The Dissertation Committee for Ross Andrew Burns Certifies that this is the approved version of the following dissertation:

Development of Scalar and Velocity Imaging Diagnostics for Supersonic Hypermixing Strut Injector Flowfields

Committee:

Noel T. Clemens, Supervisor

Ofodike A. Ezekoye

Laxminarayan Raja

Charles E. Tinney

Philip L. Varghese

Development of Scalar and Velocity Imaging Diagnostics for Supersonic Hypermixing Strut Injector Flowfields

by

Ross Andrew Burns, B.S.M.E.

Dissertation

Presented to the Faculty of the Graduate School of

The University of Texas at Austin

in Partial Fulfillment

of the Requirements

for the Degree of

Doctor of Philosophy

The University of Texas at Austin

December 2014

Acknowledgements

Above all, I would like to thank my advisor Dr. Noel T. Clemens for allowing me to work on this project. His guidance throughout my time as a graduate student has allowed me to grow as a researcher, and I appreciate the commitment he has shown to me. I would also like to thank the countless others whom I have worked with over the years. Thanks to my fellow graduate students Bryan Lochman, Chris Combs, Heath Reising, Dominik Ebi, Kevin Marr, Jonathan Ashley, Mohammed Saleem, Benton Green, Rakesh Ranjan, Dr. Justin Wagner, Dr. Mirko Gamba, Dr. Zach Murphree, Dr. Venkat Narayanaswamy, and any other lab member that I have had the opportunity to work with now or in the past. Be it helping by directly learning from you or assisting in experiments, I would not be where I am today without your help. I have also had the opportunity to work with a number of post-docs over the years whom I would like to thank, most notably Dr. Oliver Buxton, Dr. Okjoo Park, Dr. Manu Sharma, and Dr. Leon Vanstone. I would like to thank the two technicians I've worked with over the years, Eddie Zihlman and Dr. Jeremy Jagodzinski. Their help in maintaining our facilities has enabled my research and allowed me to continue making progress. I owe a great deal of thanks to both Donna Soward and Geetha Rajagopal for dealing with the majority of the administrative work over the years and the endless string of orders I've had to place to complete my research. I would also like to thank Joe Pokluda for his help in completing the machining my project has necessitated.

I finally like to acknowledge the support of both NASA and the National Science Foundation for their funding throughout the years. Additional thanks is given to the Cockrell School of Engineering for their financial support

Development of Scalar and Velocity Imaging Diagnostics for Supersonic Hypermixing Strut Injector Flowfields

Ross Andrew Burns, Ph.D.

The University of Texas at Austin, 2014

Supervisor: Noel T. Clemens

A new diagnostic technique for studying the turbulent mixing characteristics of supersonic mixing flowfields is developed and implemented in two Mach 3 mixing flowfields. The diagnostic utilizes simultaneous particle image velocimetry and quantitative planar laser-induced fluorescence of krypton gas to study the interaction between turbulent scalar and velocity fields. The fluorescence properties of krypton gas are determined; measurements of the pressure and temperature dependence of the collisional quenching rates and cross-sections are made for various mixtures with krypton. The gases tested in this fashion include helium, nitrogen, air, oxygen, and ethylene. Additional measurements are performed to measure the relative two-photon absorption cross-section for krypton gas. The non-dimensional quenching rates are found to follow a power-law dependence for temperature, while the pressure dependence of the total quenching rate is found to be linear.

Two injection flowfields are studied for their general topology and kinematic characteristcs. The first injector model is a basic injector meant to serve as a baseline case; there are no hypermixing elements present in this model. The second model is an asymmetric, unswept hypermixing injector featuring 15 degree expansive ramps flanking a central block. These studies utilize particle image velocimetry in planar and

stereoscopic configurations in various planes. Results for the mean flowfield show distinct differences between the two flowfields; the planar injector flowfield is shown to be highly two-dimensional and exhibits minimal coherent unsteady behavior. The hypermixing injector flowfield exhibits a highly three-dimensional wake, with a pair of stream-wise vortices driving both mean deviations in the flowfield and considerable vortical coupling in the span-wise direction.

Simultaneous krypton PLIF and PIV are employed in the two mixing flowfields. An assay of the dependence of the krypton mole fraction calculations on the fluorescence signal is performed. The overall sensitivity and the resulting dynamic range of the calibration is dictated largely by the reference mole fraction. Additionally, several different theoretical models of the temperature dependence of the fluorescence signal are studied to assess their validity and influence over the PLIF calibration procedure. Finally, the technique is employed in the two mixing flowfields, and a brief analysis of the mean and unsteady behavior of the two is conducted.

Table of Contents

List of Tables xiii

List of Figures xiv

Chapter 1: Introduction 1

1.1 – Literature Survey 2

1.1.1 – Compressible Shear Layer Growth 2

1.1.2 – Supersonic Injection Strategies 4

1.1.2.1 – Transverse Injection 4

1.1.2.2 – Parallel Injection 5

1.1.2.3 – Pylon Injection 7

1.1.3 – Supersonic Mixing Enhancement Strategies 9

1.1.3.1 – Transverse Injection 9

1.1.3.2 – Parallel Injection 13

1.1.3.3 – Pylon Injection 15

1.2 – Context of Present Work 24

1.3 – Details of Present Work 27

1.4 – Organization of this dissertation 28

Chapter 2: Collisional Quenching and Absorption Properties of Krypton 33

2.1 – Background and Theory 33

2.2 – Experimental Setup 39

2.2.1 – Test Facility 39

2.2.1.1 – Test Facility – Variable Pressure Runs 40

2.2.1.2 – Test Facility – Variable Temperature Runs 40

2.2.1.3 – Test Facility – Photodetectors 41

2.2.2 – Laser System and Optics 41

2.2.3 – Experimental Methodologies and Procedures 44

2.2.3.1 – Variable Pressure Runs 44

2.2.3.2 – Variable Temperature Runs 46

2.2.3.3 – Test Matrix....48
2.3 – Results and Discussion....50
2.3.1 – Spontaneous Emission Rate....50
2.3.2 – Pressure Dependence of Quenching Rates and Quenching Cross-Sections....51
2.3.3 – Temperature Dependence of Quenching Rates and Quenching Cross-Sections....52
2.3.4 – Temperature and Pressure Dependence of the Effective Two-Photon Absorption Cross-Section....55
2.4 – Conclusions....59
2.5 – Suggested Work....60
Chapter 3: Hypermixer Velocity Fields....74
3.1 – Experimental Details....74
3.1.1 – Test Facility....74
3.1.2 – Test Models....76
3.1.3 – Experimental Setup....77
3.1.3.1 – Planar PIV....78
3.1.3.2 – Stereoscopic PIV....79
3.1.3.3 – Operational Notes about PIV....81
3.2 – Results and Discussion....82
3.2.1 – Mean Flow Properties....83
3.2.2 – Turbulent and Unsteady Flow Properties....92
3.2.2.1 – General Observations....92
3.2.2.2 – Turbulence Characteristics....103
3.3 – Conclusions....110
3.4 – Suggested Work....110
Chapter 4: Application of Krypton PLIF to Supersonic Mixing Flowfields....178
4.1 – Background and Theory....178
4.1 – Fluorescence Calibration....178
4.1.2 – Estimation of Thermodynamic Conditions in Supersonic Mixing Flowfields....181

4.1.2.1 – Pressure 182
4.1.2.2 – Temperature 183
4.1.3 – Estimation of Transport Properties with Kinetic Theory 185
4.1.3.1 – Estimation of Mixture Viscosity and Thermal Conductivity 185
4.2 – Experimental Details 187
4.2.1 – Experimental Facility 187
4.2.2 – Test Models 188
4.2.3 – Experimental Setups 188
4.2.3.1 – Particle Image Velocimetry 188
4.2.3.2 – Planar Laser-Induced Fluorescence 190
4.2.3.3 – Simultaneous Measurement Application Notes 192
4.3 – Results and Discussion 194
4.3.1 – Sensitivity and Uncertainty of Kr PLIF Calibration 195
4.3.1.1 – Sensitivity 195
4.3.1.2 – Assessment of temperature model 200
4.3.1.3 – Uncertainty in mole fraction calibration 205
4.3.2 – Flowfield Analysis 207
4.3.2.1 – Mean Flowfield Analysis 207
4.3.2.2 – General Observations of Unsteady Behavior 212
4.4 – Conclusions 216
4.5 – Future and Suggested Work 218

Appendix 2A: Analytical Methods for deriving quenching rates and absorption cross-sections from fluorescence data 242
2A.1 – Calculation of Fluorescence Lifetimes 242
2A.2 – Calculation of Spontaneous Emission Rate and Reference Quenching Rates 243
2A.3 – Calculation of Temperature-Dependent Quenching Rates and Cross-Sections 244
2A.4 – Calculation of Relative Effective Two-Photon Absorption Cross-Sections 247

2A.5 – Calculation of Uncertainties....249
2A.5.1 – Uncertainty in Measured Quantities....249
2A.5.2 – Uncertainty in Derived Quantities....251
2A.5.3 – Uncertainty in Fit Quantities....252
2A.5.4 – Uncertainties in Pressure Dependent Quenching Rates and Cross-Sections....253
2A.5.5 – Uncertainties in Temperature Dependent Quenching Rates and Cross-Sections....254
2A.5.6 – Uncertainty in the Relative Effective Two-Photon Absorption Cross-Section....256
Appendix 2B: Fluorescence Lifetime Deconvolution Algorithm....258
2B.1 – Background....258
2B.2 – Numerical Method....259
2B.3 – Quantification of Accuracy....261
2B.4 – Conclusions....264
Appendix 3A – Particle Response Assessment....272
3A.1 – Introduction....272
3A.2 – Experimental Setup....273
3A.2.1 – Test Facility....273
3A.2.2 – PIV System....274
3A.3 – Numerical Methodology....274
3A.3.1 – Calculation of shock-normal velocities....274
3A.3.2 – Calculation of particle time constant....275
3A.3.3 – Calculation of Effective Particle Diameter....276
3A.4 – Results....277
3A.5 – Conclusions....278
Appendix 3B: Selection of Endview Stereoscopic PIV Parameters....281
3B.1 – Background....281
3B.2 – Selection Procedure....281
3B.2.1 – Selection of Minimum Pixel Displacements and Δt....281

3B.2.2 – Selection of Minimum Laser Sheet Thickness.....282
3B.2.3 – Other Considerations.....282
3B.2.4 – Final Selection of Parameters.....283
3B.2.5 – Additional Comments 284

Appendix 3C: PIV Uncertainty Analysis.....288
3C.1 – Background 288
3C.2 – Methodology 289
3C.2.1 – Convergence of Data.....289
3C.2.2 – Peak Locking.....289
3C.2.3 – Particle Lag Effects 290
3C.2.4 –Convergence Errors.....290
3C.2.5 – Flow-Induced Errors 291
3C.2.6 – Errors in the temporal displacement.....291
3C.2.7 – Measurement of the Total Uncertainty.....292
3C.3 – Results 292
3C.3.1 – Convergence.....292
3C.3.2 – Peak Locking.....294
3C.3.3 – Particle Lag Effects 295
3C.3.4 – Convergence Errors.....296
3C.3.5 – Flow-Induced Errors 297
3C.3.6 – Errors in temporal displacement 297
3C.3.7 – Total Uncertainty.....299

Appendix 4A: Analytical Methodologies and Uncertainty Calculations for Simultaneous Krypton PLIF and PIV Measurements.....313
4A.1 – Calibration of the Fluorescence Signal 313
4A.1.1 – Calculation of Reference Signal Ratio.....313
4A.1.2 – Calculation of Freestream Conditions.....315
4A.1.3 – Calculation of Temperature and Krypton Mole Fraction....318
4A. 2 – PIV Processing.....320
4A.3 – Spatial Mapping of Scalar Data 321

4A.4 – Uncertainty in Mole-Fraction Imaging 322
4A.5 – PIV Uncertainty 327
4A.5.1 – Convergence of Data.....327
4A.5.2 – Peak-locking.....327
4A.5.3 – Particle-lag Effects.....328
4A.5.4 – Convergence Errors.....328
4A.5.5 – Processing Errors 329
4A.5.6 – Errors in temporal displacement 329
4A.5.7 – Total Velocity Uncertainty.....329
References.....346

List of Tables

Table 2.1: Summary of runs performed in lifetime measurements.....49

Table 2.2: Summary of Reference Quenching Data 52

Table 2.3: Summary of Temperature Dependence of Quenching Rates and Cross-Sections.....54

Table 3C.1: Summary of peak uncertainties for different fields of view 299

List of Figures

Figure 1.1: Schematic of flowfield for transverse injection 30

Figure 1.2: Schematic of parallel injection flowfield 30

Figure 1.3: Schematic of partial-span pylon injection flowfield 31

Figure 1.4: Schematic of full-span pylon injection flowfield.....31

Figure 1.5: Diagram of swept-ramp injector flowfield. a) Perspective view of side-by-side injectors and b) side-view of injection flowfield 32

Figure 1.6: Illustration of the effect of averaging on a well-stirred mixing flowfield. a) Instantaneous field with interspersion and b) mean field showing mixed fluid 32

Figure 2.1: Diagram of flow reactor used in lifetime measurements. 62

Figure 2.2: Diagram of supersonic nozzle orientation within test cell with beam path and test volume. 62

Figure 2.3: Orientation of photodetectors with respect to the test facility. 63

Figure 2.4: Diagram of sum-frequency generation setup for the fluorescence lifetime studies. 64

Figure 2.5: Sample temporal trace of 214.7 nm laser pulse used in lifetime studies. 65

Figure 2.6: Excitation spectrum from sum-frequency generation setup for lifetime measurements.....65

Figure 2.7: Diagram of exciting beam path through test cell. 66

Figure 2.8: Dependence of fluorescence signal intensity as a function of excitation intensity. a) lower intensity and b) full scale. 67

Figure 2.9: Example plot of temperature vs. krypton mole fraction for a variable-mixture, variable-temperature test run. 68
Figure 2.10: Pressure dependence of krypton fluorescence lifetime and decay rate. a) lifetime and b) decay rate.....69
Figure 2.11: Pressure dependence of quenching rates for various gases. 70
Figure 2.12: Temperature dependence of krypton-krypton collisional quenching rate. 70
Figure 2.13: Temperature dependence of krypton-buffer collisional quenching rate for various gases. 71
Figure 2.14: Temperature dependence of krypton-buffer collisional quenching cross-sections for various gases.....71
Figure 2.15: Temperature and Pressure dependence of relative two-photon absorption cross-section. a) Temperature dependence and b) pressure dependence. 72
Figure 2.16: Effect of pressure on the excitation spectrum for the two-photon $5p[3/2]_2 \leftarrow 4p^6\ ^1S_o$ transition for pure krypton 73
Figure 2.17: Effect of pressure on the excitation spectrum for the two-photon $5p[3/2]_2 \leftarrow 4p^6\ ^1S_o$ transition for Kr-He mixtures.....73
Figure 3.1: Diagram of Mach 3 wind tunnel used in the kinematics studies 113
Figure 3.2: Diagram of the two injector models used in the kinematics studies. a) Planar injector with global coordinate system displayed and b) hypermixing injector.....113

Figure 3.3: Illustration of vortex-vortex interaction that occurs in transversely symmetric hypermixing injector flowfields. Top – very near-field of injector, second from top – downstream 1, third from top – downstream 2, and bottom – far-field 114
Figure 3.4: Diagram of laser setup used in PIV experiments for the flowfield kinematics studies 115
Figure 3.5: Diagram of camera and laser sheet position for side-view PIV measurements.....116
Figure 3.6: Diagram of camera and laser setup for end-view stereoscopic PIV measurements.....116
Figure 3.7: Mean centerline stream-wise velocity contours for near-field of planar injector flowfield (SV 1a) 117
Figure 3.8: Mean centerline transverse velocity contours for near-field of planar injector flowfield (SV 1a) 117
Figure 3.9: Mean centerline stream-wise velocity contours for mid-field of planar injector flowfield (SV 2a) 118
Figure 3.10: Mean centerline stream-wise velocity contours for mid-field of planar injector flowfield (SV2a) 118
Figure 3.11: Mean off-centerline ($z/h = 0.75$) stream-wise velocity contours for near-field of planar injector flowfield (SV 1b) 119
Figure 3.12: Mean off-centerline ($z/h = 0.75$) transverse velocity contours for near-field of planar injector flowfield (SV 1b) 119
Figure 3.13: Mean off-centerline ($z/h = 0.75$) stream-wise velocity contours for mid-field of planar injector flowfield (SV 2b) 120

Figure 3.14: Mean off-centerline ($z/h = 0.75$) transverse velocity contours for mid-field of planar injector flowfield (SV 2b) 120
Figure 3.15: Mean off-centerline ($z/h = 1.25$) stream-wise velocity contours for near-field of planar injector flowfield (SV 1c) 121
Figure 3.16: Mean off-centerline ($z/h = 1.25$) transverse velocity contours for near-field of planar injector flowfield (SV 1c) 121
Figure 3.17: Mean off-centerline ($z/h = 1.25$) stream-wise velocity contours for mid-field of planar injector flowfield (SV 2c).....122
Figure 3.18: Mean off-centerline ($z/h = 1.25$) transverse velocity contours for mid-field of planar injector flowfield (SV 2c) 122
Figure 3.19: Three-dimensional reconstruction of planar injector flowfield showing planes of stream-wise velocity.....123
Figure 3.20: Three-dimensional reconstruction of planar injector flowfield showing planes of transverse velocity.....124
Figure 3.21: Mean centerline stream-wise velocity contours for near-field of hypermixing injector flowfield (SV 1a).....125
Figure 3.22: Mean centerline transverse velocity contours for near-field of hypermixing injector flowfield (SV 1a).....125
Figure 3.23: Mean centerline stream-wise velocity contours for mid-field of hypermixing injector flowfield (SV 2a).....126
Figure 3.24: Mean centerline transverse velocity contours for mid-field of hypermixing injector flowfield (SV 2a).....126
Figure 3.25: Mean stream-wise end-view velocity contours for hypermixing injector flowfield ($x/h = 8$).....127

Figure 3.26: Mean transverse end-view velocity contours for hypermixing injector flowfield ($x/h = 8$).....127
Figur the corri 3.27: Mean span-wise end-view velocity contours for hypermixing injector flowfield ($x/h = 8$) 128
Figure 3.28: Mean stream-wise end-view velocity contours for hypermixing injector flowfield ($x/h = 16$) 128
Figure 3.29: Mean transverse end-view velocity contours for hypermixing injector flowfield ($x/h = 16$) 129
Figure 3.30: Mean span-wise end-view velocity contours for hypermixing injector flowfield ($x/h = 16$) 129
Figure 3.31: Example instantaneous centerline stream-wise velocity contours for near-field of planar injector flowfield (SV 1a) 130
Figure 3.32: Example fluctuating centerline stream-wise velocity contours for near-field of planar injector flowfield (SV 1a) 130
Figure 3.33: PDF of shock angle for planar injector flowfield 131
Figure 3.34: Example instantaneous centerline transverse velocity contours for near-field of planar injector flowfield (SV 1a) 131
Figure 3.35: Example fluctuating centerline transverse velocity contours for near-field of planar injector flowfield (SV 1a) 132
Figure 3.36: Example instantaneous centerline span-wise vorticity contours for near-field of planar injector flowfield (SV 1a) 132
Figure 3.37: Example instantaneous centerline span-wise vorticity contours for near-field of planar injector flowfield overlaid with fluctuating streamlines (SV 1a).....133

Figure 3.38: Example instantaneous centerline stream-wise velocity contours for mid-field of planar injector flowfield (SV 2a) 133
Figure 3.39: Example fluctuating centerline stream-wise velocity contours for mid-field of planar injector flowfield (SV 2a) 134
Figure 3.40: Example instantaneous centerline transverse velocity contours for mid-field of planar injector flowfield (SV 2a) 134
Figure 3.41: Example fluctuating centerline transverse velocity contours for mid-field of planar injector flowfield (SV 2a).....135
Figure 3.42: Example instantaneous centerline span-wise vorticity contours for mid-field of planar injector flowfield (SV 2a) 135
Figure 3.43: Example instantaneous centerline span-wise vorticity contours for mid-field of planar injector flowfield overlaid with fluctuating streamlines (SV 2a).....136
Figure 3.44: Example instantaneous centerline stream-wise velocity contours for near-field of hypermixing injector flowfield (SV 1a).....136
Figure 3.45: Example fluctuating centerline stream-wise velocity contours for near-field of hypermixing injector flowfield (SV 1a). 137
Figure 3.46: Example instantaneous centerline transverse velocity contours for near-field of hypermixing injector flowfield (SV 1a).....137
Figure 3.47: Example fluctuating centerline transverse velocity contours for near-field of hypermixing injector flowfield (SV 1a). 138
Figure 3.48: Example instantaneous centerline span-wise vorticity contours for near-field of hypermixing injector flowfield.....138

Figure 3.49: Example instantaneous centerline vorticity contours for near-field of hypermixing injector flowfield overlaid with fluctuating streamlines (SV 1a) 139
Figure 3.50: Example instantaneous centerline stream-wise velocity contours for mid-field of hypermixing injector flowfield (SV 2a) 139
Figure 3.51: Example fluctuating centerline stream-wise velocity contours for mid-field of hypermixing injector flowfield (SV 2a) 140
Figure 3.52: Example instantaneous centerline transverse velocity contours for mid-field of hypermixing injector flowfield (SV 2a) 140
Figure 3.53: Example fluctuating centerline transverse velocity contours for mid-field of hypermixing injector flowfield (SV 2a) 141
Figure 3.54: Example instantaneous centerline span-wise vorticity contours for mid-field of hypermixing injector flowfield (SV 2a) 141
Figure 3.55: Example instantaneous centerline span-wise vorticity contours for mid-field of hypermixing injector flowfield overlaid with fluctuating streamlines (SV 2a).....142
Figure 3.56: Example instantaneous off-centerline ($z/h = 0.75$) stream-wise velocity contours for near-field of hypermixing injector flow (SV 1b) 142
Figure 3.57: Example fluctuating off-centerline ($z/h = 0.75$) stream-wise velocity contours for near-field of hypermixing injector flowfield (SV 1b) 143
Figure 3.58: Example instantaneous off-centerline ($z/h = 0.75$) transverse velocity contours for near-field of hypermixing injector flowfield (SV 1b) 143
Figure 3.59: Example fluctuating off-centerlline ($z/h = 0.75$) transverse velocity contours for near-field of hypermixing injector flowfield (SV 1b) 144

Figure 3.60: Example instantaneous off-centerline ($z/h = 0.75$) span-wise vorticity contours for near-field of hypermixing injector flowfield (SV 1b) 144
Figure 3.61: Example instantaneous off-centerline ($z/h = 0.75$) span-wise vorticity contours for near-field of hypermixing injector flowfield overlaid with fluctuating streamlines (SV 1b) 145
Figure 3.62: Example instantaneous off-centerline ($z/h = 0.75$) stream-wise velocity contours for mid-field of hypermixing injector flowfield (SV 2b).145
Figure 3.63: Example fluctuating off-centerline ($z/h = 0.75$) stream-wise velocity contours for mid-field of hypermixing injector flowfield (SV 2b).146
Figure 3.64: Example instantaneous off-centerline ($z/h = 0.75$) transverse velocity contours for mid-field of hypermixing injector flowfield (SV 2b).146
Figure 3.65: Example fluctuating off-centerline ($z/h = 0.75$) transverse velocity contours for mid-field of hypermixing injector flowfield (SV 2b).147
Figure 3.66: Example instantaneous off-centerline ($z/h = 0.75$) span-wise vorticity contours for mid-field of hypermixing injector flowfield (SV 2b).147
Figure 3.67: Example instantaneous off-centerline ($z/h = 0.75$) span-wise vorticity contours for mid-field of hypermixing injector flowfield overlaid with fluctuating streamlines (SV 2b) 148
Figure 3.68: Example instantaneous off-centerline ($z/h = 1.25$) stream-wise velocity contours for near-field of hypermixing injector flowfield (SV 1c) 148
Figure 3.69: Example fluctuating off-centerline ($z/h = 1.25$) stream-wise velocity contours for near-field of hypermixing injector flowfield (SV 1c) 149
Figure 3.70: Example instantaneous off-centerline ($z/h = 1.25$) transverse velocity contours for near-field of hypermixing injector flowfield (SV 1c) 149

Figure 3.71: Example fluctuating off-centerline ($z/h = 1.25$) transverse velocity contours for near-field of hypermixing injector flowfield (SV 1c) 150
Figure 3.72: Example instantaneous off-centerline ($z/h = 1.25$) span-wise vorticity contours for near-field of hypermixing injector flowfield (SV 1c) 150
Figure 3.73: Example instantaneous off-centerline ($z/h = 1.25$) span-wise vorticity contours for near-field of hypermixing injector flowfield overlaid with fluctuating streamlines (SV 1c) 151
Figure 3.74: Example instantaneous off-centerline ($z/h = 1.25$) stream-wise velocity contours for mid-field of hypermixing injector flowfield (SV 2c) .151
Figure 3.75: Example fluctuating off-centerline ($z/h = 1.25$) stream-wise velocity contours for mid-field of hypermixing injector flowfield (SV 2c) .152
Figure 3.76: Example instantaneous off-centerline ($z/h = 1.25$) transverse velocity contours for mid-field of hypermixing injector flowfield (SV 2c) .152
Figure 3.77: Example fluctuating off-centerline ($z/h = 1.25$) transverse velocity contours for mid-field of hypermixing injector flowfield (SV 2c) .153
Figure 3.78: Example instantaneous off-centerline ($z/h = 1.25$) span-wise vorticity contours for mid-field of hypermixing injector flowfield (SV 2c) .153
Figure 3.79: Example instantaneous off-centerline ($z/h = 1.25$) span-wise vorticity contours for mid-field of hypermixing injector flowfield overlaid with fluctuating streamlines (SV 2c) 154
Figure 3.80: Example instantaneous stream-wise end-view velocity contours for hypermixing injector flowfield (EV 1, $x/h = 8$).....154
Figure 3.81: Example fluctuating stream-wise end-view velocity contours for hypermixing injector flowfield (EV 1, $x/h = 8$).....155

Figure 3.82: Example instantaneous transverse end-view velocity contours for hypermixing injector flowfield (EV 1, $x/h = 8$).....155
Figure 3.83: Example fluctuating transverse end-view velocity contours for hypermixing injector flowfield (EV 1, $x/h = 8$).....156
Figure 3.84: Example instantaneous span-wise end-view velocity contours for hypermixing injector flowfield (EV 1, $x/h = 8$).....156
Figure 3.85: Example fluctuating span-wise end-view velocity contours for hypermixing injector flowfield (EV 1, $x/h = 8$).....157
Figure 3.86: Example instantaneous end-view stream-wise vorticity contours for hypermixing injector flowfield (EV 1, $x/h = 8$).....157
Figure 3.87: Example instantaneous end-view stream-wise vorticity contours for hypermixing injector flowfield overlaid with instantaneous streamlines (EV 1, $x/h = 8$).....158
Figure 3.88: PDFs of stream-wise vortex core span-wise position for first end-view field of view (EV 1, $x/h = 8$).....158
Figure 3.89: PDFs of stream-wise vortex core transverse position for first end-view field of view (EV 1, $x/h = 8$).....159
Figure 3.90: PDF of stream-wise vortex core separation for first end-view field of view (EV 1, $x/h = 8$).....159
Figure 3.91: Example instantaneous end-view stream-wise velocity contours for hypermixing injector flowfield (EV 2, $x/h = 16$).....160
Figure 3.92: Example fluctuating end-view stream-wise velocity contours for hypermixing injector flowfield (EV 2, $x/h = 16$).....160
Figure 3.93: Example instantaneous end-view transverse velocity contours for hypermixing injector flowfield (EV 2, $x/h = 16$).....161

Figure 3.94: Example instantaneous end-view transverse velocity contours for hypermixing injector flowfield (EV 2, $x/h = 16$) 161
Figure 3.95: Example instantaneous end-view span-wise velocity contours for hypermixing injector flowfield (EV 2, $x/h = 16$) 162
Figure 3.96: Example fluctuating end-view span-wise velocity contours for hypermixing injector flowfield (EV 2, $x/h = 16$) 162
Figure 3.97: Example instantaneous end-view stream-wise vorticity contours for hypermixing injector flowfield (EV 2, $x/h = 16$) 163
Figure 3.98: Example instantaneous end-view stream-wise vorticity contours for hypermixing injector flowfield overlaid with instantaneous streamlines (EV 2, $x/h = 16$).....163
Figure 3.99: PDFs of stream-wise vortex core span-wise position for second end-view field of view (EV 2, $x/h = 16$).....164
Figure 3.100: PDFs of stream-wise vortex core transverse position for second end-view field of view (EV 2, $x/h = 16$).....164
Figure 3.101: PDF of stream-wise vortex core separation for second end-view field of view (EV 2, $x/h = 16$).....165
Figure 3.102: Centerline stream-wise velocity fluctuation contours for near-field of the planar injector flowfield (SV 1a) 165
Figure 3.103: Centerline stream-wise velocity fluctuation contours for mid-field of the planar injector flowfield (SV 2a) 166
Figure 3.104: Centerline transverse velocity fluctuation contours for near-field of planar injector flowfield (SV 1a) 166
Figure 3.105: Centerline transverse velocity fluctuation contours for mid-field of planar injector flowfield (SV 2a) 167

Figure 3.106: Centerline shear velocity fluctuation contours for near-field of planar injector flowfield (SV 1a) 167
Figure 3.107: Centerline shear velocity fluctuation contours for mid-field of planar injector flowfield (SV 2a) 168
Figure 3.108: Centerline stream-wise velocity fluctuation contours for near-field of hypermixing injector flowfield (SV 1a).....168
Figure 3.109: Centerline stream-wise velocity fluctuation contours for mid-field of hypermixing injector flowfield (SV 2a).....169
Figure 3.110: Centerline transverse velocity fluctuation contours for near-field of hypermixing injector flowfield (SV 1a).....169
Figure 3.111: Centerline transverse velocity fluctuation contours for mid-field of hypermixing injector flowfield (SV 2a).....170
Figure 3.112: Centerline shear velocity fluctuation contours for near-field of hypermixing injector flowfield (SV 1a).....170
Figure 3.113: Centerline shear velocity fluctuation contours for mid-field of hypermixing injector flowfield (SV 2a).....171
Figure 3.114: Normal Reynolds stresses for first end-view field of view (EV 1, $x/h = 8$). Top – stream-wise component, middle – transverse component, and bottom – span-wise component. Left – overlaid with stream-wise velocity contours and right – overlaid with vorticity contours.....172
Figure 3.115: Contours of turbulent kinetic energy for first end-view field of view (EV 1, $x/h = 8$). Top – overlaid with stream-wise velocity contours and bottom – overlaid with vorticity contours.....173

Figure 3.116: Normal Reynolds stresses for second end-view field of view (EV 2, $x/h = 16$). Top – stream-wise component, middle – transverse component, and bottom – span-wise component. Left – overlaid with stream-wise velocity contours and right – overlaid with vorticity contours.....174
Figure 3.117: Contours of turbulent kinetic energy for second end-view field of view (EV 2, $x/h = 16$). Top – overlaid with stream-wise velocity contours and bottom – overlaid with vorticity contours 175
Figure 3.118: Centerline two-point correlation for near-field (SV 1a) of hypermixing injector flowfield. Top left - u'u'', top right - u'v'', bottom left - v'u'', and bottom right - v'v''.....176
Figure 3.119: Centerline two-point correlation for mid-field (SV 2a) of hypermixing injector flowfield. Top left - u'u'', top right - u'v'', bottom left - v'u'', and bottom right - v'v''.....177
Figure 4.1: Variation of mixture Prandtl number with temperature and composition 220
Figure 4.2: Schematic of simultaneous PLIF/PIV laser setup used in mixing studies 221
Figure 4.3: Orientation of PIV cameras for PLIF/PIV setup. Top – perspective view showing fields of view and bottom – overhead view showing camera orientation 222
Figure 4.4: Orientation of PLIF camera for PLIF/PIV setup detailing the fields of view used in the study.....223
Figure 4.5: Effect of laser energy on calibration of Kr PLIF signal at reference conditions.....223

Figure 4.6: Effect of laser energy on calibration of Kr PLIF signal at freestream conditions 224
Figure 4.7: Effect of pressure on calibration of Kr PLIF signal at reference temperature 224
Figure 4.8: Effect of pressure on calibration of Kr PLIF signal at freestream temperature 225
Figure 4.9: Effect of temperature on the calibration of the Kr PLIF signal at reference conditions 225
Figure 4.10: Effect of temperature on the calibration of the Kr PLIF signal at freestream conditions 226
Figure 4.11: Effect of reference mole fraction on the calibration of the Kr PLIF signal at reference conditions 226
Figure 4.12: Effect of reference mole fraction on the calibration of the Kr PLIF signal at freestream conditions 227
Figure 4.13: Effect of different temperature models on calibration of PLIF signal. Left column – static temperature and right column – mole fraction. From top: standard Crocco-Busemann, instantaneous Crocco-Busemann, modified Crocco-Busemann with composition correction, and instantaneous modified Crocco-Busemann with composition correction. 228
Figure 4.14: Example calibrated fluorescence image.....229
Figure 4.15: Tabulated uncertainties for instantaneous mole fraction calibration in Fig 4.9.....230
Figure 4.16: Mean centerline stream-wise velocity contours for the planar injector flowfield.....231

Figure 4.17: Mean centerline transverse velocity contours for the planar injector flowfield.....231
Figure 4.18: Overlay of instantaneous acetone PLIF and planar laser scattering showing relative positions of barrel and recompression shocks. From [**99**].....232
Figure 4.19: Mean centerline span-wise velocity contours for the planar injector flowfield.....232
Figure 4.20: Mean centerline temperature contours for the planar injector flowfield 233
Figure 4.21: Mean centerline mole fraction contours for the planar injector flowfield 233
Figure 4.22: Mean centerline stream-wise velocity contours for the hypermixing injector flowfield.....234
Figure 4.23: Mean centerline transverse velocity contours for the hypermixing injector flowfield.....234
Figure 4.24: Mean centerline span-wise velocity contours for the hypermixing injector flowfield.....235
Figure 4.25: Mean centerline temperature contours for the hypermixing injector flowfield.....235
Figure 4.26: Mean centerline mole-fraction contours for the hypermixing injector flowfield.....236
Figure 4.27: Maximum mole fraction as a function of stream-wise distance for the two injection flowfields. The dashed lines represent the uncertainty bounds.....236

Figure 4.28: Series of instantaneous centerline mole-fraction contours for planar injector flowfield.....237
Figure 4.29: Series of instantaneous centerline mole fraction contours for hypermixing injector flowfield. Circled regions correspond to discussion in Section 4.3.2.2. 238
Figure 4.30: Instantaneous centerline mole fraction contours for planar injector flowfield overlaid with fluctuation velocity vectors.....239
Figure 4.31: Instantaneous centerline mole fraction contours for planar injector flowfield overlaid with fluctuation temperature contours 239
Figure 4.32: Instantaneous centerline span-wise vorticity contours for planar injector flowfield overlaid with mole fraction contours 240
Figure 4.33: Instantaneous centerline mole fraction contours for hypermixing injector flowfield overlaid with fluctuation velocity vectors. The circled region corresponds to discussion in Section 4.3.2.2. 240
Figure 4.34: Instantaneous centerline mole fraction contours for hypermixing injector flowfield overlaid with fluctuation temperature 241
Figure 2B.1: Sample pulse generated by deconvolution function 266
Figure 2B.2: Example of pulse conditioning used in deconvolution algorithm. Top – original signal, middle – background-subtracted signal, and bottom – conditioned signal 267
Figure 2B.3: Flowchart of functionality of deconvolution algorithm.....268
Figure 2B.4: Effect of different noise levels on accuracy of deconvolution algorithm 269
Figure 2B.5: Effect of initial condition on accuracy of solver. Top – fixed initial guess and bottom – utilizing solution of previous sample.....270

Figure 2B.6: Effect of laser pulse fall time on accuracy of solver.....271
Figure 3A.1: Mean stream-wise velocity contours in vicinity of oblique shock.279
Figure 3A.2: Mean transverse velocity contours in vicinity of oblique shock.....279
Figure 3A.3: Sample shock-normal velocity traces for different incidence angles280
Figure 3A.4: Comparison of experimental data with filtered exponential fit and theoretical step change in velocity across shock.....280
Figure 3B.1: Illustration of how particle retention was calculated as a function of laser sheet thickness 286
Figure 3B.2: Required Δt for different in-plane velocities and acceptable pixel displacements.....286
Figure 3B.3: Required laser sheet thickness for different in-plane velocities and acceptable pixel displacements.....287
Figure 3C.1: Convergence of the mean velocities for side-view fields of view.300
Figure 3C.2: Convergence of the RMS velocities for side-view fields of view .300
Figure 3C.3: Convergence of the mean velocities for end-view fields of view..301
Figure 3C.4: Convergence of the RMS velocities for end-view fields of view..301
Figure 3C.5: PDF of the stream-wise pixel displacements for side-view fields of view 302
Figure 3C.6: PDF of the transverse pixel displacements for side-view fields of view 302
Figure 3C.7: PDF of the stream-wise pixel displacements for the end-view fields of view.....303
Figure 3C.8: PDF of the transverse pixel displacements for the end-view fields of view.....303

Figure 3C.9: PDF of the span-wise pixel displacements for the end-view fields of view.....304
Figure 3C.10: Stream-wise distribution of particle Stokes number for planar injector flowfield.....304
Figure 3C.11: Stream-wise distribution of particle Stokes number for hypermixing injector flowfield.....305
Figure 3C.12: Stream-wise uncertainty due to convergence error for planar injector upstream.....305
Figure 3C.13: Transverse uncertainty due to convergence error for planar injector upstream.....306
Figure 3C.14: Stream-wise uncertainty due to convergence error for hypermixing injector upstream.....306
Figure 3C.15: Transverse uncertainty due to convergence error for hypermixing injector upstream.....307
Figure 3C.16: Stream-wise uncertainty due to convergence error for hypermixing injector end-view 307
Figure 3C.17: Transverse uncertainty due to convergence error for hypermixing injector end-view 308
Figure 3C.18: Span-wise uncertainty due to convergence error for hypermixing injector end-view 308
Figure 3C.19: Non-dimensional shear magnitude for planar injector side-view309
Figure 3C.20: Non-dimensional shear magnitude for hypermixing injector side-view.....309
Figure 3C.21: Non-dimensional shear magnitude for hypermixing injector end-view.....310

Figure 3C.22: Distribution of temporal displacements showing the jitter in the system 310
Figure 3C.23: Spatial variation in uncertainty for planar injector side-view 311
Figure 3C.24: Spatial variation in uncertainty for hypermixing injector side-view311
Figure 3C.25: Spatial variation in uncertainty for hypermixing injector end-view 312
Figure 4A.1: Estimated centerline Mach number contours for near-field of planar injector flowfield.....331
Figure 4A.2: Estimated centerline Mach number contours for near-field of hypermixing injector flowfield 331
Figure 4A.3: Estimated centerline static temperature contours for near-field of planar injector flowfield.....332
Figure 4A.4: Estimated centerline static temperature contours for near-field of hypermixing injector flowfield 332
Figure 4A.5: Estimated centerline static pressure contours for near-field of planar injector flowfield.....333
Figure 4A.6: Estimated centerline static pressure contours for near-field of hypermixing injector flowfield 333
Figure 4A.7: Uncertainty in centerline Mach number for planar injector flowfield334
Figure 4A.8: Uncertainty in centerline Mach number for hypermixing injector flowfield.....334
Figure 4A.9: Uncertainty in centerline static temperature for planar injector flowfield 335
Figure 4A.10: Uncertainty in centerline static temperature for hypermixing injector flowfield.....335

Figure 4A.11: Uncertainty in pressure for planar injector flowfield.....336
Figure 4A.12: Uncertainty in pressure for hypermixing njector flowfield 336
Figure 4A.13: Convergence of mean flow statistics for planar injector flowfield337
Figure 4A.14: Convergence of fluctuation flow statistics for planar injector flowfield 337
Figure 4A.15: PDF of stream-wise pixel displacements for planar injector flowfield, FOV 1S.....338
Figure 4A.16: PDF of transverse pixel displacements for planar injector flowfield, FOV 1S 338
Figure 4A.17: PDF of span-wise pixel displacements for planar injector flowfield, FOV 1S 339
Figure 4A.18: PDF of stream-wise pixel displacements for hypermixing injector flowfield, FOV 1S.....339
Figure 4A.19: PDF of transverse pixel displacements for hypermixing injector flowfield, FOV 1S.....340
Figure 4A.20: PDF of span-wise pixel displacements for hypermixing injector flowfield, FOV 1S.....340
Figure 4A.21: Particle Stokes numbers for planar injector flowfield, FOV 1S341
Figure 4A.22: Particle Stokes numbers for hypermixing injector flowfield, FOV 1S 341
Figure 4A.23: Displacement uncertainties due to convergence errors for planar injector flowfield, FOV 1S. Top – stream-wise, middle – transverse, and bottom – span-wise. 342

Figure 4A.24: Displacement uncertainties due to convergence errors for hypermixing injector flowfield, FOV 1S. Top – stream-wise, middle – transverse, and bottom – span-wise. 343
Figure 4A.25: Non-dimensional shear for planar injector flowfield, FOV 1S 344
Figure 4A.27: Total velocity uncertainty for planar injector flowfield, FOV 1S 345
Figure 4A.28: Total velocity uncertainty for hypermixing injector flowfield, FOV 1S 345

Chapter 1: Introduction

Supersonic mixing is a highly active area of research. Topically broad, it covers subjects ranging from ballistics to supersonic combustion [**1**]. Supersonic flows, in general, tend to be difficult flows in which to perform any variety of experimental diagnostics due to their high overall momentum flux, rapid spatial and temporal variations in thermodynamic conditions, and short convective and turbulent time scales. Mixing flowfields have the further complications of variable composition and (potentially) reactivity [**2**].

As technology has improved, the ability to perform diagnostics in flows such as these has developed considerably. With the improvement of camera and laser systems, the ability to make two- and three-dimensional measurements of velocity and scalar quantities has become possible [**3**] [**4**]. Contemporary with the development of these technologies has been the increasing desire for more complex data sets. Modern flow simulations, such as large-eddy simulations (LES) and Reynolds Averaged Navier-Stokes (RANS) simulations require complex, mulit-parameter data in order to validate the various turbulence and scalar diffusion models properly [**5**]. Data such as these are difficult to collect in even low-speed environments; collecting such data at supersonic conditions is more complex still. Thus, there is a clear and definitive need for experimental techniques and methodologies that will help make these complex measurements feasible in difficult flow environments.

The body of work contained herein covers the development and application of a new technique, the simultaneous application of krypton planar laser-induced fluorescence and particle image velocimetry in supersonic mixing flowfields. This diagnostic technique has the potential for making simultaneous measurements of velocity, scalar

concentration, and temperature in the complex flowfields described above. To begin the discussion, a brief literature survey is conducted, which details many of the flow physics associated with supersonic mixing and injection. These are complemented by interwoven discussions of the measurement techniques that have been previously applied in these types of flowfields. This survey is followed by a further discussion of the context and details of the present work.

1.1 – Literature Survey

This section will review some of the previous research done in the area of supersonic mixing and the experimental techniques which have been applied to study these flowfields. The discussion of the flow physics will cover different injection schemes and the mixing enhancement strategies applicable to each.

1.1.1 – Compressible Shear Layer Growth

Shear layers or mixing layers are an implicit component of any mixing flowfield. Any injected jet is bound by shear layers regulating the dispersion of momentum and scalar concentration. In addition, common injection schemes utilizing backward facing steps or wakes into which fuel is injected utilize the growth of these shear layers to enhance the dispersion of the jet issuing into it. Much of the early work on the subject of compressible free shear layers indicated (to varying degrees) that the growth rate of supersonic shear layers was diminished compared to their incompressible counterparts [**6**]. A survey of these studies can be found in Birch and Eggers [**7**]. Though this phenomenon was thought a consequence of the implicit density ratio across the developing shear layer at first, it was found that incompressible shear layers exhibiting similar density ratios did not show the degree of growth rate reduction present in the compressible cases [**8**]. The implication was that the reduced growth rates were a

consequence of the inherent compressibility of the flow, an observation not seen in turbulent wall-bounded compressible shear flows. This ultimately led to the concept of the convective Mach number, M_c , as a means of quantifying the compressibility of the shear layers, arguing that it was not the fact that the flow was globally compressible, but the fact that the shearing between the two flows fell within the compressible regime [**9**] [**10**]. Indeed the scaling of the velocity profiles with this convective parameter was quite successful.

The structure of the compressible shear/mixing layer has been studied in great detail. Earlier studies utilized schlieren as a means of studying the global development of structures. However, due to the spatial integration intrinsic to the schlieren technique, some of the important three-dimensional effects were masked. Clemens et al. [**11**] [**12**] [**13**] [**14**] adopted planar laser scattering techniques specifically to study the three-dimensional effects present in large-scale structures that develop in the compressible shear layer at various convective Mach numbers. Barre, Quine, and Dussauge [**15**] utilized aerodynamic probes of varying type to study the velocity, pressure, and total temperature fields, ultimately looking at the effect of compressibility on the Reynolds stresses within the shear layer. Elliot et al. [**16**] [**17**] had a series of studies utilizing both schlieren and planar laser Mie scattering to study the evolution of large-scale structures compressible shear layers of various convective Mach number. Several DNS studies by Sarkar [**18**] concluded that it was a consequence of a decreasing Reynolds stress anisotropy that resulted in the diminishing growth rate. Research on this subject continues to this day, as compressible shear layers are such a crucial element in any mixing flowfield.

1.1.2 – Supersonic Injection Strategies

1.1.2.1 – Transverse Injection

Transverse injection entails the injection of fuel in some manner perpendicular to the principle flow direction. This basic flowfield configuration can be seen in Figure 1.1 below. Following an initial bow shock, the jet is mixed with the core flow by both turbulent transition and breakdown of the jet as well as a pair of counter-rotating vortices shed from the downstream end of the injection plume. Much of the work on this subject entailed the study of jet penetration into the supersonic cross-flow and the trajectories of the injection plumes.

The former point has been studied in detail by many, including Zukoski and Spaid [**19**], Hermanson and Winters [**20**] [**21**], Cohen et al. [**22**] and Schetz et al. [**23**] [**24**]. In general, the ability of a transverse jet to penetrate a cross-flow is controlled largely by the ratio of the momentum flux of the transverse jet to that of the freestream. Cohen et al. [**22**] developed an empirical relation showing that the penetration distance as a function of the momentum flux ratio, given by

$$\frac{H}{d} = \left[\frac{2\left(1+\frac{\gamma_I - 1}{2}M_I^2\right)}{\gamma_I^2 M_I(\gamma_I+1)}\right]^{0.5}\left[\frac{1.25(1+\gamma_\infty)\gamma_\infty M_\infty^2}{(1-\gamma_\infty)+2\gamma_\infty M_\infty^2}\right]^{0.5}\left[\frac{(\rho V^2)_I}{(\rho V^2)_\infty}\right]^{0.5} \qquad 1.1$$

where Eq.1.1 encompasses not only the effect of the momentum flux, but also the composition of both the injectant and crossflows. More recent studies have attempted to quantify the potential trajectories of the injected jets, and have adopted a power law relation for the penetration distance with respect to the momentum flux ratio, noting the influence of the upstream boundary layer on the jet penetration [**25**] [**26**] [**27**] [**28**]. A comprehensive study by Gruber et al. [**26**] noted the injection trajectory to abide by the scaling law,

$$\frac{y}{d_j J} = c\left(\frac{x}{d_j J}\right)^{0.344} \qquad 1.2$$

where c is a constant associated with the jet exit geometry. A variation of this is suggested by Rothstein and Wantuck [**25**] that showed better agreement with some experimental data [**28**], though both are used throughout the literature. Regardless of the correlation used, the strong dependence of the jet penetration on the momentum flux ratio has implications on their use in scramjet combustors. At lower momentum flux ratios, the penetration of the jet into the core flow is not sufficient to have an ultimately uniform dispersion of reactants within the combustor flow. Alternatively, at higher momentum flux ratios the jets and ensuing shock structures act as a severe blockage to the flow, which can ultimately result in reduced margins of thrust. For these reasons, the use of transverse injection requires a balance between achieving an optimal fuel distribution and the resulting total pressure losses.

1.1.2.2 – Parallel Injection

Parallel or tangential injection is a wall- or strut- based injection scheme that involves the injection of fuel parallel to the principal airflow direction with lower overall disturbance to the flow than in transverse injection. This injection strategy, depicted in Figure 1.2, is distinct from both pylon injection and wall-based injection through a rearward facing step in that a) the fuel is not injected into the wake of the pylon, nor is it transverse to the primary flow direction, and b) the mixing of the reactants occurs immediately at the shear layer, rather than through recirculation as it would in rearward-facing steps. In addition, there is the theoretical capacity for thrust augmentation, as all of the injected momentum is directly added to the freestream.

As a solitary injection method, parallel injection has been studied in minor detail. Schetz and Gilreath [**29**] utilized interferometry to measure density profiles in both the

incoming boundary layer and downstream of injection into a Mach 2 freestream, ultimately comparing their results to several analytical models they develop. It was found that the parallel injection was quite effective at generating turbulence, more so than a rearward-facing step configuration. It was found that the configuration studied achieved a fully turbulent mixing region at a Reynolds number only 0.1 times that associated with a flat plate alone; however, the shear layer growth limited the mixing capabilities. Burrows and Kurkov [**30**] performed probe-based measurements of concentrations of different chemical species downstream of a parallel injector for both reactive and non-reactive cases, though their measurements were limited to a single stream-wise location. Reasonable agreement was found with a numerical solution to the boundary layer equations.

A study by Hyde et al. [**31**] made hotwire measurements of turbulent velocity fluctuations at different stream-wise locations in a supersonic parallel slot injection flowfield, which focused on the difference between heated and unheated jets. The heated slot flow, though it was found to increase the turbulence levels slightly, did not cause a notable increase in the spreading rate of the jet. A more recent study by Lewis and Schetz [**32**] tested tandem (overlaid) parallel injectors exiting into a supersonic freestream using interferometry, one of which was subsonic, the other of which was supersonic. As indicated by density profiles, the individual components closely resembled their independent counterparts. Moreover, the near-field behavior of the subsonic stream was found to be largely dispersed by roughly 6 slot heights downstream. Bogdanoff [**33**] notes that in general, this injection scheme did not exhibit strong mixing with the primary flow. However its use in tandem with other injection schemes or mixing enhancement devices (as will be discussed below) has proven effective.

1.1.2.3 – Pylon Injection

One of the principal problems experienced with both transverse and parallel injection is the inability to penetrate far into the combustor flow. In the case of the former, introducing a jet with sufficient momentum flux to penetrate the core flow inevitably leads to the formation of strong bow shocks, which can increase overall drag and decrease already small margins of thrust. The latter, as discussed above, is ineffective at transporting fuel into the core flow. Pylon injection in its most basic form attempts to bypass this problem altogether by extending the point of injection out into the flow. Pylon injection is achieved by extending some form of mechanical structure out into the flow. In some cases this can involve a strut extended part-way into the combustor [**34**] [**35**] [**36**] or fully spanning it [**37**] [**38**]. Both of these configurations can be seen in Figures 1.3 and 1.4.

Gruenig et al. [**34**] studied four different pylon configurations in a vitiated Mach 2.15 flow. Three of the struts tested were aimed at studying transverse and oblique injection from the end of the pylon, each of which was equipped with a single slot injector at its highest transverse point with the varied parameter being the angle of the injector with respect to the freestream; in this case the tested angles were 60 degrees, 90 degrees, and 120 degrees. A longer pylon with injection from its sides was also tested in these studies. To quantify the efficacy of the geometries, they defined a 'mixing efficiency parameter,' defined as

$$G_{mixing} = \frac{A_{jet}}{\dot{m}_{fuel}} \qquad 1.3$$

where the area of the injection plume was deduced with planar laser Rayleigh scattering. It was found that injection in either the 60 degree or 120 degree offered a higher ultimate mixing efficiency to that of the transverse-injection pylon, both in the near-field and far-field. The pylon with side injection ports outperformed all variations of the transverse

injection pylon. This metric was corroborated with static pressure measurements on the combustor walls, intended to measure the heat release at different stations. The authors also note that the less efficient injection strategy might be desirable in smaller combustors, as the more gradual heat release could prevent thermal choking.

The studies of Hsu et al. [**35**] observed seven different strut configurations in either a Mach 2 or 3 flow, varying the angle of the strut leading edge, root length, and the transverse sweep and taper using a combination of NO-PLIF and RANS-based simulations. It was found that the struts with larger leading edge angles tended to promote greater fuel mixing as the leading edge shocks were stronger and the subsequent wakes larger. It was found that injection from the top of the pylon with minimal momentum flux was ineffective compared to the side-injecting pylons. The authors also note that the location of injection was important, with injection downstream of the aftbody expansion being more effective at distributing the scalar than injection upstream of this point. Shorter root lengths also tended to increase fuel penetration in the transverse direction, though it also seemed to reduce the span-wise dispersion of the injectant.

Rock et al. [**36**] studied the mixing of helium injected from strut injectors in a Mach 4 flow within a circular duct. They implemented a gas-sampling and static pressure probes to measure the quantities of interest in the flow. The results were then compared to RANS-based simulations. The struts used in these experiments had a very long root length, and featured side injection ports. The experimental results indicated reasonable penetration of the injectant approximately 1.8 duct diameters downstream, at which point the individual jets had merged into a single injection plume. Overall the mixing was actually quite slow for this particular flow configuration. The authors also note a substantial total pressure loss downstream of the injectors. For this particular injection scheme, the additional mechanical structure universally leads to higher total pressure

losses, counterbalanced by the increased penetration of the fuel into the combustor flow. The two must be balanced for the pylon to be a viable injection scheme.

1.1.3 – Supersonic Mixing Enhancement Strategies

This section covers some of the literature related to enhancing the mixing in the flowfields discussed in the previous section.

1.1.3.1 – Transverse Injection

The problems associated with transverse injection have been detailed above. Increasing the overall mixing performance of transverse injection has been studied in depth by many authors. One possible mixing enhancement strategy is to vary the geometry of the injector. Gruber et al. [**39**] compared transverse injectors utilizing circular and elliptic nozzles. It was found that the elliptical nozzle promoted greater lateral spreading than the circular injector. However, there was a reduction in the transverse penetration of the jet plume, a phenomenon the authors attributed to a greater separation distance between vortex cores found in the shed pair of counter-rotating vortices.

The use of a wedge-shaped orifice was studied by Barber, Schetz, and Roe [**40**]. A 7.35 degree half-angle wedge-shaped injector was used to inject into a Mach 3 crossflow, and the resultant flowfield studied with surface oil-film visualization and a concentration probe. The wedge-shaped injector lacked a clear separation region preceding the injector (as is present in circular injectors). The wedge injector also had the advantage of penetrating farther into the crossflow. The authors concluded that it would be a superior injection scheme to that of a simple circular orifice injector.

Diamond-shaped injection orifices are another potential enhancement strategy, studied independently by a number of different groups [**41**] [**42**] [**43**]. Tomioka,

Jacobsen, and Schetz [**41**] studied a diamond-shaped orifice issuing into a Mach 3 crossflow using a concentration probe, surface oil-film visualization, and shadowgraph. It was found that at lower momentum flux ratios, the diamond-shaped orifice provided greater penetration than both a simple circular injector and the wedge-shaped injector from [**40**]. Bowersox, Fan, and Lee studied a similar diamond-shaped orifice injector issuing into a Mach 5 crossflow using surface oil-film visualization, pressure sensitive paint, shadowgraph, an aerotherm probe, and Mie scattering imaging. It was found that attachment of the jet-interaction shock was a strong function of the injector angle with respect to the freestream. The injection angle also had a direct influence on the total pressure losses, with decreasing injection angle likewise decreasing the total pressure losses. A more applied study of the diamond orifice was done by Tomioka et al. [**43**]. Both diamond and circular orifices were utilized in a model scramjet combustor (Mach 2.4). It was found that the diamond injectors had a lesser ability to stabilize the flame within the combustor, due primarily to the lesser interaction with the freestream. Additional studies by Hirano, Kouchi, et al. [**44**] [**45**] numerically studied various injector geometries and applied them to a model scramjet combustor.

Utilizing multiple interacting jets is another possible mixing enhancement mechanism. Herein, multiple injection ports are utilized to cause a positive interaction. In some cases this can be a tandem jet configuration; the counter-rotating vortex pair shed from an initial jet is used to enhance the mixing rate of a second jet injected downstream. This injection configuration has been studied by a number of authors [**46**] [**47**] [**48**]. The work by Hollo, McDaniel, and Hartfield [**46**] indicate that a large subsonic region exists between the two jets, accounting for significant mixing enhancement in the near-field, though the far-field remains relatively insensitive to the geometry. Computational studies by Lee [**47**] [**48**] indicate that the strength of the interaction is a function of the spacing

between the jets, which is itself a function of the momentum flux ratio. Reactive studies indicate a further enhancement of mixing with the addition of heat release.

Lateral interaction is another potential mixing enhancement strategy. Probably the most complex of these methods is known as the aerodynamic ramp injector (or aeroramp for brevity), credited to Schetz [**49**]. Herein, a series of laterally and axially interacting jets with different injection angles and momentum flux ratios create a virtual 'ramp' to enhance the overall mixing process. In this study by Schetz, a nine-port injector configuration was utilized in a Mach 3 flow. The flow was studied by the use of a shadowgraph, surface oil-streak visualization, and a concentration probe. The aeroramp injector induced a pair of strong counter-rotating stream-wise vortices, supported by pressure gradients resulting from the leading edge shock and the low pressure wake regions. A comparison of this injector configuration with a physical swept ramp injector was made by Fuller et al. [**50**]. It was found that the performance of the mixer was largely a function of the momentum flux ratio. With a momentum flux ratio of unity, the aeroramp injector outperformed the swept ramp injector in the near-field, but was inferior in the far-field. Increasing the ratio to 2 made the mixing performance approach that of the ramp injector. It was also noted that the higher momentum flux ratio case tended to decrease the performance of the physical ramp.

A series of studies by Cox-Stouffer and Gruber [**51**] [**52**] [**53**] performed RANS-based simulations on the geometry of Schetz et al. [**49**] in an attempt to optimize the injector configuration. The first of these studies [**51**] looked at varying the span-wise injector spacing. The results indicated that decreasing the spacing between the outer injectors and the ones along the centerline tended to increase the wall-normal plume penetration, while the converse was also true. The next study [**52**] looked parametrically at the influence of the yaw angle of the individual injectors on the overall mixing

characteristics. These studies indicated that injector yaw was not necessary to attain the desired counter-rotating vortex pair from the injector. However, much like inward displacement, adding yaw angle tended to increase the overall penetration of the jet. It was found, however, that eliminating the yaw substantially improved the mixing performance in the near-field and far-field, despite the aforementioned effect of enhancing jet penetration. The final of these studies [**53**] looked at a broader test matrix involving variations in both of the aforementioned parameters. It was found any of the metrics for quantifying the overall mixing behavior (mixing efficiency, total pressure loss, etc.) showed very little variation among the 11 test cases, the actual shape of the injection plume varied considerably, which could be a desirable design control parameter.

A study by Jacobsen et al. [**54**] and later by Maddalena, Campioli, and Schetz [**55**] [**56**] investigated a different aeroramp configuration composed of four jets. These studies used a variety of techniques including shadowgraph, surface oil-streak visualization, pressure sensitive paint, and a series of probes including those that measure Pitot pressure, cone-static pressure, and total temperature. The initial study [**54**] in a Mach 2.4 crossflow compared the new injector to a single transverse jet. It was found that in this configuration, the span-wise spreading of the injectant was far superior to that of single jet, but failed to achieve the same penetration height. It also exhibited marginally higher total pressure loss. The later studies [**55**] [**56**] investigated the same injector in a Mach 4 crossflow and compared the results to a RANS-based simulation. In these conditions, it was found that the aeroramp injector performed only slightly better than a single tangential injector, including a marginal improvement in mixing efficiency, slightly higher total pressure losses, and effectively the same plume area though the lateral spreading was enhanced. The authors noted that the injector was optimized for a Mach 2.4 flow, and that further development would be necessary to make substantial

improvements in the Mach 4 flow. The simulations were able to capture the general flow features, but were unable to accurately reproduce the experimental data for many of the desired flow parameters. The authors cite the selection of a k-ω turbulence model as the possible culprit for the observed incongruities.

1.1.3.2 – Parallel Injection

As highlighted above, parallel injection has not been shown to be an effective means of attaining effective mixing due to its poor ability to increase transverse dispersion rates. However, this can be improved in several ways. Forced interactions with shock waves can lead to vorticity-producing baroclinic torque. Looking at the inviscid vorticity transport equation,

$$\rho \frac{D}{Dt}\left(\frac{\omega}{\rho}\right) = \frac{1}{\rho^2}\nabla P \times \nabla \rho \qquad 1.4$$

it can be seen that a misalignment between the local pressure and density gradients can lead to the generation of vorticity. This effect is enhanced when fluids of different densities are present. The act of passing a shockwave through such concentration-based density gradients enhances the effect further by misaligning the pressure and density gradients. This is encouraging for use in scramjet combustors, as shockwaves tend to be present in abundance.

There have been various studies into the effects of shock-enhanced mixing [**57**] [**58**] [**59**] [**60**]. Fundamental studies into this effect were made by Jacobs [**57**]. Herein a jet of helium was pulsed into a shock tube prior to the shock passing over it, and the effect observed using PLIF of biacetyl. The formation of a distinct pair of counter-rotating vortices was formed due to the shock-induced instability, greatly enhancing the mixing of the helium with the surrounding gas. More applied studies to this effect were made by Houwing et al. [**58**], in which an oblique shockwave was made to impinge on a

two adjacent sonic jets of helium and visualized with NO PLIF. It was found that the introduction of the shockwave caused a distinct bifurcation in the jets. The authors attributed this effect both to baroclinic torque and the amplification of stream-wise vorticity by the shock. The jet also exhibited behavior consistent with the presence of a bubble shock standing off from the incident oblique shock, though further study was indicated to ascertain the cause.

Another strategy is a hybrid between parallel and transverse injection: the swept ramp injector. Herein, an aerodynamic ramp precedes an injection port which is nearly parallel to the freestream. A schematic of this flow geometry can be found in Figure 1.5. The ramp is intended to introduce stream-wise vorticity to further promote mixing between the injectant and primary flow. An early study on this subject was done by Northam et al. [**61**]; the authors studied side-by-side configurations of both swept and unswept ramp injectors using a combination of shadowgraph, wall pressure measurements, and OH luminescence in a nominally Mach 2 flow. Based on the OH luminescence, the combustion occurred primarily in the wake of the ramp injectors, with higher overall combustion efficiencies for the case of the swept injectors.

A study on the subject of ramp injectors was done by Hardfield, Hollo, and McDaniel [**62**]. A single swept-ramp injector in both Mach 2 and Mach 2.9 flows was studied using shadowgraph and iodine PLIF. They found that the injection plume, while dominated by the momentum of the underexpanded jet in the near-field, was lifted away from the wall farther downstream by the action of the induced stream-wise vortices. The fluorescence studies indicated that the vortices seemed to largely dissipate by 10 ramp heights downstream of the injector for both Mach numbers tested. A successive study by Donohue, McDaniel, and Haj-Hariri [**63**] utilized a variation on the iodine fluorescence technique to measure the time-averaged temperature, pressure, mole fraction, and

velocity fields in a similar flow configuration, though the study focused more on the application of the technique than studying the flowfield.

A combination of experimental and numerical studies by Riggins et al. [**64**] looked at the flow of a high-enthalpy Mach 5 flow over side-by-side swept ramp injectors. Their computational study was predominantly concerned with the thrust augmentation achieved by the injector. Comparisons with experimental pressure measurements provided the necessary validation. Based on the spatial distribution of thrust potential gleaned through the simulations, it was found that the thrust potential made clear gains due to the heat release, with a marked transition from jet momentum contributions in the near-field to reaction-induced gains downstream.

A combustion experiment by Hönig et al. [**65**] utilized PLIF of the OH radical in conjunction with pressure measurements to study a ramp injector in a vitiated Mach 1.9 flow. It was found that much like the non-reacting counterparts, the structure of the plume and reaction zones were dominated by the vortical-induced mixing process generated by the ramp injector. It was found that at their configured static inlet temperature of 850 K, ignition could only be stabilized in a limited region near the wall in the wake of the mixer. Flammability limits were for global equivalence ratio were found to be between ϕ=0.07 to 0.6.

1.1.3.3 – Pylon Injection

The primary means of augmenting mixing in pylon-type configurations is known as hypermixing. Much like its wall-based ramp injector counterpart, hypermixing forgoes trying to directly increase the turbulent growth rates back to their incompressible counterparts, instead trying to promote mixing through the introduction of stream-wise vorticity. This enhanced mixing is typically achieved by altering the trailing-edge

geometry of a strut or pylon, utilizing an alternating series of compressive or expansive ramps to induce pressure gradients in the flow. While this would be effective in subsonic flows as well (a similar principal to the lobed injector), the accompanying shock- and rarefaction- waves lead to even more potent pressure gradients and shed vortices.

A series of studies published by Fox, Gaston, et al. [**66**] [**67**] [**68**] [**69**] investigated a number of different hypermixing strut injector geometries. The earliest study by Gaston et al. [**69**] compared two different categories of injectors against a plane base model. These are the castellated model and swept compression-expansion ramp models, with two- and five-port injectors for the castellated type. In these studies, the combined use of shadowgraph and wall pressure measurements were used to measure drag and/or attendant heat release testing reactive and non-reactive cases. Mixing efficiencies were estimated using a one-dimensional model of supersonic flow with heat release. By assuming that all rises in pressure were associated with heat release, this allowed the authors to approximate the fraction of fuel consumed as a function of stream-wise position, which they used as a surrogate for the mixing efficiency. These studies found that for identical injector geometry, those with the five-port injection configuration tended to exhibit greater mixing than the two-port counterparts. The authors attributed this to the increase in area of the fuel-air interface. Of the geometries tested, the swept compression-expansion ramp exhibited the highest mixing efficiency. The castellated injector exhibited only modest improvements in mixing efficiency over the reference wake case, noting that the degree to which the mixing was increase was reduced as the incoming Mach number decreased from 3.7 to 2.5. The ultimate conclusion made in this study was that for the induced flow effect to impact mixing, the effect needed to be either very strong or occur very near the fuel-air interface.

A later study by Fox et al. [**66**] [**67**] introduced the use of planar laser-induced fluorescence as a means of quantifying the local mole fraction of the injectant. The studies were performed in a free-piston shock tunnel with an approximate Mach number of 4.8. The hypermixing strut injectors used in this case were a simple planar injector, a three-faceted castellated injector, a swept compressive-expansive ramp injector, and an unswept compressive-expansive ramp injector. Utilizing planar laser-induced fluorescence of NO across several distinct absorption bands, the authors were able to convert the instantaneous fluorescence images to that of mole fraction. Imaging in both the stream-wise and cross-stream planes, it was found that much as the previous study, the castellated injector performed marginally better than the plane base case in terms of mixing performance. The metric used in this comparison was a ratio of the area of stoichiometric mixture to the area of the nozzle. This comparison was not made for the swept and unswept ramp injectors. It was noted that the swept injector appeared slightly more effective at mixing based on the apparent strength of vortices present in their fluorescence images. However, there was obvious experimental jitter due to the use of an impulse facility, and as such the authors reserved judgment on these cases.

In a later study on the subject, Gaston et al. [**68**] used the same hypermixing strut injector geometries (same data set as the previous study) in comparisons with FANS-based simulations of representative flowfields. The fluorescence images were compared qualitatively with a simulated PLIF signal generated from the simulations. It was found that the simulations were able to adequately replicate the flow features found in the experimental data (inasmuch as the mean flowfield obtained in the simulations could be compared to the instantaneous experimental data). The simulation data were then used in comparing the mixing performance of the different mixers tested in three different

manners. First, the mixing efficiency of each of the tested mixers was computed as a function of the axial location. In this case the mixing efficiency was defined as

$$\eta_m = \frac{\int \rho U Y_R dA}{\dot{m}_j} \qquad 1.5$$

In Eq. 1.5, the mass fraction Y_R takes on different values for different equivalence ratios. In the case of lean mixture, Y_R would be the mass fraction of the fuel, whereas it would take on the value $f(1 - Y_f)/(1 - f)$, where f is the stoichiometric mass fraction. This metric is effectively the ratio of the mixed flow rate of fuel to the total flow rate of fuel. Second, the maximum fuel mass fraction was computed as a function of the stream-wise location. Finally, the fuel jet penetration into the coflow, defined as the distance from the transverse midplane of the strut injector to the location of 0.5 percent mass fraction. The first of these metrics indicated a similar mixing efficiency for all injector configurations in the very near-field. However, this metric diverged rapidly just a few base-heights downstream, with the swept and unswept injectors outperforming the planar and castellated cases. The other metrics corroborated this observation, with the maximum fuel mass fraction falling off rapidly in the case of the swept and unswept injectors, and the penetration into the coflow considerably greater than the planar and castellated cases. A final metric of total pressure loss indicated the swept and unswept compressive-expansive ramp injectors suffer larger overall total pressure losses. The authors also note that the losses incurred due to the mixer may be made up in higher overall combustion efficiency.

A series of studies by Doster et al. [**70**] [**71**] [**72**] developed and studied a set of three hypermixing pylon injectors in a nominally Mach 2 flow. The initial study [**70**] went through the design parameters of interest and the design choices made and performed cold-flow simulations on the test geometries using a RANS-based CFD solver.

The tested geometries included a baseline case, an alternating compressive ramp arrangement, and an alternating wedge arrangement. The dimensions were selected to have the same frontal area with respect to the flow direction. All injectors utilized upstream injection. These initial studies only looked at cases with no active injection, observing the magnitude of stream-wise vorticity introduced by the hypermixer and the total pressure loss. The alternating wedge and ramp configurations showed a decisive increase in stream-wise vorticity over the baseline case, with modest increases in drag and overall total pressure loss.

The final phase of the study [**71**] [**72**] presented experimental results for these hypermixer configurations. A combination of Raman spectroscopy and NO PLIF was utilized to discern information about fuel mass fraction at different axial locations. These studies indicate that both the alternating wedge and ramp configurations exhibit marked increases in near-field stream-wise vorticity, moving the region possessing a combustible mixture upstream. The authors note that this is potentially advantageous if the desired effect was to utilize the injector as a flame holder. The mixing efficiency (or mixing effectiveness, as it is termed in the source) is defined in the same manner as Eq. 1.5 above. There was a measurable increase in the total pressure loss accompanying the increase in mixing efficiency. The ramp injector showed a very similar total pressure loss compared with that of the baseline case, and actually exhibited less overall drag. The authors note that although these studies give insight into the mixing process, judging how well the geometries would perform in a true combustion scenario would be difficult to extrapolate.

A series of applied studies was carried out by Sunami et al. [**73**] [**74**] [**75**] [**76**]. The earliest of these studies by Sunami, Wendt, and Nishioka [69] looked at the application of a hypermixing strut injector using simulations in addition to both cold-flow

and vitiated supersonic wind tunnel experiments. The hypermixing strut injectors were varied throughout the different cases. In the simulations, two different hypermixers were examined. One hypermixer featured alternating 10 degree expansive wedges, separated from each other by a thin fence, while the other was had the same ramp angles, but each ramp was narrower and was not isolated by a fence. The simulations indicated that the vortex pairs shed from the hypermixer played an important role in the compressible shear layer; specifically, the largest growth in circulation and most of the entrainment of coflowing air occurred within $5h$. The simulations were then used to optimize the fuel injection location, in and around the region of vortex generation.

The cold flow experiments were conducted at Mach 2.45 using a scanning pitot probe. These tests were performed on four different mixer configurations. The hypermixers used in the simulations were tested along with one featuring narrower ramps and no fences and another in a so-called 'biplane' configuration, in which two of the fenceless struts were placed mid-section, separated by ~$1h$ in the transverse direction. The fenceless single mixer showed distinct counter-rotating vortices at $x/h = 1h$, $3h$, and $5h$, but they had broken down into smaller scale structures by $8h$. This vortex breakdown was not apparent in the model with the fenced case, as there was less entrainment of the shear layer from the onset. For the model with narrower ramps, it was found that the co-rotating vortex pair broke down in roughly the same length scale as the counter-rotating vortex pair. Finally, the biplane configuration yielded large-scale convective mixing, and more importantly that by arranging the position of ramps on this tiered-strut configuration, even larger-scale vortices can be generated.

The vitiated experiments utilized schlieren, bulk luminescence imaging, and gas sampling probes at the exit of the test section. In these cases, two injection configurations were tested; one hypermixer featured fenceless alternating strut injectors while the other

was a simple plane-base injector. Both schlieren and the bulk luminosity measurements indicated that the stream-wise vortices induced by the ramps served both as a mixing enhancement as well as a flameholder. The plane-base injector was capable of flameholding, but the flame base was located much farther downstream then with the hypermixing injector. The gas sampling probe measurements revealed that the hypermixing injector produced much larger region of near-stoichiometric mixtures at the exit plane of the test section.

In the next two successive studies by Sunami et al. [**74**] [**75**], a series of different alternating ramp injectors were studied for their mixing and flameholding characteristics in a vitiated Mach 2.45 flow. In the first of these studies [**74**], the global combustion performance was examined using wall static pressure measurements and bulk luminescence. Here it was found that increasing the expansive angle of the ramp yielded considerably more rapid mixing and flame ignition, in addition to a greater overall rise in total pressure. An additional injection stage was added in this study in which a wall-mounted alternating wedge injector was added at downstream end of the test section, which resulted in an even greater increase in total pressure, though extra fuel is added these cases. In the companion study [**75**], planar laser Mie scattering was used to visualize the injection plumes with the same injectors. Here it was found that the larger wedge angle was accompanied by a greater transverse spreading rate, though the span-wise growth rate of the injection plumes were roughly unaffected. The heat release associated with combustion did seem to cause the stream-wise vortices to break down more rapidly, though the authors noted that the exact nature of the breakdown could not be discerned from their data set.

In a further study by Sunami et al. [**76**], OH PLIF was utilized to study the reaction zones in several hypermixing strut injectors. Three different injection

configurations were looked at in this study. One injector featured alternating expansive wedges. In addition, an injector with overlapping alternating wedges was used, along with one featuring laterally skewed wedges. It was found in all cases that the OH PLIF signal was highly unsteady, and adhered well to the expected reaction regions perceived through Mie scattering from a previous study [**75**]. Though the wall pressure measurements indicated different amounts of heat release throughout the test section for different injector geometries, total pressure measurements downstream of these locations indicated little difference between the three mixers used.

An early study by Desikan and Kurian [**77**] utilized schlieren and planar Mie scattering to visualize the flowfield around three different hypermixing strut injectors in a Mach 1.7 flow. Accompanying simulations were performed using Fluent. The hypermixers featured slight variations on a single geometry; the basic model had dual injection ports, with an unswept compression ramp located between them. One variation featured a swept ramp, and the other had the ramp upstream of the injection point. To quantify the mixing, a parameter known as the degree of unmixedness (DU) was used, which attempts to quantify the mixing of the flow by taking the intensity of the local deviation of the Mie scattering intensity to that of the image background. The DU is defined as

$$DU = \sqrt{\frac{1}{N}\sum\sum(I(x,y) - \bar{I})^2} \Big/ \sum\sum\frac{I(x,y)}{N} \qquad 1.6$$

Mie scattering revealed the distribution of the injectant at different stream-wise locations between $x\ /\ h = 0.063$ and $x/h = 1.375$ and was used in the computation of the DU. It was observed visually that the third injector described above performed quite poorly in comparison to the other two, having the highest DU throughout the observation

volume, while the other two performed similarly. Simulation wall pressures deviated considerably from the experimental measures.

Two studies by Vergine et al. [**78**] [**79**] aimed at investigating the evolution of the vortical structures shed from a hypermixing strut injector. The first of these studies by Vergine and Maddalena [**78**] was aimed at studying the evolution of the large-scale structures shed from a single vortex generating element as they progressed downstream using simplified injector geometry. Stereoscopic PIV was used to observe the velocity in end-view planes, while two-dimensional PIV was used to observe velocity in side-view planes. It was found in these studies that the undisturbed wake structure was greatly modified by the presence of the hypermixing element. In the experimental configuration, the vorticity decayed from observation stations between 10h and 32h, though the circulation remained relatively constant between 10h and 16h. In a successive study by Vergine, Cristani, and Maddalena [**79**] the merging of adjacent vortical structures shed by two partially overlapping hypermixing elements was examined using stereoscopic PIV. It was found that the overlapping hypermixing elements generated additional spreading of the injection plume compared to the undisturbed state. The rotation of the merging vortices occurred in such a way as to induce ghost vorticity, ultimately transporting vorticity outside of the centroid of the vortex merger. Additionally, a decomposition of the merging vorticity field into symmetric and anti-symmetric components allowed the morphology of the vortex plume to be understood. An additional study by Vergine et al. [**80**] aimed at observing the effects of heat release on the vorticity-dominated flowfield. A high-enthalpy expansion tube facility operating at Mach 2.4 was used along with a hydrogen fueled hypermixing strut injector. Based on instantaneous OH-PLIF observations, it was found that the reactive injection plume behaved in a manner very similar to the cold-flow counterparts. Variations in the injection momentum flux ratio

were found not to affect the dynamics of the plume, which was capable of stabilizing a flame without the assistance of additional flameholding devices.

1.2 – CONTEXT OF PRESENT WORK

The work presented herein is broadly intended to complement the extensive body of work associated with hypermixing strut injectors. Additionally, the techniques and methodologies detailed will provide other researchers additional tools to conduct research into related flowfields and mixing phenomena. With regard to the first objective, a great deal of data is available concerning the global dispersion of injected species in supersonic mixing flowfields. That is, studies have shown where an injected species goes and in what concentration it is present for various injector configurations; this dispersive behavior has been characterized with the metrics discussed in section 1.1.3.3. However, the data currently available can be divided two broad categories: time-averaged studies and small-sample instantaneous studies. Both of these data types possess inherent limitations, which affect their utility in diagnosing the mixing flowfields in which they were collected.

When utilizing time-averaged data, the ability to discern between true mixing and stirring is lost. Stirring is the stretching and folding of intermaterial surfaces by advection, whereas mixing is the interdiffusion of different species on a molecular level. To emphasize the fundamental difference between the two, Fig. 1.6 shows the contrast between them. Figure 1.6a illustrates an instantaneous snapshot of fluid which is well ‘stirred’, i.e. the injected fluid stream has entrained large quantities of the surrounding fluid (or *vice versa*). In collecting a large number of samples at this location and averaging, the resulting concentration contours are shown in Fig 1.6b. Such mean fields may give the impression of being well-mixed on a molecular level; however, the

instantaneous realization shows the fluid is merely stirred rather than mixed. Thus, a study. A second consequence of having time-averaged data is the inability to observe instantaneous derivative quantities in the flowfield. If, for instance, there was a strong relationship between the fluctuations in concentration in the flowfield and the instantaneous shear, no observation of the behavior could be made. Since the mechanisms of mixing enhancement present in hypermixing flowfields are physically akin to the aforementioned stirring, one aspect of the present work is to enable the use of the instantaneous data in studying the mixing in these complex flowfields rather than time- or ensemble-averaged quantities. In the present study, this objective will manifest as collecting data with sufficiently short temporal integration to ensure that instantaneous scalar structures are visible. Also of concern when imaging scalar quantities in a flow is the ability to resolve the length scales of the mixing. As will be addressed in Appendix 4A, the capacity for resolving at these length scales is not currently developed, but a discussion of the resolution can be found in the aforementioned appendix.

The second category of data mentioned above is instantaneous data. These studies represent the minority of the literature, but they do have a number of advantages over the time-averaged studies. Specifically, instantaneous data provide spatial information about the flowfield not afforded by the averaged data: information about instantaneous flow structures can be gleaned, and the calculation of spatial derivatives is possible. The literature, however, still lacks any large ensembles of these data to be used for statistical calculations in supersonic flows. Moreover, the data sets that are available (at least with respect to hypermixing strut-injector flowfields) contain only scalar data. While these data are an improvement over time-averaged data sets, they are still fundamentally limited in the information that can be learned from them. Thus, it is apparent that there is a growing need for more complete data sets, featuring statistically significant quantities

of data for multiple flow parameters, either for learning about the structures of these flowfields or for the validation of simulations.

The other global objective of this work, as mentioned above, is to design and implement a series of techniques and methodologies, which can be utilized in studying these complex mixing flowfields. The novelty of the desired technique lies in two aspects: multi-parameter measurement and statistically-significant quantities of instantaneous data. However, there are currently a number of limitations that prevent the use of these extremely complex studies in supersonic mixing flowfields. First, extremely long run times are usually not a possibility because the flows are supersonic. In many circumstances this can preclude collecting statistically significant quantities of data, making computing statistics beyond the mean very difficult. Second, many diagnostics used for measuring dispersion or the velocity field can preclude the use of other diagnostics. As an example, if information regarding the temperature of a flowfield was desired, Rayleigh thermometry could hypothetically be performed. Likewise, if information about the velocity field was desired, particle image velocimetry could be performed. If it was then desired that the instantaneous scalar and velocity fields be correlated, it would not be possible to perform these two diagnostics simultaneously, since the scattering from the particles used for PIV would dominate the Rayleigh scattering signal. Similar scenarios occur frequently in the laboratory setting, and limit what kinds of data are available for analysis. Thus, it becomes an imperative in this body of work to find a means of bypassing the inherent limitation on utilizing simultaneous diagnostics. Accomplishing this objective will permit the desired multi-parameter measurements that maintain their spatial resolution.

1.3 – Details of Present Work

The present work seeks to develop and implement the krypton planar laser-induced fluorescence technique simultaneous to particle image velocimetry in a model supersonic mixing flowfield. There are several reasons for this combination of techniques. First, when considering the desirable types of data for studying mixing, the obvious selections are velocity and scalar concentration. Next, since spatially-resolved measurements (rather than point measurements) are desired, the number of techniques available for that type of measurement in the velocity field is very limited. Particle image velocimetry, global Doppler velocimetry, and in some instances I_2 PLIF are capable of such a measurement. With the facility used in these studies, PIV is the only practical choice without considerable changes in the infrastructure of the facility.

Making measurements of the scalar field are fundamentally more difficult in that the composition of the flow is tied to the thermodynamic state of the mixture. While the same could be said of the velocity field, the use of PIV allows for an indirect measurement of the velocity. While similar techniques exist for measuring the concentration of the injected scalar [**77**] based on Mie scattering, they suffer from the same particle-inertia effects present with PIV measurements, maintaining a consistent seed density is difficult, and the discrete nature of the particle images makes the data extremely difficult to interpret instantaneously. Thus, another variety of technique would be preferable. The two potential candidates are a fluorescence-based technique (PLIF), and a Rayleigh-scattering-based technique. The latter of these was ruled out very quickly; the facility operates at extremely low densities, making Rayleigh scattering a poor choice. Moreover, as mentioned in the previous section, the use of PIV at the same time would not be possible since the Rayleigh scattering would be dominated by the Mie scattering

from the particles. Thus, the most viable technique for making a spatially-resolved measurement of scalar concentration was PLIF.

The next complication was selecting the correct fluorescent tracer. As mentioned above, the selected tracer for these studies was krypton gas. First, from a chemical standpoint krypton is a superior fluorescent tracer to those commonly implemented in both low- and high-speed flows. Common tracers used in supersonic flows (NO and I_2 for example, as described above) are highly toxic and lethal in sufficient concentration. Moreover, particularly in the case of NO, they can be reactive in certain circumstances, invalidating species conservation. NO can also occur naturally in certain flows, making it difficult to distinguish between that which was intentionally seeded and the naturally occurring species. Other common tracers, for example acetone and toluene, have a limited range of thermodynamic utility; at the lower temperatures, these more complex tracers tend to condense out of their gaseous phase. At higher temperatures they can become reactive and combust, limiting the range over which they can be utilized. Krypton, being a noble gas, is non-reacting (even at combustion temperatures), nontoxic, and resistant to condensation at low temperatures. Though the details of this will be covered in later chapters, krypton PLIF also has some favorable spectral qualities, particularly a large spectral shift from excitation to emission, allowing for higher collection efficiencies and less expensive optical equipment compared to other tracers. Thus the selection of the fluorescent tracer for the work presented herein was fairly straightforward.

1.4 – ORGANIZATION OF THIS DISSERTATION

The work contained in this document constitutes a complete body of work from preliminary development of the new diagnostic technique to its application in

representative flowfields. In this way, the work naturally organizes itself into three phases. The first phase consists of the preliminary development of krypton PLIF, entailing the measurement of spectral quantities and thermodynamic data over a wide range of conditions. The second phase details the implementation of various forms of particle image velocimetry and study of two representative mixing flowfields to be used in the final phase of study. The final phase entails a study of the application of the simultaneous krypton PLIF – PIV technique to the flowfields studied in the previous phase. Each of these phases has a chapter devoted to it, in addition to the present chapter. These primary chapters are followed by a series of appendices to the work.

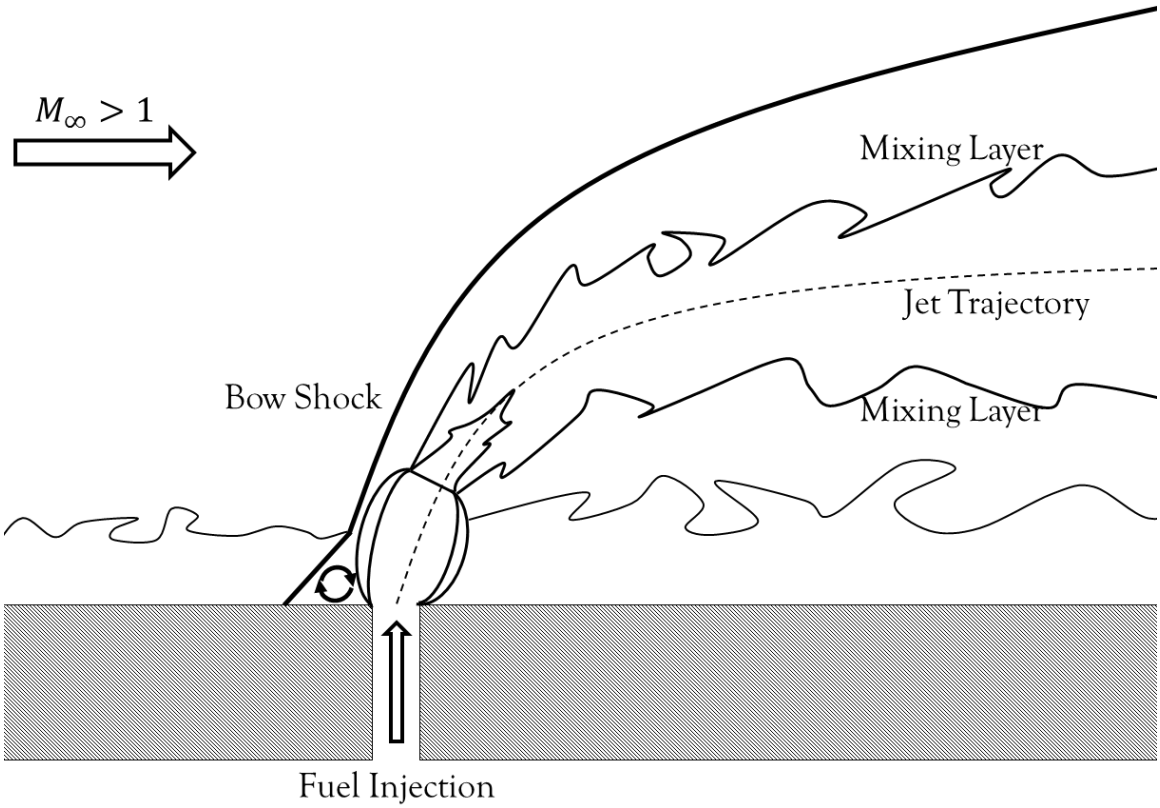

Figure 1.1: Schematic of flowfield for transverse injection

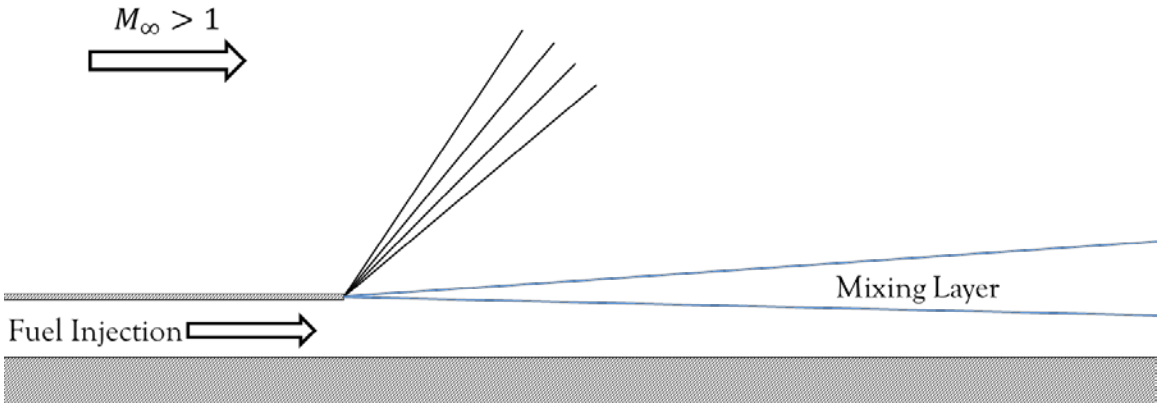

Figure 1.2: Schematic of parallel injection flowfield

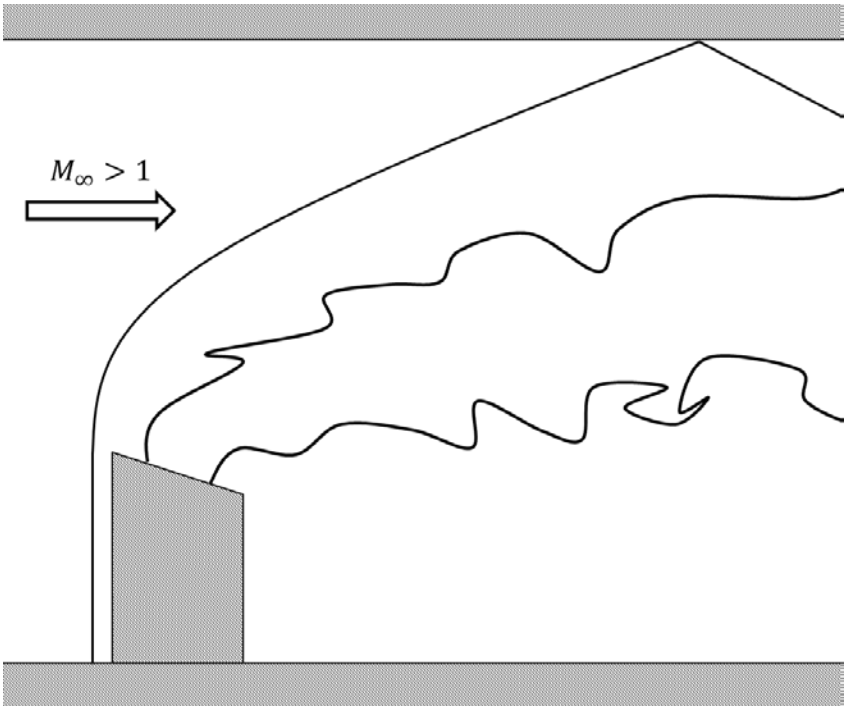

Figure 1.3: Schematic of partial-span pylon injection flowfield

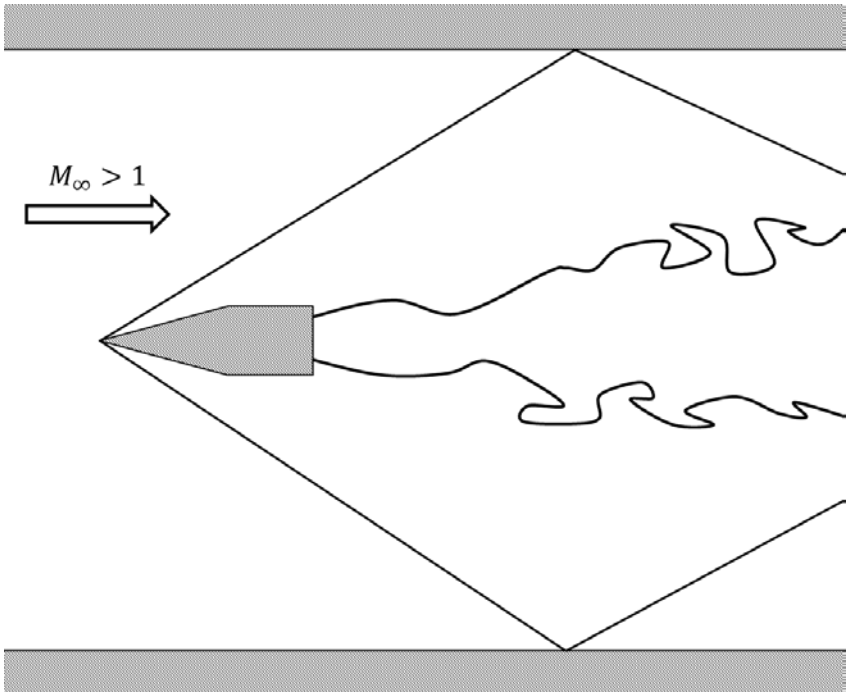

Figure 1.4: Schematic of full-span pylon injection flowfield

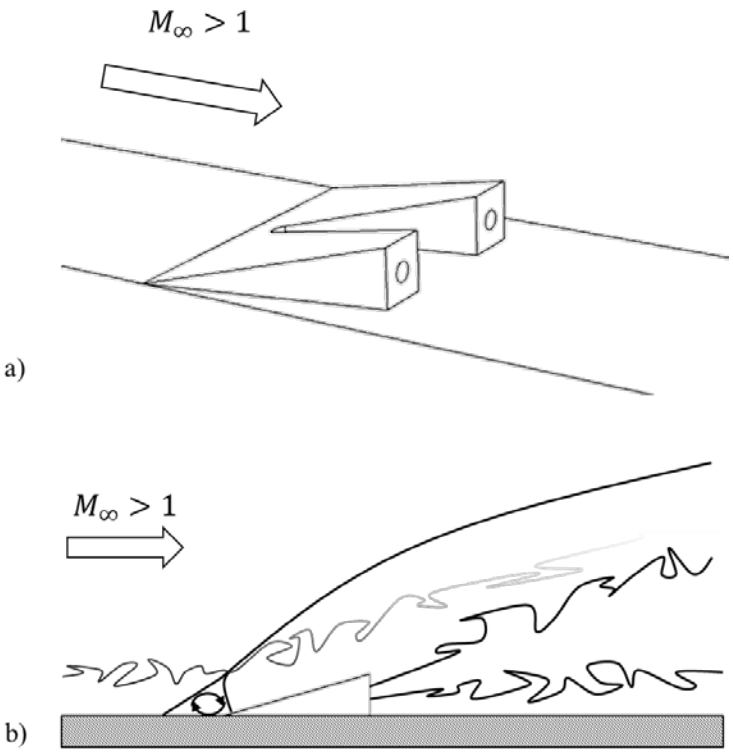

Figure 1.5: Diagram of swept-ramp injector flowfield. a) Perspective view of side-by-side injectors and b) side-view of injection flowfield

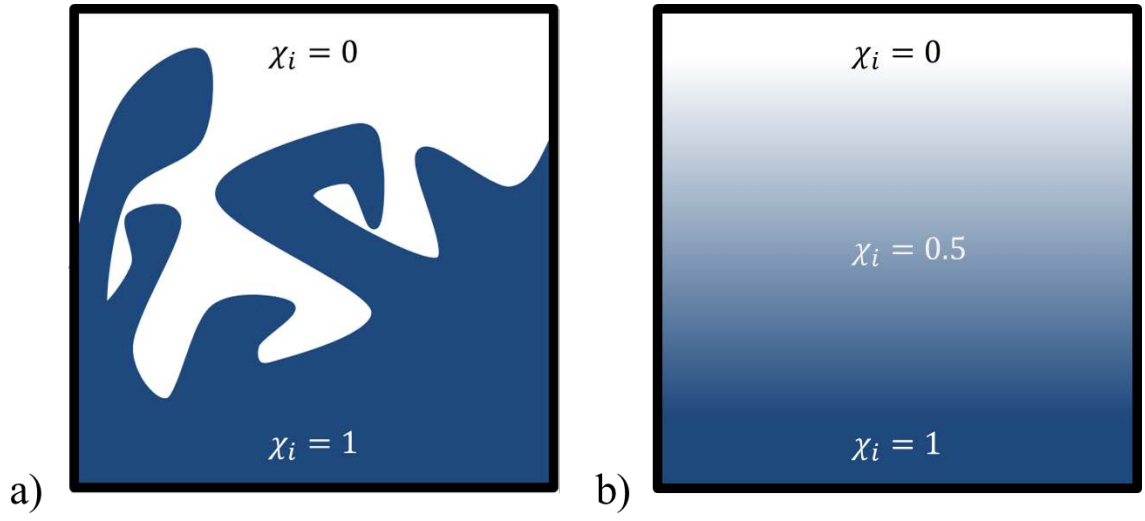

Figure 1.6: Illustration of the effect of averaging on a well-stirred mixing flowfield. a) Instantaneous field with interspersion and b) mean field showing mixed fluid

Chapter 2: Collisional Quenching and Absorption Properties of Krypton

This section details the methodology and analytical methods utilized in measuring the collisional quenching rates of the $5p[3/2]_2 \leftarrow 4p^6\ ^1S_0$ transition in krypton gas in addition to the relative two-photon absorption cross-sections. These measurements detail the pressure and temperature dependence of these quantities, as well as the design of the facility and equipment utilized.

2.1 – Background and Theory

There are several laboratory-accessible transitions in the krypton atom which could be useful for quantitative fluorescence imaging. In this context, laboratory-accessible implies that the transition can a) be excited with a wavelength that can be produced and transmitted in a laboratory setting and b) decay with a sufficiently high probability to produce a recordable fluorescence signal. For this purpose, there are three transitions which are tractable: a) $5p[3/2]_2 \leftarrow 4p^6\ ^1S_0$ with a corresponding energy change of 11.55 eV, b) $5p[5/2]_2 \leftarrow 4p^6\ ^1S_0$with an energy change of 11.45 eV, and c) $5p[1/2]_0 \leftarrow 4p^6\ ^1S_0$ with a corresponding energy change of 11.66 eV [**81**] [**82**] [**83**]. These transitions, though direct excitation is forbidden due to angular momentum conservation, permit multi-photon absorption through the existence of virtual states. The first of these transitions permits the strongest possible decay, and consequently it was selected for these fluorescence studies. The fluorescence decay from this excitation path takes two possible pathways. The largest portion of the fluorescence comes from the $5s[3/2]_2 \leftarrow 5p[3/2]_2$ decay path, having a branching ratio of 73.1 percent and corresponding wavelength of 760.4 nm, while the remaining fluorescence follows the

$5s[3/2]_1 \leftarrow 5p[3/2]_2$ path with corresponding wavelength 819 nm and a branching ratio of 21.8 percent.

In order to use the fluorescence quantitatively, the actions of excitation and decay of the desired pathways need to be modeled. A relatively simple two-level model was considered by Eichhorn [**84**] [**85**] and Löhle [**86**], who were using a similar two-photon noble gas fluorescence (xenon in this instance) for atomic oxygen density calibration. The fluorescence signal collected by the detector is given by

$$S_f = \eta_c \frac{E_L^2}{a^2} \frac{A_{21}}{A+Q} \frac{\hat{\sigma}^{(2)} n_{Kr}}{4\pi^2 (\hbar\omega)^2} \int_{-\infty}^{\infty} F^2(t) dt \qquad 2.1$$

assuming a weakly pumped transition. Eq. 2.1 considers the various excitation and kinetic processes that contribute to the fluorescence signal. Here η_c is the collection efficiency of the detector system, E_L is the pulse energy for the exciting radiation, A_{21} is the spontaneous emission rate for the transition in question, A is the Einstein A coefficient, Q is the quenching rate, $\hat{\sigma}^{(2)}$ is the effective two-photon absorption cross-section, n_{Kr} is the krypton number density, a the exciting beam radius, ω is the frequency of the exciting radiation, and $F(t)$ is the temporal profile of the exciting radiation pulse. The important things to note here are that the signal is quadratically dependent on the pumping energy due to the nature of two-photon absorption, and that the signal is dependent on the spontaneous emission rate and collisional quenching rates, expressed as the fluorescence yield in Eq. 2.1 above, in addition to the two-photon absorption cross section.

In the context of an applied measurement, relating the raw fluorescence signal back to a flow property, such as the composition, is fundamentally difficult. The reasons for this are several: considerable knowledge of the excitation and collection systems is required. These data include all of the parameters incorporated into Eq. 2.1 above

pertaining to the laser spatial, spectral, and temporal profiles, as well as the collection efficiency of the system. Additionally, the local number density, total fluorescence decay rate, and absorption cross-section are unknown. Two-dimensional imaging is particularly challenging in this regard, since the total decay rates are also dependent on the local gas conditions. For a detailed discussion on calibrating two-dimensional fluorescence images for mole-fraction sensitivity, refer to Chapter 4. The total decay rate can be written as a sum of the spontaneous emission rate for the downward transition (A) and the collisional quenching rate (Q):

$$\gamma = A + Q + k_{int} \tag{2.2}$$

For more complicated fluorescent species, the k_{int}, or the internal de-excitation rate, is often non-negligible. However, for this particular transition, a purely electronic transition, whose decay is purely radiative, the internal de-excitation rate can be neglected without a loss of accuracy. Thus, the total decay rate is only a function of the spontaneous emission rate and the collisional quenching rate. Only the collisional quenching rate possesses any thermodynamic state dependence.

The collisional quenching rate expressed in Eq. 2.2 above can be further decomposed to reveal the thermodynamic dependence:

$$Q = n_o \sum_{i=1}^{n} \chi_i \langle v_i \rangle \langle\langle \sigma_i \rangle\rangle \tag{2.3.a}$$

$$Q = P \sum_{i=1}^{n} \chi_i q_i \tag{2.3.b}$$

Eqs. 2.3 express the collisional quenching rate in two common manners. Eq. 2.3.a expresses the collisional quenching rate as a collision rate, where χ_i is the mole fraction of a given collisional partner, $\langle v_i \rangle$ is the mean relative velocity of the collisional pair (Kr-species i) given by an equilibrium Maxwell-Boltzmann distribution, $\langle\langle \sigma_i \rangle\rangle$ is the

collisional quenching cross-section of the collisional pair, and the summation is over all collisional pairs. The temperature dependence is implicit in this expression, as the total number density and relative velocity depend on temperature. The quenching cross-section maintains a temperature dependence as well in that it is relative-velocity dependent ($\langle\langle\sigma_i\rangle\rangle = \langle v_i\sigma_i\rangle/\langle v_i\rangle$). The alternative expression for the collisional quenching rate (Eq. 2.3.b) is often more convenient when computing the quenching rate, but less physically meaningful. Here, the collisional quenching rate for a given species is consolidated into a single term, q_i, where all of the temperature dependence is contained. Again, the summation is taken over all quenching species. Thus, the quantities that need to be measured to calibrate the fluorescence measurement are the spontaneous emission rate and the collisional quenching cross-sections.

The physical measurement of both the spontaneous emission and collisional quenching rates follows naturally from the definition of the terms. None of these terms can be measured directly, but they can be inferred from direct measurements. Consider the definition of the total decay rate, γ. The total decay rate can be measured by observing the decay of the fluorescence for the desired transition. The total decay rate of this transition is then given by $\tau_f = 1/\gamma$, where τ_f is the $1/e$ fall time of the fluorescence intensity. If knowledge of the temperature and pressure are also available for this measurement, it is then possible to relate these to the desired quantities. See Appendix 2A for a detailed discussion of the numerical methodologies utilized in these measurements.

Another important aspect to quantifying the fluorescence signal is to have knowledge of the absorption properties of the desired transition. Referring to Eq. 2.1 above, the absorption is expressed in terms of the effective two-photon absorption cross-section, $\hat{\sigma}^{(2)}$. Following a similar development to Bamford et al. [**87**], the probability of an electronic transition from the ground state ($4p^6\ {}^1S_o$) to the excited upper state

$(5p[3/2]_2)$ is $\hat{\sigma}^{(2)}\Phi^2$, where Φ is the laser photon flux and is related to the irradiance I by $\Phi = I/\hbar\omega_o$. ω_o is the mean (radian) frequency in the laser linewidth defined as $\omega_o = \int_0^\infty \omega g_L(\omega)d\omega$ and $g_L(\omega)$ is the laser lineshape function. The important thing about this definition is that both the two-photon absorption coefficient and the photon flux are spectrally integrated. The implication of this integration is that the effective two-photon absorption cross-section as defined in Eq. 2.1 is implicitly dependent on the laser lineshape function, $g_L(\omega)$.There is also an implicit dependence on the absorption lineshape, $g_a(\omega)$. Furthermore, since there are various mechanisms for broadening the absorption line (pressure broadening, Doppler broadening, etc.), there is an inherent thermodynamic dependence contained in the effective two-photon absorption cross-section as well.

The two-photon absorption cross-section being possessed of the various dependences described above is problematic. The reason for this is that the laser lineshape function is dependent on the excitation system, and changing any part of the system will inherently change the spectral integral and alter the thermodynamic dependences of the cross-section. Thus, any experiment measuring the integrated two-photon absorption coefficient in the matter described below may not be directly applicable to those conducted in other facilities. To avoid this undesirable outcome, the works of Glauber [**88**] and subsequently McKenzie and Gross [**89**] can be considered. Glauber defined a second-order correlation function, $G^{(2)}$ to help account for the coherence of the exciting radiation fields when considering the interplay between coherent and incoherent states. Bamford simplified the form of this correlation function for experiments similar to those described below as follows:

$$G^{(2)} = \frac{\langle f^2(t)\rangle}{\langle f(t)\rangle^2} = \frac{\langle f^2(t)\rangle}{F^2(t)} \qquad 2.4$$

where $f(t)$ is the temporal profile of the laser as measured by and infinitely fast detector (i.e. one which could measure on the coherence length scales of the exciting laser radiation). This correlation function takes on a range of values depending on the characteristics of the exciting radiation: $G^{(2)} = 1$ for a single-mode laser, $G^{(2)} = 2$ for a chaotic field, and $G^{(2)} = i$ for coupled multi-mode lasers with i coupled modes [**89**]. It is often assumed in the literature that this correlation function takes on the value of 2 for the type of systems described in Section 2.2.2. With this information, the measured two-photon absorption cross-section could be related to the system-independent effective cross-section by

$$\int_0^\infty \hat{\sigma}^{(2)}(\omega)d\omega = G^{(2)} \int_{-\infty}^{\infty} \sigma_0^{(2)} g_L(\omega - \omega_o)\, d\omega \qquad 2.5$$

where $\sigma_0^{(2)}$ is the system-independent effective cross-section. In expressing the equivalency in Eq. 2.5, it is assumed that the laser linewidth is much broader than the absorption linewidth, which is expected for the two-photon transition in question at the pressure range in consideration. With an analytical or measured form for g_L, the system-independent cross-section can expressed as follows,

$$\sigma_0^{(2)} = \frac{\hat{\sigma}^{(2)}}{G^{(2)} \int_{-\infty}^{\infty} g_L(\omega - \omega_o)d\omega} \qquad 2.6$$

Since the laser lineshape function is normalized such that $\int_0^\infty g_L(\omega)d\omega = 1$, the system-independent two-photon absorption cross-section is related to the system-dependent variety by the proportionality constant of $1/G^{(2)}$ evaluated for the current system. Likewise, conversion back to the dependent variety with for use with a new laser system merely requires information about the modal quality of the laser system. Note that the effective cross-section still contains the thermodynamic dependences, which are described in Section 2.3.4.

2.2 – Experimental Setup

This section details the equipment and methodologies used in measuring the quenching and spontaneous emission rates of krypton and its collisional partners. The discussion includes information about the test facility, the laser system, and all photodetectors used during the experiments, as well as the matrix of different test conditions used throughout the different experiments.

2.2.1 – Test Facility

The facility used in these experiments needed the capability of controlling and monitoring the thermodynamic conditions and composition of a mixture of gases in a test cell. A schematic of the facility can be seen in Fig 2.1 below. The primary body of the designed facility consisted of a 2 ¾-inch CF cross (6 ports), which was fitted with three UV-grade fused silica windows in three of its six ports to allow for optical access and transmission of the exciting radiation. An additional port was outfitted with a flange equipped with a static pressure probe and a K- or T-type thermocouple used in measuring the thermodynamic conditions within the cell. The static pressure was measured using a temperature-compensated vacuum pressure transducer (MKS Baratron 626A). The remaining two ports allowed the passage of the test gases into and out of the cell. The outlet section was connected to an additional 2 ¾-inch tee (three ports). The side port of this tee was outfitted with a static pressure port for measuring the static back pressure in the cell, which was done with an absolute pressure transducer (Omega PX309). The outlet of the CF-tee was connected through one-inch tubing to a needle or ball valve (depending on the situation), and then further connected to the vacuum system present in the room, which allowed the pressure to be reduced down to approximately 2.2 kPa. The section upstream of the primary test cell varied depending on the type of test being conducted (see the two following sections for the specific modifications).

All gases entering the facility were monitored for molar flowrate (SLPM) using calibrated flowmeters (Omega FMA-1612A, -1610A, -1609A, -1605A, depending on the flow rates). These along with the pressure transducers, thermocouples, and the signal outputs from the various photodetectors were recorded and monitored using a custom-built Labview VI.

2.2.1.1 – Test Facility – Variable Pressure Runs

When running an experiment at a constant temperature, variable pressure condition, the inlet port of the test cell was fit with an otherwise blind flange equipped with a single ¼-inch Swagelok tube fitting. In addition, the static back pressure transducer was removed and replaced with ¼-inch tubing leading to a metering valve and subsequently a secondary vacuum pump (Edwards RV). Additionally, the valve connecting the facility to the primary vacuum system was closed. This modification allowed for a much lower cell pressures, down to 400 Pa, though the smaller vacuum pump was unable to handle a flow of gas and hence the experiments were conducted on static fluid. This arrangement led to the best control of the pressure and minimized the leak rate (observed leak rate of 3-5 Pa/min at lowest pressures, reducing to 1-2 Pa/min above 10 kPa) in the test cell.

2.2.1.2 – Test Facility – Variable Temperature Runs

When conducting an experiment with a variable temperature, the inlet port to the test cell was equipped with a larger nozzle-block flange, which allowed for the insertion of supersonic nozzles prior to the injection into the test cell. Upstream of the nozzle block, an in-line gas heater was equipped (Omega AHP-7561 or AHPF-121, depending on the desired flow rates), which was in turn connected to a variable AC transformer to control the power output of the heater. All test gases were passed through this heater prior

to entering the test cell. The aforementioned supersonic nozzles were used when the desired temperature was below the static temperature in the room. Two nozzles were designed for this purpose, a Mach 2 and a Mach 3 design. A schematic of the test cell/nozzle block configuration with a supersonic nozzle inserted can be found in Fig 2.2.

2.2.1.3 – Test Facility – Photodetectors

There were three primary photodetectors used in this facility. The incoming and outgoing laser pulses were recorded with fast biased photodiodes (Thorlabs DET-10A and DET-210, respectively). The beam was split from the primary beam using fused silica wedges to direct them into the detector with sufficiently low amplitude to avoid damaging or saturating the detectors. A photomultiplier tube (Hamamatsu R636-10) was used to capture the fluorescence of the excited krypton gas. A narrow bandpass filter ($\lambda_c = 760$ nm, 10 nm FWHM) was used to isolate the stronger of the two fluorescent transitions for detection. The placement of the PMT and incident photodiode can be seen in Fig 2.3. The photomultiplier tube was supplied with voltages ranging from 700 to 1350 V using a regulated high-voltage power supply (SRS PS350). The outputs from these various photodetectors were read using a fast oscilloscope (Tektronix TDS 3054, 5 GS/s). The oscilloscope was subsequently read into, and recorded by, a custom Labview VI using a GPIB connector.

2.2.2 – Laser System and Optics

The $5p[3/2]_2 \leftarrow 4p^6\ {}^1S_0$ transition is excited via two-photon absorption at 214.7 nm. To generate this wavelength a method known as sum-frequency generation (SFG) was employed. Here, two beams of like polarization but different frequency are combined in a nonlinear birefringent crystal to generate light at the sum of the two combined frequencies. To generate the 214.7 nm light, wavelengths of 354.7 nm (third harmonic of

an Nd:YAG laser) and 544 nm were combined in the aforementioned fashion. The 354.7 nm light is generated by a frequency-tripled Nd:YAG laser (Coherent Infinity 40-100). Though other, higher-pulse-energy lasers were available, this particular laser has a shorter pulse duration (4 ns FWHM at 1064 nm, 2 ns FWHM at 354.7 nm), in addition to a narrower line width of 250 MHz. The 544 nm light was produced by a dye laser (Lumonics HD-300), operated with Fluorescein 548 dye doped with NaOH (2:1 molar ratio) to shift the peak output wavelength closer to the desired 544 nm. The dye laser was pumped with an independent Nd:YAG laser (SpectraPhysics PIV-400, frequency doubled). The temporal pulse width of the dye laser was much longer than that of the 354.7 pulse (11 ns FWHM). Both of these beams were directed through half-wave plates and telescopic lens pairs to match the polarization and improve the spatial overlap, respectively. These two pulses were then combined in a Type-I BBO (beta-Barium Borate) crystal. To optimize the temporal overlap of the two pulses, the two separate pulses were monitored with a single photodiode (Thorlabs DET-210) and oscilloscope (Tektronix TDS 224, 1 GS/s) before entering the BBO crystal enclosure, and the delays on the triggering hardware (SRS DG535 pulse generators) adjusted accordingly. A full schematic of this laser layout with all relevant optics is shown in Fig. 2.4. The resulting pulse of 214.7 nm light had a pulse width 1.2 ns; a sample temporal trace of this laser pulse can be found in Fig. 2.5.

To optimize the fluorescence signal, an excitation scan was conducted. An intensified camera (Roper Scientific PI-MAX III) replaced the photomultiplier tube in the test facility, and the beam of exciting radiation was passed through the test cell. To increase the fluorescence signal, the beam was focused using a 300 mm UV-fused silica spherical lens, with the focus lying at the center of the camera's field of view. The dye laser was then scanned over a range of wavelengths around the desired 544 nm, and the

resulting images of the fluorescence were recorded for later post-processing. The results of this scan are shown in Fig. 2.6; the peak at 544 nm was found to have a linewidth of 0.006 nm FWHM, though this does represent the convolution of the laser linewidth with that of the electronic transition. Since this atomic transition linewidth is quite narrow, its contribution to the overall recorded lineshape was negligible. Note also the slight shift of wavelength from the expected peak; this was an effect of slight miscalibration in the dye laser positioning parameters.

In these experiments, controlling the intensity of the light proved crucial in acquiring consistent data. The intensity was controlled in two fashions. First, the overall energy of the pulse was set by first maximizing the energy through optimal spatial and temporal overlap, in addition to the phase-matching angle of the BBO crystal. The maximum energy was then attenuated by shifting the temporal overlap of the lasers until the desired energy was attained. Second, the focus of the light through the test cell was used to optimize signal while avoiding either saturating the PMT or inducing stimulated emission on the desired transition. To meet these criteria, a low pulse energy was used, ranging from 30 to 200 μJ (usually a mean of 75 μJ, though the RMS shot-to-shot variations were nearly 50%), and a long-focal-length spherical lens (750 mm) was used, with the focus lying outside the test section. To determine the acceptable pulse energy to use in these studies, the integrated fluorescence signal (obtained by integrating the signal from the PMT with respect to time) was compared to the exciting laser energy with the desired lens in place. By Eq. 2.1, the fluorescence signal should be quadratically dependent on the laser pulse energy for weak pumping. The results for this investigation are presented in Fig. 2.8. As can be seen in Fig 2.8a, this quadratic dependence was held quite accurately for lower pulse energies, the maximum energy used in the observed range being 440 μJ. When the range of this analysis was extended, the effect of

stimulated emission became apparent (see Fig 2.8b). While the signal continued to increase with increasing energy, the behavior changed to that of a nearly linear trend. Therefore, it was crucial for these studies to keep the pulse energy well below that threshold. Given the variability in the pulse energy, it was prudent to keep the maximum energy below half of this threshold.

In addition to properly attenuating the laser pulse energy, many different lens combinations were tried when optimizing the optical system including a focused and defocused 300 mm spherical lens, a focused and defocused 500 mm spherical lens, a focused 500 mm cylindrical lens, and a focused 750 mm spherical lens in addition to the aforementioned defocused 750 mm spherical lens. With the exception of the single cylindrical lens, the focused cases induced stimulated emission in the krypton and were consequently not used. The defocused cases all gave consistent results (repeatable runs with fixed conditions), but the 750 mm gave the strongest signal (higher than the focused 500 mm cylindrical) likely due to the higher intensity over a longer path. Though this observation would suggest that an even longer focal length would be preferable, the physical limitations of the space precluded the use of a slower optic. The beam path through the test facility is depicted in Fig 2.7.

2.2.3 – Experimental Methodologies and Procedures

To obtain consistent results in these experiments, a fixed protocol of activities was followed to ensure that there was no contamination or other unknown bias in the results that could skew the interpretation of the data.

2.2.3.1 – Variable Pressure Runs

These experiments were done statically, i.e. the same fixed volume of gas was used throughout the run rather than flowing. This method was used for several reasons.

First, as krypton is quite expensive, it conserved the amount of gas used. Second, this method ensured that the mixture did not vary during the test. Finally, by allowing the use of the secondary vacuum pump, lower pressures could be attained, allowing a more accurate extrapolation to find the spontaneous emission rate.

During these runs, the system was first inspected for leaks by pulling the vacuum as low as was possible (around 400 Pa), and allowing it to sit for several minutes to ensure the leak rate was minimal. Following that, the cell was back-filled with krypton to 100 kPa and subsequently pulled to full vacuum again. This step is essentially a purge to ensure that the composition of the 400 Pa is as close to pure krypton as is possible. If the previous run was with a gas that was a strong quencher (air, ethylene), this step was repeated. Next, the desired mixture of gases was injected into the cell. The mole fractions of the individual gases were set by observing the rise in pressure associated with each injected species. For example, if a mixture of 0.75-0.25 Kr-air mixture was used with a maximum pressure of 20 kPa, the cell was first filled with 15 kPa (including the residual from the previous step) of Kr and then 5 kPa of air. The run was then conducted by recording a set of waveforms and pressure/temperature readings at each given pressure (usually 30-50 samples per set), after which the pressure in the cell was reduced by opening the metering valve between the vacuum pump and the test cell. Usually, at pressures above 20 kPa, the pressure was dropped in decrements of 5 kPa, and below that in decrements range from 2.5 to 0.5 kPa, with the finer resolution at lower pressures. The temperature was monitored in these runs to ensure that it stayed constant. Generally, the tests were conducted at room temperature of around 291 K, and this was used as a reference condition in all measurements.

2.2.3.2 – Variable Temperature Runs

The variable temperature runs differed from the variable pressure runs in that the test gases were flowing during the run. While the option existed to statically heat the cell was viable, the low temperature runs were problematic as temperatures as low as 90 K were desired (which would require a cryogenic pump). This process required more elaborate measures to prevent needlessly wasting krypton (although it would have simplified the analysis considerably if similar mixtures to those used in the variable pressure runs were used). Thus, the runs were all run with a buffer gas (helium or nitrogen), krypton, and the quenching species. See the numerical methods (Appendix 2A.3) for the methods used in extracting the desired information from these compound runs.

The variable temperature runs were initiated by conducting the same sort of leak test performed during the variable pressure runs. This was more of an issue with the temperature runs since the repeated thermal cycling on the system annealed the copper gaskets used in the construction of the facility. Thus, it was commonplace to have to replace one or two gaskets each day of testing, even when proper gaskets (silver/gold-plated or fully annealed copper) were used. Since the gases were flowing in these experiments, it was not, in general, necessary to purge the facility beyond opening the valve to the large vacuum system. Often, as a precautionary measure, the system was initially purged with helium. Next, the desired mixture was set using the flow meters. In general, the krypton was set to a flow rate of 0.3 to 1 SLPM (usually on the lower end), followed by the desired quenching species, and finally the buffer gas if one was used. Generally the buffer gas was only necessary for the supersonic runs, as a minimum flowrate was needed to start the nozzle correctly (depending on the back pressure). Following this, the heater was activated. Once a desired temperature was reached (usually

increments of 25 K stagnation temperature), a set of 30-50 samples was taken in the same manner as the pressure runs. It should be noted that the krypton was only flowing when the samples were being collected. Since it generally comprised a small fraction of the overall mixture, the effect on the temperature was negligible. It should also be noted that the pressure did tend to vary slightly during these runs. However, this deviation was recorded with the data sets and compensated for in the data processing.

For the low temperature runs, an alternate method was employed in some cases to test the validity of the methodology. The premise behind this technique was that, instead of relying on the in-line heater to change the temperature, the flowrate through one of the supersonic nozzles was varied. To begin a run of this variety, a fixed mixture of the krypton and quencher was set (e.g., 0.5 SLPM Kr and 0.8 SLPM air). Then, with one of the supersonic nozzles in place, the buffer gas (again, usually helium) was added in increments of 5 SLPM. This procedure would drop the temperature gradually until the point that the nozzle choked, after which the temperature would begin dropping precipitously (an example temperature trace from one of these runs can be seen in Fig 2.9 plotted against the krypton mole fraction). This method allowed a broad range of temperatures to be measured with a single nozzle as the flow transitions from subsonic to perfectly-expanded to underexpanded. An uncertainty arises because the condition between being choked and fully started could potentially cause a shock to sit in the nozzle before the measurement point. However, the probes measuring the temperature and pressure also sit behind this point, and as such they were seeing essentially the same thermodynamic conditions. In general, the results were very similar to those taken in the other method, but both were usually taken to ensure consistency.

A final note about the low temperature runs; regardless of the exact method used in data collection, the position of the probe volume (where the fluorescence was being

excited) was crucial. The probe volume had to sit exactly at the exit of the supersonic nozzle; in some instances the beam was made to clip the downstream edge. This step ensured that the region of interest did not receive interference from any flow structures (i.e. shockwaves). In the fluorescence facility, the thermodynamic probes sat roughly 7 mm downstream of the exit of the nozzle. If the probe volume resided too far downstream of the nozzle, it was possible the probe volume would clip behind the bow shock that formed on the stagnation temperature probe. Subsequently, all the data points collected at this location would be at the thermodynamic conditions before the shock, after the shock, or a mixture of the two. Without any means of distinguishing between the thermodynamic state in which each sample resided, the data from these cases were rendered useless. The precautionary movement of the beam to clip the nozzle was sufficient to fix the problem, once the exact cause of the stated problem was found.

2.2.3.3 – Test Matrix

These experiments sought to quantify the temperature and pressure dependence in the quenching rates of two different gases, nitrogen and air. In addition, the quenching rates of helium, oxygen, and ethylene are measured as well. The sets of different runs and gas compositions are shown in Table 2.1 below.

Summary of Runs

Pressure dependent runs		
Gas Mixture	Mole fraction of each component	Number of runs at each condition
Kr	Kr-Kr: 1	14
Kr-N_2	Kr – 0.875; N_2 – 0.125	6
	Kr – 0.75; N_2 – 0.20	9
	Kr – 0.50; N_2 – 0.50	4
Kr-He	Kr – 0.75; He – 0.25	2
	Kr – 0.50; He – 0.50	2

Table 2.1: Summary of runs performed in lifetime measurements

	Kr – 0.25; He – 0.75	5
	Kr – 0.10; He – 0.90	3
Kr-air	Kr – 0.875; air – 0.125	4
	Kr – 0.75; air – 0.25	6
Kr-O_2	Kr – 0.95; O_2 – 0.05	4
	Kr – 0.90; O_2 – 0.10	4
	Kr – 0.875; O_2 – 0.125	1
	Kr – 0.75; O_2 – 0.25	2
Kr-C_2H_4	Kr – 0.95; C_2H_4 – 0.05	6
	Kr – 0.90; C_2H_4 – 0.10	1
	Kr – 0.875; C_2H_4 – 0.125	2
	Kr – 0.75; C_2H_4 – 0.25	1

Temperature Dependent Runs

Gas Mixture	Mole fraction of each component	Temperature Range (K)
Kr-He	Kr – 0.010; He – 0.99	290 – 550
	Kr – 0.004; He – 0.996	290 – 600
	Kr – 0.004; He – 0.995	150 - 270
	Kr – 0.005; He – 0.995	120 – 230
	Kr – 0.005; He – 0.995	99 – 210
Kr-N_2	Kr – 0.025; N_2 – 0.975	290 – 610
	Kr – 0.017; N_2 – 0.983	285 – 655
	Kr – 0.016; N_2 – 0.984	155 – 260
	Kr – 0.016; N_2 – 0.984	110 – 220
Kr-He-N_2	Kr – 0.025; N_2 – 0.025; He – 0.950	95 – 215
	Kr:N_2 – 1:1; He – variable	100 – 285
Kr-air	Kr – 0.038; air – 0.962	290 – 600
	Kr – 0.017; air – 0.983	280 – 630
	Kr – 0.016; air – 0.984	140 – 250
	Kr – 0.016; air – 0.984	115 – 220
Kr-He-air	Kr – 0.025; air – 0.025; He – 0.950	105 – 215
	Kr:air – 1:2; He – variable	95 – 275
Kr-He-O_2	Kr – 0.04; N2 – 0.01; He – 0.950	285 – 580
		150 – 240
	Kr:O_2 – 1:3; He – variable	100 – 280
Kr-He-C_2H_4	Kr – 0.025; C_2H_4 – 0.025; He – 0.950	290 – 540
		295 – 600
		145 – 235
	Kr:C_2H_4 – 1:3; He – variable	105 – 290
Kr-N2-C_2H_4	Kr – 0.025; C_2H_4 – 0.075; N_2 – 0.900	285 – 630
	Kr – 0.050; C_2H_4 – 0.038; N_2 – 0.912	295 – 655

Table 2.1: Summary of runs performed in lifetime measurements

2.3 – Results and Discussion

This section details the results of the above-described experiments, focusing separately on the spontaneous emission rate, reference quenching rates, temperature-dependent quenching rates, and two-photon absorption cross-section.

2.3.1 – Spontaneous Emission Rate

The spontaneous emission rate was inferred from the variable pressure runs taken for pure krypton. Here, since the mole fraction was constant, the sum over all data sets was used to fit the quenching rate and spontaneous emission rate. The spontaneous emission rate was taken to be the value of the total decay rate extrapolated to zero pressure. A plot of the fluorescence lifetime versus pressure for the pure krypton runs can be seen in Fig 2.10a, while the total decay rate versus pressure for these same runs can be seen in Fig 2.10b. Note here that the best least-squares fit is given by the red line, while the 2σ uncertainty bounds are shown by the black lines. Here, it can be seen that the spontaneous emission rate is 37.861 ± 2.972 MHz. This corresponds to a natural fluorescence lifetime of 26.41 ± 0.46 ns. The values for these quantities for this particular transition vary mildly throughout the literature, ranging from 21.5 to 27.35 ns for the natural lifetime, though most are clustered at the higher end of this range. A summary of these data can be found in Whitehead, et al. [**82**]. It should be noted that the data used in performing these fits were limited to the data taken below 20 kPa. Beyond this point, the response time of the PMT began to interfere with the measurements, and so the data were not considered in these studies. However, the data needed for the runs in both the wind tunnel and subsonic jets/jet flame fall within this range either in terms of total or partial pressure, respectively.

2.3.2 – Pressure Dependence of Quenching Rates and Quenching Cross-Sections

The pressure dependence of the collisional quenching rate of krypton-krypton collisions can be found in Fig 2.10b. Here the slope of the least-squares linear fit represents the product of the quenching rate and the pressure. Since the composition for these runs is pure krypton, no consideration needs to be given to the mole fraction, and the total quenching rate and the specific quenching rate are directly related by the cell pressure. From this, the quenching rate is measured to be 2875 $\pm$ 185 Hz/Pa or 0.383$\pm$0.025 MHz/Torr. This value serves as the reference quenching rate for the later temperature dependent runs.

The tested buffer gases each possess a characteristic quenching rate. In these runs, a series of different mixtures of the desired buffer gas and krypton were tested, and the resulting total quenching rates were corrected for the spontaneous emission rate, the quenching rate of krypton, and the mole fractions of the mixture. This procedure allowed the specific quenching rate of the buffer gas to be extracted from the data. The reference specific quenching rates for Kr-He, Kr-N_2, Kr-air, Kr-O_2, and Kr-C_2H_4 are plotted in Fig 2.11. Here it can be seen that ethylene is the most efficient quencher, followed by oxygen, air, nitrogen, and helium. The air studied here is not a fixed N_2/O_2 mixture, but rather the air taken from the high-pressure compression system for the lab. Despite the potential contamination by trace quantities of water and oil vapors, the results for the air were quite consistent with the measurements made in nitrogen and oxygen, with the weighted sum of their reference quenching rates falling within 2 percent of the measured air quenching rate. A summary of these quenching rates is presented in Table 2.2.

As a further refinement to this data, the collisional quenching cross-section for the different collisional pairs can be extracted from the measured quenching rates. These are directly related through their respective definitions. That is, $\langle\langle\sigma_i\rangle\rangle = q_i\sqrt{\pi k\mu_i T/8}$, where

k is Boltzmann's constant and μ_i is the reduced mass for the collisional pair, here defined as $\mu_i = (m_{Kr} + m_i)/(m_{Kr}m_i)$. The reference quenching rates and cross-sections are presented in Table 2.2.

Summary of Reference Quenching Data

Collisional Pair	q_{ref} *(kHz/Pa)*	$q_{ref}/q_{Kr,ref}$	σ_{ref} (Å^2)	$\sigma_{ref}/\sigma_{Kr,ref}$
Kr-Kr	2.875 ± 0.185	1.000	3.016 ± 0.576	1.000
Kr-He	0.917 ± 0.135	0.319	0.290 ± 0.043	0.096
Kr-N_2	18.88 ± 1.25	6.540	13.96 ± 0.93	4.629
Kr-O_2	58.32 ± 1.07	20.29	45.51 ± 4.19	15.09
Kr-C_2H_4	91.02 ± 4.53	31.66	67.61 ± 3.36	22.14
Kr-air	27.46 ± 2.14	9.553	---	---

Table 2.2: Summary of Reference Quenching Data

2.3.3 – Temperature Dependence of Quenching Rates and Quenching Cross-Sections

The temperature dependence of the krypton quenching rate was derived from runs of krypton-helium and krypton-nitrogen as described in Appendix 2A. The temperature dependent quenching rate is plotted in Fig 2.12. Since the mole fractions of krypton in these runs were minimal (peaking near 5 percent), the uncertainty in the pure krypton quenching rate measurements was quite large. Table 2.3 below shows the corresponding range of the temperature exponents.

The same buffer gases tested in the pressure-dependence runs are studied for the temperature dependence as well. The results of these tests are summarized in Fig 2.13 while the uncertainty bounds are listed in Table 2.3. Note here that the uncertainties in the buffer gases are much smaller than that of pure krypton. This is due to the fact that the quenching gas was the dominant species, and thus the krypton rate could essentially be neglected. As the original fit to the total quenching rate was generally of high quality,

this means that the uncertainty arose predominantly from the krypton fit rather than that of the buffer gas. Here it can be seen that the oxygen quenching rate diminishes most rapidly, followed by krypton, ethylene, air, helium, then nitrogen. A few notes regarding these fits for the temperature variation: first, the variation rates for nitrogen and oxygen match the measurements of Hsu et al. [**83**], taken at high temperatures. From those studies, the power-law fit for nitrogen was seen to vary to the -0.26, whereas the present studies show the variation to be to the -0.269. Likewise the variation in oxygen was seen to be -0.64 in the Hsu studies and -0.643 in the present studies. Both of these deviations (in either the Hsu studies or the present studies) fall well within the experimental uncertainties. Thus, it is seen that, at least at the ranges over which the measurements were made, the same trends hold.

Second, with regards to the variation of the air quenching rate; it is observed that it still tracks very closely as a weighted sum of the nitrogen and oxygen over the temperature range presented. Despite this, it still adheres well to a power-law dependence. This observation is not surprising when the uncertainties in the nitrogen and oxygen fits are considered. That is, even though the algebraic weighted sum cannot be fit with a single power law ($AT^n \neq BT^{n_1} + CT^{n_2}$ for $n_1 \neq n_2$), the discrepancy in the fit can be accommodated by the overall uncertainty in both the constituent O_2 and N_2 fits and that of the air. While this result is consistent with the pressure-dependent quenching measurements, there is still some lingering question as to the true constituents of the mixture. However, from a practical standpoint the simple power-law dependence is sufficient for capturing the temperature dependence of the air.

Likewise similar fits can be made for the quenching cross-sections for each collisional pair. Again, these fits are detailed in Fig 2.14 and Table 2.3. A few notes should be made regarding the data therein presented. First, the temperature dependence of

the fits is found to be universally $\sqrt{T}$ higher than that of the quenching rates. This observation is due to the definition of the quenching cross-section as expressed in Eq. 2.3a above. The only exception to this point is the krypton-krypton cross-section, which suffers from the same noise-related issues found in the quenching rate. Nonetheless, the deviation lies within 4 percent (well within the experimental uncertainty), so the accuracy is not questioned in this regard.

Next, the quenching cross-section for krypton is seen to vary minimally throughout the entire temperature range. This observation is very consistent with the observations made by Narayanaswamy, et al. [**90**] in studying an underexpanded jet structure. Therein, the quenching cross-section of krypton was assumed constant in using the LIF signal as a measure of flow density, and the results were found to be very consistent with theoretical predictions. Since the quenching cross-section has been shown to vary roughly 6 percent across the entire measured temperature range, this observation is easily explained, and can also help to estimate some of the discrepancies they observed in the vicinity of the terminating Mach disk, where the Mach number and temperature are the lowest.

Summary of Temperature Dependence of Quenching Rates and Cross-Sections

Collisional Pair	$\boldsymbol{n}\,(\boldsymbol{q})$	$\boldsymbol{n^{+}(q)}$	$\boldsymbol{n^{-}(q)}$	$\boldsymbol{n(\sigma)}$	$\boldsymbol{n^{+}(\sigma)}$	$\boldsymbol{n^{-}(\sigma)}$
Kr-Kr	-0.524	-0.682	-0.317	-0.041	$+0.139$	-0.184
Kr-He	-0.364	-0.415	-0.294	$+0.138$	$+0.201$	$+0.064$
Kr-N_2	-0.269	-0.283	-0.243	$+0.230$	$+0.310$	$+0.209$
Kr-O_2	-0.643	-0.703	-0.521	-0.148	-0.034	-0.204
Kr-C_2H_4	-0.491	-0.611	-0.452	$+0.010$	$+0.044$	-0.105
Kr-air	-0.428	-0.488	-0.403	---	---	---

Table 2.3: Summary of Temperature Dependence of Quenching Rates and Cross-Sections

2.3.4 – Temperature and Pressure Dependence of the Effective Two-Photon Absorption Cross-Section

The effective two-photon absorption cross-section for the $5p[3/2]_2 \leftarrow 4p^6\ {}^1S_0$ transition exhibits a strong thermodynamic dependence as well, owing largely to the broadening of the absorption lines with both pressure and temperature [**81**]. Thus, quantifying this dependence is critical in attempting to calibrate the LIF signals obtained in experiments. In both the case of the temperature dependence and the pressure dependence, a ratiometric method was utilized as detailed in Appendix 2A. The results of these studies are presented in Fig 2.15a and 2.15b. It can be seen here that there is a marked decrease in the effective absorption cross-section with increasing temperature. Following the same power law dependence used for the temperature-dependent quenching rates, the variation with respect to temperature can be expressed as

$$\frac{\sigma_0^{(2)}}{\sigma_0^{(2)}} = \left(\frac{T}{T_{ref}}\right)^{-0.310} \qquad 2.7$$

A few comments can be made regarding this observation. First of all, the variation in the absorption cross-section is relatively minor in the flows of interest in to the present study. More specifically, in a typical temperature variation seen in one of the hypermixing flowfields, the two-photon absorption cross-section varies by only 10 percent (over approximately a 60 K temperature variation). The exception to this statement is a flow such as a flame in which there is a very large temperature gradient. Consider an ethylene jet flame with an approximate peak temperature of 1900 K. Such a flow could easily exhibit a variation in the effective absorption cross-section of up to 40 percent throughout the field, if the data could be faithfully extrapolated to those temperatures.

The pressure dependence of the effective absorption cross-section is far more drastic than the temperature variation; here the reference pressure was taken to be the maximum pressure at which accurate lifetime measurements could be made (just about

20 kPa). It is seen that the absorption coefficient follows a positive power-law dependence given by

$$\frac{\sigma_0^{(2)}}{\sigma_0^{(2)}} = \left(\frac{P}{P_{ref}}\right)^{0.893} \qquad 2.8$$

Some increase in the effective absorption cross-section is to be expected due to pressure broadening of the absorption line, and the nearly linear behavior corroborates this notion. That is, the absorption linewidth scales linearly with the pressure, which when spectrally integrated with the fixed laser lineshape results in the nearly linear increase in the overall absorption. Regardless of the extent of the observed change in effective cross-section, the variation observed is likely to be inconsequential in the fluorescence measurements made in situ. This is due to the fact that most of the regions where fluorescence is imaged are essentially isobaric. Consider the wind tunnel measurements described in Chapter 4; here the static pressures vary mildly around 4 kPa. Over this range, the variations in effective absorption cross-section are about 5 percent. Likewise, in free-jet situations, the partial pressure varies in much the same fashion. Thus, even though the variation with pressure is significant, the actual pressure variations in the flows are not significant.

To examine this pressure dependence further, a number of excitation spectra were collected over various pressures for both pure krypton and krypton-helium mixtures. The spectra for pure krypton are shown in Fig 2.16, showing pressures ranging from 5 kPa to atmospheric pressure. An unexpected trend is found for increasing pressures; as the pressure is increased, a significant asymmetric broadening is observed. As the frequency of the exciting radiation is tuned off resonance, with increasing frequency a mild broadening is observed with increasing pressures. In contrast, decreasing the excitation frequency below resonance causes a long tail to form on the spectra, which grows in magnitude with increasing pressure. These same total pressures were then assayed in

krypton-helium mixtures by fixing the partial pressure of krypton (at 5 kPa) and increasing the total pressure by adding helium to the test cell. The results of these scans are presented in Fig 2.17; the spectra are seen to remain unchanged at all pressures tested. It can be concluded that the linewidths measured in Fig 2.17 represent the true laser linewidth, which has been quoted in Section 2.2.2.

These experiments show that krypton exhibits a strong self-broadening effect with pressure. However, this broadening does not represent simple pressure broadening, as it is asymmetric [**91**]. The appearance of these various lineshapes are visibly akin to the amplified spontaneous emission (ASE) observed by Miller [**81**] when pumping the nearby $5p[5/2]_2 \leftarrow 4p^6\ {}^1S_0$ transition of krypton. However, it is unlikely that ASE is the cause of this distortion due to the fact that the emission is observed when the excitation is tuned far off resonance (several full laser linewidths for the highest pressure cases) and it is not directional (i.e., it does not strictly follow the beam path). This does not conclusively preclude ASE, but further tests would need to be conducted to verify this result. There are several other possibilities for the appearance of the observed self-broadening lineshapes. Halfmann et al. [**92**] examined the effects of non-resonant excitation of two-photon xenon transitions. These studies found that the absorption lineshape broadened considerably when higher energies were utilized in pumping the transition off-resonance. However, the asymmetric form of the excitation spectrum was only visible when probing with mutli-photon ionization (MPI), not the collection of fluorescence, and the broadening was much narrower than observed in the present studies. Additional investigations into effects of pressure and resonance broadening in krypton transitions can be found in the studies of Vaughan [**93**] [**94**] and Ferrell et al. [**95**]. At present, it is unclear exactly what the mechanism of this broadening is. Regardless, it is apparent that the broadening of the absorption line is pressure-dependent

and only occurs for krypton-krypton interactions. From this, it can be concluded that the present data for the two-photon absorption lineshape stays valid up to the reference pressure in these experiments (20 kPa), where the broadening is of similar order to the laser lineshape.

One of the shortcomings of the present measurements is that only the stronger fluorescence transition is being observed. It has been observed that the addition of self-quenching changes the effective branching ratio for these two-state decaying transitions [**96**] [**97**]. Thus, particularly in the case of the pressure runs (since the total quenching rate is a much stronger function of pressure than temperature), it is likely that part of the missing signal, which is numerically resulting in a decreased effective absorption cross-section, is found in the other fluorescence band. Likewise, the mild decrease in total quenching rate seen with temperature would have a similar effect.

One of the difficulties faced in making these measurements is that there is virtually no literature on the thermodynamic dependence of the effective absorption cross-section for two-photon transitions in noble gases. The studies which have covered this subject in detail utilize the fluorescence species as a marker for density measurements of a different species [**84**] [**85**] [**86**]. Thus, while the ratio of the effective two-photon absorption cross-sections is relevant, the thermodynamic condition experienced is always the same. It was implicitly assumed in these studies, in which xenon was used to measure atomic oxygen densities, that the ratio was fixed. In addition, theoretically predicting the cross-section at a fixed thermodynamic state is nontrivial [**97**]. As such, it is difficult to know if the effects observed are truly variations in the effective two-photon absorption cross-section or are from unresolved thermodynamic dependences not accounted for in the fluorescence model. Nonetheless, the measurements are critical in calibrating the LIF signals since they clearly encompass some portion of the

thermodynamic dependence of the signal. That is, assuming the fluorescence model presented in Eq. 2.1 is utilized, the inclusion of this parameter is necessary.

2.4 – CONCLUSIONS

The collisional quenching rates for the two-photon excited $5p[3/2]_2 \leftarrow 4p^6\ {}^1S_0$ transition in krypton are measured for various buffer gases. It was observed that krypton exhibit some minor self-quenching, though the quenching caused by other collisional partners far exceeded this rate. Of the gases tested, ethylene proved to be the most efficient quenching species, followed by oxygen, air, nitrogen and helium. The quenching rates were found to universally decrease with temperature. For some gases, particularly krypton and ethylene, the temperature dependence was shown to be an effect almost purely of the density and relative molecular velocity, rather than a strong variability in the collisional quenching cross-section. The other gases tested did not follow this trend; exhibiting a much stronger temperature dependence in the aforementioned cross-section. The relative effective two-photon absorption cross-section was measured as a function of the temperature and pressure. A weak temperature dependence was found, trending downward as the temperature increased. The pressure dependence was much more pronounced, with the effective absorption cross-section increasing nearly linearly with pressure up to nearly 20 kPa. Additional inquiries into the pressure effect revealed an asymmetric pressure-dependent broadening of the absorption lineshape, with fluorescence signal visible when the laser line was tuned far off resonance. It is unclear at present whether the results for the pressure-dependence of the effective two-photon absorption cross-section are correct or simply a function of an unaccounted thermodynamic dependence in the fluorescence model. Regardless, should the fluorescence model in question be utilized in quantifying LIF measurements the inclusion

of this term is essential as it encompasses a fraction of the thermodynamic dependence of the fluorescence signal.

2.5 – SUGGESTED WORK

There were a number of shortcomings in the present studies that could be amended in future work to both extend the range of thermodynamic validity of the measurements and also attain a higher degree of confidence. First and foremost is to utilize a photomultiplier tube with a shorter response time. This simple modification will allow the measurements taken to be extended to higher pressures while also allowing for more dilute mixtures of krypton to be utilized. Second, when trying to perform the low-temperature runs, it would be beneficial to use a liquid-N_2-cooled cryogenic test cell instead of the supersonic nozzle flow reactor used in the present studies. The reason for this change is that it would permit lower, volumetrically uniform temperatures. In conjunction with a static heater, the gaseous mixture temperature could be varied from approximately 70 K up to ambient temperatures without having to dilute the krypton substantially (since the tests could be done statically). One potential issue that could arise with a setup such as this would be condensation of gases (water vapor and oxygen) on the internal surfaces of the cell. However, the higher integrity of the data would be worthwhile tradeoff for more rigorous monitoring of the temperature to help avoid these issues. Next, it would be extremely useful to understand the thermodynamic dependence of the fluorescence signal by measuring the temperature and pressure dependences of the emission spectra. Apart from being generally informative, these data could inform a number of the present studies, particularly the effects of changing quenching rates on the relative branching ratio of the fluorescence and the effective two-photon absorption cross-section calculations. Finally, devising a way of quantifying the collection efficiency

of the optical system would make measurement of the two-photon absorption cross-section in the absolute sense possible and would remain more accurate than an extinction-based method, assuming the same limitations in the excitation system described above.

A tangential study that would be informative to the present would be a parametric investigation into the observed excitation spectra in Fig 2.16. Specifically, conducting the scans at a fixed pressure but variable energy would be quite interesting. The excitation spectrum shown in Fig 2.6 was collected in atmospheric pressure krypton but without any focusing optics for the beam, but a higher pulse energy. The significantly diminished tail on that spectrum in comparison to those present in Fig 2.16, which were taken with a defocused positive focal length cylindrical lens, suggest an intensity-dependent effect. However, at the time these data were taken, too many variables were changed to conclusively say this was the case; the laser dye was recently changed, the bandwidth was slightly narrower, and the spatial and temporal profiles of the beam were different. Thus, no one-to-one comparison can be made at present. However, repeating these scans with uniform experimental conditions would help elucidate the cause the phenomenon, and adding the effect of laser intensity would further help isolate the source.

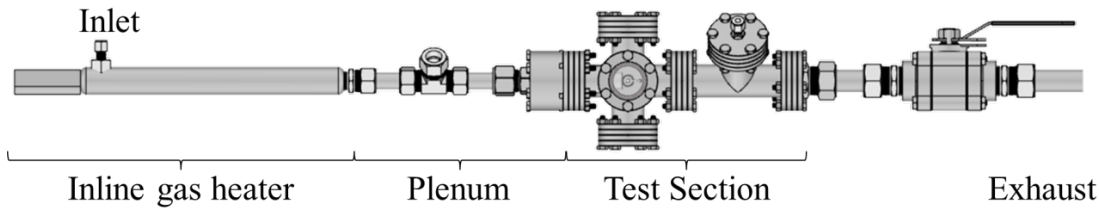

Figure 2.1: Diagram of flow reactor used in lifetime measurements.

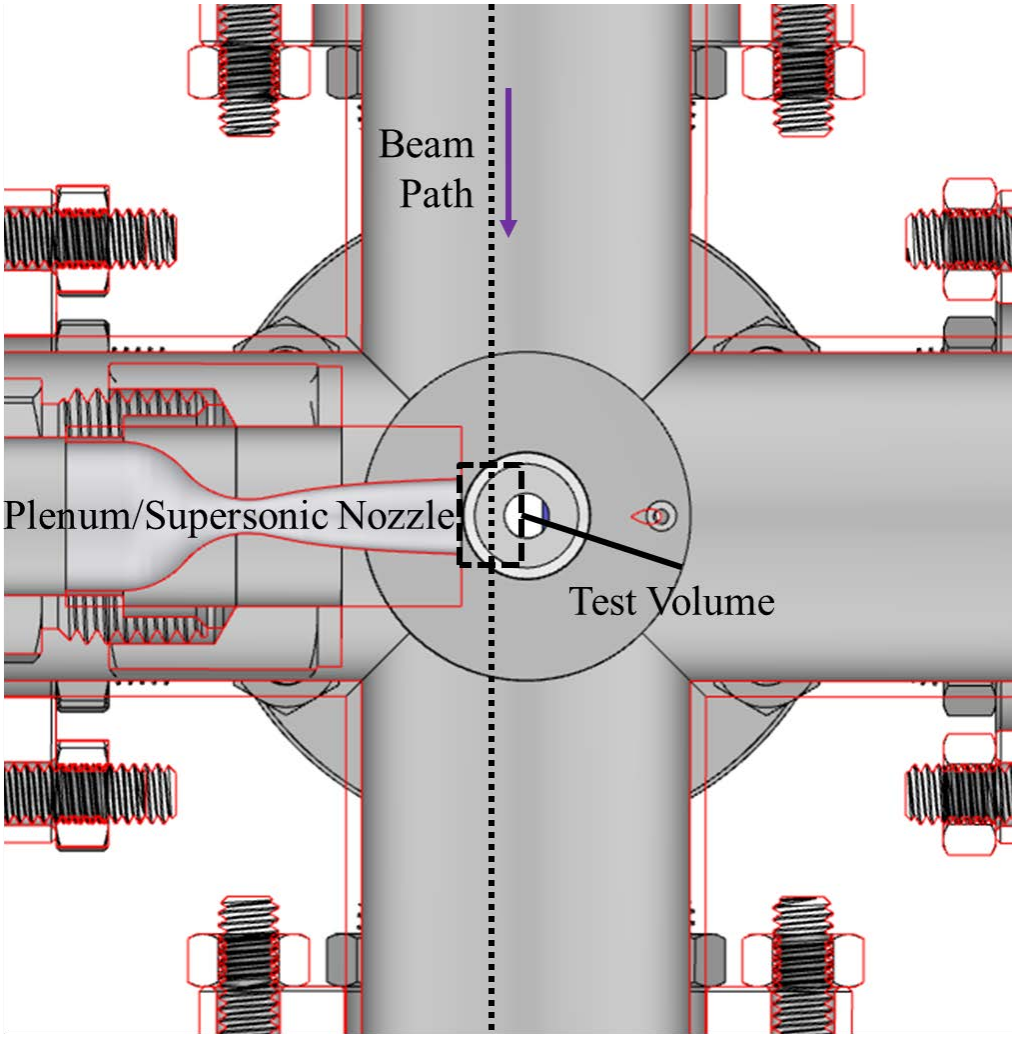

Figure 2.2: Diagram of supersonic nozzle orientation within test cell with beam path and test volume.

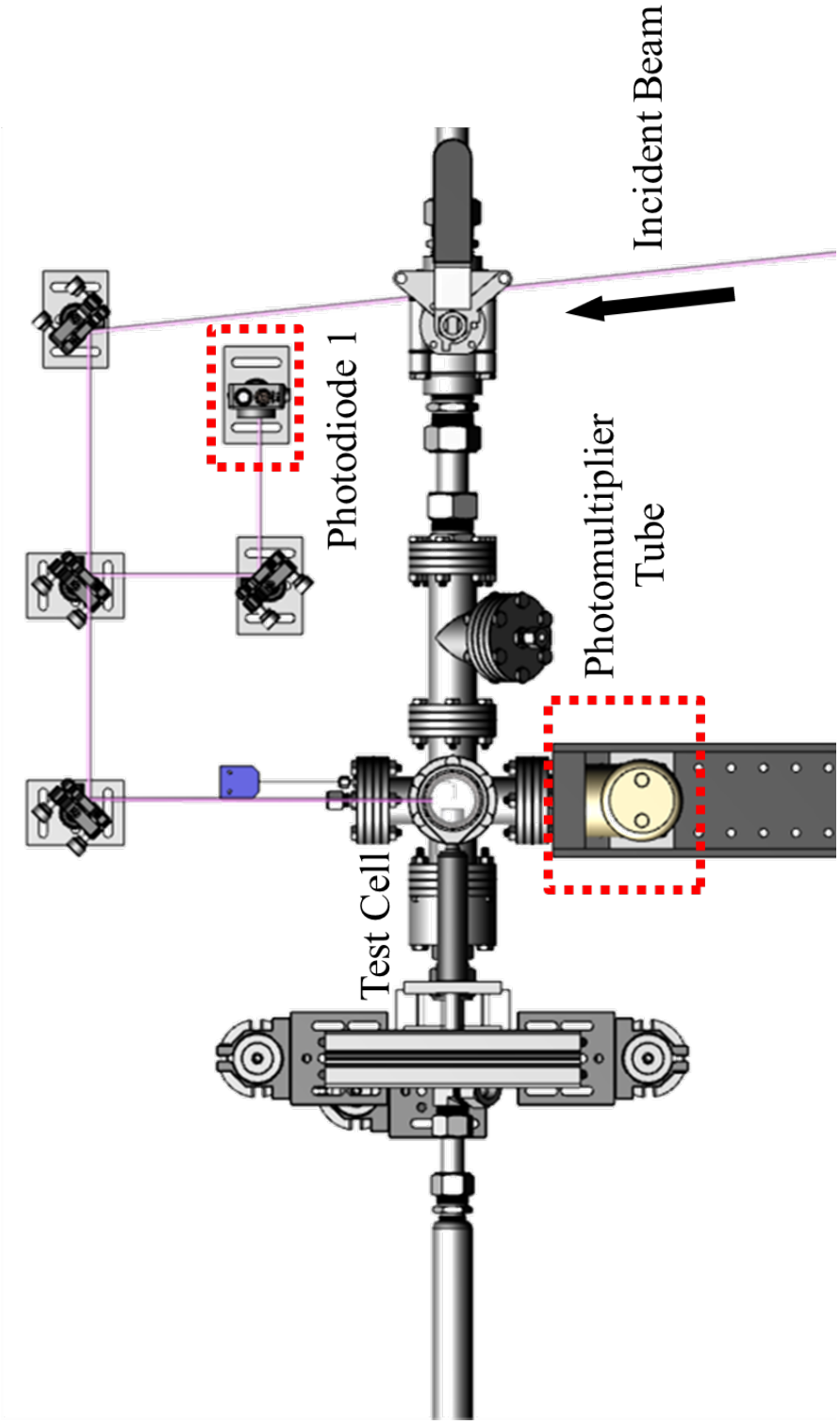

Figure 2.3: Orientation of photodetectors with respect to the test facility.

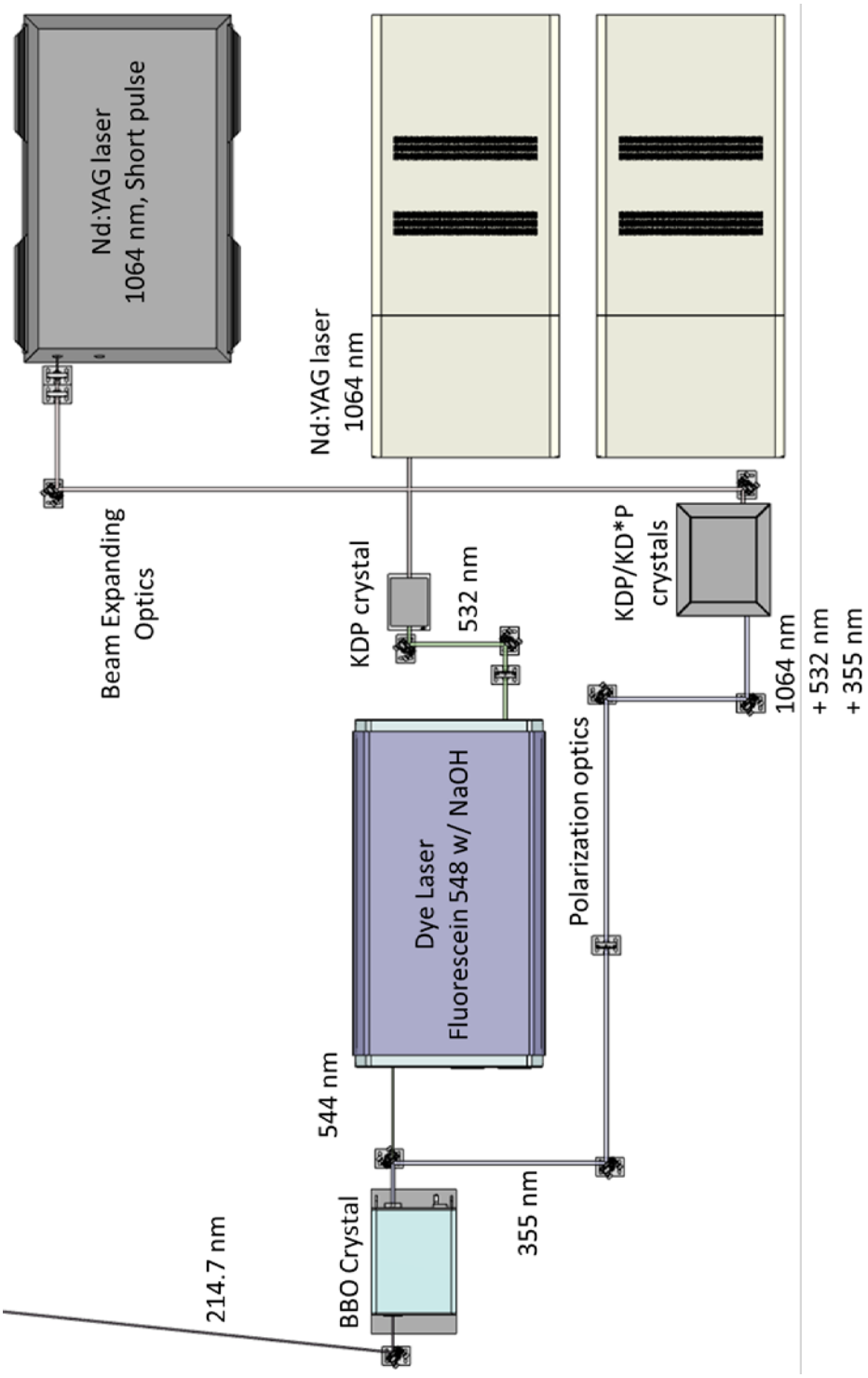

Figure 2.4: Diagram of sum-frequency generation setup for the fluorescence lifetime studies.

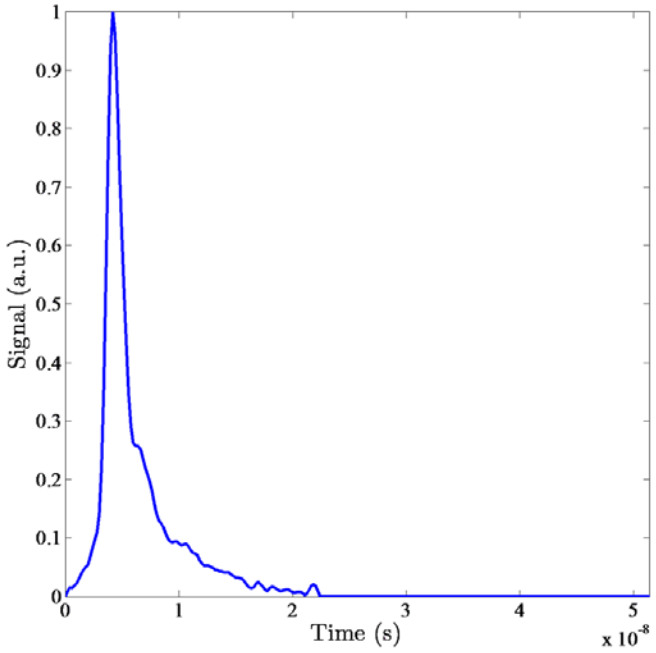

Figure 2.5: Sample temporal trace of 214.7 nm laser pulse used in lifetime studies.

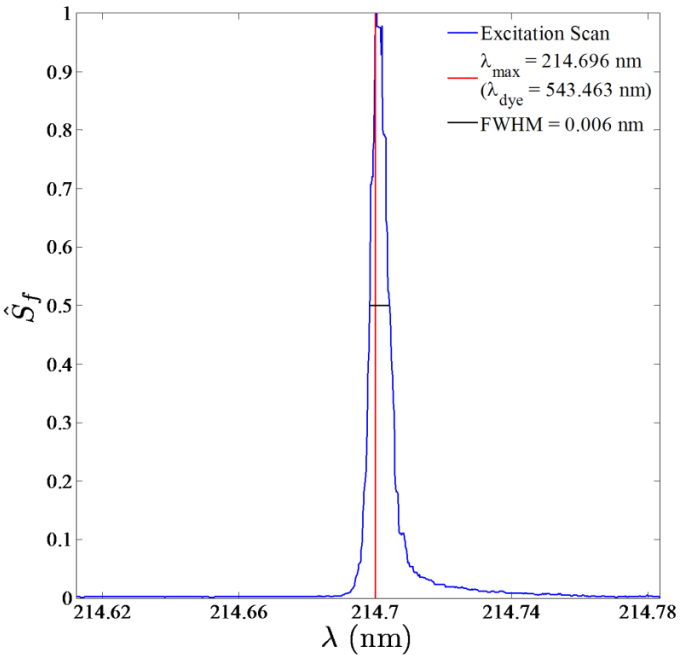

Figure 2.6: Excitation spectrum from sum-frequency generation setup for lifetime measurements

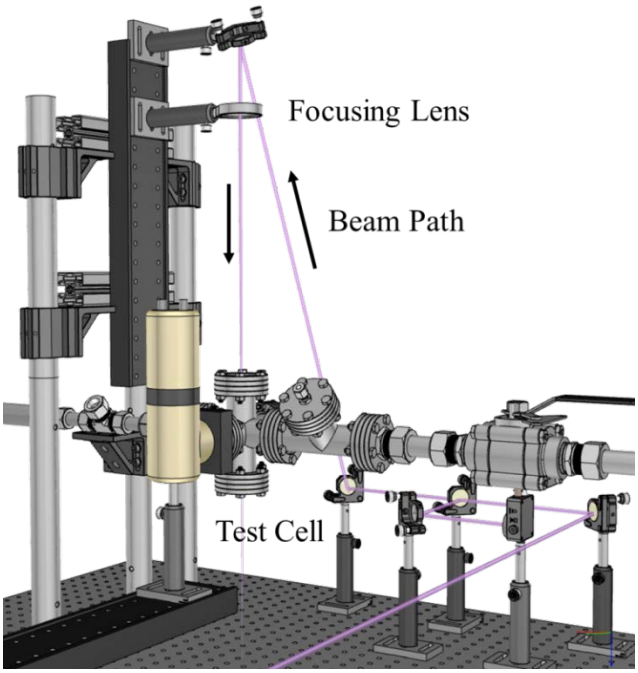

Figure 2.7: Diagram of exciting beam path through test cell.

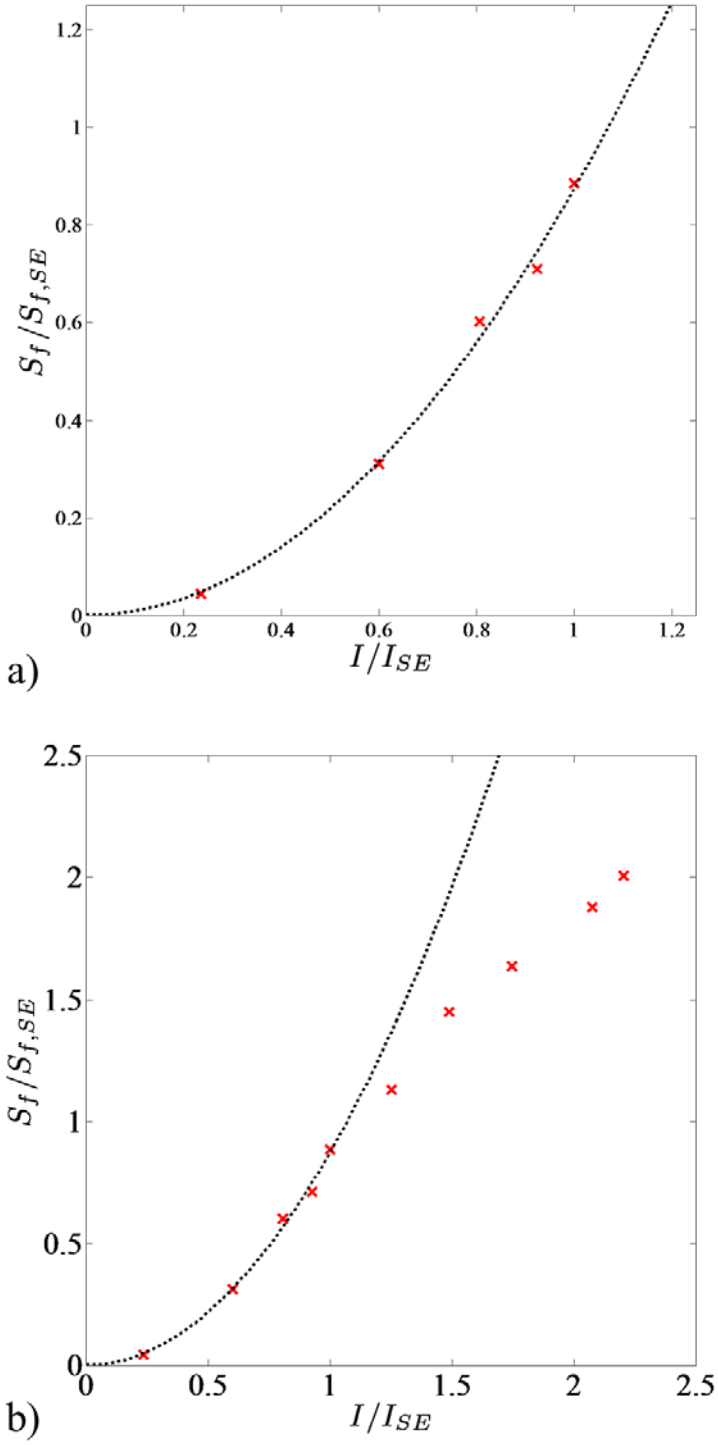

Figure 2.8: Dependence of fluorescence signal intensity as a function of excitation intensity. a) lower intensity and b) full scale.

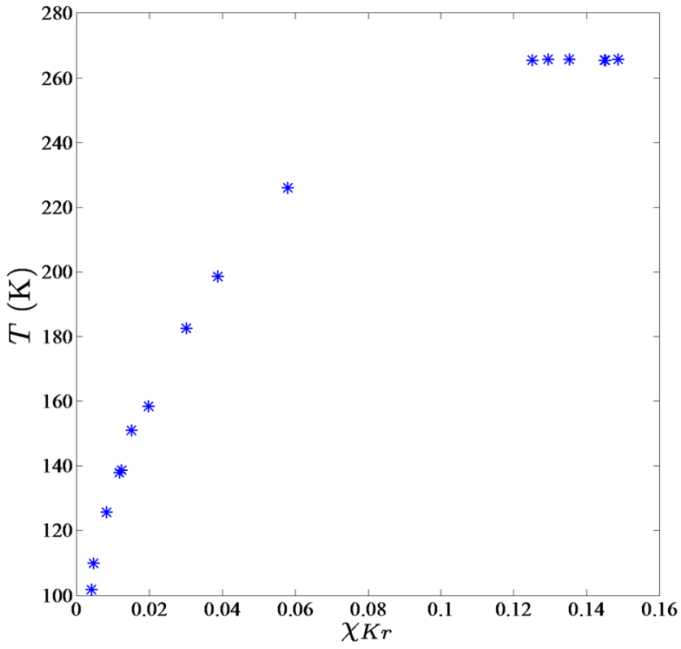

Figure 2.9: Example plot of temperature vs. krypton mole fraction for a variable-mixture, variable-temperature test run.

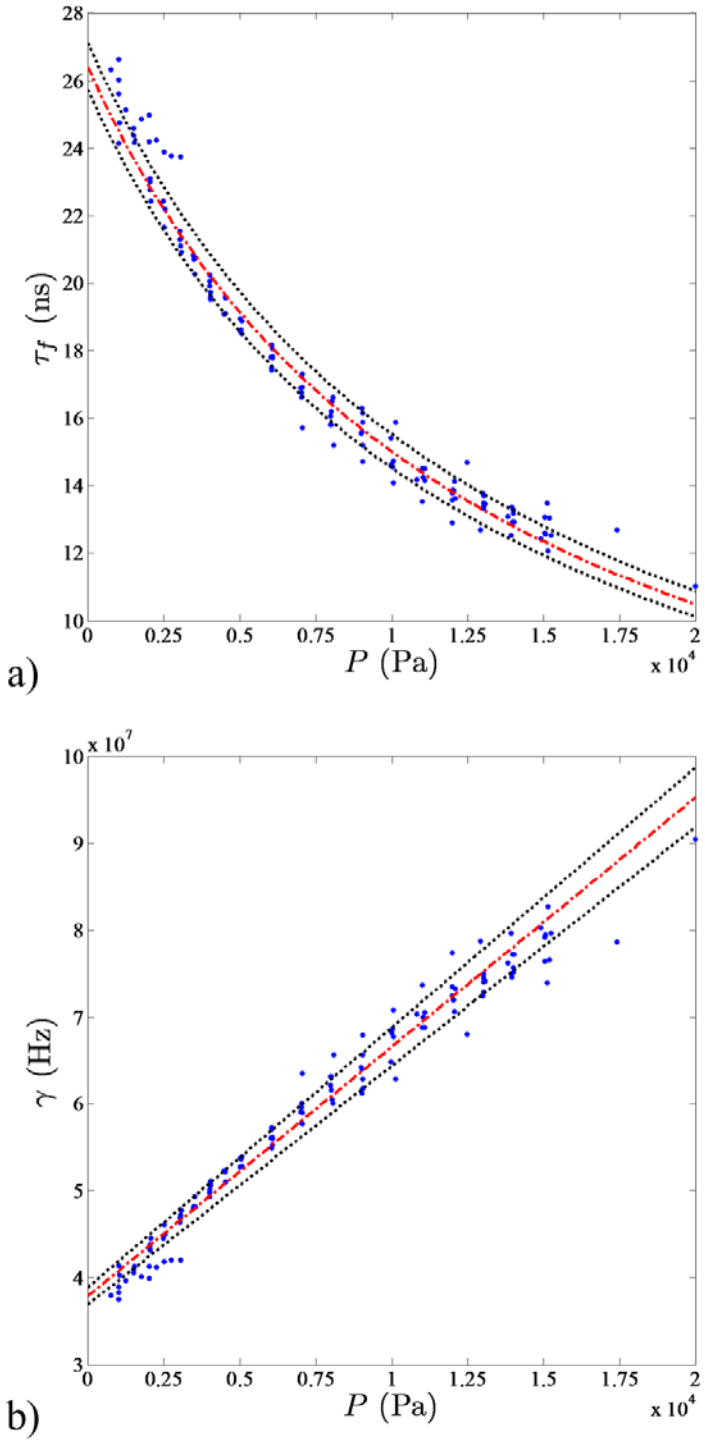

Figure 2.10: Pressure dependence of krypton fluorescence lifetime and decay rate. a) lifetime and b) decay rate.

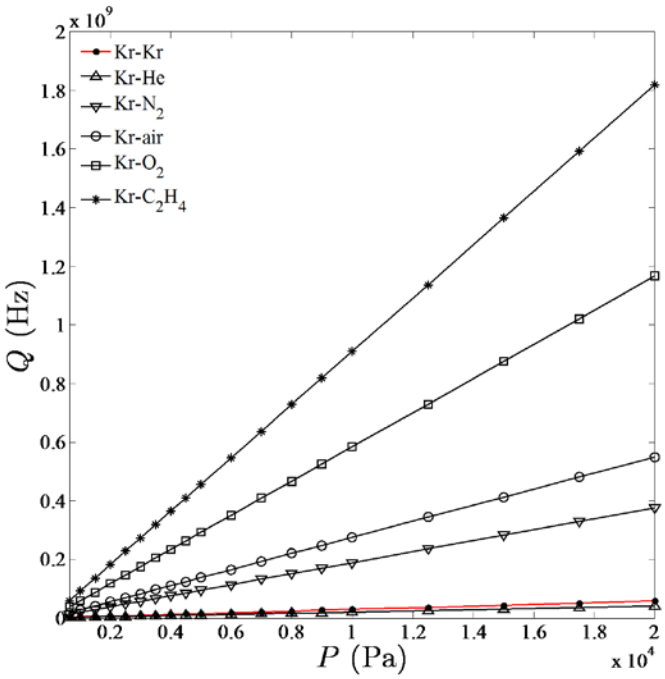

Figure 2.11: Pressure dependence of quenching rates for various gases.

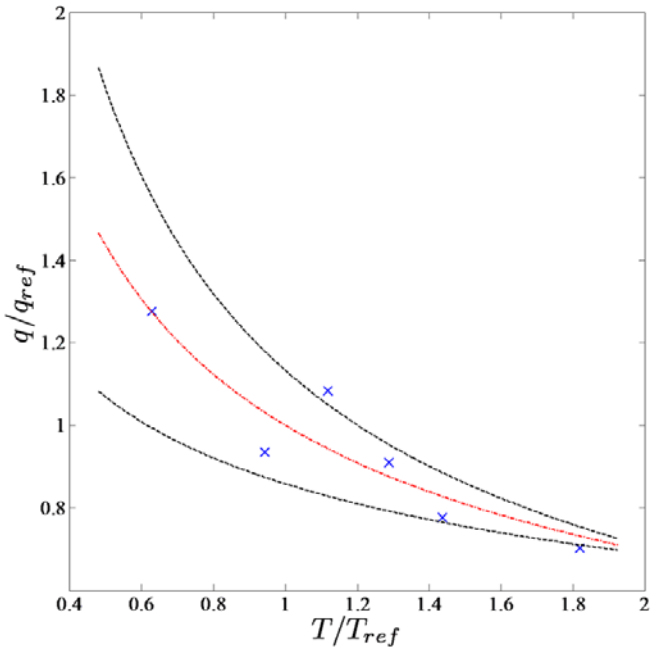

Figure 2.12: Temperature dependence of krypton-krypton collisional quenching rate.

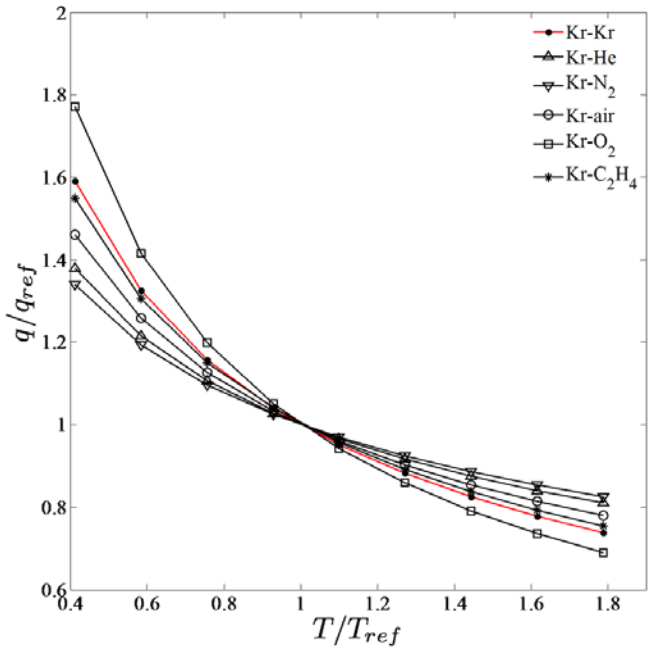

Figure 2.13: Temperature dependence of krypton-buffer collisional quenching rate for various gases.

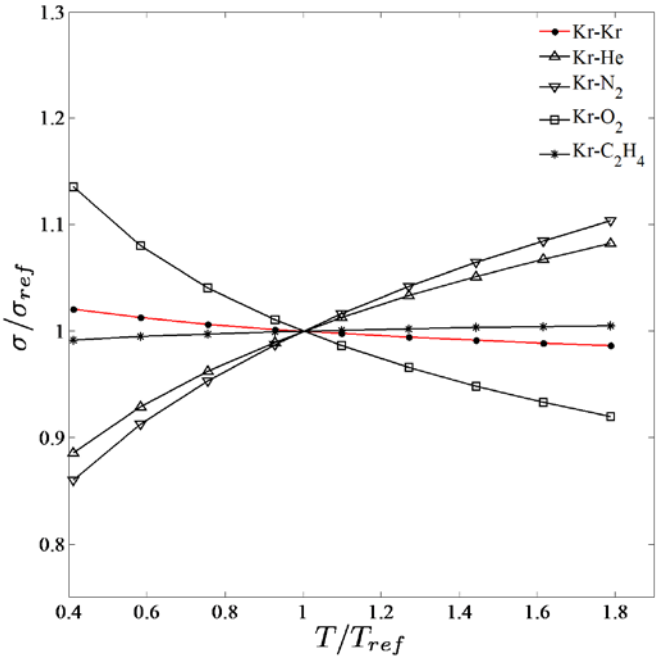

Figure 2.14: Temperature dependence of krypton-buffer collisional quenching cross-sections for various gases.

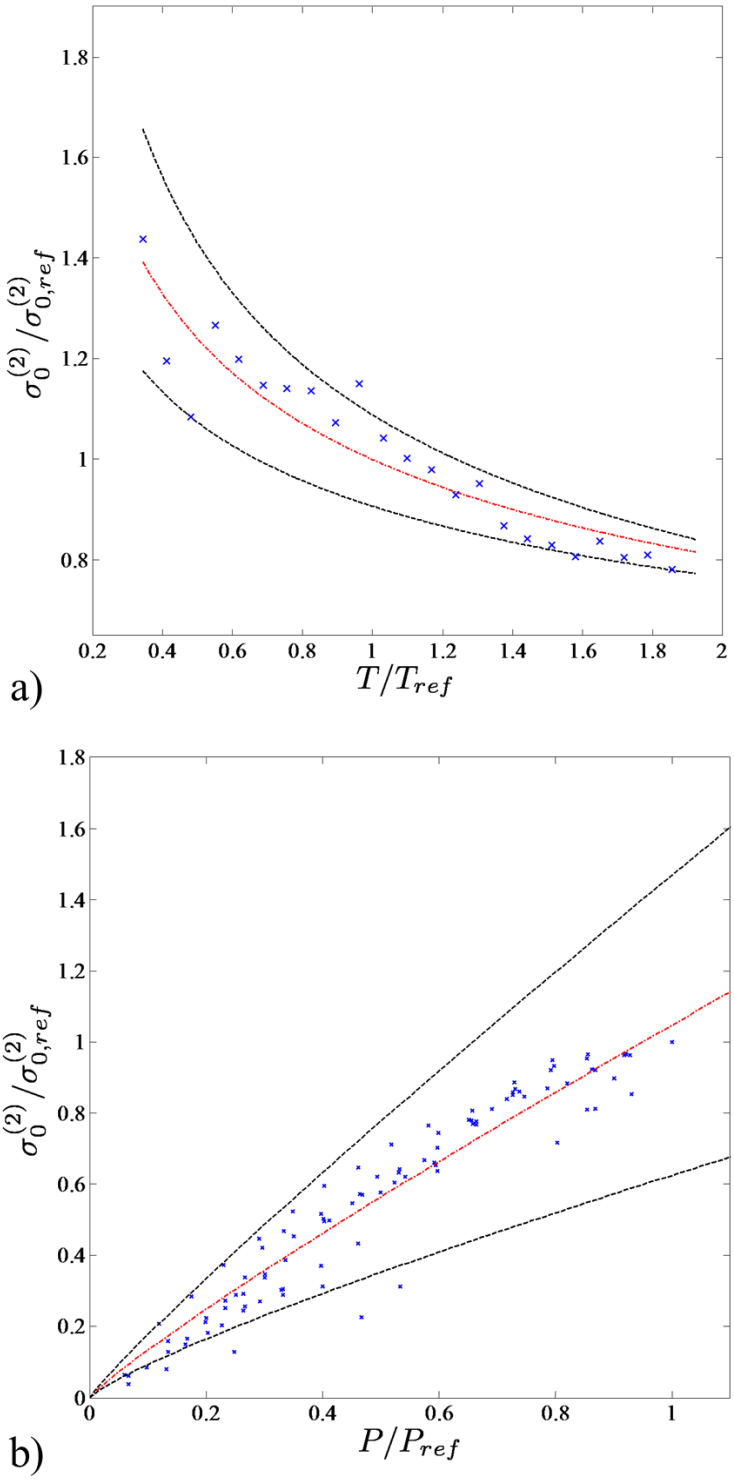

Figure 2.15: Temperature and Pressure dependence of relative two-photon absorption cross-section. a) Temperature dependence and b) pressure dependence.

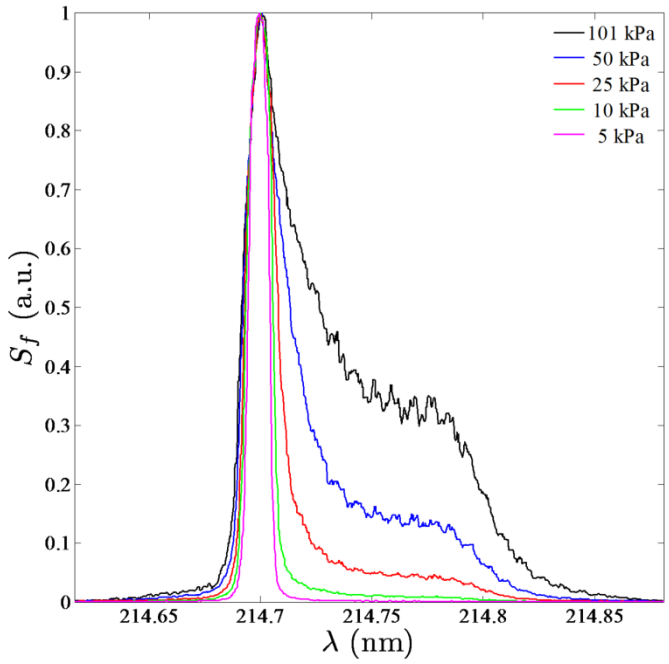

Figure 2.16: Effect of pressure on the excitation spectrum for the two-photon $5p[3/2]_2 \leftarrow 4p^6\ {}^1S_o$ transition for pure krypton

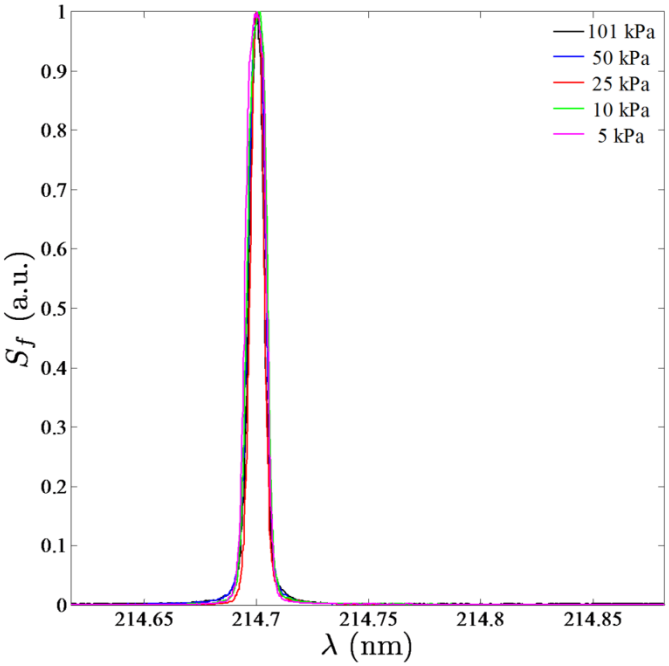

Figure 2.17: Effect of pressure on the excitation spectrum for the two-photon $5p[3/2]_2 \leftarrow 4p^6\ {}^1S_o$ transition for Kr-He mixtures.

Chapter 3: Hypermixer Velocity Fields

This chapter discusses the general characteristics of the two strut injector flowfields used in this and the succeeding chapter. Through the discussion of the two strut-injector flowfields, a basic understanding of the mean and unsteady velocity fields is established, which informs further studies of the mixing behavior in the subsequent chapter. The details of the experimental setup including the test facility, test models, and experimental techniques are discussed, followed by a presentation and discussion of the results.

3.1 – Experimental Details

This section details the test facilities, test geometries, and diagnostics used in the kinematics studies.

3.1.1 – Test Facility

The facility used in these experiments was the Mach 3 located at the flowfield imaging lab at PRC. This is a relatively small blowdown-suction supersonic wind tunnel. The plenum of this tunnel is connected to a large high-pressure reservoir held at roughly 1.1 MPa, and the flow is throttled through the use of a needle valve located within the lab itself. The diffuser is connected directly to the high-volume vacuum system, capable of pulling a vacuum down to 1.5 kPa. Attainable unit Reynolds numbers for this tunnel range from 7.7×10^6 to 1.83×10^7, limited on the low end by difficulty starting the tunnel (sub-atmospheric plenum pressures) and on the high end by both insufficient run time and tank pressure. For these experiments, the plenum pressure was held constant at 185 kPa, which resulted in a developing turbulent boundary layer. The Re_θ for this condition is estimated at 3450 based on a momentum thickness of 0.25 mm. Additionally, the estimated displacement thickness was 0.4 mm, with an overall shape factor of 1.65. It

should be noted that the velocity data used for this calculation was taken downstream of the end of the injector model. Consequently, the velocity profiles show signs of the separation from the model and do not adhere well to a typical turbulent boundary layer profile. Thus these values only represent estimates based on those profiles. As a further point of reference, the boundary layer data of Naryanaswamy [**98**], which were taken in the same facilities with the same hardware, suggest that the Re_θ would be around 3300 for the current stagnation conditions. In those experiments, the boundary layer was shown to be developing/transitional (the turbulence was not fully-developed), which suggest the same is true of the current boundary layer given the similarity in conditions. The plenum temperature ranged from 295 to 310 K from day to day, though the magnitude of the fluctuations during a given day (and thus a given set of experiments) was no higher than 3 K. The maximum runtime for the stated conditions was around 45 seconds, though this depended on the strength of the vacuum.

The test-section of this wind tunnel has cross-sectional dimensions of 50.8 mm × 50.8 mm (2" × 2"). Each of the four bounding walls possesses optical access; the ceiling and floors of the tunnel feature UV-grade fused silica windows mounted in the window plugs of the inner and outer walls. The sidewalls had large acrylic plugs to provide optical access. Each of the 6 plugs could be interchanged with alternate versions if necessary to alter the position of the optical access. The false floor and ceiling in this tunnel are connected to a mechanism allowing for a variable diffuser area. For these experiments, the diffuser was left parallel to the principal flow direction.

This tunnel has a splitter plate built into the nozzle block and part of the test section to allow for controlled wake formation within the test section; the height of the splitter plate is 6.35 mm. This nozzle can be interchanged with a normal supersonic nozzle to allow for a more uniform flow within the test section as was done in the

particle response assessment (see Appendix 3A), though it was advantageous to leave the splitter plate installed for these studies. A diagram of the test facility in the splitter-plate configuration can be seen in Fig 3.1.

3.1.2 – Test Models

The hypermixer models used in the flowfield kinematics studies are shown in Fig 3.2 below. The models are affixed directly to the downstream end of the splitter plate and are of the same thickness. The first model (Fig 3.2a) is the most basic configuration possible for these studies; it is a simple planar injector with no hypermixing elements. The injection port is located at the zero-point in the transverse direction and is 3.175 mm in diameter. This model was selected to act as the control for these experiments. The second model was an asymmetric, unswept expansive injector as depicted in Fig 3.2b. The central block containing the injector port (identical in size and location to the planar model) is 12.7 mm wide. The expansive ramps take up the remainder of the span; they are 15 degree ramps taking up the full transverse extent of the model. For brevity, this injector will simply be called the hypermixing injector or hypermixer for the remainder of this document. Note also in Fig 3.2a the coordinate system used throughout these studies; the x-direction corresponds to the stream-wise direction, y-direction the transverse direction, and z-direction the span-wise direction.

In previous experiments [**99**] [**100**], a wide array of different hypermixer configurations were studied. In these studies, the configuration and size of the injector ports varied considerably. For the present studies, it was decided that the scope of the studies should be limited to a single hypermixing injector and a control-case, which share as many geometric similarities as possible (i.e. injector port location/diameter, length, and base height) such that the effects of only the hypermixing elements could be

ascertained. The actual selection of the configuration shown in Fig. 3.2b, was based both on the experience gleaned in previous works and in consideration of the literature. Specifically, a strong, well-defined pair of stream-wise vortices was desired. Results from previous studies [**100**] indicated that the use of transversely symmetric injectors tended to cause the vortices to break down in the near-field of the mixer because of the anti-symmetric vortex pairing (see Fig. 3.3 for an illustration). Thus, using an asymmetric mixer was preferable in this instance.

Additionally, the configuration used in these studies was very similar in external geometry to that used by Vergine et al. [**78**] (transversely asymmetric and laterally symmetric, unswept, no compressive elements). Selecting a similar geometry provided a basis for comparison in the present study. Finally, the specific angles used in the hypermixing geometry were selected in consideration of the work of Kondo, Arai, et al. [**101**] [**102**]. These studies showed that for purely expansive hypermixing elements such as those used in the present study, the strongest vortices were generated for a ramp angle of around 14 degrees. Thus, an angle of 15 degrees was selected for the hypermixing geometry utilized in these studies.

3.1.3 – Experimental Setup

The principal diagnostic used in these studies was particle image velocimetry (PIV). Two primary configurations were utilized for investigating these flowfields: planar and stereoscopic. For both of these configurations, the laser configuration was identical; this setup can be seen in Fig 3.4 below. The particles used for seeding the flow were atomized olive oil droplets created through a six-jet atomizer (TSI 9306); the particles were injected through half-inch tubing upstream of the plenum of the wind tunnel. For a

detailed discussion of the response and size of the particles generated by this atomizer, see Appendix 3A.

3.1.3.1 – Planar PIV

For this diagnostic, the double-pulsed PIV laser was brought into the test section through the ceiling window. In this case the beam was first deflected upward and then redirected with appropriate mirrors to align the beam with the center of the desired field of view. Finally the beam was passed through sheet-forming optics, in this case a first a -75 mm plano-cylindrical lens followed by a +500 mm spherical lens. The spacing of the lenses was such to collimate the sheet in the stream-wise direction, while still focusing the sheet in the span-wise direction. The measured sheet thickness for this configuration was measured to be between 0.6 and 0.7 mm using the burn-spot method, while the overall width was fixed at 50.8 mm. The temporal separation between laser pulses was set to 0.85 μs for these experiments, while the pulse energy was set at around 60 mJ.

The scattering from the particles was captured with a frame-straddling CCD camera with 2048 px × 2048 px resolution (Roper ES 4020) with a 105 mm Nikon lens stopped at f/5.6. A diagram of the camera and laser configuration for these experiments is shown in Fig 3.4 below. All system timing was controlled by a series of digital pulse generators (SRS DG535) operating in a master-slave configuration. The camera operated with EPIX software, while all PIV processing was done in LaVision's DaVis v.7.2 software package. The PIV used an adaptive, multi-pass interrogation scheme, with initial interrogation windows starting at 128 px × 128 px, reducing to 32 px × 32 px with 75 percent overlap. The threshold Q-ratio was set to be 1.4 in these cases because the seeding and illumination was very close to optimal, and thus over 95 percent of vector

correlations were still attainable. Post-processing of the data was done using custom MATLAB scripts.

For this PIV configuration, 6 separate fields of view were used for each injector. To make the nomenclature as clear as possible, the fields of view were divided into two groups: SV 1, extending from $x/h = 0$ to $x/h = 8$, and SV 2, extending from $x/h = 8$ to $x/h = 16$. Each of these groups was then subdivided into three separate fields of view corresponding to the span-wise location: a) corresponded to the centerline, b) to $z/h = 0.75$, and c) to $z/h = 1.25$. As an example, SV 2b refers to a field of view spanning from $x/h = 8$ to $x/h = 16$ located at $z/h = 0.75$. Between 800 and 900 image pairs were collected for each of these fields of view to ensure sufficient convergence of the mean properties.

3.1.3.2 – Stereoscopic PIV

Stereoscopic PIV was utilized for imaging the stream-wise vortices shed from the hypermixing injector. In this configuration, the double-pulsed laser beam was first diametrically contracted in a 3:1 ratio using a Galilean telescoping lens pair (a + 300 mm spherical lens and -100 mm spherical lens). Following this, the beam was passed beneath the test section and then through an iris; the iris acted to control the eventual thickness of the laser sheet. After the iris, the beam was brought up to the desired height and then passed through a negative focal length cylindrical lens to expand the beam into a sheet. The sheet was then passed through a second iris before entering the test section to ensure the sheet did not clip the ceiling or floor of the test section and cause unnecessary reflections. In these experiments the temporal separation of the laser pulses was set to 1.2 μs. For a detailed discussion of the selection of the laser sheet thickness and temporal separation, see Appendix 3B.

For these experiments, a pair of the same cameras used in the planar PIV was set up in a stereoscopic configuration; this layout is depicted in Fig 3.6 below, along with the laser configuration described above. Each camera utilized an identical lens (105 mm Nikon) connected to a Scheimpflug adapter to accommodate the tilting of the image plane. The decision to place both cameras on one side of the wind tunnel was done to accommodate a more accurate calibration procedure. Both camera axes were oriented roughly 25 degrees off the axis of the wind tunnel. The selection of this angle was mostly trial-and-error; initially the angle was set to be closer to 40 degrees. However, there were two issues with this selection. First, since the imaging was being done through the same window as the laser sheet transmission, there were (relatively) strong reflections near the boundaries of the tunnel in the images. The more obtuse the angle of the camera axis was made, the more these reflections occluded the desired field of view. Second, due to the fact that the out-of-plane velocity component was so much larger than the in-plane motion, the projected pixel displacements grew with increasing camera axis angle. Thus, the 25 degree angle represents the maximum angle at which both of these problems have been sufficiently mitigated.

The data processing procedures required extra care over the simple planar case. In this case a similar adaptive, multi-pass interrogation scheme was utilized, but the selected parameters were quite different. The initial interrogation window size was set to 256 px × 256 px and reduced to 32 px × 32 px with 75 percent overlap. The allowable velocity vector range had to be set quite accurately (u: 600 $\pm$ 100 $m\,s^{-1}$, v, w: 0 $\pm$ 120 $m\,s^{-1}$). The multi-pass post-processing parameters also needed to be set to reject vectors with a Q-ratio less than 1.3. Likewise, the stereo-reconstruction error tolerance was set to only 1 px. Typically, these parameters allowed for nearly 85 percent valid vectors, with missing

vectors arising principally around the tunnel boundaries where the reflections mentioned above were located. Additional post-processing was done in MATLAB.

Two different fields of view were imaged with this technique: one located at $x/h = 8$ and another at $x/h = 16$. For further clarity in presentation, these fields of view will be referred to as EV 1 and EV 2, respectively. To ensure sufficient convergence of the mean properties, roughly 2000 image pairs were collected for each field of view. Data was only collected for the hypermixer model rather than both, mostly due to the extended amount of time it took to collect this quantity of data and the planar model was expected to produce a symmetric flowfield based on three-dimensional reconstruction of the planar PIV.

3.1.3.3 – Operational Notes about PIV

There were a number of non-trivial issues to overcome when performing PIV in this facility due to its small cross-sectional are. Typically, one must reach a balance between attaining a sufficient seeding density and preventing the buildup of the seeding material on the walls of the tunnel. The previous experiments of the author attempted to use both solid particles and liquid droplets for seeding to no particular success. In the case of solid particles, the particle density was usually so high that maybe one to two image pairs could be captured during a run before the walls and windows of the tunnel would be completely coated with particles. On the other hand, the use of liquid droplets would yield completely insufficient seeding, and streaks of the seeding material would obscure the field of view each run.

These experiments and those that follow in Chapter 4 were distinctly different in that the seeding density was well-managed. The modifications to the procedure were largely the reason for the success. First, a new atomizer was used (same model, just new).

Though not compared quantitatively in any way, the output of the new seeder was visually superior to that of the older one in terms of density and was less prone to spraying large agglomerates of oil. Second, the size of the tubing between the seeder and the tunnel plenum was crucial to achieving sufficient seeding density. The previous experiments used a ¼-inch tube between the seeder and the tunnel plenum in many different configurations. Increasing the size of this tube from ¼-inch to half-inch diameter greatly increased the observed seeding density. Finally, the actual operating procedures were quite important. First, the valve between the seeder and the plenum was closed and the pressure to the seeder started. Then maybe one to two seconds before the wind tunnel flow was started, the valve between the seeder and plenum was opened. This step allowed the built-up seeded gas to fill the plenum. Finally, the run was started. Before the wind tunnel flow was stopped, the valve between the seeder and the plenum was closed. This kept the pressure seen by the seeder above atmospheric at all times.

Regarding the buildup of seeding material on the walls; the only effective means of stopping this was preventatively removing the excess oil from the system after each run. This entailed pushing an absorbent cloth all the way through the test section and up into the nozzle block on both sides of the splitter plate, and finally opening up the plenum and removing the stagnant oil. This latter step was not possible in the previous construction of the tunnel, and it made a tremendous difference in this set of experiments.

3.2 – RESULTS AND DISCUSSION

This section will discuss the overall results of the experiments described above. The mean flow properties will first be discussed with a particular emphasis on the comparison between the two different injectors. This discussion will be followed by a discussion of the turbulent and general unsteady flow properties related to both injectors.

3.2.1 – Mean Flow Properties

The mean centerline near-field velocity fields for the planar injector (SV 1a) can be found in Figs 3.7 and 3.8 (stream-wise and transverse components, respectively). Note in these figures that the blackened region in the extreme near-field of the injector corresponds to unacceptably low number of vector correlations (due to reflections off of the injector model); thus these data will not be considered in the analysis. The structure of this flowfield is identical to that of a two-dimensional supersonic wake. The flow enters the interrogation region at the nominal freestream velocity of 630 m/s. Note here that the incoming boundary layer thickness (assumed to be the difference between the injector's half-height and the $0.99U_\infty$ line) is 4.75 mm and is quite symmetric about the mid-plane of the flowfield. The flow undergoes an expansion as it turns around the corner of the injector, indicated both by the increase in the transverse component of velocity and the acceleration of the stream-wise component to nearly 650 m/s. It is observed in Figs. 3.7 and 3.8 that the expansion is not exactly anchored at the corner of the injector model, a phenomenon observed by others [**103**]. This is due to the fact that the incoming boundary layer has a finite thickness and thus possesses a distinct radius of curvature as it detaches from the model. Additionally, as the flow undergoes a rapid change in velocity near the corner of the model, it is probable that there are effects from particle lag that ultimately broaden the base of the expansion (as observed through PIV). The expansion waves are followed by a symmetric pair of recompression shocks, emanating from roughly $x/h = 2.5$. After traversing the shock, the flow remains relatively parallel to the tunnel boundaries, with the weak transverse velocity flanking the centerline of the wake gradually decreasing in magnitude toward the downstream end of the field of view.

Moving downstream to the mid-field of this flowfield (SV 2a, see Figs 3.9 and 3.10), the general trends of the flow's behavior continue. Here, the recompression shocks

continue to propagate rather symmetrically through the test section, visualized very clearly as both the terminating line between the transverse velocity component (Fig 3.9) and parallel flow and as the border separating the high stream-wise velocity and the lower post-shock velocity in the streamwise component (Fig 3.8). These shocks continue through most of the field of view, with a vague suggestion of reflection at the very downstream edge of this field of view (particularly apparent in the transverse velocity component). The wake structure exhibits a relatively minimal growth rate throughout the upstream and downstream fields of view, starting at roughly $y/h = \pm 0.4$ and growing to $y/h = \pm 0.7$. The overall velocity deficit is reduced to only 10 percent of the freestream velocity by the downstream field of view.

The planar injector flowfield exhibits notable two-dimensionality throughout the test section as well. The stream-wise and transverse velocity components for both fields of view are depicted in Fig 3.11 through 3.14 for $z/h = 0.75$ (SV 1b and 2b) and in Fig 3.15 through 3.18 for $z/h = 1.25$ (SV 1c and 2c). Through these figures, it is demonstrated that the overall velocity magnitudes stay consistent throughout the span of the tunnel. Moreover, the growth rate of the wake appears unchanged as well. For a clearer visualization of the span-wise distribution of velocities, the individual planes of velocity can be reconstructed into a mean volumetric representation. The stream-wise velocity for this reconstruction is shown in Fig 3.19, while the transverse component of velocity is seen in Fig 3.20. The thickness of the wake (as visualized in the stream-wise velocity component) is shown in this perspective to be larger near the center of the test section in the very near-field. That is, the wake bulges at the center and tails off with increasing span-wise distance (made evident by the contour lines). This bulging diminishes rapidly downstream, though there is still a slight suggestion of it at the end of these fields of view. The transverse velocity component exhibits the general bulging

observed in the stream-wise component as well. With increasing stream-wise distance, the extreme (span-wise) tails of the wake begin to turn upward while the center of the flow turns parallel. It is unclear from this analysis what the cause of this bulging is. However, as will be demonstrated below in discussion of the other injector, the flow in the test section is inherently three-dimensional due to the limited size relative to the injectors. Thus, this observed deviation from purely two-dimensional flow is likely a consequence of the interaction with the sidewalls, though this cannot be confirmed without a span-wise velocity measurement. It should also be noted that the deviations are quite minor, with the deviations from two-dimensionality residing to within 5 percent of the centerline velocity. Thus it is also possible that the deviations observed are an artefact of the measurement, since they fall within the measured uncertainties presented in Appendix 3C. In this instance, the uncertainty found in the incoming boundary layers is roughly 9 to 10 percent, which does permit the thickened wake observed in Fig 3.19.

The centerline near-field wake structure following the hypermixing injector is depicted in Figs 3.21 and 3.22 (SV 1a). A number of distinct differences between this flowfield and the planar injector flowfield are observable in this field of view. First, as shown in Fig 3.21 the incoming boundary layer appears to be asymmetric. This is accompanied by an upward deflection of the entire wake structure and a transverse asymmetry in both the expansions and recompression shocks (more clearly visible in the transverse component in Fig 3.26). Second, primarily visible in the transverse velocity component, is the development of a strong upward velocity near the reattachment point, which grows in breadth further downstream. It is also worth noting that the upper edge of this high velocity region corresponds to the lower edge of the wake structure visible in the stream-wise velocity component. The appearance of this centerline wake structure is reminiscent of the split-stream wake of Smith and Dutton [**104**], wherein two streams of

differing Mach number were combined with a finite-thickness base. However, the effect observed in this flow has a much different origin. Considering the work of Vergine and Maddalena [**78**], wherein the mid-field of a very similar hypermixing injector was studied, the same lifting effect was observed and attributed to the much higher circulation present in the stream-wise vortex pair than that of the span-wise vortices.

The final observation to be made in this flowfield, though not visible in this data, is the decrease in the observed base pressure; the measured base pressure decreased from 4400 Pa in the planar injector flowfield to 3200 Pa in the hypermixing injector flowfield. The cause of this deviation is twofold. The first is a strengthened expansion on the bottom half of this flowfield. This particular feature stems from the both the thinner boundary layer on the bottom surface of the mixer, allowing the expansion to attach closer to the shoulder of the hypermixing injector, and the lifting effect of the counter-rotating vortex pair, which pulls the detached shear layer up and effectively increases the angle through which the flow expands. The second potential cause of the lower base pressure is the depressurizing effect of the counter-rotating vortex pair (CVP), which acts to depressurize the flow on the top surface of the injector by allowing it to escape to the expansive ramps flanking the central block. Thus, even though the top expansion is more limited in turning angle than in the case of the planar injector, the pressure is ultimately lower.

The mid-field field of view (SV 2a, Figs 3.23 and 3.24, stream-wise and transverse, respectively) shows a continuation of the aforementioned trends. The wake structure continues to propagate upward at the same angle of inclination, with the lower edge of the low velocity region still following the growth of the high-transverse-velocity region developing within the wake. With regard to the aforementioned region, the transverse velocities reached in this field of view nearly double in magnitude from the

upstream edge to the downstream edge. All of these observed variations seen along the centerline are the direct result of the presence of the counter-rotating vortex pair emanating from the hypermixer, which imposes a lifting force on the centerline. This effect will be discussed below in more detail.

The endview PIV reveals much about the three-dimensional nature of the hypermixing injector flowfield. Figs 3.25 through 3.27 show the three mean components of velocity (stream-wise, transverse, and span-wise, respectively) overlain with the in-plane velocity vectors taken at $x/h = 8$ (EV 1). Perhaps the most obvious feature to point out, revealed by the velocity vectors, is the large pair of counter-rotating vortices. The cores of these vortices are located at approximately (1,0.2) and (-0.65,0.2) in (z/h,y/h) coordinates. These vortices are shed from the hypermixer due to the pressure differential experienced between the central block and the expansive ramps. With respect to that point, it should be noted that the edges of the central block, which act as the locus of the vortex shedding, are located at $/h = \pm 1$. In that regard, the vortices have not traversed the span of the flowfield significantly relative to their initial position. Perhaps just as noteworthy is the distortion of the flowfield resulting from the counter-rotating vortex pair. The stream-wise velocity component shown in Fig 3.25 shows the wake has become corrugated by the action of this same vortex pair. The central portion of the wake nested between the two primary vortex cores is raised, corresponding to the upward tilting of the wake seen in Fig 3.21 and 3.23. In contrast, the span-wise outboard region of the wake have remained parallel to the principal flow direction. A similar wake organization has been observed by others. Kondo et al. [**101**] and Arai et al. [**102**], both of whom were studying wall-based injector similar in geometry to the hypermixer injector in the present study, found similar lifting and growth effects of the central portion of the wake due to the action of the vortex pair. In addition, the three-dimensional mapping of a supersonic

ramp injector by Donohue and McDaniel [**105**] exhibits a similar mean profile. Finally, Mie scattering images from Burns and Clemens [**100**], Sunami [**75**], and Vergine and Maddalena [**78**] in similar flowfields exhibit the same distortion observed in the present study.

The transverse component of velocity shown in Fig 3.26 exhibits the same central lobe of increased velocity observed in Figs 3.22 and 3.24 (SV 1a and 2a, respectively). Here it is seen that the high positive velocity is contained within a central lobe structure with an inclusion near the centerline where the two vortices merge. This structure is flanked on each side by a lobe of negative velocity of roughly the same magnitude. Additionally, the regions of zero transverse velocity flanking the central lobe of positive velocity are collocated with the transition region between the raised central wake and the span-wise outboard edges of the wake observed in Fig 3.25. The span-wise velocity component is shown in Fig 3.27. Here it is seen that this component of velocity exhibits a distinct anti-symmetry with respect to the flowfield centerline. Corresponding to the entrainment of fluid from below the CVP, there is a lobe of inward velocity on both sides of the centerline below $y/h = 0$ (transverse midplane). Likewise, above the transverse mid-plane there is a lobe of outward velocity present on each side of the centerline. These structures correspond to the motion of fluid out from the interaction region of the two vortices. Much like the transverse component suggested further vertical spreading of the central wake, this span-wise component further suggest that the wake below the midplane will be forced inward, while that above the midplane will be forced out.

While not especially pronounced in this field of view (EV 1, Figs 3.25-27), it is worth noting for future discussion that there is subtle asymmetry present in the span-wise direction. This is revealed in a number of ways. First, the two tails of the wake structure shown in Fig 3.25 are shaped differently in addition to the presence of slightly lower

velocities in the $-z$ direction. Second, the flow surrounding the wake is also seen to possess similar asymmetries. Specifically, beneath the wake the $-z$ direction shows higher velocities than the $+z$ direction. The opposite trends are observed above the wake, with higher velocities present in the $+z$ direction. The transverse and span-wise components of velocity reveal a similar asymmetry to the stream-wise component. In the transverse component (Fig 3.25), the region of negative velocity is much stronger on the $-z$ side of the centerline. This observation is also consistent with what was observed in the stream-wise component, in which the $-z$ side of the wake was depressed to some extent. The span-wise velocity contours (Fig 3.27) show a less pronounced asymmetry compared to the other components, with the cross-flow velocities of similar magnitudes and shape on both sides of the centerline. However, the $-z$ lobe within the wake structure is shifted downward in the same manner as stream-wise component of velocity. The reason for this asymmetry is not immediately apparent. It is possible that the model was slightly asymmetric or mounted at a slight angle, though measurements of the relevant dimensions seem to exclude these as a possibility. Thus, it is likely an artefact of the test section itself. That is, the flow entering the test section is either asymmetric, or the model is potentially interacting with the side wall boundary layers. As will be observed in the next field of view (EV 2), the latter of these is likely responsible for the observed asymmetries in the present field of view.

While certainly not apparent from the side-view PIV, the end-view PIV shows how dramatically the flowfield evolves spatially. Figs 3.28 through 3.30 (stream-wise, transverse, and span-wise components of velocity, respectively) detail the second end-view field of view (EV 2) located at $x/h = 16$. The stream-wise component shows that the evolution of the wake into a mushroom-like structure (in comparison to Fig 3.25); the central wake, which was lifted in the previous end-view plane has expanded both upward

and outward by the action of the counter-rotating vortex pair. It is seen through the velocity vectors that the centers of the two vortices have also moved upward, likely contributing to the overall expansion of the wake structure. Much as was seen in the Mie scattering visualizations by Vergine and Maddalena [**78**], the structure of the wake continues to grow in the central region while being pinched in closer to the base. Interestingly, the Mie scattering visualizations of Burns and Clemens [**100**] and Sunami [**75**] differ from this wake profile for similar mixers; the very top of the wake in those cases showed a weak indent or inclusion. The primary difference between these cases was the presence of a co-rotating vortex pair in the transverse direction. This observation suggests that the co-rotational merging of the transverse vortex pair allows the vortices to persists farther downstream than the span-wise counter-rotating vortex pair, since the inclusion was attributed to the co-rotating vortices. Further study of this effect is warranted, though it lies outside of the scope of the present study.

The transverse component of the velocity field (Fig 3.29) shows that the strong upward velocity induced by the vortices merging with one another has strengthened considerably. The magnitude and location of this velocity closely matches the observation made with the side-view PIV. Additionally, the downward velocity component on either side of the centerline has stayed constant in magnitude. A new feature has developed in this fields of view; a strong upward velocity component has developed above the overall vortex structure. Based on the side-view PIV and the overall shape of the structure, it is likely the reflection of the recompression shock off the ceiling of the tunnel. The magnitude of the span-wise velocity component has remained relatively constant as well (Fig 3.30).

While many features have remained consistent between the two end-views, the subtle span-wise asymmetry has become far more pronounced downstream. Consider

first the stream-wise velocity component (Fig 3.28) in comparison to the upstream field of view (EV 1, Fig 3.25). The most notable feature here is the large, low velocity lobe seen emanating from outside the field of view attached to the smaller outboard edges of the wake ($|z/h| > 2$). These outermost regions have, in general, grown more asymmetric; the one located in the $-z$-direction has moved down considerably from its previous location while the other has remained fairly level relative to the upstream field of view (EV 1, Fig 3.25). It is difficult to know from what these low-velocity outboard lobes result. One possibility is that the action of the stream-wise vortices causes a suction effect on the side-wall boundary layer. With the growth of the vortex pair via the entrainment of the surrounding air, the span-wise extent of the vortices begins interacting with the sidewall boundary layer. Near the top of the vortices, the span-wise velocity would push into the walls, and as the rotation continued, the vortices would first push down on and then pull against the boundary layer, locally pulling it into the wake. This view of the flow pattern is supported by the general orientation of the velocity vectors visible in Figs. 3.28 through 3.30, which point down and toward the centerline in the vicinity of the wake. If this mechanism is accurate, the observed effect on the boundary layer is remarkable considering how far from the sidewall this field of view is (sidewalls are located at $z/h = \pm 4$), suggesting that each boundary layer has grown to $1.75h$ or around 11 mm in thickness on average in these regions.

Comparing the transverse component (Fig 3.29) to the previous end-view field of view (EV 1, Fig 3.26), the two lobes of negative velocity have become more asymmetric as well, with the lobe in the $-z$-direction becoming much larger in extent and greater in magnitude, particularly close to the edge of the field of view. Given the previous observation regarding the enhanced boundary layer growth and/or flow separation on the side walls of the facility, it is possible that this large region above the two vortex cores

could be some form of flow separation in this general vicinity. However, it is unlikely that this structure is flow separation due both to shape of the structure and the generally low Reynolds stresses that were observed in this region (more on this below). Finally, the span-wise asymmetry has become more pronounced in the span-wise velocity as well (Fig 3.30 in contrast to Fig 3.27), particularly in the upper left lobe of negative velocity. Here the magnitude is considerably weaker than that of the other three lobes, disturbing the overall anti-symmetry of this velocity component. Again, the cause of this asymmetry is not immediately apparent, though the interaction of the CVP with the sidewall boundary layer is likely the cause, as described above.

3.2.2 – Turbulent and Unsteady Flow Properties

The wake flowfields heretofore established are inherently unsteady in nature. This unsteadiness manifests itself in two ways; first, a global unsteadiness is present associated with large-scale motions of the respective wake structures. Second, the flows are highly turbulent; this turbulence is both naturally generated and convected into the flowfield from the incoming boundary layers. This section will first discuss some general observations of the unsteadiness of the flow followed by a discussion of the turbulence characteristics present in the test flowfields.

3.2.2.1 – General Observations

There are three key flow features to discuss in regard to the unsteadiness of the flow: the incoming boundary layer, the system of shocks and expansions, and the wake structure. The most straightforward of these to characterize is the incoming boundary layer. As mentioned in the experimental setup, the Reynolds number for the tunnel was adjusted such that incoming boundary layer was turbulent; this corresponded to a unit Reynolds number of 1.4×10^7 and an Re_θ of 3450. As mentioned in the experimental

setup (Section 3.1.1), the turbulent boundary layer is likely transitional/not fully-developed. The mean incoming boundary layer thickness was found to be 4.75 mm.

The incoming boundary layer consists of large turbulent eddies, which are convected from upstream and have a mean transverse extent of ~1.5 mm or $0.24h$ along the centerline. These structures can be visualized in the instantaneous stream-wise velocity contours found in Fig 3.31, or the fluctuating velocity contours in Fig 3.32. It can also be seen that the shedding of these structures is quite symmetric. That is, the shedding is equal in magnitude on both sides of the splitter plate. This observation is in contrast to some of the previous studies [**99**] [**100**], in which an intermittent shedding pattern was found corresponding to transitional behavior in the incoming boundary layers. As these structures expand around the corner, they are stretched into much longer strand-like structures. This observation is similar to the structures observed via planar laser scattering in several of the author's previous works on the subject [**100**] [**99**] [**106**]. Following the expansion, these wispy structures are convected along the outer region of the wake, where they ultimately merge with the turbulent structures present within the wake.

With regards to the expansion and shock structures, their positions were very much constant throughout these runs, with oscillations due primarily to the incoming turbulent structures rather than fluctuations in the freestream conditions as has been observed in this facility in past experiments [**99**]. This deviation from past behavior is again attributable to a higher Reynolds number during test runs. With regards to the unsteadiness of the recompression shocks, a PDF of the approximate shock angle for the centerline of the planar injector is shown in Fig 3.33. It can be seen that the variations in angle are minor, suggesting (and confirmed below) that the expected RMS velocities in

the vicinity of the shockwaves will be very low compared with the turbulence in the wake. Similarly the expansions emanating from the injector are quite stable.

The wake of the planar injector flowfield is inherently the most unsteady feature in these flows due to the fact that there are both turbulence and large-scale instabilities present in this region of the flow; these two properties will be examined in the next section. First, consider the upstream planar injector flowfield; a set of instantaneous velocity and vorticity contours are depicted in Figs 3.31 and 3.33 through 3.37 (SV 1a). The stream-wise velocity and associated fluctuations (Figs 3.31 and 3.33, respectively) show that the instantaneous wake possesses a weak undulating pattern, exhibiting intermittently inclined and declined regions with respect to the transverse direction. Furthermore, there are turbulent structures of diverse scale interspersed throughout the wake. In this particular realization (Fig 3.33), these structures lie principally along the top of the wake and are positive in direction. The transverse velocity component (Fig 3.34) and fluctuations (Fig 3.35) in this region exhibit regions of positive and negative velocity corresponding to the undulation observed in the stream-wise component in addition to the more randomized fluctuations caused by the turbulence in the flow. Finally, in considering the span-wise vorticity fields shown in Figs 3.36 and 3.37, it is seen that clusters of high negative vorticity line the top of the wake structure. Likewise, regions of positive vorticity align with the bottom of the wake. Similar instantaneous structures are observed by Scarano and van Oudheusden [**103**] in their consideration of a planar supersonic wake. In contrast the unmodified wake studied by Vergine and Maddalena [**78**] exhibits a nearly identical vorticity topology to the present flow including the size and magnitude of the structures. The undulations described in the stream-wise velocity component do not have any appreciable signature in the vorticity field; this observation is made apparent by observing the overlaid streamlines in Fig 3.37. It should be noted that

the majority of the vortex structures appear to originate in the wake, rather than being convected into the region by the incoming boundary layer.

In the downstream field of view (SV 2a), the undulating pattern observed in the SV 1a has become more organized. The stream-wise velocity contours detailed in Fig 3.38 and 3.39 (total and fluctuating velocities, respectively) show that the undulations in the wake have become more pronounced while the overall breadth of the wake has continued to grow. An interesting note here is that the instantaneous width of the wake is found to be considerably thinner than the mean in Fig 3.9 suggests. Furthermore, the transverse velocity (Figs 3.40 and 3.41) shows that the once random fluctuations seen in the near-field of the injector have become more organized, showing alternating positive and negative pockets of velocity throughout the wake. The vorticity contours (Fig 3.42 and 3.43) show that the weak vortical structures that presented upstream have become more organized as well, manifesting as coupled vortex pairs on alternating sides of the wake. These are particularly apparent by looking at the streamlines in Fig 3.43. These structures could represent a growing instability in the wake, akin to the Kelvin-Helmholtz instability. However, the pairings of vortices present in this instantaneous realization are not coupled in the correct manner for this to be the exact instability. It is possible that these structures result from intermittent upstream oscillations in either the incoming boundary layers or the shedding shear layers [**107**]. These structures are discussed in greater detail in Appendix 3D.

The hypermixing injector flowfield exhibits some marked differences from the planar injector flowfield that are apparent even in the near-field of the injector. Figures 3.44 through 3.49 show an instantaneous set of velocity and vorticity contours for the near-field of the hypermixing injector. The stream-wise velocity contours (Figs 3.44 and 3.45) suggest that the wake takes on a similar character to the mean overlaid with some

mild turbulence. However, this is contradicted by the transverse velocity contours (Fig 3.46 and 3.47); the top of the wake has periodic regions of high velocity growing in extent with downstream distance. These regions are at a much higher velocity than the mean in these regions, suggesting the intermittency is intrinsic to the flow. Accompanying these regions of high transverse velocity are span-wise vortices lining the top portion of the wake; these can be seen in Figs 3.48 and 3.49. Though not fully organized, the degree of organization present here far exceeds that observed in the planar injector flowfield.

The downstream field of view exhibits a similar behavior to the upstream; a sample instantaneous field is shown in Figs 3.50 through 3.55. The stream-wise velocity contours (Figs 3.50 and 3.51) show a similar spatial evolution to the upstream contours; the wake does not seem to exhibit the same undulation seen in the planar injector flowfield. Likewise, observing the transverse contours (Fig 3.52 and 3.53) shows a continued growth of the high velocity structures along the top of the wake. Here again, there is a marked intermittency in the appearance of these high velocity structures; moreover, they are growing in stream-wise extent with downstream distance. Observing the vorticity field in this region (Fig 3.54 and 3.55), it is seen that the appearance of these structures correspond to the pairing of span-wise vortices, which alternatingly push the wake up and down with their interaction. While this will be discussed in detail below, it is worth noting at this point that the appearance of these structures is likely a secondary manifestation of the stream-wise vortex pair that is propagating downstream.

As was made apparent with the study of the mean velocity fields, the hypermixing injector flowfield is highly three-dimensional in character. Given the periodic vortex structures observed along the centerline of this flowfield, it is worth considering how these structures vary spatially. Consider the two out-board side-view planes detailed in

Figs 3.56 through 3.67 (SV 1b and 2b) and Figs 3.68 through 3.79 (SV 1c and 2c); here the structural differences are made apparent. The first of these outboard planes, located at $x/h = 0.75$ (SV 1b and 2b), shows something of a hybrid wake. That is, the wake exhibits traits both of the centerline and of the wake emanating from the expansive ramps (Figs 3.68 through 3.79). The upstream field of view detailed in Figs 3.56 through 3.61 appears in many ways indistinguishable from the centerline. The transverse protrusions in the wake are here appear at a much higher velocity and with less distinguishable intermittency. Rather than strengthening (increasing in transverse velocity) with downstream distance, they appear to stay constant in magnitude throughout the field of view. The weak vortex structures, which lined the top of the wake along the centerline, are present here as well.

As can be observed in the downstream field of view (SV 2b, Figs 3.62 through 3.67), the wake is seen to vary substantially from the centerline at the same stream-wise location. The vortex structures visible in Fig 3.66 and 3.67 suggest the wake structure has considerable span-wise vortical motion, though the flowfield lacks the organization or periodicity observed along the centerline at this location. The top of the wake still has much larger (spatial extent) and stronger vortices in terms of the vorticity magnitude than the bottom of the wake, but they no longer appear in counter-rotating pairs. Instead, larger vortices appear to form in conjunction with multiple smaller vortices of the opposite orientation. In addition, the entire wake is replete with these large-scale vortices, rather than them being isolated to the top of the wake. As was mentioned above, and will be discussed in detail below, the stream-wise vortices propagating downstream are unsteady in their core position. Since this location is rather close to the shedding locus (at $z/h = 1$), it is likely that this vortical motion is induced by vortex stretching, and appears so chaotic because of the instability in the stream-wise vortex cores.

The next out-board plane is equidistant from the shedding locus (SV 1c and 2c, $z/h = 1.25$) as the previous plane, but on the opposite side. The structure of the flowfield at this plane is detailed in Figs 3.68 through 3.79; this position again is associated with a greatly altered flowfield. First, the upstream stream-wise velocity contours (SV 1c, Figs 3.68 and 3.69) show a much thinner wake structure emanating from the expansive ramps; the overall transverse extent of the wake is only $0.5h$, but is flanked on the top side with faint turbulent structures convecting from the upstream boundary layer. Since the location of this measurement lies along the expansive wedge of the model, the flow doesn't experience an abrupt change in the geometry as it would along the central block. Thus, the flow is able to stay attached to the injector more readily, and the incoming turbulent structures don't immediately become incorporated into the turbulence of the wake as they have in the previous two data planes. The transverse velocity component (Figs 3.70 and 3.71) shows the thin central wake to be flanked on both sides by velocities of similar magnitude, though the actual fluctuations lack any large-scale organization. The previous observation made regarding the incoming turbulent structures staying detached from the central wake for most of this field of view is confirmed by the vorticity contours/streamlines seen in Fig 3.72 and 3.73. The small vortical structures present in the incoming boundary layer are convected into the field of view and remain detached from the vortex structures present in the wake. Much like the vortex structures observed in the other data planes, the wake is still lined on the top and bottom surfaces with structures of negative and positive vorticity, respectively. However, unlike fields of view SV 1a,b and 2a,b, no large regions of circulation are present in the wake until the very edge of the field of view, which was a consistent observation in this span-wise location.

The downstream field of view (SV 2c, Figs 3.74 through 3.79) shows a consistent but nonetheless dramatic evolution in that the stream-wise velocity contours (Figs 3.74 and 3.75) show that the wake has taken on an undulating pattern. The remnants of the incoming boundary layer still appear occasionally along the top of the wake. These are accompanied by large vertical streaks of high velocity in the same location. These same structures are visible in the transverse velocity contours as well (Figs 3.76 and 3.77). Large vertical bands of negative velocity are present as well, stretching down into the thin wake structure. These structures occur out-of-phase with the vertical streaks of high stream-wise velocity. Moreover, within the wake these vertical streaks occur between small pockets of positive transverse velocity. The vorticity contours/streamlines in Fig 3.78 and 3.79 show that this intermittent velocity pattern corresponds to alternating vortex pairs occurring within the thinnest part of the wake. This vortex pattern is very similar to a vortex street; this region of the wake behaves far more like a simple wake than the other fields of view due to the expansive ramp present upstream. The vertical velocity streaks observed above the wake are likely an effect of the stream-wise vortex pair; the spatial periodicity is identicl to that of the lobes of high transverse velocity occurring along the centerline wake.

Since many of the deviations to this point can be mechanistically related to the stream-wise vortex pair, the end-view PIV can help illuminate the exact mechanisms responsible for the aforementioned phenomena. Consider the first end-view field of view; while the mean velocity fields shown in Figs 3.25 through 3.27 suggest a highly stable vortex pattern propagating downstream, the various side-views suggest a large degree of instability in the vortex structures. The end-view PIV corroborates this assertion; an example instantaneous field is shown in Figs 3.80 through 3.87. The stream-wise velocity contours (Fig 3.80 and 3.81) show that the general profile of the wake is retained

instantaneously, but is far more chaotic in nature. The transverse velocity (Figs 3.82 and 3.83) maintains a strong upward velocity on the centerline flanked by negative velocity lobes, while the span-wise component (Figs 3.84 and 3.85) exhibits a similar anti-symmetry to the mean. However, in viewing the instantaneous velocity vectors overlaid on these velocity components, it is clear that the mean vortex structure has been almost completely lost. The left vortex remains in some ways intact (there is a recognizable vortex core), but the right vortex does not exhibit the same degree of organization. This observation is further supported by the in-plane vorticity (ω_x) contours in Fig 3.86 and 3.87; it can be seen that unlike the mean field, there are no large vortex structures indicative of the stream-wise vortices. Rather, the vorticity is concentrated in smaller clusters of very high magnitude (nearly an order of magnitude higher than those seen in the side-view).

When trying to understand some of the phenomena observed in the side-view fields of view, it is useful to quantify the motion of the stream-wise vortices. Figures 3.88 and 3.89 show probability density functions of the position of the vortex cores in the span-wise and transverse directions, respectively. The core position was calculated by the method of Jiang et al. [**108**], though simply calculating the centroid of vorticity in these cases showed minimal difference. It can be seen here that the two vortices have nearly identical motion widths in both directions. In both cases the width is roughly $0.07h$ in extent. Furthermore, the motion is symmetric, not favoring any particular directional shift from the center. Complementary to this observation is the separation of the two vortex cores. Fig 3.90 shows a PDF of the vortex core separation for the first end-view field of view (EV 1). Here it is seen that the mean separation is almost precisely equal to that measured through the PDFs of the individual vortex core motion. However, the important thing to note here is that the overall width of the motion is much broader than the motion

of the individual vortices. There are a number of possibilities for the motion of the two vortices. First, if they move exactly in-phase with one another (cores are displaced in the same amount and direction at the same time), the separation PDF would identically be a delta function at the mean separation distance. Second, if the motion was exactly out-of-phase, the separation PDF would be of the same form as the individual motion PDFs, but would be twice as broad since the separation would implicitly increase or decrease by twice the amount of either of two vortex cores. The final extreme is completely incoherent motion (the two vortices move independent of each other), which would result in a PDF having a total width equal to twice the individual linewidths, but the distribution would be acquired by multiplying the two individual distributions. What this suggests in regard to the observed vortex motion is that two vortices move primarily out-of-phase with one another, though not exactly. Thus, it can be concluded that (statistically), the two vortices most commonly move either toward or away from each other, though not exactly out-of-phase.

The second end-view plane shows similar behavior to that of the first; an instantaneous set of velocity and vorticity fields are shown in Figs 3.91 through 3.98. As depicted in Figs 3.91 and 3.92, the stream-wise velocity contours show that the wake has an instantaneous profile similar to the mean. Much like the previous field of view, there is a considerable degree of turbulence superimposed on the flowfield in this instance. In like manner, the transverse (Fig 3.93 and 3.94) and span-wise (Fig 3.95 and 3.96) velocity components behave in a much more chaotic fashion than their mean would suggest. The velocity vectors overlaying these velocity contours show that in this particular instantaneous realization, there are two well-defined vortex cores present, which are visible in the vorticity contours (Fig 3.97 and 3.98) as two large vortical structures. The instantaneous streamlines in Fig 3.98 show that the two vortex cores lie

coincident with the regions of high vorticity, suggesting a higher degree of organization in this field of view than in the previous.

Similar to the analysis performed on the previous field of view, PDFs of vortex core position and separation are shown in Figs 3.99 through 3.101. From Figs 3.99 and 3.100, it can be seen that the span-wise motion of the two vortex cores is nearly identical in breadth to that seen in the previous field of view, though just about 6 percent lower. Furthermore, the motion in the transverse direction has increased by roughly 16 percent. Finally, the separation of the two vortex cores was found to be identical to that seen in the previous field of view. The anisotropy exhibited in the vortex motion in this field of view suggests that the motion of the vortices is becoming more confined as they grow in extent. The reasons for this are several; first, there is physically more space in the transverse direction for the vortices to move. Second, as was shown in the mean, the wake from the hypermixing injector begins interacting with the other flow structures within the test section, namely the side wall boundary layers and recompression shocks. In the upstream field of view, the influence of the shedding source (namely the hypermixing injector) is still dominant in controlling the motion. Moreover, since the vortices are relatively limited in spatial extent, there is not much interaction with the physical boundaries of the tunnel (or resulting flow structures). The limited size of the vortices thus allows the motion of the vortices to remain isotropic. However, as the flow becomes more turbulent and chaotic with downstream progression, the tendency would seem to be that the vortex motion would become similarly chaotic but remain isotropic. However, as the interaction with the side-wall boundary layer commences, the span-wise motion of the vortex cores is restricted, and the energy is more frequently diverted to transverse motion.

In examining the span-wise vortex structures that were found throughout the flowfield, the motion of the stream-wise vortices is critical to understanding their occurrence. Consider the centerline case seen in Figs 3.44 through 3.55; therein large counter-rotating span-wise vortex pairs were found to line the top of the wake. With knowledge of the unsteady behavior of the stream-wise vortex cores, a mechanism for this coupling begins to reveal itself. Consider a situation in which the two vortex cores were to approach each other. In this scenario, the interfacial area between the two vortices would increase. Consequently, the additive effect resulting in the band of positive transverse velocity observed at this location would momentarily strengthen, resulting in a band of increased transverse velocity. Since the vortices are interacting more strongly with one another, they would ultimately weaken and move apart, either returning to their equilibrium position or possibly moving beyond. Thus, the transverse velocity would return to its equilibrium value or decrease. While this is a simplified conceptualization of what is occurring in the hypermixer flowfield, it is nonetheless a potential mechanism to explain the observations made in this. Only time-resolved measurements of the velocity field could verify if this mechanism was responsible for the observed behavior.

3.2.2.2 – Turbulence Characteristics

The previous section detailed some general observations about the unsteady behavior of the two test flowfields used in these studies. This section will discuss some of these same features from a statistical standpoint. Consider first the planar injector flowfield; the ensemble-averaged velocity fluctuations for the centerline are depicted in Figs 3.102 through 3.107. The stream-wise fluctuations are depicted in Figs 3.102 and 3.103. It is found here that the fluctuations peak within the outer regions of the wake and

incoming boundary layer, in this case peaking at around 5 percent of the freestream velocity (that is, $\sqrt{\langle u'^2 \rangle}/U_\infty$). The fluctuations in the freestream are quite minor, below 0.1 percent. A few things should be noted here; the fluctuations are found to increase in magnitude with increasing downstream distance within SV 1a. However, it is also found that the regions surrounding the wake also increase in fluctuation magnitude with this component; this behavior is due to a lower correlation percentage in this region (due to the laser sheet placement). However, based on the downstream field of view, the values found in the wake are fairly accurate; the magnitude of the fluctuations matches across the two fields of view. Continuing downstream, much the same behavior is observed, with the noted difference being that the fluctuations begin to trail off with further downstream progression. Additionally, in both fields of view, there is little observed fluctuation around the recompression shocks or expansions, which is consistent with the observation made in the previous section with regard to the steadiness of the shocks. The PIV investigation of Scarano [**103**] in a planar supersonic wake exhibited similar flow topology with regards to the stream-wise component of the Reynolds stresses. Specifically, the strongest fluctuations aligned in two distinct bands on either side of the transverse midplane. However, the fluctuations were of much higher magnitude in those data. This is due in part to the fact that the field of view was limited to just $2.5h$ in those studies, which is contained mostly in the region of low correlation discounted in the present study. This general structure is corroborated by other supersonic wake data as well [**109**] [**107**] [**110**] [**111**].

The transverse fluctuations (Figs 3.104 and 3.105) behave in a manner quite opposite that of the stream-wise fluctuations. Specifically, the peak of the transverse fluctuations is found within the very center of the wake. With downstream distance, the magnitude of these fluctuation decreases much like was observed in the stream-wise

component. Additionally, there is a relatively high degree of fluctuation (relative to the stream-wise component) found at the trailing edge of the expansion/recompression shock. Again, these data match the general structure of the supersonic wakes in [**103**], [**110**], and [**109**]. Much like the previous component, there is noise found at the downstream end of the first field of view due to the lower correlation percentage in this region. These trends continue in the downstream field of view, with the strongest fluctuations found within the center of the wake and additional fluctuation found in the vicinity of the recompression shocks. Finally, the Reynolds shear stress ($\langle u'v' \rangle$) shown in Figs 3.106 and 3.107 are found to peak within the shear layers surrounding the wake. The magnitude of these fluctuations is much smaller in magnitude than those seen for either the stream-wise or transverse components, peaking around 3 percent. Much like the other components, the fluctuations are found to decrease with downstream distance, but in this case the rate of decay is much slower.

The hypermixing injector flowfield, as would be expected from the discussion of the unsteadiness above, exhibits very different turbulent flow characteristics from that of the planar injector flowfield. The stream-wise contours (Figs 3.108 and 3.109) show that, unlike the planar injector, the peak of the fluctuations aligns solely with the top of the wake and is concentrated in a much narrower band. There is an additional band along the bottom of the wake, but is a much lower magnitude than that seen in the top band. These behaviors continue downstream; the two bands for both sides of the wake merge into a single profile and decrease with increasing downstream distance. The transverse fluctuations seen in Fig 3.110 and 3.111 show that, much like the planar injector, the peak of the transverse fluctuations is found within the center of the wake. Again, there is some degree of fluctuation aligning with the recompression shocks, but the vast majority is concentrated within the center of the wake. Finally, the shear component found in Figs

3.112 and 3.113 exhibits a similar trend to that seen in the planar injector flowfield. That is, the shearing component aligns with the top and bottom of the wake. The primary difference here is that the negative component is quite a bit stronger than the positive. The literature is very limited in its study of hypermixers like the one utilized in the present study, particularly in regard to the turbulence properties of such flows. A similar concept for use in subsonic flows is the lobed injector, for which more data is available. McCormick and Bennet [**112**], in studying a lobed injector in subsonic flow noted a similar double-banded Reynolds stress near the peak of one of their mixing elements. The complex mixer of Hu et al. [**113**], though axisymmetric, also showed a turbulent intensity profile organizing into a banded structure much as was observed in the present studies.

The stream-wise component of the fluctuations viewed from the end-view perspective is shown in Fig 3.114 along with the other components. For discussion, they have been shown overlaid with the mean stream-wise velocity and vorticity contours. It is seen here that, as the side-view PIV would suggest, the majority of the turbulent fluctuations are contained within the wake. Note here that the fluctuations are much more spread-out across the wake than they were in the side-view. This observation results from the experimental noise observed in this field of view. Particularly in the vortex cores, the vector correlation percentage was quite low due to low particle density. Thus, the wake appears far more turbulent in these regions because the degree of convergence is smaller than the side-view. Nonetheless the analysis taken from the data can still be quite useful for understanding the flow physics, if only qualitatively. The remaining components of the normal stresses presented in Fig 3.114 differ slightly from the stream-wise component; in the transverse component, the fluctuations are contained almost entirely within the raised central portion of the wake, while the span-wise component shows a similar trend with additional fluctuations present in the $+z$ direction. These results

collapse concisely by looking at the turbulent kinetic energy, k, as depicted in Figure 3.115.

Figure 3.116 depicts the three normal Reynolds stresses for the second end-view field of view. Here, some distinctly different trends were observed than in the upstream field of view. Consider first the stream-wise component. Here, it can be seen that majority of the fluctuations are contained within the outer regions of the wake; this fact is particularly true in the regions approaching the separated side-wall boundary layers. Much like the side-view PIV, the central wake structure shows that the fluctuations are much more spread out than along the sides of the wake. Additionally, there appears to be very little correlation between the local vorticity and the magnitude of the stream-wise fluctuations. The transverse component shows much the opposite trend; the majority of the fluctuations are contained within the center of the wake, both along the centerline and on the sides of the wake. However, the most dominant region of transverse fluctuations lies directly within the vortex cores. It should also be noted that regions of highest fluctuating velocity are not strictly vertical but are tilted on both sides of the centerline. Similar observations can be made in the span-wise fluctuations, where again the fluctuations are contained within the center of the wake and concentrated in the vortex cores.

Looking at the overall turbulent kinetic energy in this field of view (Fig 3.117) shows, again, that the strongest fluctuations are found in the vortex cores (an almost exact overlap is seen when looking at the corresponding vorticity contours). It is impossible to tell from this analysis whether this overlap is a function of increased turbulence in the vicinity of the vortex cores or is it simply a function of the unsteadiness in the position of the vortex cores. However, given that the positional PDFs of the vortex core positions exactly coincide with these regions of highest velocity fluctuation suggest that the motion

of the vortex cores is culpable for this observation. This view also suggests that the stream-wise fluctuations contribute less to the total TKE; in making this claim, it is important to remember that the laser sheet was quite thick in these experiments (3 mm), and thus there is an inherent smoothing of fluctuations seen within the thickness of the sheet.

One limitation of the previous analysis is that it avoids any mention of the structures observed instantaneously. To complement this, a slightly different analysis could assist in examining the structure of the turbulent flowfield – multi-point statistical correlations. In this analysis, the two-point correlation, R_{ij}, will be utilized. The two-point correlation is defined as:

$$\langle u_i' u_j'' \rangle = \langle \left(u_i(x_0, y_0) - \overline{u_i(x_0, y_0)}\right)\left(u_j(x, y) - \overline{u_j(x, y)}\right) \rangle \qquad 3.1$$

In Eq. 3.1, point (x_0, y_0) represents the fixed reference point for the correlation (indicated by the $'$), and (x, y) is the location at which the correlation is being computed (indicated by the $''$). The angled brackets $\langle\rangle$ indicate the statistic is ensemble averaged over the data sets. In this context, u_1 is the stream-wise component of velocity, u, and u_2 is the transverse component, v.

Consider first the centerline of the hypermixing injector flowfield. It was observed instantaneously that there appeared to be a series of vortical structures lining the top of the wake. One of the issues with using a higher-order statistic is that the turbulence in these flows is neither homogeneous nor isotropic; thus, the selection of the correlation point is crucial in finding structure within these flowfields. Consider a point located on one of these perceived structures in an instantaneous realization of the flowfield. For the upstream field of view, the four components of this tensor are shown in Fig 3.118. It can be seen for the $\langle u'u'' \rangle$ component, there is little correlation to be found except for the autocorrelation at $(5.5, 0.5)$. A similar observation can be made of the $\langle v'u'' \rangle$

component. On the other hand the $\langle u'v'' \rangle$ component does exhibit some degree of correlation; near the downstream edge of the field of view, there is some suggestion of alternating positive and negative structures approximately $1h$ in diameter starting at $x/h = 4$, though there is little correlation with any of the surrounding structures. A similar correlation is observed in the $\langle v'v'' \rangle$ component, with the exception being that the sign of the correlation is opposite. The downstream field of view (SV 2a) visualized in Fig 3.119 show similar trends. The $\langle u'u'' \rangle$and $\langle v'u'' \rangle$ components of the correlation show little sign of organized structures in the mean beyond the autocorrelation point. The $\langle u'v'' \rangle$ component is the most striking observed in this data; the appearance of alternating positive and negative lobes appear all along the wake. These structures still maintain a diameter of roughly $1h$ and match in location very closely with the occurrence of the vortices noted in Section 3.2.2.1. What this suggests is that the stream-wise vortex pair present in this flowfield imposes a periodicity to the velocity fluctuations in this flowfield. In the present analysis, this periodicity has manifested itself as a strong coupling between the stream-wise and transverse velocity fluctuations. As was discussed at the end of Section 3.2.2.1, a likely mechanism for this periodic behavior is the motion of the vortex cores relative to one another. However, without a time-resolved, three-dimensional measurement of the velocity field, discerning the exact mechanism of this coupling is very difficult. Nonetheless, the present analysis provides further evidence for the coupling between the stream-wise vortices and the observed circulating structures in the various side-views. As an addendum to this section, refer to Appendix 3D for a short analysis of the flowfield utilizing proper orthogonal decomposition.

3.3 – CONCLUSIONS

This chapter sought to examine the general structure and kinematics of two supersonic mixing flowfields. The two models tested were a simple hypermixing injector featuring expansive ramps flanking a central block and a planar injector featuring no hypermixing elements or castellation. It was found that the planar injector strongly resembled a two-dimensional wake within the data reduction planes. The hypermixing injector too was similar when observed in a side-view configuration, but featured a distinct upward deflection of the central wake and strong transverse velocity component along the centerline. Examining this flow in an end-view configuration revealed a strong stream-wise vortex pair responsible for the lift along the centerline. Furthermore, the vortex pair caused significant distortion of the overall wake structure. This phase of the analysis also revealed a span-wise asymmetry in the flow of the tunnel when approaching the side-wall boundary layers.

Both flowfields exhibited different unsteadiness characteristics. Instantaneously, the planar injector flowfield was found to exhibit sporadic vortex shedding, but lacked any strong organization in the statistical sense. The hypermixing injector flowfield, on the other hand, was found to exhibit notable periodicity in the occurrence of span-wise vortices and circulation. Furthermore, the strongest fluctuations present in the end-view planes were directly coincident with the motion of the stream-wise vortex cores. Additional studies utilizing two-point turbulent correlations revealed evidence of coherent spatial structures within the hypermixing flowfield, while the planar injector flowfield lacked such organization.

3.4 – SUGGESTED WORK

The work presented in this chapter provides a fairly comprehensive overview of the structure and unsteady behavior of the two strut-injector flowfields used in this study.

However, in conducting this research a number of potential studies either tangential or complementary to the body of work presented here were made apparent. The first of these relates to the merging and cancelation of vortex structures within the hypermixing flowfields used in previous studies. It was tacitly assumed in the current body of work that stronger and/or more persistent stream-wise vortices were desirable to enhancing mixing in the flowfield. However, this is not necessarily true insofar as the turbulence generated by the breakdown of stream-wise vortices is also instrumental at augmenting mixing. In all likelihood, some optimal combination of vortical persistence and breakdown is optimal for mixing the flow in a desired length. An interesting area of study could utilize the multi-plane and stereoscopic PIV arrangements used in this chapter to observe the breakdown process in several hypermixing injectors with incremented degrees of asymmetry in the transverse direction, thereby allowing for a variation in the persistence and breakdown of the vortex structures with downstream distance.

A further point of inquiry arises regarding the motion of the vortex cores relative to one another. The present study utilized statistics to describe the motion of the cores, but the actual relative motion could not be observed directly. While the equipment does not yet exist to both image and illuminate the particle fields at the required temporal resolution for these studies (approximately 1 MHz or so assuming the temporal separation used in the present studies), the motion could at least be observed over short intervals (3 μs or so) by attempting the following experiment. Using the six Nd:YAG cavities available to the author (and any new cavities that have become available) in addition to two dye lasers, a string of pulses of various wavelength could be generated. For example, two 532 nm pulses followed by two 570 nm pulses and two 610 nm pulses could be generated with the aforementioned equipment. Subsequently, after combining and illuminating a single volume with these pulses, the resulting scattering from seeded

particles could be imaged with three frame-straddling CCD cameras (filtered to the desired wavelengths) to observe the evolution over this 5 μs period. In addition to the qualitative information these data would reveal about the motion of the vortex cores, the data could potentially be processed for a short sequence of time-resolved PIV if the imaging angles were sufficiently narrow with respect to the tunnel axis. This sort of experiment would be extremely useful for diagnosing the stream-wise vortex motion, though it would be quite difficult to conduct due to the complexity of the experiment.

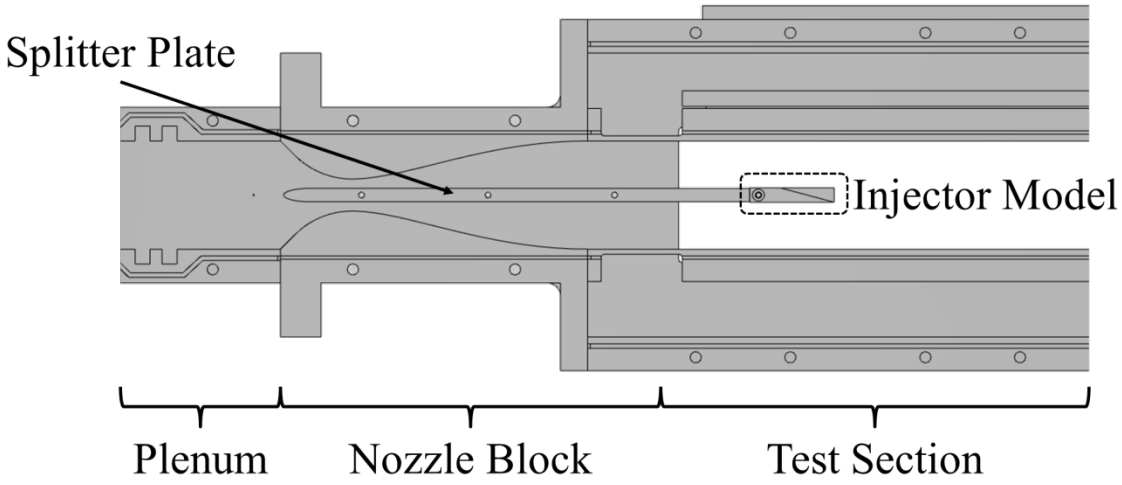

Figure 3.1: Diagram of Mach 3 wind tunnel used in the kinematics studies

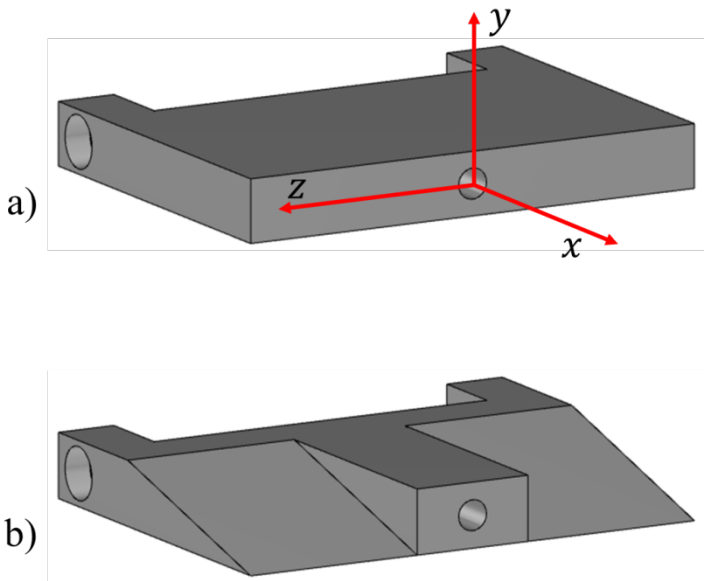

Figure 3.2: Diagram of the two injector models used in the kinematics studies. a) Planar injector with global coordinate system displayed and b) hypermixing injector

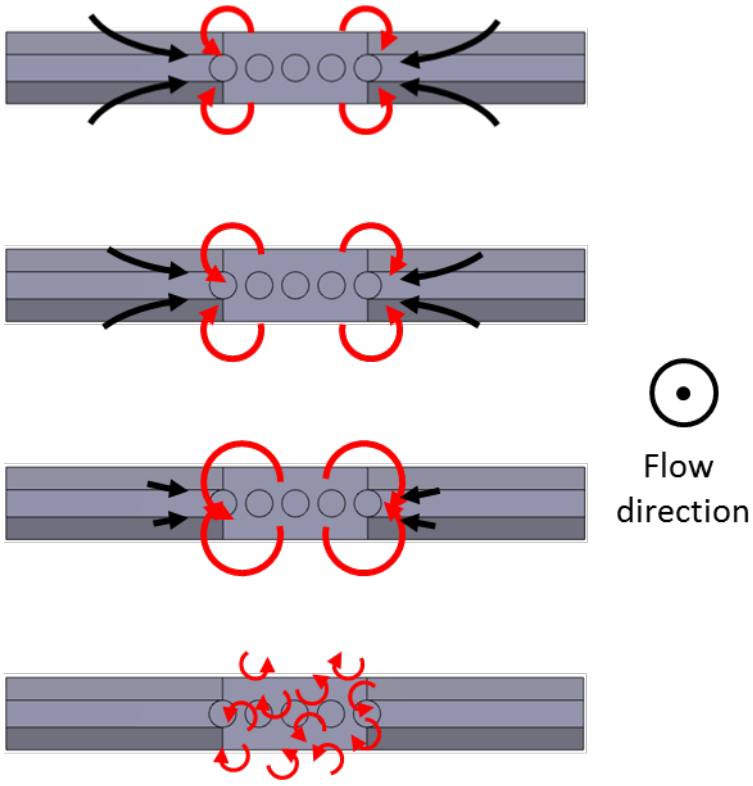

Figure 3.3: Illustration of vortex-vortex interaction that occurs in transversely symmetric hypermixing injector flowfields. Top – very near-field of injector, second from top – downstream 1, third from top – downstream 2, and bottom – far-field

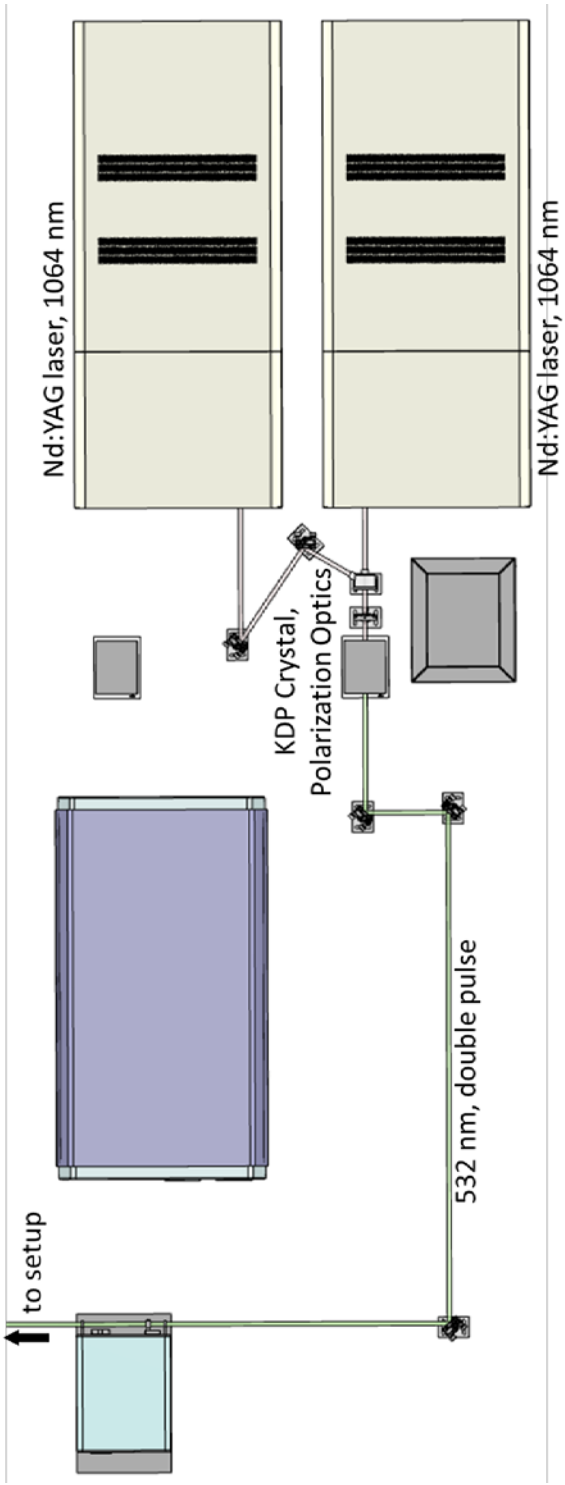

Figure 3.4: Diagram of laser setup used in PIV experiments for the flowfield kinematics studies

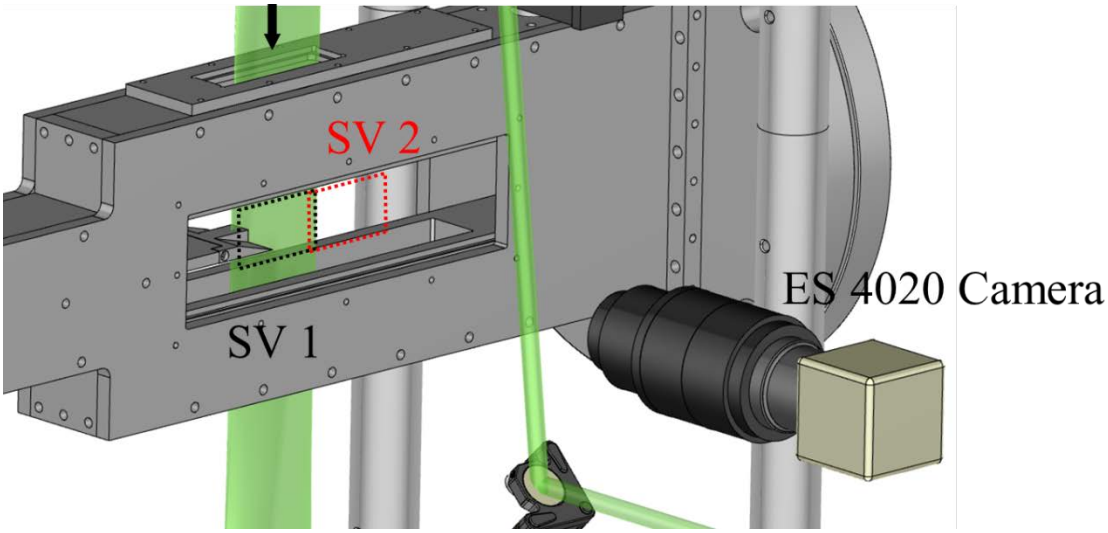

Figure 3.5: Diagram of camera and laser sheet position for side-view PIV measurements.

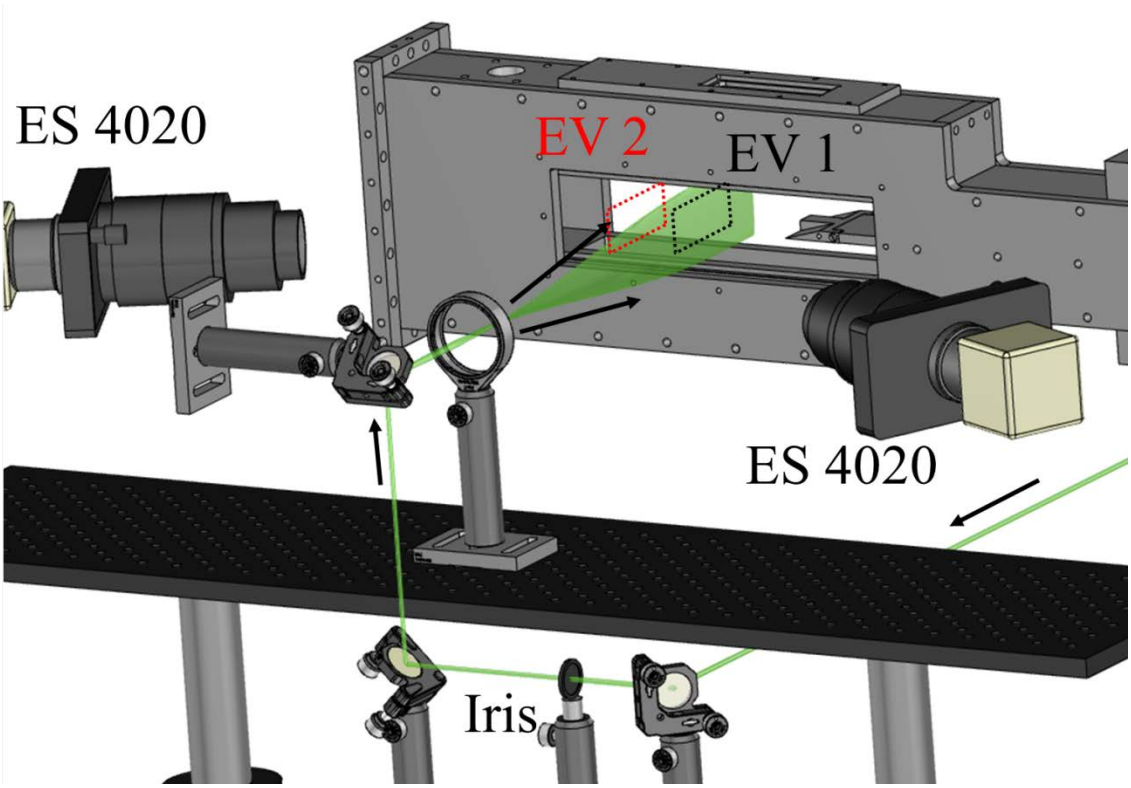

Figure 3.6: Diagram of camera and laser setup for end-view stereoscopic PIV measurements.

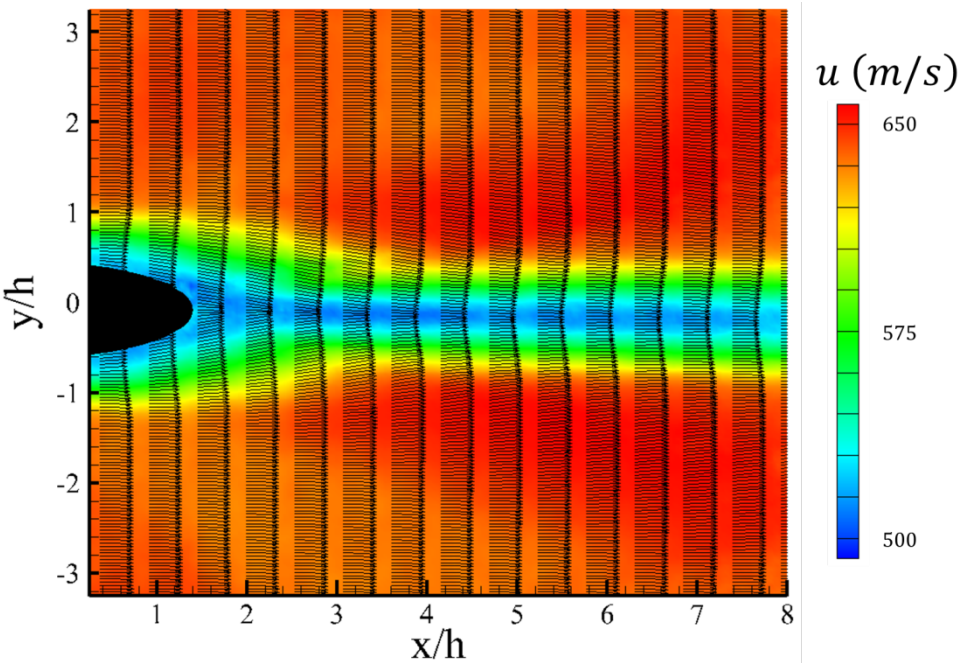

Figure 3.7: Mean centerline stream-wise velocity contours for near-field of planar injector flowfield (SV 1a)

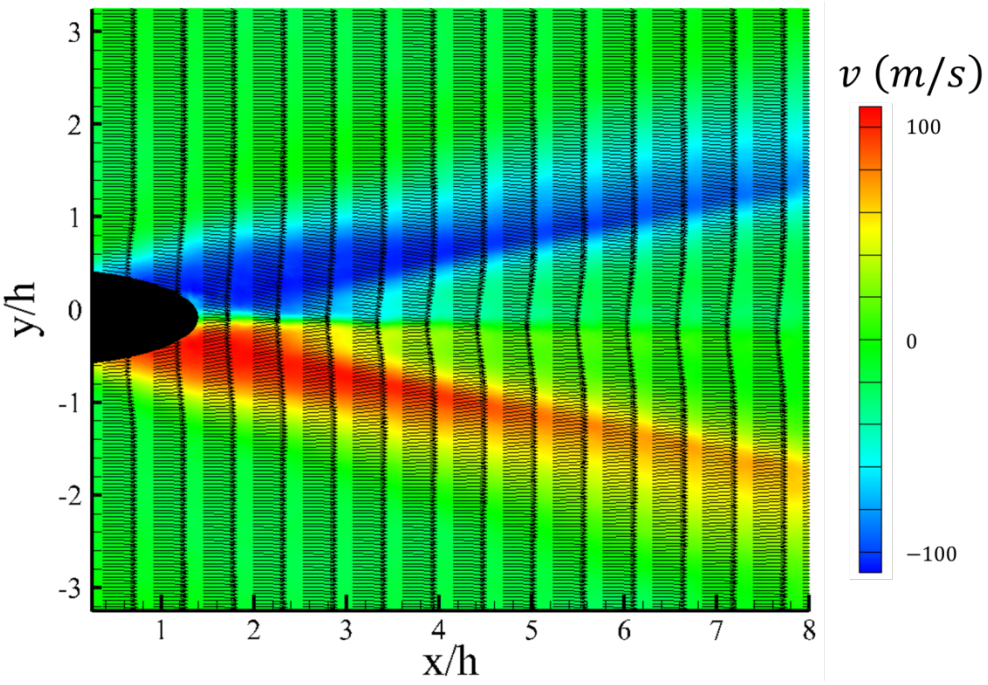

Figure 3.8: Mean centerline transverse velocity contours for near-field of planar injector flowfield (SV 1a)

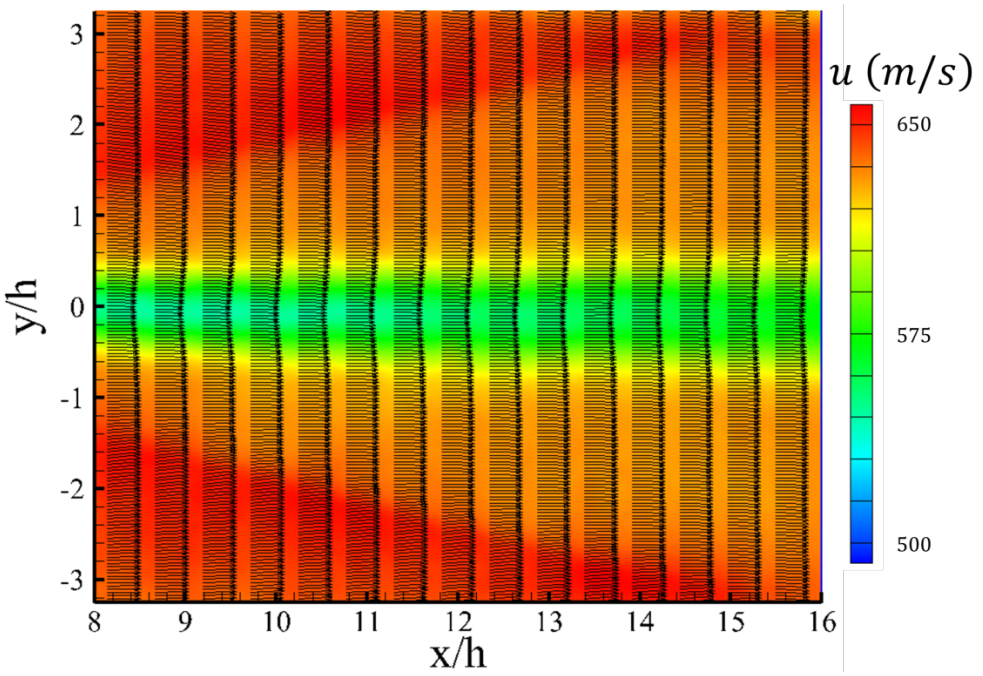

Figure 3.9: Mean centerline stream-wise velocity contours for mid-field of planar injector flowfield (SV 2a)

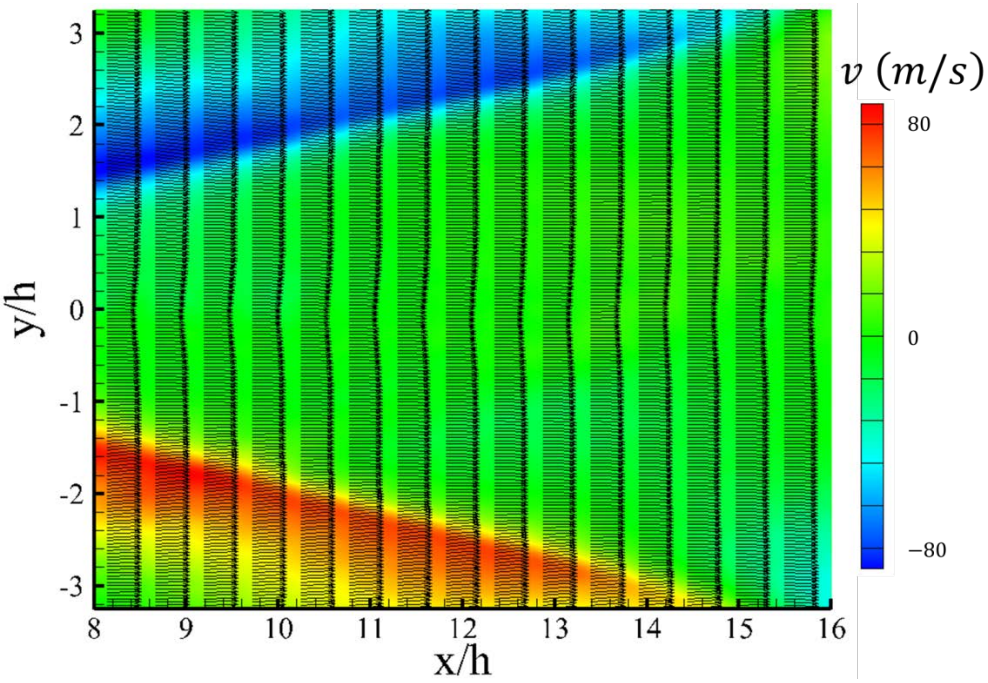

Figure 3.10: Mean centerline stream-wise velocity contours for mid-field of planar injector flowfield (SV2a)

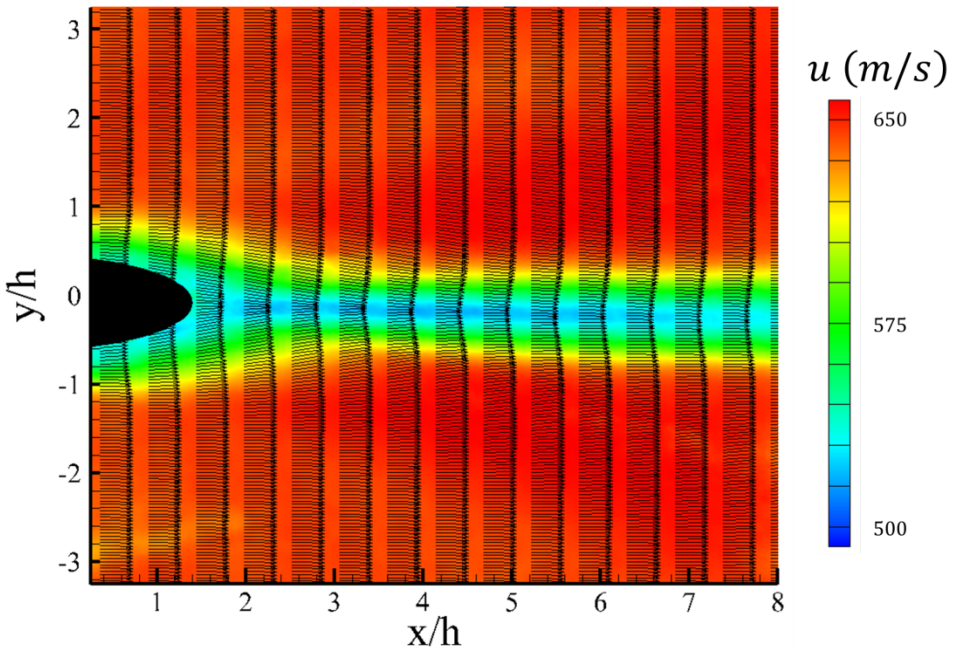

Figure 3.11: Mean off-centerline ($z/h = 0.75$) stream-wise velocity contours for near-field of planar injector flowfield (SV 1b)

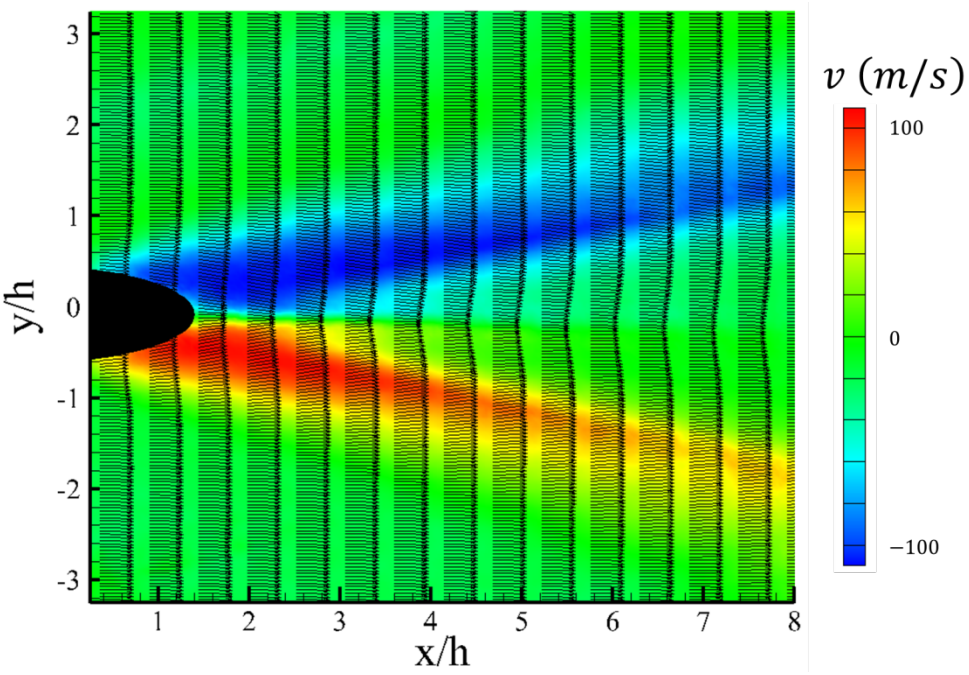

Figure 3.12: Mean off-centerline ($z/h = 0.75$) transverse velocity contours for near-field of planar injector flowfield (SV 1b)

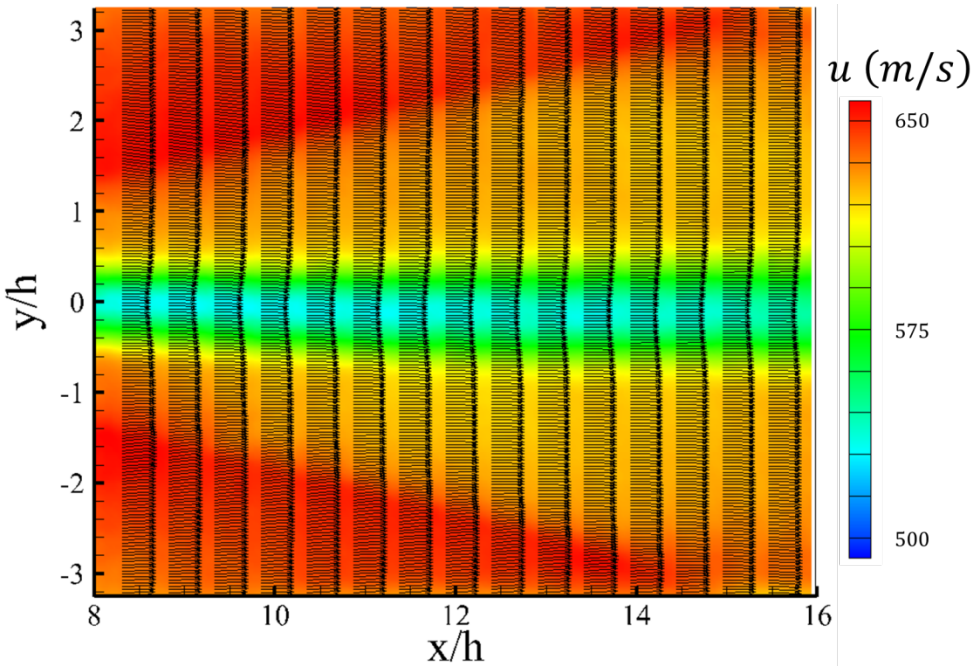

Figure 3.13: Mean off-centerline ($z/h = 0.75$) stream-wise velocity contours for mid-field of planar injector flowfield (SV 2b)

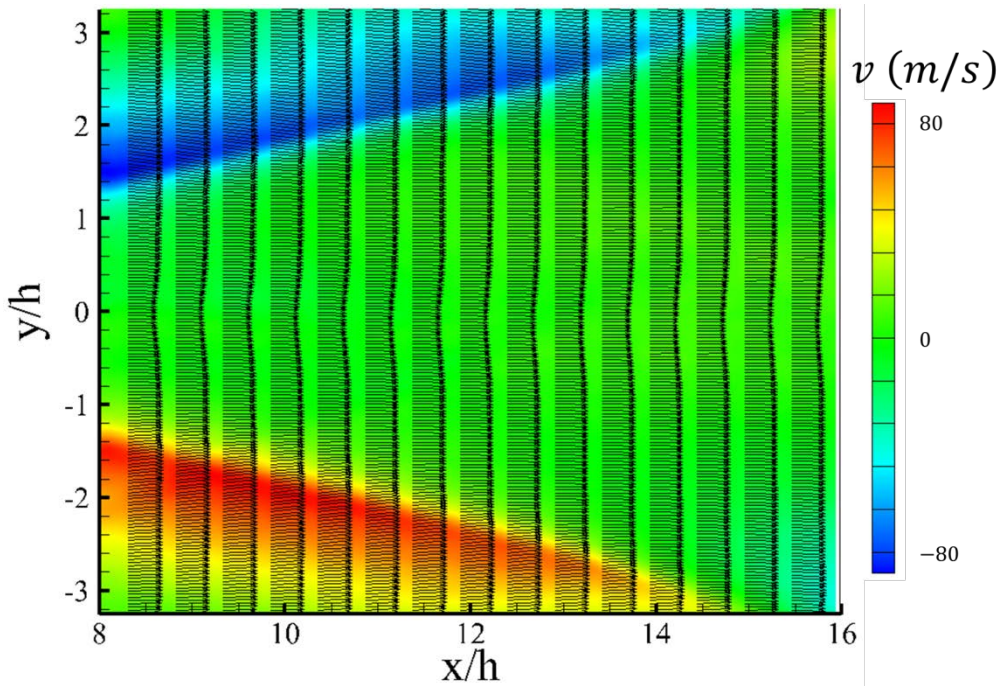

Figure 3.14: Mean off-centerline ($z/h = 0.75$) transverse velocity contours for mid-field of planar injector flowfield (SV 2b)

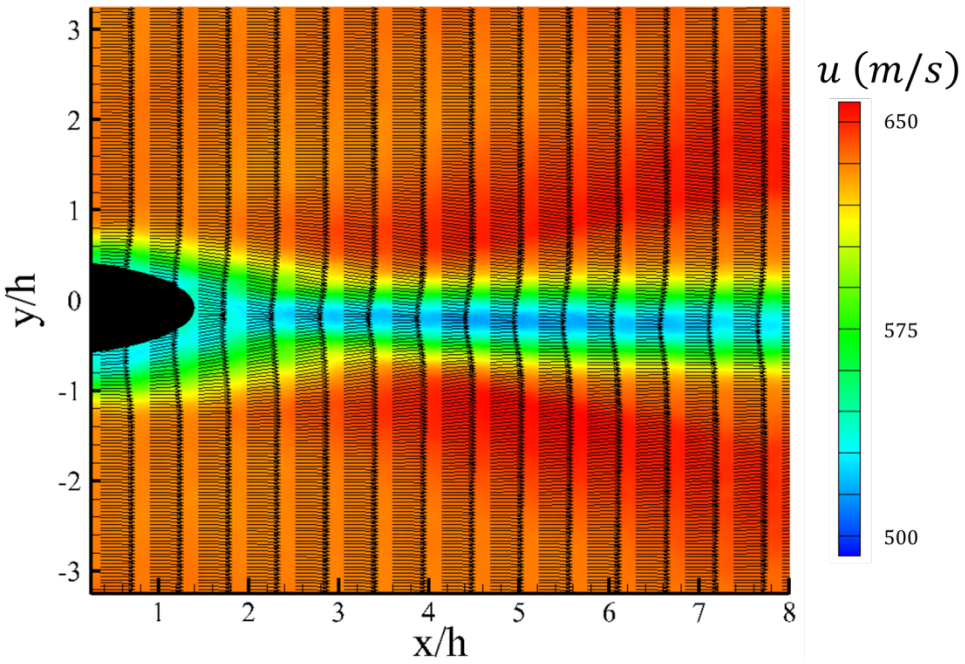

Figure 3.15: Mean off-centerline ($z/h = 1.25$) stream-wise velocity contours for near-field of planar injector flowfield (SV 1c)

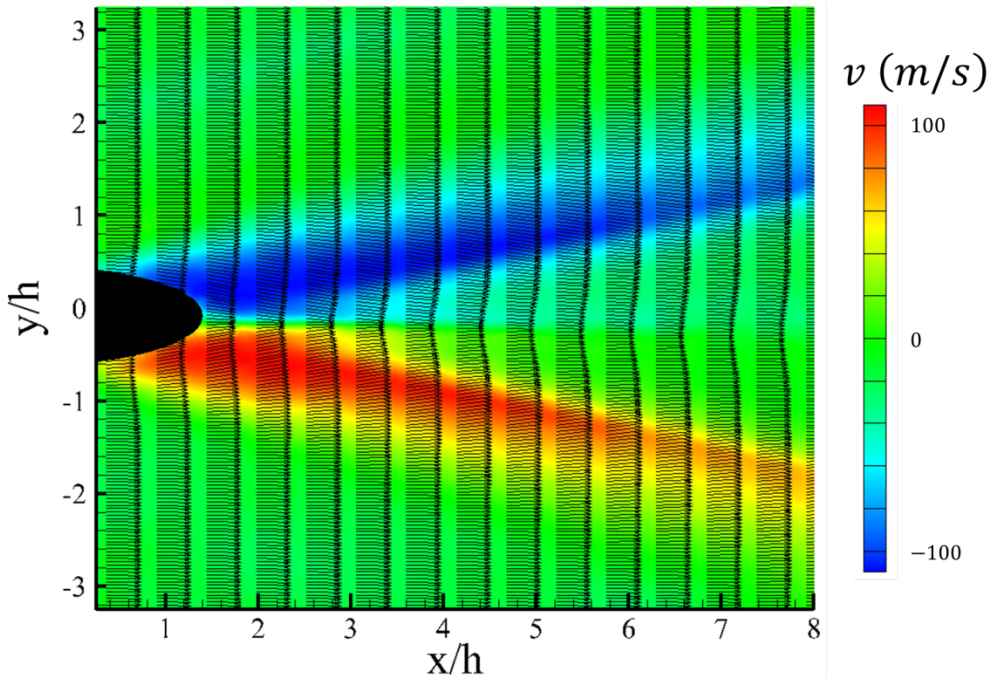

Figure 3.16: Mean off-centerline ($z/h = 1.25$) transverse velocity contours for near-field of planar injector flowfield (SV 1c)

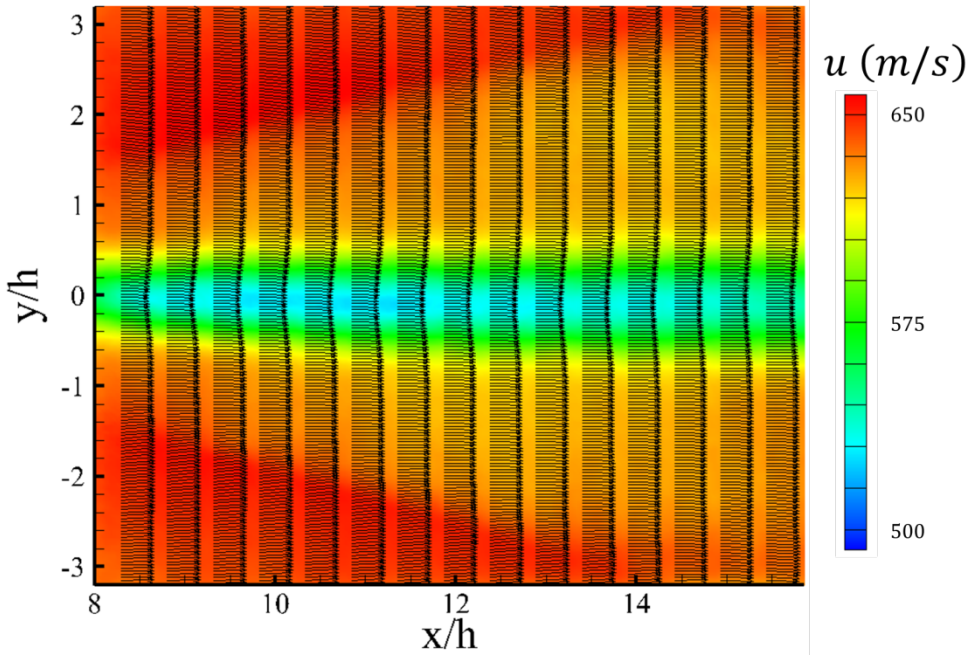

Figure 3.17: Mean off-centerline ($z/h = 1.25$) stream-wise velocity contours for mid-field of planar injector flowfield (SV 2c)

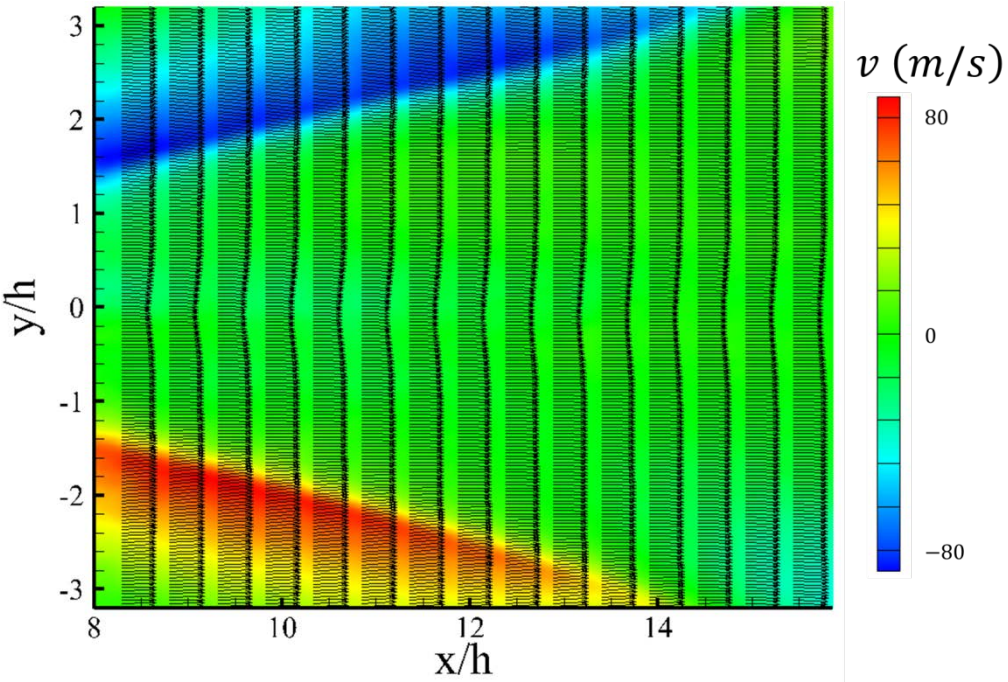

Figure 3.18: Mean off-centerline ($z/h = 1.25$) transverse velocity contours for mid-field of planar injector flowfield (SV 2c)

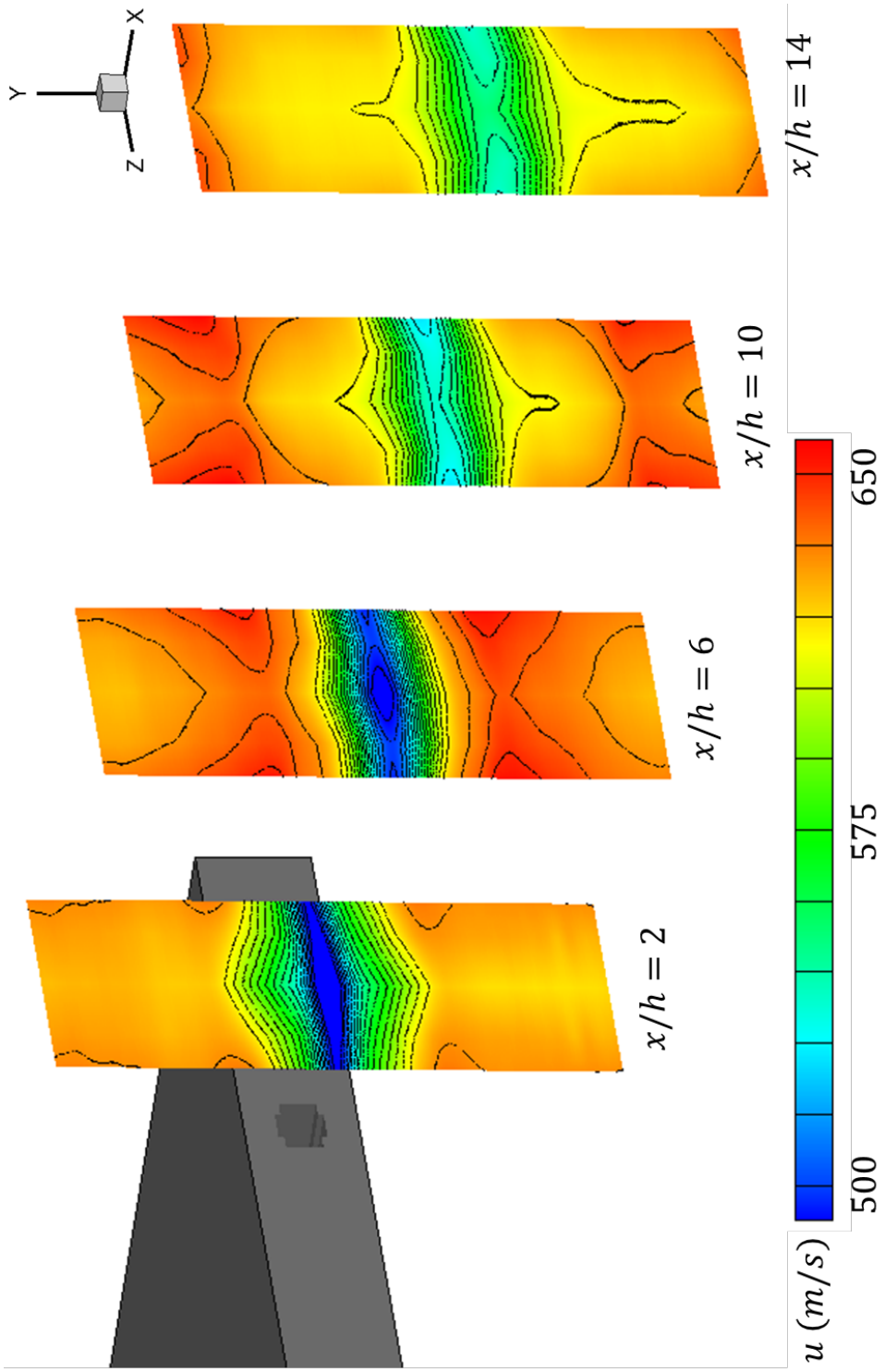

Figure 3.19: Three-dimensional reconstruction of planar injector flowfield showing planes of stream-wise velocity

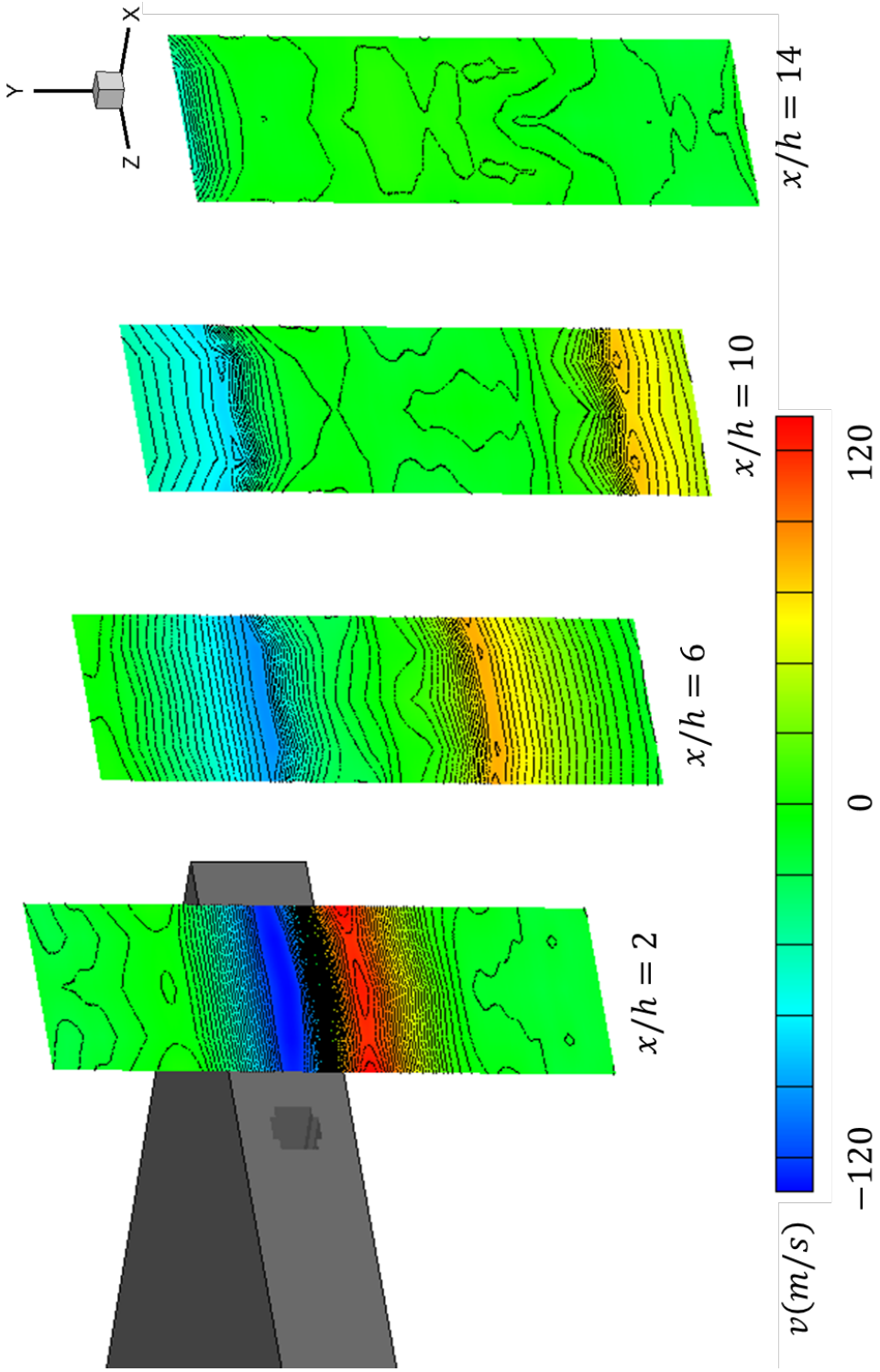

Figure 3.20: Three-dimensional reconstruction of planar injector flowfield showing planes of transverse velocity

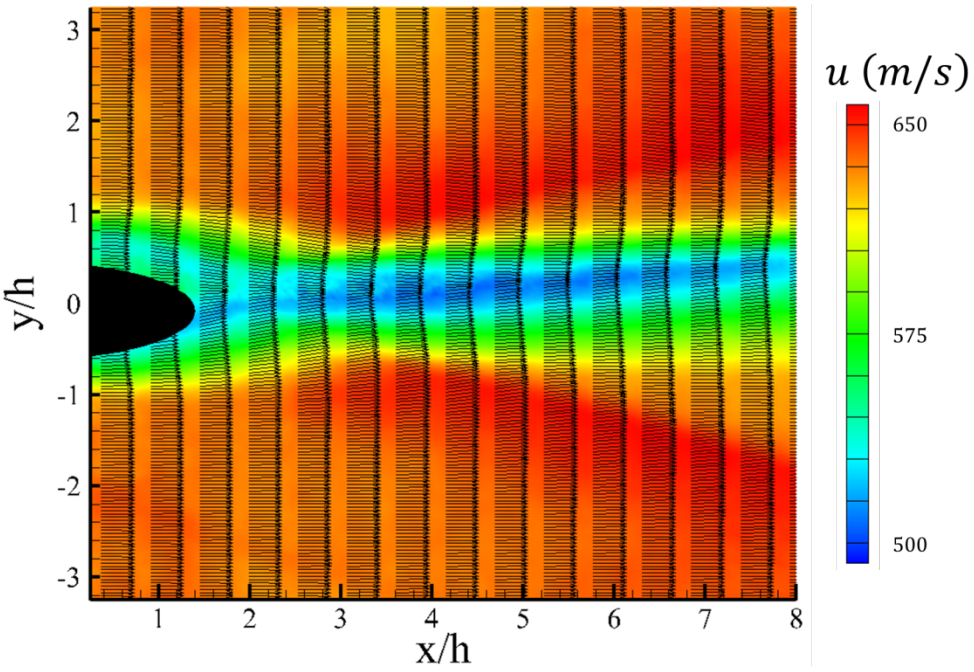

Figure 3.21: Mean centerline stream-wise velocity contours for near-field of hypermixing injector flowfield (SV 1a)

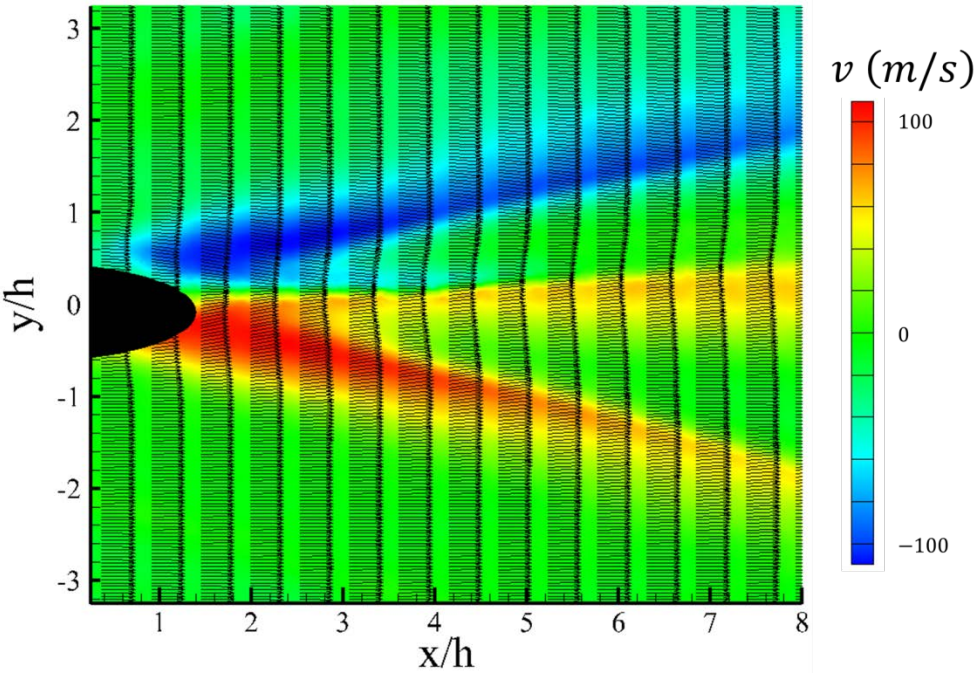

Figure 3.22: Mean centerline transverse velocity contours for near-field of hypermixing injector flowfield (SV 1a)

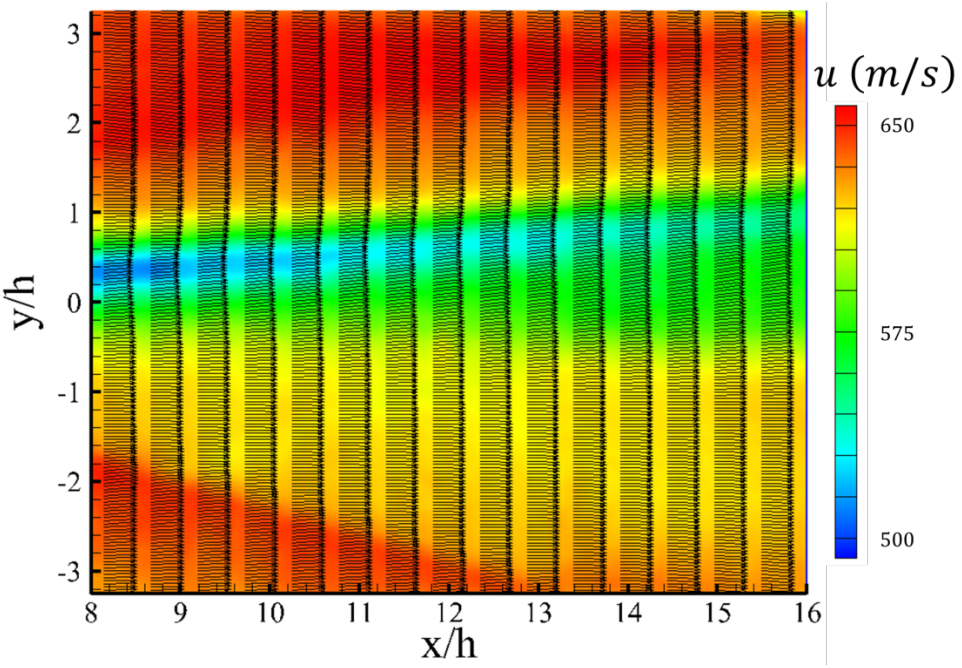

Figure 3.23: Mean centerline stream-wise velocity contours for mid-field of hypermixing injector flowfield (SV 2a)

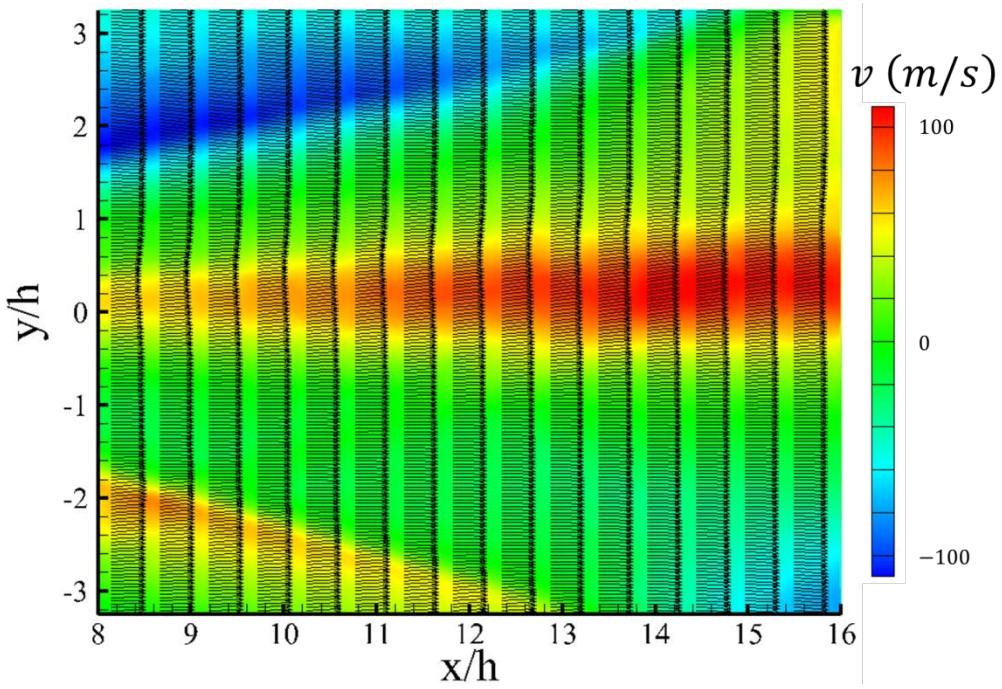

Figure 3.24: Mean centerline transverse velocity contours for mid-field of hypermixing injector flowfield (SV 2a)

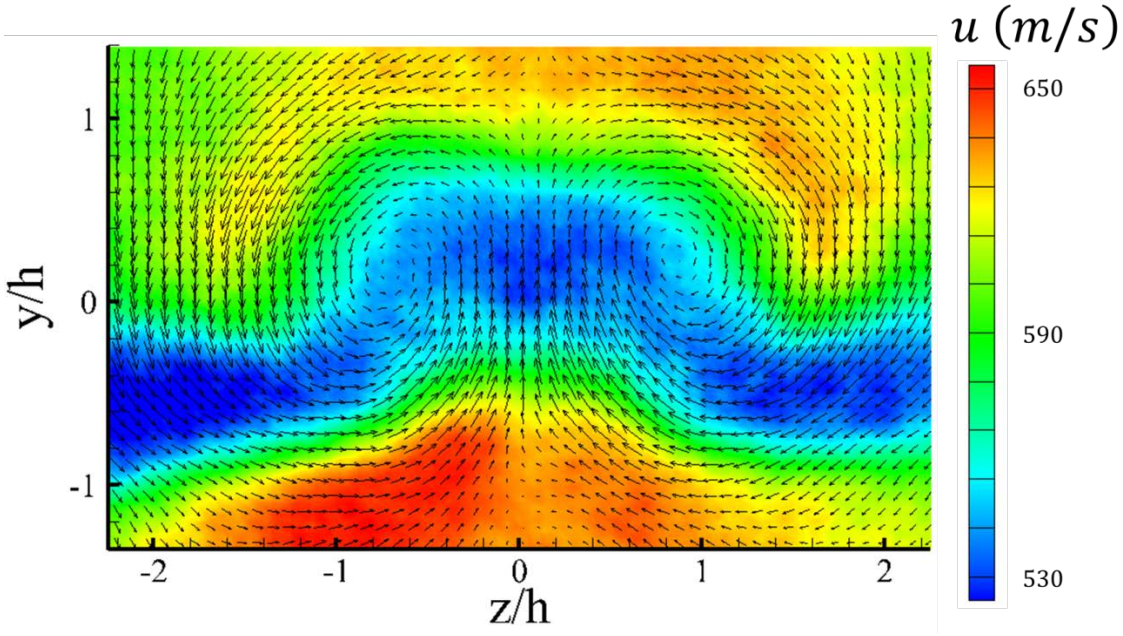

Figure 3.25: Mean stream-wise end-view velocity contours for hypermixing injector flowfield ($x/h = 8$)

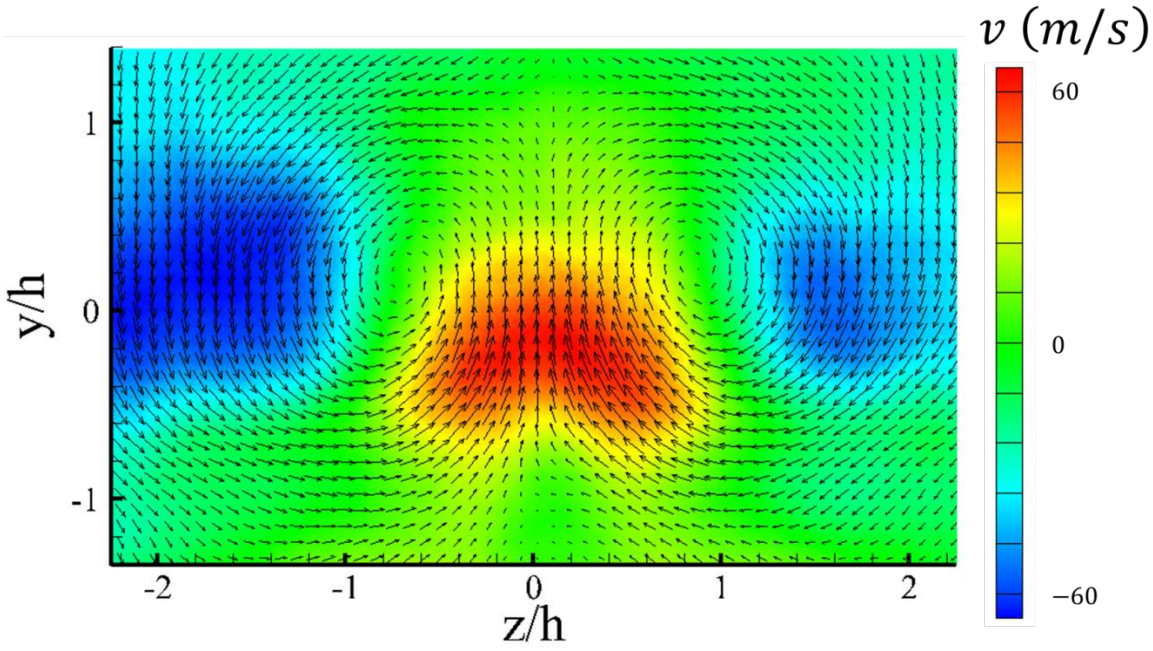

Figure 3.26: Mean transverse end-view velocity contours for hypermixing injector flowfield ($x/h = 8$)

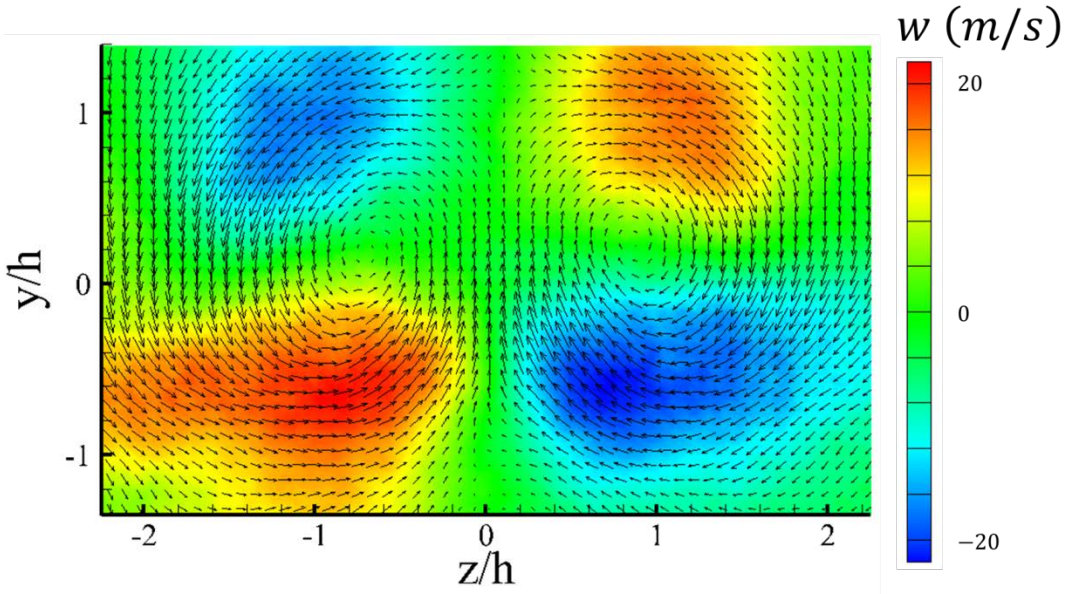

Figur the corri 3.27: Mean span-wise end-view velocity contours for hypermixing injector flowfield ($x/h = 8$)

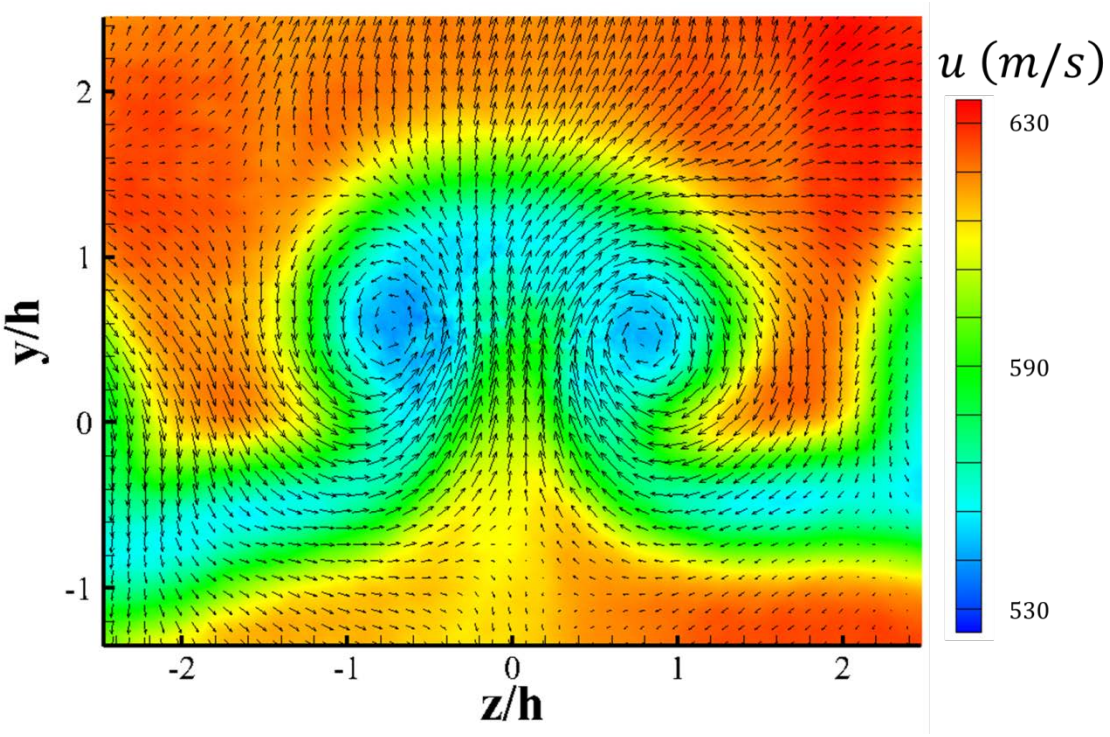

Figure 3.28: Mean stream-wise end-view velocity contours for hypermixing injector flowfield ($x/h = 16$)

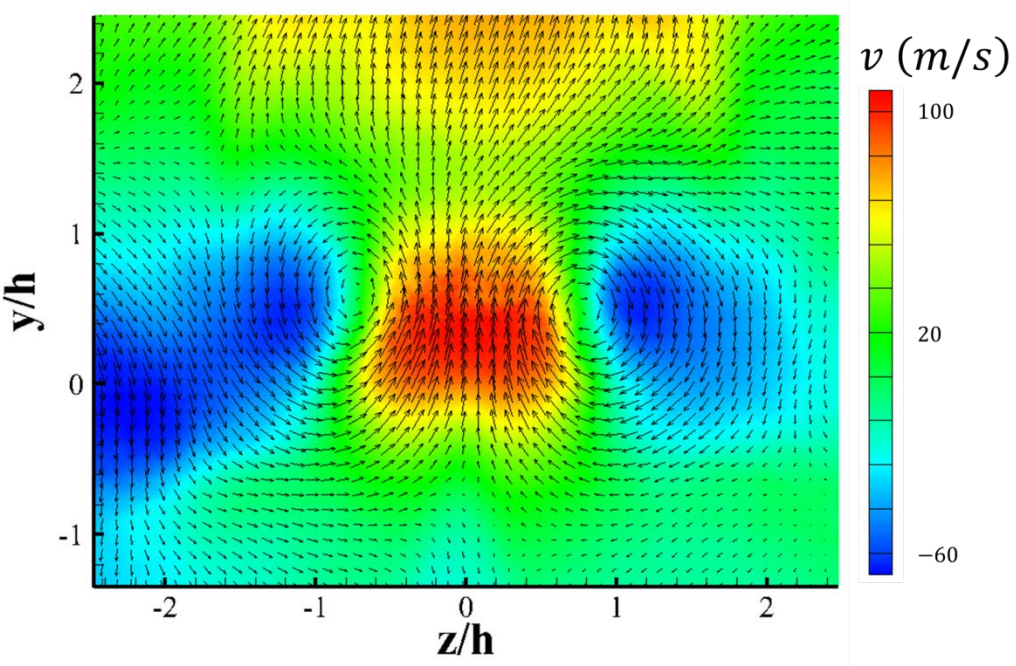

Figure 3.29: Mean transverse end-view velocity contours for hypermixing injector flowfield ($x/h = 16$)

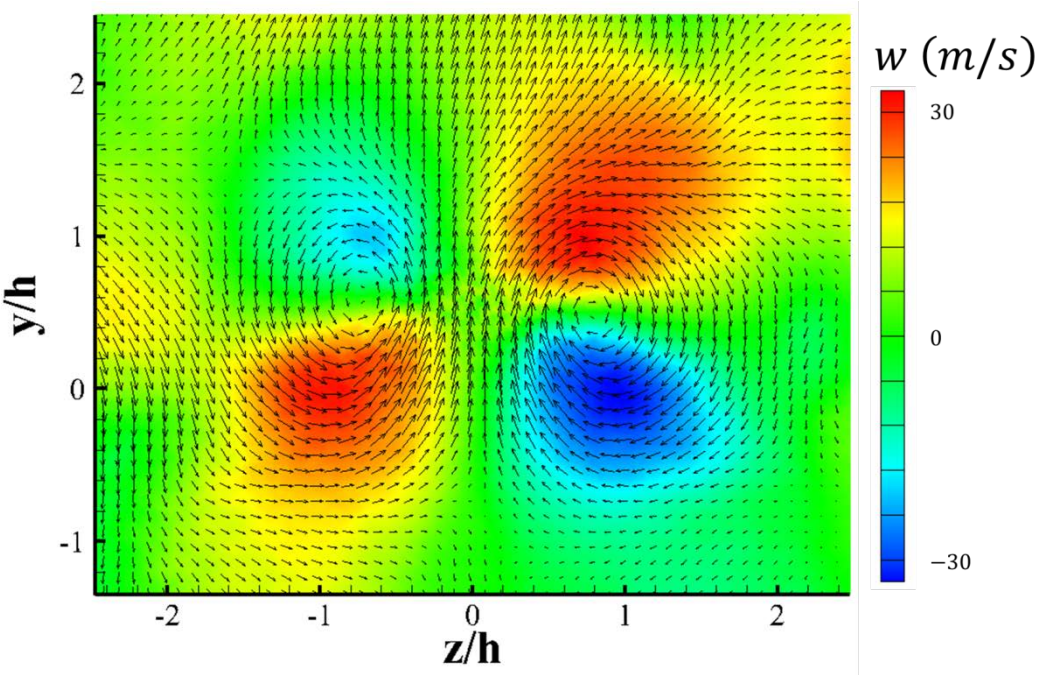

Figure 3.30: Mean span-wise end-view velocity contours for hypermixing injector flowfield ($x/h = 16$)

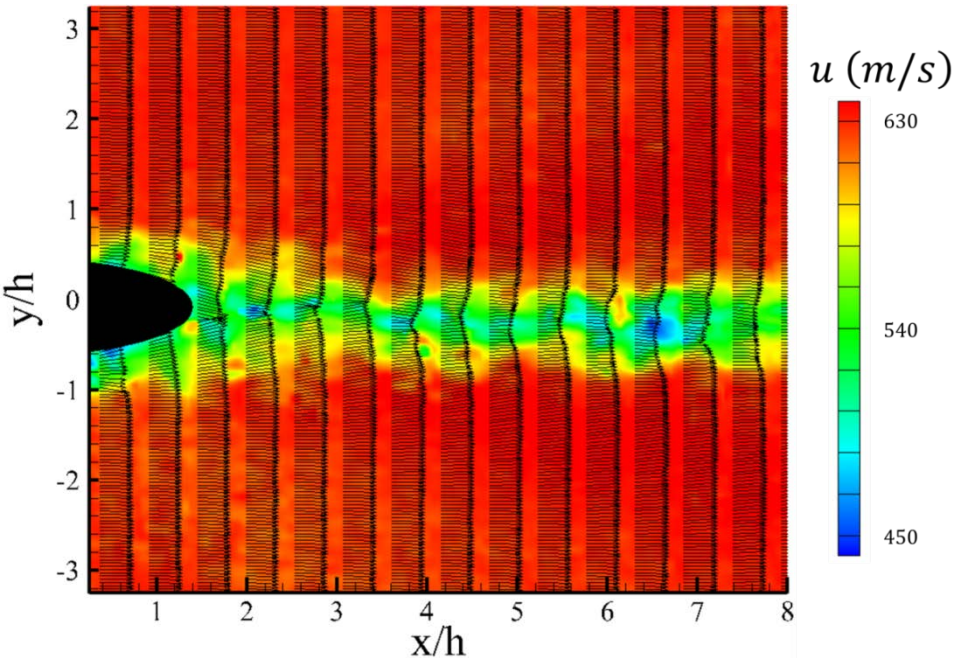

Figure 3.31: Example instantaneous centerline stream-wise velocity contours for near-field of planar injector flowfield (SV 1a)

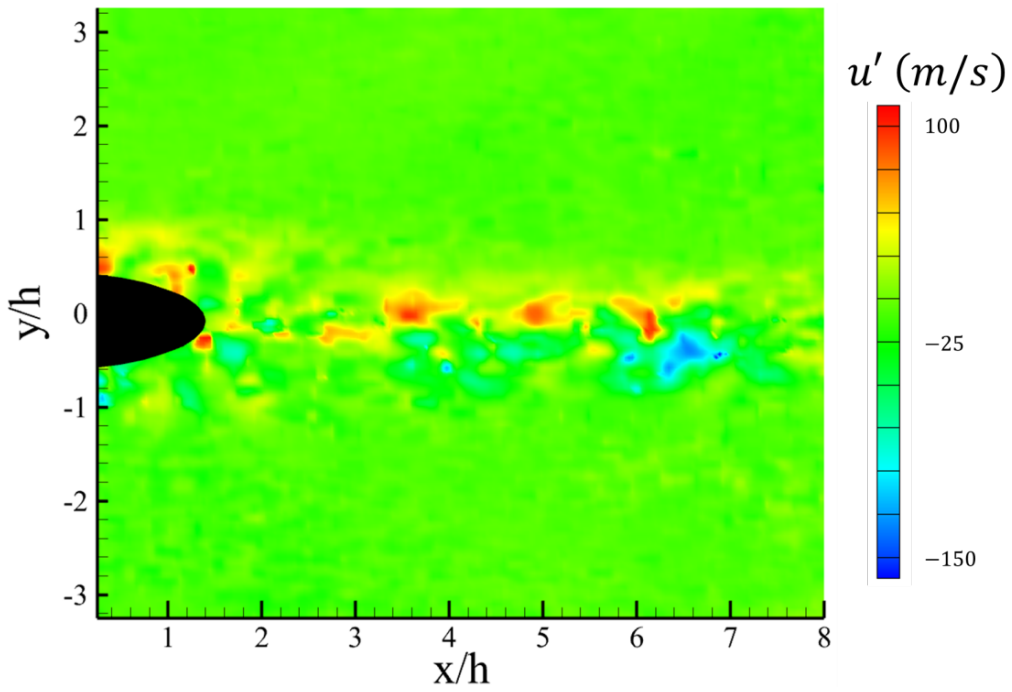

Figure 3.32: Example fluctuating centerline stream-wise velocity contours for near-field of planar injector flowfield (SV 1a)

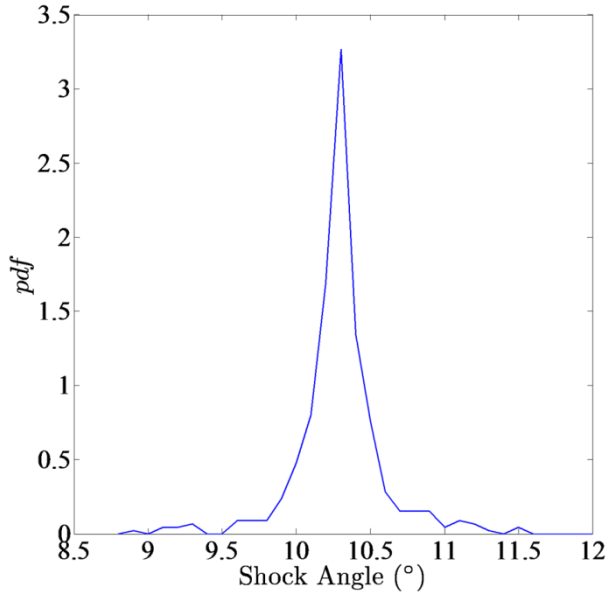

Figure 3.33: PDF of shock angle for planar injector flowfield

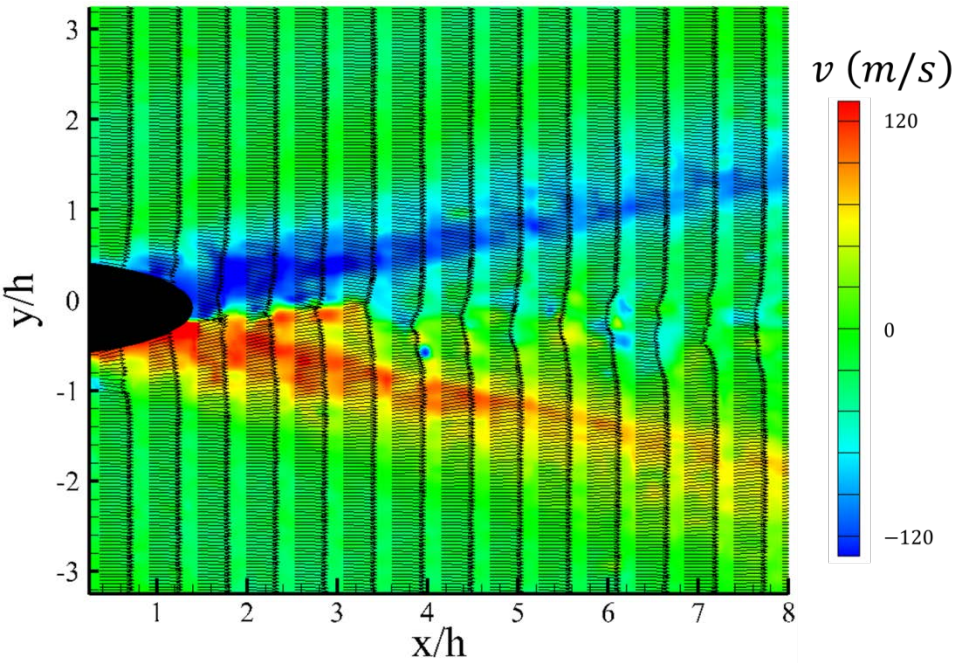

Figure 3.34: Example instantaneous centerline transverse velocity contours for near-field of planar injector flowfield (SV 1a)

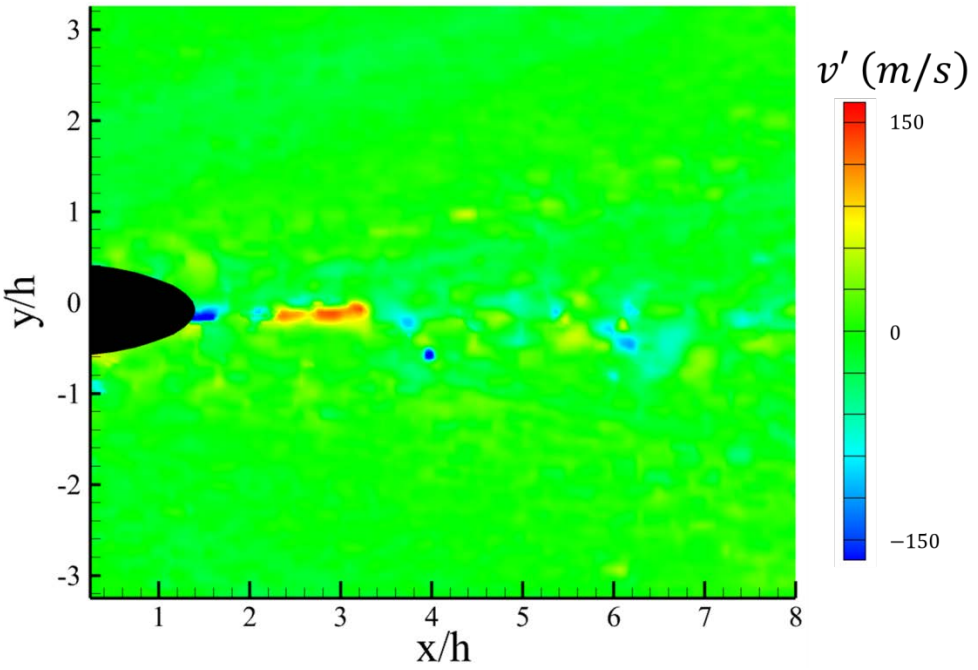

Figure 3.35: Example fluctuating centerline transverse velocity contours for near-field of planar injector flowfield (SV 1a)

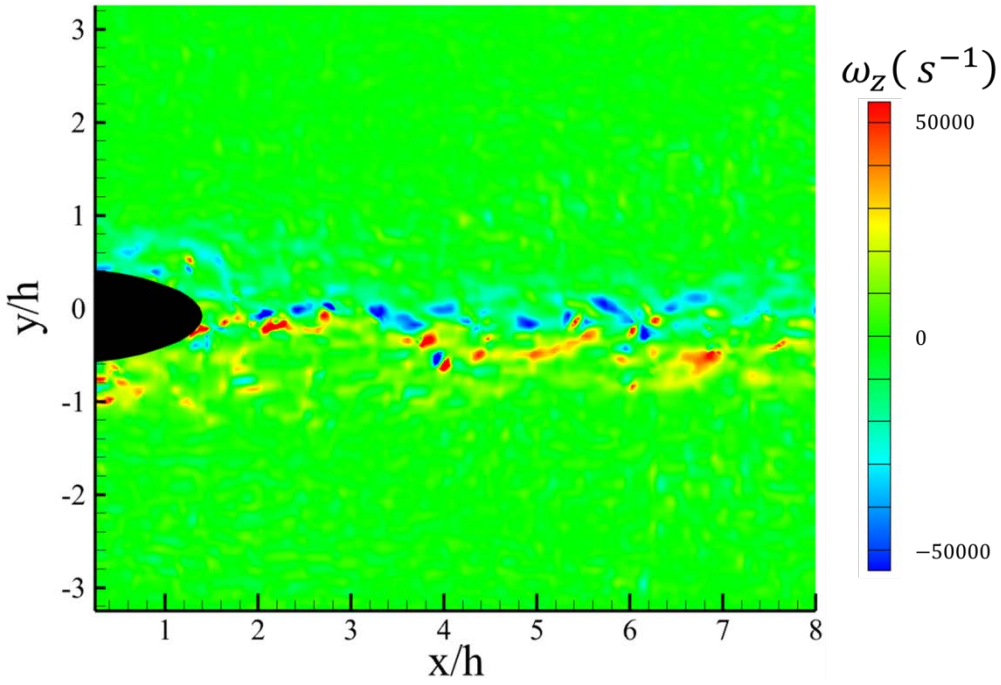

Figure 3.36: Example instantaneous centerline span-wise vorticity contours for near-field of planar injector flowfield (SV 1a)

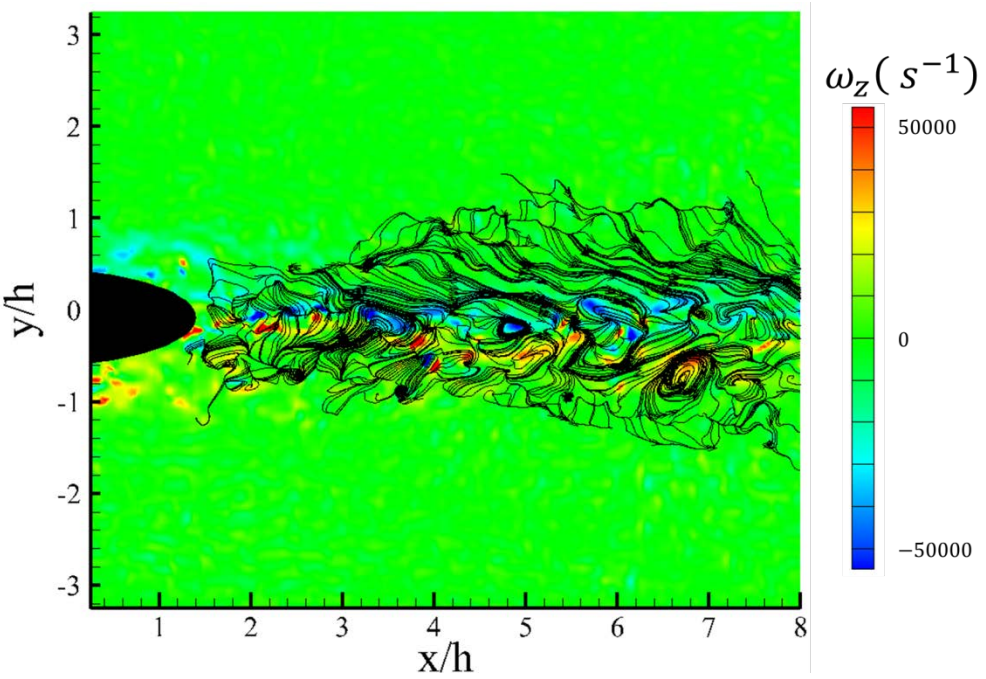

Figure 3.37: Example instantaneous centerline span-wise vorticity contours for near-field of planar injector flowfield overlaid with fluctuating streamlines (SV 1a)

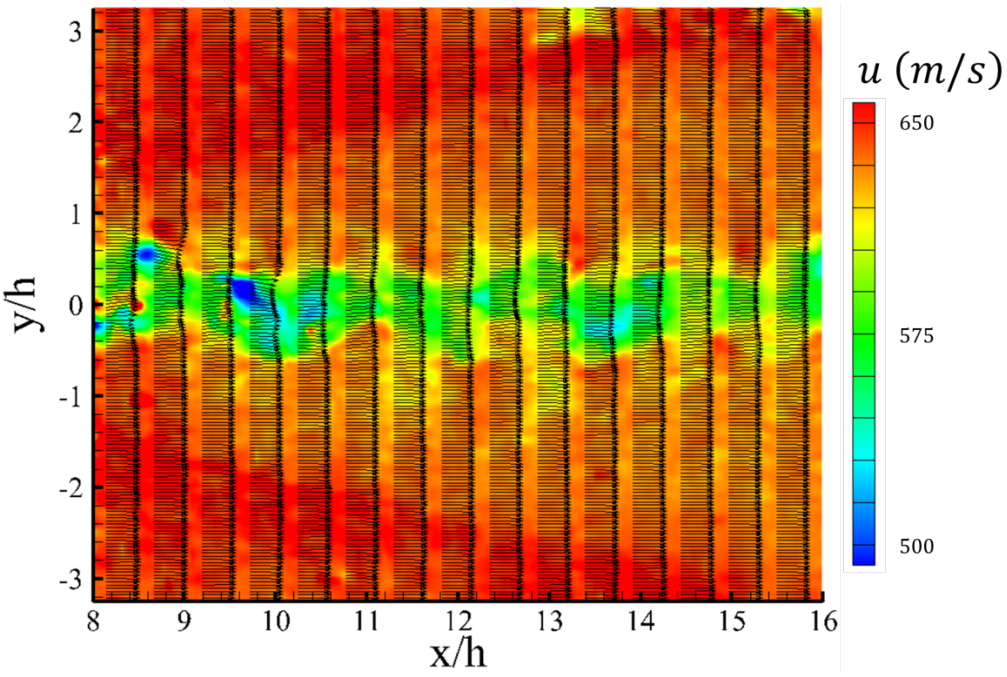

Figure 3.38: Example instantaneous centerline stream-wise velocity contours for mid-field of planar injector flowfield (SV 2a)

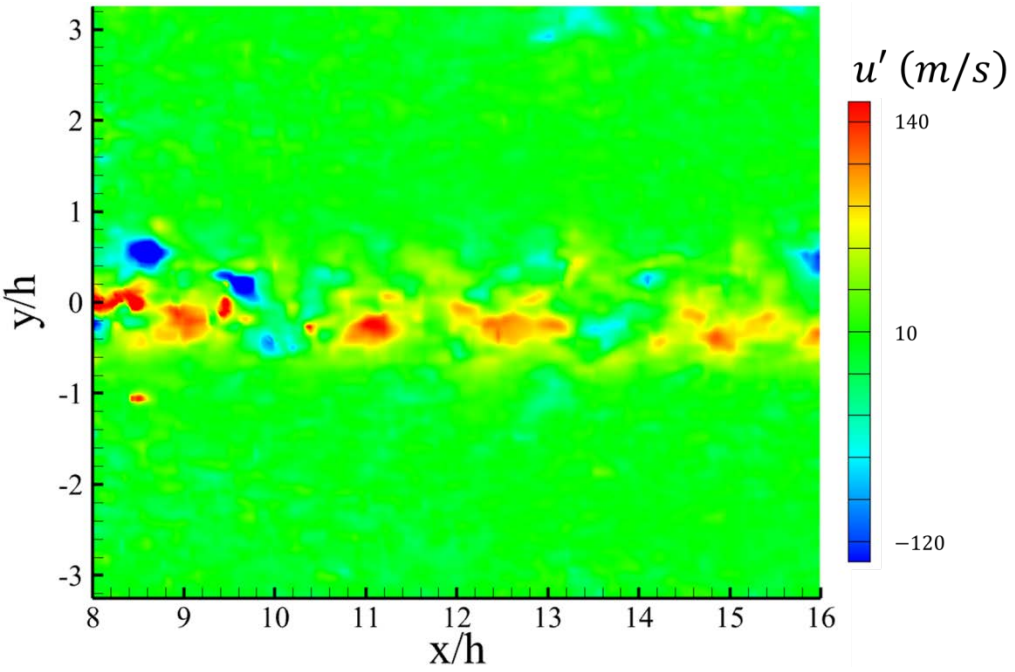

Figure 3.39: Example fluctuating centerline stream-wise velocity contours for mid-field of planar injector flowfield (SV 2a)

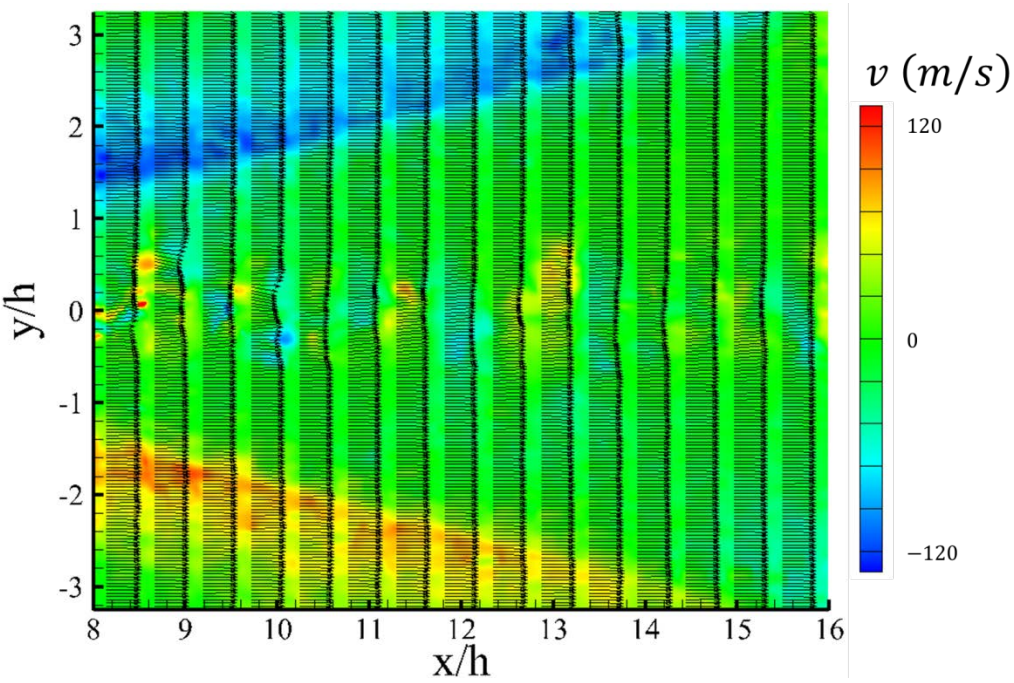

Figure 3.40: Example instantaneous centerline transverse velocity contours for mid-field of planar injector flowfield (SV 2a)

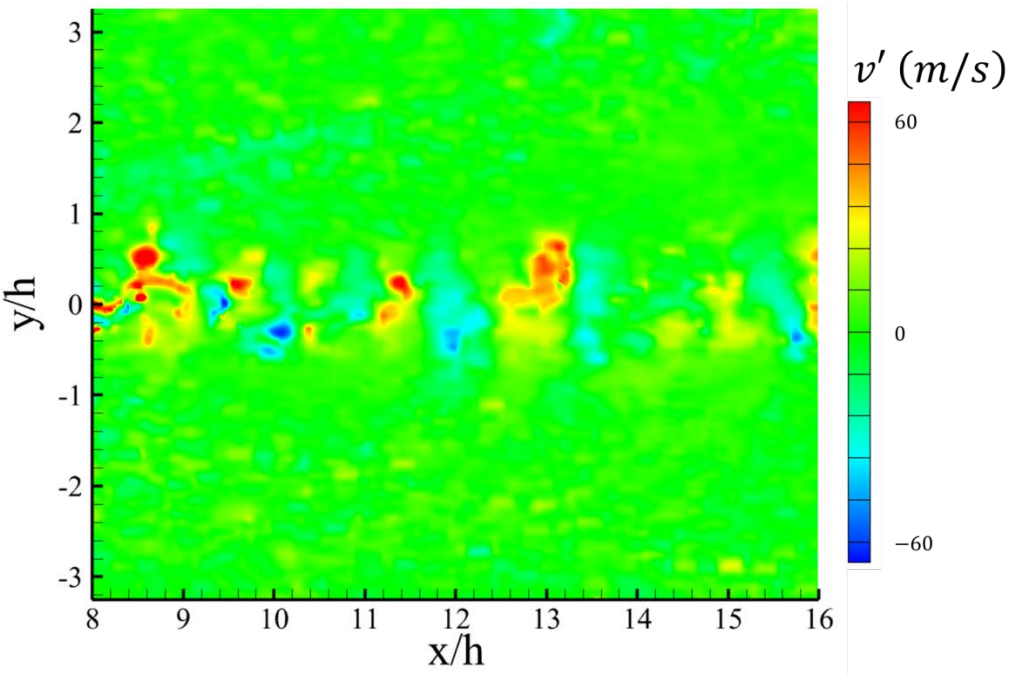

Figure 3.41: Example fluctuating centerline transverse velocity contours for mid-field of planar injector flowfield (SV 2a)

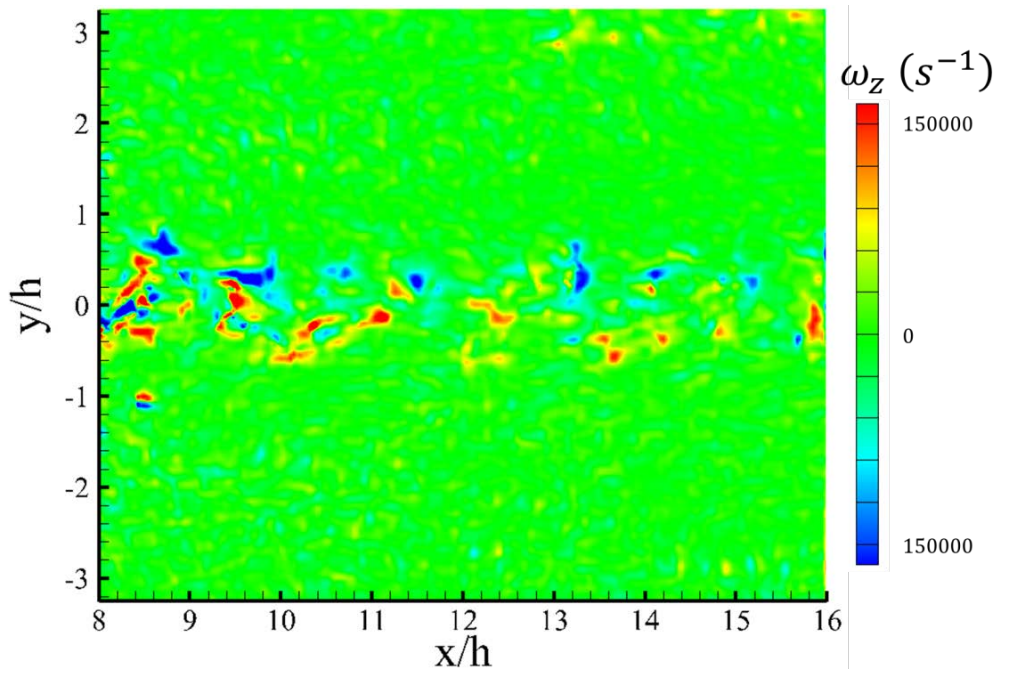

Figure 3.42: Example instantaneous centerline span-wise vorticity contours for mid-field of planar injector flowfield (SV 2a)

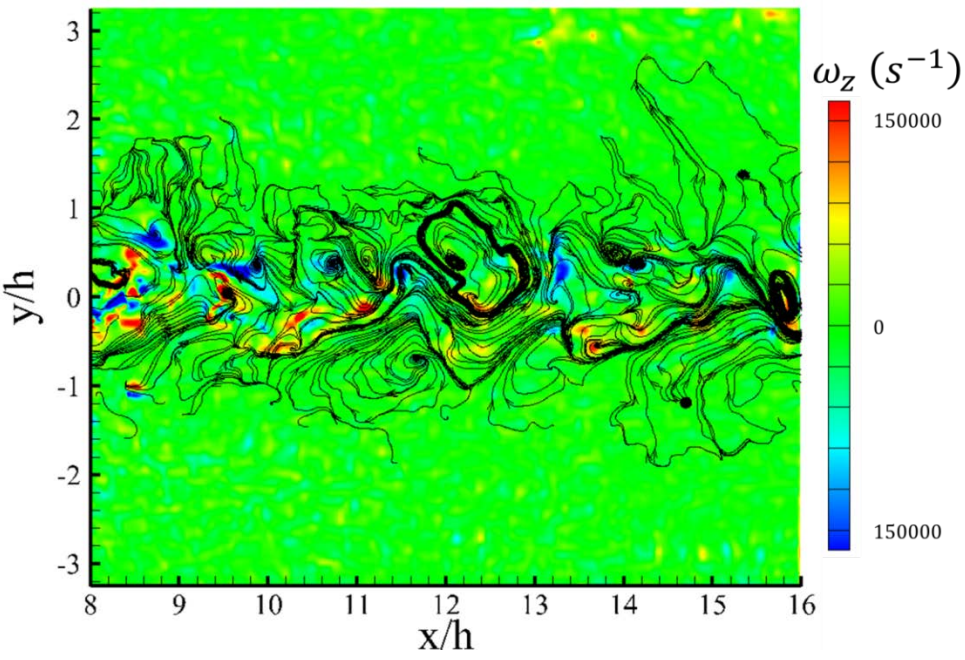

Figure 3.43: Example instantaneous centerline span-wise vorticity contours for mid-field of planar injector flowfield overlaid with fluctuating streamlines (SV 2a)

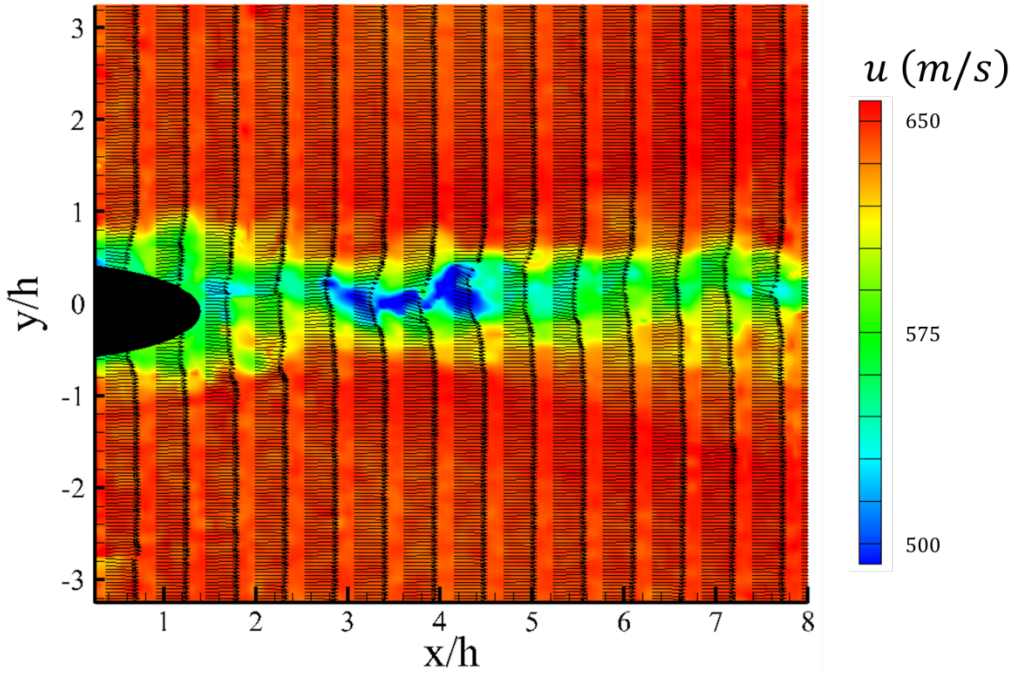

Figure 3.44: Example instantaneous centerline stream-wise velocity contours for near-field of hypermixing injector flowfield (SV 1a)

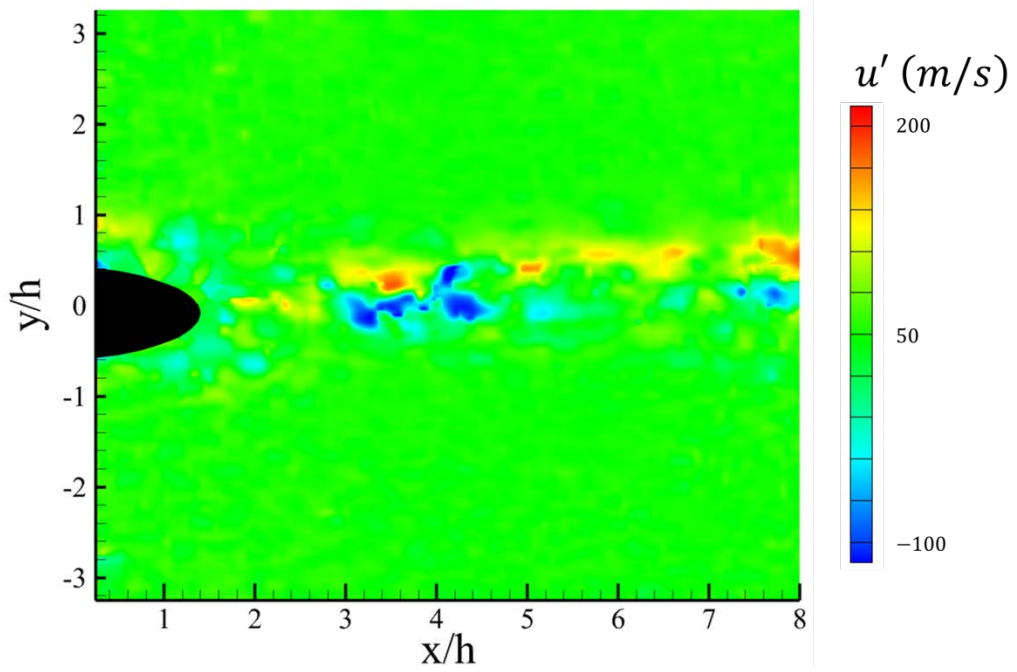

Figure 3.45: Example fluctuating centerline stream-wise velocity contours for near-field of hypermixing injector flowfield (SV 1a).

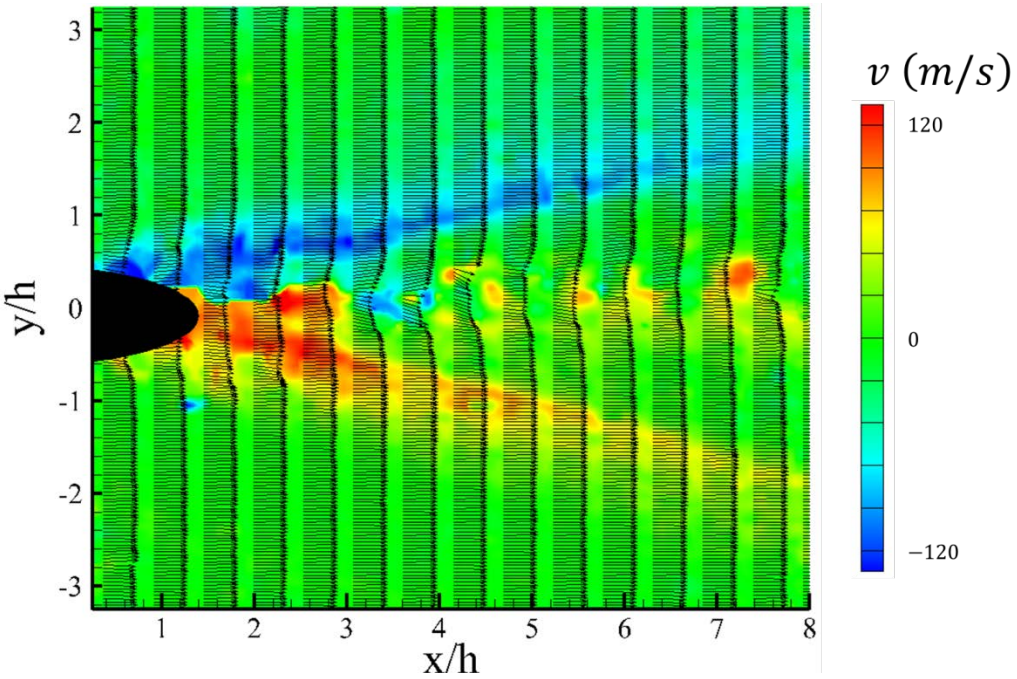

Figure 3.46: Example instantaneous centerline transverse velocity contours for near-field of hypermixing injector flowfield (SV 1a)

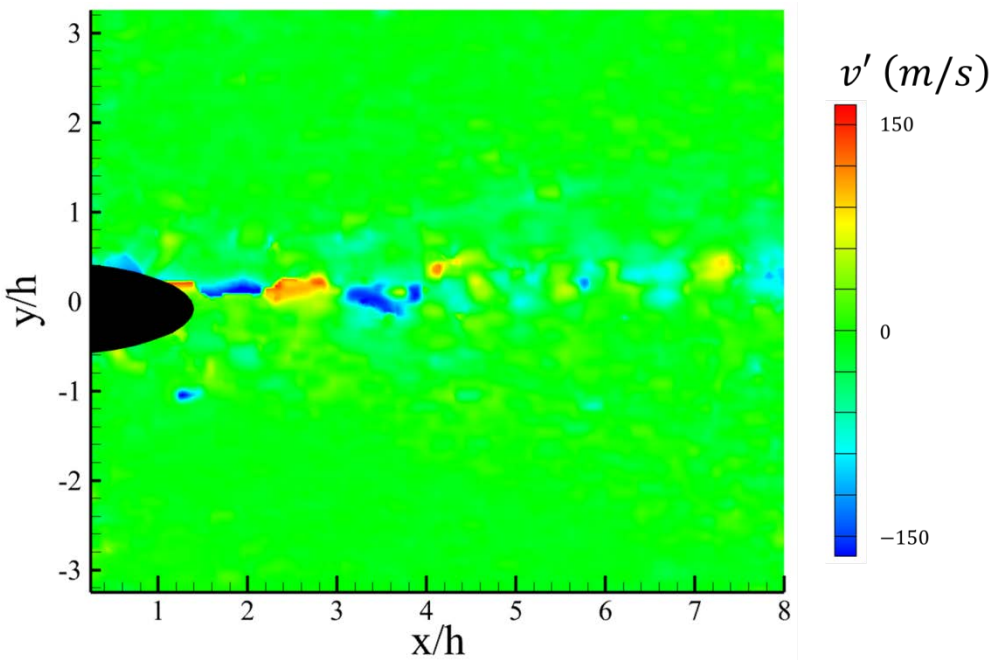

Figure 3.47: Example fluctuating centerline transverse velocity contours for near-field of hypermixing injector flowfield (SV 1a).

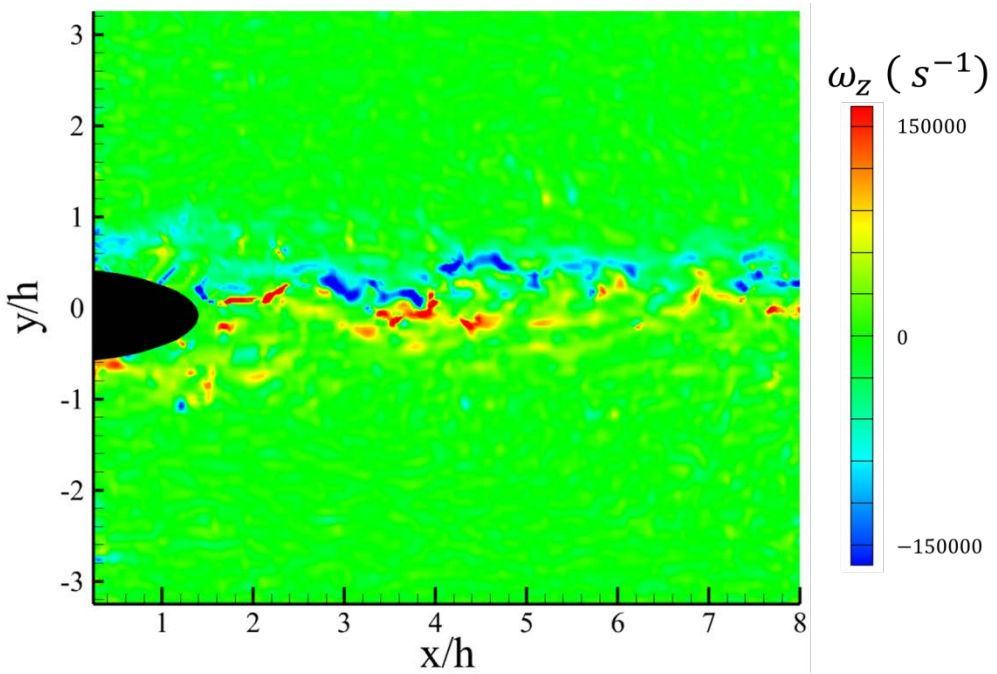

Figure 3.48: Example instantaneous centerline span-wise vorticity contours for near-field of hypermixing injector flowfield.

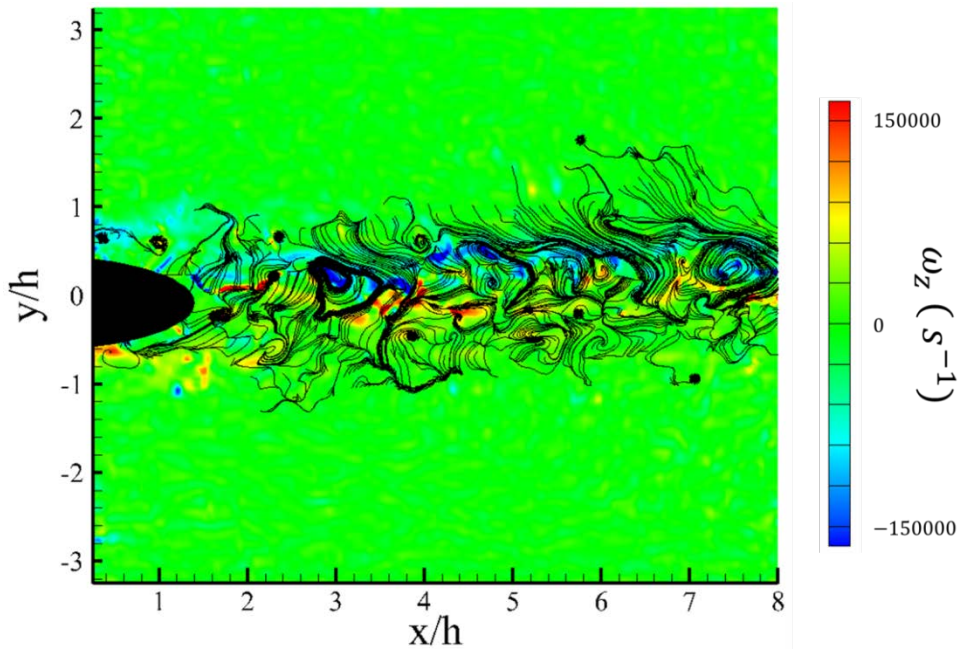

Figure 3.49: Example instantaneous centerline vorticity contours for near-field of hypermixing injector flowfield overlaid with fluctuating streamlines (SV 1a)

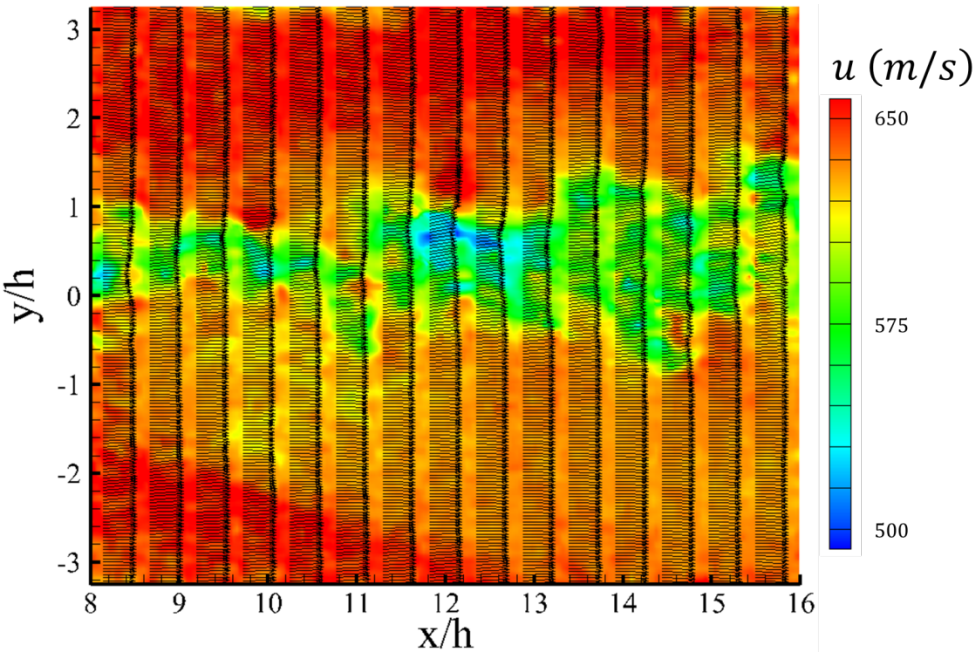

Figure 3.50: Example instantaneous centerline stream-wise velocity contours for mid-field of hypermixing injector flowfield (SV 2a)

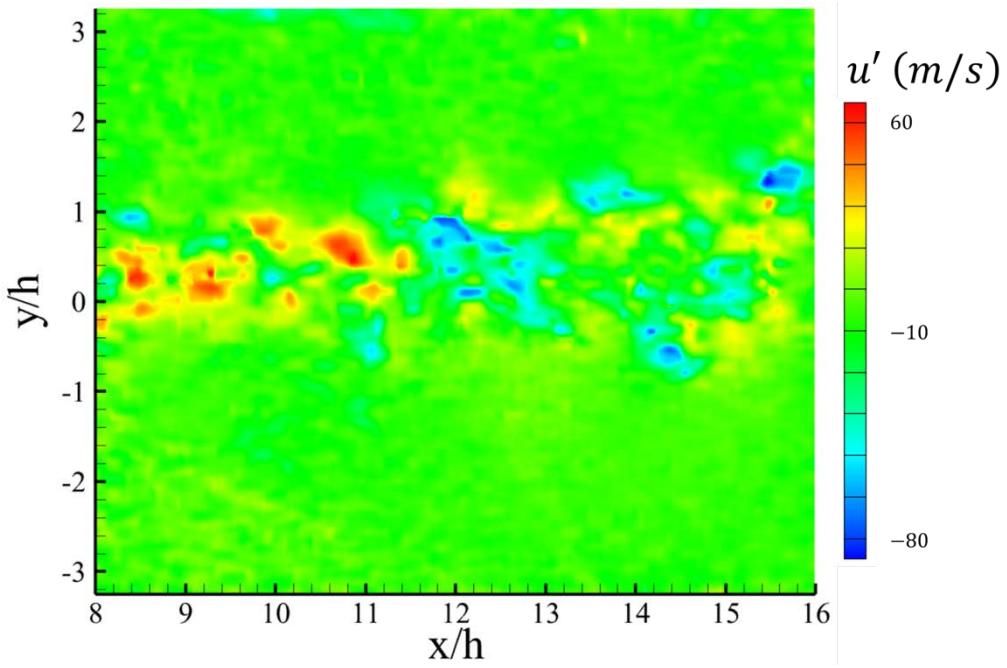

Figure 3.51: Example fluctuating centerline stream-wise velocity contours for mid-field of hypermixing injector flowfield (SV 2a)

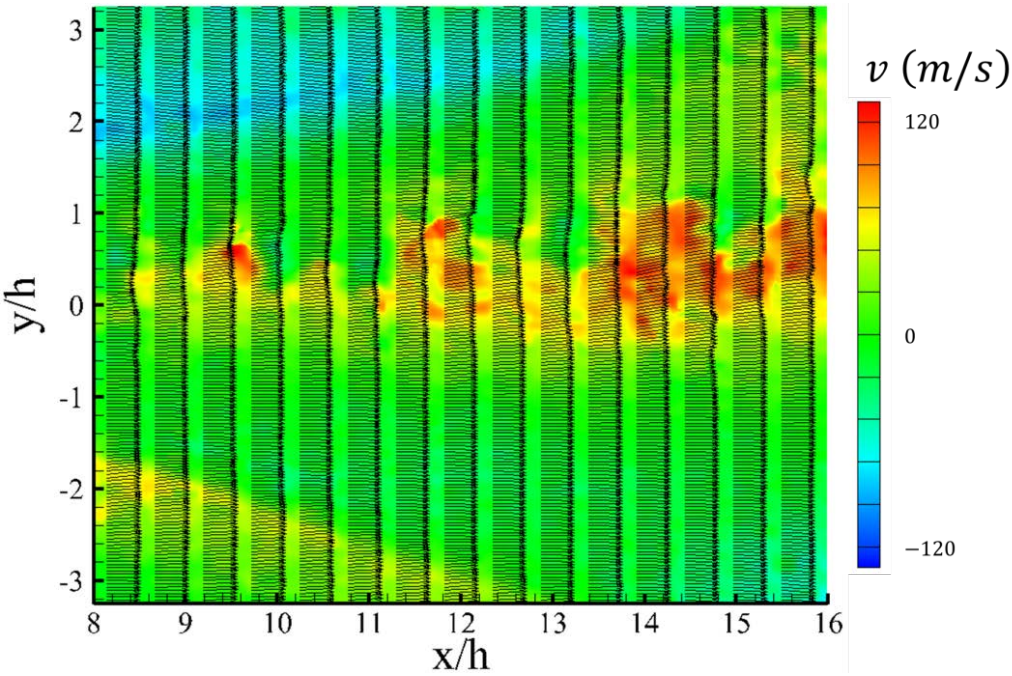

Figure 3.52: Example instantaneous centerline transverse velocity contours for mid-field of hypermixing injector flowfield (SV 2a)

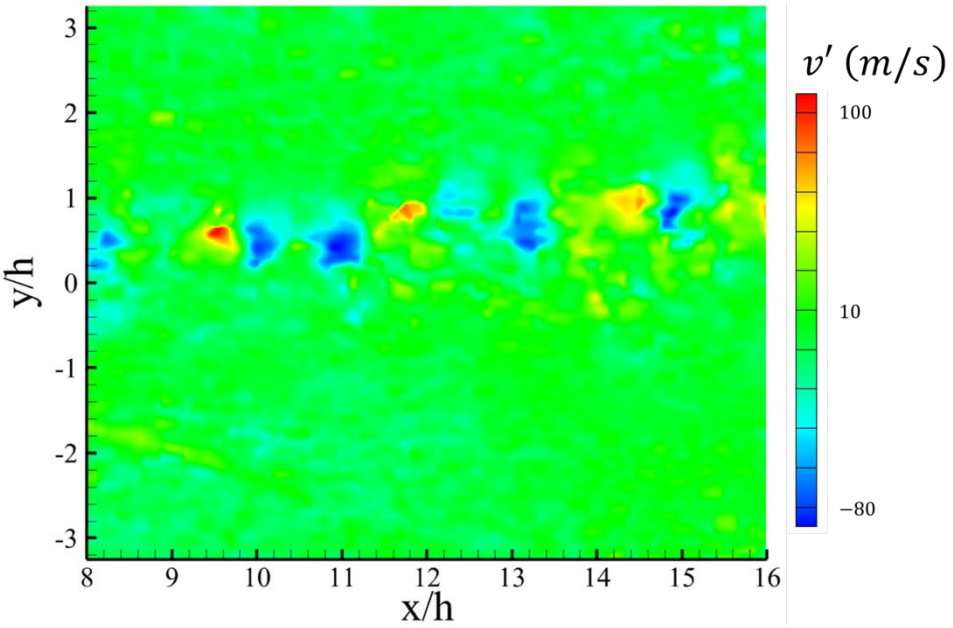

Figure 3.53: Example fluctuating centerline transverse velocity contours for mid-field of hypermixing injector flowfield (SV 2a)

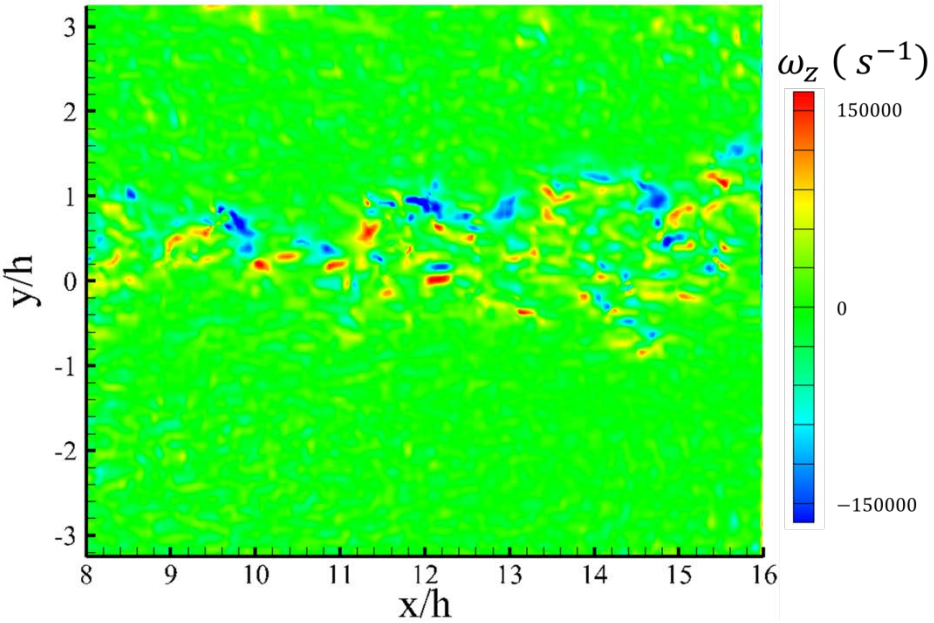

Figure 3.54: Example instantaneous centerline span-wise vorticity contours for mid-field of hypermixing injector flowfield (SV 2a)

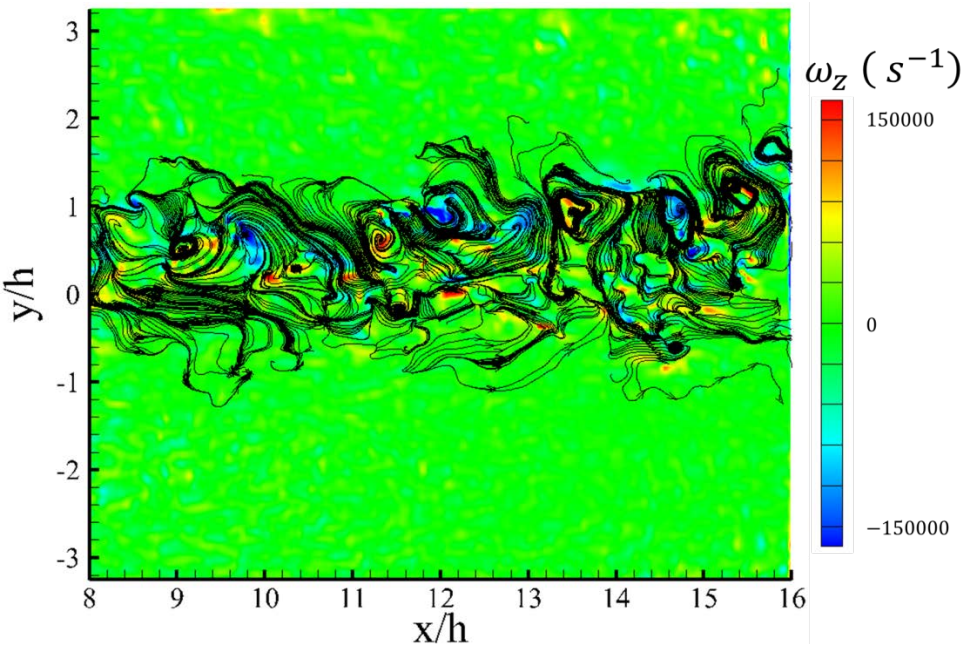

Figure 3.55: Example instantaneous centerline span-wise vorticity contours for mid-field of hypermixing injector flowfield overlaid with fluctuating streamlines (SV 2a)

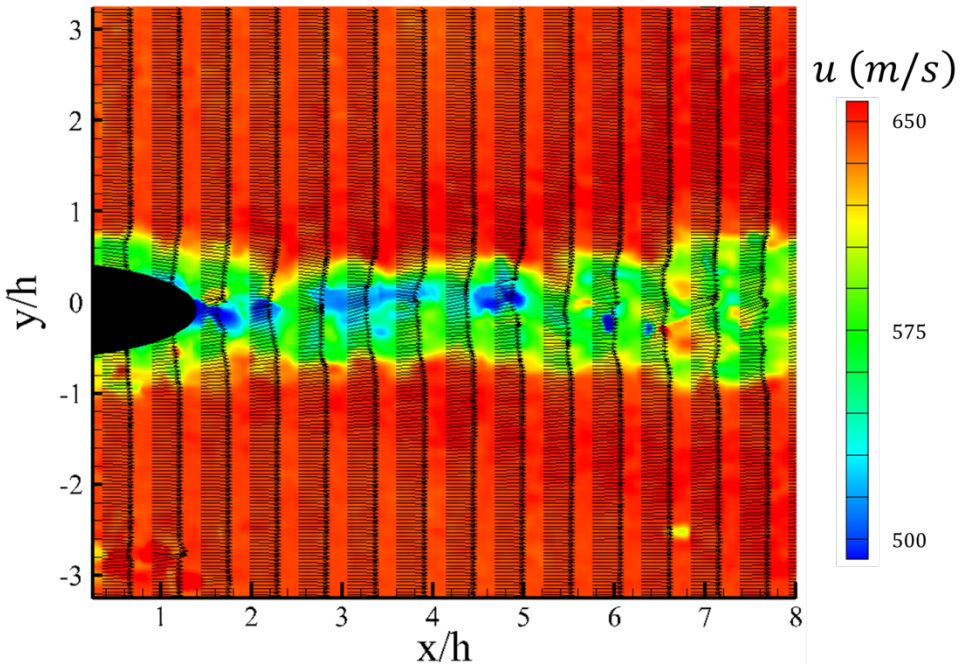

Figure 3.56: Example instantaneous off-centerline ($z/h = 0.75$) stream-wise velocity contours for near-field of hypermixing injector flow (SV 1b)

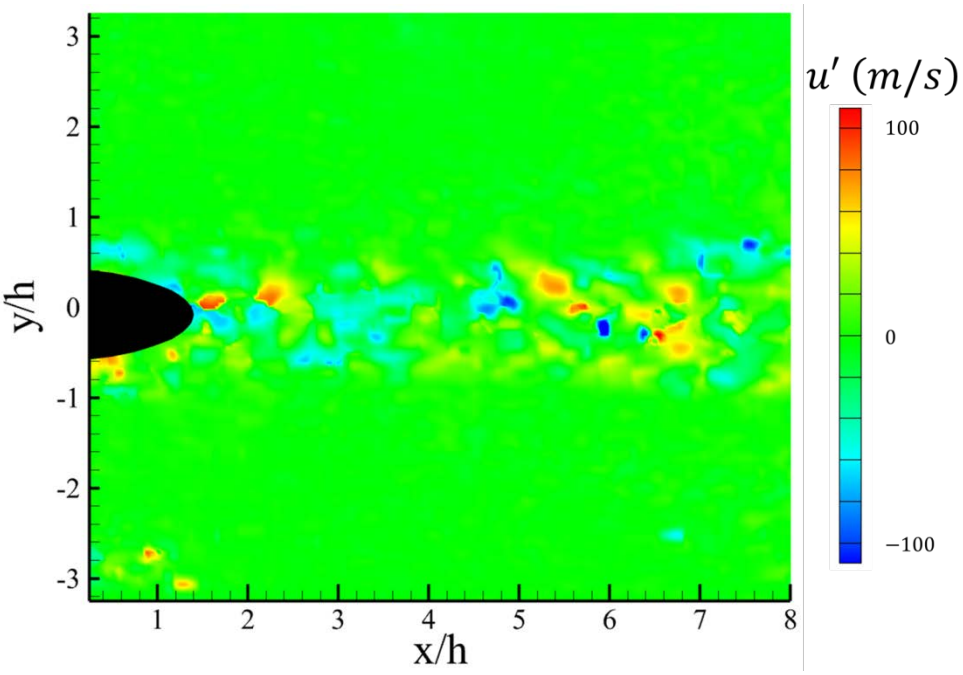

Figure 3.57: Example fluctuating off-centerline ($z/h = 0.75$) stream-wise velocity contours for near-field of hypermixing injector flowfield (SV 1b)

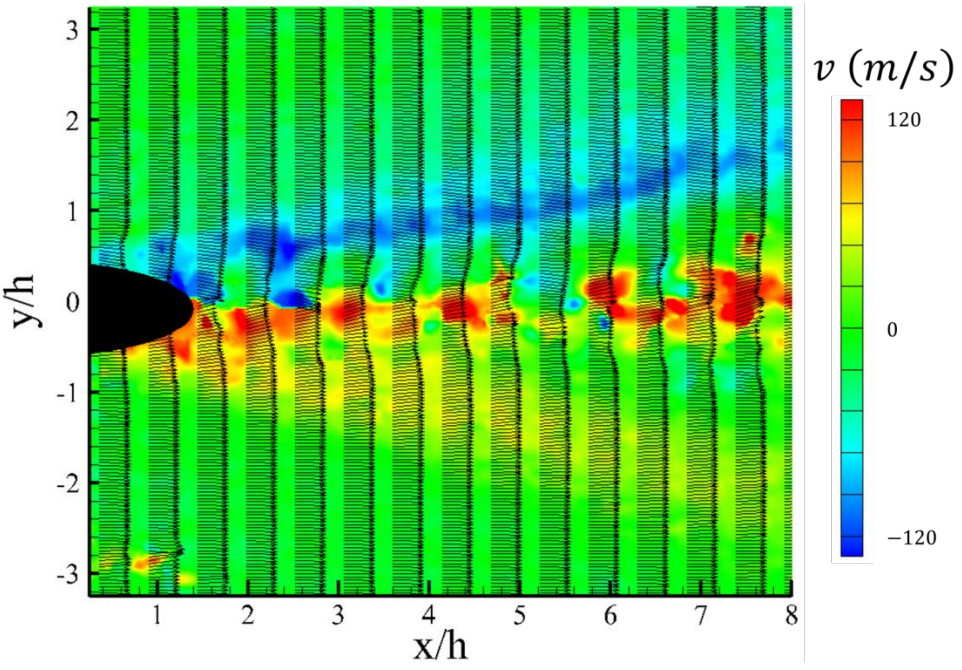

Figure 3.58: Example instantaneous off-centerline ($z/h = 0.75$) transverse velocity contours for near-field of hypermixing injector flowfield (SV 1b)

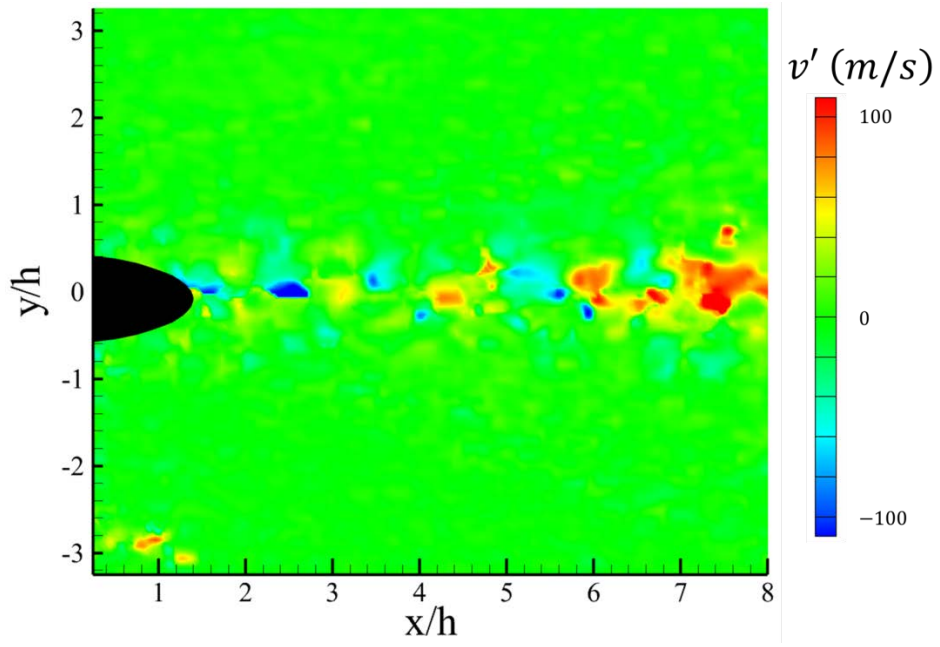

Figure 3.59: Example fluctuating off-centerlline ($z/h = 0.75$) transverse velocity contours for near-field of hypermixing injector flowfield (SV 1b)

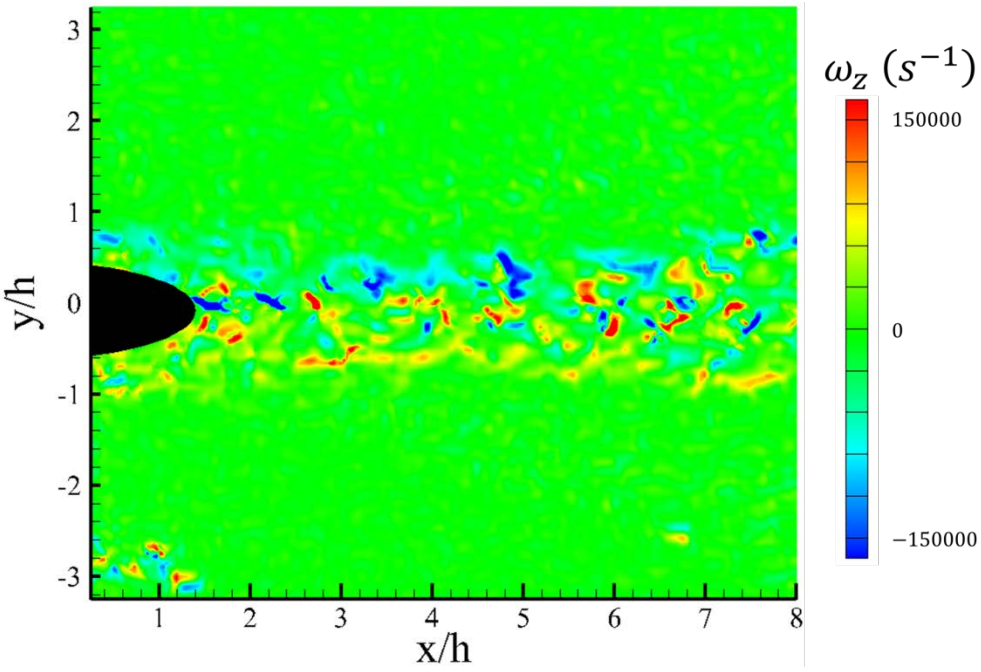

Figure 3.60: Example instantaneous off-centerline ($z/h = 0.75$) span-wise vorticity contours for near-field of hypermixing injector flowfield (SV 1b)

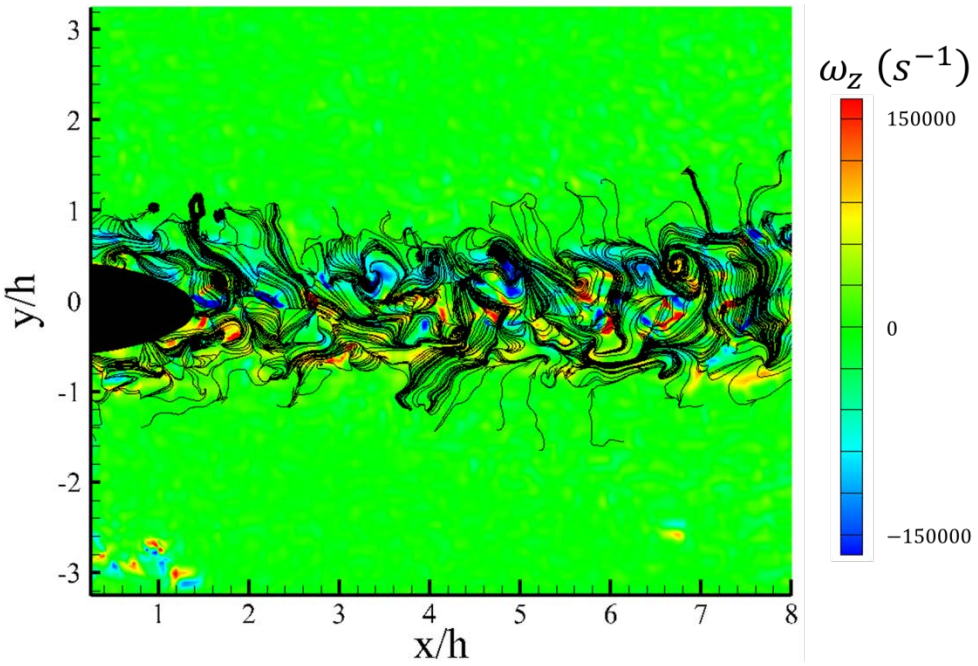

Figure 3.61: Example instantaneous off-centerline ($z/h = 0.75$) span-wise vorticity contours for near-field of hypermixing injector flowfield overlaid with fluctuating streamlines (SV 1b)

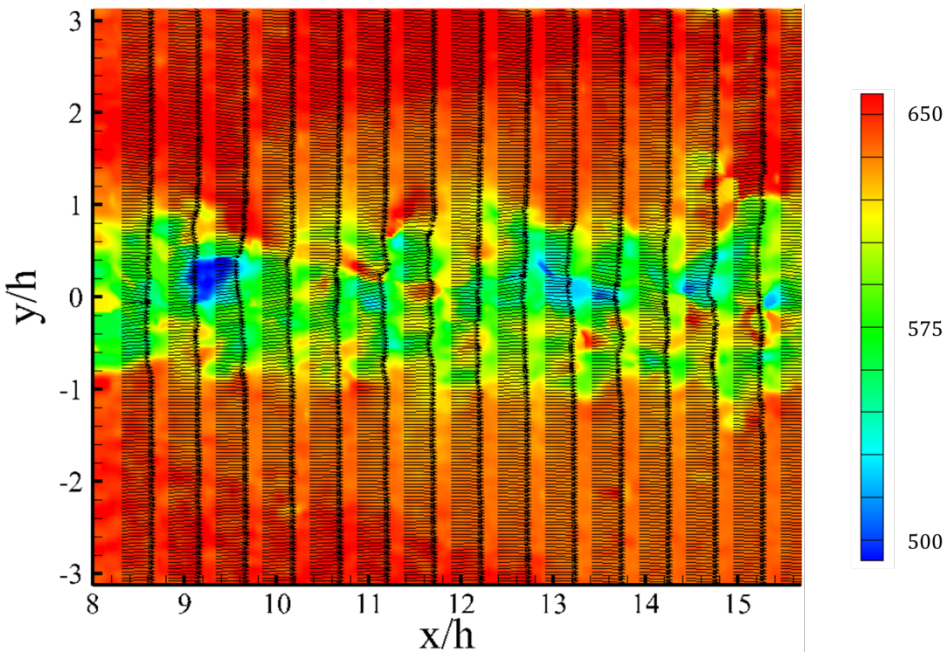

Figure 3.62: Example instantaneous off-centerline ($z/h = 0.75$) stream-wise velocity contours for mid-field of hypermixing injector flowfield (SV 2b)

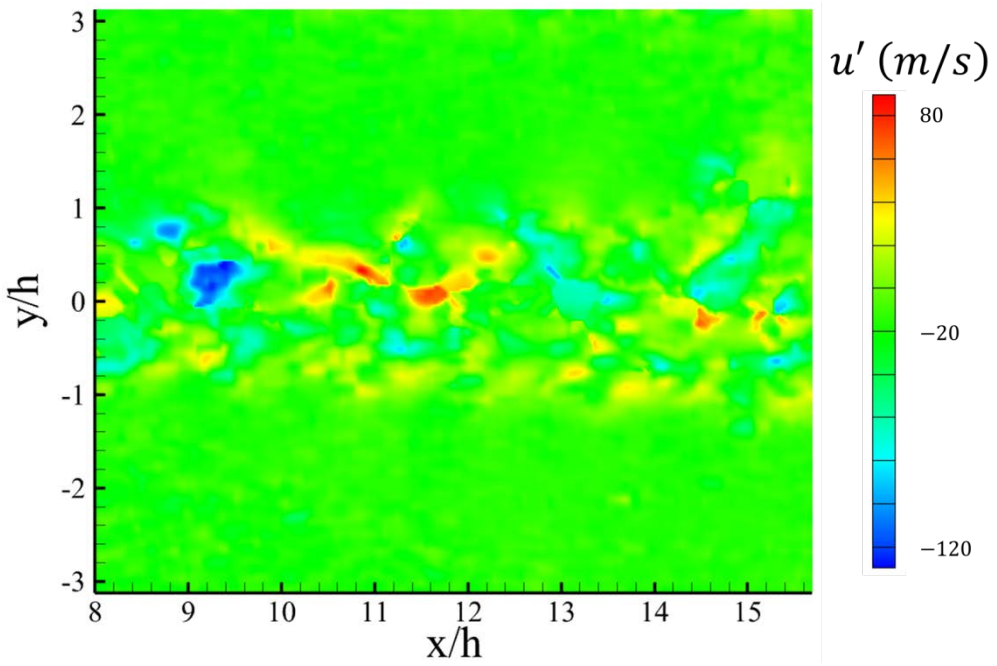

Figure 3.63: Example fluctuating off-centerline ($z/h = 0.75$) stream-wise velocity contours for mid-field of hypermixing injector flowfield (SV 2b)

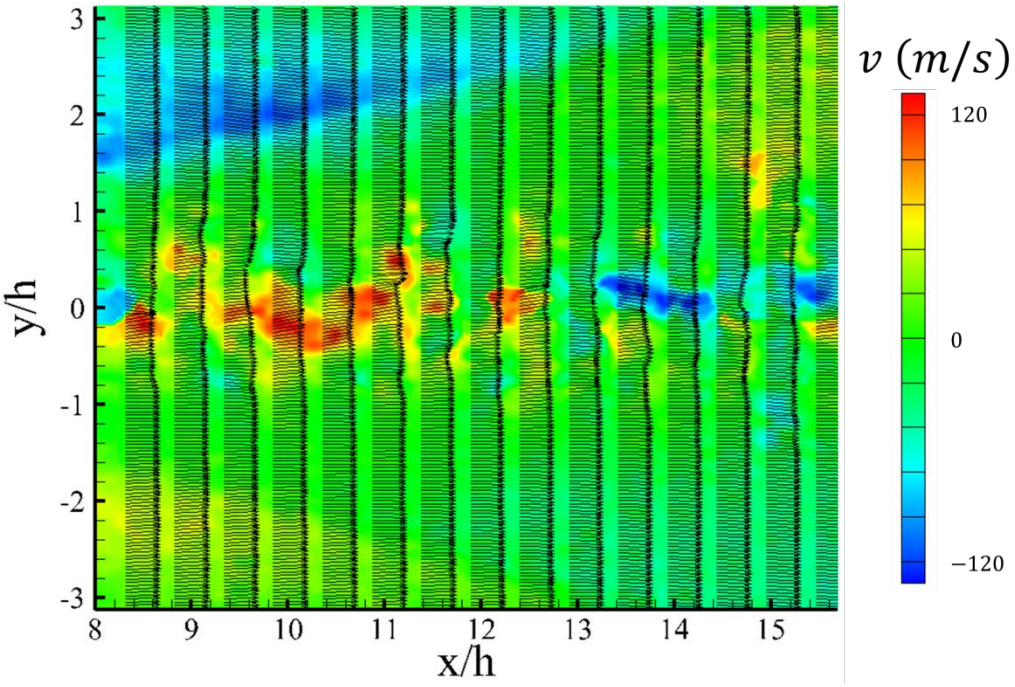

Figure 3.64: Example instantaneous off-centerline ($z/h = 0.75$) transverse velocity contours for mid-field of hypermixing injector flowfield (SV 2b)

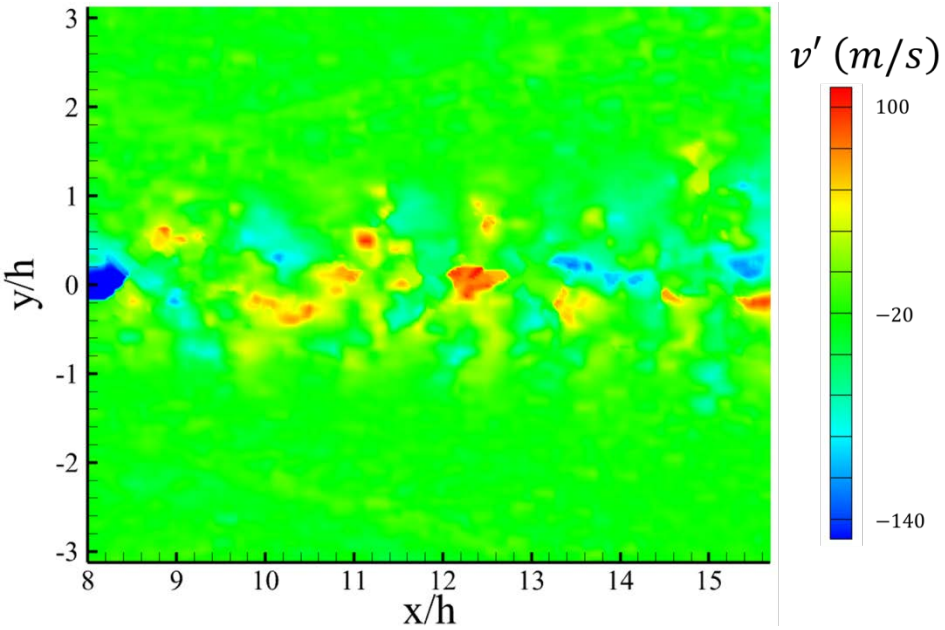

Figure 3.65: Example fluctuating off-centerline ($z/h = 0.75$) transverse velocity contours for mid-field of hypermixing injector flowfield (SV 2b)

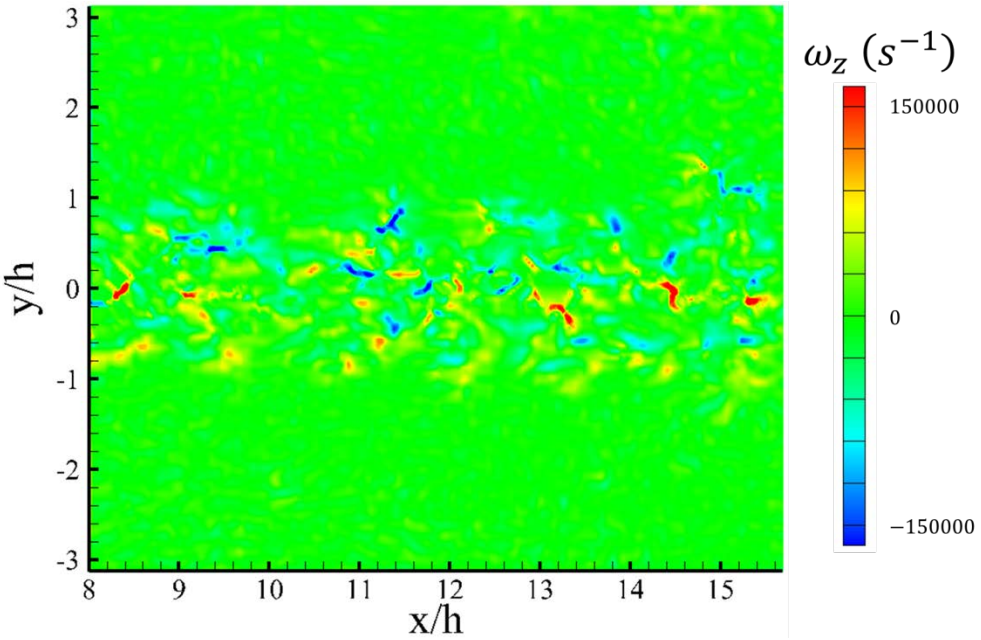

Figure 3.66: Example instantaneous off-centerline ($z/h = 0.75$) span-wise vorticity contours for mid-field of hypermixing injector flowfield (SV 2b)

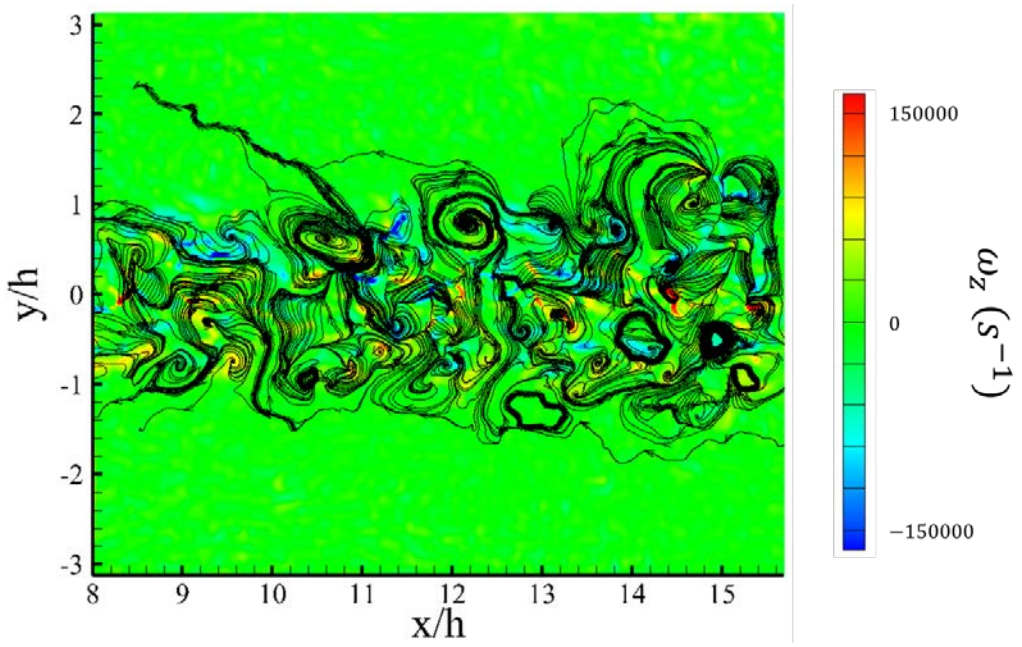

Figure 3.67: Example instantaneous off-centerline ($z/h = 0.75$) span-wise vorticity contours for mid-field of hypermixing injector flowfield overlaid with fluctuating streamlines (SV 2b)

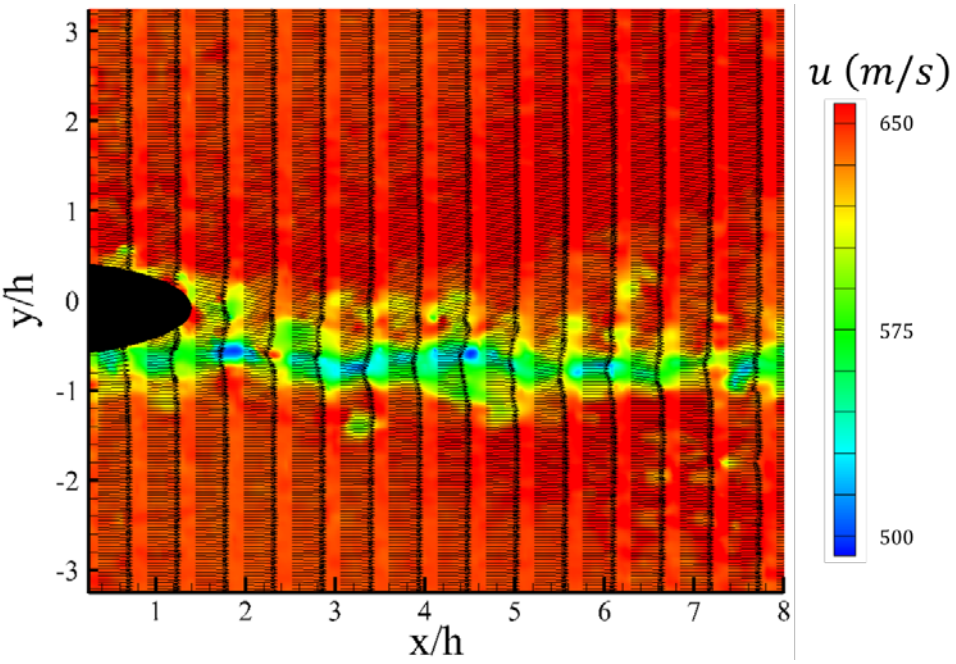

Figure 3.68: Example instantaneous off-centerline ($z/h = 1.25$) stream-wise velocity contours for near-field of hypermixing injector flowfield (SV 1c)

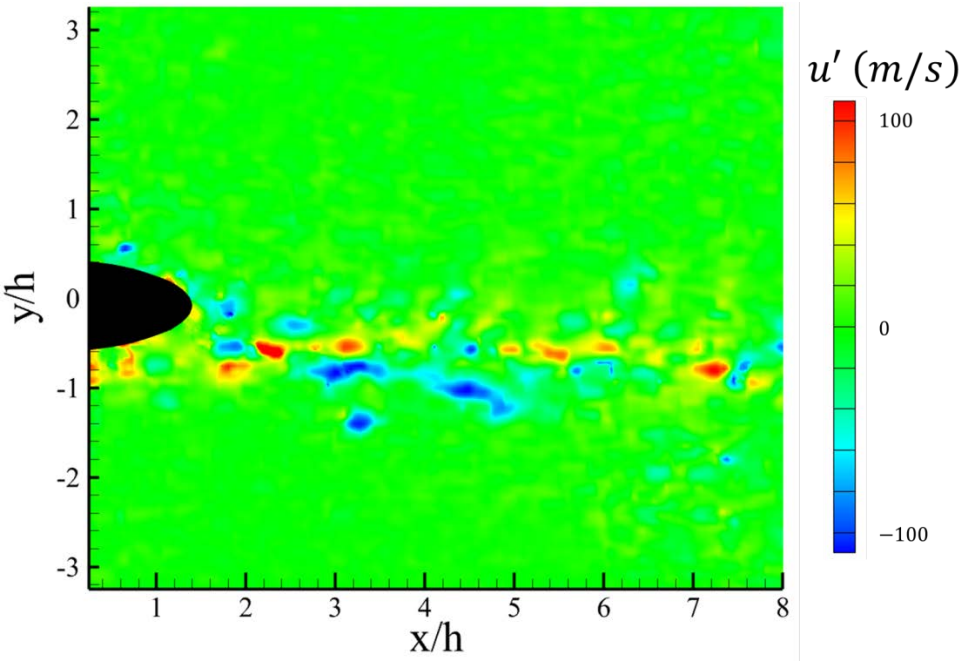

Figure 3.69: Example fluctuating off-centerline ($z/h = 1.25$) stream-wise velocity contours for near-field of hypermixing injector flowfield (SV 1c)

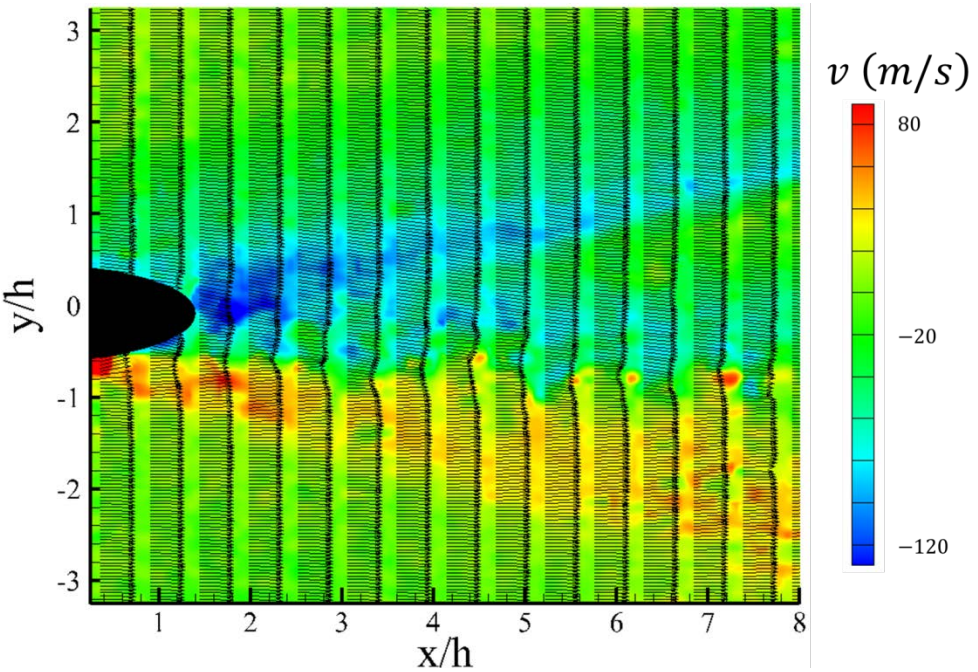

Figure 3.70: Example instantaneous off-centerline ($z/h = 1.25$) transverse velocity contours for near-field of hypermixing injector flowfield (SV 1c)

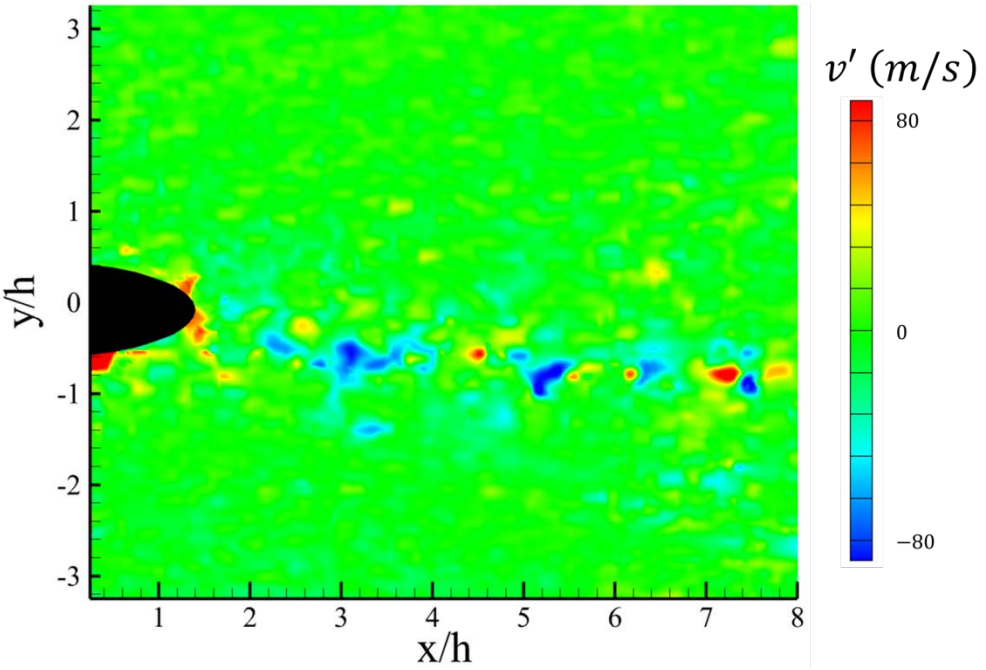

Figure 3.71: Example fluctuating off-centerline ($z/h = 1.25$) transverse velocity contours for near-field of hypermixing injector flowfield (SV 1c)

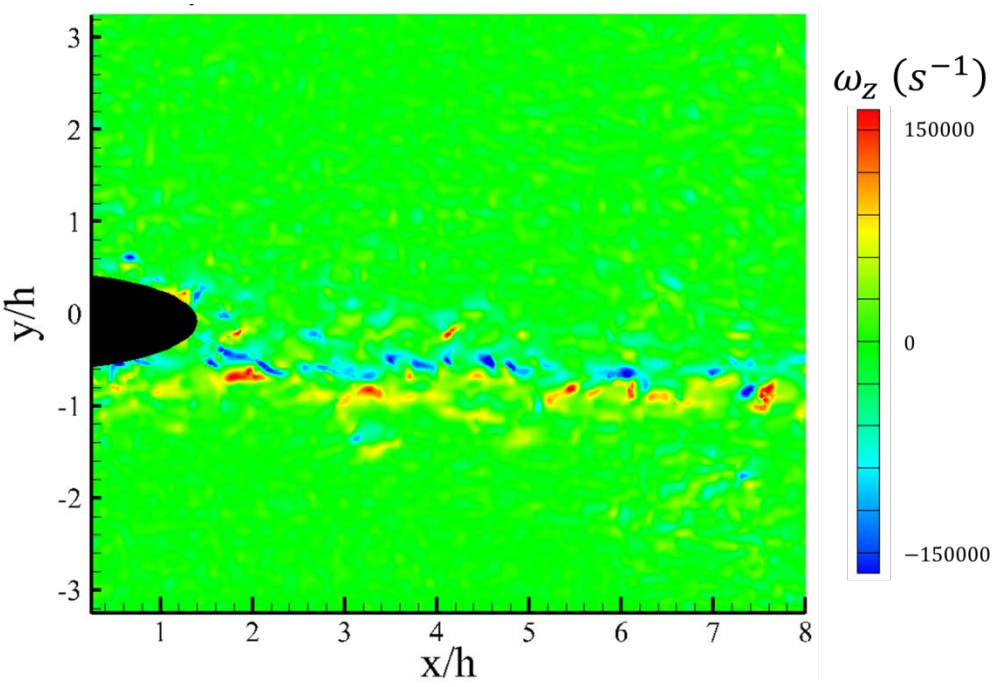

Figure 3.72: Example instantaneous off-centerline ($z/h = 1.25$) span-wise vorticity contours for near-field of hypermixing injector flowfield (SV 1c)

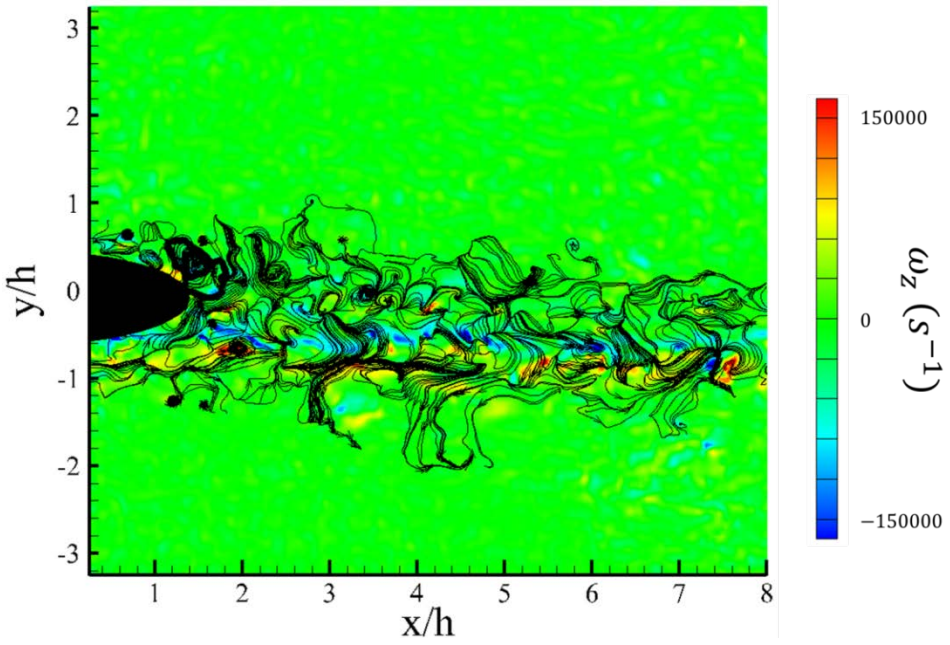

Figure 3.73: Example instantaneous off-centerline ($z/h = 1.25$) span-wise vorticity contours for near-field of hypermixing injector flowfield overlaid with fluctuating streamlines (SV 1c)

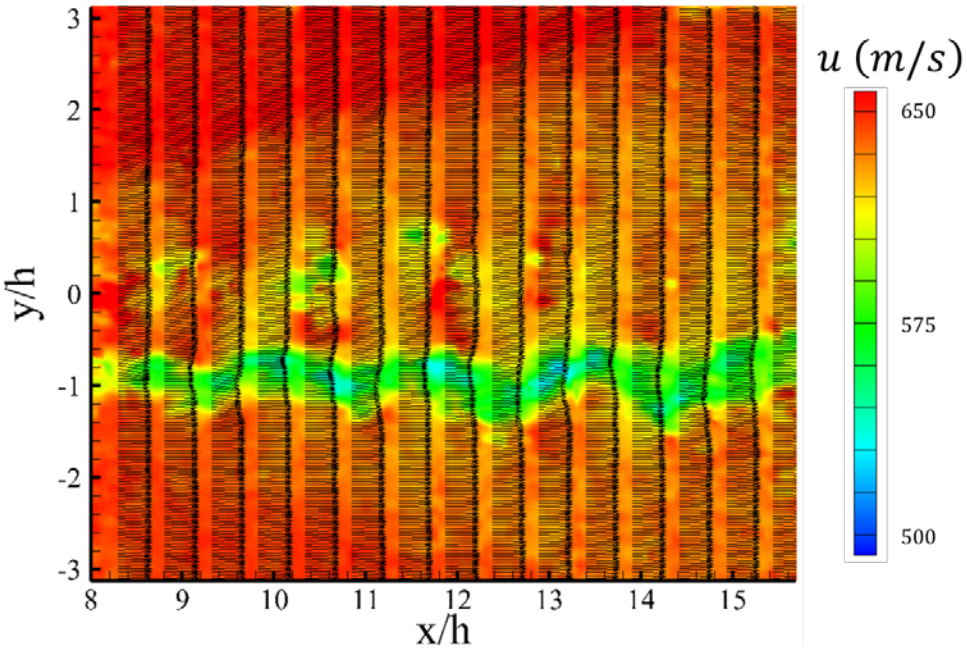

Figure 3.74: Example instantaneous off-centerline ($z/h = 1.25$) stream-wise velocity contours for mid-field of hypermixing injector flowfield (SV 2c)

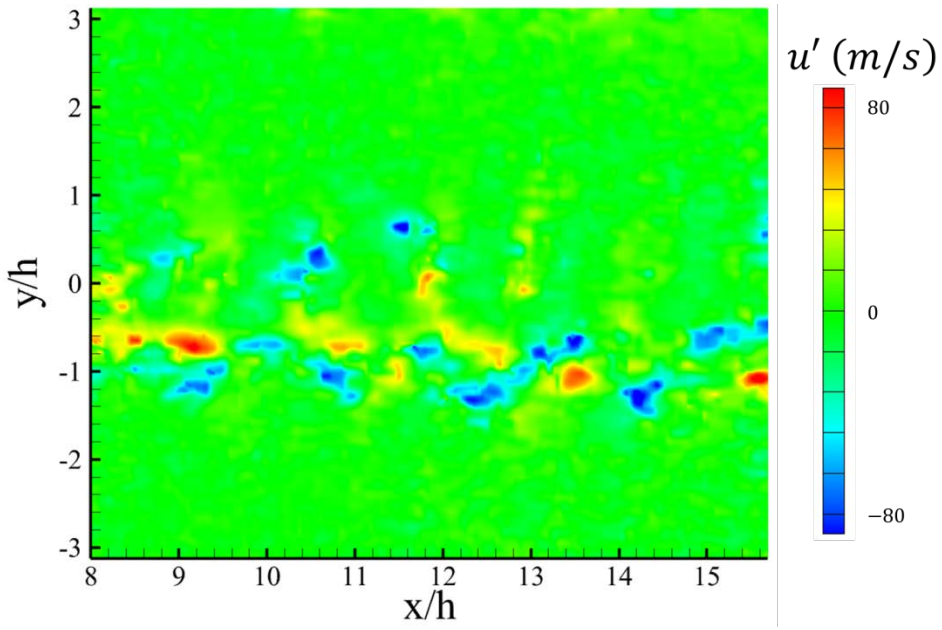

Figure 3.75: Example fluctuating off-centerline ($z/h = 1.25$) stream-wise velocity contours for mid-field of hypermixing injector flowfield (SV 2c)

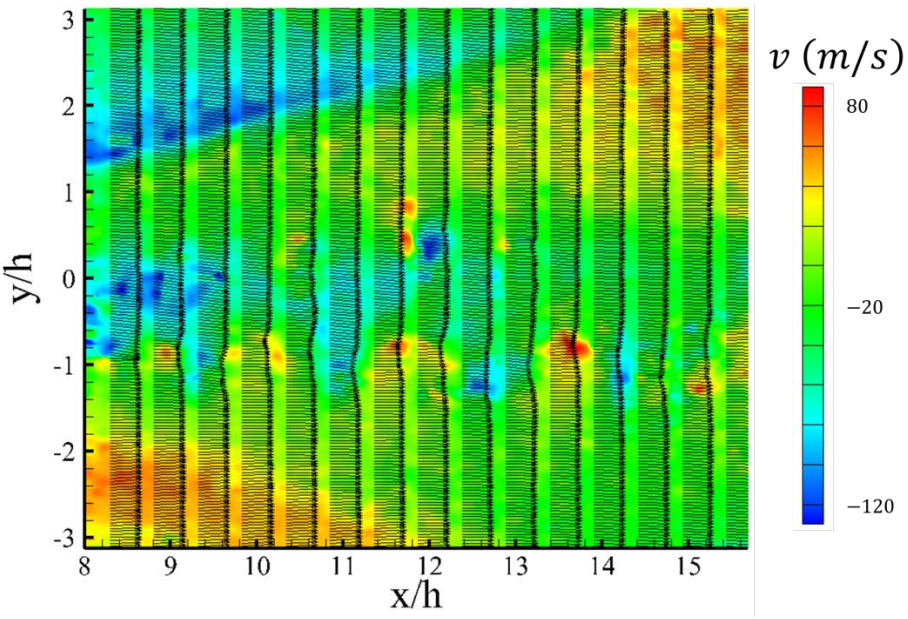

Figure 3.76: Example instantaneous off-centerline ($z/h = 1.25$) transverse velocity contours for mid-field of hypermixing injector flowfield (SV 2c)

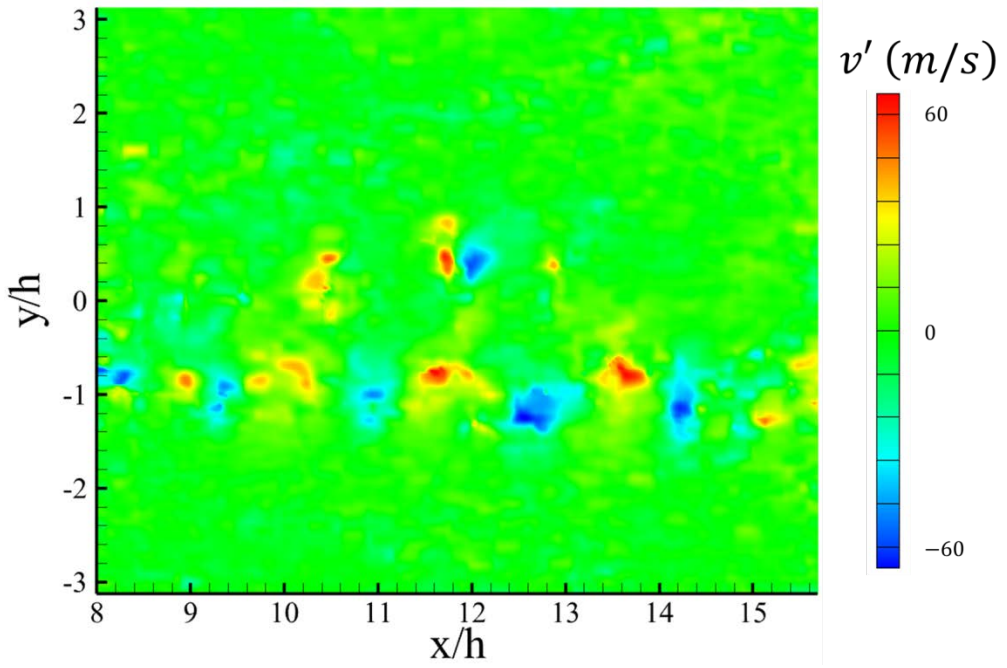

Figure 3.77: Example fluctuating off-centerline ($z/h = 1.25$) transverse velocity contours for mid-field of hypermixing injector flowfield (SV 2c)

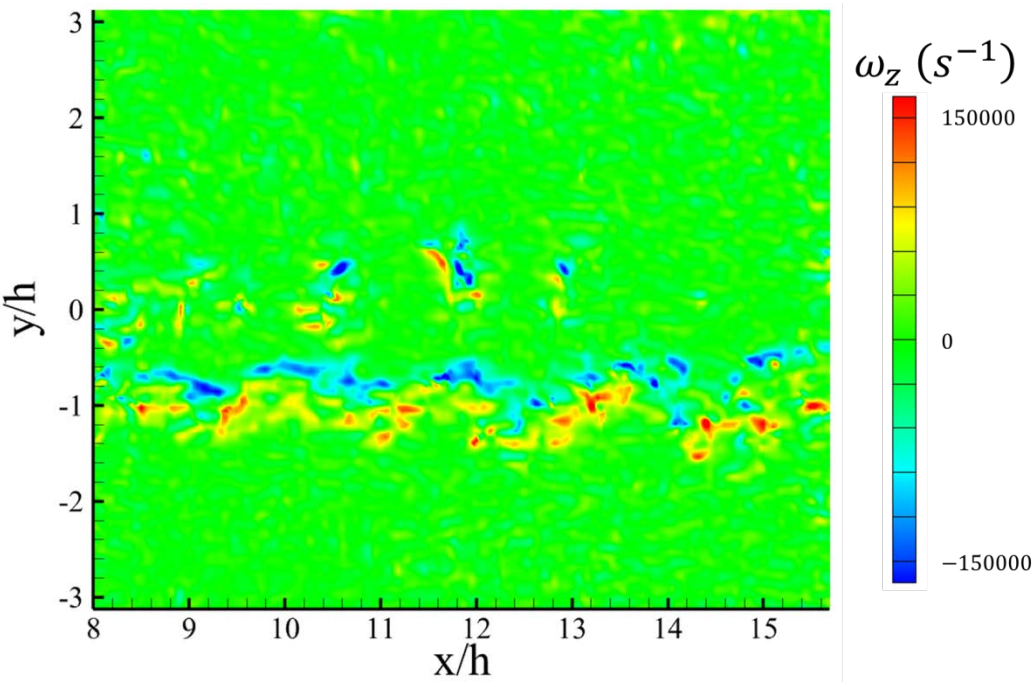

Figure 3.78: Example instantaneous off-centerline ($z/h = 1.25$) span-wise vorticity contours for mid-field of hypermixing injector flowfield (SV 2c)

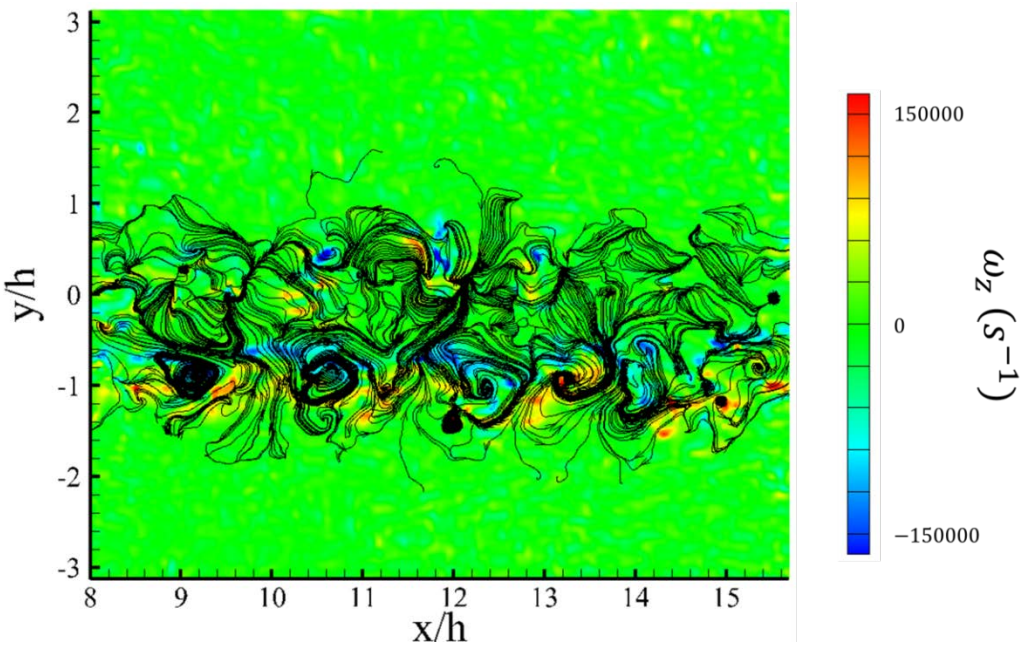

Figure 3.79: Example instantaneous off-centerline ($z/h = 1.25$) span-wise vorticity contours for mid-field of hypermixing injector flowfield overlaid with fluctuating streamlines (SV 2c)

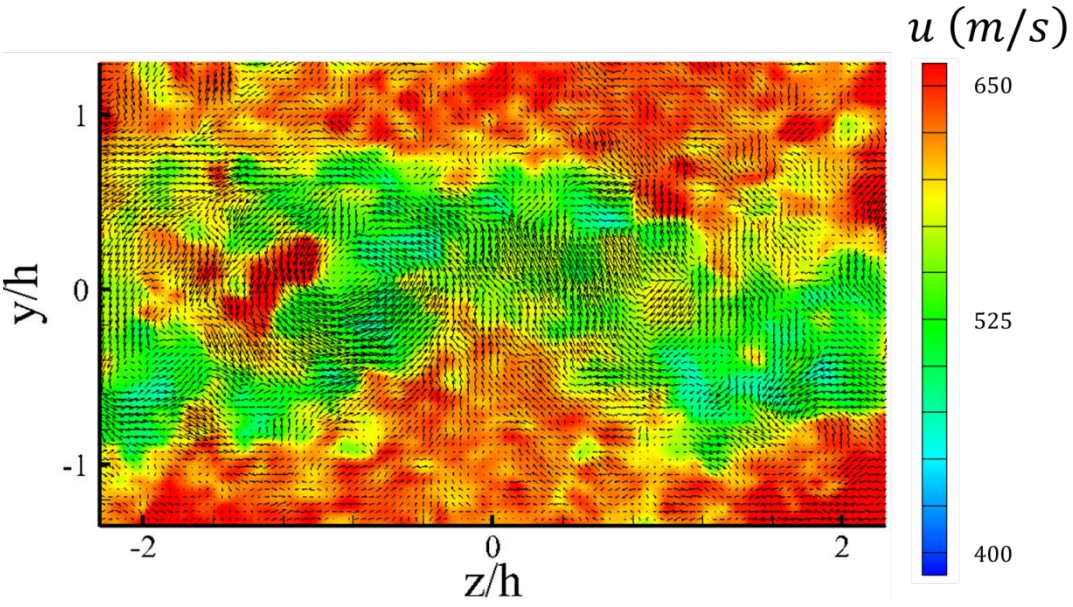

Figure 3.80: Example instantaneous stream-wise end-view velocity contours for hypermixing injector flowfield (EV 1, $x/h = 8$)

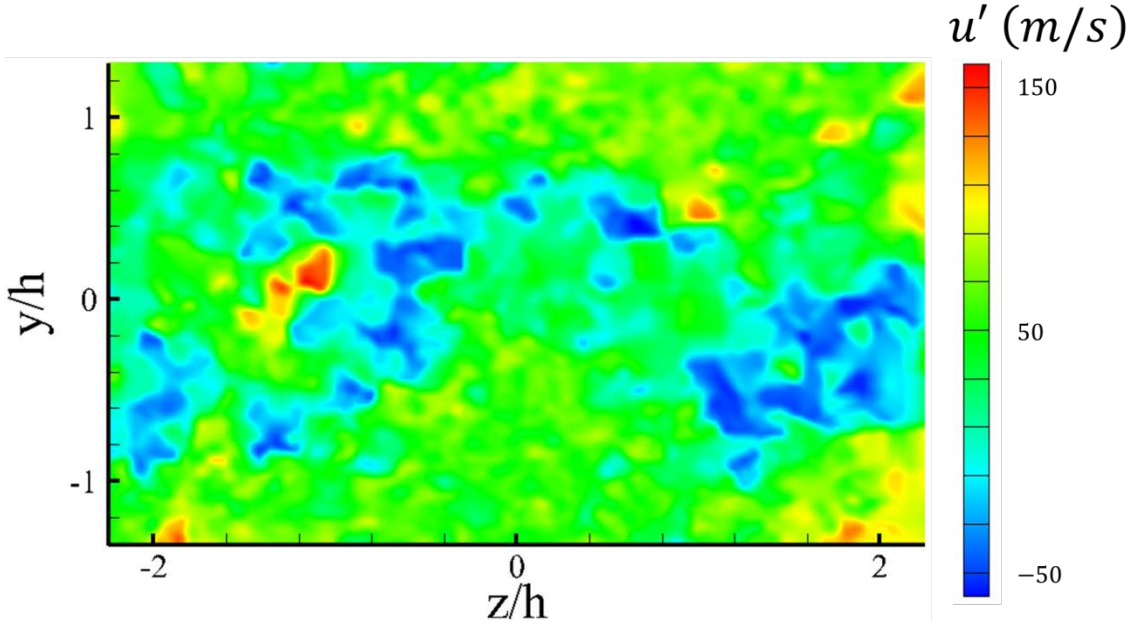

Figure 3.81: Example fluctuating stream-wise end-view velocity contours for hypermixing injector flowfield (EV 1, $x/h = 8$)

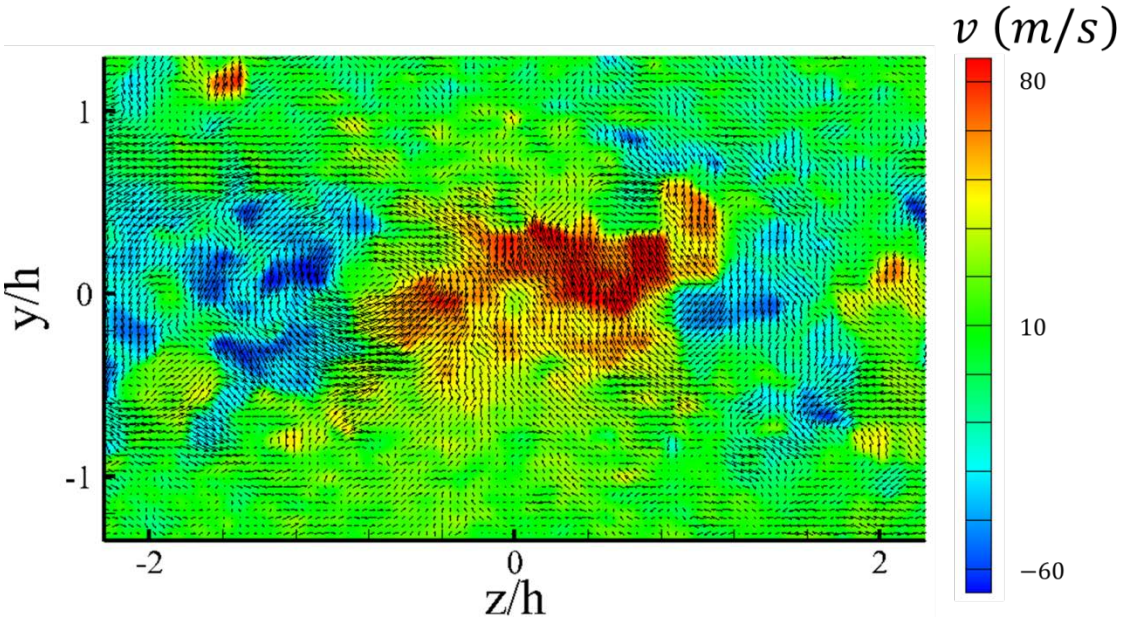

Figure 3.82: Example instantaneous transverse end-view velocity contours for hypermixing injector flowfield (EV 1, $x/h = 8$)

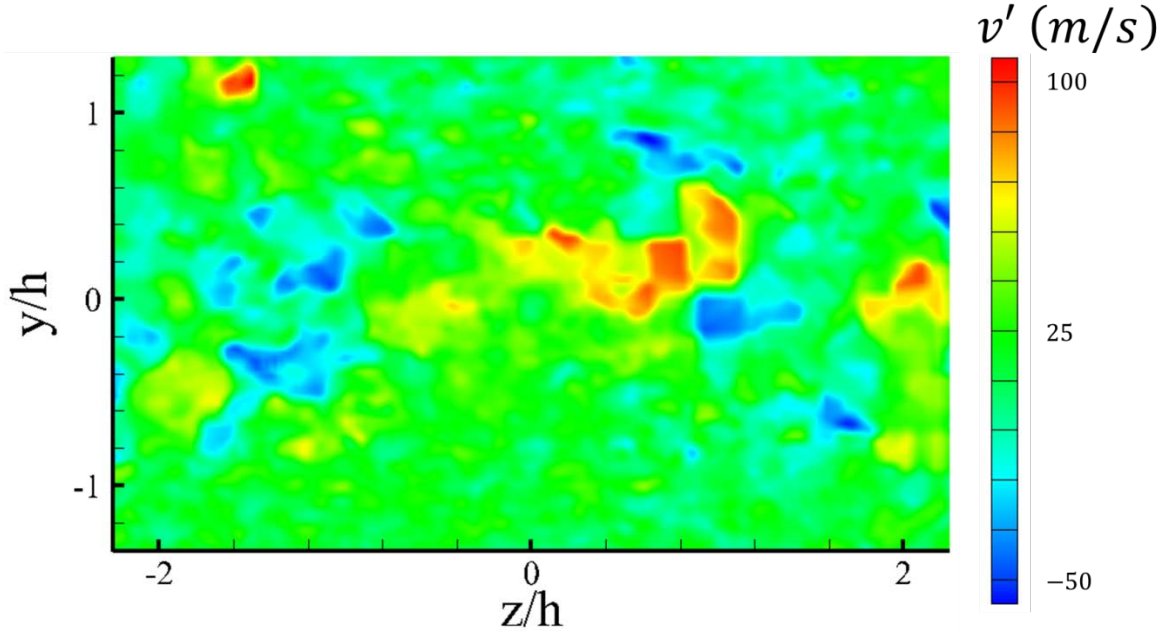

Figure 3.83: Example fluctuating transverse end-view velocity contours for hypermixing injector flowfield (EV 1, $x/h = 8$)

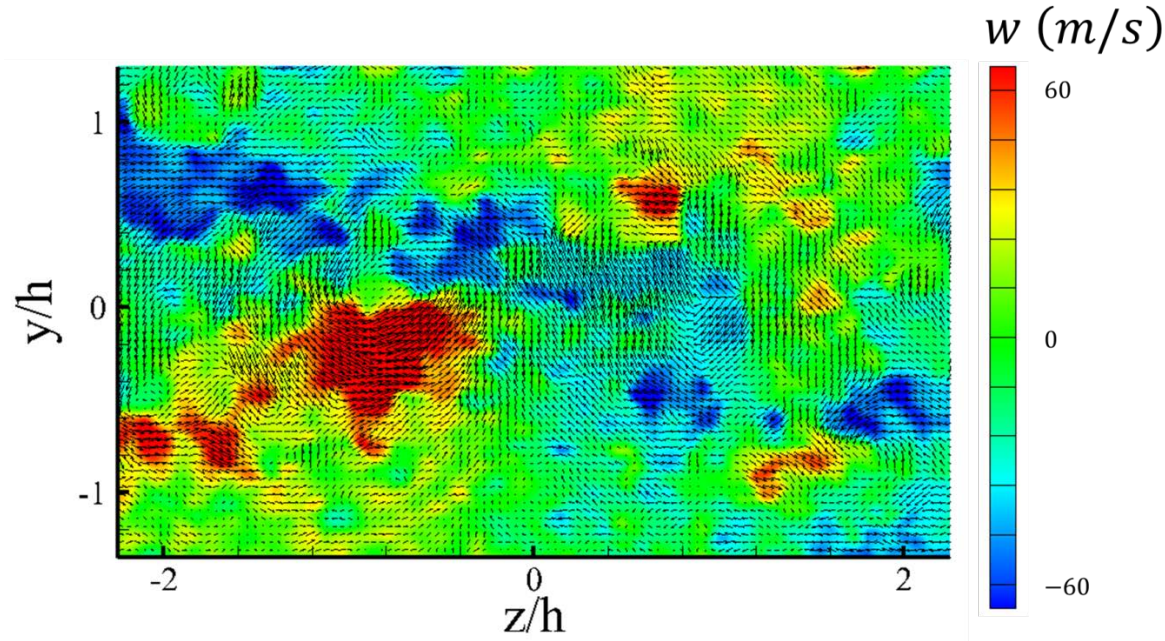

Figure 3.84: Example instantaneous span-wise end-view velocity contours for hypermixing injector flowfield (EV 1, $x/h = 8$)

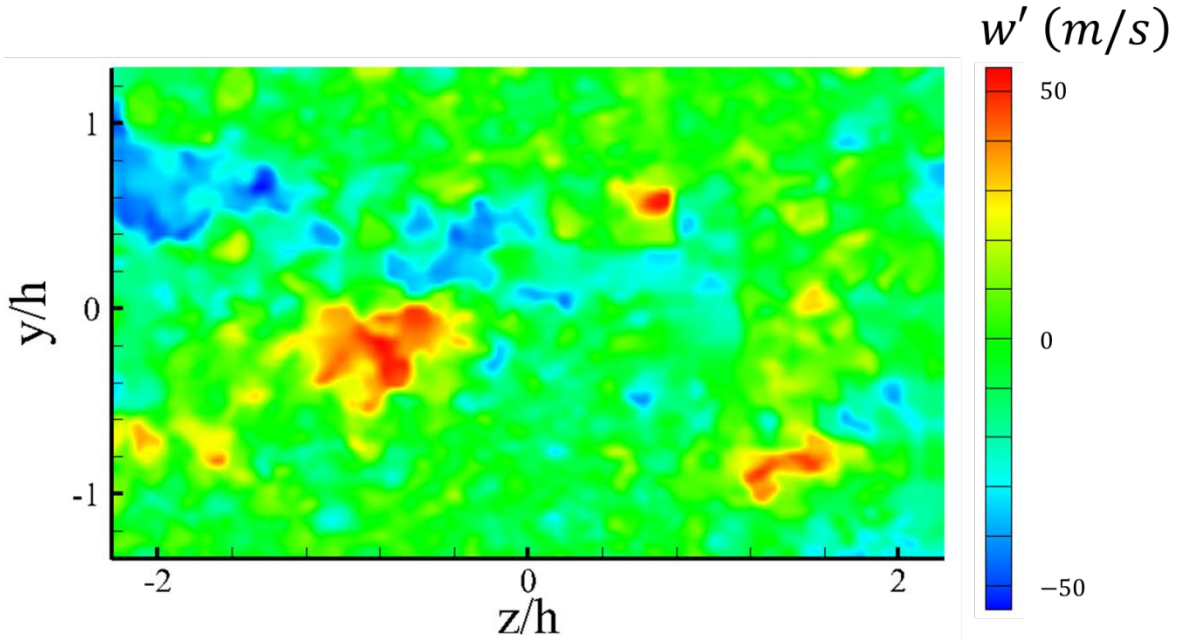

Figure 3.85: Example fluctuating span-wise end-view velocity contours for hypermixing injector flowfield (EV 1, $x/h = 8$)

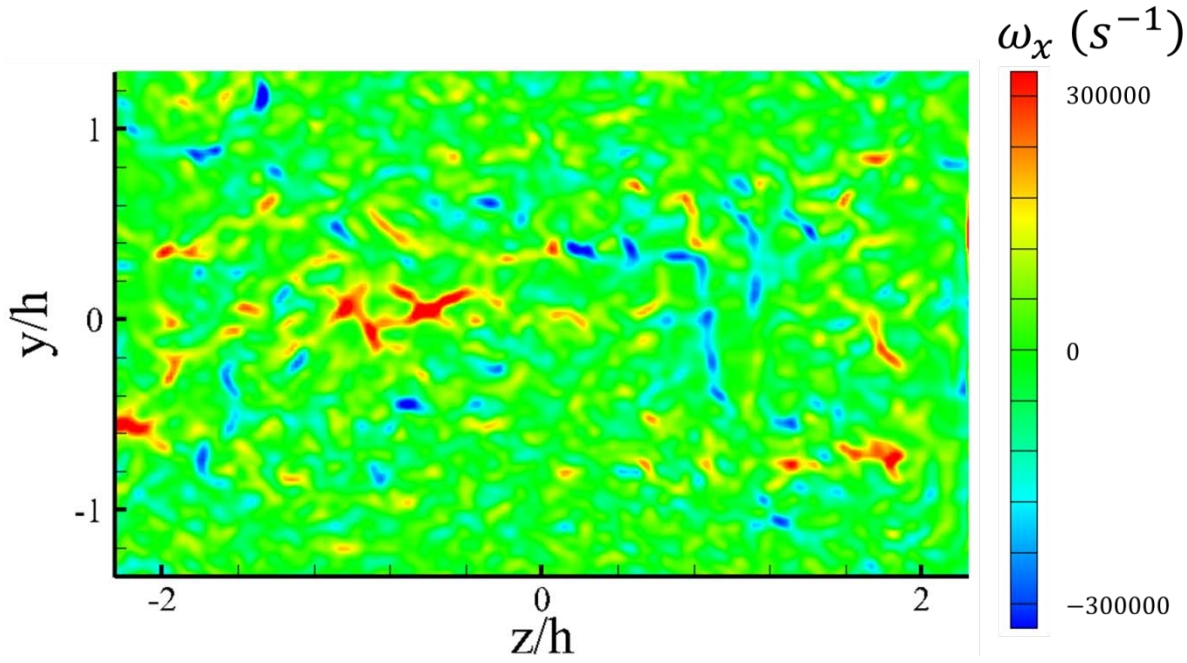

Figure 3.86: Example instantaneous end-view stream-wise vorticity contours for hypermixing injector flowfield (EV 1, $x/h = 8$)

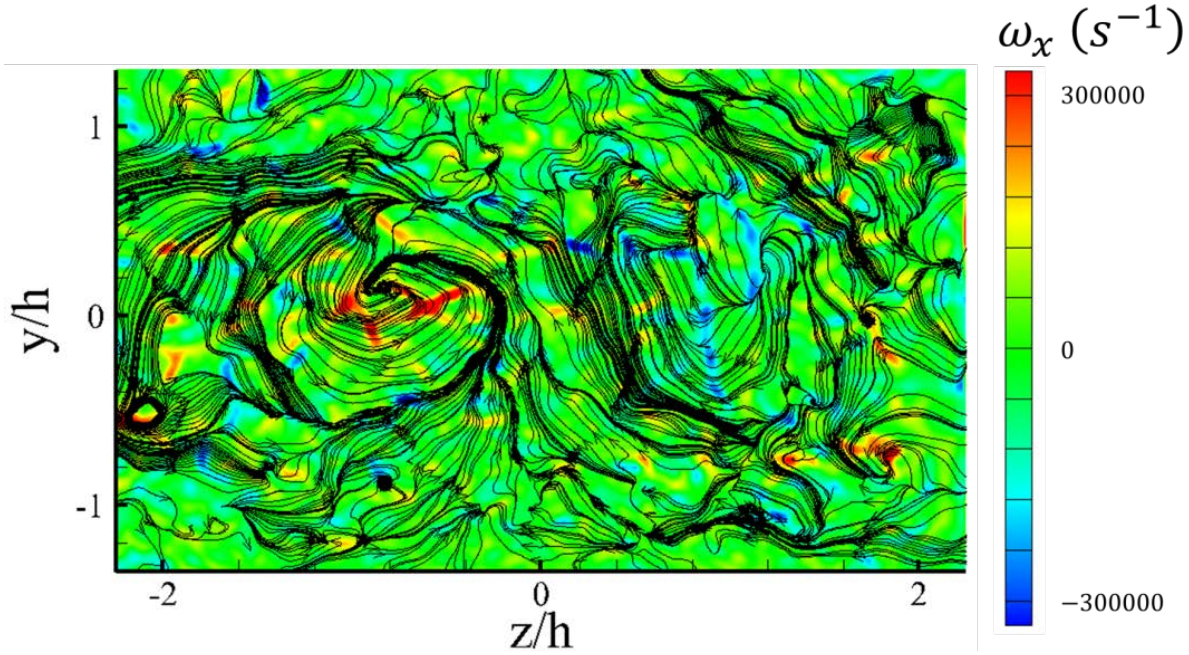

Figure 3.87: Example instantaneous end-view stream-wise vorticity contours for hypermixing injector flowfield overlaid with instantaneous streamlines (EV 1, $x/h = 8$)

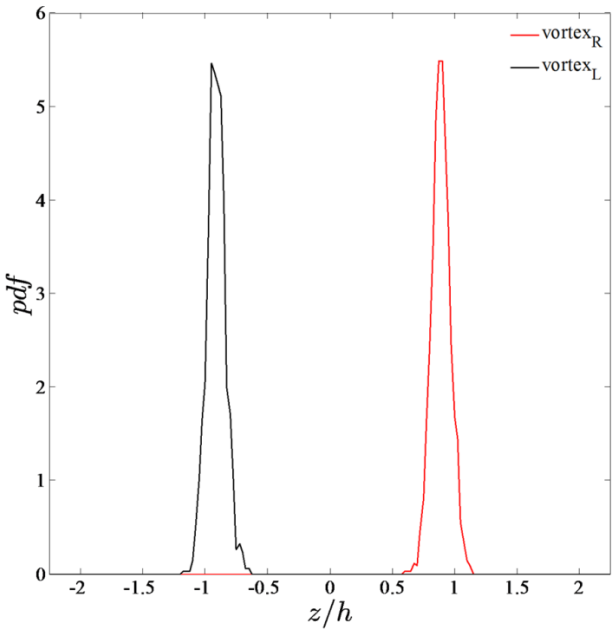

Figure 3.88: PDFs of stream-wise vortex core span-wise position for first end-view field of view (EV 1, $x/h = 8$)

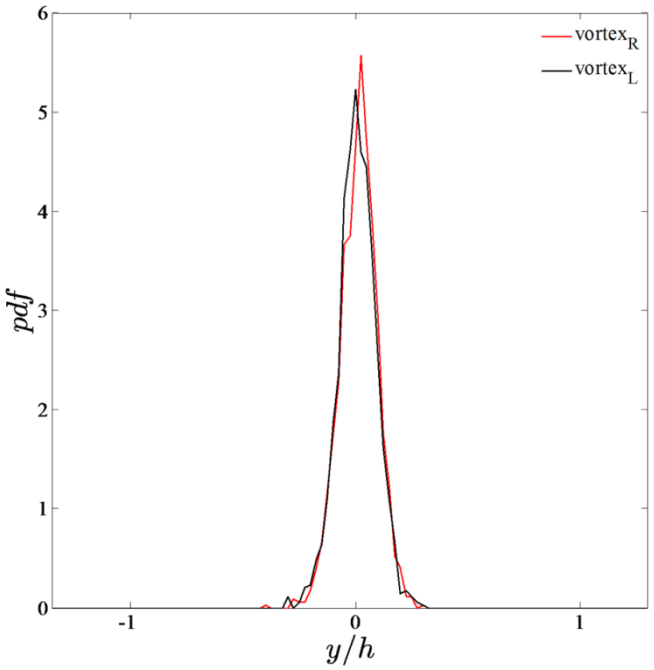

Figure 3.89: PDFs of stream-wise vortex core transverse position for first end-view field of view (EV 1, $x/h = 8$)

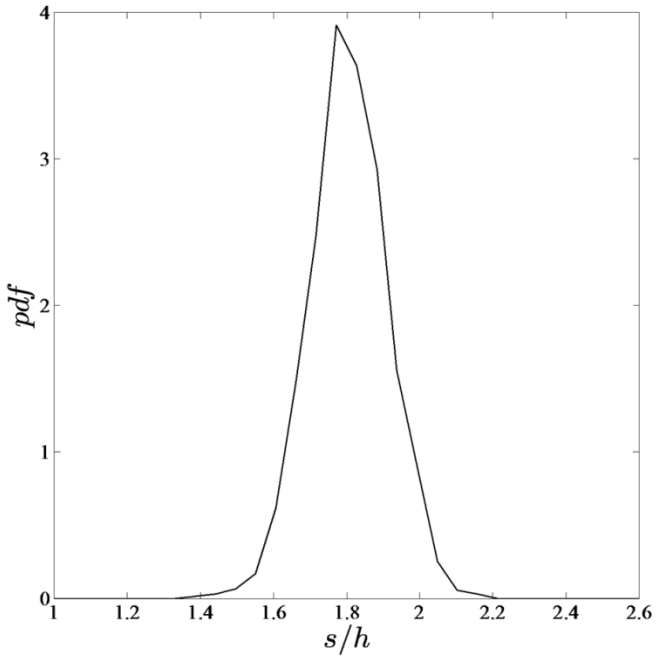

Figure 3.90: PDF of stream-wise vortex core separation for first end-view field of view (EV 1, $x/h = 8$)

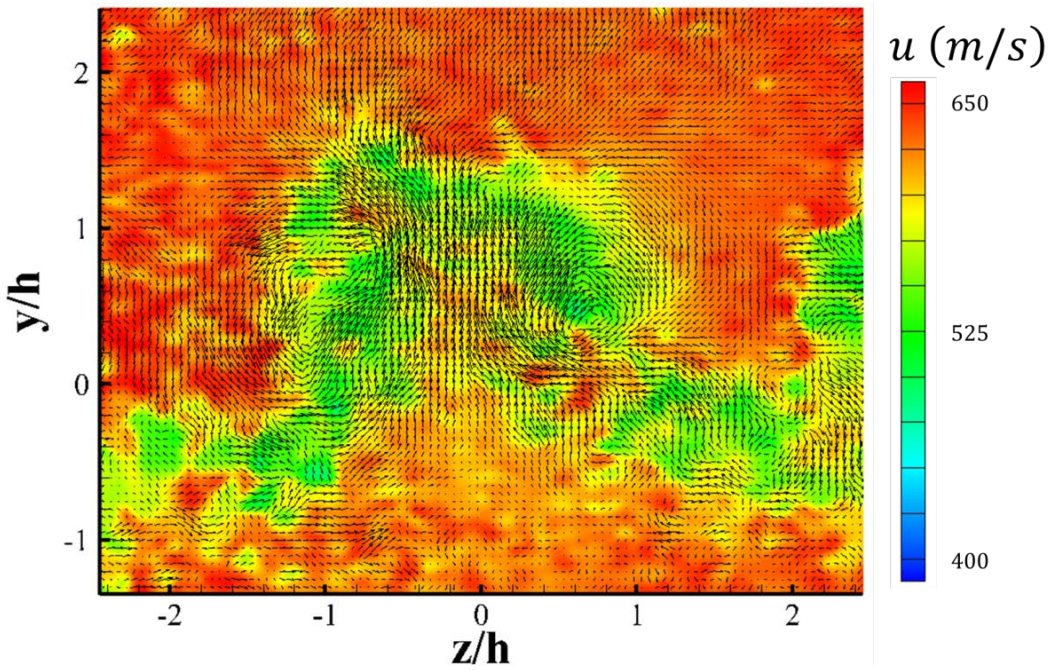

Figure 3.91: Example instantaneous end-view stream-wise velocity contours for hypermixing injector flowfield (EV 2, $x/h = 16$)

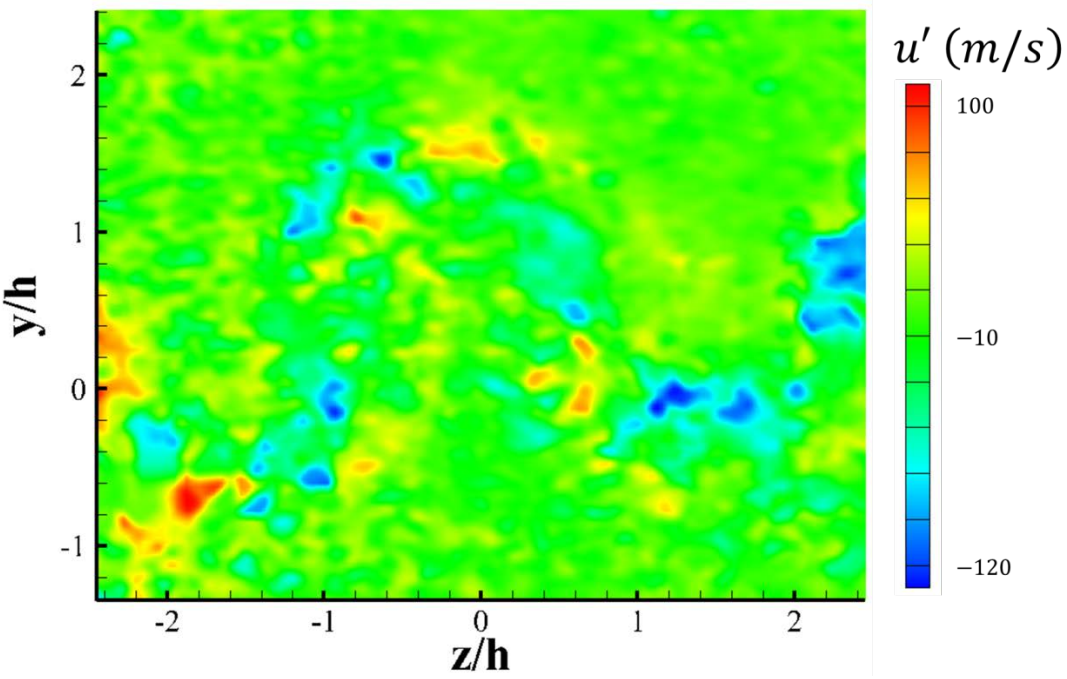

Figure 3.92: Example fluctuating end-view stream-wise velocity contours for hypermixing injector flowfield (EV 2, $x/h = 16$)

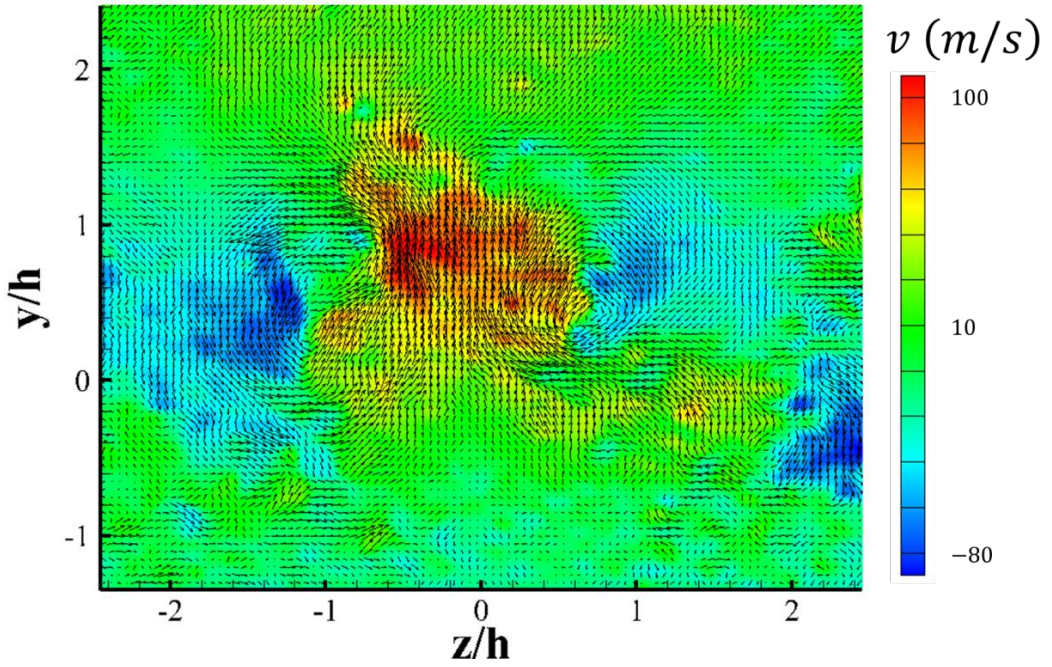

Figure 3.93: Example instantaneous end-view transverse velocity contours for hypermixing injector flowfield (EV 2, $x/h = 16$)

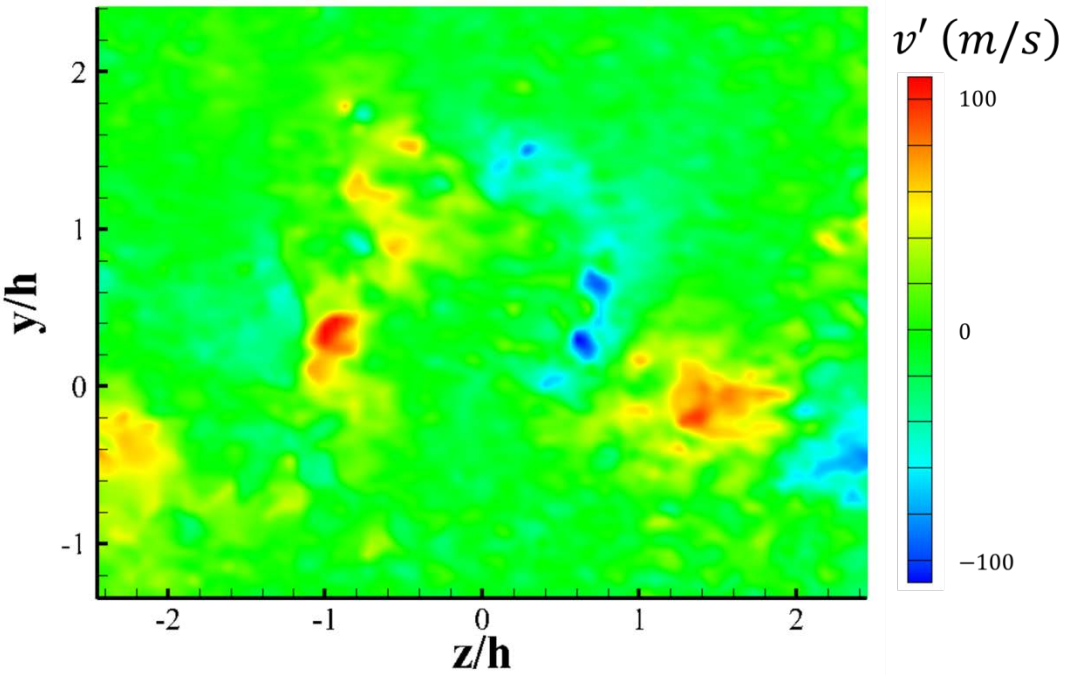

Figure 3.94: Example instantaneous end-view transverse velocity contours for hypermixing injector flowfield (EV 2, $x/h = 16$)

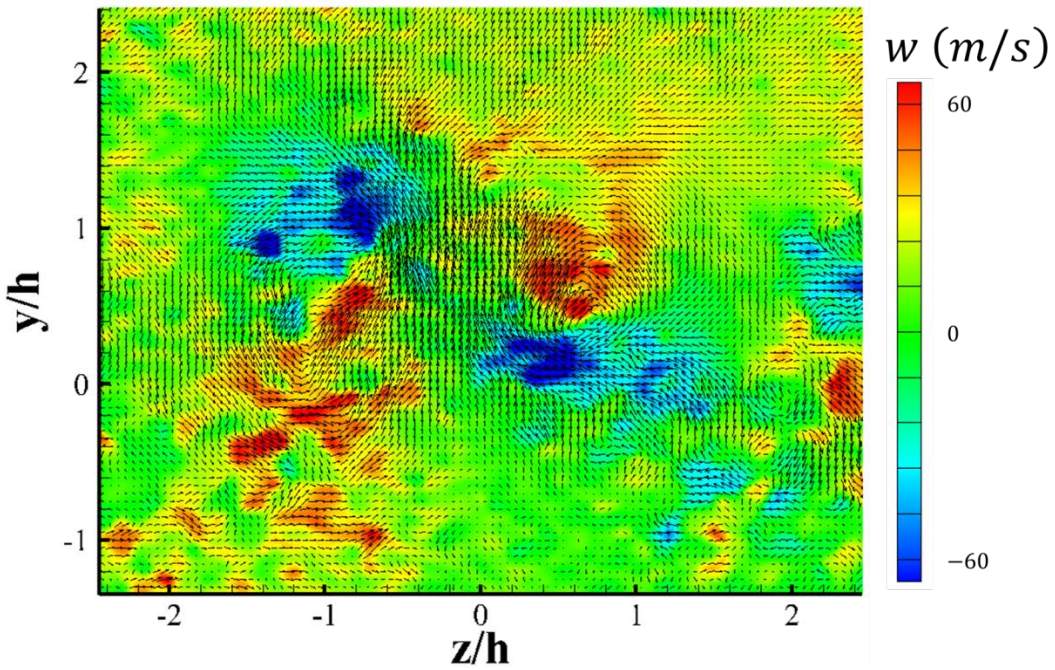

Figure 3.95: Example instantaneous end-view span-wise velocity contours for hypermixing injector flowfield (EV 2, $x/h = 16$)

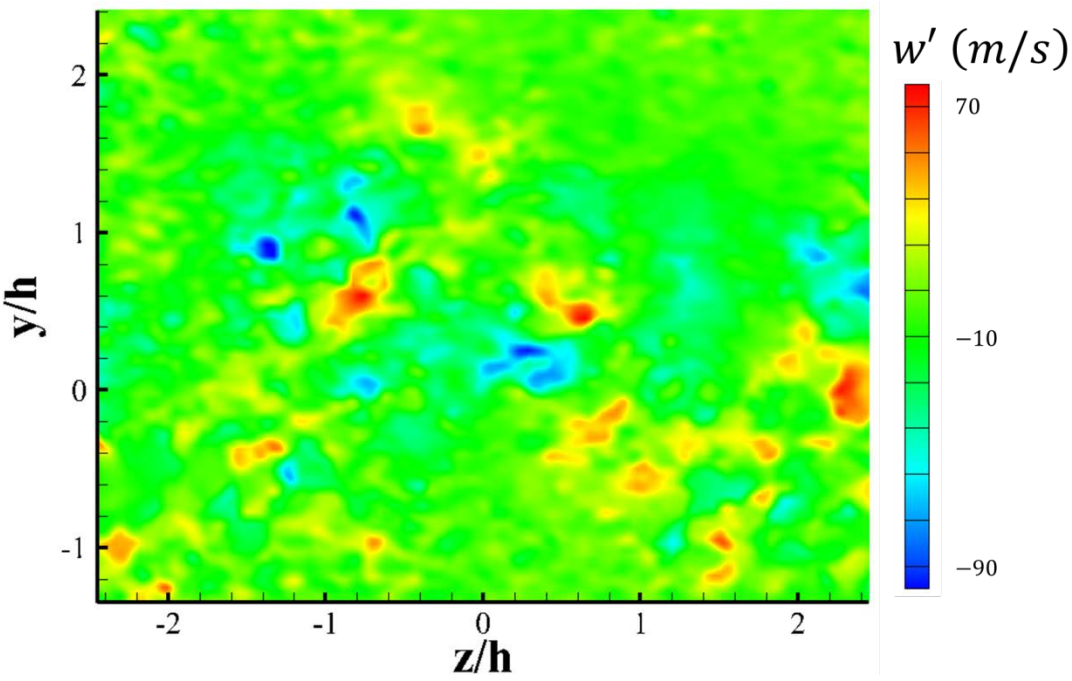

Figure 3.96: Example fluctuating end-view span-wise velocity contours for hypermixing injector flowfield (EV 2, $x/h = 16$)

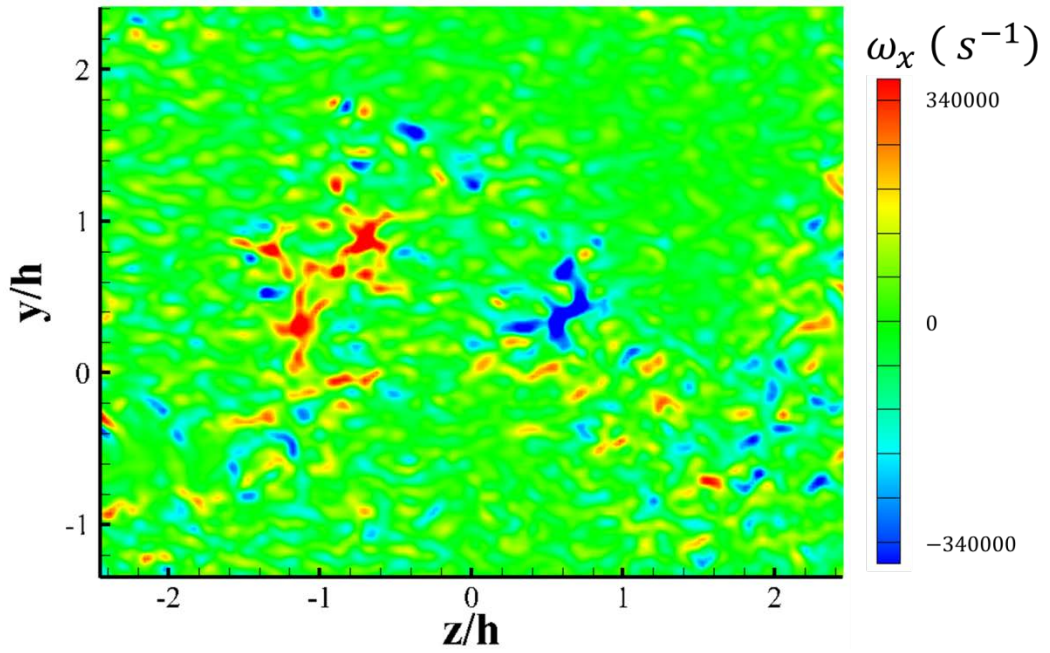

Figure 3.97: Example instantaneous end-view stream-wise vorticity contours for hypermixing injector flowfield (EV 2, $x/h = 16$)

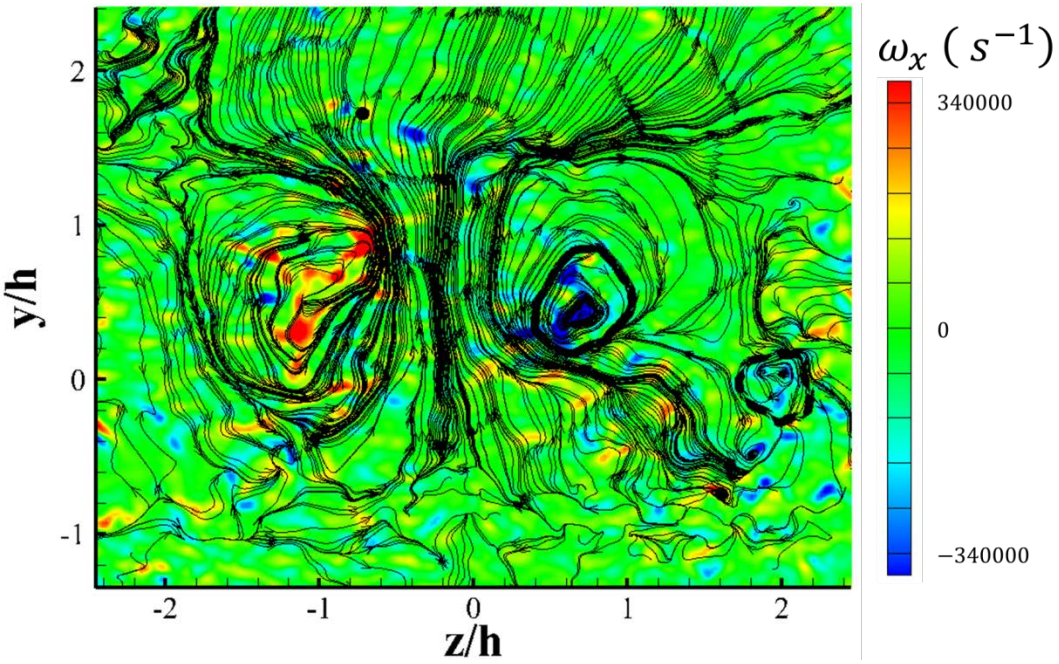

Figure 3.98: Example instantaneous end-view stream-wise vorticity contours for hypermixing injector flowfield overlaid with instantaneous streamlines (EV 2, $x/h = 16$)

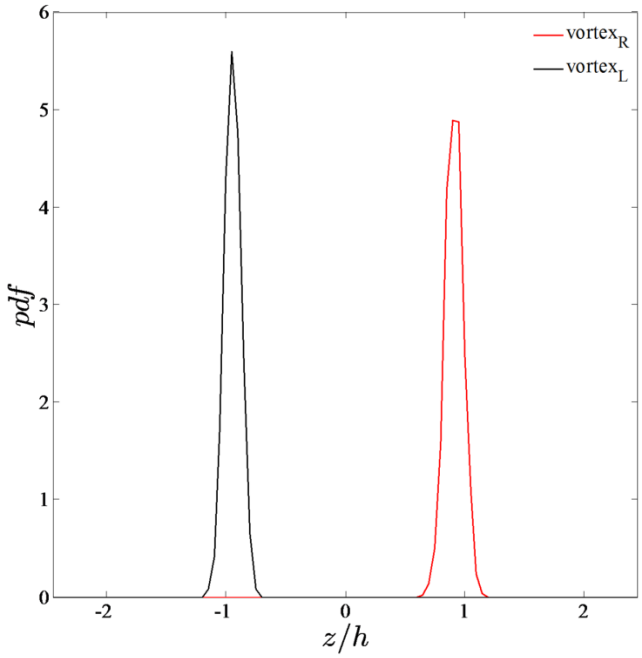

Figure 3.99: PDFs of stream-wise vortex core span-wise position for second end-view field of view (EV 2, $x/h = 16$)

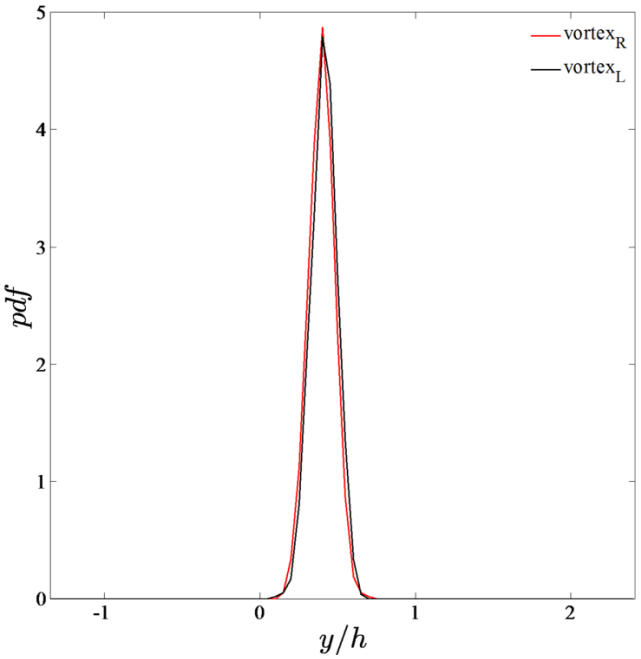

Figure 3.100: PDFs of stream-wise vortex core transverse position for second end-view field of view (EV 2, $x/h = 16$)

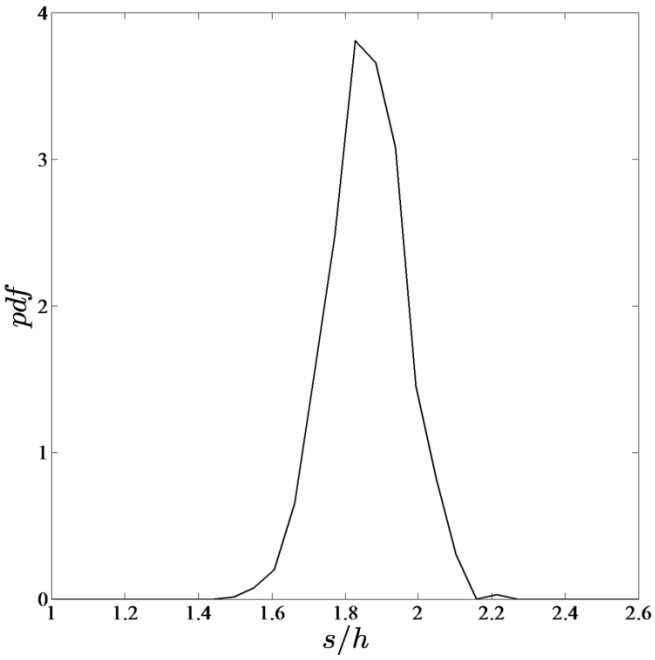

Figure 3.101: PDF of stream-wise vortex core separation for second end-view field of view (EV 2, $x/h = 16$)

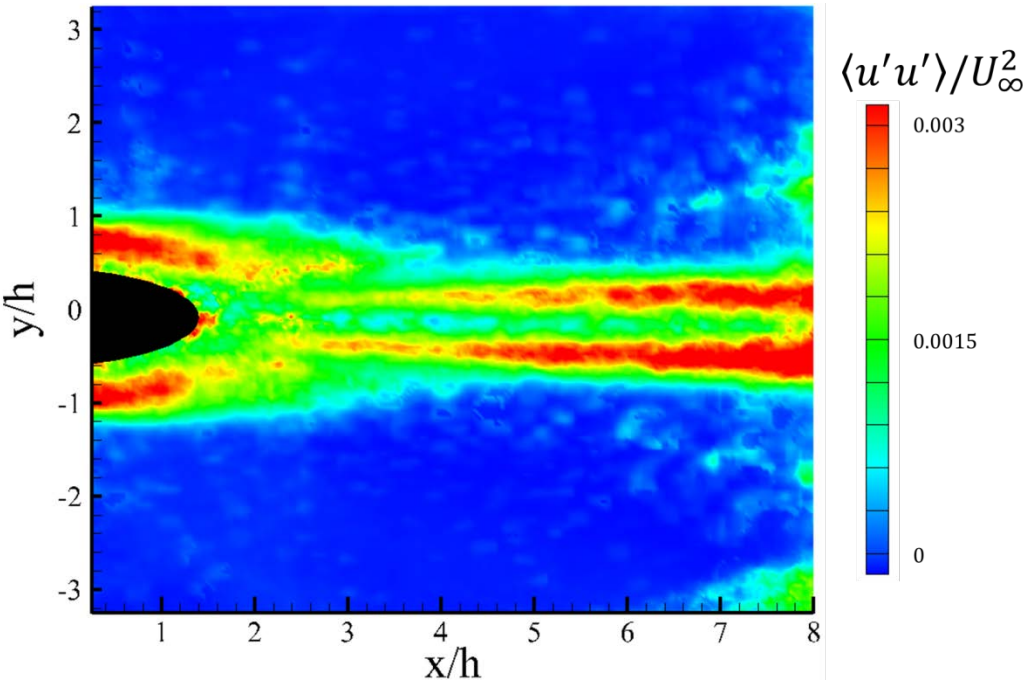

Figure 3.102: Centerline stream-wise velocity fluctuation contours for near-field of the planar injector flowfield (SV 1a)

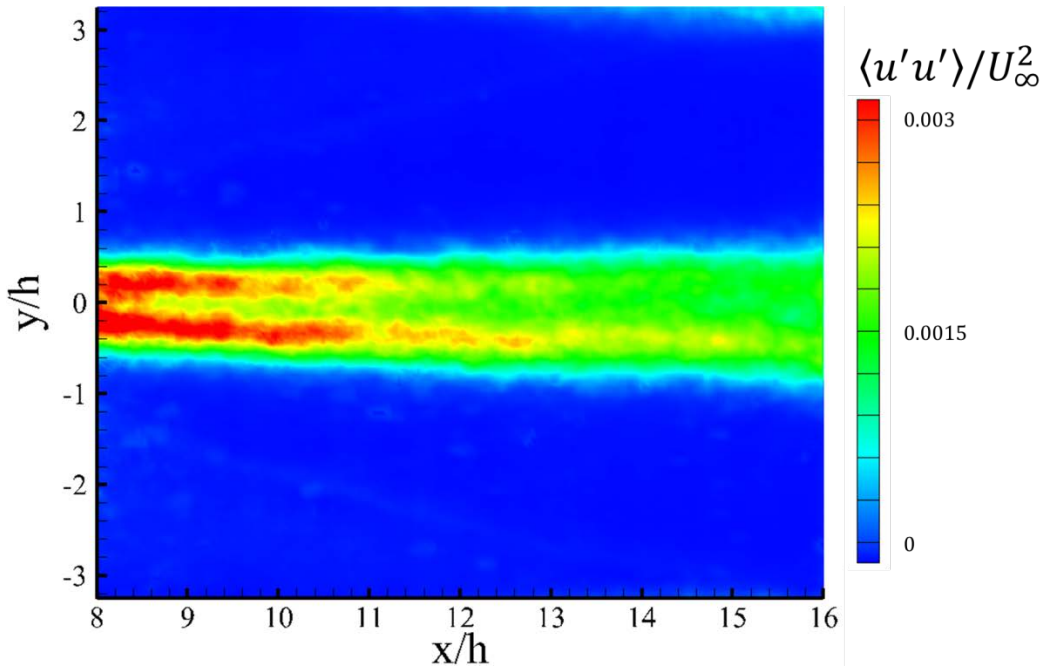

Figure 3.103: Centerline stream-wise velocity fluctuation contours for mid-field of the planar injector flowfield (SV 2a)

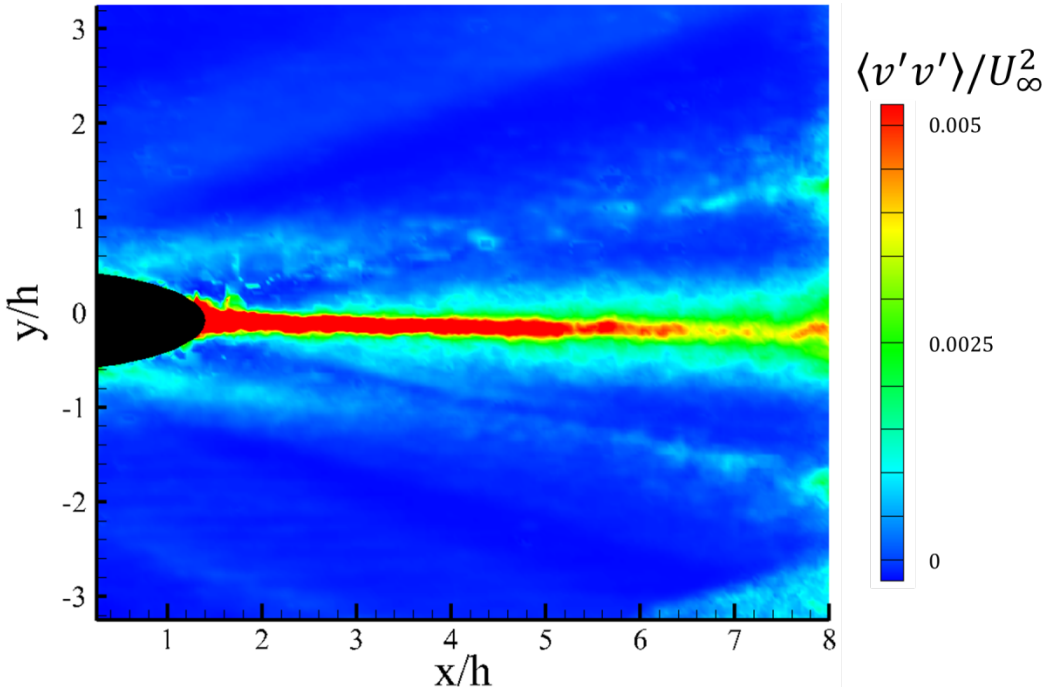

Figure 3.104: Centerline transverse velocity fluctuation contours for near-field of planar injector flowfield (SV 1a)

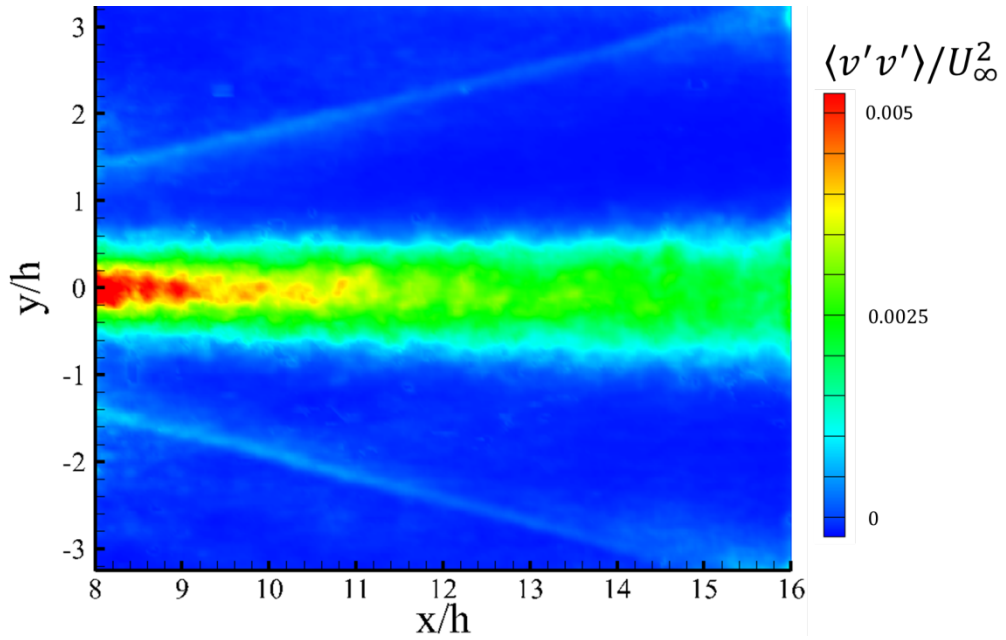

Figure 3.105: Centerline transverse velocity fluctuation contours for mid-field of planar injector flowfield (SV 2a)

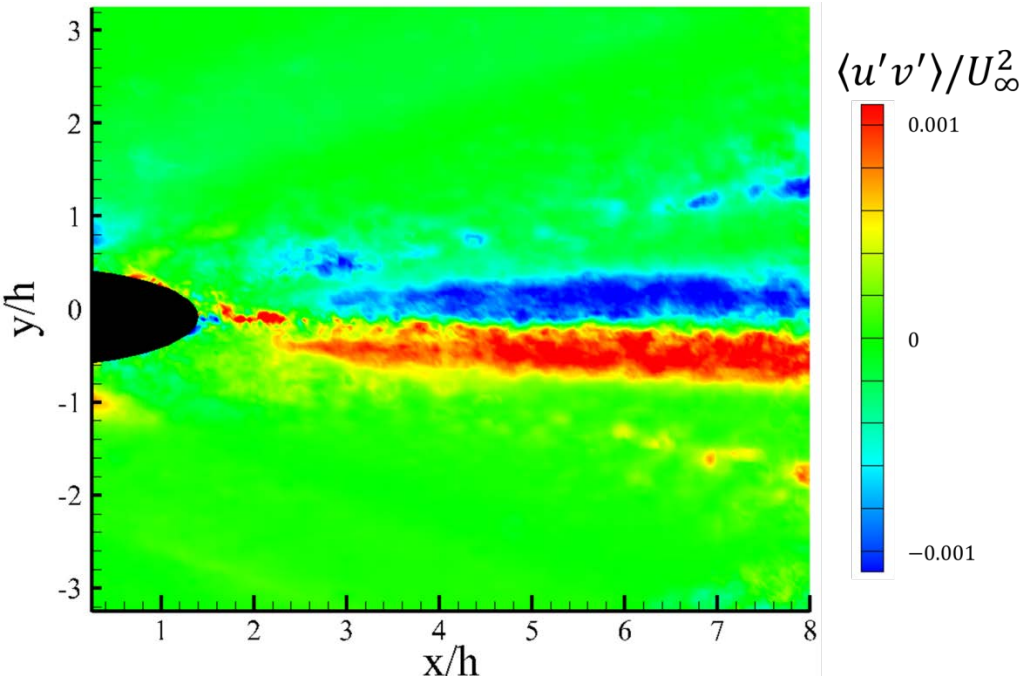

Figure 3.106: Centerline shear velocity fluctuation contours for near-field of planar injector flowfield (SV 1a)

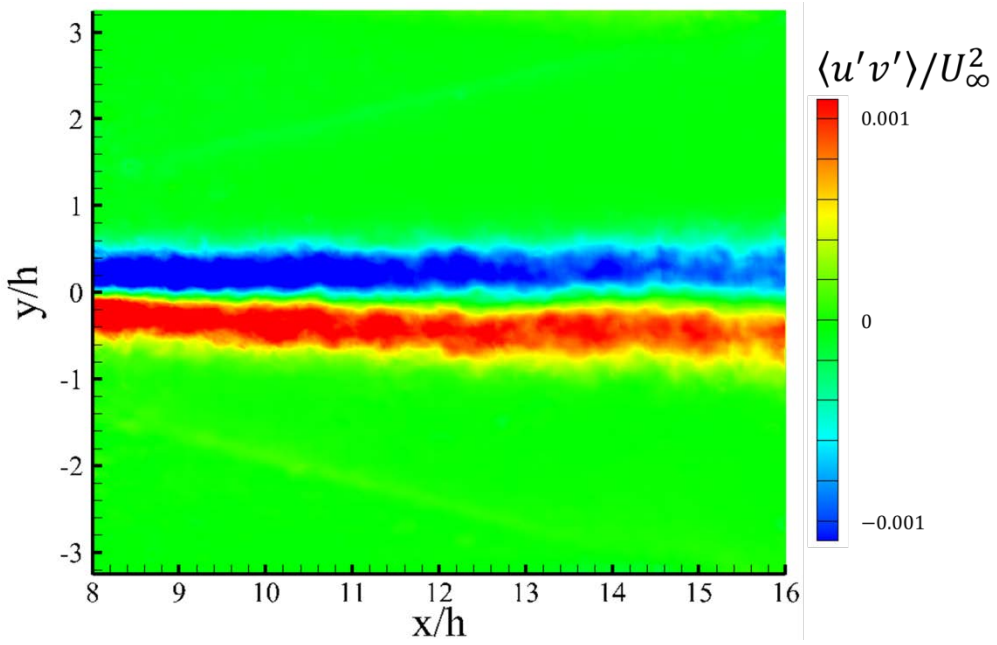

Figure 3.107: Centerline shear velocity fluctuation contours for mid-field of planar injector flowfield (SV 2a)

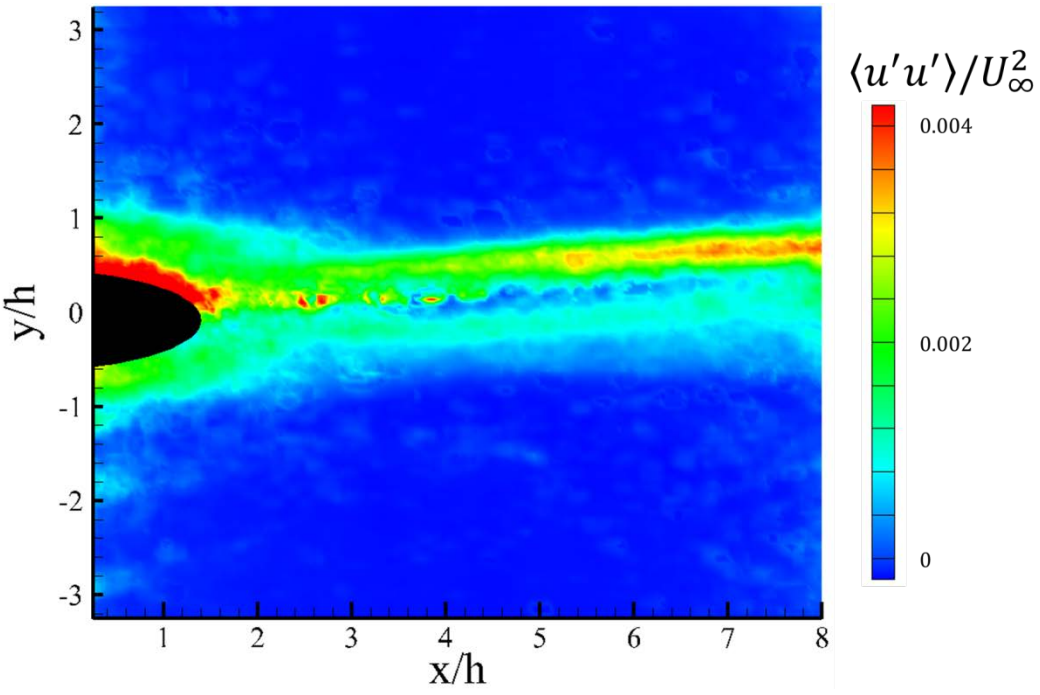

Figure 3.108: Centerline stream-wise velocity fluctuation contours for near-field of hypermixing injector flowfield (SV 1a)

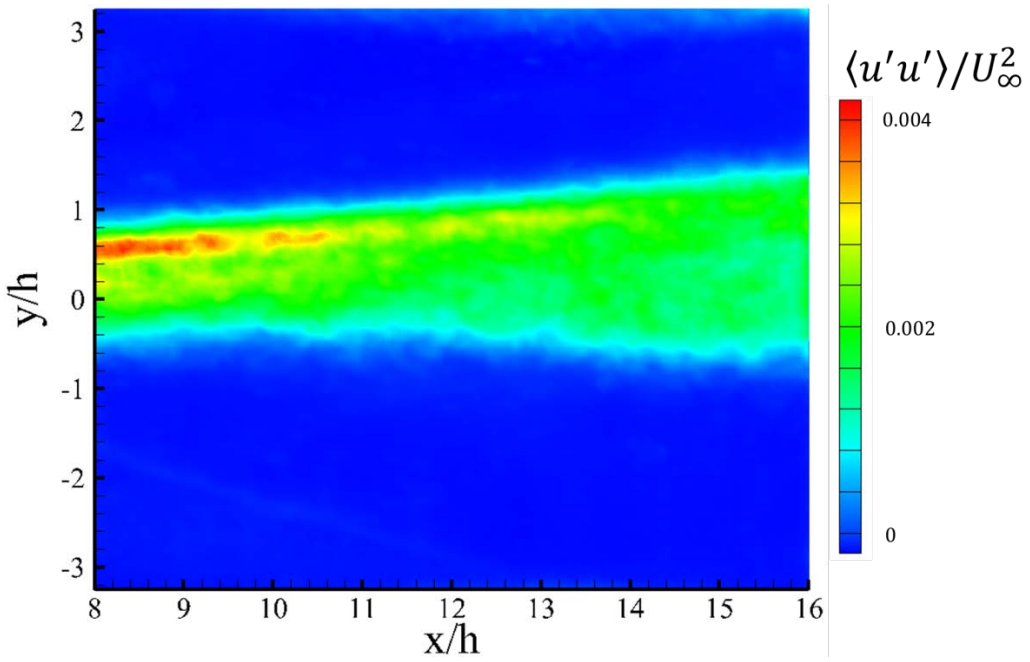

Figure 3.109: Centerline stream-wise velocity fluctuation contours for mid-field of hypermixing injector flowfield (SV 2a)

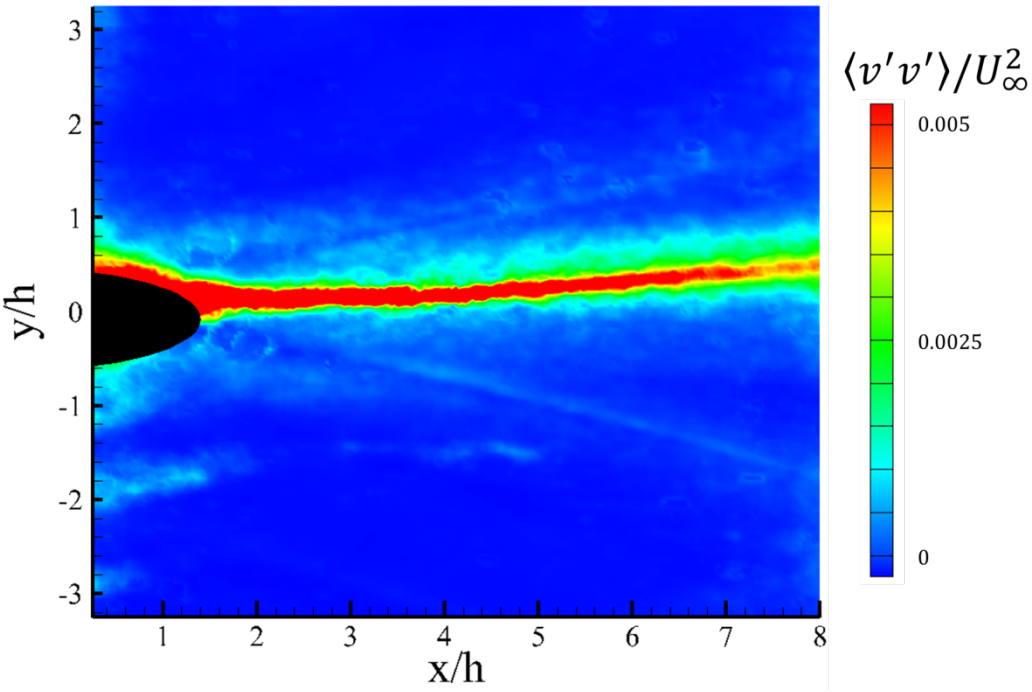

Figure 3.110: Centerline transverse velocity fluctuation contours for near-field of hypermixing injector flowfield (SV 1a)

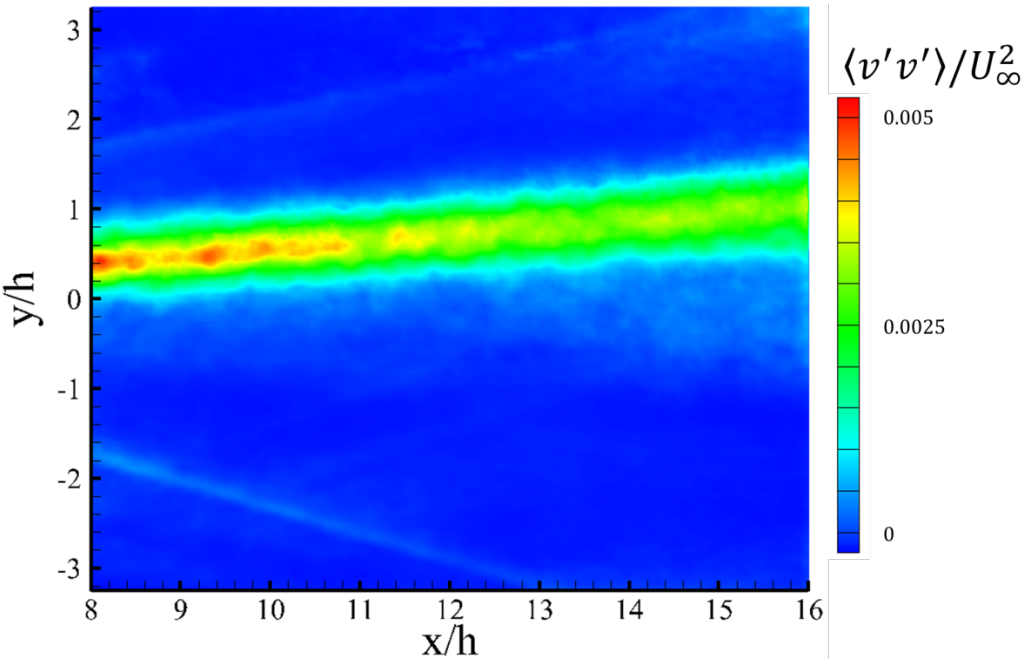

Figure 3.111: Centerline transverse velocity fluctuation contours for mid-field of hypermixing injector flowfield (SV 2a)

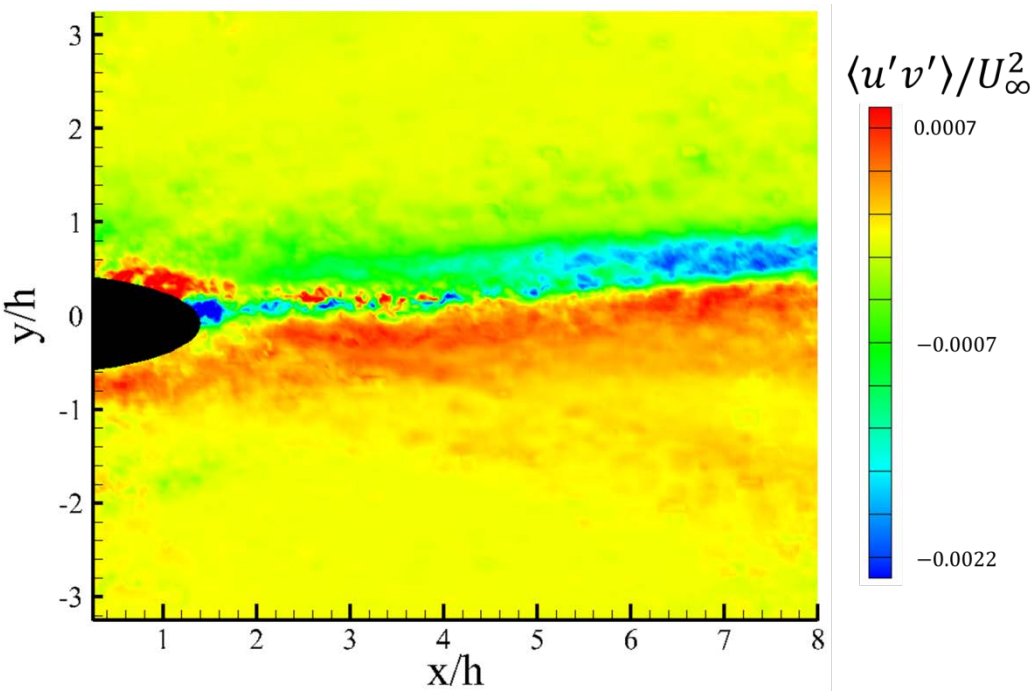

Figure 3.112: Centerline shear velocity fluctuation contours for near-field of hypermixing injector flowfield (SV 1a)

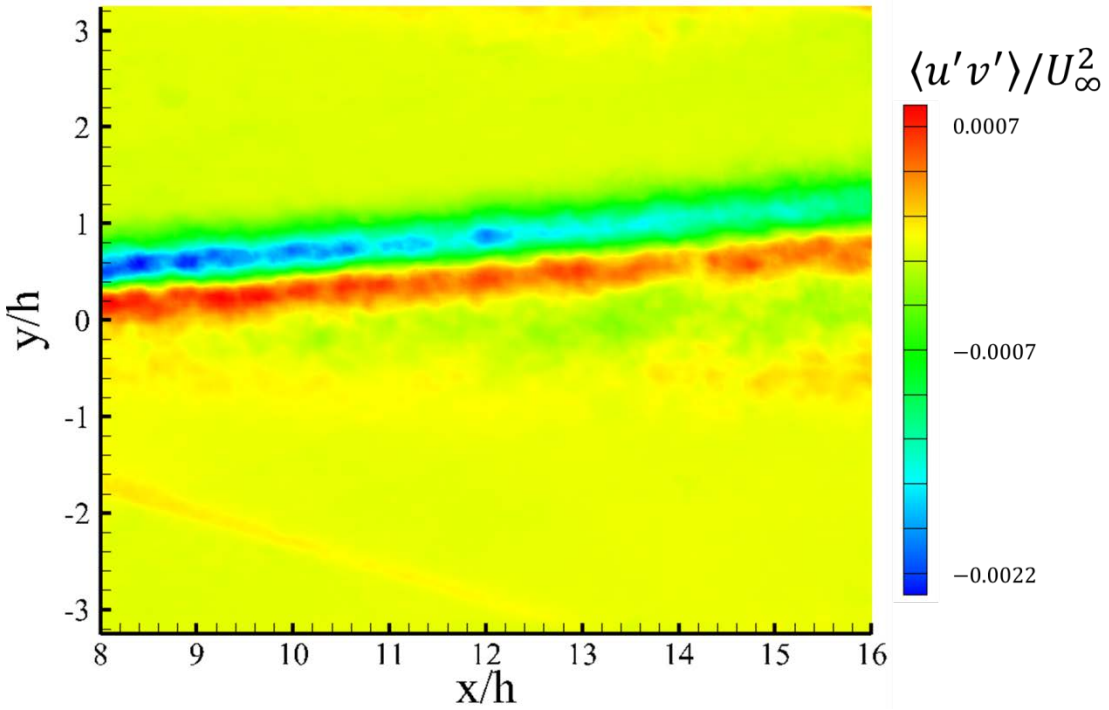

Figure 3.113: Centerline shear velocity fluctuation contours for mid-field of hypermixing injector flowfield (SV 2a)

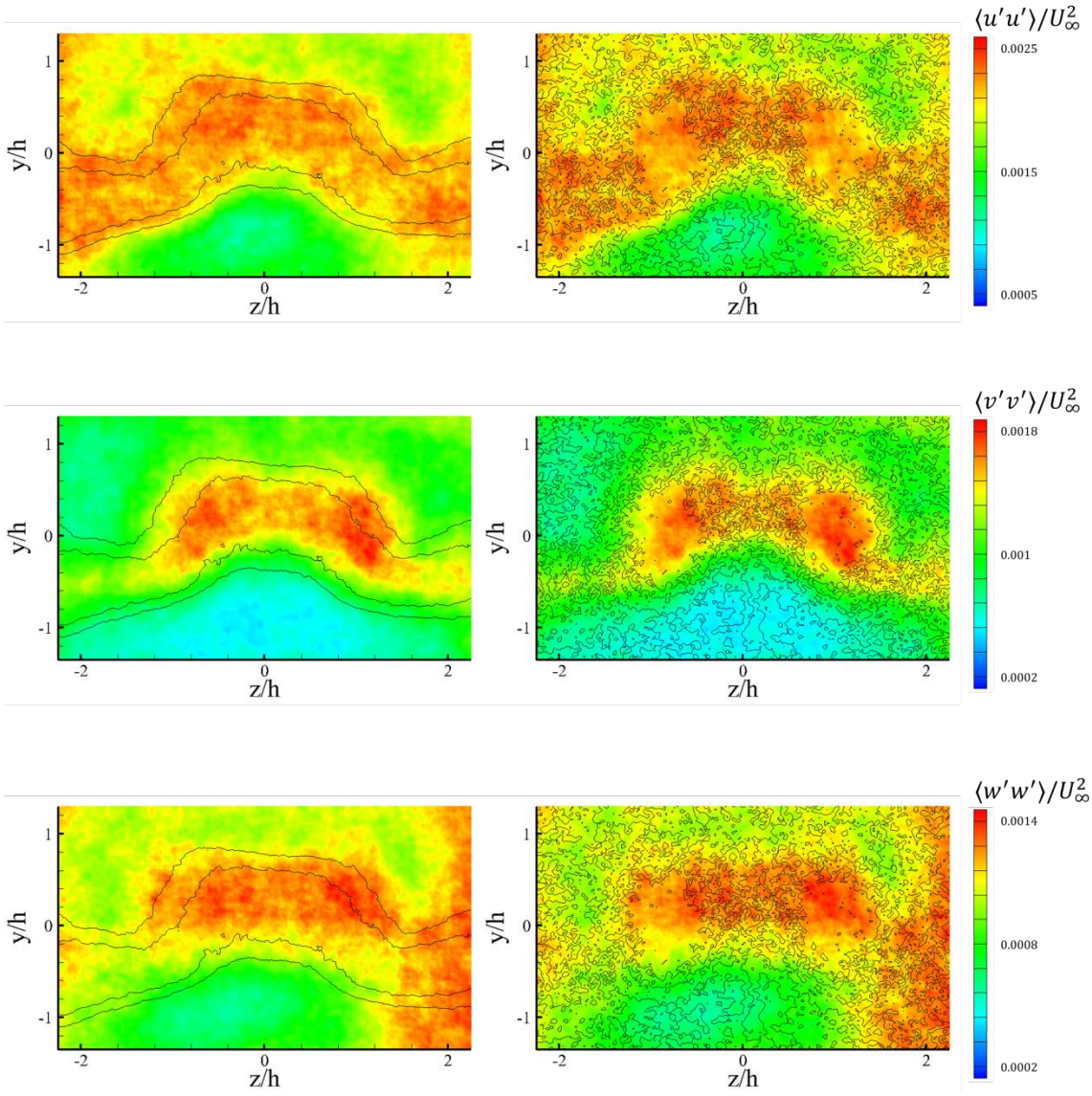

Figure 3.114: Normal Reynolds stresses for first end-view field of view (EV 1, $x/h = 8$). Top – stream-wise component, middle – transverse component, and bottom – span-wise component. Left – overlaid with stream-wise velocity contours and right – overlaid with vorticity contours

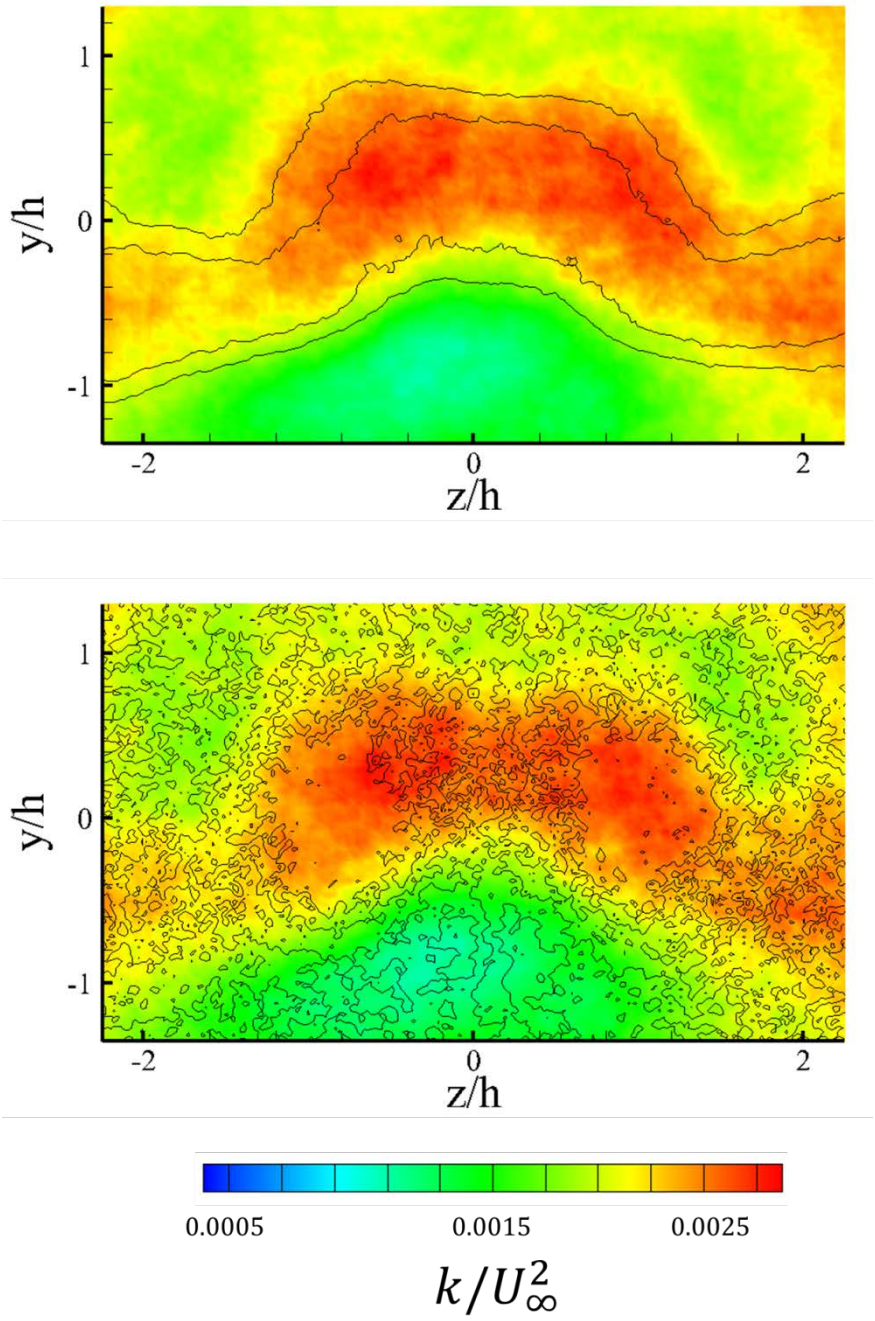

Figure 3.115: Contours of turbulent kinetic energy for first end-view field of view (EV 1, $x/h = 8$). Top – overlaid with stream-wise velocity contours and bottom – overlaid with vorticity contours

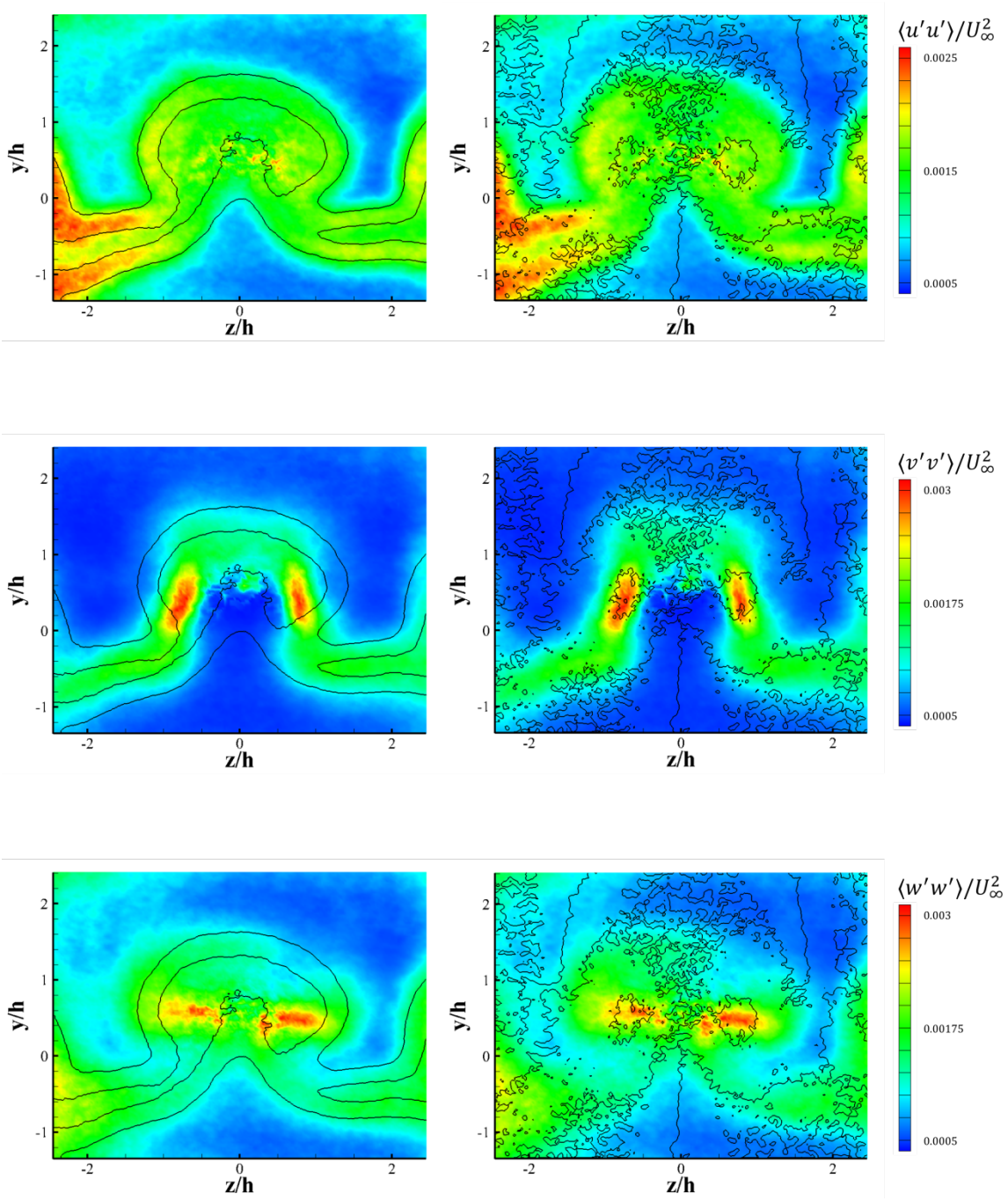

Figure 3.116: Normal Reynolds stresses for second end-view field of view (EV 2, $x/h = 16$). Top – stream-wise component, middle – transverse component, and bottom – span-wise component. Left – overlaid with stream-wise velocity contours and right – overlaid with vorticity contours

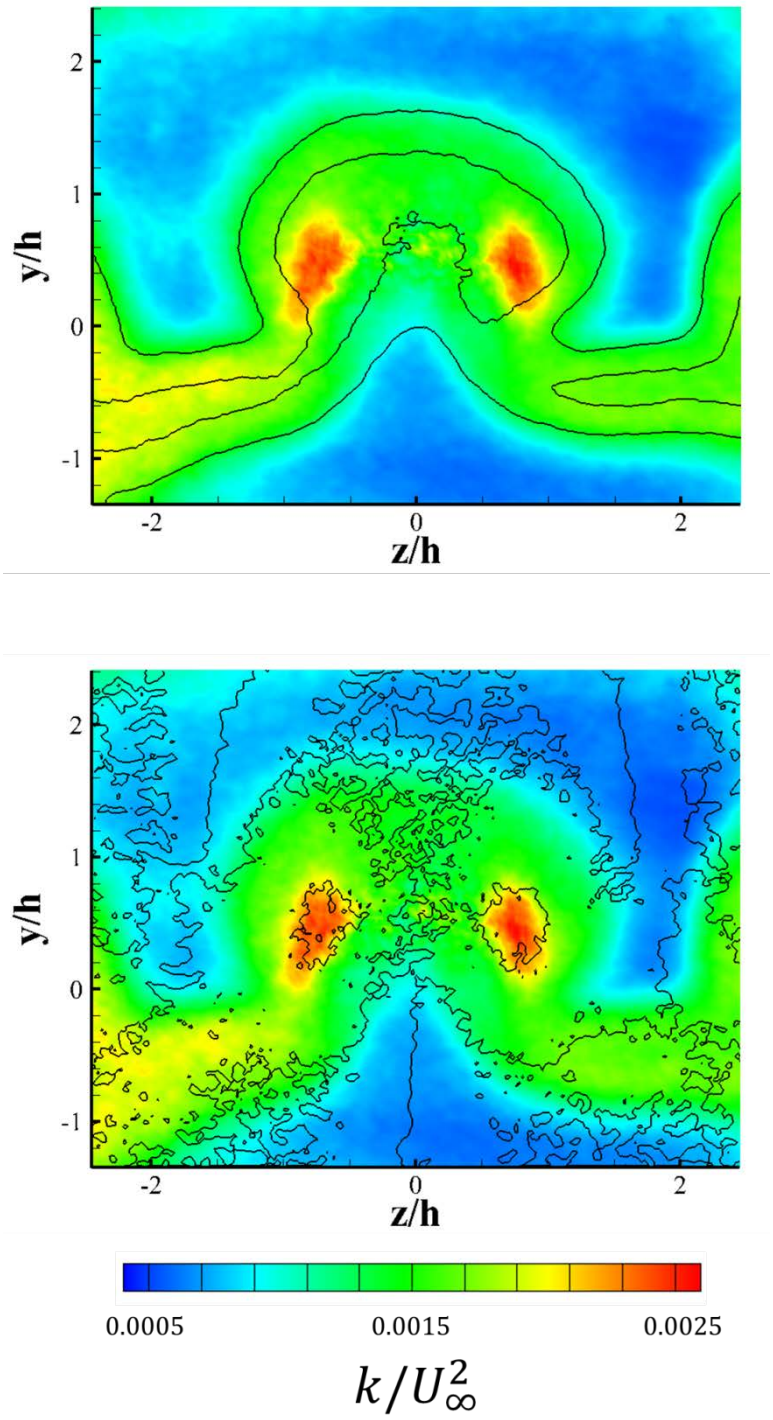

Figure 3.117: Contours of turbulent kinetic energy for second end-view field of view (EV 2, $x/h = 16$). Top – overlaid with stream-wise velocity contours and bottom – overlaid with vorticity contours

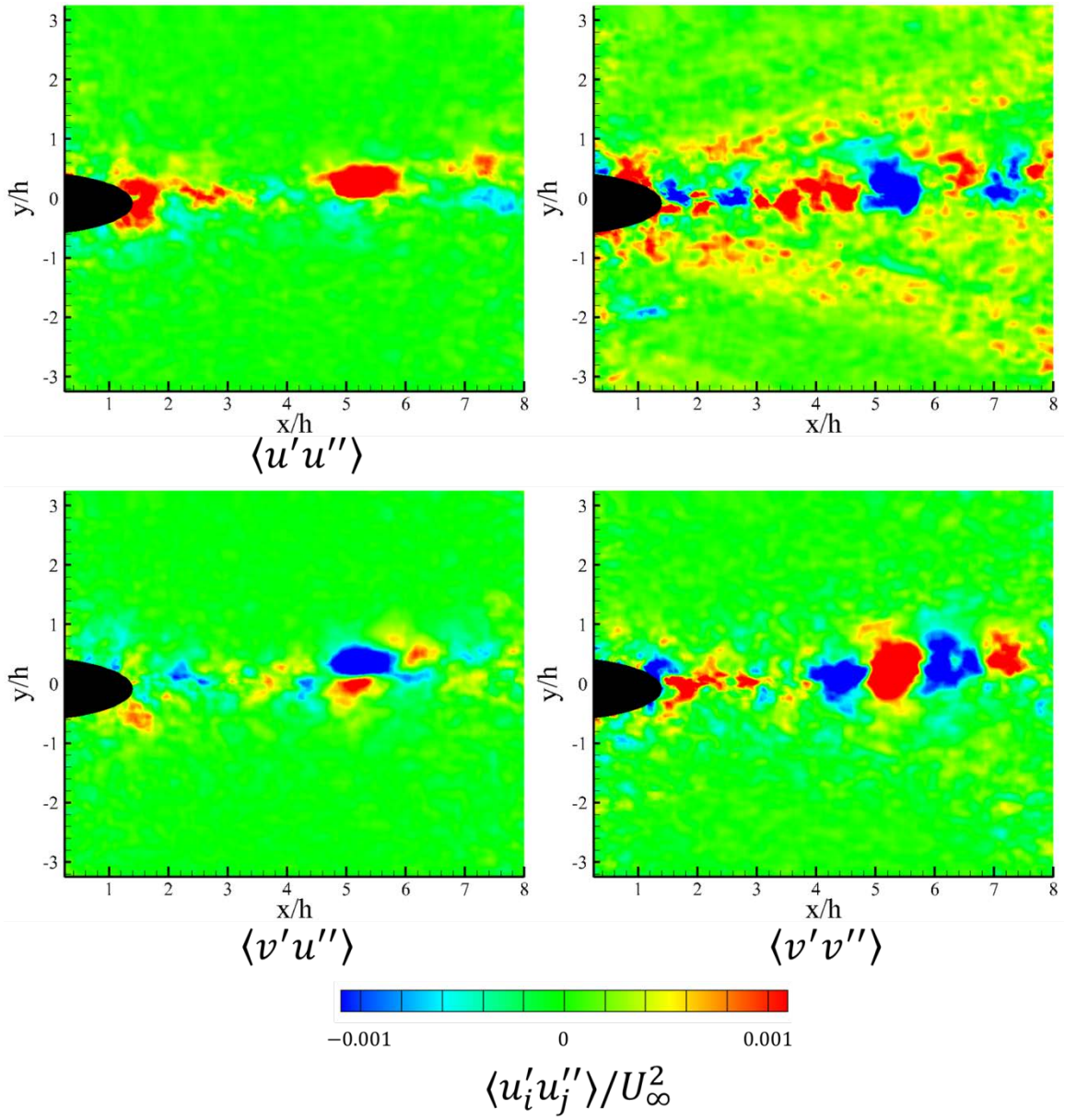

Figure 3.118: Centerline two-point correlation for near-field (SV 1a) of hypermixing injector flowfield. Top left - $\langle u'u'' \rangle$, top right - $\langle u'v'' \rangle$, bottom left - $\langle v'u'' \rangle$, and bottom right - $\langle v'v'' \rangle$

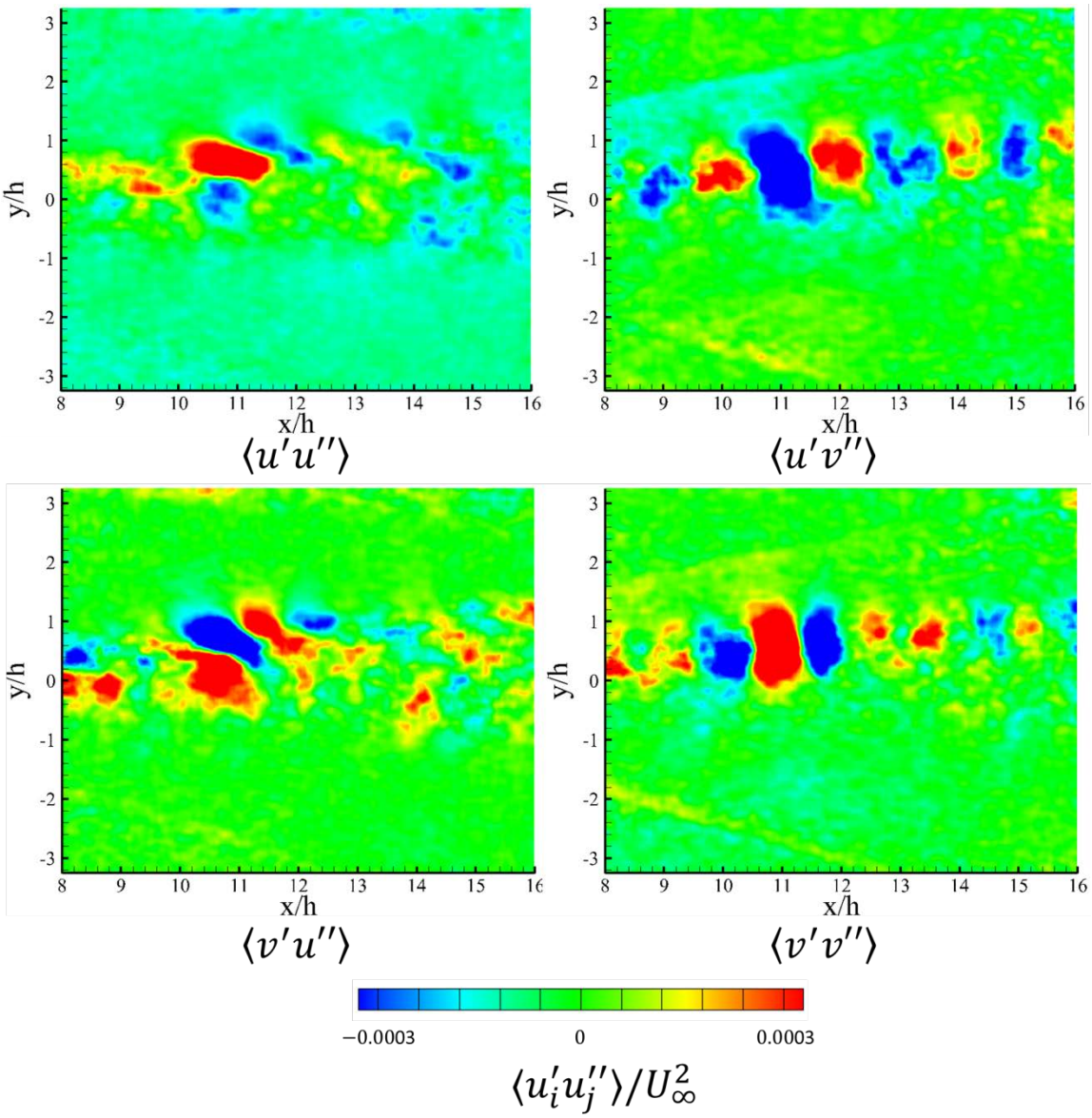

Figure 3.119: Centerline two-point correlation for mid-field (SV 2a) of hypermixing injector flowfield. Top left - $\langle u'u'' \rangle$, top right - $\langle u'v'' \rangle$, bottom left - $\langle v'u'' \rangle$, and bottom right - $\langle v'v'' \rangle$

Chapter 4: Application of Krypton PLIF to Supersonic Mixing Flowfields

This chapter details the experimental and analytical methods utilized in implementing simultaneous krypton PLIF and PIV in supersonic mixing flowfields. Theory relevant to the fluorescence calibration is followed by a discussion of the experimental setup. An analysis of the sensitivity of the Kr PLIF technique to various input parameters and a comparison of the different potential temperature models used in these studies follows. A brief analysis of two supersonic mixing flowfields, both mean and instantaneous, follows. Finally, some suggestions for future work and analysis using these data are proposed.

4.1 – Background and Theory

This section details the background information and theory relevant to the calculation of the krypton mole fraction from the raw fluorescence signal. The topics covered herein include a restatement of the fluorescence calibration theory in the context of two-dimensional imaging, the coupling between the velocity, temperature, and concentration fields in compressible mixing flowfields, and some background on kinetic theory relevant to the calculation of thermodynamic properties of gases.

4.1 – Fluorescence Calibration

The various dependences of the nonlinear fluorescence signal found in Kr LIF have been covered extensively in Chapter 2 and consequently will not be reexamined here. However, no formal discussion has yet been given on utilizing the krypton fluorescence signal as a measure of the local concentration of krypton in a flow. In Chapter 2, the thermodynamic dependence of the fluorescence signal was established. Specifically, the species-specific quenching rates have been measured as a function of

temperature and pressure, as have the relative two-photon absorption cross-sections. However, these represent only a fraction of the total dependences of the fluorescence signal. To recapitulate Eq. 2.1 will be restated here:

$$S_f = \eta_c \frac{E_L^2}{a^2} \frac{A_{21}}{A+Q} \frac{\hat{\sigma}^{(2)} n_{Kr}}{4\pi^2(\hbar\omega)^2} \int_{-\infty}^{\infty} F^2(t)dt \qquad 2.1$$

Eq. 2.1 can be further restated in terms of measureable thermodynamic quantities as follows:

$$S_{f,Kr} = \eta_c \left(\frac{E_L}{a}\right)^2 \frac{A_{21}}{A+Q} \frac{\hat{\sigma}^{(2)}}{4\pi^2(\hbar\omega)^2} \frac{P}{kT} \chi_{Kr} \int_{-\infty}^{\infty} F^2(t)dt \qquad 4.1$$

Thus, the explicit thermodynamic dependences are revealed. Now, in principle Eq. 4.1 could be directly solved for χ_{Kr} by first expanding the total quenching rate via Eq. 2.3a or 2.3b and subsequently rearranging the equation. In making this substitution, however, a number of problems are revealed. First, the mole fraction calculated in this fashion holds a dependence on the collection efficiency of the optical system, which is unknown and very difficult to measure [**87**]. Second, there are dependences (both explicit and implicit) on the local thermodynamic conditions. When in a test cell where the temperature and pressure are controlled and measured, knowing these conditions doesn't pose a tremendous difficulty. However, in a practical flow these quantities are very difficult to measure without disturbing the flow (which is one reason a non-intrusive diagnostic is preferable to physical probes). Third, especially true if the measurement taken is planar in nature, the distribution of laser energy and spatial excitation parameter (a) are not well-defined.

Some of the three aforementioned points can be overcome with sufficient theoretical development. However, there are two unavoidable shortcomings in the procedure: there is insufficient knowledge of the collection efficiency of the optical

system being used as well as the true intensity profile of the laser sheet if making planar measurements. A similar problem was encountered in Chapter 2 when measuring the thermodynamic dependence of the two-photon absorption cross-section. In that situation, a ratiometric method was utilized, and the relative absorption cross-section was measured instead. In a similar manner, the same procedure can be used in calibrating the fluorescence signal for mole fraction sensitivity while simultaneously overcoming both of the aforementioned limitations. Consider first a practical measurement of fluorescence in a wind-tunnel – the *in situ* signal dependence is described by Eq. 4.1. Now consider another measurement, taken with the same optical collection system, but in this circumstance the thermodynamic conditions of the measurement are known *a priori* (taken in a test cell or something similar). In this second measurement, since all of the thermodynamic conditions are known in addition to the bulk laser energy, the quenching rates are known by extension. If the signal from the original fluorescence measurement was then divided by that from this second measurement or reference state, the ratio would be defined by:

$$\frac{S_f}{S_{f,ref}} = \frac{E_L^2}{E_{L,ref}^2} \frac{\gamma\left(\chi_{ref}, P_{ref}, T_{ref}\right)}{\gamma(\chi_i, P, T)} \frac{\hat{\sigma}^{(2)}}{\hat{\sigma}_{ref}^{(2)}} \frac{\chi_{Kr}}{\chi_{Kr,ref}} \frac{P}{P_{ref}} \frac{T_{ref}}{T} \qquad 4.2$$

By utilizing this procedure, the collection efficiency (and laser intensity profile) is removed from the dependence since both measurements share the same excitation and acquisition systems. Should the bulk laser pulse energy be constant as well, Eq. 4.2 would simplify further. However, to maintain generality, it has been included in this circumstance. Also eliminated from this equation are the mean excitation photon energy and temporal profile of the exciting laser pulse. Note here that in utilizing this ratio method for calibration, the effective two-photon absorption cross-section has been converted to its relative form as measured in Chapter 2.

Once this simplification has been made, the mole fraction of krypton can be solved for explicitly. To accomplish this, the total decay rates (γ) must first be expanded by the appropriate definition. Utilizing Eq. 2.3b, the solution obtained for the mole fraction of krypton (specialized for a binary Kr-air mixture) is given by:

$$\chi_{Kr} = \frac{\dfrac{A + P q_{air}(T)}{P\left(q_{Kr}(T) - q_{air}(T)\right)}}{\dfrac{S_{f,ref}}{S_f}\dfrac{E_L^2}{E_{L,ref}^2}\dfrac{\gamma\left(P_{ref}, T_{ref}\right)}{P\left(q_{Kr}(T) - q_{air}(T)\right)}\dfrac{\hat{\sigma}^{(2)}}{\hat{\sigma}_{ref}^{(2)}}\dfrac{T_{ref}}{T}\dfrac{P}{P_{ref}}\dfrac{1}{\chi_{Kr,ref}} - 1} \qquad 4.3$$

Eq. 4.3 is sufficient for calculating the mole-fraction of krypton in a krypton-air mixture if the pressure and temperature are known. If these conditions are unknown, then the calibration procedure becomes far more complex. These complications will be discussed in Section 4.1.2.

4.1.2 – Estimation of Thermodynamic Conditions in Supersonic Mixing Flowfields

As was described in Section 4.1.1, even with a robust calibration methodology, the calibration of the krypton fluorescence signal still requires knowledge of the local thermodynamic conditions. If the flowfield was purely subsonic and non-reacting, this would be a relatively simple requirement to meet. That is, the conditions could be approximated as constant (and potentially equal to ambient conditions if the flow was external). Should these criteria not be met, the mole fraction calibration becomes more complicated; an additional procedure is needed to assess the thermodynamic conditions. In performing krypton PLIF in a jet flame (a reacting flow), Hsu et al. [**83**] performed simultaneous Rayleigh thermometry measurements to correct for the local temperature field, using the jet core conditions as the reference. However, in the current supersonic mixing flowfields no such measurements can be made. As noted in Chapter 1, the low density of the flows of interest precludes the use of Rayleigh scattering, and the use of

krypton changes the local differential Rayleigh scattering cross-section sufficiently that the typical calibration of Rayleigh thermometry could not be directly applied regardless. Thus, an alternative means of evaluating the thermodynamic state of the flow is required.

Another approach to evaluating the state of the flow is to attempt to use an equation of state to couple the unknown thermodynamic variables to other known quantities in the flow. In these supersonic mixing flowfields, the coupling of the energy, momentum, and species transport equations requires that the thermodynamic conditions, composition, and velocity fields are strongly related [**114**]. Thus, in order to apply this strategy in calibrating the fluorescence signal, Eq. 4.3 will have to be modified to incorporate effects related to the momentum and energy of the flow rather than just the bulk thermodynamic properties.

In addition to compositional effects on the flowfield, as was demonstrated in Chapter 3 there are a number of flow features, which cause variations in the thermodynamic conditions. These include expansion waves, recompression shocks, and shear flows of various forms. With information about the flowfield structure from Chapter 3, these data can be utilized in estimating the local thermodynamic conditions within the supersonic mixing flowfields. Each of the relevant properties will be discussed in the sections to follow.

4.1.2.1 – Pressure

The flowfields studied in Chapter 3 are, for the most part, complex shear flows. Should the measurement location be sufficiently far downstream that other flow structures (shocks or expansions) pose little interference, these regions of the flow could be assumed isobaric in the mean by virtue of the compressible boundary layer equations [**114**]. However, in making this assumption it is required that the freestream pressure is

known throughout the flowfield. As mentioned in the introduction to this section, the flowfield has a series of shock- and expansion waves that alter the thermodynamic conditions throughout the flowfield. In order to accommodate the presence of these structures, the freestream conditions can be estimated with the use of simple compressible flow relations in addition to knowledge of the flow structure (specifically, the direction of the flow and the ratio of velocities across shockwaves). However, to use these relations, it is required that both the Mach number of the flow be known, and that the flow remains either isentropic or adiabatic in the case of shockwaves. The procedures for estimating the Mach number and subsequently estimating the pressure field are described in Appendix 4A. The one shortcoming of this approach is that it neglects turbulent fluctuations throughout the wake. At present, the model used for estimating the pressure will estimate the turbulent fluctuations in the pressure via the fluctuations in the velocity, but they will be incorporated into the uncertainty of the calibration as explained in Section 4.3.1.3 and Appendix 4A.

4.1.2.2 – Temperature

In much the same manner that the freestream conditions were predicted for use in the pressure calculations, the freestream temperature throughout the flowfield can be estimated as well. However, the wake/jet structures also need to be accommodated in the estimation of the temperature. Due to viscous dissipation, deceleration of the flow, and in this case a variable composition as well, the temperature does not remain uniform across these shear flows as the pressure does in the mean.

For a fixed composition, one method for estimating the temperature across a shear flow such as this is given by the Crocco-Busemann relation [**114**]:

$$T(y) = T_{aw} - r\frac{\|\vec{u}(y)\|^2}{2c_p} \qquad 4.4$$

Here, r is a viscous recovery factor that depends on the flow in question, but is generally a function of the local Prandtl number (ν/α), and $\vec{u}(y)$ is the total velocity of the flow. The basis for this formula is that the shear flow, despite the transverse velocity gradients, still possesses a constant total enthalpy ($H_o = h + u^2/2$), which allows the temperature to be estimated. There are two limitations to this assumption. First, the relation has only been shown valid in the mean flow, which means that turbulent fluctuations will pose a problem in the calibration procedure. Second, the relation assumes a constant composition. With regard to the turbulent fluctuations, while Eq. 4.4 becomes invalid, the utilization of the Crocco-Busemann model can assist in making first order corrections to temperature fluctuations in the flow in lieu of a separate temperature measurement or a more sophisticated model for the coupling between the temperature and velocity fluctuations (as is discussed in Section 4.3.1.2). The second limitation, regarding the variable composition of the flow, can be amended in the current circumstances. Specifically, if we can estimate the total enthalpy as a function of the transverse position, the temperature can be estimated as well. The total enthalpy of a krypton-air mixture can be written as:

$$H_o(y) = \chi_{Kr}(y)H_{o,Kr}(y) + \chi_{air}(y)H_{o,air}(y) \qquad 4.5$$

Thus, if the composition can be estimated, and the velocity field is known, the total enthalpy field can be calculated and, subsequently, the temperature. Since the temperature is needed to calculate the composition, and the composition is needed to estimate the total enthalpy, these equations (4.3 and 4.5) must be solved simultaneously. For a detailed description of this procedure, refer to Appendix 4A.

4.1.3 – Estimation of Transport Properties with Kinetic Theory

In attempting to estimate the temperature for the LIF calibration, it is necessary to estimate the total enthalpy of the flow using the various material and transport properties as described in the above section. However, computing the thermodynamic and transport properties is more complex when there is a variable composition. Some properties, such as the specific heat of the mixture, simply act a mole-fraction-weighted sum of the constituent gases. That is:

$$c_{p,mix} = \sum_{i=1}^{N} \chi_i c_{p,i} \tag{4.6}$$

This mixture weighting is not valid for all flow properties. Examples of this included the thermal conductivity and dynamic viscosity. This complication arises from the fact that the atoms/molecules don't simply interact with themselves, but also interact across species (i.e., krypton doesn't just collide with krypton, but with the N_2 and O_2 present within the air as well). Consequently the formulae need to be modified to accommodate this interatomic/intermolecular potential when trying to study a mixture. These properties are particularly important when trying to estimate the temperature; the Prandtl number incorporated into the recovery factor in Eq. 4.4 has a dependence on both the viscosity and thermal conductivity, so it is required that these properties are estimated based on the local composition of the mixture.

4.1.3.1 – Estimation of Mixture Viscosity and Thermal Conductivity

A model for estimating the viscosity of gaseous mixtures was put forth by Wilke [**115**]. The dynamic viscosity of the mixture can be approximated by:

$$\mu_{mix} = \sum_{i=1}^{N} \frac{\chi_i \mu_i}{\sum_{j=1}^{N} \chi_j \Phi_{ij}} \tag{4.7}$$

Here, χ_i is the mole fraction of constituent gas i, μ_i is the dynamic viscosity of constituent gas i, and Φ_{ij} is the interatomic/intermolecular potential between species i and j. Thus, it can be seen that this model expresses the viscosity of the mixture as a mole-fraction-weighted sum of the component viscosities, which has been further weighted by the potential between all the species. The potential used in Eq. 4.7 is defined as:

$$\Phi_{ij} = \frac{1}{\sqrt{8}}\left(1 + \frac{M_i}{M_j}\right)^{-1/2}\left[1 + \left(\frac{\mu_i}{\mu_j}\right)^{1/2}\left(\frac{M_j}{M_i}\right)^{1/4}\right]^2 \quad 4.8$$

Where M_i is the molecular/atomic weight of species i. This formulation then requires that the viscosity is known as a function of temperature. For this, the Chapman-Enskog theory suffices [**115**], which expresses the viscosity as:

$$\mu_i = 2.6693 \times 10^{-5}\frac{\sqrt{M_i T}}{\sigma_i^2 \Omega_\mu} \quad 4.9$$

In Eq. 4.9, the viscosity is expressed in units of $[g\ cm^{-1}s^{-1}]$, σ_i is the Lennard-Jones collisional diameter, and $\Omega_\mu$is an interaction term with a dependence on the non-dimensional temperature kT/ϵ. The values for these different constants are given in Appendix 4A.

A parallel formulation can be followed for estimating the thermal conductivity of a mixture. The mixture thermal conductivity can be estimated as:

$$k_{mix} = \sum_{i=1}^{N}\frac{\chi_i k_i}{\sum_{j=1}^{N}\chi_j \Phi_{ij}} \quad 4.10$$

Here, the potential term is identical to that given in Eq. 4.8. For the constituent thermal conductivities, two separate models are used for the monatomic krypton and the hybrid-diatomic mixture of air. For the former, Chapman-Enskog theory is again utilized:

$$k_i = 1.9891 \times 10^{-4}\frac{\sqrt{T/M_i}}{\sigma_i^2 \Omega_k} \quad 4.11$$

Here the collision diameter and interaction term are identical to those used in the viscosity calculation. The units of k in Eq. 4.11 are $[cal\ cm^{-1}s^{-1}K^{-1}]$. For air, the formulation of Eucken [**115**] was used, which expresses the thermal conductivity as:

$$k_i = \left(c_{p,i} + \frac{5}{4}\frac{R}{M_i}\right)\mu_i \qquad 4.12$$

Here, the mass-specific heat can be taken from empirical data, R is the universal gas constant, and μ_i is calculated via Eq. 4.9. With the combination of these data, the Prandtl number can be calculated as:

$$Pr_{mix}(T) = \mu_{mix}(T)\ C_{p,mix}(T)/k_{mix}(T) \qquad 4.13$$

The Prandtl number as a function of temperature and mole fraction for krypton-air mixtures are depicted in Fig 4.1.

4.2 – Experimental Details

This section will detail the experimental apparatus and setups utilized in the PLIF application studies. This will include information about the experimental facilities, test models, experimental techniques, and setups.

4.2.1 – Experimental Facility

The experimental facility and conditions utilized in these studies were the same used in the studies of Chapter 3. Please refer to the experimental details section of Chapter 3 (section 3.1) for details thereto related. As a brief summary, the tunnel is again arranged with the splitter plate installed in the nozzle block. The freestream Mach number is 2.97, and the incoming boundary layer has a thickness of 4.75 mm and $Re_\theta = 3450$.

4.2.2 – Test Models

The models utilized in these studies were the same used in the studies of Chapter 3. The addition of secondary injection in these studies was achieved by utilizing the internal channels machined into the injectors. The injectors featured at straight injection duct (no nozzle contour, $d = 3.175$ mm) with an l/d ratio of 10. These were supplied by external tubing sealed to the model with silicone RTV.

The injected species was pure krypton for these studies. To regulate the flow into the tunnel, the high-pressure cylinder storing the gas was fed into a regulator to reduce the pressure to 240 kPa (20 psig), which was then run through a metering valve and flow meter (Omega 1610A). The flowrate used was 12 SLPM, which corresponded to an injection momentum flux ratio ($\rho_j u_j^2/\rho_\infty u_\infty^2$) of 0.27; therefore, the jet momentum is significantly less than the freestream momentum and so the flow should behave much like a wake.

4.2.3 – Experimental Setups

Two diagnostics were utilized in these studies: particle image velocimetry (PIV) and planar laser-induced fluorescence (PLIF) of krypton, conducted simultaneously. Experimental details for each technique will be discussed separately, and then further notes regarding their simultaneous application will be detailed.

4.2.3.1 – Particle Image Velocimetry

Two PIV configurations were used in the present studies: planar (2D, 2-component) and stereoscopic (2D, 3-component). As in the studies of Chapter 3, seeding of the primary flow was accomplished using a six-jet atomizer (TSI 9306). For the injected gas, a fluidized-bed seeder was utilized with particles of TiO2. The particles were shown in previous studies [**116**] to have a nominal diameter of 0.26 μm with

corresponding response time of 2.6 μs, which matches closely with the particles used in the freestream as shown in Appendix 3A. The seeder was positioned between the flow meter and the injector model.

The actual laser setup varied from the studies in the previous chapter. The motivation for the change was that one of the laser cavities used for PIV in that body of work was better-suited for use in the PLIF experiments, and so the overall setup needed to be altered as a consequence. A schematic of the complete laser setup for the simultaneous experiments is shown in Fig 4.2 below. Two Nd:YAG lasers were utilized; the first came from a short-pulsed Nd:YAG laser (Coherent Infinity 40-100, 1064 nm, 4 ns), whose beam was first expanded with a telescopic lens pair (Galilean) to improve the spatial overlap of the two pulses and prevent damage to optics downstream of the laser. The second pulse came from one cavity of a dual-cavity Nd:YAG laser (Spectra-physics PIV-400, 1064 nm, 11 ns). The two beams were individually passed through $\lambda/2$-plates before being combined with a plate polarizer and run through another $\lambda/2$-plate. The combined beams were then frequency-doubled to 532 nm using a KDP crystal and directed to the test section. The timing for the two lasers was controlled with two separate digital pulse generators (SRS DG-535). For the simultaneous studies, a temporal separation of 400 ns was used between the pulses.

The camera-laser sheet setup for these studies is shown in Fig 4.3. Here the laser sheet was first expanded into a narrow sheet (~25 mm wide) and then directed through the bottom of the test section. The expansion of the sheet was achieved using a +750 mm spherical lens and a -100 mm cylindrical lens. The sheet in this case was slightly converging in thickness (and diverging in width), but was approximately 1 mm thick at the center of the test section. Laser energy of 30 mJ/pulse was used to illuminate the particles in this sheet. Two frame-straddling CCD cameras (Roper MegaPlus ES 4020)

were used to capture the scattering from the illuminated particles. Both cameras were equipped with a Scheimpflug mount and a 105 mm Nikon lens to bring the full field of view into focus. The angle between the two cameras was approximately 60 degrees as is shown in Fig 4.3. The field of view extended from $0.5h$ to $3.35h$ downstream of the injectors.

4.2.3.2 – Planar Laser-Induced Fluorescence

The laser setup used for the laser-induced fluorescence studies was slightly different than that used in the studies of Chapter 2. The reason for the alteration was to drastically increase the amount of energy at the desired wavelength, at the expense of having a longer overall pulse duration. Much as in the quenching studies of Chapter 2, the wavelength needed for exciting fluorescence from the krypton gas was 214.7 nm. This wavelength was generated using sum-frequency generation (SFG), combining wavelengths of 355 nm and 544 nm. Refer to Fig 4.2 for a schematic of the laser layout for the PLIF system. A pulsed Nd:YAG laser (Spectra-physics PIV-400, 1064 nm, 11 ns) was first run through a $\lambda/2$-plate and then frequency-doubled (to 532 nm) with a KDP crystal. This beam was then used to pump a dye laser. The dye laser (Lumonics HD-300) was operated with Fluorescein 548 dye (in methanol) doped with NaOH in a 2:1 molar ratio to shift the peak output wavelength to a higher frequency. The oscillator and amplifier were operated at slightly different dye concentrations to maximize the energy from the laser ($4.194 \times 10^{-4}\ M$ for the oscillator and $3.49 \times 10^{-4} M$ for the amplifier). The wavelength could be tuned over a limited range, with a peak around 546 nm. This beam was then expanded using a telescopic lens pair (Galilean) and polarization-rotated with a $\lambda/2$-plate.

The 355 nm light was generated by another Nd:YAG laser (Spectra-physics PIV-400, 1064 nm, 11 ns), which was first passed through a $\lambda/2$-plate. The beam was then frequency-doubled with a KDP crystal and subsequently tripled with a KD*P crystal. This beam was then run through a $\lambda/2$-plate to rotate the polarization. The two beams were then combined using a simple dielectric mirror, which transmitted the 544nm light and reflected the 355 nm light. The timing for the two pulses was controlled by digital pulse generators (SRS DG-535). The overlapped beams were then mixed with a BBO (beta barium borate, type I) crystal, whose phase-matching angle was continuously adjusted with a controller assembly (Inrad Autotracker II). The output beam was then separated using a series of dielectric mirrors and was simultaneously redirected to the test section. The two pulses were continuously monitored for temporal overlap using a fast photodiode (Thorlabs DET 210) and an oscilloscope (Tektronix TDS224).

In these experiments, the beam was brought above the test section and then passed through beam expanding optics. These optics consisted of a + 300 mm spherical lens and a -150 mm cylindrical lens spaced to collimate the sheet laterally; the sheet thickness was measured to be 0.2 mm. When using the PLIF simultaneously with the PIV, the PLIF sheet was centered in the PIV sheet. Fluorescence was imaged using an intensified CCD camera with enhance near-IR response (Roper PI-Max III with Unigen II filmless Gen III photocathode). The camera was equipped with a 50 mm Nikon F/1.2 lens further outfitted with extension tubes totaling 30 mm and a narrow bandpass filter (760 nm cwl, 10 nm FWHM) to isolate the fluorescence. The FOV spanned from $1.57h$ to $3.14h$ downstream of these injector models; this field of view and the camera position are shown in Fig 4.4.

4.2.3.3 – Simultaneous Measurement Application Notes

Utilizing PIV and PLIF simultaneously in this application was quite challenging for a number of reasons. First, at high energies, the PLIF system described above became extremely unstable. Specifically, maintaining the peak pulse energy was very difficult. The lasers, upon initial startup, required anywhere from 2 to 3 hours to reach peak pulse energy in addition to allowing the various harmonic generators used to thermally stabilize. Once the system was online and stable, the alignment of the two component beams was performed. This step allowed the frequency-mixed beam to be optimized for pulse energy. However, this peak pulse energy only remained for approximately 20 minutes before the crystals, dye laser, and alignment would need to be readjusted. After the initial realignment, the energy would only remain stabilized for 8 to 10 minutes before subsequent realignments/readjustments were required. Thus, keeping the systems stable for a sufficient amount of time to run the experiments (which took approximately 7 hours per data set) required constant vigilance. The stability of the PLIF system was further compromised by the overall jitter in the laser system. Since the pulses were of identical pulse length, the frequency-mixed pulse energy and spatial profile fluctuated considerably each time the pulses moved with respect to each other temporally. This unsteadiness was ultimately considered in the uncertainty analysis, but it is important to note for any researcher attempting to replicate the SFG system used in these studies.

The next complication faced in operating the PLIF and PIV systems simultaneously was that experiments required precise control of the timing of not only the laser systems but the cameras as well, all which operate on slightly different frequencies. The two lasers used for PIV had very different system characteristics; in particular, the optimal Q-switch delays were different. The Coherent Infinity used had an optimal Q-switch delay of 271 μs from the lamp trigger, while the PIV-400 had an

optimal delay of 169 μs, which had to be compensated for when adjusting the temporal overlap. The two PLIF pulses had the same optimal Q-switch delay of 175 μs, but the delays had to be adjusted to compensate not only for their timings with respect to the PIV pulses, but also the different beam-path lengths. To further complicate the situation, there was a delay of unknown duration imposed by chaining multiple pulse-generators together in a master-slave configuration. Often, the temporal delays had to be adjusted empirically. It was critical to monitor the timing of the laser pulses in the optical system using an oscilloscope and photodiodes to prevent any timing errors. The timing used in the simultaneous experiment was set to a 400 ns delay between PIV pulses, with the combined PLIF pulse situated approximately 200 ns from the first PIV pulse.

The camera timing was also quite complicated for the simultaneous measurement. The laser systems both fire at exactly 10 Hz, while the natural framing rate of the PIV cameras was 6 Hz and that of the PLIF camera is 5 Hz. Thus, it was also quite critical to get the triggering of the cameras set up correctly. As mentioned above, the timing was controlled by a series of SRS DG-535 pulse generators. In this experiment, three such units were chained together in the following manner: the master clock was chosen to correspond to the pulse from the Coherent Infinity 40-100 laser pulse utilized as the first PIV pulse. The reason for this is that this laser had the longest Q-switch delay, and thus all other pulses could be delayed positively to the master clock. This same pulse generator controlled the second PIV pulse as well, with both the lamp and Q-switch delays set to trigger at the desired delay time of 400 ns. A second timing box was used to control the two PLIF laser pulses, while the final pulse generator was used to control the three cameras. To allow the cameras to sync with the laser pulses, the frequency used in the final timing box was set to 5 Hz by increasing the delay on the first channel to 0.1 s, thereby forcing the box to trigger at half the frequency of the 10 Hz master clock.

Triggering the PLIF camera with the correct delay was straightforward; the camera has a monitor on the intensifier to indicate when it was gating. Monitoring the output from the intensifier while adjusting the software delays sufficed for optimizing the timing. For these studies, the intensifier gate width was set to 50 ns, with the rising edge leading the rising edge of the PLIF laser pulse by approximately 5 ns. This was a sufficient delay that it could capture the entirety of the fluorescence signal while also allowing for some delay between the pulse measurement location and the center of the test section where the actual measurement was taking place. The PIV cameras were more complicated to trigger accurately. First, there is no monitor on the exposure, so it is difficult to know when the cameras are firing relative to the laser pulses. Second, the cameras have a number of built-in delays, which make it difficult to know when the cameras will capture relative to the input trigger. Ultimately, the timing is done empirically for these cameras by viewing when the laser pulses show up in the correct frames. The minimum possible temporal separation between pulses for one of these cameras was measured at just 300 ns. However, when using multiple cameras simultaneously, the bus speed of the computers became an issue. Specifically, depending on the motherboard in the computer, different CCD readout speeds had to be used in the software. Moreover, they had to be used at the same speed for the two camera acquisitions to be synchronized. These cameras have two different readout speeds, 30 MHz and 38 MHz. Because of the bus-speed limitation, the cameras needed to be run in the low-speed readout mode, increasing the minimum inter-frame delay to the 400 ns that was used in these experiments.

4.3 – Results and Discussion

This section details the results of the application of krypton PLIF to the two supersonic injector flowfields. The results include a discussion of the sensitivity and

uncertainty of the calibration procedure described above and in Appendix 4A. This is followed by a discussion of the calculated thermodynamic conditions within the regions of interest in the flow, and finally a basic analysis of the mean and unsteady flow behaviors observed in the two injection flowfields.

4.3.1 – Sensitivity and Uncertainty of Kr PLIF Calibration

This section discusses the overall sensitivity of the Kr PLIF technique in its application to supersonic mixing flowfields. This discussion will include a description of the sensitivity of the calibration to different system inputs, followed by an examination of the temperature model on the overall calibration of the fluorescence signal, and finally an estimation of the uncertainties for a single-shot mole fraction calibration.

4.3.1.1 – Sensitivity

While Eq 4.3 describes the overall sensitivity of the Kr PLIF calibration for mole fraction sensitivity, the inclusion of the data from Chapter 2 in many ways obscures the dependence of the mole-fraction calibration on the signal intensity. That is, it remains unclear exactly how the krypton mole fraction depends on the signal when considering the thermodynamic conditions and other aspects of the calibration procedure. There are many parameters to examine in this context, including the effects of variable laser energy, temperature, pressure, and the reference state conditions. To simplify this analysis a bit, Eq. 4.3 can be rewritten in the following form:

$$\chi_{Kr} = \frac{A + P q_{air}(T_s)}{P\left(q_{air}(T) - q_{Kr}(T)\right) + S^{-1}\mathrm{E}^2 \gamma_{ref} \hat{\Sigma}^{(2)} \Theta^{-1} \Pi \chi_{Kr,ref}^{-1}} = \frac{N_f}{D_f} \qquad 4.14$$

Apart from algebraic manipulation, Eq. 4.14 differs from Eq. 4.3 in that several substitutions have been made. Here, S is the ratio of the local fluorescence signal to the local reference fluorescence signal, $S_f/S_{f,ref}$, E is the ratio of the instantaneous bulk laser pulse energy to the reference state energy, $E_L/E_{L,ref}$, $\hat{\Sigma}^{(2)}$ is the relative effective two-

photon absorption cross-section, Θ is the ratio of the local temperature to the reference temperature, T/T_{ref}, and Π is the ratio of the local pressure to that of the reference pressure, P/P_{ref}. For consolidating the terms in performing an uncertainty analysis later in this section, the numerator and denominator of Eq. 4.14 have been combined into the terms N_f and D_f, respectively. The effects of each ratio, in addition to the reference krypton mole fraction, need to be considered for their effect on the overall calibration.

The effects of the laser energy on the signal calibration are shown in Figs 4.5 and 4.6. In Fig 4.5, the temperature, pressure, and reference mole fraction have been fixed at their reference values to isolate the dependence of the aforementioned laser energy ratio. In contrast, Fig 4.6 shows the same plots of sensitivity with the temperature and pressure fixed at their freestream values (the comparison is intended to show how the trends differ at the extremes of the thermodynamic conditions encountered in the present experiments). In this context, the sensitivity is defined as the derivative of the mole fraction (or relative mole fraction) with respect to the signal ratio S, $\partial(\chi/\chi_{ref})/\partial S$; this quantity indicates how much the mole fraction changes per unit of signal change. If there was no thermodynamic dependence to the signal, it would be expected that a linear relation would exist between the two quantities. However, as evinced in these plots, that is not the case with this calibration. A few general comments regarding the similarities between the two different conditions represented in Figs 4.5 and 4.6: it is observed that increasing the laser pulse energy relative to the reference energy results in a more uniform sensitivity across the range of values. Specifically, as the laser energy ratio approaches 0, the sensitivity is seen to decrease dramatically – for the reference conditions, this is true for $S > 0.3$, and is only slightly higher for the freestream conditions at $S > 0.35$. In either circumstance, the implication is that the mole fraction is approaching unity beyond that value, and as such the signal would not increase further.

However, the further implication is that the entire dynamic range is contained within 30-35% of the reference signal levels. From a practical standpoint, this isn't that much of a detriment. Since the fluorescence signal increases quadratically with the bulk laser pulse energy (all other things equal), a higher pulse ratio is desired anyway, provide that stimulated emission, saturation, and ionization are avoided. From the opposite perspective, it would seem quite advantageous to take the reference fluorescence images at the minimum possible energy, provided the signals were sufficiently high to capture the laser sheet intensity profile accurately. The advantage of doing this, as made evident by Figs 4.5 and 4.6, is that the overall sensitivity of the measurement is made more uniform. Without an ideal, uniform sensitivity, any fluctuations in the laser energy would be disproportionately amplified or attenuated through the calibration procedure. This situation is undesirable if the exact shot-to-shot noise is unknown, since the effects of the fluctuation will only be understood in the mean sense in these studies. Consequently, having the most uniform sensitivity will make the calibration less sensitive to such occurrences and thus more accurate if such signal fluctuations occur. In the present experiments, this energy ratio was fixed around unity, and thus the sensitivity is seen to be relatively uniform over the experimental conditions compared to lower relative pulse energies.

A far less pronounced effect on the sensitivity is seen when looking at the pressure dependence, shown in Figs 4.7 and 4.8. Again, with increasing pressure the overall sensitivity of the calibration decreases while simultaneously becoming more uniform. Unlike the laser energy dependence, the sensitivity appears to asymptote to a fixed pattern as the pressure ratio is increased toward unity. That being said, the overall change in the sensitivity is minimal over the pressure range examined here (0.01 to 1). It is also observed in comparing Figs 4.7 and 4.8 that decreasing the temperature to the

freestream value results in a reduction in the overall sensitivity. This is accompanied by the sensitivity becoming more uniform over the signal range presented and a less drastic change with differing pressures. This analysis does not suggest much amendment needs to be made with regard to the pressure in the reference state, though pressure ratios approaching unity do have marginally more uniform sensitivity. In the present experiments, the ratio of the freestream pressure to that of the reference state is approximately 0.05, so the pressure isn't expected to affect the overall sensitivity of the calibration procedure drastically.

The effect of temperature is slightly more pronounced than that observed in the pressure; the overall effect of temperature ratio is shown in Figs 4.9 and 4.10. In Fig 4.9, the pressure was fixed at the reference value, while in 4.10, it was decreased to the freestream value. Overall, the effect of temperature is seen to differ greatly with that of pressure. First, increasing the temperature ratio is seen to increase the sensitivity and make it less uniform over the range of signals presented. Furthermore, changing the pressure from the reference state to the freestream conditions is not found to impact the sensitivity considerably. Given the previous analysis of the pressure sensitivity, this is to be expected. Additionally, no asymptotic behavior is observed in this sensitivity analysis, as was observed in the pressure dependence. This temperature dependence has various implications on the practical calibration of fluorescence images. The supersonic mixing flowfields examined in the present body of work exhibit considerable temperature fluctuation, which means that the calibration will have to sweep through the complete envelope of the curves presented in Fig 4.10 during such a calibration. If the temperature model is inaccurate, then the sensitivity of the calibration will be misrepresented, and the value obtained for mole fraction will likely be wrong by a considerable margin. In the context of the present experiments, this effect will need to be accounted for in the

uncertainty analysis, but it also informs the focus of future studies as well to establish a more accurate temperature model.

Finally, and perhaps the most informative from an experimental standpoint, is the effect that the reference krypton mole fraction has on the sensitivity. Sensitivity plots for different mole fractions are shown in Figs. 4.11 and 4.12. As with the previous three ratios examined, these plots differ in that the former is taken at the reference conditions, while the latter is taken at the freestream conditions. These plots indicate that a very pronounced change in sensitivity occurs for different reference mole fractions. An increase in this condition causes the sensitivity at the low end of the signal ratios to become extremely high, while losing sensitivity at the higher registers. Decreasing the reference mole fraction then makes the sensitivity more uniform across the field, asymptotic to a constant with a mole fraction of 0.1. When collecting intensity calibration images, one might be inclined to use pure krypton as the reference condition, since this selection would provide the strongest signals and consequently the best possible sheet correction. However, what this analysis suggests is that doing so will result in almost a complete loss of sensitivity. Specifically, if the signal is within the top 90 percent of the register, the variation in mole fraction will only be on the order of 10 percent. From the perspective of imaging the fluorescence, the implication is that only 10 percent of the full dynamic range of the signal will be utilized in make the calculation while the remaining 90 percent of the signal will be seen as (nearly) uniform. Thus, even though the sensitivity of the calibration increases dramatically at low signal levels, the uncertainty it imposes on the measurement will be equally dramatic. It is observed that lowering the reference mole fraction even slightly decreases the sensitivity substantially at the lower register while increasing it at the upper. In comparing Fig 4.11 with 4.12, it is seen that this effect is further enhanced by decreasing the reference temperature and pressure to

freestream values, causing the values' sensitivity to cover a much broader envelope of the same range of conditions. Based on the observations made above, the change in sensitivity is the result of the temperature decrease rather than the pressure. In the present experiments, the reference mole fraction was approximately 0.7, and thus the sensitivity is reasonably uniform over the desired range (on the same order as the pressure and temperature variations). However, the sensitivity to the reference state mole fraction is a crucial point to note for any future research attempting to calibrate krypton fluorescence in the same manner, since it can have such a dramatic influence on the uncertainty in the calibration.

4.3.1.2 – Assessment of temperature model

The direct implementation of the standard Crocco-Busemann model (Eq. 4.4) proved problematic when attempting to compensate for the local concentration. That is, if the specific heats and Prandtl number alone were adjusted for the local composition of the flow, the temperatures required to allow for a convergent solution were far beyond the total temperature of the flow. A discussion of this can be found in Appendix 4A. This discrepancy resulted from the fact that the total enthalpy throughout the flow was not equal to the freestream value due to the changing composition, requiring the modification resulting from coupling Eq. 4.3 and 4.5. With the exclusion of this erroneous model, there remained four potential methods for estimating the temperature throughout the wake/jet in the desired flowfields. The first of these was to utilize the Crocco-Busemann relation assuming the composition of the flow was solely air. An example of this method applied to the hypermixing injector flowfield can be seen in Fig. 4.13 (top left) along with the scalar concentration contours that correspond to that correction (top right). The next method is to make the same assumption as the first, but utilize the instantaneous

velocity rather than the mean velocity. Applying this model to the same flowfield, the resulting temperature and concentration fields can again be seen in Fig. 4.13 (second from top). The next method utilized the Crocco-Busemann relation, which had been corrected for a variable total enthalpy and utilized the mean velocity fields. That is, in addition to allowing the composition to vary, the mean velocity profiles were used in the estimation of the temperature. The application of this method is demonstrated in Fig. 4.13 (third from top). The final temperature model utilizes the both the correction for variable composition and the instantaneous velocity fields. A demonstration of this is shown in Fig. 4.13 (bottom).

Before any further discussion regarding these different models is undertaken, it first needs to be reiterated that, as was mentioned in Section 4.1.2.2, the instantaneous CB models are inherently flawed. That is, total enthalpy is not conserved in an unsteady flow. Rather, changes in enthalpy can manifest in the form of pressure fluctuations, and consequently the assumption that changes in enthalpy are only coupled to the velocity is invalidated. However, in the present context this direct coupling is assumed in order to make a first-order temperature correction, which would otherwise require a separate measurement. With this objective in mind, the different temperature models described above can be evaluated for their effect on the overall calibration procedure.

It is first worth noting the general similarities between the resultant mole fractions for all four methods. In all cases the peak mole fractions are found to be around 0.94, and the lower end of the range in all calibrated fields is identical as well. Thus, it could be argued that from the perspective of estimating the general behavior, it doesn't really matter which method is selected. However, the dramatic differences observed in the temperature fields and the calibrated signals at the higher end of the spectrum suggest otherwise. Consider first the effect of utilizing the mean velocity fields versus that of the

instantaneous velocity fields. In observing the two mole fraction contours calculating using mean velocity fields, in the central region where the mole fraction is highest, a distinct difference can be seen. In both the fields utilizing instantaneous velocity data, the concentration throughout this region is fairly uniform, coming to a single peak around $(x/h, y/h)$ = (2,0.1). The actual distributions are slightly different in each, but they are topologically quite similar. In contrast, the scalar fields utilizing the mean velocity data show two peaks within this same region (as denoted by the contour lines). While the actual patterns seen in the mole fraction contours do not suggest much from a diagnostic standpoint, a deficiency in the model is revealed. Specifically, attempting to correct the fluorescence signal using a mean temperature field effectively denies the possibility of instantaneous signal variations being caused by any source other than the mole fraction. It can be shown that instantaneous velocity fluctuations can also lead to changes in the fluorescence signal. As an example, consider a negative stream-wise velocity fluctuation ($u' < 0$). It is expected (and assumed in the case of the instantaneous temperature corrections) that the local static temperature would increase in this circumstance (i.e. kinetic energy is converted to thermal energy). Based on the various data from Chapter 2, an occurrence such as this would lead to a decrease in the quenching rates, a decrease in the absorption, and a decrease in the density. Thus, the response of the signal would ultimately be to decrease without necessitating a decrease in the krypton concentration. In this regard, the mole fraction would intermittently be over- and under-predicted, and consequently the uncertainty in the measurement rises considerably.

Before addressing the quality of the two instantaneous corrections, a few notes should be given on temperature fields used in the two mean corrections. The first thing to notice is that the shapes of the two wakes/jets differ slightly. Specifically, the correction accounting for variable composition is broader and is inclined at a higher angle than the

wake found in the standard model. Furthermore, the two temperature ranges vary slightly, with peak temperatures in the standard CB model reaching 260 K and that for the modified CB model extending to 275 K. The first of these differences result from the lower specific heat of krypton, which amounts to higher temperatures when decelerated to the same velocities. Thus, the wake appears broader. The second difference is due to the fact that the scalar field does not *exactly* follow the jet/wake structure, tending in the mean to be angled up slightly more. Consequently, the wake becomes a hybrid of the two structures when viewed in the mean.

As mentioned above, the two instantaneous models have the potential for performing a more accurate temperature correction due to their accommodation of fluctuating velocities. However, the two corrections themselves are quite different. At first glance, the two temperature fields are quite similar – the temperature ranges are nearly identical (100 K to 285 K for the standard CB model, 100 K to 290 K for the corrected CB model). To understand the fundamental impact of the corrected model, the actual shape of the turbulent structures must be considered. First note the large turbulent eddy on top of the wake/jet spanning from $x/h = 2$ to 2.45 in Fig 4.13 (second from top and bottom). It can be seen in the standard model that this structure takes on the form of a bulge in the wake. In contrast, the same temperature field using the modified CB model shows that this particular structure appears as more of a large detached arm extending from the wake followed by an indentation. The difference may seem subtle, but when these two results are then compared to their respective mole fraction contours, the reason for the difference is made apparent. Collocated with this detached arm structure is a region of low mole fraction (and low fluorescence signal) cutting into the center of the injection plume. In this region, using the standard CB model yields lower mole fractions (about 20 percent lower throughout) than the modified CB model. This suggests that,

based on the coupled velocity and scalar data, at least some portion of this decrease in signal was due to a temperature fluctuation rather than a change in the mole fraction. As a result, when attempting to study the scalar fluxes in a region such as this, the standard model is again subject to intermittent over- and under-prediction and a greater degree of uncertainty versus using the corrected model.

This section has shown some of the incongruities that arise when using different temperature models for calibrating the fluorescence signal for mole-fraction-sensitivity. While the selection of the instantaneous, composition-corrected temperature model may seem the obvious choice, caution must be exercised. As has been mentioned previously, the accuracy of the instantaneous CB model has not been established. While it is likely that this model is beneficial in correcting for temperature fluctuations, the possibility exists that the CB model performs poorly instantaneously. The deviations that arise from the utilization of this model in such situations might imply that the use of the mean model would be preferable, as it is immune to such erroneous fluctuations. A large portion of the future work will be devoted to analyzing this model such that a more definitive statement of the model accuracy can be made.

Assuming that all of the temperature models have benefits and drawbacks, a few application-specific notes can be made with regard to their utilization. It is rarely the case in a supersonic mixing flowfield such as the two studied in this chapter that simultaneous velocity and scalar data are available. Moreover, the use of the instantaneous, composition corrected model is quite computationally intensive and may prove unwieldy for large data sets. Consequently, while it is likely preferable to use the most advanced temperature model available, the selection of model is dependent on the circumstances. Consider first a situation in which the krypton was in trace concentrations (a few percent) such as at a measurement location further downstream. In this instance,

the use of either the standard CB or the instantaneous CB would be quite valid; the concentration of krypton is sufficiently low that the transverse variation in total enthalpy need not be considered. Moreover, if a general flow structure is all that is desired, it was shown that all variations on the CB temperature model yield similar results. In the aforementioned situation all temperature models would be applicable, but the extensive computational time required for the final two models (particularly the final one) would likely make the cost/benefit ratio unfavorable. The next situation to consider is one in which simultaneous data is not available or not possible to collect. In this case, either mean-velocity-based model could be used with the understanding that there are uncertainties inherent to their utilization. Given the option, it would likely be beneficial in this scenario to utilize the composition-corrected version since it is more general. In this situation, the variance in the velocity data could also help to account for the uncertainty in the temperature model, though this still lacks the direct coupling of the velocity and scalar data afforded by the simultaneous data.

4.3.1.3 – Uncertainty in mole fraction calibration

The estimation of the uncertainty in the measurement of krypton mole fraction from the raw fluorescence signal will follow a similar development to that used in Appendix 2A. The basis for these calculations is Eq. 4.14, which is complemented by the estimation of uncertainties in the temperature model and freestream pressure found in Appendix 4A. In applying the uncertainty operator to Eq. 4.14, the overall uncertainty in the calculated mole fraction is found to be:

$$|\delta\chi_{Kr}| = \left\{\left(\frac{\partial\chi_{Kr}}{\partial A}\delta A\right)^2 + \left(\frac{\partial\chi_{Kr}}{\partial P}\delta P\right)^2 + \left(\frac{\partial\chi_{Kr}}{\partial q_{air}}\delta q_{air}\right)^2 + \left(\frac{\partial\chi_{Kr}}{\partial q_{Kr}}\delta q_{Kr}\right)^2 + \left(\frac{\partial\chi_{Kr}}{\partial S}\delta S\right)^2 + \left(\frac{\partial\chi_{Kr}}{\partial E}\delta E\right)^2 + \left(\frac{\partial\chi_{Kr}}{\partial\gamma_{ref}}\delta\gamma_{ref}\right)^2 + \left(\frac{\partial\chi_{Kr}}{\partial\hat{\Sigma}^{(2)}}\delta\hat{\Sigma}^{(2)}\right)^2 + \left(\frac{\partial\chi_{Kr}}{\partial\Theta}\delta\Theta\right)^2 + \left(\frac{\partial\chi_{Kr}}{\partial\Pi}\delta\Pi\right)^2 + \left(\frac{\partial\chi_{Kr}}{\partial\chi_{Kr,ref}}\delta\chi_{Kr,ref}\right)^2\right\}^{1/2} \quad 4.15$$

Each of these partial derivatives is given in Appendix 4A. Also located therewith is a synopsis of the constitutive uncertainties that comprise each of the component uncertainties in Eq. 4.15.

To demonstrate the extent that each of the component uncertainties affects the overall uncertainty in the mole fraction calibration, an example is demonstrated here. Figure 4.14 shows a calibrated fluorescence image taken in the planar injector flowfield; the corresponding total and component uncertainties are presented in Fig. 4.15. Note that only the 5 most dominant components are shown, which comprise about 97 percent of the total uncertainty. Here it can be seen that the total uncertainty is quite substantial, nearing 40 percent uncertainty within the shear layers surrounding the primary injection plume. While this is not an unexpected result, the source of the uncertainty needs to be discerned in order to understand how improvements can be made to the experiments. Examining the component uncertainties, it is seen that the source of the greatest uncertainty is the fluorescence signal ratio. The reasons for this are several. As discussed in Appendix 4A, the shot-to-shot fluctuations in the profile of the laser sheet were substantial, which applies a fixed uncertainty pattern across most of the field of view. Since these fluctuations are only understood in the mean sense, if the intensity pattern of a single shot differs significantly from the mean, the uncertainty in regions of low signals is amplified

considerably. Thus, it is apparent that a single-shot sheet correction is required for reducing the uncertainty in the mole-fraction calculation.

The other components in Fig 4.15 contribute far less to the overall uncertainty in the mole fraction calibration. The fluctuations in the bulk laser energy cause a relatively minor uncertainty in the calibration procedure, with maximum uncertainties of about 7 percent. In like fashion, the uncertainty due to the local temperature and the reference krypton mole fraction are quite minimal, reaching maxima at 5 percent and 2.5 percent, respectively. The exception to these lies in the uncertainty in the pressure ratio, which exhibits a peak uncertainty of roughly 25 percent. The reason for this is that the pressure affects the total quenching rates, which has a substantial influence on the tabulated uncertainties. However, all of these components still lie well below that caused by the reference signal ratio. With the previous discussion in mind, it is important to note that these calculations represent the uncertainty in the measurement, not the accuracy. One suggestion that is made in the future and suggested work at the end of this chapter will be applying the technique in a flowfield that has a well-defined mean concentration profile. In so doing, the accuracy of the technique could be quantified in addition to the uncertainty in the calculation.

4.3.2 – Flowfield Analysis

This section will discuss the general characteristics of the mixing flowfields. The analysis will first look at the mean characteristics of both flowfields followed by an overview of some of the unsteady behavior exhibited.

4.3.2.1 – Mean Flowfield Analysis

Consider first the planar injector flowfield; in the previous chapter, it was shown to be virtually identical to a two-dimensional supersonic wake. The velocity, temperature,

and mole fraction contours for this flowfield are shown in Figs. 4.16 through 4.20. The inclusion of the injection is seen to have a number of effects on the flowfield. First, the jet is seen to have lower velocities than that of the undisturbed wake structure from Chapter 3, observed most readily in the stream-wise velocity contours of Fig. 4.16. In previous studies [**100**], this same observation was made in similar flowfields. Correspondingly, the studies of Vergine and Maddalena [**78**] showed a similar wake-like profile for the undisturbed flowfield, though their imaging location was much farther downstream. Another observation to be made in this flowfield is a shift in the foot of the recompression shocks; the downstream side of these shockwaves can be seen in Fig. 4.17. In the undisturbed flowfield, the recompression shocks were (in the mean) situated at roughly $x/h = 3$. An explanation of this behavior can be found in the a previous work of the author [**99**]. Figure 4.18 shows planar laser scattering of the turbulent injection flowfield overlaid with qualitative acetone PLIF (refer to [**99**] for the details of the experiments), which illustrates the point described below. In those studies, the underexpanded jet exiting from the injector caused the incoming boundary layers to attach to the jet boundary, rather than expanding around the corner as was observed in the undisturbed case. Subsequently, at the termination of the barrel shock, the surrounding flow was forced to turn parallel to the wake/jet structure. Since this phenomenon would normally occur near the neck of the wake, the natural wake neck was eliminated, and the recompression shocks sat at this reattachment point. In the present case, since the flow rates and pressure ratios are roughly equal to those used in the studies of [**99**], it is likely that a similar phenomenon is occurring in this flowfield. It should also be noted that despite the shift in location, the velocities observed here are very similar to those seen in wide-field PIV taken in the last Chapter 3. This observation lends validity to the method whereby the freestream conditions were mapped into the new wake structure described in

Appendix 4A for the mole-fraction calibration, since the discrepancies would be apparent in this region. Finally, with respect to the out-of-plane velocity; there is little to no mean structure to note. The contours of this velocity component are shown in Fig. 4.19. Here it is seen that the velocity magnitudes are quite small with respect to the other velocity components. Given the symmetry of the flowfield, it is not expected that there is a large span-wise velocity.

Continuing with the temperature field shown in Fig 4.20, there is not much to mention that hasn't been discussed above. The method used in computing this temperature was the modified CB model with compensation for the mean composition of the flow. As defined by this temperature model, the regions of lowest velocity correspond to the regions of highest temperature. Here, the peak temperatures reach roughly 280 K, while the minimum temperatures are found to drop to approximately 100 K. The peak temperature is found to be considerably higher than that observed in the undisturbed wake. The reason for this is both the smaller velocity magnitudes throughout the wake and the lower specific heat of krypton. Thus, the same enthalpy change will result in a higher temperature. Finally, the mean mole fraction contours are shown in Fig 4.21. Here the peak mole fractions are found to sit upstream and decrease fairly rapidly with downstream distance. The peak mean mole fraction is approximately 0.89 and reduces to approximately 0.45 by the downstream end. A number of general observations can be made with regard to the mole fraction field presented in Fig 4.21: the shape of the mean concentration profile is misleading, as is the rapid drop off in mole fraction with downstream distance. The unsteadiness of the flow in this region is considerable, and thus the mean contours make the mole fraction seem much lower than it is instantaneously; this effect will be illustrated in the next section, but is a reasonable demonstration of the stirring effect described in Fig. 1.6. Second, there is an odd

transverse indentation at about $x/h = 3$; this artifact comes from the sheet correction process. In this region, there was a lower mean sheet intensity due to a burn in one of the optical access windows of the wind tunnel. After correcting for the variations in the sheet intensity, this region was brought up to a higher intensity level and appears nearly continuous with respect to the surrounding mole fraction levels. As this region had very little signal before the intensity correction, this actually shows how effective the iterative sheet correction is, though obviously the ideal correction would show no sign of such a systematic flaw. The presence of this mean feature must be kept in mind when considering the instantaneous data in the next section.

Continuing with the discussion of the mean flowfield properties, the velocity and thermodynamic contours for the hypermixing injector flowfield are shown in Figs. 4.22 through 4.26. Much like the planar injector flowfield, the stream-wise velocity (Fig 4.22) takes on lower values when compared to the undisturbed case. The similar wake of Vergine and Maddalena [**78**] followed this same trend, though again the field of view used in those studies was much farther downstream. It is also observed that the angle of inclination of the wake/jet in the present flow is identical to that seen in the undisturbed flowfield. This observation suggests that the stream-wise vortices are able to influence the injection plumes considerably, even considering the additional momentum imparted to the flow.

In the same manner as was observed in the planar injector flowfield, the same shift in the recompression shocks is observed in the transverse velocity component (Fig. 4.23). Additionally, the upward transverse velocity below the wake (noted in Chapter 3) caused by the two vortices interacting is apparent in this field of view. An interesting note here is that despite the jet, these flowfields appear remarkably undisturbed. This is due to the low momentum flux ratio of the jet versus the freestream; the jet lacks the momentum

to change the overall structure of the flow. Since the flowfields behave in a manner identical to those observed in the undisturbed flowfields, extrapolating the results from Chapter 3 to these structures should be valid.

Much like the planar injector flowfield, there is little notable structure in the out-of-plane velocity (Fig 4.24). Again, since this is a highly symmetric flow (away from the side-wall boundary layers at least), this result is not surprising. The temperature field depicted in Fig 4.25 needs little discussion outside of Section 4.3.1.2. It should be noted for completeness that the method used in calculating this temperature was the modified CB relation with the mean velocity and scalar fields. Finally, mean mole fraction contours for this flowfield are shown in Fig 4.26. The structure observed here is very similar to the in the planar injector flowfield. The notable exception to this generalization is that the injection plume has taken on the inclination of the undisturbed wake, though the mole fractions appear similar in magnitude. As a brief comparison of the two flowfields, one metric that can be used is the peak mole fraction at each stream-wise location. A comparison of these two mean injection plumes is shown in Fig 4.27. Here it can be seen that both flowfields take on a similar character. At the upstream edge of this field of view, both mixers start with a relatively high peak mole fraction; the hypermixing injector is found to be slightly lower to begin, with a peak mole fraction around 0.8 rather than the 0.89 for the planar injector flowfield. However, both mole fractions drop off in similar fashion until the edge of the field of view, which also is nearing the edge of the laser sheet. This pattern suggests that within this region of the flow, the mechanism for dispersion is the same. That is, if the interaction with the vortices was the primary mechanism for the redistribution of the injectant gas, the trends which the two peak mole fraction contours follow would differ. This result is to be expected in this vicinity of the flow; the imaging location is extremely close to the injector, so little influence of the

injector geometry is likely to be observed. The work of Fox, Gaston, et al. [**66**] [**67**] [**68**], in their studies of various hypermixing injectors found that the mole fraction differed little in the near-field between mixers, despite the considerable variation in injector geometry. Such general agreement was found throughout the literature (see Chapter 1), though no studies utilizing these exact mixer configurations were found.

4.3.2.2 – General Observations of Unsteady Behavior

The instantaneous view of the injector flowfields shows that the dispersion of the scalar is highly intermittent and unsteady. To demonstrate this observation, a number of different instantaneous realizations are presented in Figs 4.28 and 4.29. Consider the instantaneous mole fraction contours for the planar injector flowfield (Fig 4.28). A number of general behaviors are evinced in this series of images. First, the injection plume is seen to be highly turbulent and unsteady. That is, the structure is not that of a simple turbulent jet but instead appears to be entirely composed of intermittent scalar structures. These structures take on a number of common forms. In many of these instantaneous realizations, the upstream area of the plume appears broad, much like the mean, but appears to be sheared into a long filament-like structure towards the center of the field of view. Alternatively, the plume appears to take on an undulating characteristic similar to that seen in the undisturbed wake (see Chapter 3 and Appendix 3D). Specifically, the jet is seen to be intermittently inclined and declined relative to the transverse mid-plane. Furthermore, some of the instantaneous realizations exhibit completely chaotic behavior, with the entire plume broken down into weakly attached or completely detached structures. In all of these realizations, a common trend is that the peak mole fraction as a function of downstream distance is much greater than that seen in the mean and is, in fact, quite constant throughout the field of view.

The hypermixing flowfield differs slightly in its unsteady behavior. Figure 4.29 shows a series of instantaneous mole-fraction contours for the hypermixing injector flowfield. Unlike the planar injector flowfield, the injection plume is seen to resemble the mean for the most part. That is, the injection plume is broad and high in concentration on the upstream end of the field of view while decreasing in breadth and concentration with further downstream distance. However, some general behaviors can be observed instantaneously. The injection plume is seen be quite turbulent, observed clearly the various convolutions in the shear layers surrounding the jet. Furthermore, the breakdown of the injection plume is visible towards the downstream end of the field of view, with the coherent plume frequently breaking apart into small, detached turbulent structures. One feature that is observed in some instantaneous shots is large turbulent protrusions below the primary injection plume. In Fig 4.29, these structures are indicated by the white circles. These same structures were not observed, at least not to the same extent, on the top of the wake. Similar structures were observed in previous studies [**100**] when considering a similar hypermixing injector. Additionally, these large structures were observed both by Vergine and Maddalena [**78**] and Sunami et al. [**75**] in their Mie scattering images, though these studies were all taken further downstream stations than the present field of view. Additionally, the instantaneous schlieren images of Arai et al. [**102**] and Kondo et al. [**101**] showed suggestion of similar structures in their wall-based hypermixing inejctors when injecting helium. It is observed that the plume structure is relatively consistent upstream of $x/h = 2.5$. However, beyond this point the injection plume is seen to take on a greater degree of unsteadiness of similar magnitude with that observed in the planar injector flowfield. The likely reason for this observation is that the base pressure is lower in the wake of the hypermixing injector. Consequently, the jet exiting the mixer is underexpanded to a further degree (i.e., the ratio of the jet total

pressure to the base pressure is higher, even if the momentum flux ratio relative to the freestream is identical), and more momentum is imparted to the injection plume. This observation is corroborated by the mean velocity contours, which show 10 percent higher velocities in the upstream region of this field of view. With a higher jet momentum, the injection plume is able to stay more self-contained, before the primary breakdown begins at a further downstream distance.

To further examine this unsteadiness of these flowfields, the interplay between the velocity and scalar fields can be observed. An example instantaneous set of mole-fraction contours for the planar injector flowfield are shown in Figs 4.30 through 4.32. As was noted in the above discussion about uncertainty, these instantaneous contours appear to have very little in common with the mean mole fraction contours. Notably, the barrel-shaped structure present in the mean is absent instantaneously. Rather, this instantaneous realization shows a high concentration near the mid-plane with large turbulent eddies extending out into the freestream. Much like other instantaneous images in Fig 4.28, the value of the peak mole fraction throughout the field of view appears universally higher than the mean. In regard to the interaction between the velocity and scalar fields, a few things of note can be taken from this instantaneous field shown in Figs 4.30 through 4.32. Looking first at the fluctuating temperature contours shown in Fig 4.31, there appears to be a strong correlation between the instantaneous mole fraction contours and that of the temperature fluctuations along the top of the wake/jet. Specifically, the large eddy spanning from $x/h = 2.1$ to $x/h = 2.35$ as well as the one to follow it fall almost exactly within the confines of the temperature contours. This observation is indicative of strong mixing with the freestream occurring at this location. Since both changes in mole fraction and those in velocity are indicative of mixing with the freestream, there is expected to be a strong correlation between the mole fraction and velocity field. Since the temperature

field is strongly coupled to the velocity field by the modified CB, it will exhibit a similar correlation.

Looking further into the instantaneous behavior, Fig. 4.32 depicts the instantaneous span-wise vorticity contours for the same flowfield overlaid with mole fraction contours. One trend which is quite dominant in this realization is that regions of rapidly changing mole fraction (more closely spaced contours) align very closely with regions of high vorticity. This is particularly apparent on the top of the injection plume both before and after the turbulent protrusion between $x/h = 2.1$ and $x/h = 2.35$, as well as the mixing layer beneath the injection plume from $x/h = 2.5$ to $x/h = 3$. Since these regions are associated with the primary interaction between the injection plume and freestream, having the gradient in the scalar field coincide with the vorticity is not surprising as the shear between the two flows is the primary source of the mixing behavior.

As was mentioned in the discussion of Fig 4.29 above, the injection plume in the hypermixing injector flowfield possesses different unsteady characteristics than that found in the planar injector flowfield. To examine this further, the interaction between the scalar and velocity fields can be examined. Figures 4.33 through 4.35 show an instantaneous realization of the hypermixing injector flowfield. Much like the other instantaneous fields shown in Fig 4.29, this image shows very similar behavior to the mean, most notably a large central plume, which begins rapidly breaking up downstream of $x/h = 2.7$. Examining the fluctuating velocity vectors in Fig 4.33, a number of interesting observations can be made. First, it is seen that the along the top of the injection plume, there is a large region of low mole fraction between $x/h = 2.1$ and $x/h = 2.35$, which is circled in Fig 4.33.This is seen to correspond to a rather strong positive stream-wise velocity fluctuation. Looking at the corresponding fluctuating

temperature contours in Fig 4.34, it is seen that immediately upstream of this region is a very sharp gradient in the fluctuating temperature (negative fluctuation). Finally, looking at the span-wise vorticity in this region, it is revealed that there is a region of strong negative vorticity aligned with this region as well. Collectively, these data suggest that this region of low mole fraction resulted from a large turbulentstructure, which was at some point upstream detached from the wake. Through the interaction with the freestream, this structure was forced back into the wake, in the process engulfing some of the cold, krypton-lean freestream. Thus, the mole fraction was reduced, and the temperature decreased. As a further general observation, the turbulent fields (velocity, temperature, and vorticity) are much more chaotic in this flowfield than they appeared in the planar injector flowfield (though it is difficult to judge from a single instant shot). This is particularly obvious by looking at the vorticity field, which shows large pockets of high vorticity throughout the flowfield. This results from two sources. First, the jet has a higher momentum and is likely to be subject to a higher degree of turbulence. Additionally, the action of the stream-wise vortices is likely to cause minor vortex stretching in this region, resulting in a profusion of span-wise vorticity structures.

4.4 – CONCLUSIONS

This chapter has detailed the development and implementation of the simultaneous krypton PLIF – PIV technique in a supersonic mixing flowfield. The theoretical and analytical methods utilized in calibrating raw fluorescence images were discussed in depth. The sensitivity of the calibration procedure to the reference conditions, particularly the mole fractions of the mixture, was quite high and had implications vis-à-vis the potential dynamic range of the technique when utilizing digital acquisition methods. Specifically, reducing the mole fraction of the reference state

dramatically increased the sensitivity of the fluorescence technique to changes in reference signal ratio. Moreover, it was shown that there was no unique combination of signal ratios and mole fractions with which to quickly calibrate the images, requiring more complicated numerical methods to perform the calibration.

This chapter also covered the development of different theoretical models for the temperature distribution and investigated their effect on the overall PLIF calibration. The initial model was a variation of the Crocco-Busemann relation, which was further modified to allow for variations in the total enthalpy of the flow to more accurately recreate the temperature profiles. It was shown that the use of either the standard Crocco-Busemann model or the composition-corrected version allowed for the general features of the scalar field to be discerned, but will inevitably over- and under-predict the fluctuations. Both versions utilizing the instantaneous velocity data were superior to the mean versions, but the version that compensated for local composition the composition more faithfully extracted scalar data and revealed regions where signal fluctuations were due to the thermodynamic fluctuations rather than true changes in composition.

The implementation of the technique was demonstrated in this chapter as well. The mean data showed that the addition of the injection had little influence on the overall topology of the flow for either injector. It was also observed in the instantaneous data that there was an interesting correlation between the turbulent motions of the flow with the corresponding changes in the scalar field topology. In addition to the standard fluctuating velocities, the calculated temperature fluctuations and vorticity fields proved a useful tool in understanding the nature of the change is in the scalar field topology.

4.5 – FUTURE AND SUGGESTED WORK

With the collection of the data required for these studies as well as data not herein presented, a sufficient database has been constructed to perform a detailed statistical analysis of the flowfield. Most notably this analysis will entail the study of the correlations between the turbulent velocity fluctuations and those of the scalar field. To the first order, this analysis would consist of simple correlations such as PDFs of the scalar field versus the velocity field (e.g., u' vs ϕ') to determine of any particular trends present in the flow and the also to help further assess the validity of the temperature model utilized in the above study. Next, the study of more compounded statistics would begin to describe the relative mixing behaviors of the two flowfields, for instance the relation between and distribution of the scalar fluxes $\langle u'\phi' \rangle$ and $\langle v'\phi' \rangle$. Finally, correlations between the fluctuating strain, vorticity, and swirling strength fields and the scalar fields would reveal the influence of the unsteady flow behavior on the dissemination of the injectant species and possibly offer insight into turbulent flow characteristics imparted to the flow by the two test geometries.

Another possible path to take in the analysis of these flowfields, rather than the traditional statistical route, is to approach the problem using proper orthogonal decomposition. However, instead of its application to simply the velocity field, joint application to both the velocity fields and the scalar fluxes (for instance) would help reveal dominant spatial modes present in the flow, which could help isolate the mechanisms responsible for mixing enhancement within the hypermixing flowfield.

Another potential path of future work is analyzing the temperature model used in these studies. It was noted in Section 4.3.1.2 that there are discrepancies that arise from utilizing different temperature models in the Kr PLIF calibration. While the composition corrected Crocco-Busemann model was a definite improvement over the basic model, it

is still uncertain whether the use of instantaneous velocity data provides more accurate results than that of the mean. Thus, a number of different studies could be devoted to validating this model. If an experimental approach was taken, the experiments could range from a simple scanning total temperature and composition probes to measure the true temperature and concentration profiles or potentially utilizing something more complicated such as NO PLIF to measure the temperature field. Additionally, a high-fidelity simulation such as DNS of a related flowfield would be tremendously useful for assessing the validity of the temperature model, particularly in regard to the instantaneous velocity and composition corrections. Another related study would apply the Kr PLIF technique to a flowfield with a well-known mean concentration profile, thereby allowing for an assessment not only of the uncertainty as conducted herein, but also of the accuracy of the technique.

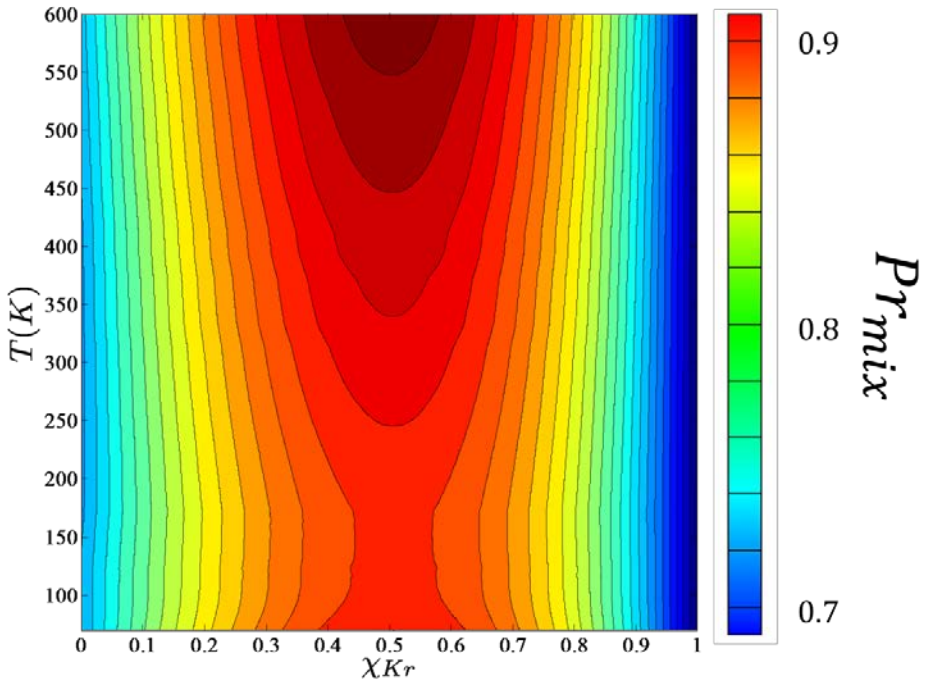

Figure 4.1: Variation of mixture Prandtl number with temperature and composition

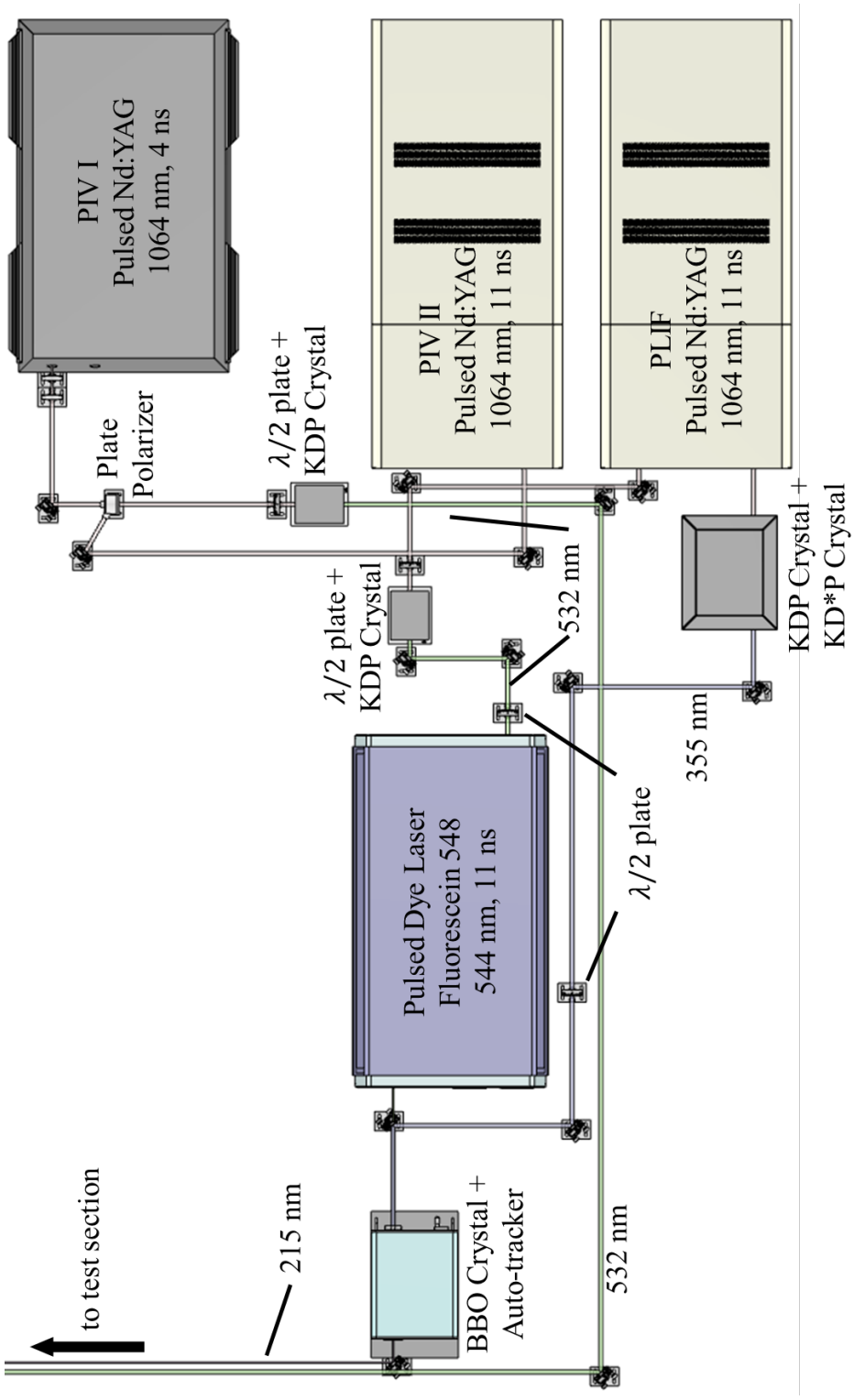

Figure 4.2: Schematic of simultaneous PLIF/PIV laser setup used in mixing studies

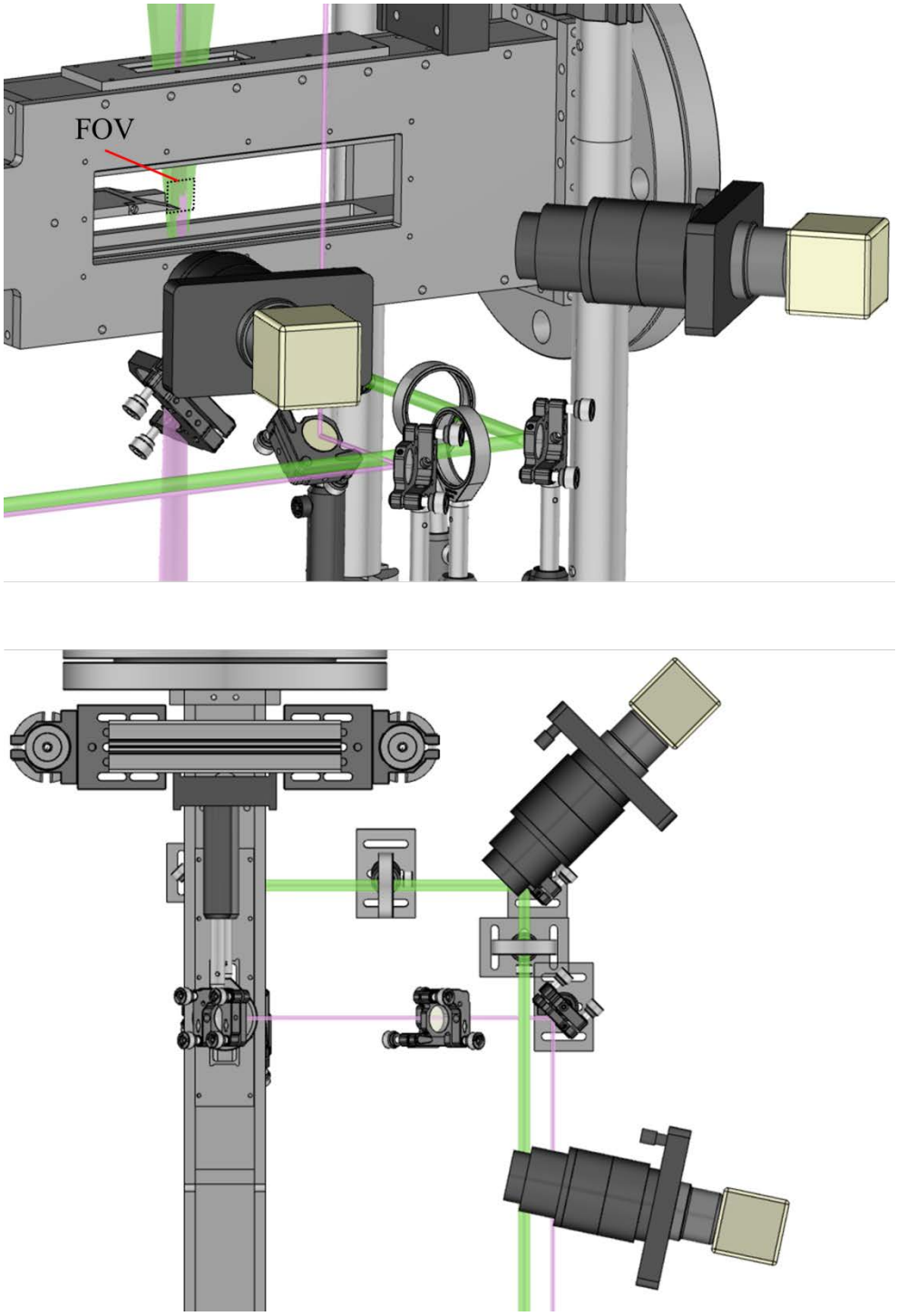

Figure 4.3: Orientation of PIV cameras for PLIF/PIV setup. Top – perspective view showing fields of view and bottom – overhead view showing camera orientation

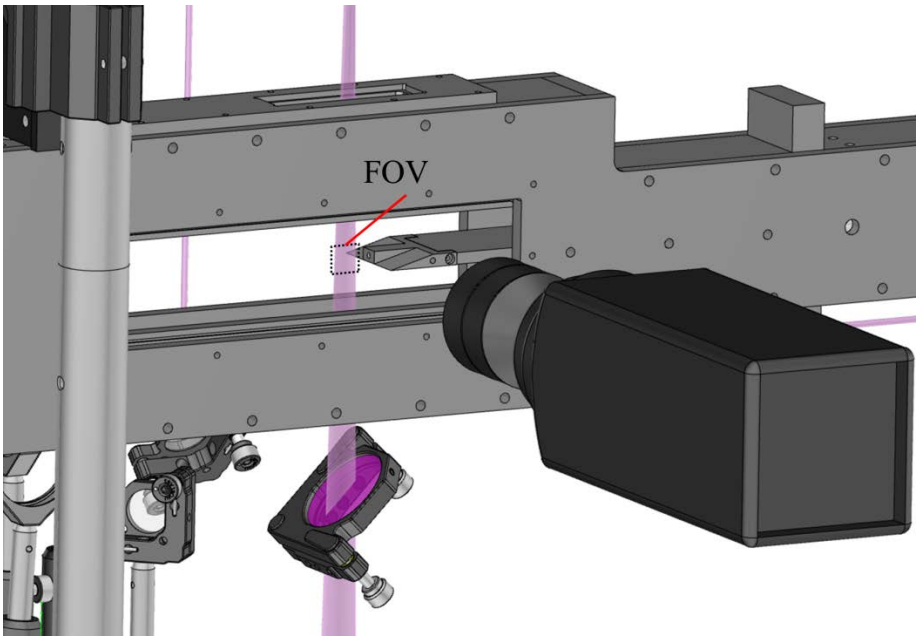

Figure 4.4: Orientation of PLIF camera for PLIF/PIV setup detailing the fields of view used in the study.

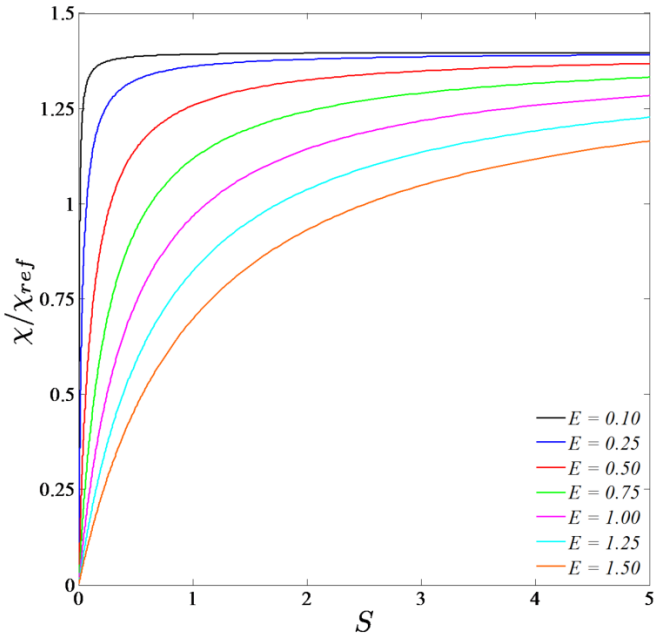

Figure 4.5: Effect of laser energy on calibration of Kr PLIF signal at reference conditions

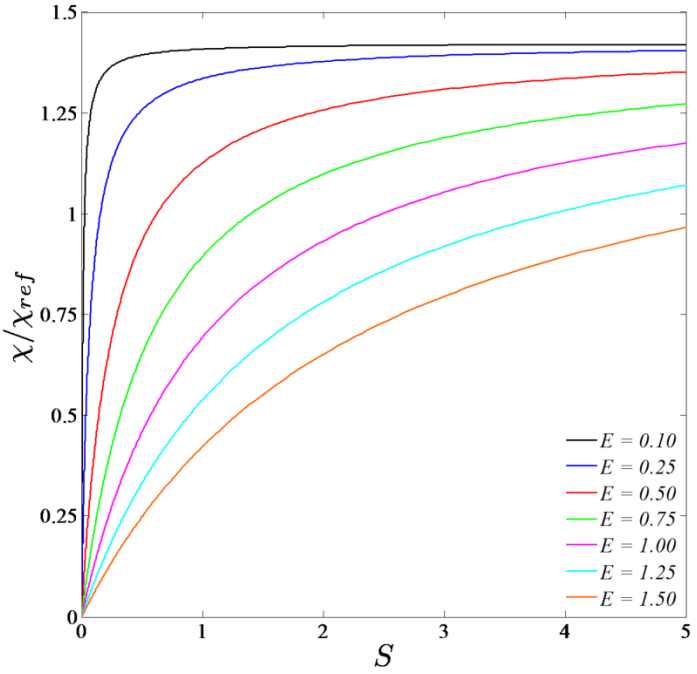

Figure 4.6: Effect of laser energy on calibration of Kr PLIF signal at freestream conditions

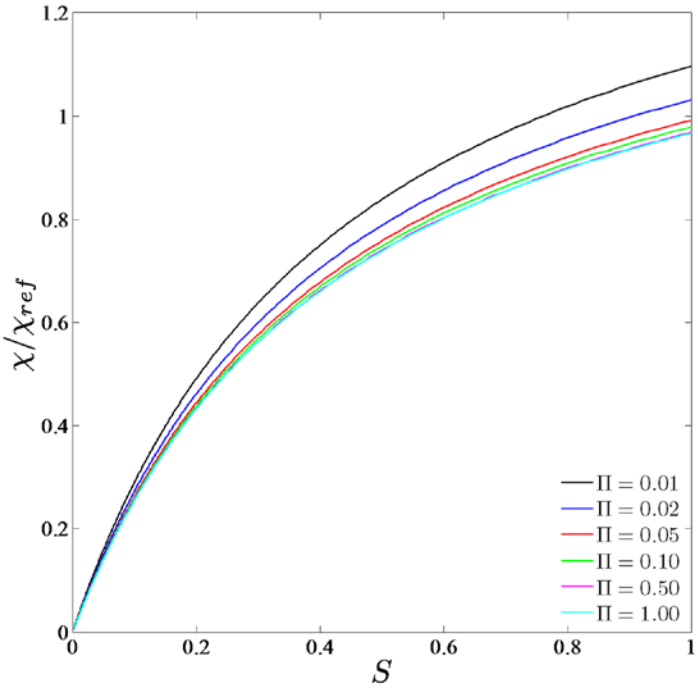

Figure 4.7: Effect of pressure on calibration of Kr PLIF signal at reference temperature

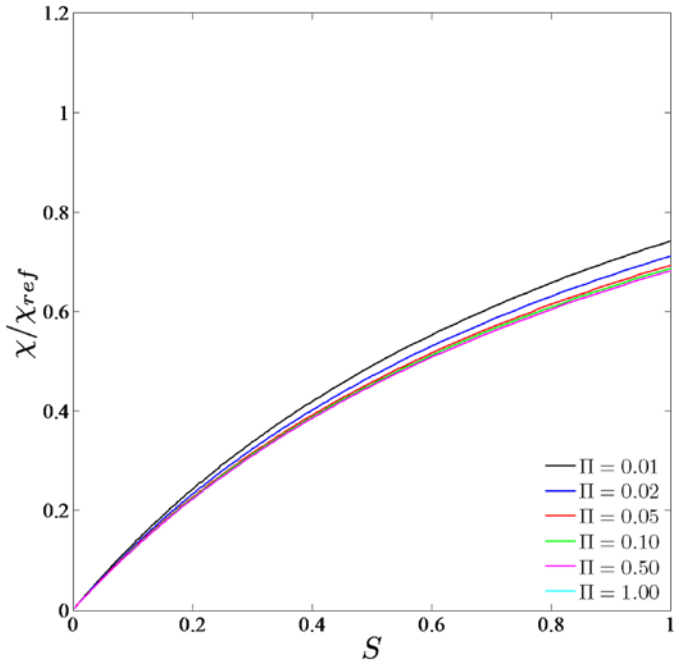

Figure 4.8: Effect of pressure on calibration of Kr PLIF signal at freestream temperature

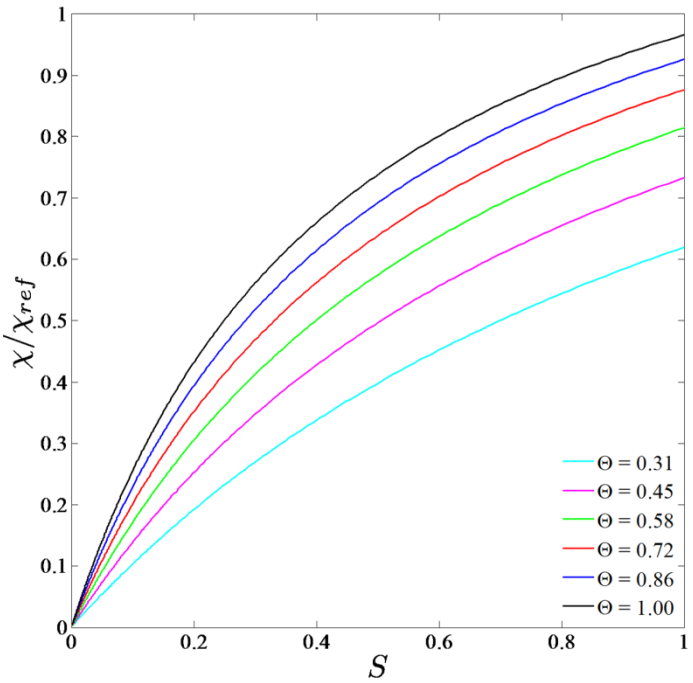

Figure 4.9: Effect of temperature on the calibration of the Kr PLIF signal at reference conditions

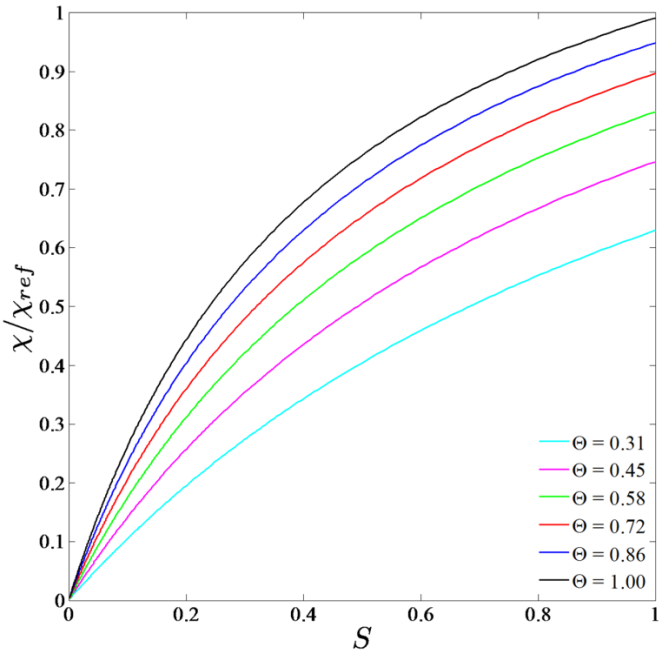

Figure 4.10: Effect of temperature on the calibration of the Kr PLIF signal at freestream conditions

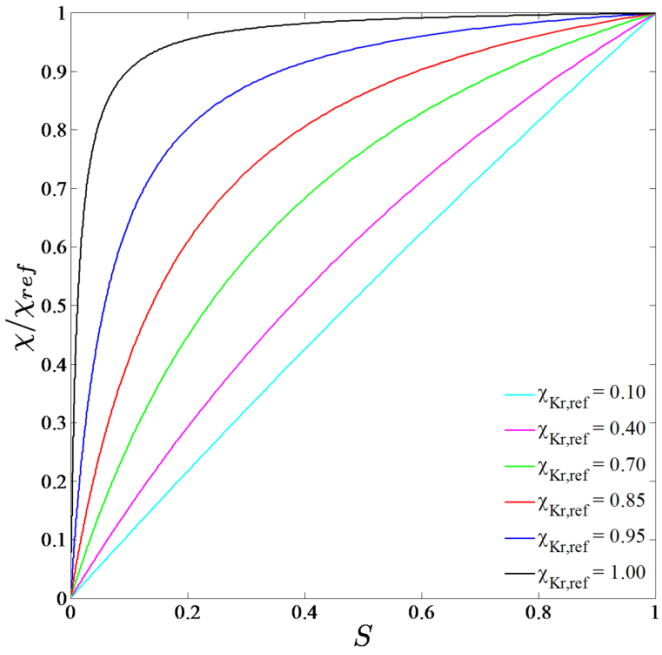

Figure 4.11: Effect of reference mole fraction on the calibration of the Kr PLIF signal at reference conditions

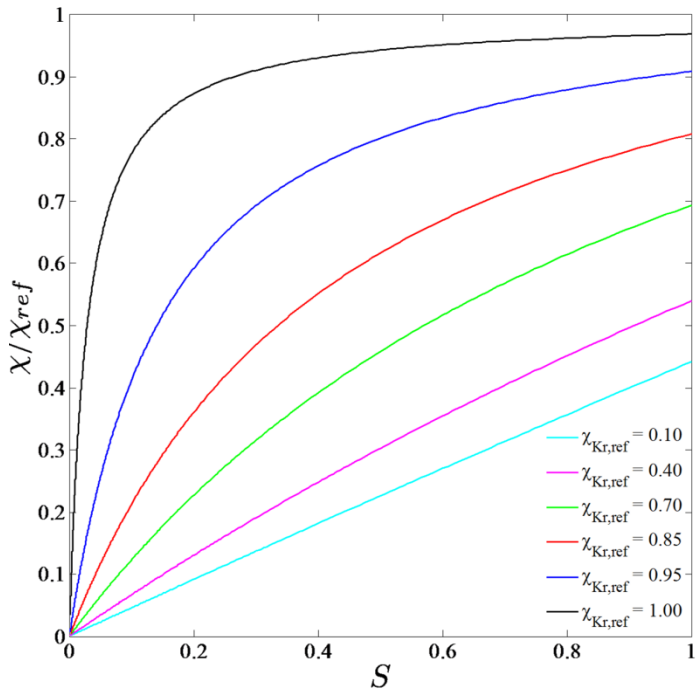

Figure 4.12: Effect of reference mole fraction on the calibration of the Kr PLIF signal at freestream conditions

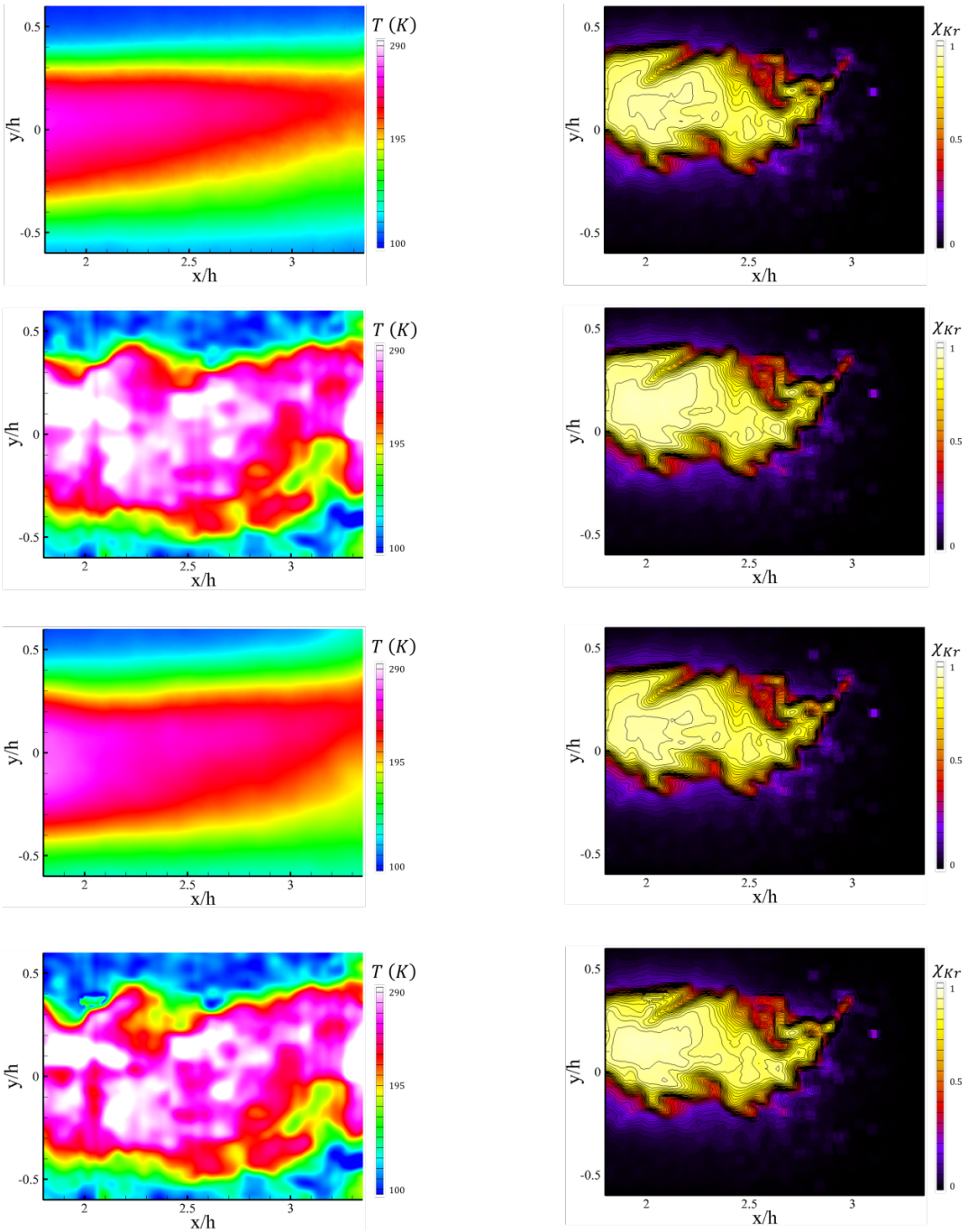

Figure 4.13: Effect of different temperature models on calibration of PLIF signal. Left column – static temperature and right column – mole fraction. From top: standard Crocco-Busemann, instantaneous Crocco-Busemann, modified Crocco-Busemann with composition correction, and instantaneous modified Crocco-Busemann with composition correction.

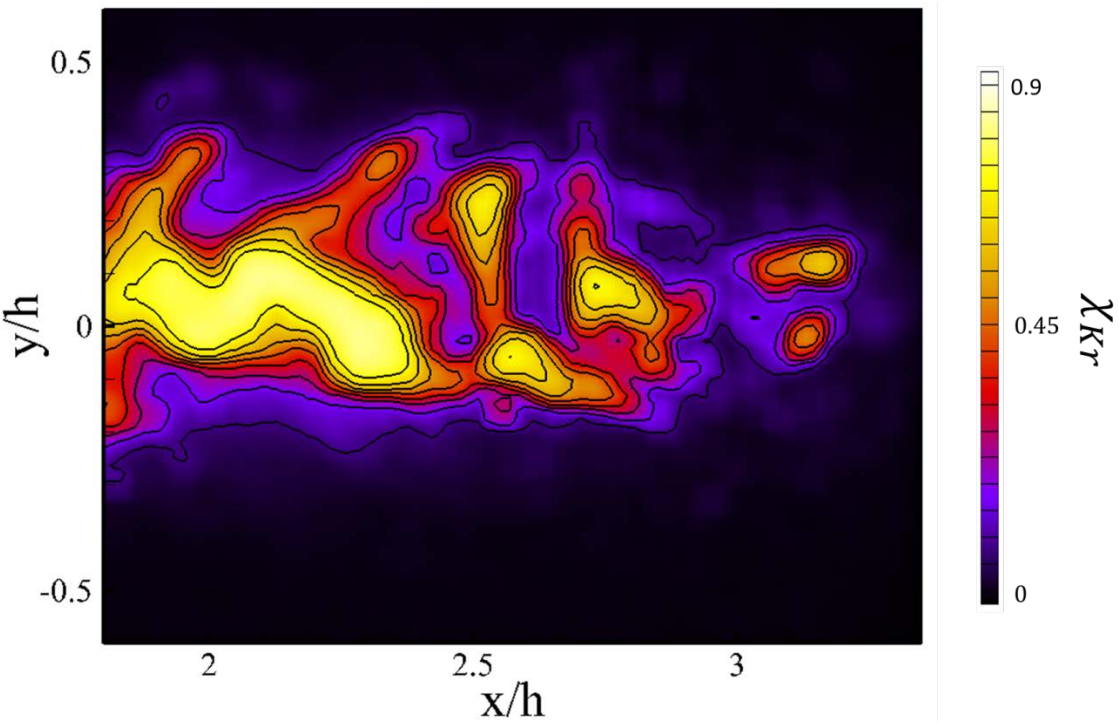

Figure 4.14: Example calibrated fluorescence image

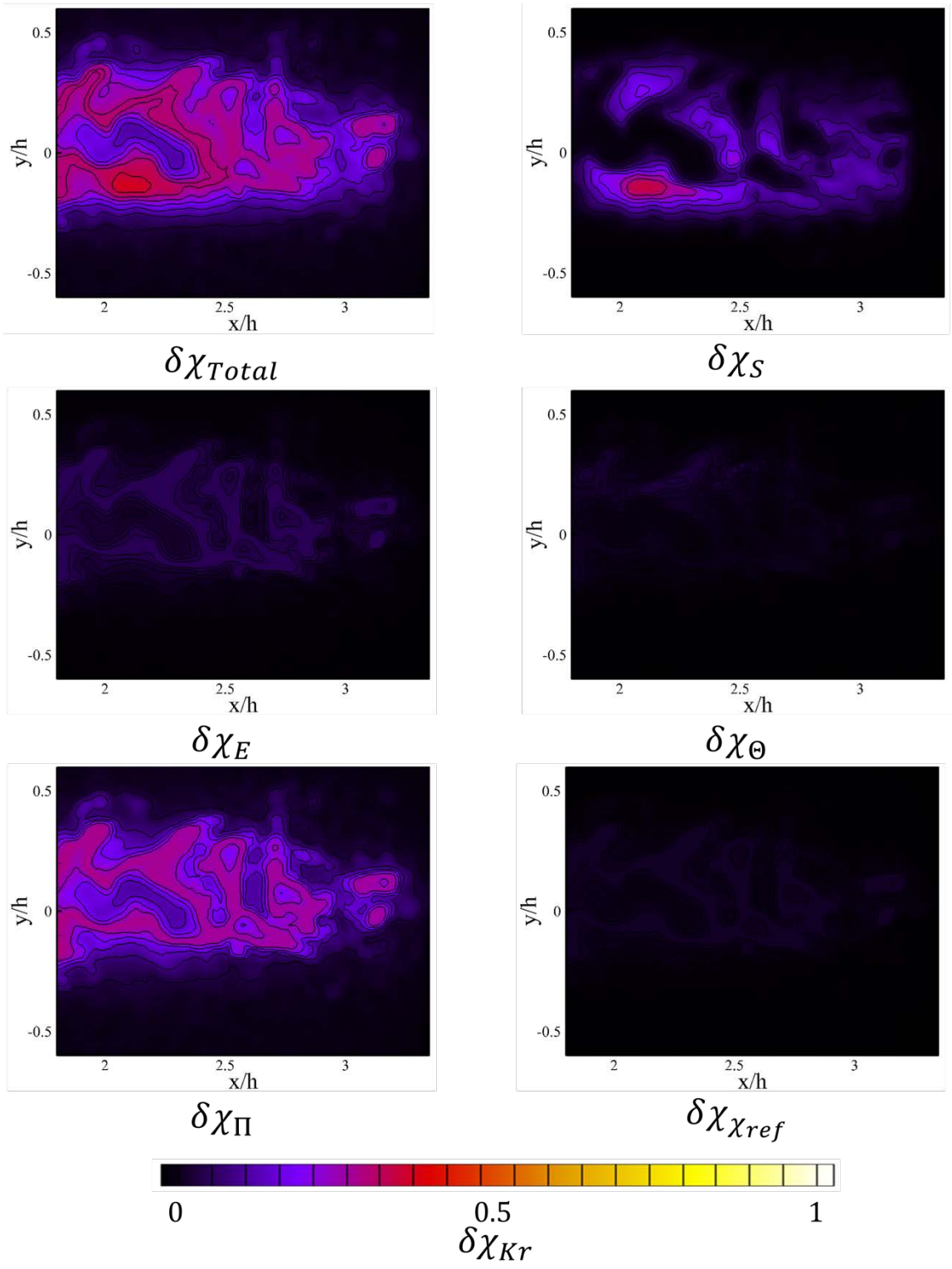

Figure 4.15: Tabulated uncertainties for instantaneous mole fraction calibration in Fig 4.9

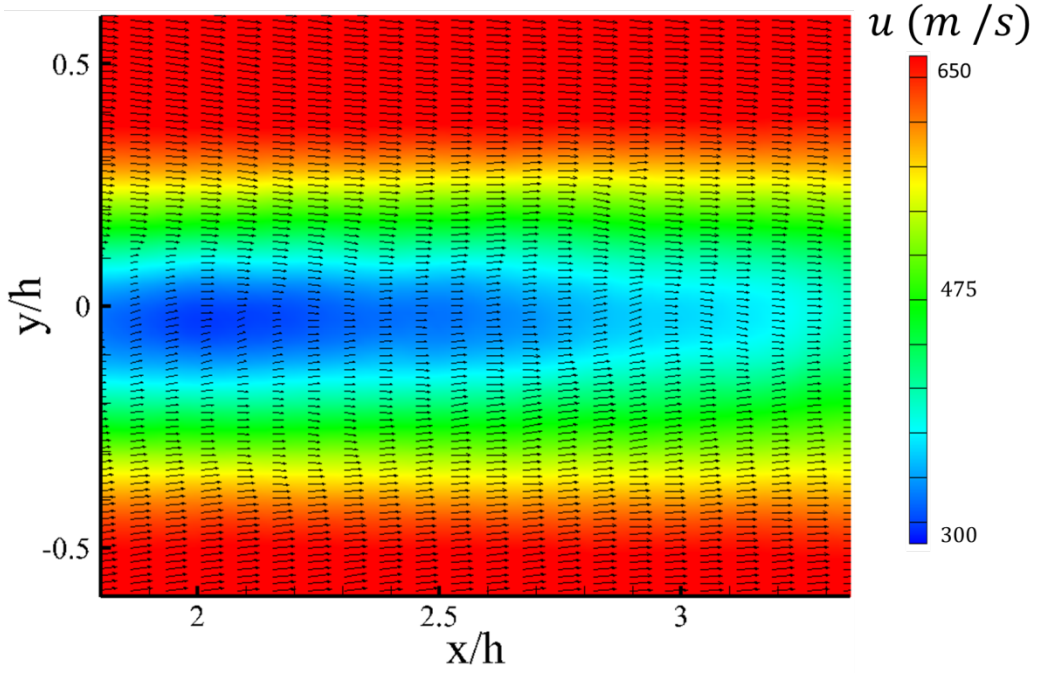

Figure 4.16: Mean centerline stream-wise velocity contours for the planar injector flowfield

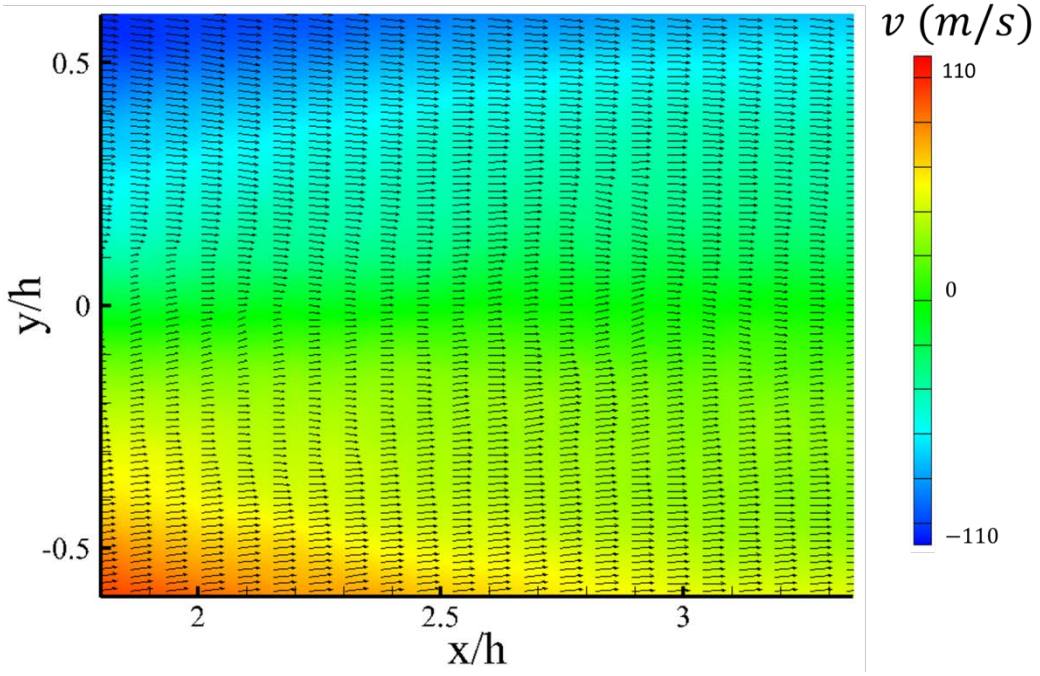

Figure 4.17: Mean centerline transverse velocity contours for the planar injector flowfield

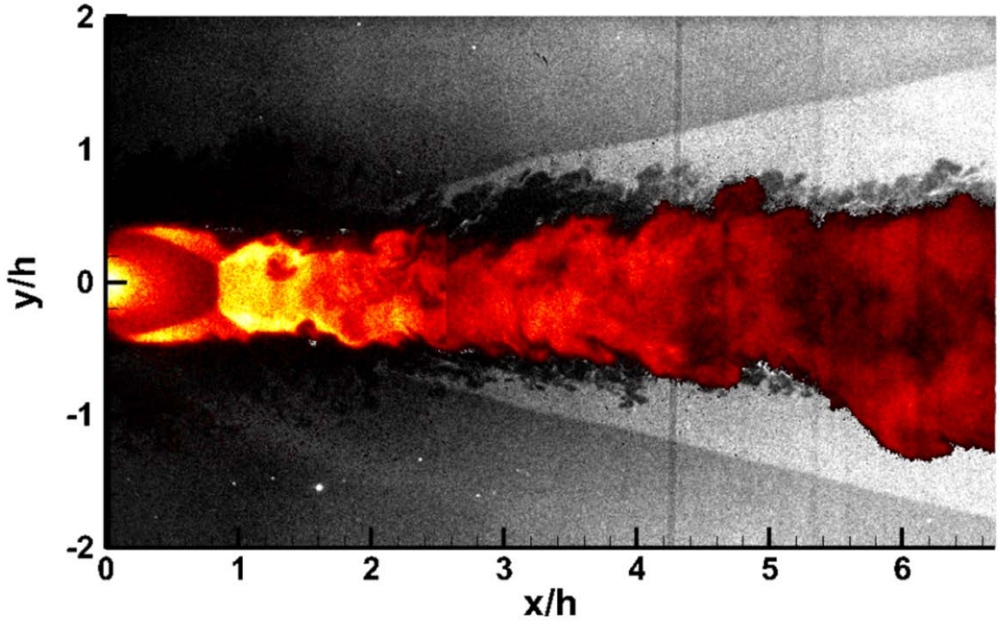

Figure 4.18: Overlay of instantaneous acetone PLIF and planar laser scattering showing relative positions of barrel and recompression shocks. From [**99**].

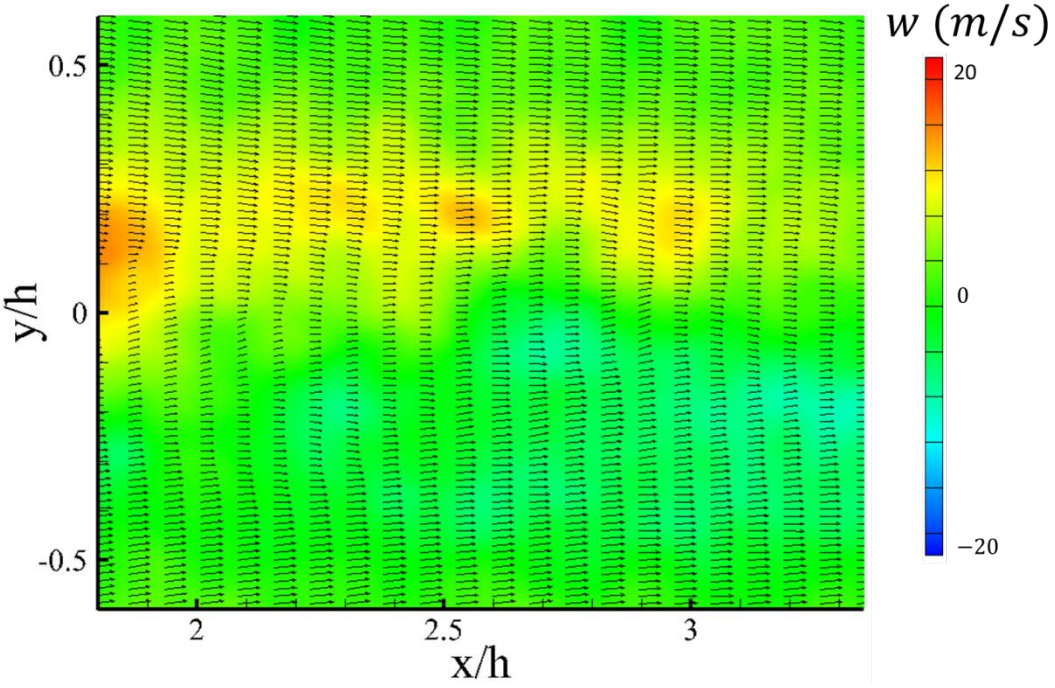

Figure 4.19: Mean centerline span-wise velocity contours for the planar injector flowfield

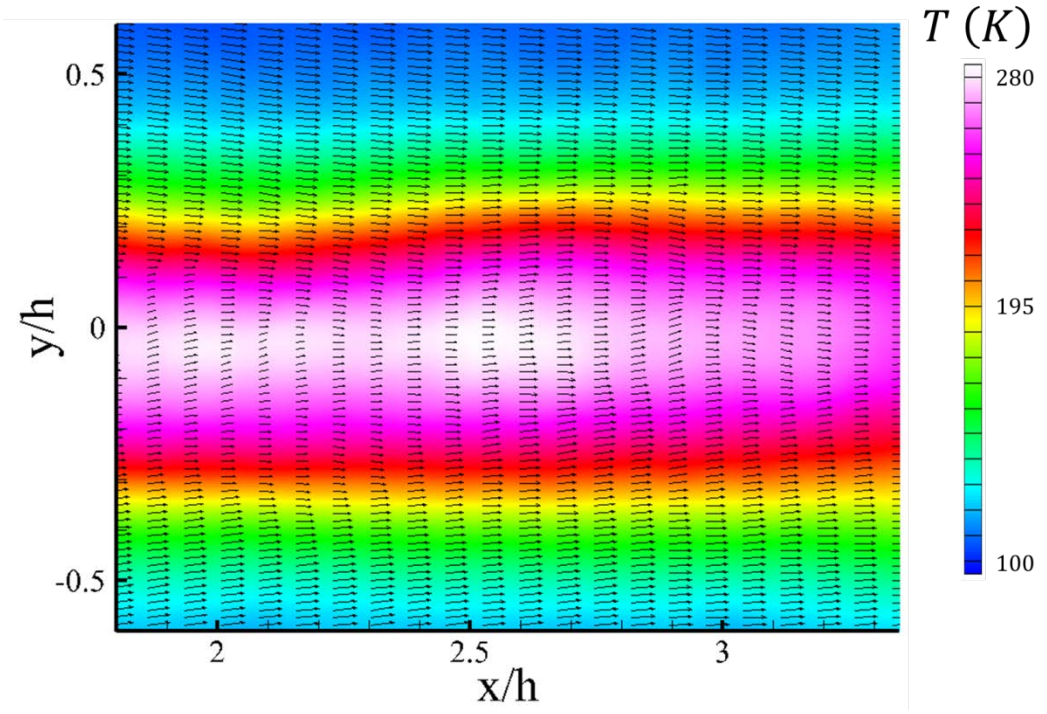

Figure 4.20: Mean centerline temperature contours for the planar injector flowfield

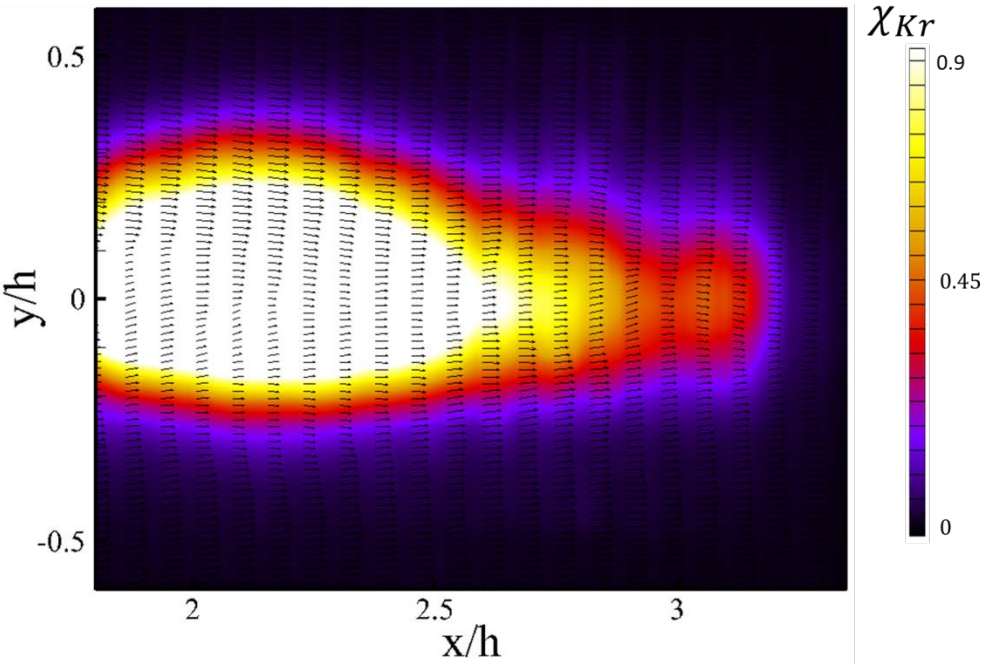

Figure 4.21: Mean centerline mole fraction contours for the planar injector flowfield

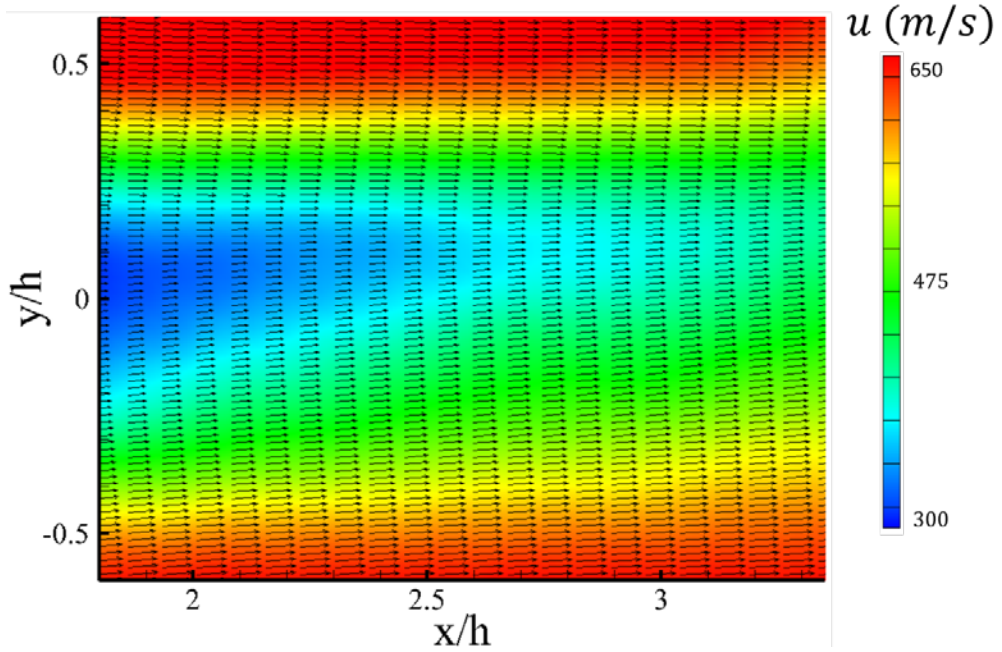

Figure 4.22: Mean centerline stream-wise velocity contours for the hypermixing injector flowfield

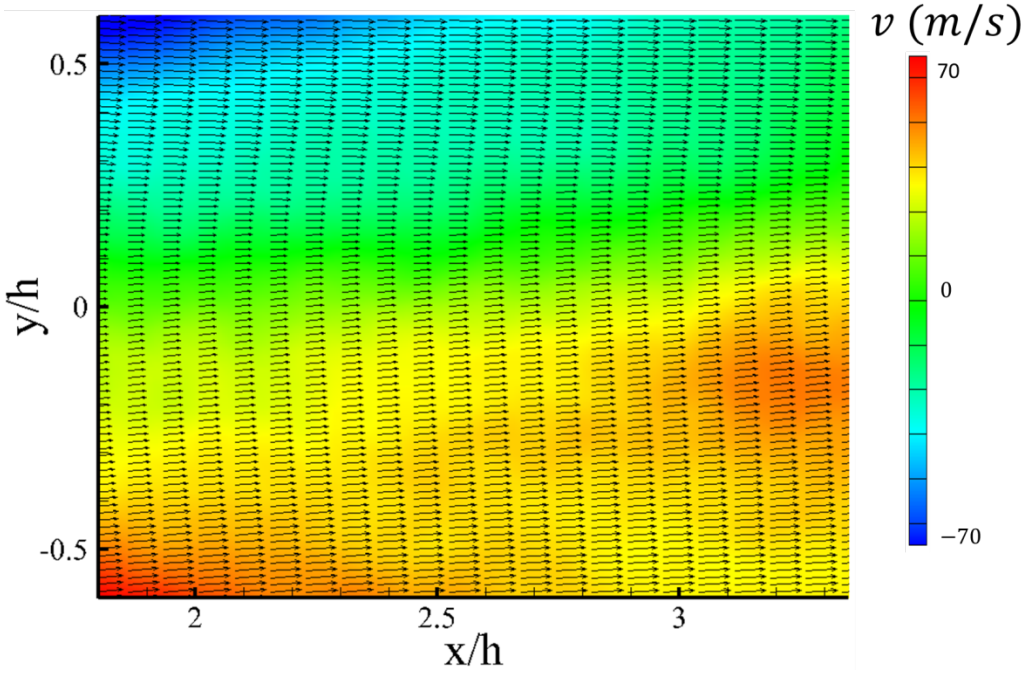

Figure 4.23: Mean centerline transverse velocity contours for the hypermixing injector flowfield

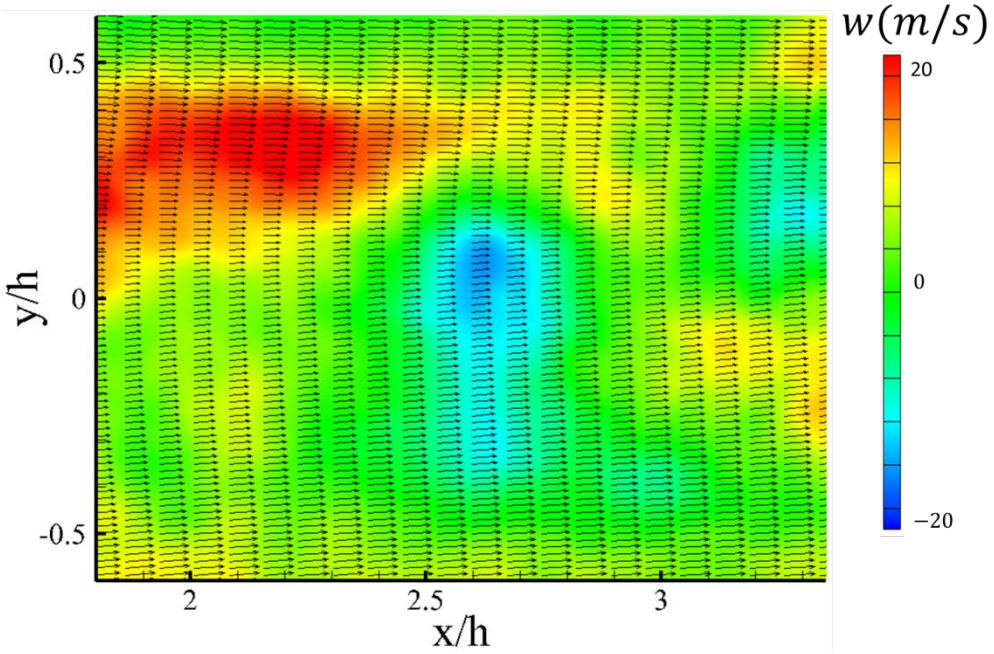

Figure 4.24: Mean centerline span-wise velocity contours for the hypermixing injector flowfield

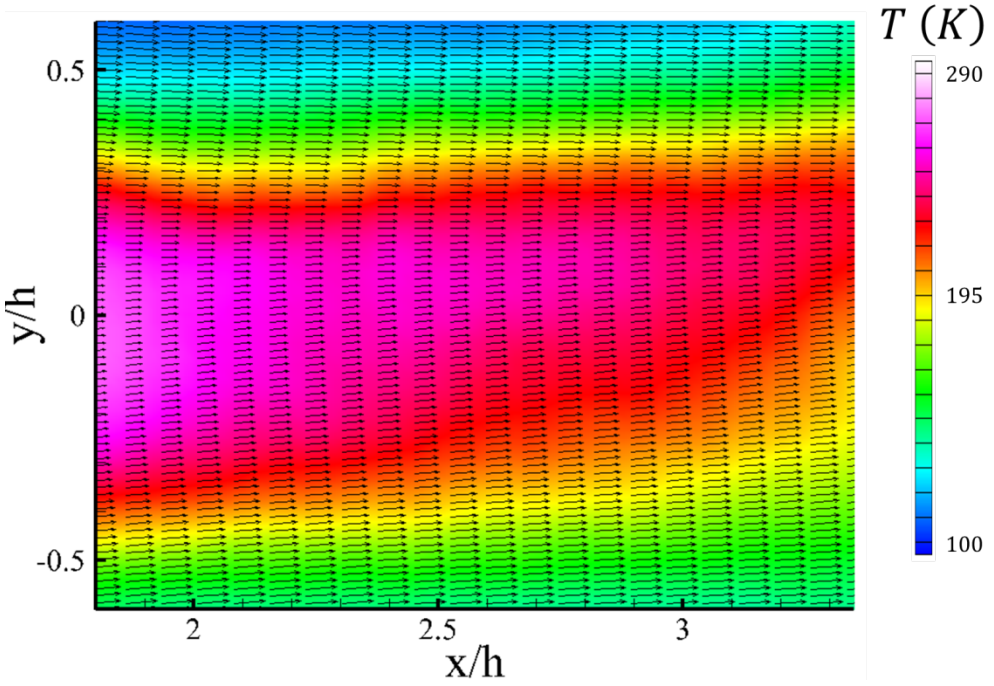

Figure 4.25: Mean centerline temperature contours for the hypermixing injector flowfield

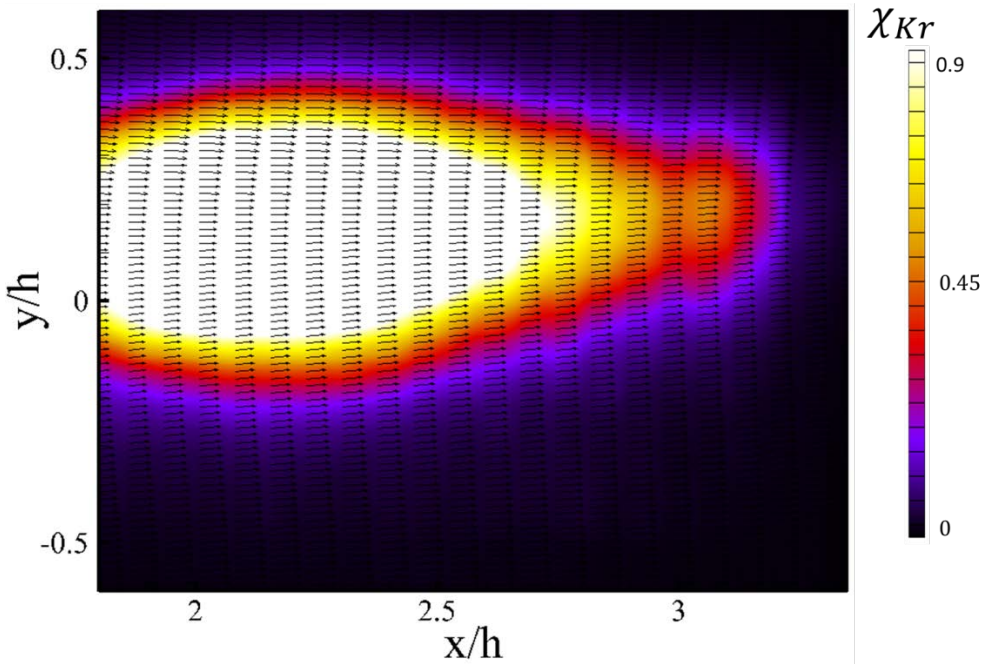

Figure 4.26: Mean centerline mole-fraction contours for the hypermixing injector flowfield

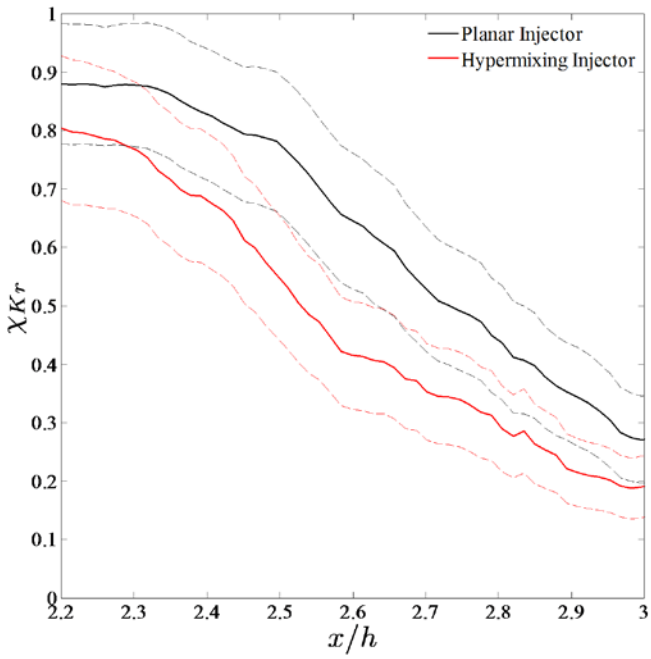

Figure 4.27: Maximum mole fraction as a function of stream-wise distance for the two injection flowfields. The dashed lines represent the uncertainty bounds.

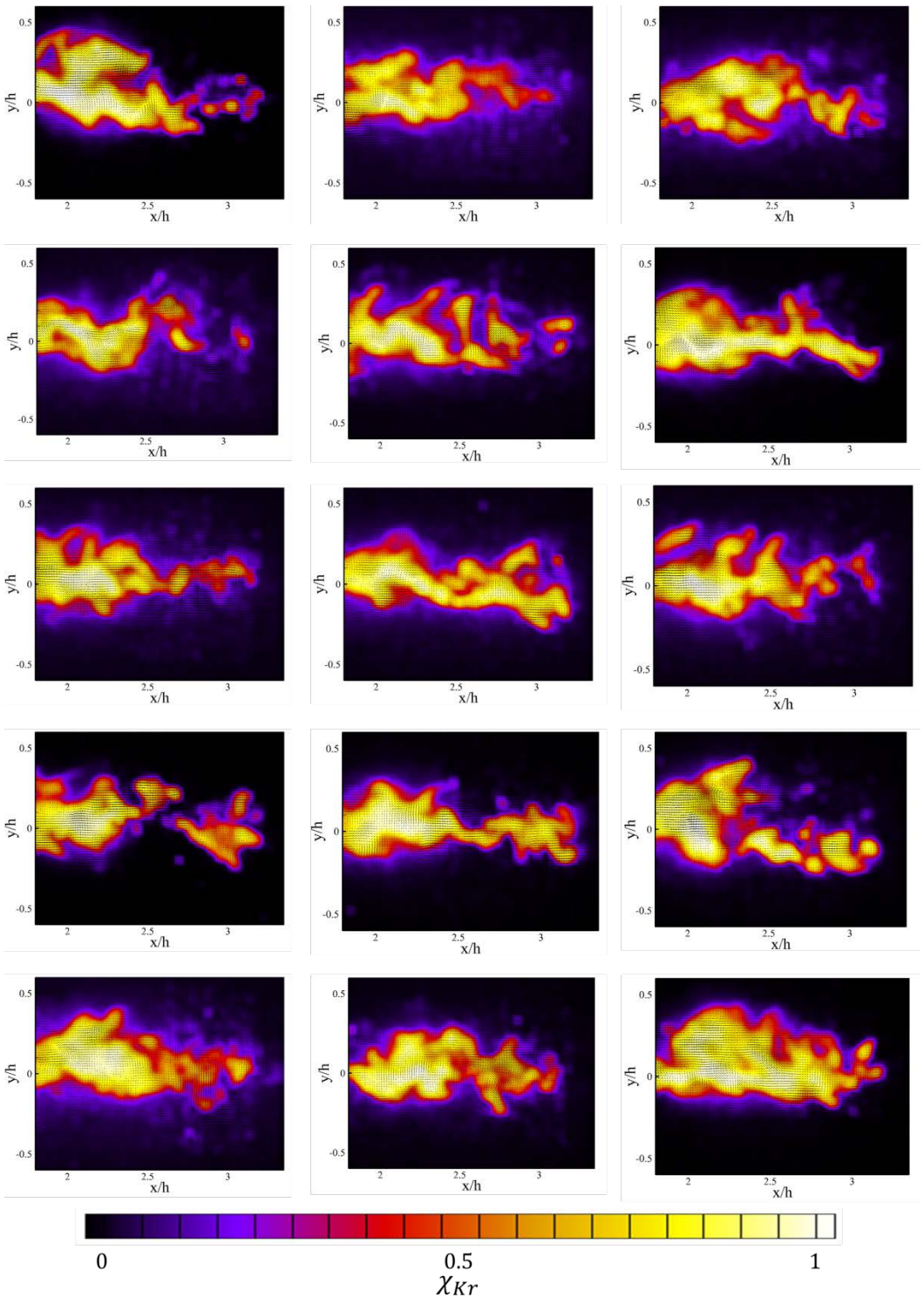

Figure 4.28: Series of instantaneous centerline mole-fraction contours for planar injector flowfield

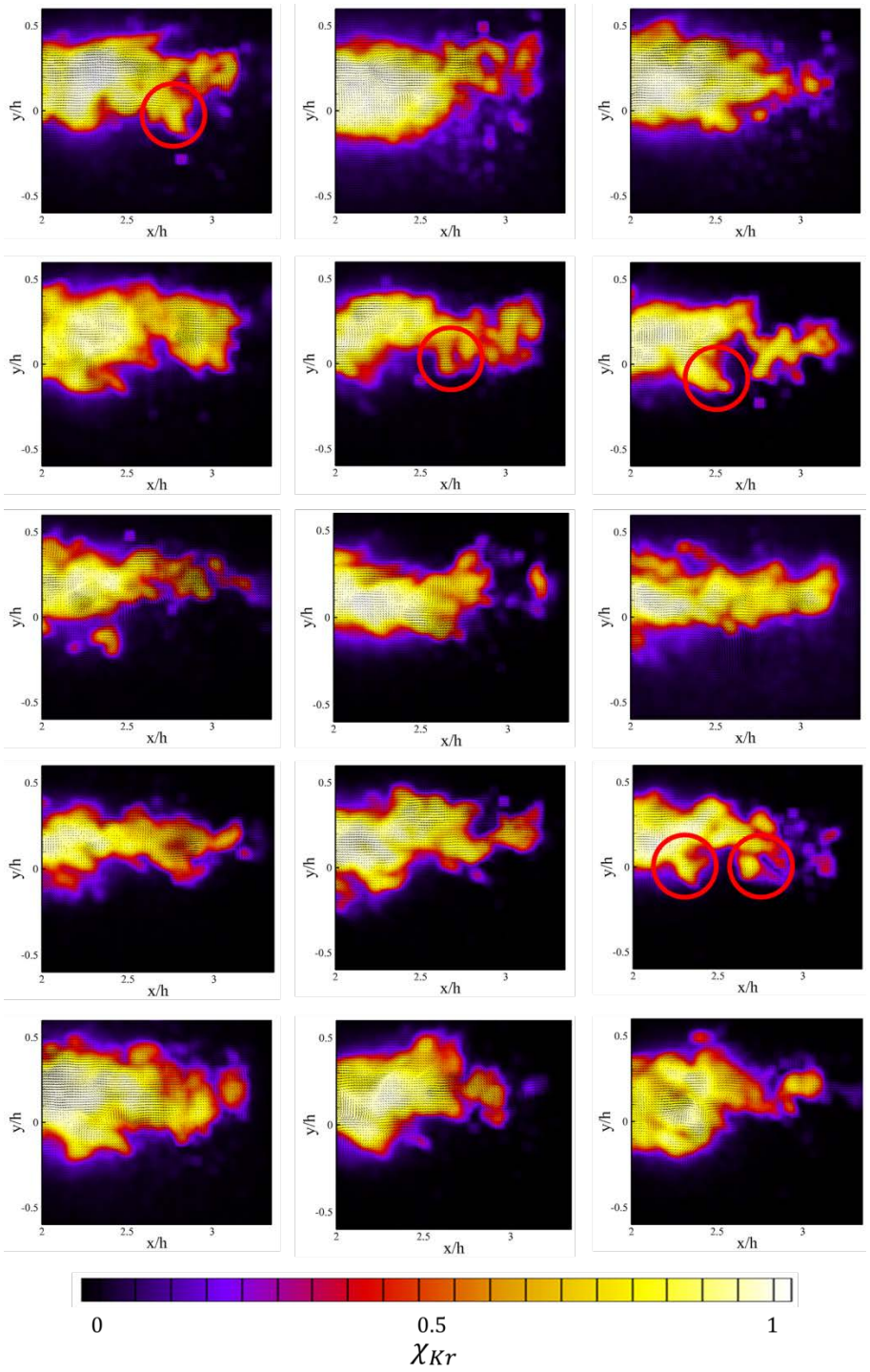

Figure 4.29: Series of instantaneous centerline mole fraction contours for hypermixing injector flowfield. Circled regions correspond to discussion in Section 4.3.2.2.

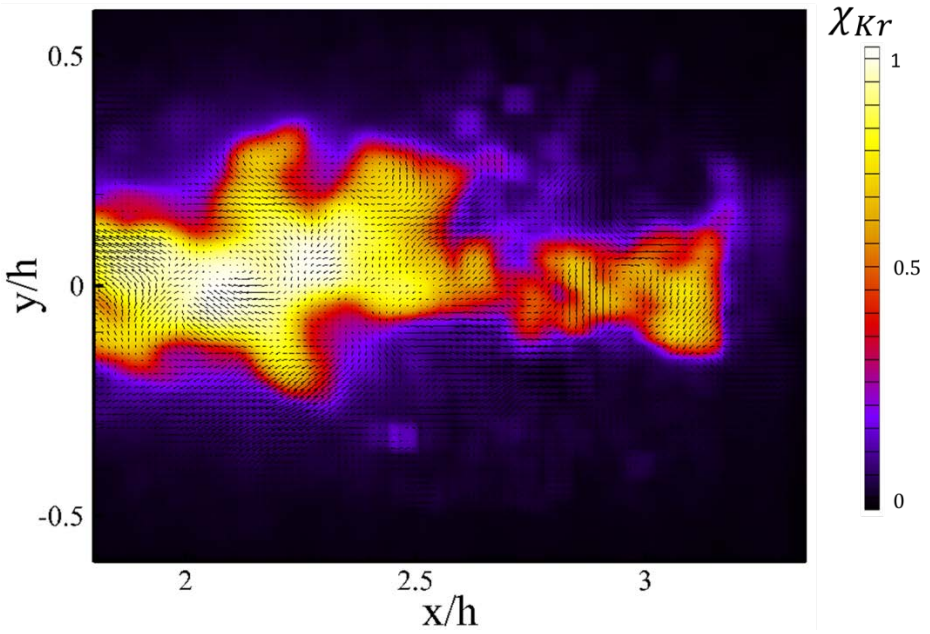

Figure 4.30: Instantaneous centerline mole fraction contours for planar injector flowfield overlaid with fluctuation velocity vectors

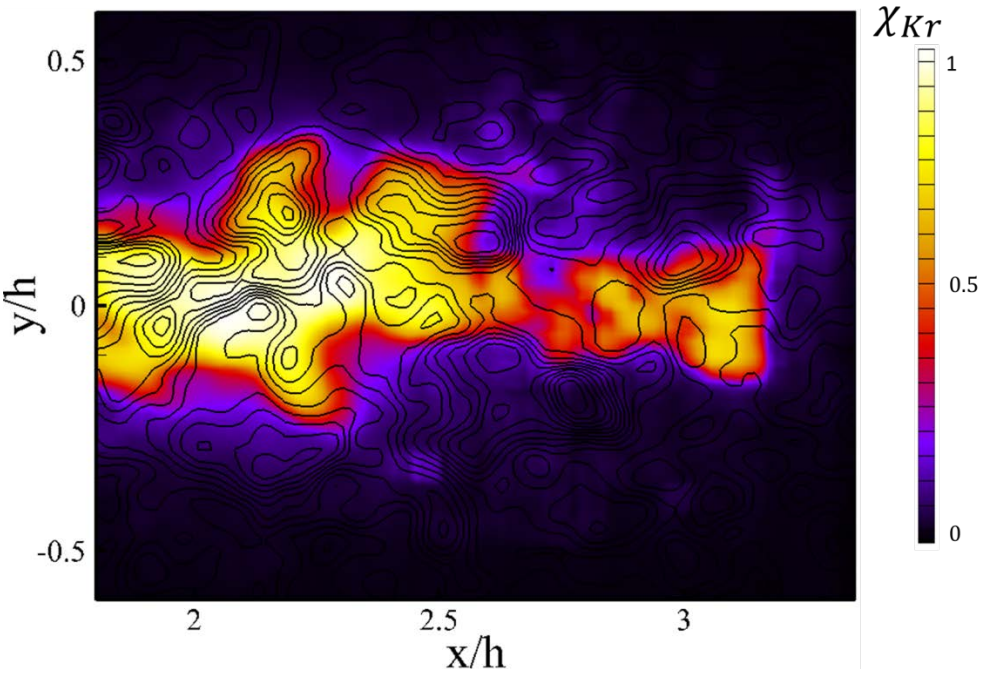

Figure 4.31: Instantaneous centerline mole fraction contours for planar injector flowfield overlaid with fluctuation temperature contours

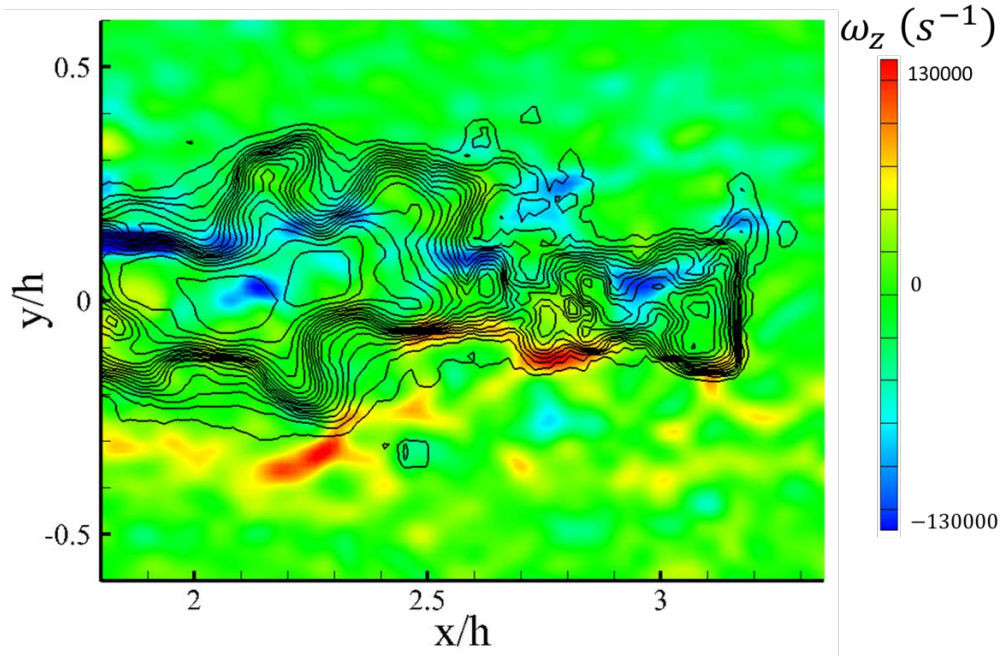

Figure 4.32: Instantaneous centerline span-wise vorticity contours for planar injector flowfield overlaid with mole fraction contours

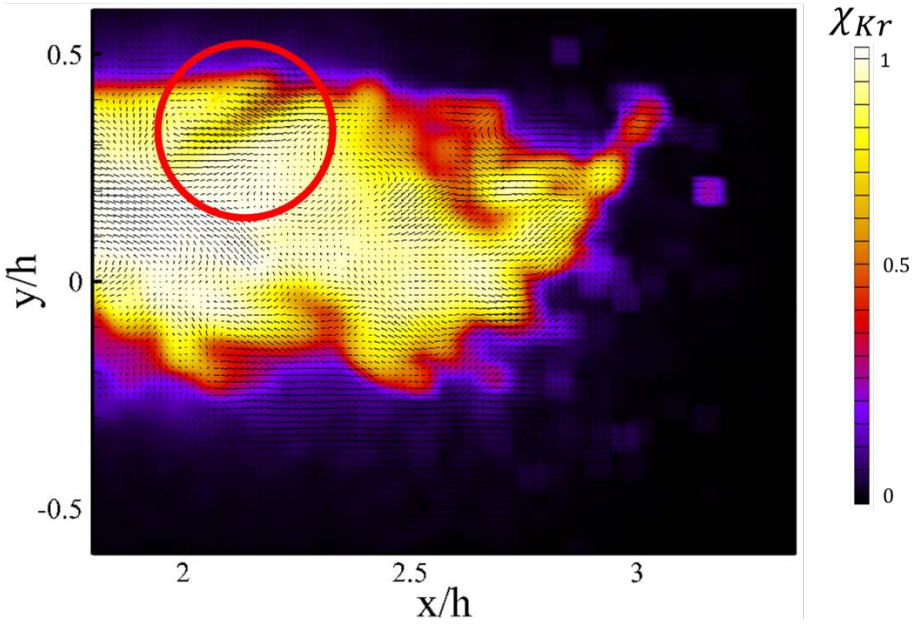

Figure 4.33: Instantaneous centerline mole fraction contours for hypermixing injector flowfield overlaid with fluctuation velocity vectors. The circled region corresponds to discussion in Section 4.3.2.2.

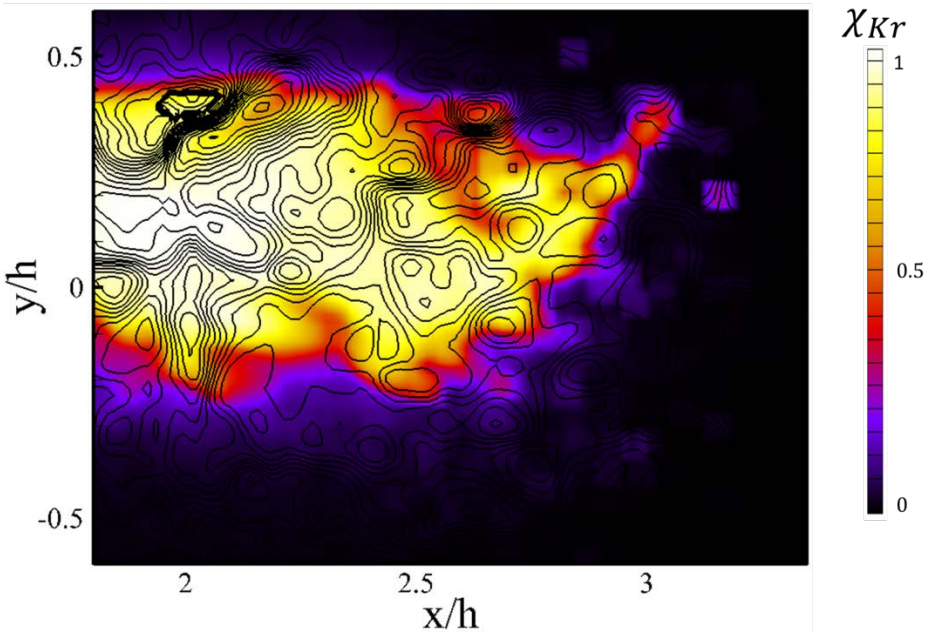

Figure 4.34: Instantaneous centerline mole fraction contours for hypermixing injector flowfield overlaid with fluctuation temperature

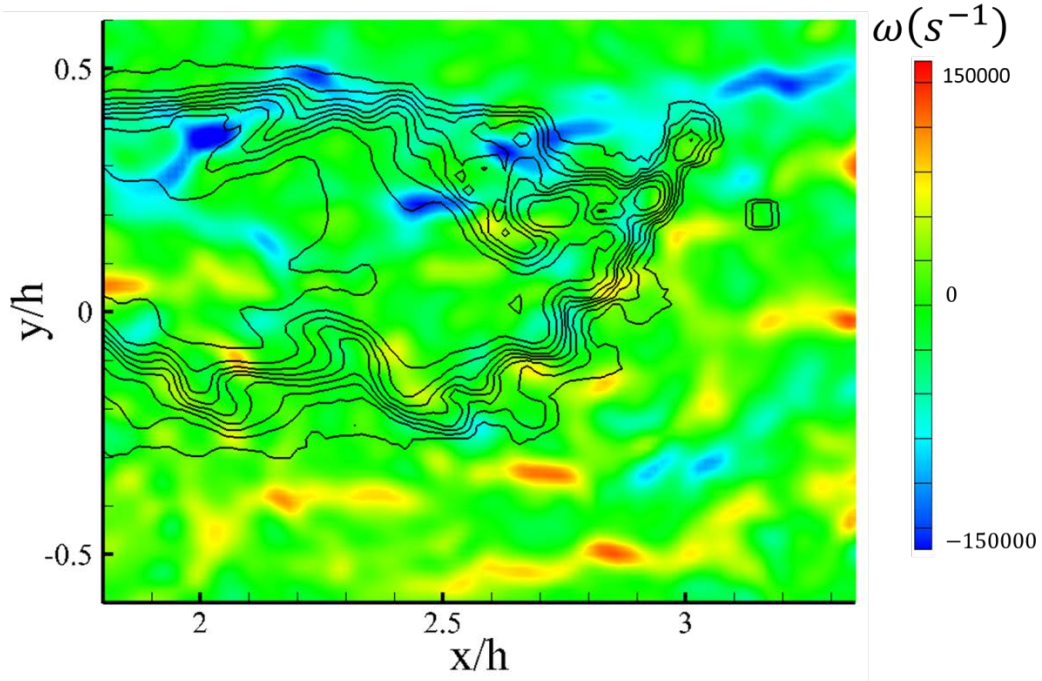

Figure 4.35: Instantaneous centerline vorticity contours for hypermixing injector flowfield overlaid with mole fraction contours

Appendix 2A: Analytical Methods for deriving quenching rates and absorption cross-sections from fluorescence data

This section details the numerical methods and uncertainty calculations used in the measurements of quenching rates found in Chapter 2. The data processing for these measurements was quite detailed and intensive, and the documentation of the procedures could prove helpful for future researchers attempting to make similar measurements.

2A.1 – Calculation of Fluorescence Lifetimes

It is not a trivial matter to infer the fluorescence decay constant from these measurements because the fluorescence, particularly under quenched conditions, is of the same order of magnitude as the laser pulse duration. The fluorescence decay time is the inverse of the fluorescence decay rate,

$$\tau_f = \frac{1}{\gamma} = \frac{1}{A + Q} \qquad \text{2A.1}$$

In the case when the laser pulse width is much smaller than the fluorescence decay time one can take the natural logarithm of the observed fluorescence time history and attempt a linear curve fit on the falling edge of the fluorescence signal [**117**] [**86**] [**82**] [**85**] [**96**]. However, in the present case, the expected fluorescence lifetimes are at most 26 ns since this is the natural lifetime of the transition of interest. Therefore, despite the short duration of the pulse described in Chapter 2, its presence in the fluorescence signal will still be observed. The solution to this problem was the development of an iterative deconvolution method to back out the impulse response of the fluorescence. A detailed explanation of the theory and functionality of this algorithm can be found in Appendix 2B.

2A.2 – Calculation of Spontaneous Emission Rate and Reference Quenching Rates

The calculation of the spontaneous emission rates in addition to the collisional quenching rates at the reference conditions are accomplished with the variable pressure runs described above. The raw data extracted from these runs are vectors of τ_f and pressure. Extending the equivalency expressed in Eq. 2A.1:

$$\tau_f = \frac{1}{A + P\sum\chi_i q_i\left(T = T_{ref}\right)} \tag{2A.2}$$

Alternatively, expressing Eq. 2A.2 as its inverse, it becomes apparent that for a fixed mole fraction and quenching rate, the inverse fall time (total decay rate) should be linearly dependent on the pressure.

$$\frac{1}{\tau_f} = A + P\sum\chi_i q_i\left(T = T_{ref}\right) \tag{2A.3}$$

As Eq. 2A.3 further suggests, by taking the data points and plotting the aforementioned quantities ($1/\tau_f$ vs P), performing a linear regression (something of the form $f(x) = Ax + B$) on the resulting curve will yield the spontaneous emission rate (as the y-intercept value of the regression) and the summation term in Eq. 2A.6. The natural lifetime can also be extracted in this manner as simply the inverse of the spontaneous emission rate.

The easiest of these data to calculate, and the most important in terms of conditioning the remaining data, is that of pure krypton. Here, since it is no longer a mixture, the χ_i and summation terms vanish, and the resulting fit parameter is exactly q_{Kr} at the reference temperature. Further calculation can yield the reference quenching cross-section with this data:

$$A + P\sum\chi_i q_i = A + n_o\sum\chi_i\langle v_i\rangle\sigma_i = A + \frac{P}{kT}\sum\chi_i\left(\frac{8kT}{\pi\mu_i}\right)^{\frac{1}{2}}\sigma_i \tag{2A.4}$$

The final step is to replace the total number density and the relative velocity terms with their respective thermodynamic definitions, where k is the Boltzmann constant and μ_i is the reduced mass of the collisional pair, defined as $\mu_i = (m_{Kr}m_i)/(m_{Kr} + m_i)$, giving:

$$P\sum\chi_i q_i = P\sum\chi_i \left(\frac{8}{\pi kT\mu_i}\right)^{\frac{1}{2}} \sigma_i \qquad \text{2A.5}$$

From Eqs. 2A.4 and 2A.5, it is made apparent that there is a simple relationship between the quenching cross-section and the quenching rate.

Given the quenching and spontaneous emission rates for krypton, the rates for the other quenching species can be calculated in turn. Procedurally this calculation was conducted by first extracting the decay times, pressure, and composition data from the raw data sets. These data were part of the raw data files saved in the Labview VI, which included all of the information about the test cell including the total and static temperatures, current waveform taken from the oscilloscope, flow rates of gases, and Mach number if applicable. Once these data were extracted, a linear regression was performed in a like manner to that used for the pure krypton case. In this instance, the calculated slope of the linear regression is equivalent to the summation term. Since both the mole fraction and reference quenching rates for krypton were previously determined, it follows that the remaining part of the summation is from the additional quenching species. These quenching rates (and cross-sections) were calculated over many runs using a wide range of mole fractions to both validate the procedure and allow for a more converged average.

2A.3 – Calculation of Temperature-Dependent Quenching Rates and Cross-Sections

Calculating the temperature dependence (that is, deviations from the reference conditions) is slightly more intensive than the procedure used for calculating the

reference conditions. The reason for this is that there is no pure krypton case, and in the case of the low-temperature runs, the buffer gas adds extra complications to the calculations. Since the cost of krypton is so high (and generally available in small quantities), openly flowing a sufficient amount of the gas to start the facility and extract enough heat from the inline heater is not a realistic possibility. The first step in the calculation procedure is to find the temperature dependence of the krypton quenching rates. Procedurally, this is fairly straightforward; the krypton is run with a buffer gas. If two runs at the same temperature are performed, but with very different compositions, the relative quenching rates can be solved for through a system of equations:

$$\gamma_1(T) = A + P_1(T)\sum\chi_{i,1}q_i(T) \qquad \text{2A.6}$$
$$\gamma_2(T) = A + P_2(T)\sum\chi_{i,2}q_i(T)$$

Here, the sum is over two terms (Kr-Kr and Kr-He). Making this substitution, Eq. 2A.6 can be expressed in matrix form:

$$\begin{bmatrix}\chi_{Kr,1} & \chi_{He,1}\\ \chi_{Kr,2} & \chi_{He,2}\end{bmatrix}\begin{bmatrix}q_{Kr}(T)\\ q_{He}(T)\end{bmatrix} = \begin{bmatrix}\left(\frac{\gamma_1(T)-A}{P_1(T)}\right)\\ \left(\frac{\gamma_2(T)-A}{P_2(T)}\right)\end{bmatrix} \qquad \text{2A.7}$$

Since all of the terms in Eq. 2A.7 are known apart from the quenching rates, it is a simple matter of solving the system of equations to extract the relative quenching rates. Note here that this procedure explicitly accounts for variations in the mole fractions and pressure that were present during the run (as explained in Chapter 2). However, this process enhances noise significantly, and as a result was conducted over many runs and multiple buffer gases (He and N_2) to allow for convergence of the result. Once the raw data was processed to this point, a power-law curve fit was made. The functional form of this power law fit is given by:

$$\left(\frac{q}{q_{ref}}\right) = c_1\left(\frac{T}{T_{ref}}\right)^{c_2} \quad \text{2A.8}$$

The fit given by Eq. 2A.8 has one small issue in that it essentially contains a correction for the reference quenching rate. While this certainly could be left out of the fit, it was used as a metric of the overall procedure. That is, if the constant c_1 is not equal to unity, in all likelihood there is something wrong with the procedure or the data is not of sufficient quality. For all the final data presented in Chapter 2, the fit parameter was always within the range [0.98, 1.03], and as such this was omitted from the functional form of the temperature dependence since this was within the experimental uncertainties for the reference state conditions.

Expanding on the above procedure, before any of the described calculations for finding specific quenching rates were conducted, the raw data (the total decay rates, γ) were fit to a functional form. A power-law fit was adopted for this purpose (anticipating the functional form of the quenching rate dependence). The form of this fit is given by:

$$\gamma = c_1 T^{c_2} \quad \text{2A.9}$$

There were two reasons for applying this initial curve fit in Eq. 2A.9. The first reason was that it helped to reduce experimental noise early in the data processing before it was amplified by subsequent steps. That is, the procedure gives an analytic form for the raw data and is more resistant to the accumulation of noise through the calculations than the raw data themselves. Second, this procedure allowed for the isolation of low-quality data before they were integrated into the averages and further post-processing. It was a requirement that the data was of sufficient quality to perform this curve fit; if it was not, it usually indicated a problem with the data. This metric is how the problem regarding the positioning of the laser pulse described in Section 2.2.3.2 was found. Data that could not

support an initial curve fit as described in this section was generally rejected, as its quality was insufficient.

Once the quenching rates of krypton and the buffer gas were calculated, the temperature dependence of the other quenching rates could be calculated in a more simplistic manner. Specifically, referring back to Eq. 2A.3, the temperature dependence of a single quenching rate can be calculated by expanding the summation:

$$\gamma(T) = A + P(T)[\chi_{Kr}(T)q_{Kr}(T) + \chi_{He}(T)q_{He}(T) + \chi_n(T)q_n(T)] \quad \text{2A.10}$$

$$q_n(T) = \frac{1}{\chi_n(T)}\left[\frac{\gamma(T) - A}{P(T)} - \chi_{Kr}(T)q_{Kr}(T) - \chi_{He}(T)q_{He}(T)\right] \quad \text{2A.11}$$

Here, the subscript n denotes the species being calculated. Since the temperature dependence of the krypton and buffer quenching rates in Eqs. 2A.10 and 2A.11 are already known at this stage of the calculation, the temperature dependence of the additional quenching species can be evaluated directly. Much as was the case with krypton and helium, it took many runs to achieve convergence of these data. Once these individual rates have been calculated and compiled, the temperature dependence was fit to the functional form given by Eq. 2A.8.

2A.4 – Calculation of Relative Effective Two-Photon Absorption Cross-Sections

In principle, the effective two-photon absorption cross-sections could have been measured directly in this set of experiments. That is, photodiodes before and after the test cell could have been calibrated used to measure the laser energy at both locations. With little assumption, the absorption in the cell could have been calculated based on the path length of the beam and the thermodynamic conditions within the cell. However, in practice this was nearly infeasible. First, the beam used to excite the fluorescence tended to drift spatially over time (quite rapidly), making any attempt to calibrate the

photodiodes futile. Secondly, when performing the temperature-dependent studies the krypton concentration in the cell was not spatially uniform nor was the spatial distribution known. One of these conditions are required for making the absorption measurement quantitative.

An alternative method to infer the effective absorption cross-section was employed instead; this method utilized the ratio of the fluorescence signals of the unknown condition against a known condition to measure how much the effective cross-section varied with the desired quantity. Such methods have been used to calibrate the effective two-photon absorption cross-section of disparate species (e.g., organic dyes [**118**] or two gaseous species [**86**]). In this case, the same method is used, but the ratio is taken against a different thermodynamic condition. As the methods employed in calibrating the LIF signal only require the relative effective absorption cross-section (see Chapter 4), these data will suffice for the experiments to follow.

The basic idea is that the ratio of two fluorescence signals represents the ratio between various excitation and thermodynamic quantities as expressed in Eq. 2A.12. This ratio is formally expressed as

$$\frac{\hat{\sigma}^{(2)}}{\hat{\sigma}^{(2)}_{ref}} = \frac{S_f}{S_{f,ref}}\left(\frac{E_{L,ref}}{E_L}\right)^2 \frac{A+Q}{A+Q|_{ref}} \frac{P_{ref}}{P} \frac{T}{T_{ref}} \frac{\chi_{Kr,ref}}{\chi_{Kr}} \qquad \text{2A.12}$$

Equation 2A.12 is simply the ratio of Eq. 2.1 at two different conditions and subsequently rearranged for the desired quantity. Note here that a number of the excitation properties (the temporal profile of the laser pulse, the excitation photon energy, and the beam area) have been neglected. Since the only excitation property that varied throughout a given run was the pulse energy, the explicit dependence on these terms was removed in the ratio.

In practice, this method required the use of nearly all data collected during the lifetime measurements – cell pressures (P, P_{ref}), temperatures (T, T_{ref}), fluorescence and laser signal traces, and the flow rates for computing the mixture mole fractions ($\chi_{Kr}, \chi_{\{Kr,ref\}}$). While most of these terms are self-explanatory, two require minor clarification. The fluorescence signal, S_f, is here defined as the temporal integral of the fluorescence signal seen by the PMT, kept in units of V-S (or mV-ns for more reasonable values). That is $S_f = \int_{-\infty}^{\infty} V_f dt$, where V_f is the voltage seen by the photomultiplier tube. In like manner, the laser energy was measured as the temporal integral of the incident photodiode voltage. During the runs, the energy of the incoming pulse was monitored to ensure only minor variations occurred, so even if this parameter was not accurately captured by the photodiode as described above, any egregious deviations were noted to ensure a more accurate measurement.

2A.5 – Calculation of Uncertainties

Estimating the uncertainties in all of the derived quantities in Chapter 2 required formulae to relate the calculated quantities to the data measured during the experiments. To accomplish this, uncertainty propagation formulae were first derived for the calculated quantities and subsequently related back to the measured quantities. An outline of the methodology is given below, while a comprehensive discussion of the formulae derived and used in the calibrations follows.

2A.5.1 – Uncertainty in Measured Quantities

The acquired data in these experiments is comprised of the fluorescence and laser waveforms, the stagnation temperature in the cell, the static pressure in the test cell, the stagnation pressure of the inflowing gas (if used), and the flowrates of specific gasses into the test cell. Each of these quantities has an associated uncertainty that arises from

unsteadiness in the measured quantity, experimental noise (dark current, shot noise, RF interference, etc.), and the accuracy of the instrument. To calculate the uncertainty in the measured quantities, which subsequently affect all the derived quantities expressed in the above sections, these different variations must be taken into account.

The basic tool utilized in this analysis is the standard uncertainty operator:

$$|\delta f(x_1, x_2, \dots, x_n)| = \left[\sum_{i=1}^{n} \left(\frac{\partial f}{\partial x_i}\delta x_i\right)^2\right]^{\frac{1}{2}} \quad \text{2A.13}$$

Eq. 2A.13 expresses the uncertainty of a given quantity as the length of a vector in the parameter space of a measured quantity, that vector being the gradient of the measured quantity with respect to all constitutive quantities. Here, the standard Euclidean norm is used as the metric of the vector length. Application of Eq. 2A.13 to all measured quantities requires that the quantity in question can be shown as the sum of its constitutive parts. To demonstrate this process, consider the flowrate of a given gas:

$$\dot{N} = \dot{N}_{actual} + \dot{N}_{inst} + \dot{N}_{rep} \quad \text{2A.14}$$

Eq. 2A.14 decomposes the flowrates into the component quantities that result from the uncertainties mentioned above. Here, the subscript $actual$ refers to the true molar flowrate of the gas, while the subscripts $inst$ and rep refer to the additional (either positive or negative) measured flowrate resulting from the accuracy of the instrument and non-repeatability of the measurement of the same quantity (accounting for unsteadiness and external interference), respectively. Application of the uncertainty operator (Eq. 2A.13) to Eq. 2A.14 yields the uncertainty for the measured molar flowrate:

$$\left|\delta\dot{N}\right| = \left[\delta\dot{N}_{inst}^2 + \delta\dot{N}_{rep}^2\right]^{\frac{1}{2}} \quad \text{2A.15}$$

From this analysis, the uncertainty in a given measurement of the flowrate is shown to be the quadratic sum of the corresponding individual uncertainties. The values used for the uncertainties come from different sources. The instrumentation uncertainties for a given

measurement are taken from the stated accuracy of the measurement device. Continuing with the example of a molar flowrate, the flow meters have a stated accuracy of 0.2 percent of full scale plus 0.8 percent of the reading. Therefore, for a measurement of 5.00 slpm on a 100 slpm flowmeter, the given uncertainty due to the instrument is 0.24 slpm. The uncertainty taken from repeated measurements (resulting from unsteadiness, RF interference, etc.) is taken to be two standard deviations of the measured quantity (e.g. $\delta\dot{N}_{rep} = 2\sigma_{\dot{N}}$). To complete this example, assume the standard deviation of the measurement is 0.25 slpm. This measurement would yield a repeated measurement uncertainty of 0.50 slpm, and an aggregate uncertainty for the measured flowrate of 0.55 slpm (i.e. $\dot{N} = 5.00 \pm 0.55$ slpm). This same basic procedure was followed for all measured quantities. The exception to this was the calculated fall time of the fluorescence signal, which replaced the instrumentation uncertainty with an uncertainty due to the fitting procedure described in Appendix 2B..

2A.5.2 – Uncertainty in Derived Quantities

Calculating the uncertainty in a derived quantity was accomplished in a similar fashion to that used in calculating those of the measured quantities. Again, Eq. 2A.13 is applied to the given quantity, but in this case the parameter space consists of individual measured quantities rather than the component uncertainties in a single measurement as expressed in Eq. 2A.14. An example of this procedure is given below.

Consider the derived quantity of the mole fraction of a given species n:

$$\chi_n = \frac{\dot{N}_n}{\dot{N}_n + \sum_{i \neq n} \dot{N}_i} \qquad \text{2A.16}$$

Eq. 2A.16 expresses the mole fraction as a ratio of the measured molar flow rate of species n to the sum of all molar flow rates. Applying the uncertainty operator to Eq. 2A.16 yields:

$$|\delta\chi_n| = \frac{1}{\dot{N}^2}\left[\left(\delta\dot{N}_n \sum_{i\neq n}\dot{N}_i\right)^2 + \sum_{i\neq n}\left(\dot{N}_n\delta\dot{N}_i\right)^2\right]^{\frac{1}{2}} \quad \text{2A.17}$$

where $\dot{N}$ is the total molar flow rate. As an example of the application of this example, consider the measurement of flow rate given in the previous section ($\dot{N} = 5.00 \pm 0.55$ slpm). For this example, let the gas in question be a trinary mixture with equal flow rates and uncertainties. Applying the operator in Eq. 2A.17 to any of the three species would give a measured value of $\chi_n = 0.33 \pm 0.03$.

2A.5.3 – Uncertainty in Fit Quantities

The results presented were also largely based on the curve-fitting of different quantities. These include not only the final curves for $q_n(T)$, but also more basic quantities such as the spontaneous emission rate (A) and the reference quenching rates. Calculating the uncertainty in a given fit was done by considering the uncertainty in the constitutive data points, which were generally calculated in the manner presented in the previous section. To calculate the bounds in the fit, two additional fits were performed on the data; one was done at the positive edge of the uncertainty bound, while another was done at the negative edge of the uncertainty bound. To clarify, consider a quantity such as the spontaneous emission rate (A), which was tabulated from the variable pressure runs. For a visual depiction, see Fig. 2.10b. Here, a plot of γ vs. P is shown; the nominal curve fit is given by the red line. To calculate the uncertainty bounds, additional lines (plotted in black) are fit to data points corresponding to $\gamma + \delta\gamma$ vs. $P - \delta P$ and $\gamma - \delta\gamma$ vs. $P + \delta P$. The value of the spontaneous emission rate is found by taking the value of the nominal fit at $P = 0$, while the uncertainty in this measurement comes from taking the maximum deviation of the two uncertainty fits from the nominal value. That is, $|\delta A| = \max(|A - A_1|, |A - A_2|)$. In similar fashion, uncertainty curves can be constructed for

the fits of $q_n(T)$, the difference being that instead of a singular value, the uncertainties are a function of the independent fit parameter.

2A.5.4 – Uncertainties in Pressure Dependent Quenching Rates and Cross-Sections

Consider first the pressure dependence of the spontaneous emission rate and quenching rate for pure krypton. As described in the section above, the uncertainty in the spontaneous emission rate is taken from the uncertainty bounds of the quenching rate. Specifically, the series of pressure dependent total decay rates are assigned an uncertainty based on the uncertainty in the fluorescence lifetime measurement. This uncertainty is expressed as

$$|\delta\gamma| = \gamma \frac{\delta\tau_f}{\tau_f} \qquad \text{2A.21}$$

Once this value has been given to each point, the upper and lower bounds thereby described are then each given a linear fit. Subsequently, the uncertainty in the quenching rate is described by taking the maximum of the deviation in slope between these two bounds and the best fit to the original data. Finally, the uncertainty in the spontaneous emission rate δA is taken to be the maximum of the deviation of these two bound from the best fit line.

A similar procedure was used for the other gases in question in these experiments. To begin, the specific quenching rate for one of these gases is defined by

$$q_n = \frac{1}{\chi_n}\left[\frac{Q}{P} - \sum \chi_i q_i\right], i \neq n \qquad \text{2A.22}$$

A set of data was constructed over multiple runs, and subsequently a set of measured quenching rates was constructed. The quenching rate was taken to be the mean of this set of data. There are several uncertainties to consider in these cases. First is the shot-to-shot variation seen within the data set constructed in this manner, quantified as the 2σ uncertainty bounds. Second are the uncertainties that arise from variations in composition

and the quenching rate of krypton previously measured. Applying the uncertainty operator to Eq. 2A.19 yields Eq. 2A.20.

$$|\delta q_n| = \left\{\left[\frac{q_n \delta \chi_n}{\chi_n}\right]^2 + \left[\frac{\delta Q}{\chi_n P}\right]^2 + \left[\frac{Q \delta P}{\chi_n P^2}\right]^2 + \left[\sum \frac{q_i \delta \chi_i}{\chi_n}\right]^2 + \left[\sum \frac{\chi_i \delta q_i}{\chi_n}\right]^2\right\}^{\frac{1}{2}}, \; i \neq n \qquad \text{2A.20}$$

Here, several of the terms can be neglected. Specifically, the second term and the fourth term represent quantities that the previous 2σ method already accommodates. The remaining uncertainties come from the measurement of the pure krypton quenching rate. The only omission is the uncertainty in the mole fraction which in this case was measured via the uncertainty in the initial partial pressures. With this set of uncertainties, the total uncertainty was taken to be the quadratic sum of all four terms, though the 2σ value was found to dominate the other sources.

The uncertainty in the quenching cross-section measurements follows from the quenching rate calculations. Since the quenching cross-section is defined per Eq. 2A.5 the uncertainty which follows is defined as

$$|\delta \sigma_i| = \sqrt{\frac{\pi k \mu_i T}{8}} \left\{\left(\frac{1}{2}\frac{\delta T}{T}\right)^2 + (\delta q_i)^2\right\}^{\frac{1}{2}} \qquad \text{2A.21}$$

Since the uncertainty in the temperature here is relatively small (taken to be the 2σ bound from the repeated measurements), the percentage uncertainty between the quenching cross-section and the quenching rate is virtually identical.

2A.5.5 – Uncertainties in Temperature Dependent Quenching Rates and Cross-Sections

The procedure for calculating uncertainties in the temperature dependent fits is very similar to that of the pressure-dependent fits. The only exception is that the uncertainty in the temperature measurement needs to be considered in the fitting procedure rather than that of the pressure. In the case of the high-temperature runs (i.e.,

$T > T_{ref}$) this was a straightforward 2σ uncertainty taken from repeated measurements at (nominally) the same temperature, taken from the total temperature probe. The low temperature runs were far more complicated in that the static temperature was calculated based on the pressure measurements and stagnation conditions rather than directly from the temperature probe. In these cases, the temperature was calculated using the isentropic flow relations, wherein the Mach number and ratio of specific heats were calculated from the various component measurements taken during the run. Eqs. 2A.22 through 2A.29 summarize these equations and their respective uncertainties:

$$T = T_o \Big/ \left(1 + \frac{\gamma_{mix} - 1}{2} M^2\right) \tag{2A.22}$$

$$|\delta T| = T \left\{ \left(\frac{\delta T_o}{T}\right)^2 + \left(\frac{1}{2} \frac{M^2}{1 + (\gamma_{mix} - 1)/2 \ M^2} \delta\gamma\right)^2 + \left(\frac{(\gamma_{mix} - 1)M}{(1 + (\gamma_{mix} - 1)/2 \ M^2} \delta M\right)^2 \right\}^{\frac{1}{2}} \tag{2A.23}$$

$$\gamma_{mix} = \frac{\sum \chi_i c_{p,i}}{\sum \chi_i c_{v,i}} = \frac{c_{p,mix}}{c_{v,mix}} \tag{2A.24}$$

$$|\delta\gamma| = \left[\sum \left(\frac{c_{p,i} c_{v,mix} - c_{v,i} c_{p,mix}}{\left(c_{v,mix}\right)^2} \delta\chi_i \right)^2 \right]^{\frac{1}{2}} \tag{2A.25}$$

$$M = \left\{ \frac{2}{\gamma - 1} \left[\left(\frac{P_o}{P}\right)^{\frac{\gamma_{mix} - 1}{\gamma_{mix}}} - 1 \right] \right\}^{\frac{1}{2}} \tag{2A.26}$$

$$|\delta M| = \left\{ \left[\frac{1}{M(\gamma_{mix}-1)} \left(\frac{1}{\gamma_{mix}^2} \left(\frac{P_o}{P} \right)^{\frac{\gamma_{mix}-1}{\gamma_{mix}}} \ln\left(\frac{P_o}{P} \right) - \frac{M^2}{2} \right) \delta\gamma_{mix} \right]^2 \right. \quad \text{2A.27}$$
$$+ \left[\frac{1}{\gamma_{mix} M} \left(\frac{P_o}{P} \right)^{\frac{\gamma_{mix}-1}{\gamma_{mix}}} \frac{\delta P_o}{P_o} \right]^2$$
$$\left. + \left[\frac{1}{\gamma_{mix} M} \left(\frac{P_o}{P} \right)^{\frac{\gamma_{mix}-1}{\gamma_{mix}}} \frac{\delta P}{P} \right]^2 \right\}^{\frac{1}{2}}$$

$$\chi_n = \frac{\dot{N}_n}{\dot{N}_n + \sum \dot{N}_i} \quad \text{2A.28}$$

$$|\delta\chi_n| = \chi_n \left\{ \left[(1-\chi_n) \frac{\delta\dot{N}_n}{\dot{N}_n} \right]^2 + \left[\sum \frac{\delta\dot{N}_i}{\dot{N}_n + \sum \dot{N}_i} \right]^2 \right\}^{\frac{1}{2}} \quad \text{2A.29}$$

Here, T is the static temperature, T_o is the total temperature, γ_{mix} is the ratio of specific heats for the mixture of gases, M is the Mach number, P_o is the total pressure, P is the local static pressure, χ_i is the mole fraction of species i, and $\dot{N}_i$ is the molar flow rate of species i. The uncertainty in T_o, P_o, and P were taken to be the 2σ bounds taken from repeated measurements along with the inherent instrument accuracy. In this manner, the uncertainty in the temperature and the quenching rate were used to perform a fit on the upper and lower bound in much the same manner as the pressure fits.

2A.5.6 – Uncertainty in the Relative Effective Two-Photon Absorption Cross-Section

The calculation of the uncertainties in the effective absorption cross-section includes the uncertainties from almost all measured quantities. Application of the uncertainty operator to Eq. 2A.15 yields

$$\left|\delta\left(\frac{\hat{\sigma}^{(2)}}{\hat{\sigma}^{(2)}_{ref}}\right)\right| = \frac{\hat{\sigma}^{(2)}}{\hat{\sigma}^{(2)}_{ref}}\left\{\left(\frac{\delta S_f}{S_f}\right)^2 + \left(2\frac{\delta E_L}{E_L}\right)^2 + \left(\frac{\delta\gamma}{\gamma}\right)^2 + \left(\frac{\delta P}{P}\right)^2 + \left(\frac{\delta T}{T}\right)^2 + \left(\frac{\delta\chi_{Kr}}{\chi_{Kr}}\right)^2\right\}^{\frac{1}{2}} \quad \text{2A.30}$$

Much like the fits for temperature and pressure in the quenching rates, the uncertainty in the relative effective cross-section was used for creating the upper and lower bounding fits for the final data.

Appendix 2B: Fluorescence Lifetime Deconvolution Algorithm

In collecting the data for measurement of the fluorescence lifetime of krypton, the ideal situation would be an infinitesimally short pulse of exciting radiation. With such an application, the fluorescence in the gas would be excited impulsively, and purely the rise and decay of the fluorescence could be observed. Practically, this situation is not attainable, and thus the data must be corrected for the finite width of the laser pulse.

2B.1 – Background

Strictly speaking, this problem is representative of a deconvolution process. That is, what is observed as the fluorescence signal $P_f(t)$) is the temporal profile of the laser pulse ($P_L(t)$) convolved with the impulse response of the fluorescence ($I_f(t)$), or

$$\Big(P_L(t) * I_f(t)\Big) = P_f(t) \qquad \text{2B.1}$$

Posed in this fashion, the Fourier transform of $I_f(t)$ in Eq. 2B.1 ($\mathcal{F}\{I_f\}$) represents a transfer function between the temporal profile of the laser pulse and the temporal profile of the fluorescence. It can be thought of as the impulse response of the fluorescence.

A few problems arise when trying to evaluate $I_f(t)$. In principle, if $P_L(t)$ and $P_f(t)$ are known, then it should be possible to evaluate $I_f(t)$ using deterministic deconvolution if the form of $I_f(t)$ is known. In frequency space, the deconvolution could be done by simple division. However, attempting to directly evaluate this function with the raw data would likely yield unsatisfactory results. This observation was due to the fact that the two known quantities are actual experimental data with a non-negligible noise component. Since the aforementioned method of deconvolution is inherently noise-enhancing, it is not surprising to find that the procedure does not perform well. Thus, another method must be used.

With the deconvolution problem described above, two paths could be taken to solve for the impulse response. First, the noise issue could be overcome by fitting analytical functions to the laser and fluorescence pulses ($P_L(t)$ and $P_f(t)$, respectively). Doing so would allow for the direct deconvolution described above, since the noise is effectively removed from the signals by the fitting procedure. The second solution method would be to iteratively solve for the fluorescence impulse response. In this methodology, the laser and fluorescence pulses act as the inputs to the solution procedure. A form for the fluorescence impulse response is assumed, which is then iteratively convolved with the laser pulse profile until its adjustable parameters converge to the true fluorescence signal observed in the experiment. The second method was employed in the present studies.

2B.2 – NUMERICAL METHOD

To begin the deconvolution procedure a functional form for I_f must be assumed *a priori*, and a least-squares fitting algorithm employed to optimize the fit parameters of the impulse response. Since the process being described by the impulse response is a general exponential rise and decay, the functional form should incorporate both of these behaviors. For these experiments the generalized form of I_f was assumed to be

$$I_f(t) = H(t-\tau_1)\left(1-\exp\left(-\frac{t-\tau_1}{\tau_2}\right)\right)\left(1-H(t-\tau_3)+H(t-\tau_3)\exp\left(-\frac{t-\tau_3}{\tau_4}\right)\right) \qquad \text{2B.2}$$

where $H(t-\tau)$ is the Heaviside function active at $t=\tau$. Eq. 2B.2 has four separate fit parameters. τ_1 is an initial shift in the exponential rise component, while τ_3 is a shift in the exponential decay component. τ_2 and τ_4 are the time constants for the exponential rise and decay, respectively. An example of this family of functions can be seen in Fig 2B.1 below, with a rise and fall time of 1 ns and 15 ns, respectively. In posing the actual deconvolution problem, an additional fit parameter is included, τ_5, which allows for a

general shift in the overall fluorescence impulse function. In this manner, noise or a small ledger before the laser and/or fluorescence pulse does not interfere with the fitting procedure. The location of this additional fit parameter is given in Eq. 2B.3.

$$\left(P_L(t-\tau_5) * I_F(t-\tau_5)\right) = P_F(t) \qquad \text{2B.3}$$

Eq. 2B.3 also suggests that performing the deconvolution over the entire recorded time interval (in this case 2 μs) will lead to undue computational time resulting from the large number of points that need to be included in the fit. As a result, an additional algorithm is utilized that finds and isolates the fluorescence and laser pulses from the background. This procedure takes the individual signal traces from the photodiodes (laser) and PMT (fluorescence) and finds the peak signal in each. To ensure accuracy, the peak had to be at least 5 times the RMS background noise in that particular trace. Once the peak is located, the algorithm scans down the rising and falling edges of the pulse until it comes within some tolerance of the background noise floor (typically within 1×10^{-4} on the rising edge and 1×10^{-3} on the falling edge). Once these bounds are located, this portion of the pulse is isolated, rescaled so that peak min-to-max magnitude is equal to unity, and extracted for use in the overall deconvolution procedure. As a final check on accuracy, the approximate rising and falling edge time constants are compared to the original signal to ensure that there was no inadvertent stretching or compression of the pulse when the signal was rescaled. This procedure is illustrated in Fig. 2B.2 below. The overall deconvolution algorithm is described in Fig. 2B.3 below. This procedure also has the advantage of handling any and all issues related to scaling that are incurred in the simple linear fit procedure.

2B.3 – Quantification of Accuracy

While conceptually this algorithm is necessary, there are some practical limitations on its utility. These limitations stem from three problems: 1) fitting errors incurred due to noise in the signals, 2) fitting errors incurred due to non-uniqueness of solutions, and 3) fitting errors due to the finite width of the laser pulse. To address each of these problems, a battery of tests was performed on the deconvolution algorithm. In this assay, an actual laser pulse profile was convolved with a theoretical impulse response. The resulting synthetic fluorescence signal was then run through the deconvolution algorithm to test its accuracy in recreating the theoretical impulse response.

Noise is the biggest area of concern in these studies; the fluorescence was generally of low signal amplitude, and the resulting signal to noise ratios suffered accordingly. To assess the effects of different levels of noise, an array of fluorescence responses ranging in time decay times from 0.4 ns to 1000 ns was used as a baseline. Then, a randomly generated Gaussian noise signal was superimposed on the synthetic fluorescence signal. This noise was then varied such that the RMS amplitude of the noise ranged from an SNR (relative to the peak amplitude of the signal) of 10^4 to 10. Fig 2B.4 below shows the effects of this noise at these different levels. In Fig 2B.4, τ_f is the theoretical fall time of the fluorescence (τ_4 in Eq. 2B.2), while $\tau_{f,las}$ is the measured fall time of the laser pulse. Finally, τ_c is the fall time of the fluorescence, which has been calculated through the deconvolution algorithm described above. Thus, the vertical axes in Fig 2B.4 represent a percent error, while horizontal axis is indicating how long the theoretical lifetime is relative to the laser fall time.

A few notes regarding the solution parameters. First, the lower and upper bounds for the time solver are set to two times the smallest resolvable time in the measurement system (0.4 ns) and a time far beyond the expected natural fluorescence lifetime (100 ns), respectively. Note in Figure 2B.4, the response to this upper limit, regardless of the noise level, is to cause a step decrease in the accuracy of the solver. While this is to be expected, it is a reasonable check that the solver is behaving correctly. As the fluorescence lifetime increases relative to the laser fall time (increasing direction on the x-axis), there is a general trend toward increasing accuracy. Specifically, the discrepancy between the calculated and theoretical fall times decreases. This improvement is due largely to the increased disparity between the laser fall time and the fluorescence. That is, as the impulse response becomes less rapid, the overall contribution of the laser pulse to the convolution is diminished. The percent error ranges from nearly 10 percent at the shortest resolvable lifetimes, decreasing by nearly two orders of magnitude as the upper limit of the solver is reached. In the context of the fluorescence experiments, the fluorescence lifetimes ranged from (approximately) 5 to 15 times the laser fall time, to give some context on where the errors fall.

With regard to the noise, the effects are seen to minimal down to a signal-to-noise ratio (SNR) of 100. That is, the general trend and magnitude of the deviation is preserved. Various noise-reduction filters are in place to help mitigate its effect when processing the signal, so this lack of deviation is to be expected. For all time scales of relevance in the current study (7 to 30 ns approximately), the approximate error resulting from noise was below 1 percent across the board. The only exception to this is the case

with the highest noise levels (SNR = 10), which saw errors climb to approximately 10%. As explained in the previous section, signals with this degree of noise were rejected *a priori*, so it can be expected that the fitting errors resulting from noise were below 1 percent for all studies.

One of major concerns with this fitting procedure is the large degree of uncertainty introduced by having 4 different constants controlling the shape of the fluorescence impulse response. That is, the possibility exists that there is not a unique solution for a given deconvolution problem. A brief illustration of this can be seen in Fig 2B.5, where two different initial conditions were used in the solution procedure. The axes in Fig. 2B.5 are the same as in Fig 2B.4. While this view of the error may exaggerate the effect to some extent, it is apparent that at least two separate solutions to the same problem are possible over a wide range of conditions. A similar phenomenon is possible when the bounds of the solver are changed. The correct solution can be obtained with proper rigor in the solution selection process. Referring to the operational flow chart in Fig 2B.3; first, a simple metric of the fit quality needs to be utilized. In this case, the basic R^2 criterion is used as a basis for rejection. By observation, the threshold must be exceptionally high to prevent false fits, in this case in excess of 0.995. In most instances this criterion is sufficient to keep the fits accurate, but in some cases (particularly with the highest acceptable noise limits) an extra filtering step was necessary. The second filtering step used the fit fluorescence impulse response to calculate the residual noise in the original signal. Subsequently, the RMS value of this noise was calculated and compared to a threshold based on the integrated fluorescence signal. Typically, if there was a fit that

was able to get through this procedure, the fit was considered optimized. Finally, all fits were visually checked to ensure the fit was converged.

The third source of uncertainty arises from the actual width and decay time of the laser pulse. Though not of particular concern for these experiments, this effect could manifest itself if longer exciting pulses were used. To examine this effect, the true laser pulse profile was numerically stretched in time to increase the effective fall time, $\tau_{f,las}$, and an examination of the solver accuracy was conducted. Stretching the laser pulse in this manner allows for shorter relative fluorescence decay times without dropping below the lowest resolvable time scale in the system (0.4 ns). The results of this study are shown in Fig 2B.6. Much like what was observed in the studies shown in Fig 2B.4, the accuracy remains high for fluorescence lifetimes above 10 percent of the laser pulse fall time, with errors of order 10^{-3} to 10^{-2} up to the solver upper limit. However, the interesting thing to note is that, regardless of the laser pulse fall time, the error begins increasing dramatically for lifetimes below 10 percent of the laser fall time. Thus, from this analysis a practical limitation on the solver was found. If the lifetimes are very short and/or the fall time of the laser pulse is quite long, the error obtained through the fitting procedure begins increasing dramatically with lifetimes shorter than 10 percent of the laser fall time. Note that the SNR used in these studies was 100.

2B.4 – CONCLUSIONS

An iterative deconvolution algorithm was developed for use in extracting the fluorescence impulse response desired in the quenching experiments. An assessment of

its accuracy show that for signal-to-noise ratios in excess of 10, the overall uncertainty imparted by the solver was on the order of 1 percent. Additionally, the sensitivity to the initial and boundary conditions of the solver was explored. This study elucidated the need for the rigorous filtering of solution results described in the general operational procedure. Finally the effect of the laser pulse width and fall time was investigated, showing that the accuracy of the solver remained within 10 percent for fluorescence decay times greater than 10 percent of the laser fall time.

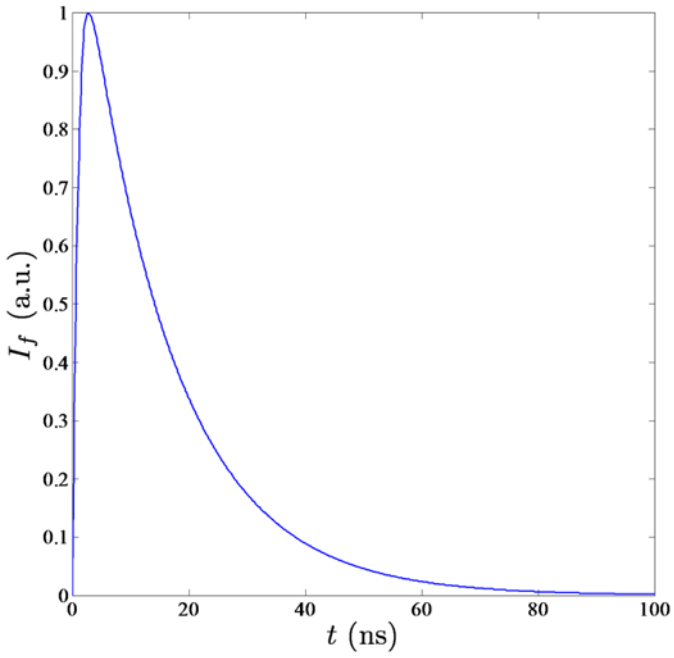

Figure 2B.1: Sample pulse generated by deconvolution function

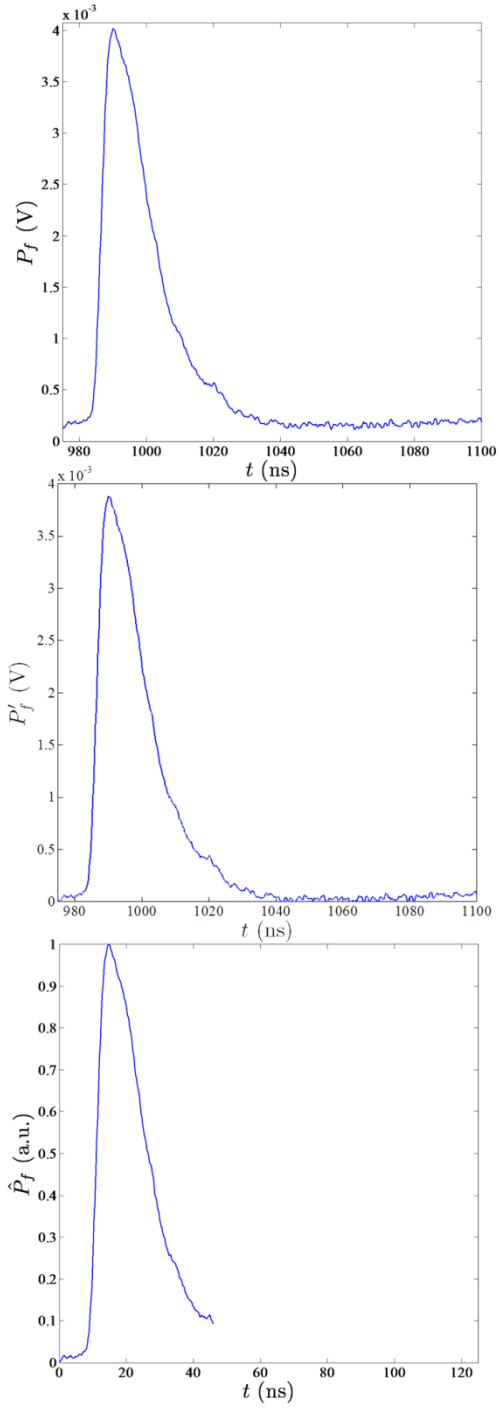

Figure 2B.2: Example of pulse conditioning used in deconvolution algorithm. Top – original signal, middle – background-subtracted signal, and bottom – conditioned signal

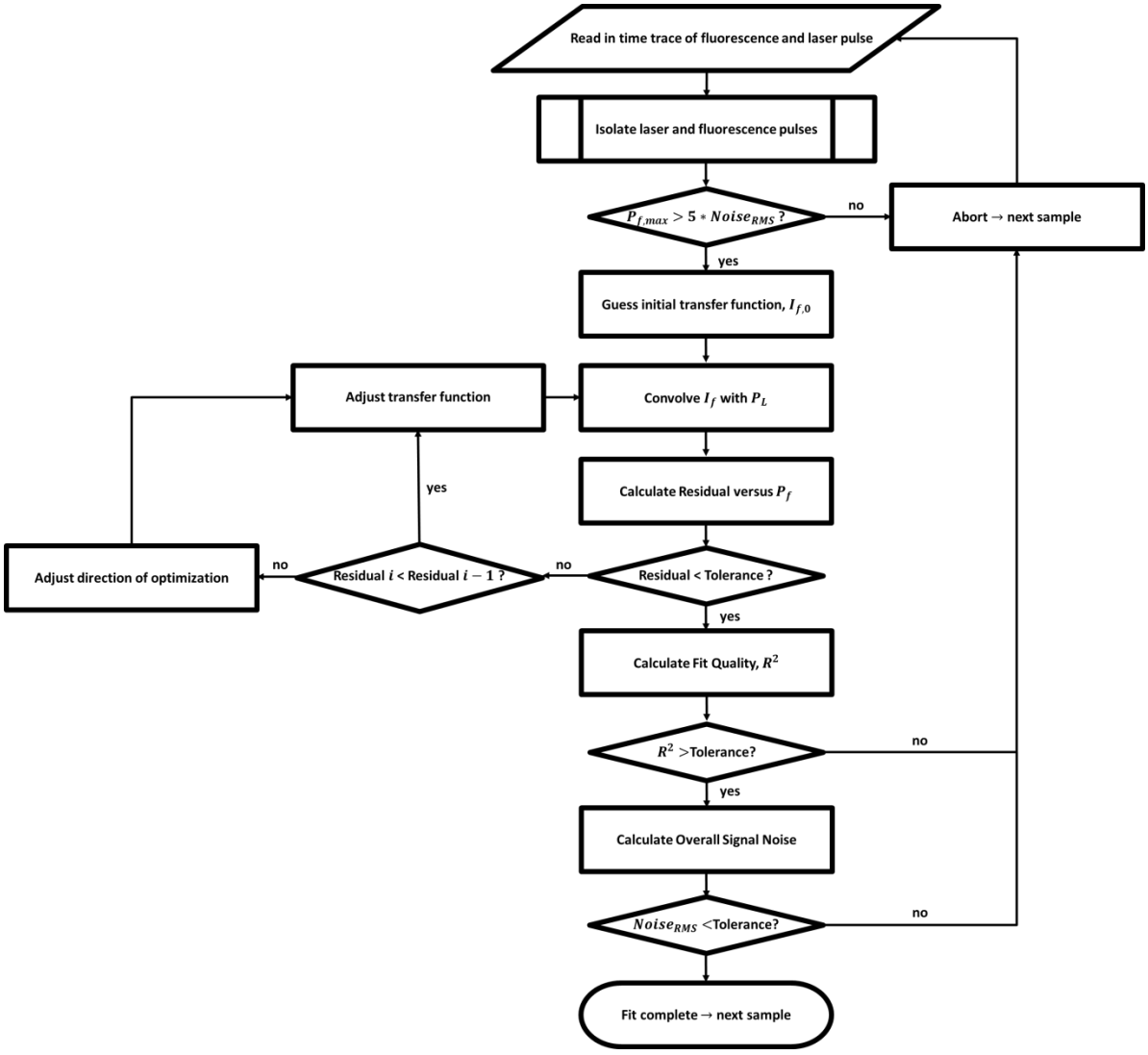

Figure 2B.3: Flowchart of functionality of deconvolution algorithm

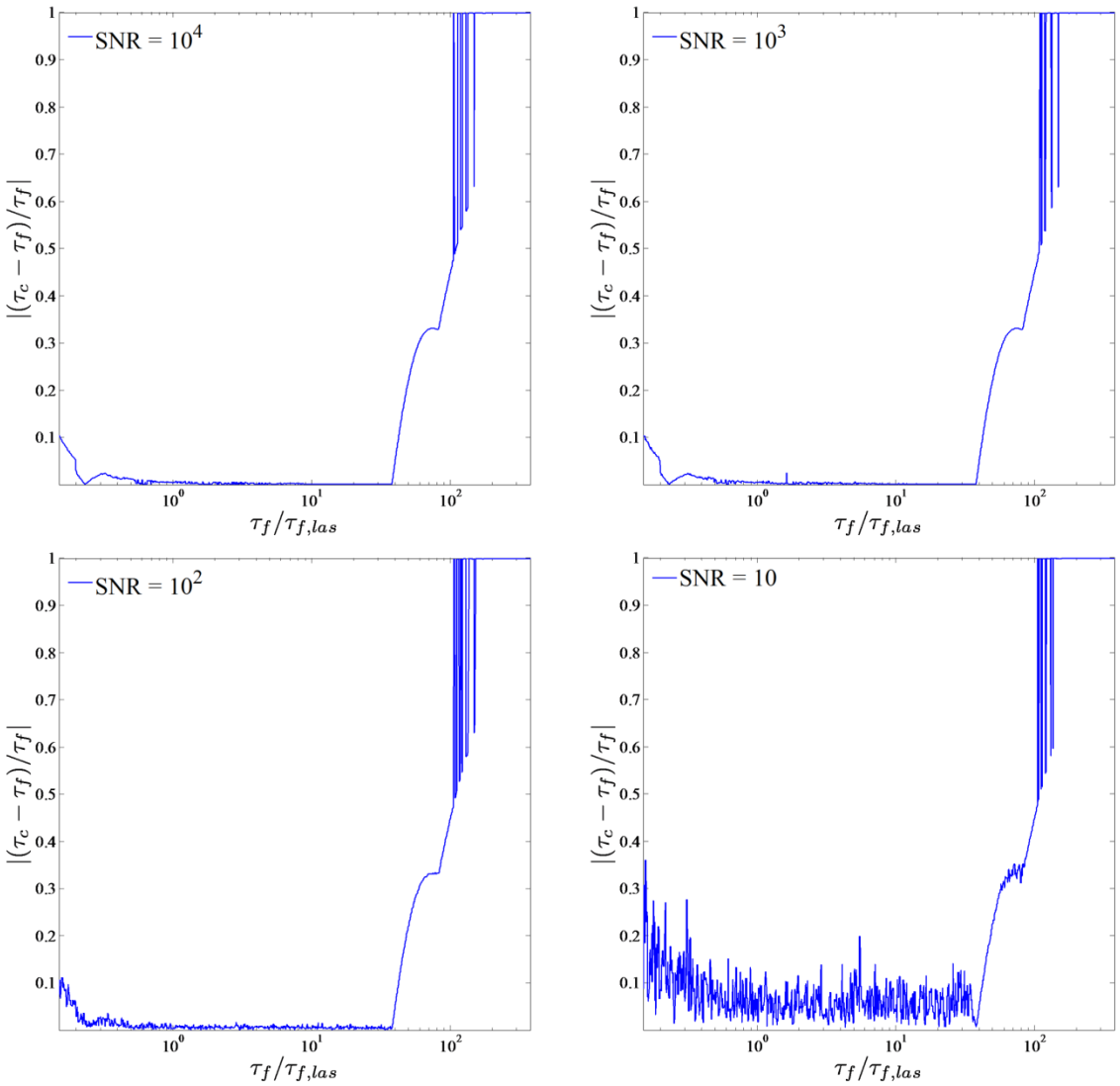

Figure 2B.4: Effect of different noise levels on accuracy of deconvolution algorithm

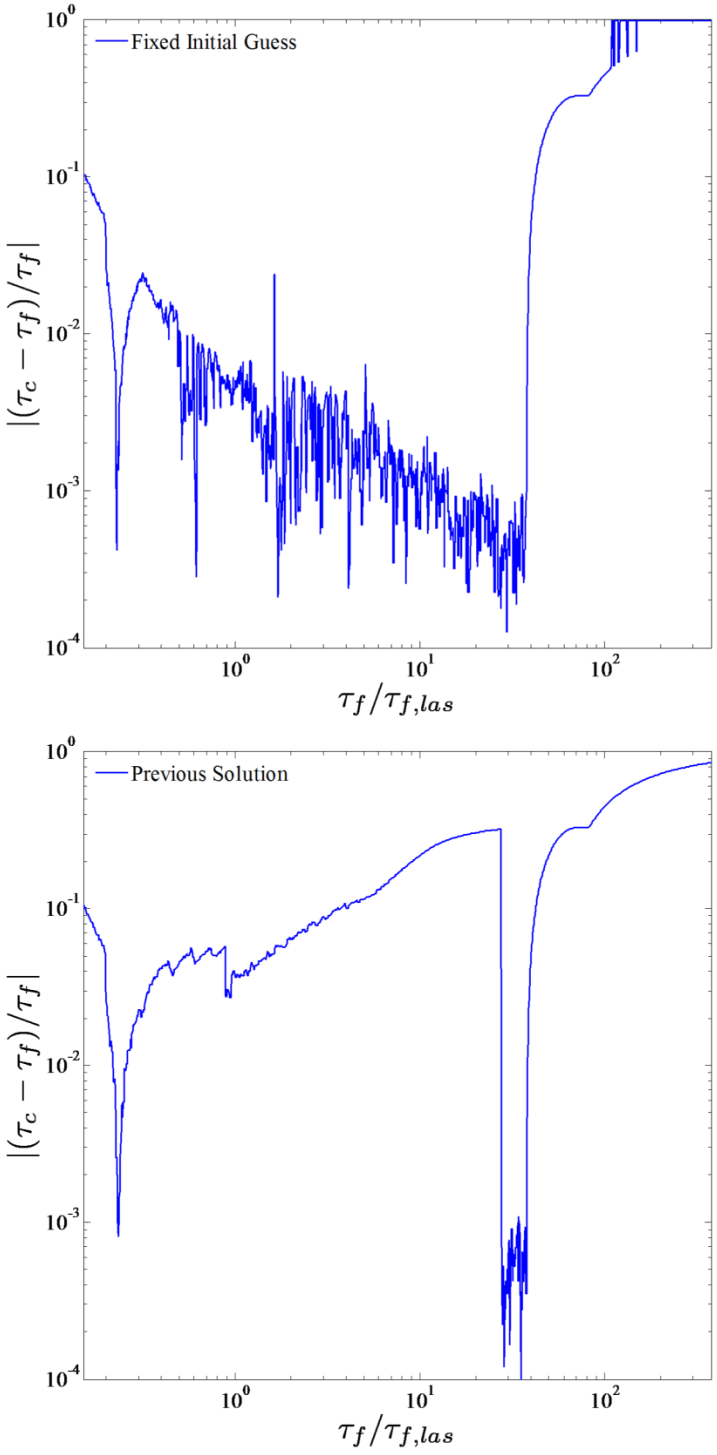

Figure 2B.5: Effect of initial condition on accuracy of solver. Top – fixed initial guess and bottom – utilizing solution of previous sample

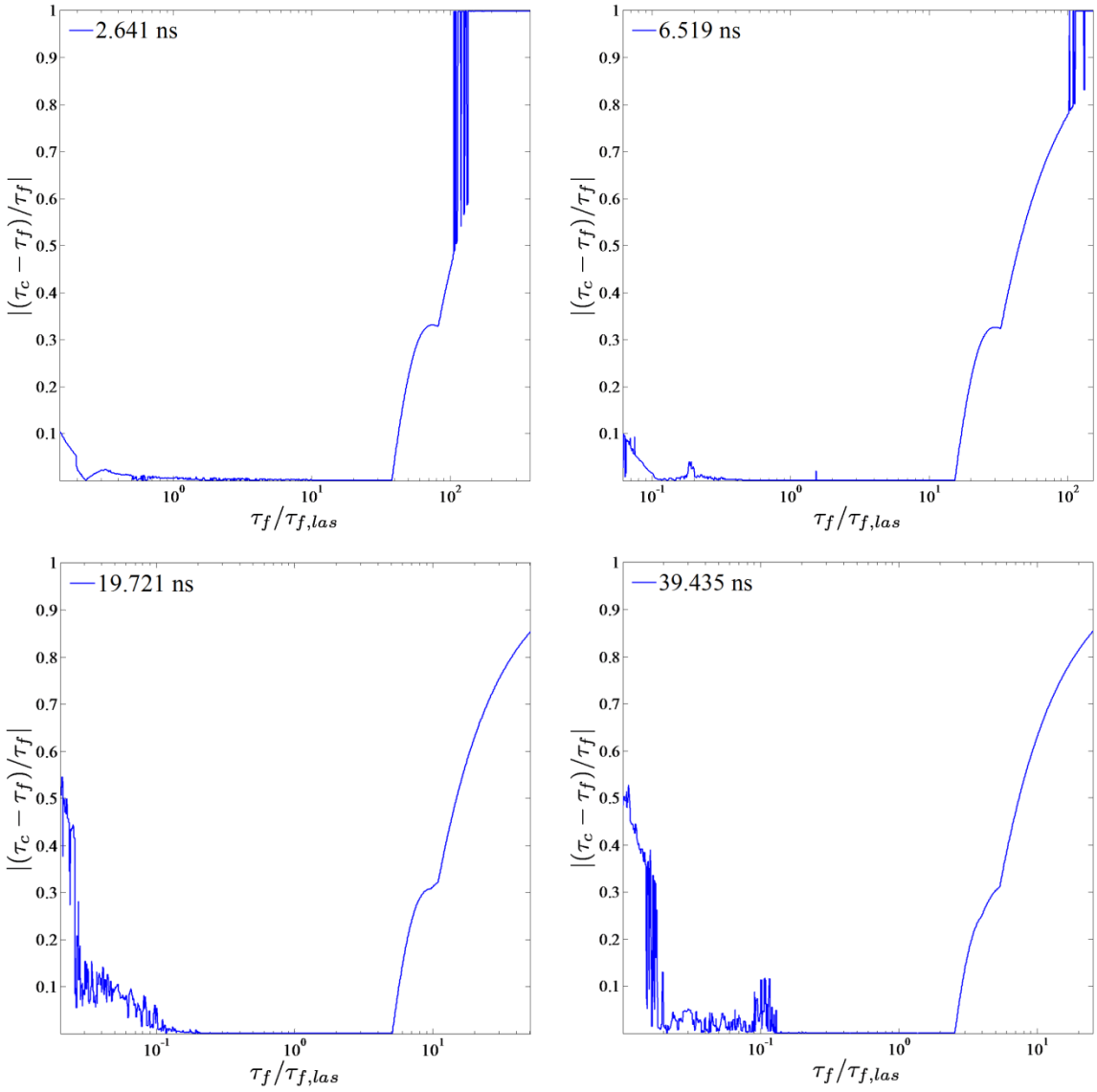

Figure 2B.6: Effect of laser pulse fall time on accuracy of solver

Appendix 3A – Particle Response Assessment

This appendix documents the work done to assess the effective response time of the particles used for seeding the flow for PIV performed in Chapters 3 and 4.

3A.1 – Introduction

One of the fundamental problems encountered when trying to perform particle image velocimetry is that its implementation must faithfully reproduce the flowfield of interest. This effect can manifest in two ways. First, adding particles to the flowfield can fundamentally change the character of the flow. In the case of relatively low particle loading, the principal area where this effect is observed is in the turbulence of the flow. That is, the particles, being of finite size and mass, can act as a physical damper to rapid changes in the flow properties. Thus the turbulence, which operates over a wide range of time scales, is the dominant receptor of this effect. Should the particle loading become exceptionally high, it is also possible for the mean field to be effective, though this effect far exceeds to acceptable limits for use in PIV.

The second effect is related to the inertia that the particles possess; even if the particles do not directly affect the flow, the inertia of the particles can lead to them not following the flow properly. That is, if there is a sudden change in the direction or velocity of the flow, the ability of the particle to immediately respond to the changes in the flow is influenced by the inertia of the particle, effectively limiting the range of time scales to which the particles can respond. Thus, as the PIV technique relies on the particle velocity rather than the fluid velocity directly, this effect can cause errors to be incurred by the measurement technique.

Typically, the first of the aforementioned effects is considered negligible. A summary of work on particle-laden flows given by Crowe, et al. [**119**]. In essence, below

a relatively large particle loading, either in terms of mass or volume, the feedback of the particles to the flow can be considered negligible. This assumption has in large part been confirmed experimentally by Humble et al. [**120**]where the freestream turbulence intensity in their facility was found to vary by only 0.2 percent. In their experiments, the particles were used to seed the freestream of a Mach 2.07 flow and the undisturbed turbulence intensity was around 1 percent. Likewise, the boundary layer thicknesses ($\delta_{99}, \delta^*, and\ \theta$) and friction velocity were unaffected.

The second effect is a much more pronounced problem, particularly in supersonic flows. The reason for this is certainly the presence of turbulence, but also due to rapid velocity changes associated with wave structures. This issue of particle lag has been investigated experimentally by a number of authors [**120**] [**121**] [**103**] [**122**] [**123**]. In general, the response of the particles is tested by observing the velocity change across a step change in velocity. Typically this entails passing the particles through an oblique shockwave. By tracking the velocity seen through PIV in this flowfield, an effective particle response time can be calculated. This general methodology has been followed herein and is detailed below.

3A.2 – Experimental Setup

This section details the experimental setup utilized in the particle response assessment. Since the details of the PIV system have been detailed elsewhere, this section will only cover the specific details of these experiments.

3A.2.1 – Test Facility

The facility used in these experiments is a modified version of the Mach 3 tunnel utilized for the experiments found in Chapters 3 and 4. The facility has been modified to remove the splitter plate; in this case, a new nozzle block was installed to maintain the

same freestream Mach number. The plenum pressure used in these experiments was 156 kPa, while the freestream velocity was found to be around 630 m s^{-1}. A shock generator (7 degrees) was installed in the test section to produce the desired oblique shock.

3A.2.2 – PIV System

The PIV system (lasers and cameras) have been detailed elsewhere in this document (see Chapter 3). In the present experiments, planar PIV was utilized in which the laser sheet was brought into the test section through the ceiling window. The PIV field of view is detailed in Fig 3.4, capturing the shock while avoiding any reflections from the shock generator. The temporal separation between pulses was set to 0.85 μs. PIV raw data was processed using DaVis v.7.2 [**124**], while all post-processing was done using custom MATLAB scripts.

3A.3 – NUMERICAL METHODOLOGY

This section details three different aspects of the data post-processing procedures: the calculation of the shock-normal velocities, the calculation of the particle time constant, and the calculation of the effective particle size.

3A.3.1 – Calculation of shock-normal velocities

There were two difficulties faced in trying to calculate the shock-normal velocities in these experiments. First, the flow through the test section had a series of wave structures reflecting from the nozzle. Some of these waves can be seen in Figs. 3A.1 and 3A.2 below. The consequence is that the shockwave is, in some areas a far more complex interaction than desired. Thus, judicious selection of the sampling location was required. The second (and related) problem is that the flow isn't aligned with the camera axis. Thus, the absolute shock angle is different from the angle measured relative to the image axis.

To get around these issues with the highest precision, an iterative method was used to optimize the shock angle. This procedure worked by fixing a point behind the shockwave then sweeping a numerical probe of length 10 mm through the field in finely incremented angles. Subsequently, each of these angles was considered to be the shock-normal angle, and the shock-normal velocity computed. Numerically,

$$U_N = U_{total} \sin(\theta_i - \theta_f) \qquad \text{3A.1}$$

Here, U_N is the shock-normal velocity, U_{total} is the total velocity calculated as $\{u^2 + v^2\}^{\frac{1}{2}}$ using the image axes, θ_i is the current angle of the iteration, and θ_f is the angle of the flow relative to the image axis. Once these values have been tabulated, the standard deviation of the velocity in the regions before and after the shock were calculated. To clarify, the value being calculated was not the RMS of the entire set of data, but rather the standard deviation of the few points before and after the shock. The correct angle was taken to be the point where the RMS velocity in these regions was found to be a minimum. The idea behind this method is that when the standard deviation of the velocity in these regions is a minimum, the velocity before and after the shocks is the closest it could be to a constant. A few samples of these velocity profiles are seen in Fig 3A.3.

3A.3.2 – Calculation of particle time constant

After the shock-normal velocity has been determined, the data were non-dimensionalized for fitting of an exponential; this scaling is expressed as

$$\widehat{U}_N = \frac{U_N - U_2}{U_1 - U_2} \qquad \text{3A.2}$$

U_1 is taken to be the pre-shock normal velocity, while U_2 is taken to be the final velocity post-shock. Apart from this non-dimensionalization, there are two effects that have to be considered. First is the form of the function to fit to the decay. In general this is an exponential decay of the form, $\exp(-t/\tau)$, which requires that the spatial coordinate be

transformed into a temporal coordinate. This transform is accomplished by dividing the spatial coordinate by the local fluid velocity. In that way, the time coordinate appears dilated after the shock since the velocity is inherently lower. To accommodate the transform and account for the constant-velocity condition both before and after the shock, the following function was used for fitting:

$$\widehat{U}_N = \big(1 - H(t-\tau_1)\big) + \big(H(t-\tau_1)\exp(-(t-\tau_1)/\tau_2) \qquad \text{3A.3}$$

Here $H(t-\tau)$ is the Heaviside function which activates at $t=\tau$, and the particle response time is τ_2. It should be noted that if the velocity following the shock was not constant as it is in these experiments, a more sophisticated space-time transform would be required. An explanation of this transform can be found in [**116**].

The second point which needs consideration in the fitting procedure is the averaging effect of PIV. The velocity vectors obtained through PIV represent an average over the interrogation volume. As such, the fitting procedure described above will not be able to accurately recreate the falling slope without giving this effect consideration. See [**103**] for a discussion of this spatial averaging effect. In order to mimic the averaging effect, a spatial filter was convolved with the decay function during the fitting to ensure its effect was considered during the least-squares fitting process. This filter was assumed to be a uniform filter with a width equal to one of the PIV interrogation volumes. To perform the fit, a simple least-squares algorithm was employed much like that used in Chapter 2 for the deconvolution procedure (see appendix 2B for details).

3A.3.3 – Calculation of Effective Particle Diameter

Once the fall time was found from the exponential fit, the particle size could be calculated based on theoretical models of the particle response behavior. There are a number of ways of going about this modeling. The most appropriate and widely used

model for the current flow regime is a modified version of the Stokes drag law given by Melling [**125**], which accounts for the effects of gas rarefaction on the response time:

$$\tau_p = \frac{\rho_p d_p^2}{18\mu}\left(1 + 2.7\, Kn_p\right) \qquad \text{3A.4}$$

This inclusion of the Knudsen number is done to account for the fact that there is slip at the surface of the particle under rarefied conditions. The Knudsen number was calculated by the method of Schaaf, et al. [**126**], where:

$$Kn_p = 1.26\gamma_{air}^{1/2} M_{\Delta V}/Re_{\mathrm{d}} \qquad \text{3A.5}$$

Here, γ_{air} is the ratio of specific heats for air, $M_{\Delta V}$ is the slip Mach number, defined as $(U_1 - U_2)/(\gamma R T_2)^{1/2}$, and Re_d is the Reynolds number based on the slip velocity and particle diameter. Utilizing the perfect gas law and the respective definitions of the Reynolds number and slip Mach number, Eq. 3A.6 simplifies to

$$Kn_p = \frac{1.26\mu(RT_2)^{1/2}}{P_2 d_p} = \frac{\lambda}{d_p} \qquad \text{3A.6}$$

In Eq. 3A.6, λ is the mean free path for the gas at state 2 after the shock.

3A.4 – RESULTS

The mean flowfield can be seen in Figs 3A.1 and 3A.2 below; this mean was taken over 750 samples to ensure sufficient convergence. These mean velocity components show the wave structures emanating from the nozzle block. These can be seen intersecting the primary oblique shock around $x = 11$ mm and $x = 24$ mm. The effect on of these interactions is apparent, causing distorted velocity fields behind the primary oblique shock. To avoid these complex interactions, the sampling location for the particle response assessment was anchored at ($x = 21.76$, $y = 5.616$).

The velocity profile seen across the shock is detailed in Figure 3A.4. Here the PIV data is compared to the fit velocity profile and the theoretical fluid velocity through this region. A few notes; the fit is seen to match the experimental data very closely. This

lends credence to the spatial filtering effect described above, particularly by observing the slope of the initial fall. From this fitting procedure, the characteristic particle response time was found to be 2.098 μs. This response time corresponds to a characteristic frequency of roughly 477 kHz.

From this characteristic response time, the effective particle size can be calculated as described above. For these studies, the particles used were atomized olive oil. While the bulk density varies from source to source, the density generally falls in the range of 800 to 950 kg m^{-3}. Computing the characteristic diameter gives a range from 0.284 μm to 0.359 μm for the same density range indicated above. A few notes about this procedure. First, the calculated shock-normal Mach number was found to be 1.123 using the ratio of velocities across the shock, with corresponding temperature and pressure ratios of 1.080 and 1.305, respectively. These ratios admitted a post-shock density of 0.160 kg m^{-3} and viscosity of 7.864×10^{-6} Pa-s. Furthermore, the calculated slip Mach number for this regime was 0.35 and the Reynolds number ranged from 0.434 to 0.512, well within the Stokes regime upon which the theoretical model is constructed.

3A.5 – CONCLUSIONS

From this analysis, fairly rigorous bounds on the temporal and/or spatial resolution of the PIV measurements have been set by performing a particle response assessment. Through the use of an oblique shock generator to create a step change in velocity within the flowfield, the effective response time for the particles used in the PIV seeding has been discerned. Furthermore, by utilizing a modified version of the Stokes drag law, an effective particle diameter has been calculated.

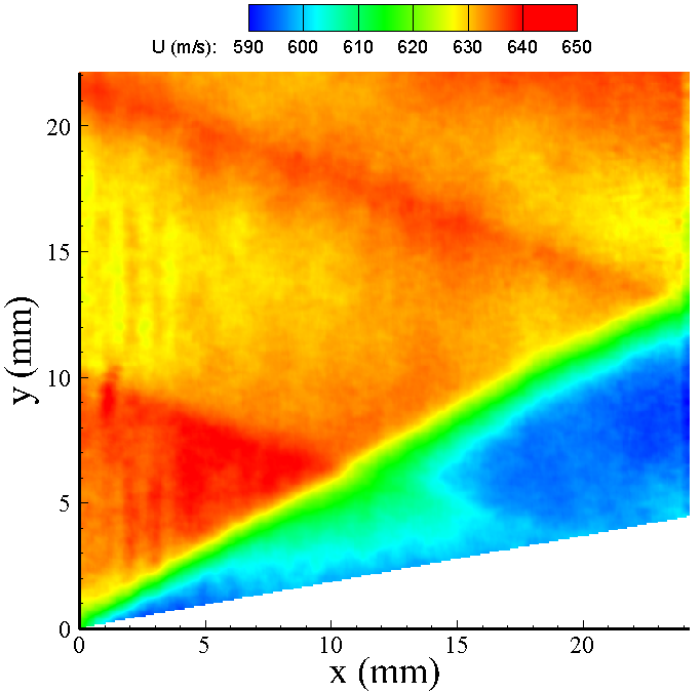

Figure 3A.1: Mean stream-wise velocity contours in vicinity of oblique shock

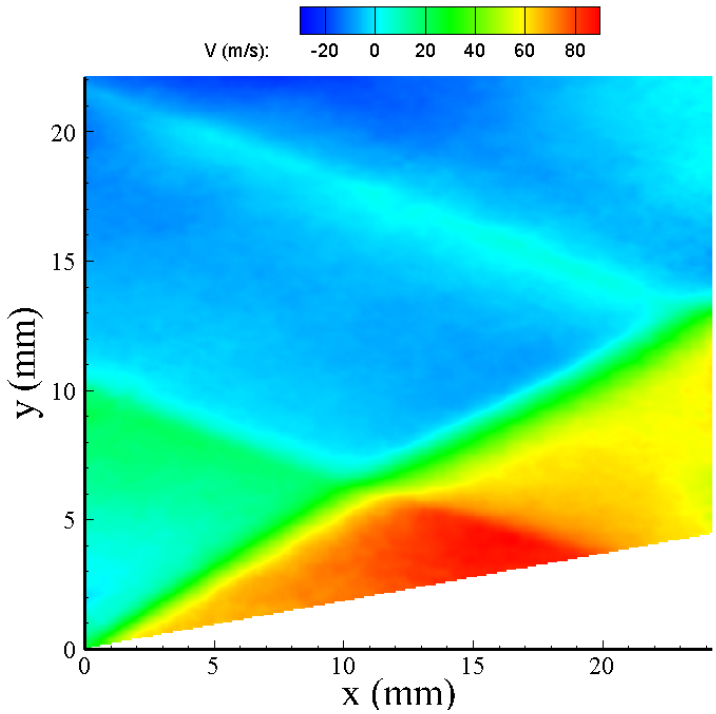

Figure 3A.2: Mean transverse velocity contours in vicinity of oblique shock

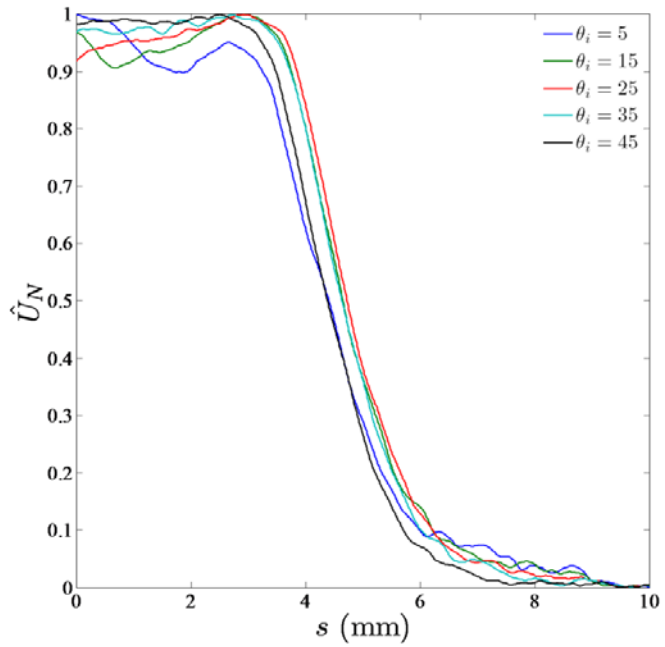

Figure 3A.3: Sample shock-normal velocity traces for different incidence angles

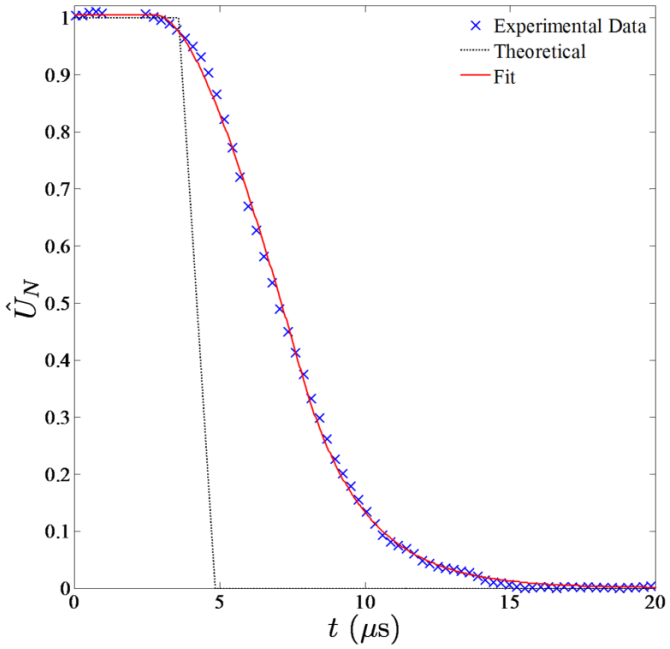

Figure 3A.4: Comparison of experimental data with filtered exponential fit and theoretical step change in velocity across shock

Appendix 3B: Selection of Endview Stereoscopic PIV Parameters

This section details the procedure of selecting the laser sheet thickness and temporal separation between laser pulses for use in endview stereoscopic PIV.

3B.1 – Background

The major problem with this variety of PIV is that the principal velocity component of the flow is normal to the direction of the sheet. While this isn't ordinarily a problem, in the case of these experiments the difference between the in-plane and out-of-plane velocity components is more than order of magnitude. Thus, while the desired pixel displacements are one of the primary factors to consider, additional consideration must be given to the potential loss of particles within the laser sheet. This general problem is illustrated in Fig 3B.1, and shows particle pairs are not expected for flow that enters and leaves the laser sheet.

To be more specific about the flow in question, the approximate out-of-plane velocity for these flows was 630 $m\,s^{-1}$. The in-plane velocities were largely unknown, but estimates from the side-view PIV measurements suggested that the maximum velocities were 100 $m\,s^{-1}$. It is likely that the velocities experienced elsewhere are much lower than this figure.

3B.2 – Selection Procedure

3B.2.1 – Selection of Minimum Pixel Displacements and Δt

It became necessary to approach this problem semi-empirically, but to determine the correct Δt roughly required estimating the minimum resolvable in-plane pixel displacements. This procedure starts by assuming a camera is viewing the laser sheet at normal incidence. This gives the approximate digital resolution of the camera; in the case

of the ES 4020 cameras described in Chapter 3, and assuming the full width of the test section as the field of view, the digital resolution was 24.8 μm/px.

The next step in the procedure was to select the minimum resolvable pixel displacements, which are a function of the Δt and the in-plane velocity. For the *a priori* assessment, a series of different velocities were plotted along with a series of different pixel displacements, effectively prescribing different Δt's. These results are plotted in Fig 3B.2 below.

3B.2.2 – Selection of Minimum Laser Sheet Thickness

The final step in this analysis is to translate the Δt into a laser sheet thickness. The ideal situation would obviously be that all of the particles would be retained, a situation only possible with an infinitely thick laser sheet, no flow, or a very short Δt. Thus, it becomes necessary to set a threshold for particle retention. For these studies, the minimum particle retention was taken to be 75 percent.

The fractional retention of particles is a function of the Δt, out-of-plane velocity, and thickness of the laser sheet. Specifically,

$$R = \left(t_L - u_{op}\,\Delta t\right)/t_L \qquad \text{3B.1}$$

where t_L is the thickness of the laser sheet, u_{op} is the out-of-plane velocity component, and R is the fraction particle retention. From this definition and the threshold for retention, it is seen that the minimum thickness of the laser sheet is exactly four times the out-of-plane convective distance, $u_{op}\Delta t$. The minimum laser sheet thickness for the same Δt's selected in Fig 3B.2 are plotted in Fig 3B.3.

3B.2.3 – Other Considerations

The procedure does not account for the projected displacements caused by the angle of the camera relative to the imaging plane. Thus, most of the pixel displacements

seen by the camera are projected from the out-of-plane components. As an estimation of this, the camera-plane displacements caused by this projection can be expressed as

$$\Delta px_{z,proj} = u_{op}\Delta t \sin\phi \,/DR \qquad \text{3B.2}$$

where $\Delta px_{z,proj}$ is the projected displacement in the camera plane due to out-of-plane motion, ϕ is the angle of the camera plane relative to the imaging plane, and DR is the digital resolution of the optical system in m/px. Likewise, the in-plane displacements are projected in a similar fashion:

$$\Delta px_{x,proj} = u_{ip}\Delta t \cos\phi \,/DR \qquad \text{3B.3}$$

$\Delta px_{x,proj}$ is the projected displacement in the camera plane due to in-plane motion and u_{ip} is the in-plane velocity. Thus, the smaller the angle between the camera plane and the imaging plane, the more dominant the in-plane component of the displacements becomes. As an example of this application, consider a Δt of 1μs and a camera angle of 25 degrees. For the out-of-plane velocity given above, the projected out-of-plane displacements would be roughly 13 px, while the in-plane varies with the velocity, but roughly 90 percent are projected. Thus, the pixel displacements are likely to be dominated by the out-of-plane projection even at the shallow viewing angle

3B.2.4 – Final Selection of Parameters

The initial selection of the Δt for these experiments was 0.85 μs with a camera angle of 40 degrees. By the assessments provided above, this would amount to an in-plane displacement of 2-4 px depending on the velocity, while the estimated out-of-plane projection would 14 px and in-plane projection of 1.5-3 px. Thus, the total pixel displacements were in the optimal range. These parameters required a laser sheet thickness of 2.1 mm. However, this analysis was neglects the minimal resolvable pixel displacements by the PIV processing algorithm. It was found that very few correlations

were made with this setup (less than 20 percent). Thus, this setup was found not to function practically, and many different revisions were made.

Ultimately the selected parameters that worked for the experiments were as follows: $\Delta t = 1.2\,\mu$s, $\phi = 25$ degrees, and t_L = 3 mm. These parameters lead to the following estimations for the displacements: $\Delta px_{ip} = 2 - 8$ px, $\Delta px_{z,proj} = 13$ px, and $\Delta px_{x,proj} = 1 - 7$ px. These conditions proved sufficient for these experiments.

3B.2.5 – Additional Comments

The shortcomings of this technique lie in the extremely thick laser sheet needed for sufficient particle retention. That is, even if the vector correlations are very high, the solution will be averaged over a large volume. If higher resolution is demanded by the application, tomographic PIV would be necessary since this would allow for more vectors throughout the thickness of the sheet rather than averaging over the entire volume.

A final note regarding the selection of the temporal displacement; when looking at the range of in-plane velocities measured in Chapter 3, velocities corresponding to pixel displacements below the minimum threshold prescribed in this appendix are found. This observation would suggest that the threshold is much lower than estimated in this section, and thus a shorter Δt (and thinner laser sheet) is viable. However, shorter Δt's were tested with the final camera orientation and resulted in very few valid vectors during the processing. The reason for this disparity is that the interrogation algorithm needs to be able to assess the bulk in-plane motion of the particles. If it is able to do this on the first few passes of the interrogation process, then the lower velocities can be measured in subsequent passes. If the pixel displacements are so small that no bulk motion can be discerned in the coarse interrogation, then the lower velocities will not be resolvable

either. Thus, the appropriate velocity scale to use for estimating the temporal displacement seems to be the mean velocity of the bulk motion of the fluid rather than the peak, as this would have given a more accurate assessment for these studies.

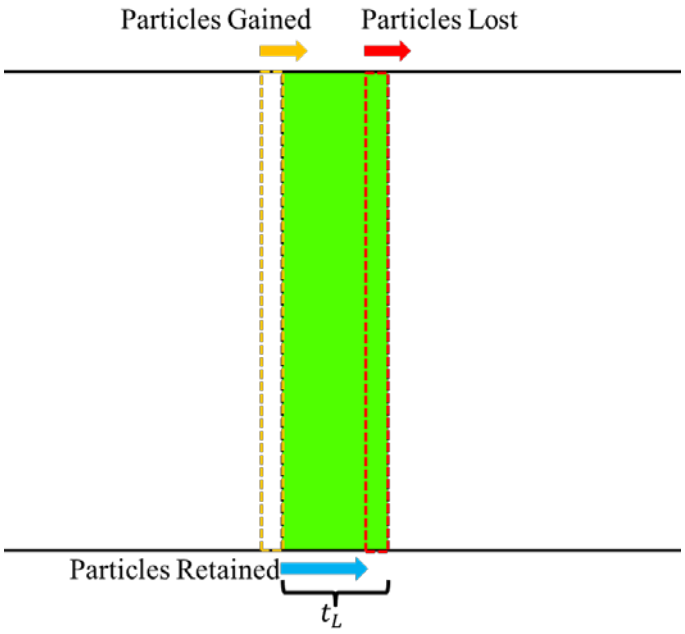

Figure 3B.1: Illustration of how particle retention was calculated as a function of laser sheet thickness

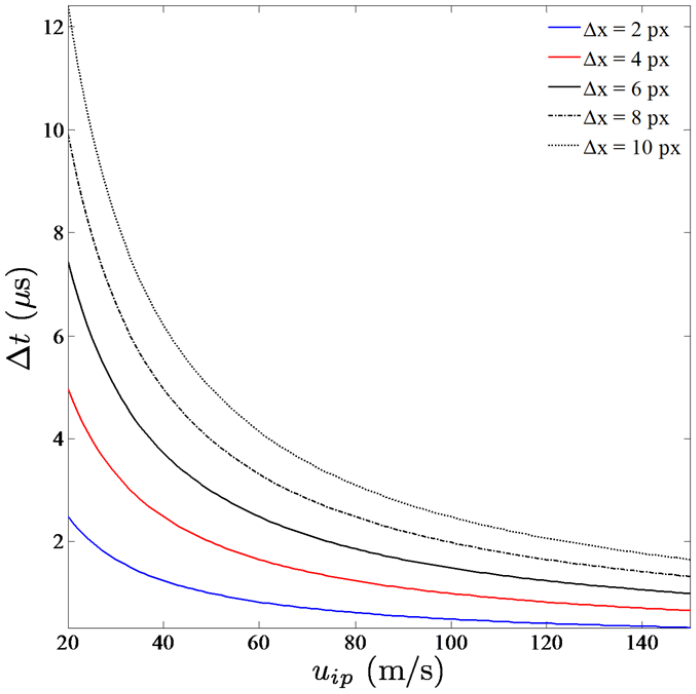

Figure 3B.2: Required Δt for different in-plane velocities and acceptable pixel displacements

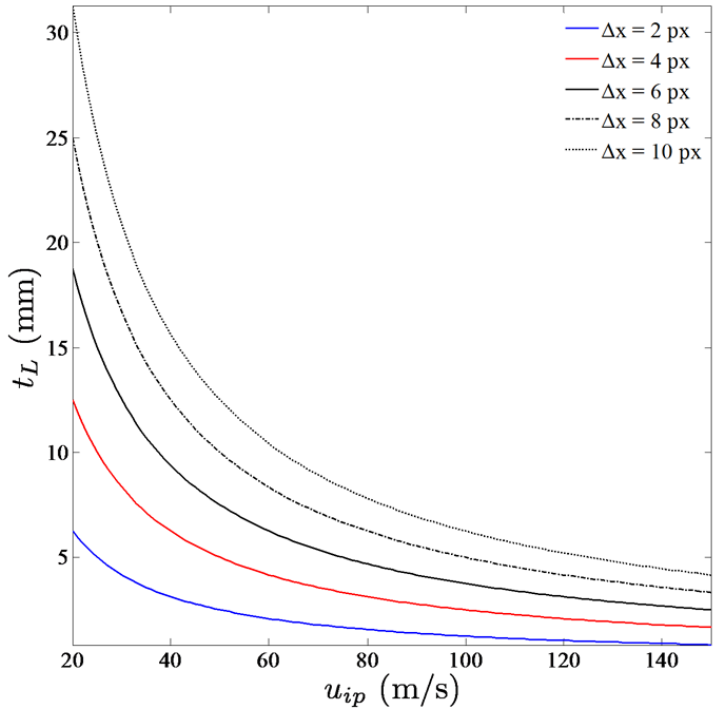

Figure 3B.3: Required laser sheet thickness for different in-plane velocities and acceptable pixel displacements

Appendix 3C: PIV Uncertainty Analysis

This section details the methodology and results of the uncertainty analysis performed on the particle image velocimetry (PIV) data from Chapter 3.

3C.1 – BACKGROUND

PIV uncertainty is still a poorly understood topic for a number of reasons. A traditional approach to uncertainty analysis would consider the component errors involved in PIV. That is:

$$U = \Delta x/\Delta t \qquad \text{3C.1}$$

or the calculated velocity (U) is equal to the measured displacement (Δx) divided by the temporal separation (Δt). The difficulty with this procedure is that the measurement of the displacement is achieved via a cross- or auto-correlation algorithm applied to an image pair or double-exposed image, respectively. While this is really the only statistically viable methodology for achieving sufficient resolution (in lieu of particle tracking), it is not without its problems. There are well documented errors associated with this interrogation procedure, generally divided into random and biasing errors. In the former category, the errors generally arise from the spurious calculation of vectors either because of similar vector choices or random noise in the images. Sufficient sample size and ensemble/temporal averaging are usually sufficient for mitigating random errors. In the case of biasing errors, the sources of uncertainty can be further sub-divided into many categories. There are errors involved with the calibration procedure, errors induced by image and/or physical boundaries in the image, pixel-locking effects, particle-lag effects, and errors caused by the actual interrogation algorithm due to challenging flow environments.

The methodology used herein is not intended to be holistic in its approach; that is, the estimation of the accuracy, precision, and uncertainty will not be distinguished. Rather, the desired effect is to achieve a conservative assessment of the overall uncertainty in the statistical quantities (which may contain elements of accuracy and precision) so that the reader can attain some sense of the quality of the data as well as its shortcomings. To achieve this, a three-part approach is taken. First, some common sources of uncertainty are examined to measure their influence on the current data. Second, the convergence-related errors are quantified, and finally, the possible biases imparted by the flow are investigated.

3C.2 – METHODOLOGY

3C.2.1 – Convergence of Data

The data were first checked for convergence to ensure that the remaining results were not contaminated. For the mean, the metric used was the mean change per iteration divided by the local value of the statistic. For the RMS velocities, the ratio of the RMS velocity to the mean velocity was the test quantity, and the fractional change per iteration used as the residual metric.

3C.2.2 – Peak Locking

Peak or pixel locking is a phenomenon in which the calculated displacements tend to favor integer-valued pixel displacements. To study the effects of pixel locking on the current data, a rather straightforward approach was taken. The measured particle displacements in the data immediately post-interrogation (before any post-processing) were consolidated, and PDFs of these displacements were generated.

3C.2.3 – Particle Lag Effects

The methodologies used to study this effect in the current data are detailed extensively in Appendix 3A. In general, since the majority of the studied flows consist of shear layers, the analysis will focus on time scales thereto relevant. Samimy and Lele [**127**] suggest a fluid timescale of $\tau_f = 10\delta_\omega/\Delta U$ for the compressible shear layer, where δ_ω is the vorticity thickness defined as $\Delta U/\ (du/dy)_{max}$, where du/dy is the transverse derivative of the stream-wise velocity taken at its maximum value through the shear layer, and ΔU is the velocity difference across the shear layer. The Stokes number based on the particle response time then allows for the calculation of an RMS slip velocity for the particle behavior.

3C.2.4 –Convergence Errors

To study the errors due to the incomplete convergence of the data, two processing stages were used. First, the data were checked for numerical convergence; this was done in the mean and RMS of the flow statistics. Second, a method utilizing repeated averaging and subsets of the complete data set was used to measure the uncertainty due to incomplete convergence.. This process involved selecting a subset sample size, which was done by first finding the maximum degree of convergence for the statistic, and then setting the sample size at 75 percent of the samples required to reach this degree of convergence. The actual threshold set for the convergence errors was a bit arbitrary. For instance, subsets ranging from 2 samples to 2000 samples could be used, and the degree of convergence would change with each sample size. Thus, a fixed, conservative threshold was set in this circumstance, which was then applied to all data to be consistent. This quantity of samples was then randomly selected from the entire data set, and the mean of the data were calculated. The convergence-related errors for this subset were then considered to be the difference between the mean calculated in this subset and the

mean calculated over the entire data set. This process was then repeated for at least 1000 unique subsets, with the errors found with each subset being averaged over the repeated subset sampling. The idea behind this method is that the mean and fluctuating components of the velocity will impart their signature to the flow statistics, which are already fairly well-converged at the subset sample size. Therefore any changes seen beyond this are unlikely to be a result of the flow, but of errors related to the overall convergence of the data.

3C.2.5 – Flow-Induced Errors

The principal effect considered in these studies was the effect of strong shearing gradients in the flow. For advanced digital correlation algorithms, this has generally been found to be the most difficult issue to resolve, even in light of the adaptive interrogation schemes that have been developed within the past decade. The simplest of these methods utilizes the measured shear in the flow (quantified by a non-dimensional vorticity) against well-quantified interrogation errors based on synthetic displacements. To do this measurement, the vorticity in the flow was measured and multiplied by the Δt utilized in that particular field of view, and then ultimately compared to the reference data of Fincham and Delerce [**128**].

3C.2.6 – Errors in the temporal displacement

While this may seem like the lesser of the overall uncertainties (in comparison to the uncertainties in displacement), this was not found to be the case. There are two primary sources for errors in the temporal displacement. The first of these stems from jitter in the overall timing circuits used in the experiments. These can arise from jitter in the digital pulse generators, jitter in the laser systems, or possibly ringing in the lines linking slaved pulse generators to the master. To quantify this jitter, a photodiode was set

up to observe the two PIV pulses. The voltage signal from the photodiode was read into a digital oscilloscope and then into a custom LabView VI for acquisition. Several thousand of these samples were recorded for this set of measurements, which were post-processed to measure the fluctuation in the temporal displacement between the two pulses.

The second of the sources of uncertainties in the temporal displacement arises from the voltage fluctuations in the lasers themselves. Due to adjusting the voltage, across the flashlamps to maintain pulse energy or repeatedly inhibiting and enabling the laser emission, the temporal separation tended to vary by a substantial amount if not monitored closely. To quantify this error, the difference was observed over the course of the experiments, and the maximum deviation seen was used as the metric.

3C.2.7 – Measurement of the Total Uncertainty

Once all of the component uncertainties described above have been quantified, the uncertainty is assumed to propagate as the root of the sum of squares:

$$|\delta u_i| = \left\{ \left(\frac{\delta \Delta x_i}{\Delta t} \right)^2 + \left(u_i \frac{\delta \Delta t}{\Delta t} \right)^2 \right\}^{1/2} \qquad \text{3C.2}$$

3C.3 – RESULTS

3C.3.1 – Convergence

The degree of convergence was found to vary for the different statistics. Fig. 3C.1 and 3C.2 show a plot of the residuals for the mean and fluctuating velocities, respectively for the side-view PIV. In these plots, the residuals were calculated as the mean residual over the entire field. These traces were taken for the upstream view in the planar injector, but they are representative of all side views taken. It is seen here that the mean stream-wise velocity converges quite a bit more rapidly than the transverse

component. Here the residual is plotted as a fraction of the mean value, and thus the stream-wise component is found to approach a smaller value. Nonetheless the transverse component is found to be converged to within one percent of the mean and the stream-wise component within 0.01 percent of the mean value. This value is sufficient for the analysis here, though it is likely that derivatives of these quantities will exhibit some noise. Note also that there is a high level of noise in the transverse component; this is a consequence of the velocities being symmetric about zero. The RMS velocities were found to converge very similarly in rate to that of the mean values. The transverse component converges to within one percent, while the stream-wise component converges to 0.1 percent. Note also that the noise characteristics follow the trends seen in the mean velocities.

The convergence of the end-view PIV mean and fluctuating velocities is shown in Figs 3C.3 and 3C.4, respectively. These plots are taken from the second field of view, but they are representative of both fields of view. The end-view PIV was found to converge more slowly than the side-view, likely due to more noise in the measurement. Here, the stream-wise component was found to be converged to within 0.1 percent, while both the transverse and span-wise velocities converged to within 1 percent. This fact was one of the reasons that so many samples were taken for this measurement. Nonetheless, these data converged to values similar to those found in the side-view, and thus similar deficiencies would arise. Note here that both the transverse and span-wise velocities exhibit the noise characteristics seen in the transverse component of the side-view fields of view. The cause again the fact that the velocities are centered around zero rather than the high velocities seen in the stream-wise component. The RMS velocities behaved similarly as well, so not much discussion will be given to them.

3C.3.2 – Peak Locking

The results for this analysis for the fields of view considered in Chapter 3 are presented in Figs 3C.1 through 3C.10 below. The data for the side-view fields of view are presented in Figures 3C.5 and 3C.6 below. Here the distributions of pixel displacements within the field of view are presented. These PDFs are generated from the upstream field of view for the planar injector, but they are representative of the other geometry and fields of view. Upon initial inspection of the stream-wise component of velocity (Figs 3C.5), there is little sign of pixel locking. A great deal of the velocities are concentrated at the high-end of the displacement spectrum, but upon more detailed inspection of the lower velocity tail, a minor degree of pixel locking can be seen. This observation is made even more apparent by considering the transverse component of velocity (Fig 3C.6). Here, apart from the central peak, there are several minor 'humps' concentrated around integer pixel values. It is worth noting here that the resolution in the PDF is 0.1 px, so the sub-pixel displacements are fully represented in this histogram. Now, the observed pixel locking is not directly characteristic of the traditional effect; if it were, then the peaks would be much sharper. Instead, they appear quite spread out, particularly on the negative velocity side. This observation suggests the mitigating processing steps, for instance the selection of the correct sub-pixel interpolation scheme (a 4:1 elliptical Gaussian function in this case), are functioning as desired. Nonetheless, this does add a bit of uncertainty to the overall calculation, since the observed displacements are in some way biased by the interrogation process.

The end-view fields of view do not exhibit the same evidence of peak locking seen in the side-view PIV orientation. PDFs of all three velocity components are shown in Figs 3C.7 through 3C.9. Here, no evidence of pixel locking is evident. Consequently, the overall uncertainty is largely unaffected by this uncertainty.

3C.3.3 – Particle Lag Effects

As was shown in the Appendix 2A, the approximate response time of the particles used in the PIV was found to be 2.098 μs. The effect this has on the shockwaves has already been demonstrated in Appendix 3A. In short, there is a distance downstream of the shocks, defined coarsely as $\tau_p u_2$ (particle response time multiplied by the velocity after the shock), in which the particles will have a pronounced slip velocity. For the flows in question, this distance is 1.33 mm in the stream-wise direction, or approximately 6 interrogation windows at the current overlap setting. In this regard, there is notable uncertainty of velocity in this region, though it is difficult to define since the velocity is varying continuously behind the shock. As most of the analysis avoids these regions, it is not of much concern in the present studies.

The second region of interest, noted in the numerical methods above, is in the shear layers. For these flows, the top and bottom shear layers were analyzed to find the vorticity thickness, and the result used to compute a particle Stokes number as described above. The fluid time scale vs the downstream distance is shown in Figs 3C.10 and 3C.11 for the planar and hypermixing injector flowfields, respectively. Here it is seen that the maximum St_p is found to be 0.0175 for the planar injector flowfield and 0.022 for the hypermixing injector flowfield. For the planar injector flowfield, the maximum RMS slip velocity (based on the analysis of Samimy and Lele [**127**]) is 1.75 percent, while the hypermixing injector flowfield is at 2 percent. From this, it is apparent that particle lag effects should nominally be negligible outside of the shock-relaxation region. As an aside to this analysis, it is interesting to note that the Stokes number for the top shear layer exhibits much shorter fluid time scales (and thus larger Stokes numbers) than the lower shear layer. This result is a consequence of lift imposed by the counter-rotating vortex pair and the distortion of the wake; the top shear layer is effectively thinned while lower

shear layer is expanded. Thus, the magnitude of the shearing is different and the timescales follow.

3C.3.4 – Convergence Errors

The results for the convergence error analysis are depicted in Figs 3C.12 through 3C.18, with the side-view fields of view ranging from 3C.12 through 3C.15 and the end-view spanning the remainder. Figs 3C.12 and 3C.13 detail the uncertainties found for the planar injector; here it can be seen that the largest uncertainty was found within the near-field wake region near the reattachment point. The maximum uncertainty is found in the transverse component, collocated with the region of highest RMS velocity. It is seen here that the maximum displacement uncertainty is approximately 3 pixels, or just about 14 percent of the local velocity. The entire wake region here is found to have a rather high uncertainty (due to the lower fractional correlations in this location), while the freestream has a rather low uncertainty, generally sub-pixel in magnitude. Overall the uncertainties are fractionally quite low, and are bound here at the aforementioned 14 percent.

The hypermixing injector exhibits similar properties with respect to its wake structure (see Figs 3C.14 and 3C.15). In this instance, the stream-wise uncertainty is concentrated in the near-field wake region (near the border of the low correlation bubble) and extending out into the wake. The peak uncertainty exhibited by the data here is roughly 1.75 px or about 8 percent. The transverse uncertainty is again found to be concentrated in the center of the wake, with similar magnitudes to the planar injector. Again, the peak uncertainty in these instances is about 14 percent within the wake, trending to about 3 percent within the freestream.

The uncertainties in the end-view PIV are actually quite a bit smaller than that found in the side-view. Refer to Figs. 3C.16 through 3C.18 to see the tabulated

uncertainties due to random errors in the end-view field of view. These particular data are from the first field of view, where the overall uncertainties were found to be higher than the downstream FOV. The uncertainties in this region peak at around 1.5 px found in the streamwise component of velocity. This value is also quite consistent with the uncertainty seen in the side view analysis, which is to be expected since the degrees of convergence were quite similar. Likewise, the other velocity components are seen to match closely; both in-plane velocity components exhibit similar uncertainties, and the transverse uncertainty matches closely with that seen in the side view.

Ultimately this analysis allows for an uncertainty in pixels to be applied to the total uncertainty. While there is an obvious spatial dependence, the goal here was to find an upper bound on the uncertainty, which was found in each field of view. For each of the side-view fields of view, the peak uncertainty was around 3 px, while it peaked at 1.5 px for the endview.

3C.3.5 – Flow-Induced Errors

The mean non-dimensional vorticity for these fields of view are shown in Figs 3C.19 through 3C.21. Considering all three fields of view presented here (and all considered in these studies as well), the maximum non-dimensional shear seen is just about 0.045. By the work of Fincham and Delerce [**128**], it is found that the error in pixel displacement for even this peak value is a mere 0.1 pixel. Consequently, these did not contribute exceedingly to the overall uncertainty.

3C.3.6 – Errors in temporal displacement

As mentioned above, there are two possible sources of uncertainty in the temporal displacement. The first is an overall jitter in the system due to various sources. The results for one of the sampling runs are shown in Fig 3C.22, shown here for a nominal Δt

of 400 ns. The measured jitter from this scan was 1.86 ns, which is fractionally quite minor compared to the overall temporal displacement. Likewise, scans of the 0.85 μs and 1.2 μs temporal displacements yielded jitters of 2.12 ns and 1.53 ns, respectively. Based on day-to-day repetition of the procedure, the jitter is independent of the temporal displacement. As an additional note on the jitter, the overall current-draw in the room was a strong contributing factor. That is, if something in the lab or room was drawing an excessive amount of electrical current, the jitter would increase considerably.

The second source of temporal uncertainty as discussed above is due to changes in the flashlamp voltage in the lasers. The change due to this effect was observed during the experiments, though no waveforms showing its effect were recorded. This temporal uncertainty was found to cause a variation of nearly 40 ns sweeping the energy from 30 mJ/pulse to 75 mJ/pulse. Likewise, increasing further (up to ~120 mJ for some experiments) increased this difference to nearly 60 ns. A similar observation was seen when adjusting the ratio of flashlamp delay to Q-switch delay, though the effect was smaller. It is unknown exactly why these effects are present, but they have a definite influence on both the PIV measurements and the stability of the PLIF laser system used in later experiments. To establish a basic uncertainty for use in the PIV experiments, a mean value of 30 ns was used. In practice, it became necessary to continuously monitor the pulse separation during the experiments after the discovery of this temporal drift. However, since this monitoring was not done throughout the entirety of the experimental cycle, and the energy was often adjust during runs, including this uncertainty is necessary in this analysis.

3C.3.7 – Total Uncertainty

The component uncertainties from the above-mentioned sources are as follows: pixel-locking – 0.25 px for side-view FOVs, 0 for end-view FOVs, convergence errors – 2.5 px for side-view FOVs, 1.5 px for end-view FOVs, correlation biasing (due to shearing) – 0.1 px for all FOVs, 1.86 ns for temporal jitter, and 30 ns for the voltage-induced error in the timing. A summary of the peak consolidated uncertainties is presented in table 3C.1:

Summary of peak uncertainties for different fields of view

FOV	$\delta\Delta x$ (m)	$\delta\Delta t$ (ns)	δu ($m\ s^{-1}$)	$\delta u/u$
SV (SV 1a-c, 2a-c)	7.18×10^{-5}	30.06	87.37	13.87
EV 1	2.12×10^{-5}	30.06	28.43	4.51
EV 2	2.56×10^{-5}	30.06	31.82	5.05

Table 3C.1: Summary of peak uncertainties for different fields of view

These values represent the absolute upper bound on the uncertainty for the PIV measurements in Chapter 3. However, there is an obvious spatial variation in this value. For completeness, the spatial variations in uncertainty are presented below for the three fields of view in Figs 3C.23-25.

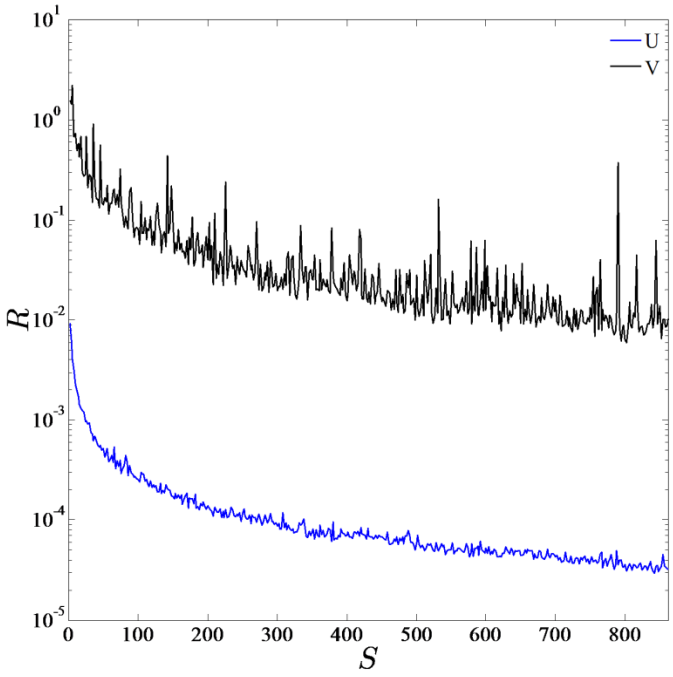

Figure 3C.1: Convergence of the mean velocities for side-view fields of view

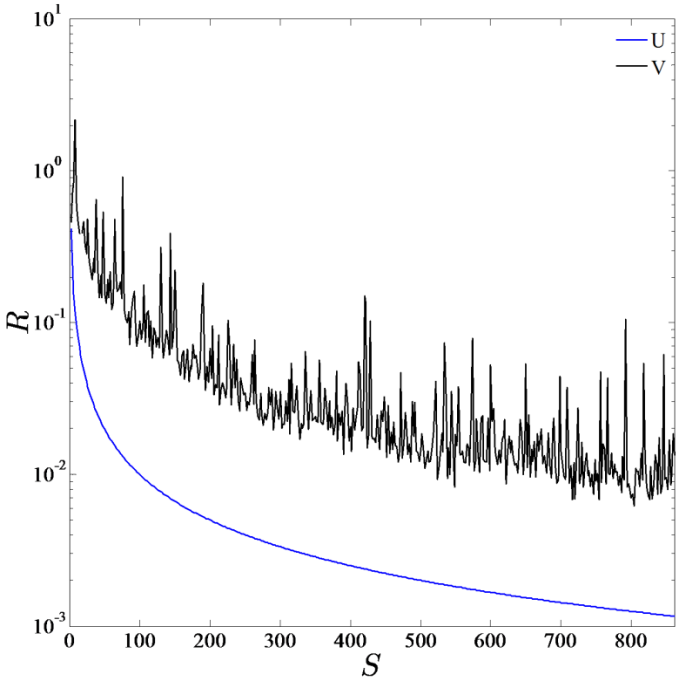

Figure 3C.2: Convergence of the RMS velocities for side-view fields of view

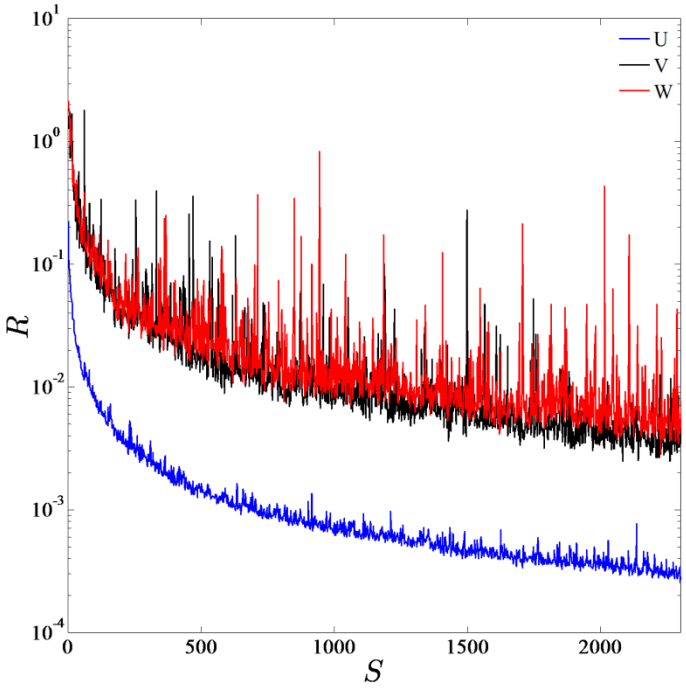

Figure 3C.3: Convergence of the mean velocities for end-view fields of view

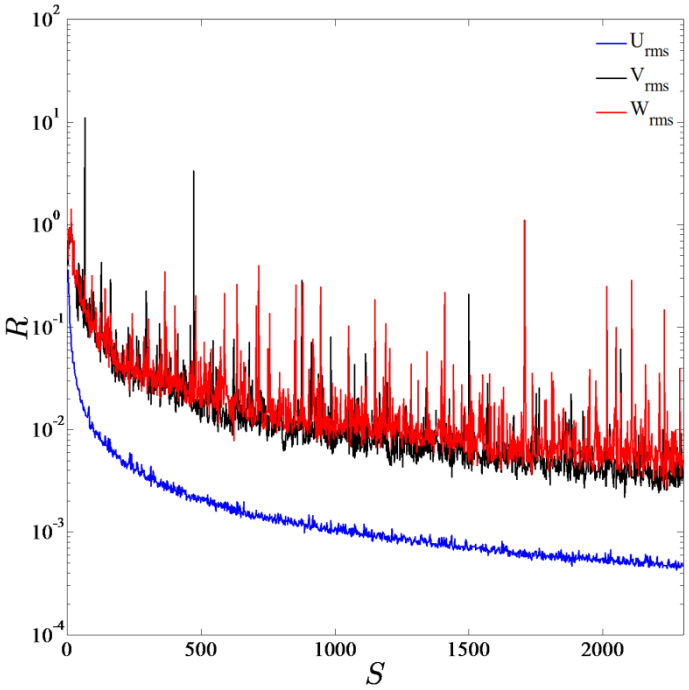

Figure 3C.4: Convergence of the RMS velocities for end-view fields of view

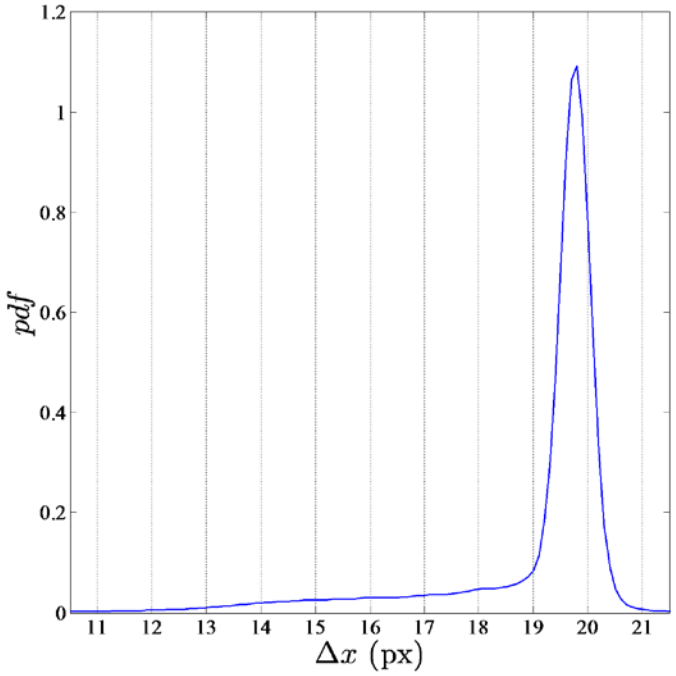

Figure 3C.5: PDF of the stream-wise pixel displacements for side-view fields of view

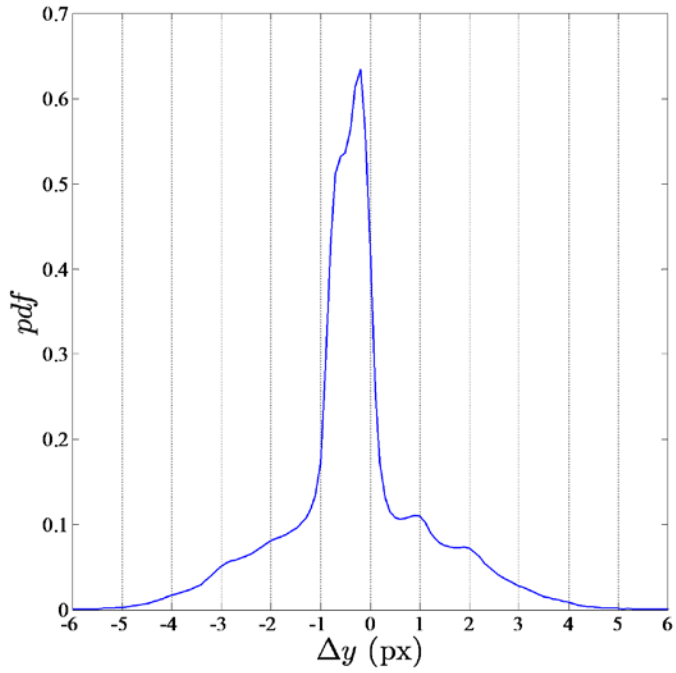

Figure 3C.6: PDF of the transverse pixel displacements for side-view fields of view

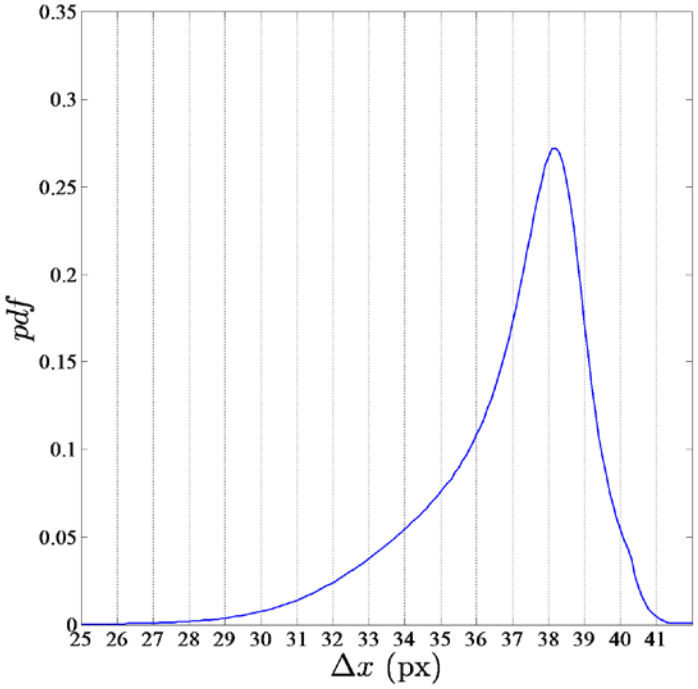

Figure 3C.7: PDF of the stream-wise pixel displacements for the end-view fields of view

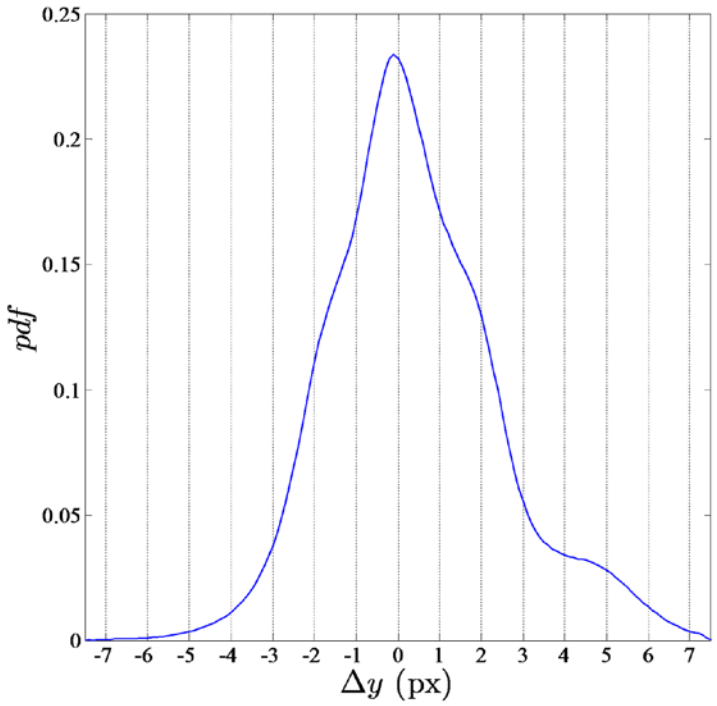

Figure 3C.8: PDF of the transverse pixel displacements for the end-view fields of view

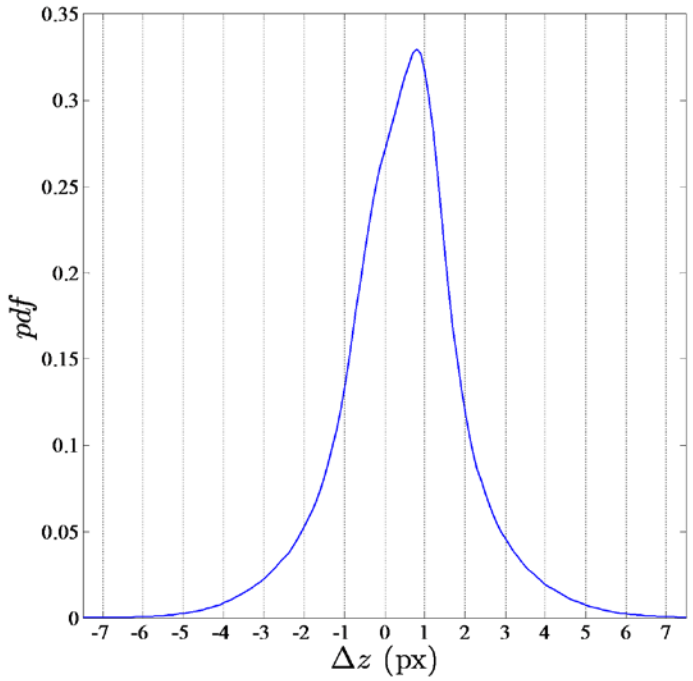

Figure 3C.9: PDF of the span-wise pixel displacements for the end-view fields of view

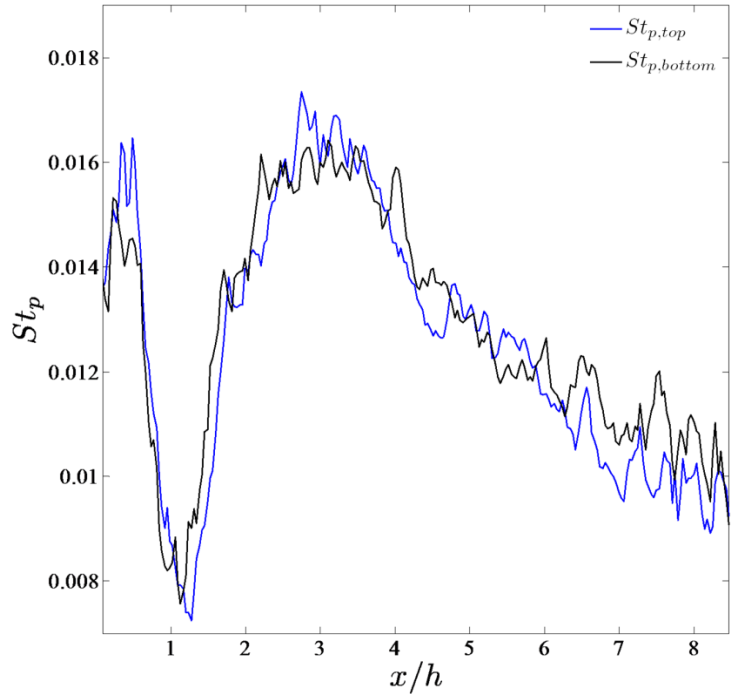

Figure 3C.10: Stream-wise distribution of particle Stokes number for planar injector flowfield

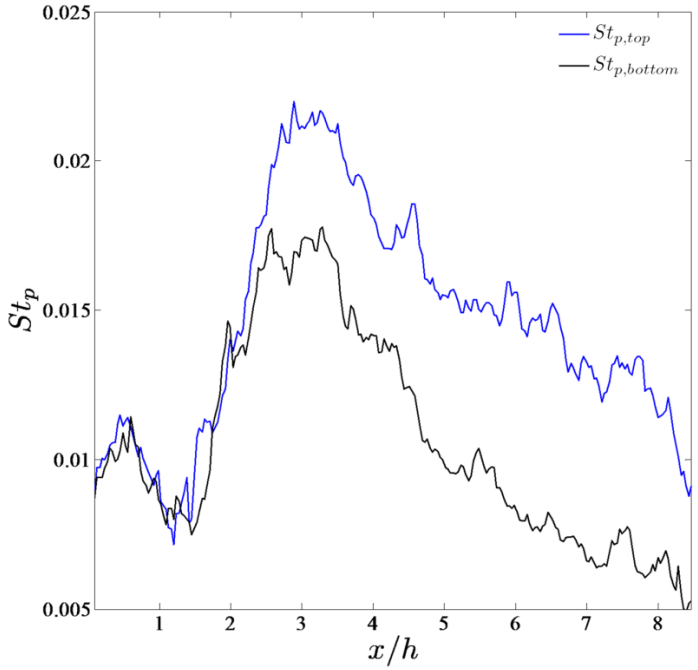

Figure 3C.11: Stream-wise distribution of particle Stokes number for hypermixing injector flowfield

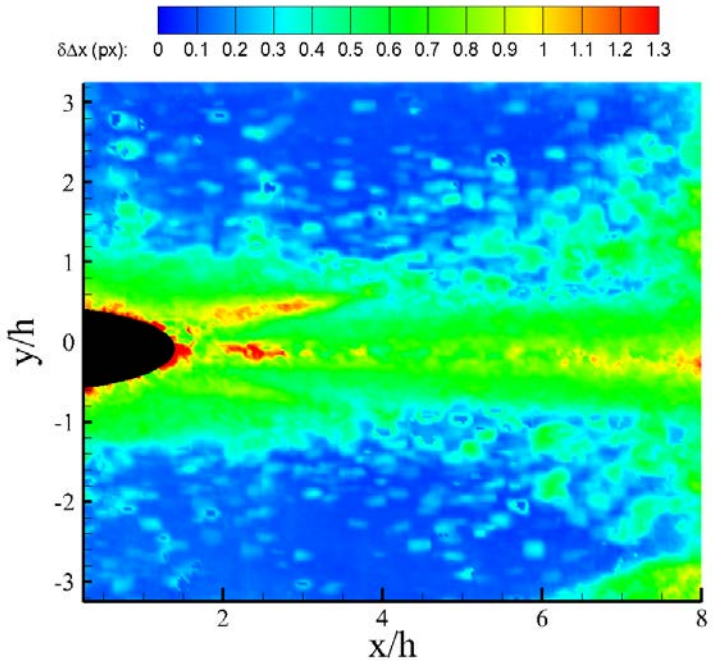

Figure 3C.12: Stream-wise uncertainty due to convergence error for planar injector upstream

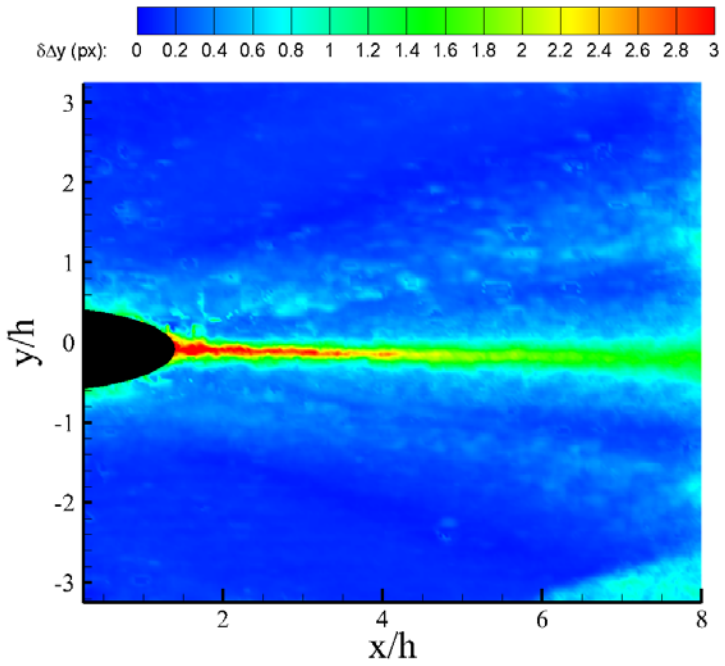

Figure 3C.13: Transverse uncertainty due to convergence error for planar injector upstream

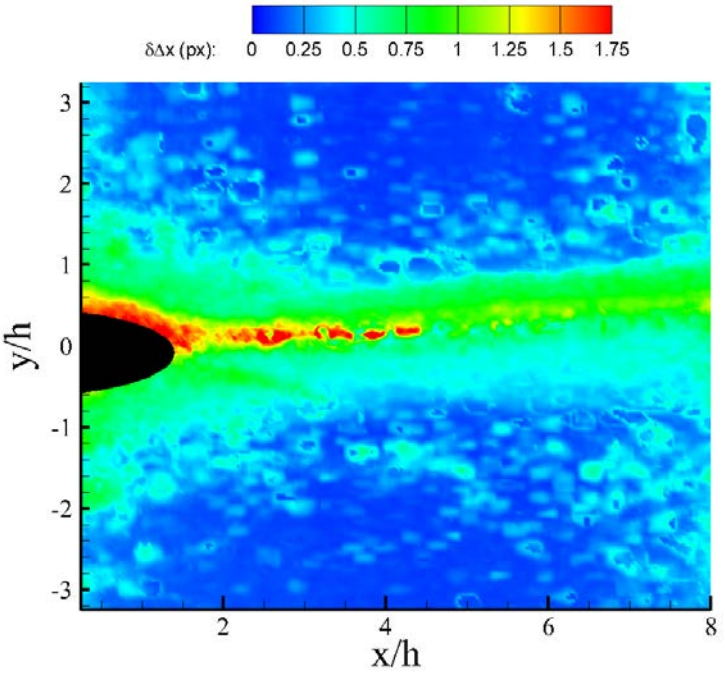

Figure 3C.14: Stream-wise uncertainty due to convergence error for hypermixing injector upstream

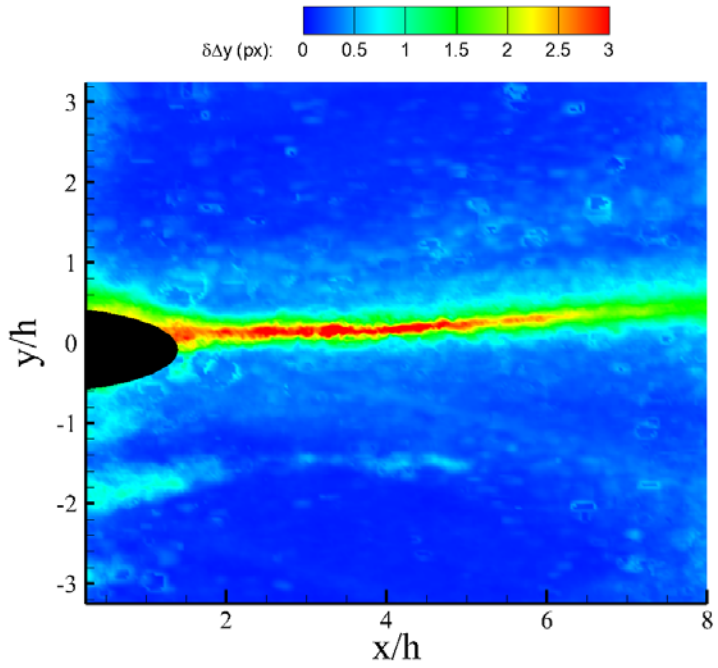

Figure 3C.15: Transverse uncertainty due to convergence error for hypermixing injector upstream

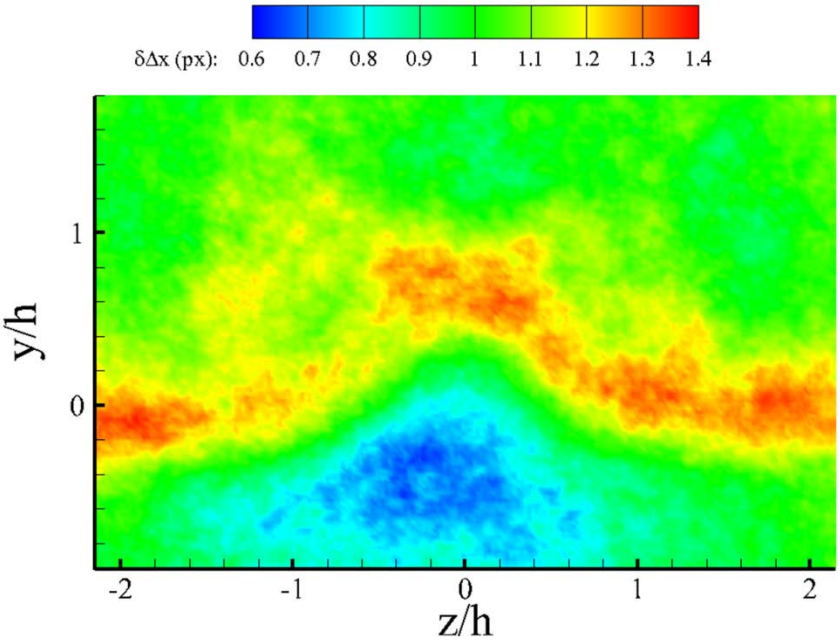

Figure 3C.16: Stream-wise uncertainty due to convergence error for hypermixing injector end-view

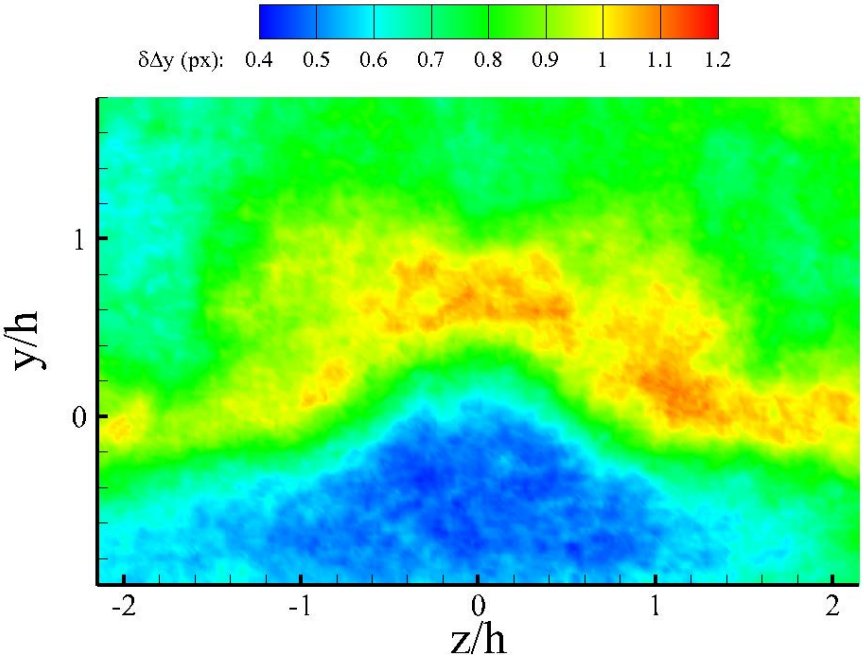

Figure 3C.17: Transverse uncertainty due to convergence error for hypermixing injector end-view

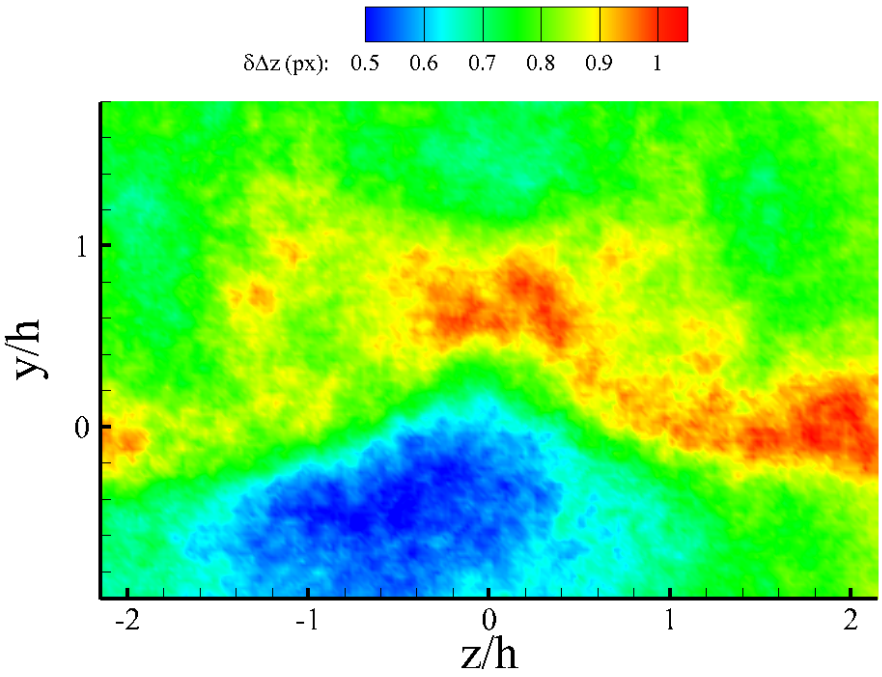

Figure 3C.18: Span-wise uncertainty due to convergence error for hypermixing injector end-view

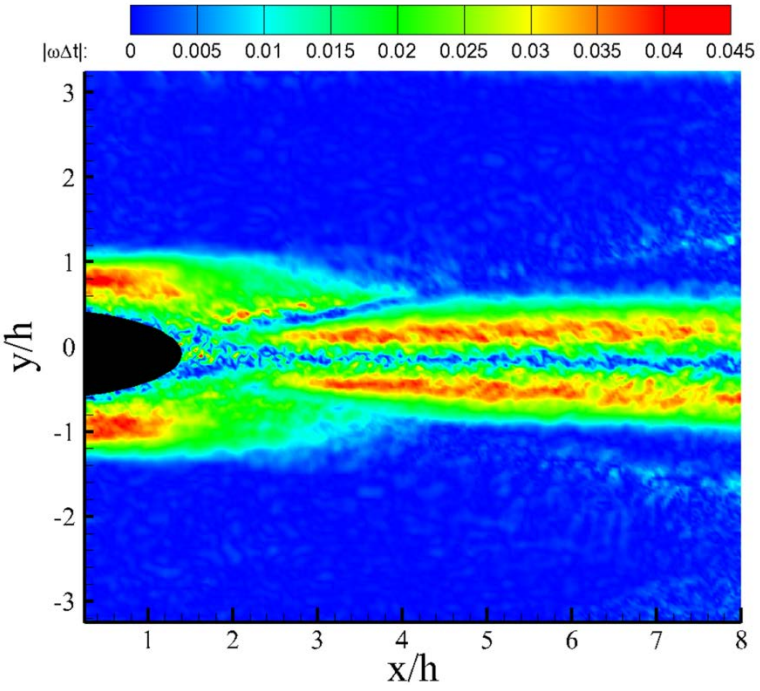

Figure 3C.19: Non-dimensional shear magnitude for planar injector side-view

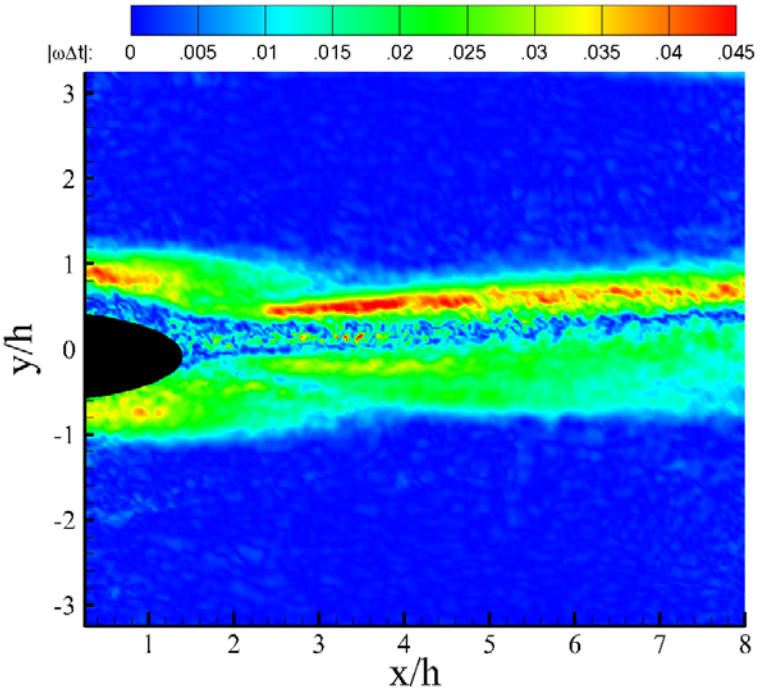

Figure 3C.20: Non-dimensional shear magnitude for hypermixing injector side-view

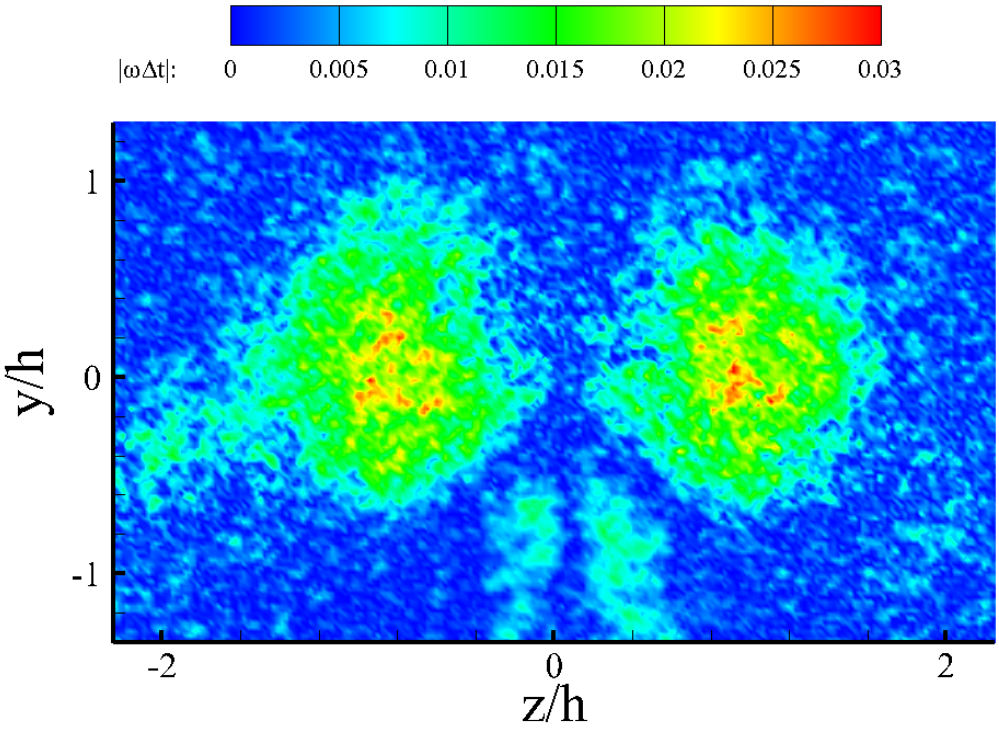

Figure 3C.21: Non-dimensional shear magnitude for hypermixing injector end-view

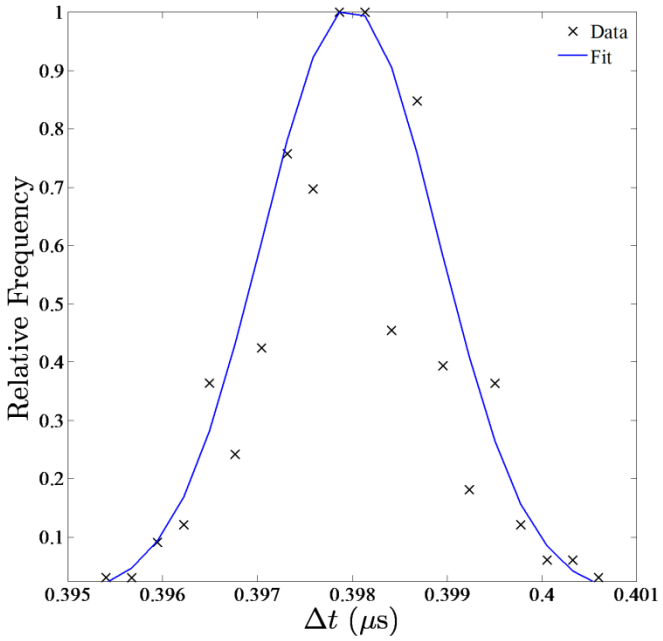

Figure 3C.22: Distribution of temporal displacements showing the jitter in the system

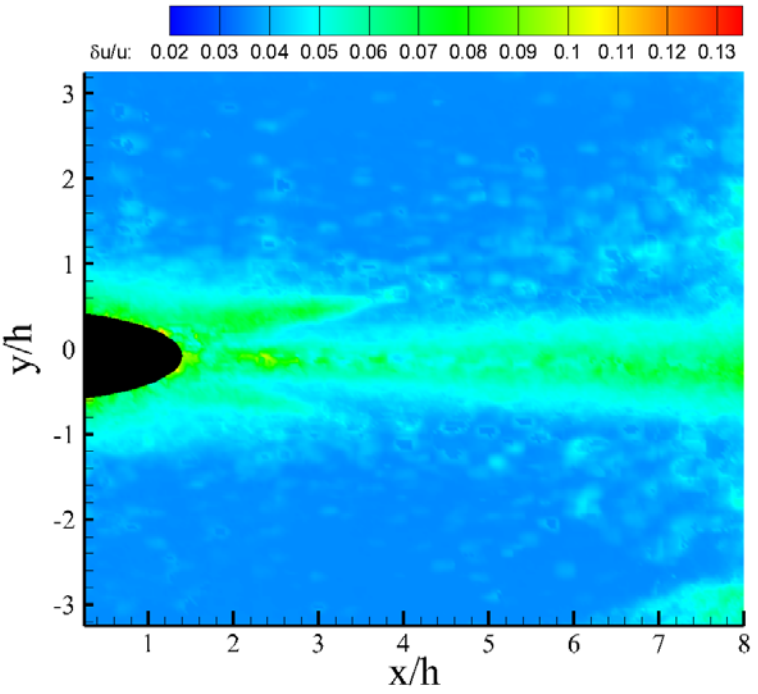

Figure 3C.23: Spatial variation in uncertainty for planar injector side-view

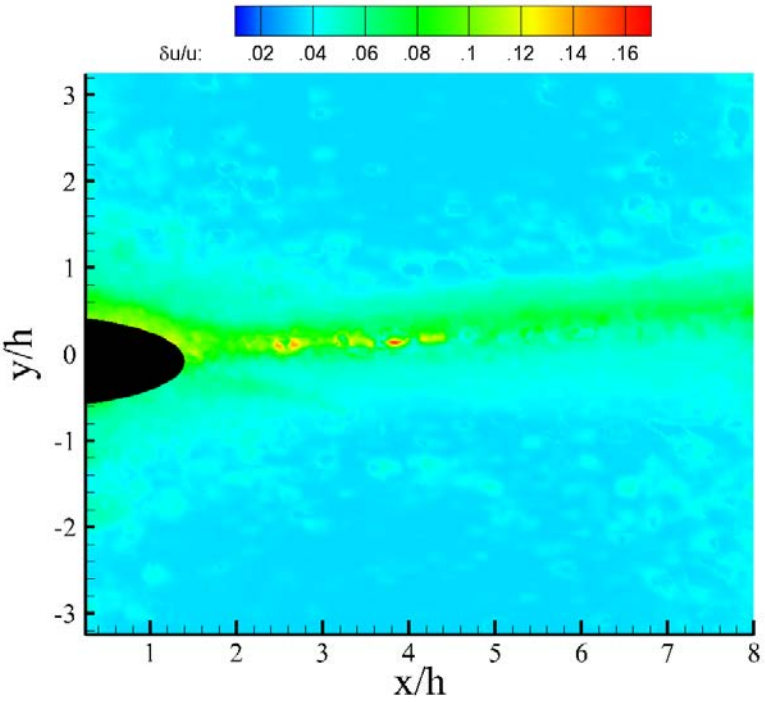

Figure 3C.24: Spatial variation in uncertainty for hypermixing injector side-view

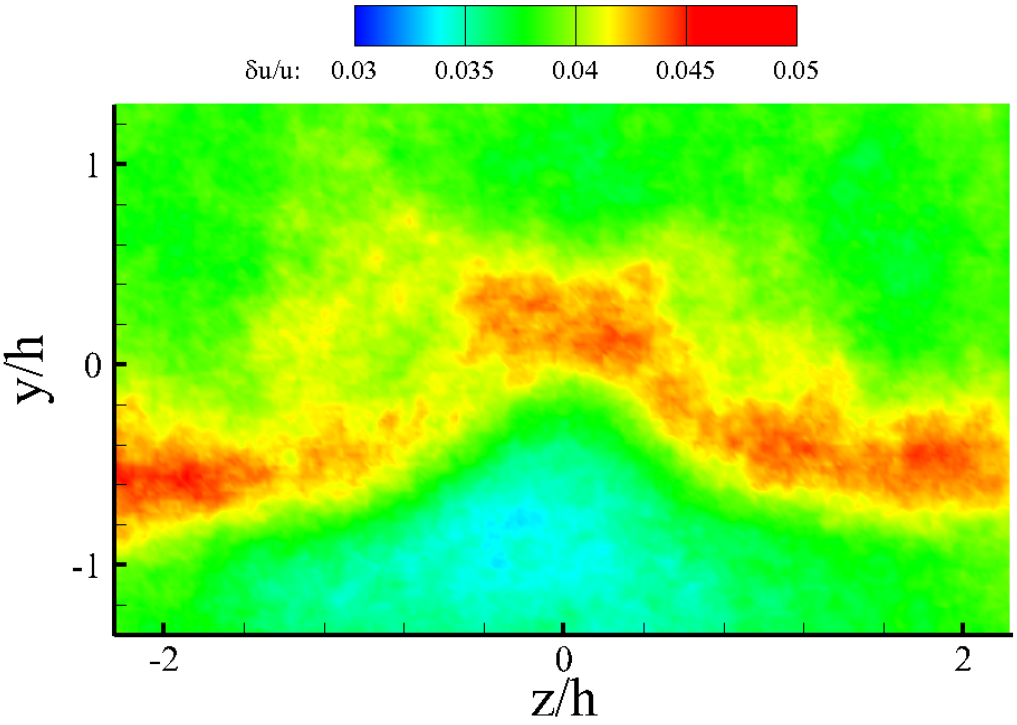

Figure 3C.25: Spatial variation in uncertainty for hypermixing injector end-view

Appendix 4A: Analytical Methodologies and Uncertainty Calculations for Simultaneous Krypton PLIF and PIV Measurements

This appendix will outline the analytical methodologies and uncertainty calculations relevant to the work in Chapter 4.

4A.1 – Calibration of the Fluorescence Signal

This section will cover the various procedures conducted in the calibration of the raw Kr fluorescence signal to determine Kr mole-fraction.

4A.1.1 – Calculation of Reference Signal Ratio

The reference signal ratio represents the ratio between the fluorescence image taken in the flow and those taken at the reference state condition. The calculation of the reference signal ratio requires two separate operations. First, dark-field images were acquired to remove the mean accumulated dark noise in the images. These were taken by shutting off the laser during the image acquisition, with all other camera and system parameters (lens focus and aperture, intensifier settings) being the same. Images were also taken with the lens cap in place, though there was no distinguishable difference between the two sets due to the filter in place during the imaging. The dark-field image used for this correction was the mean of a set of 100 images. The background subtraction was applied to both the reference fluorescence images and the experimental data for these studies.

The next part of this procedure is to calculate the signal ratio. At its most basic, this step of the procedure is little more than a calibrated sheet correction [**129**] [**130**] [**131**]. In a simple sheet correction, the spatial intensity variations in the laser beam profile, which cause vertical or horizontal streaks to form in the fluorescence signal when expanded into a sheet, are numerically corrected. Typically, a fluorescence image of the

sheet profile is taken in a uniform background of the fluorescence species, allowing the intensity profile to be viewed without interference from spatial variations in concentration. Thereafter, the signal from this correction image is scaled from 0 to 1, and the image mapped onto the same coordinate system as the original data. By then dividing the signal of the original data by the sheet correction image, the variations in signal due to non-uniformity in the laser sheet are removed. To use this procedure to calculate a reference signal ratio, two addition steps have to be considered in this procedure: the raw intensities must be used rather than a scaled version, and the thermodynamic conditions when the sheet correction was taken must be known. In regard to the first of these conditions, this procedure is not intended to merely visually correct the fluorescence image. Rather, the actual value of the ratio of the two signals is desired; that the intensity variations are corrected in this procedure is a secondary consequence. Knowledge of the thermodynamic conditions is achieved by utilizing the ambient conditions of the room, which are well-known.

While the above procedure is quite straightforward, attempting to apply it directly to the images captured for these studies yielded unsatisfactory results. The reasons for this are several. Unlike more simplistic harmonic laser excitation, the laser beam created through SFG in this context is difficult to characterize. It is extremely susceptible to temporal jitter in the timing system as well as the spatial overlap and even the intensity variations present in both beams. Thus, there is considerable shot-to-shot variation in the laser intensity ($I(x,t_1) \neq I(x,t_2)$). Second, the fluorescence is nonlinear in the excitation intensity. Thus, it is critical that the calibration images be taken with the intended fluorescing species to ensure that the correct intensity pattern is collected. Another consideration is that obtaining a sheet correction using a profiling cell requires that some fraction of the excitation beam is redirected to the cell, but the signals were low enough

that there was not sufficient residual energy for this purpose. With these problems, it becomes difficult to generate accurate reference image signal ratios.

As a first-order correction, the mean calibration image can be applied to the fluorescence images. The problem that arises from this procedure is that the shot-to-shot variations in laser intensity will not be corrected. Practically, little can be done to amend this issue without instantaneous sheet profiles. Two steps were thus taken to accommodate this shortcoming. First, a more limited stream-wise extent of the data was used in the calculations of this chapter. Specifically, only the area of the sheet which possessed the highest intensity was used. These regions were less susceptible to the shot-to-shot variations than the fringes of the beam, and thus had a lesser effect on the data. Second, the shot-to-shot variations observed in the data sampling regions were incorporated into the uncertainty calculations to ensure their influence on the calibration procedure is well-established.

4A.1.2 – Calculation of Freestream Conditions

As was noted in Chapter 4, the estimation of the local thermodynamic state is required in order to calculate the mole fraction from the fluorescence signal. The general theory behind this is outlined in Section 4.1. However, there are some details of the procedure which have not been elucidated. The first step in this procedure was to estimate the Mach number field. This procedure utilized the velocity data presented in Chapter 3. Based on the measured stagnation conditions, the Mach number distribution allows the thermodynamic conditions throughout the two supersonic mixing flowfields to be estimated. The basis of this analysis is a combination of isentropic flow relations, Prandtl-Meyer theory, and the Rankine-Hugoniot equations for calculating conditions after the recompression shocks. The procedure entailed three distinct steps. The process

starts by estimating the incoming Mach number from the velocity measurement and the stagnation temperature. In this case the Mach number was estimated as 2.97, which is consistent with the design Mach number of 3. After the incoming Mach number was estimated, the corresponding Prandtl-Meyer angle of the flow was calculated. Subsequently, the turning angles of the flow relative to the splitter plate angle (very close to zero degrees) were calculated. This step allowed for the Prandtl-Meyer angle to be calculated everywhere in the field, and subsequently, the Mach number based on the Prandtl-Meyer angle was tabulated in the complete field as well. This initially included the turbulent regions (where PM theory is not valid), though this was corrected in a later step and ultimately was not used in the analysis that follows. Using isentropic flow relations, associated static and stagnation pressure fields were calculated.

The next step in the procedure was to estimate the conditions after the recompression shocks, which first required an algorithm for finding the shocks. A similar (though coarser) methodology used for finding the shock in Appendix 3A (particle response assessment) was utilized. Herein, sampling points were placed on both sides of the shock and the angle between them was adjusted to optimize the shock angle relative to the flow direction. Using this methodology, the shock location could be discerned, while the flow direction and deflection angle were calculated from the velocity data. As an input to the shock relations, the incoming Mach number was taken from the previously calculated Mach number contours based on Prandtl-Meyer theory; this Mach number, along with the turning angle of the flow and shock angle were used to calculate the static and stagnation conditions after the shock. Once these data were calculated, new Mach number and thermodynamic conditions after the shocks were calculated with the Prandtl-Meyer method as was described above, with the total Mach number following the shock used as the input. One caveat to this procedure is that the shocks all appear spread out

over a few interrogation windows due to particle-lag effects. Thus, the conditions were smoothed out over the relaxation region by averaging them with the Prandtl-Meyer-theory-based temperature and pressure contours calculated with the new conditions after the shock. With the calculation of the Mach number contours after the recompression shocks, the new static conditions could be calculated as well. As a final step in the procedure, the estimated temperature through the wake was calculated using the basic Crocco-Busemann relation (Eq. 4.4). The Mach number, temperature, and pressure contours estimated for these flowfields are found in Figs 4A.1 through 4A.6.

A final note should be made here regarding the mapping of the conditions between the two different experiments. The first comment is that the two flowfields are implicitly different because the flowfields in the present studies utilize injection, whereas those in Chapter 3 were merely a wake structure. Based on previous studies [**100**] [**99**], several modifications are seen when the injection is considered. First, the fundamental wake/recompression shock system is altered by the jet. Specifically, the termination of the barrel shock from the jet (which in this case occurs at $0.9h$ downstream of the injector) is coincident with the foot of the recompression shocks. The shift in the recompression shocks is caused by the incoming detached boundary layers from the mixer moving along the jet boundary. Next, since the jet is present to contribute to the momentum of the flow, the wake does not reach its natural neck as it does in the undisturbed flowfields seen in Chapter 3. Consequently, the flow turns parallel further upstream to match the jet, and the recompression shocks move upstream. This is important to remember when considering the mapping of freestream conditions. Specifically, since the wake and jet have the same transverse extent, the freestream conditions are mapped after the recompression shocks, assuming they are seated at the previously noted $0.9h$. Now this is not universally applicable, but in this case since the

pressure variation is quite minor throughout this region, it is not that problematic. It would have been preferable to have velocity data for a wider field of view to use for this purpose, but it is not currently available.

4A.1.3 – Calculation of Temperature and Krypton Mole Fraction

As described in Section 4.1, the calculation of temperature and krypton mole fraction are coupled; the fluorescence signal calibration is dependent on the local temperature, and the total enthalpy of the flow (used to calculate the temperature) is dependent on the composition of the flow. Thus, the two relations (Eqs. 4.3 and 4.5) must be satisfied simultaneously. The approach taken in these studies was to solve the two equations recursively.

The solution procedure began by estimating the values of the freestream temperature and pressure. The simultaneous velocity data was loaded, and the temperature and pressure data calculated in Section 4A.1.2 were mapped onto the same grid. Once this was done, the $0.99U_\infty$ location was found in the velocity data, and the temperature and pressure at these locations were taken as the freestream values. Following this, a preliminary temperature profile was calculated using Eq. 4.4 with the mean velocity data. Finally, a preliminary guess for the mole fraction in the field was set at a uniform 0.5. These data combined served as the input data for the solution procedure.

A number of different temperature models were employed when solving for the mole fraction. These included the basic Crocco-Busemann (CB) relation tabulated with the mean velocity data, the basic CB relation tabulated with the instantaneous velocity data, the composition-variable CB tabulated with the mean velocity data, and the composition-variable CB tabulated with instantaneous velocity data. The employment of

each of these required a slightly different solution procedure. For simplicity, the composition-variable CB solution procedure will be described first, since all other versions are simplifications thereon. The initial temperature and composition data are first used to calculate the total enthalpy distribution. In so doing, the transport properties were evaluated at the estimated temperature. Using these data, the temperature field was re-evaluated. Furthermore, the quenching rates and two-photon absorption cross-sections were calculated at these same conditions, after which the mole fraction relation Eq. 4.3 was evaluated. After the composition was recalculated, the total enthalpy field was evaluated using the new composition, but the instantaneous velocity data was used in this case rather than the mean field. Finally, the temperature was reevaluated at the new condition. These steps represent one iteration, and the procedure was repeated as many times as required to achieve convergence. The scaled residual tolerance in this case was set to 1×10^{-14} for both the temperature and the mole fraction. In some rare instances, such as the data having a particularly large deviation from the initial guess, the iterative procedure would not converge. In these circumstances, an alternative iterative procedure was employed; the mole fraction was instead stepped in extremely small increments, and the temperature reevaluated at each step. This alternative procedure converged much more slowly than the recursive variety, but it was more reliable in terms of achieving convergence in difficult situations. Regardless of the exact iterative method employed, the overall procedure was repeated for all instantaneous data sets.

When using the variations on this solution method, several of the evaluation parameters described above were changed. In the simplest variation, in which the basic CB relation was employed with mean velocity data, the total enthalpy field was not allowed to vary, and the composition was evaluated as a function of the mean temperature. The second variation that used the basic CB relation with instantaneous

velocity data was identical to the previous description, but the temperature field was evaluated using the instantaneous velocity data instead. In much the same fashion, the composition was evaluated independent of the total enthalpy. The final variation used the full solution procedure described above, but instead of using the instantaneous velocity data, the mean velocity data was used. The results utilizing these different temperature models are discussed in Chapter 4.

4A. 2 – PIV PROCESSING

All PIV processing was done in DaVIS v.7.2 [**124**]. The interrogation scheme was an iterative, multi-pass, adaptive scheme. The interrogation windows ranged in size from 128 px on the first iteration to 32 on the final iteration with 75 percent overlap. The traditional selection of 50 percent overlap was increased to allow for less truncation error in calculating spatial derivative with the velocity data. Moreover, there tended to be a higher degree of valid vectors when utilizing the larger spatial overlap. The Q-ratio used for vector acceptance/rejection was set to 1.2 for these data. Typical vector fields had 85 percent valid correlations, with the majority of missing vectors lying on the horizontal bounds of the images rather than in any particular flow structure.

Given the camera/lens configuration used in these studies, the digital resolution was 11 μm/px. Thus, the spatial resolution of the PIV measurement with the interrogation scheme described above was 346 μm. Estimating the relevant length scales with the velocity data, the minimum Kolmogorov length scale is 1μm based on the minimum vorticity thickness or 1.15 μm based on the minimum thickness of the wake. The Batchelor scale is smaller due to its scaling with Schmidt number. These scale lengths were calculated from the relations found in Su and Clemens [**4**]. Specifically, the Kolmogorov scale (η) is equal to $\delta Re_{\delta}^{-3/4}$, while the Batchelor scale (η_B) is equal to

$\eta Sc^{-1/2}$. Research on low speed jets suggest that the true dissipative length scales may be up to an order of magnitude larger [**4**] [**132**], but this estimation is meant to serve as a lower limit. It should also be noted that these scales will grow with downstream distance. Regardless, it is clear that the dissipation scales are far from being resolved with either the PIV or simultaneous measurements. The PLIF by itself is at a higher resolution than the PIV since no interrogation scheme is required (though the calibration must be done at the scale of the PIV measurements), with a minimum resolution of roughly 18 μm/px. Comparing this to the local Batchelor scale, the PLIF resolution is still roughly an order of magnitude larger than that of the relevant length scales in the flow, though they are potentially of the same order considering the argument for the true dissipative scales mentioned above. However, the scaling of the data required for the calibration of the fluorescence signal (discussed in Section 4A.3) reduces the resolution to that of the PIV, so the PIV still serves as the upper limit on the resolution. .

4A.3 – Spatial Mapping of Scalar Data

When utilizing the scalar data simultaneously with the velocity data, it is critically important to map the two data sets to each other properly. The first part of this procedure is to scale and deform the PLIF data. Using the calibration data taken prior to the experiments, the spatial data for the PLIF data was generated using LaVision's DaVIS software. The application of said calibration allowed for the two data to be correctly overlapped spatially.

The next phase of the process is to map the two data sets onto each other. The inclination is to map the velocity data onto the PLIF data via interpolation; the PLIF data is at a much higher resolution, and as such the amount of information gleaned from the analysis would be greater. However, this process is fundamentally flawed. The resolution

of the simultaneous experiment is limited by the lowest resolution experiment, which in this case is the PIV. To perform the mapping correctly, the interrogation process involved in the PIV post-processing must be accommodated. That is, at a given velocity vector location (which is centered within the final interrogation window), the velocity within the cell is averaged. Thus, instead of a simple interpolation scheme to map the scalar data to that of the velocity, a window around each grid node is made, and all PLIF points which lie within that window are averaged. As a final note, it is also important to consider the overlap percentage used in the PIV processing when performing this mapping. That is, when the standard 50 percent overlap is used, the resolution is given by $\pm\Delta x$ (in grid units) in either direction. However, at the 75 percent overlap used in these studies, the resolution is still limited by the final interrogation window size, and as such requires that the filter window has an extent of $\pm 2\Delta x$.

4A.4 – Uncertainty in Mole-Fraction Imaging

The general methodology for the calculation of uncertainties was outlined in Section 4.3.1.3 with a discussion of the results. This section is meant to consolidate the formulae used in the calculations. The total uncertainty in the mole fraction was expressed in Eq. 4.15, which will be repeated here for convenience:

$$\begin{aligned}|\delta\chi_{Kr}| = \Bigg\{ &\left(\frac{\partial\chi_{Kr}}{\partial A}\delta A\right)^2 + \left(\frac{\partial\chi_{Kr}}{\partial P}\delta P\right)^2 + \left(\frac{\partial\chi_{Kr}}{\partial q_{air}}\delta q_{air}\right)^2 \\ &+ \left(\frac{\partial\chi_{Kr}}{\partial q_{Kr}}\delta q_{Kr}\right)^2 + \left(\frac{\partial\chi_{Kr}}{\partial S}\delta S\right)^2 + \left(\frac{\partial\chi_{Kr}}{\partial E}\delta E\right)^2 \\ &+ \left(\frac{\partial\chi_{Kr}}{\partial\gamma_{ref}}\delta\gamma_{ref}\right)^2 + \left(\frac{\partial\chi_{Kr}}{\partial\hat{\Sigma}^{(2)}}\delta\hat{\Sigma}^{(2)}\right)^2 + \left(\frac{\partial\chi_{Kr}}{\partial\Theta}\delta\Theta\right)^2 \\ &+ \left(\frac{\partial\chi_{Kr}}{\partial\Pi}\delta\Pi\right)^2 + \left(\frac{\partial\chi_{Kr}}{\partial\chi_{Kr,ref}}\delta\chi_{Kr,ref}\right)^2 \Bigg\}^{1/2}\end{aligned} \qquad 4.15$$

Each of the corresponding partial derivatives are summarized below:

$$\frac{\partial \chi_{Kr}}{\partial A} = \frac{1}{D_f} \tag{4A.1}$$

$$\frac{\partial \chi_{Kr}}{\partial P_s} = \frac{\left(D_f(q_{air}) - N_f(q_{air} - q_{Kr})\right)}{D_f^2} \tag{4A.2}$$

$$\frac{\partial \chi_{Kr}}{\partial q_{air}} = \frac{\left(D_f(P_s) - N_f P_s\right)}{D_f^2} \tag{4A.3}$$

$$\frac{\partial \chi_{Kr}}{\partial q_{Kr}} = \frac{N_f P_s}{D_f^2} \tag{4A.4}$$

$$\frac{\partial \chi_{Kr}}{\partial S} = \frac{-N_f S^{-2} E^2 \gamma_{ref} \hat{\Sigma}^{(2)} T^{-1} P \chi_{Kr,ref}^{-1}}{D_f^2} \tag{4A.5}$$

$$\frac{\partial \chi_{Kr}}{\partial E} = \frac{2N_f S^{-1} E \gamma_{ref} \hat{\Sigma}^{(2)} T^{-1} P \chi_{Kr,ref}^{-1}}{D_f^2} \tag{4A.6}$$

$$\frac{\partial \chi_{Kr}}{\partial \gamma_{ref}} = \frac{-N_f S^{-1} E^2 \hat{\Sigma}^{(2)} T^{-1} P \chi_{Kr,ref}^{-1}}{D_f^2} \tag{4A.7}$$

$$\frac{\partial \chi_{Kr}}{\partial \hat{\Sigma}^{(2)}} = \frac{-N_f S^{-1} E^2 \gamma_{ref} T^{-1} P \chi_{Kr,ref}^{-1}}{D_f^2} \tag{4A.8}$$

$$\frac{\partial \chi_{Kr}}{\partial T} = \frac{N_f S^{-1} E^2 \gamma_{ref} \hat{\Sigma}^{(2)} T^{-2} P \chi_{Kr,ref}^{-1}}{D_f^2} \tag{4A.9}$$

$$\frac{\partial \chi_{Kr}}{\partial P} = \frac{N_f S^{-1} E^2 \gamma_{ref} \hat{\Sigma}^{(2)} T^{-1} \chi_{Kr,ref}^{-1}}{D_f^2} \tag{4A.10}$$

$$\frac{\partial \chi_{Kr}}{\partial \chi_{Kr,ref}} = \frac{N_f S^{-1} E^2 \gamma_{ref} \hat{\Sigma}^{(2)} T^{-1} P \chi_{Kr,ref}^{-2}}{D_f^2} \tag{4A.11}$$

In Eqs. 4A.1 through 4A.11, the terms N_f and D_f are taken from Eq. 4.14, and represent the numerator and denominator, respectively, of the fluorescence calibration equation. In

addition to the application of these partial derivatives, each of the corresponding uncertainties must be calculated as well.

The uncertainty in the spontaneous emission rate, which is found in the total decay rates, comes from the quenching measurements found in Chapter 2; it was measured to be 2.97 MHz. In similar fashion, the uncertainties in the quenching rates for air and krypton in addition to the relative two-photon absorption cross-section are temperature dependent, and are again taken from the data of Chapter 2. The remaining uncertainties related to the fluorescence excitation are in the fluorescence signal and laser pulse energy ratios. The former of these uncertainties is calculated in a manner consistent with calculating the convergence uncertainties in the PIV data (see Appendix 3C). The uncertainty in the reference signal was found by first finding the average and standard deviation of the set of dark-field corrected calibration images. The uncertainty in the reference intensity was then taken to be twice the standard deviation. The total uncertainty in the signal ratio S can then be expressed as:

$$\delta S = \left\{ \left(\frac{\delta S_f}{S_{ref}} \right)^2 + \left(\frac{S_f \delta S_{ref}}{S_{ref}^2} \right)^2 \right\}^{1/2} \qquad 4A.12$$

Typically this uncertainty was on the order of 18 percent. A similar method can be used in the calculation of the uncertainty of the laser energy ratio:

$$\delta E = \left\{ \left(\frac{\delta E_L}{E_{L,ref}} \right)^2 + \left(\frac{E_L \delta E_{L,ref}}{E_{L,ref}^2} \right)^2 \right\}^{1/2} \qquad 4A.13$$

The uncertainty in the laser energy is calculated based on the standard deviation of the pulse energy; during the runs, the pulse energy of 500 pulses was measured and analyzed to find the mean and standard deviation, the latter of which was used as the uncertainty. In general the 2σ uncertainty was found to be 10 percent of the mean pulse energy, which corresponded to a combined uncertainty of roughly 13 percent.

The final step was to estimate the uncertainty in the other thermodynamic ratios. These can be expressed as:

$$\delta\Theta = \left\{\left(\frac{\delta T}{T_{ref}}\right)^2 + \left(\frac{T\delta T_{ref}}{T_{ref}^2}\right)^2\right\}^{1/2} \quad \text{4A.14}$$

$$\delta\Pi = \left\{\left(\frac{\delta P}{P_{ref}}\right)^2 + \left(\frac{P\delta P_{ref}}{P_{ref}^2}\right)^2\right\}^{1/2} \quad \text{4A.15}$$

The individual uncertainties in the temperature, pressure, and reference conditions then need to be considered as well. The temperature based on the modified CB model, in addition to its uncertainty are expressed as:

$$T(y) = T_\infty + \frac{Pr_{mix}^{1/3}}{2C_{p,mix}(y)}\left(U_\infty^2 - U^2(y)\right) \quad \text{4A.16}$$

$$\begin{aligned}\delta T = \Bigg\{ & (\delta T_\infty)^2 + \left(-\frac{Pr_{mix}^{1/3}}{2C_{p,mix}^2}\left(U_\infty^2 - U^2(y)\right)\delta C_{P,mix}\right)^2 \\ & + \left(\frac{Pr_{mix}^{-2/3}}{6C_{P,mix}}\left(U_\infty^2 - U^2(y)\right)\delta Pr_{mix}\right)^2 \\ & + \left(\frac{Pr_{mix}^{1/3}}{C_{p,mix}}U_\infty \delta U_\infty\right)^2 + \left(-\frac{Pr_{mix}^{1/3}}{C_{p,mix}}U\ \delta U\right)^2\Bigg\}^{1/2}\end{aligned} \quad \text{4A.17}$$

From Eq. 4A.17, it is apparent that in addition to the uncertainties found in the velocity and freestream temperature, there are additional uncertainties due to the mixture-based properties. The uncertainty associated with the mixture specific heat is:

$$\begin{aligned}\delta C_{P,mix} = \Big\{ & \left(\left(C_{P,Kr} - C_{P,air}\right)\delta\bar{\chi}_{Kr}\right)^2 + \left(\bar{\chi}_{Kr}\delta C_{P,Kr}\right)^2 \\ & + \left(\left(1 - \chi_{Kr}\right)\delta C_{P,air}\right)^2\Big\}^{1/2}\end{aligned} \quad \text{4A.18}$$

With regards to the uncertainty in the Prandtl number, the total uncertainty is expressed as:

$$\delta Pr_{mix} = \left\{ \left(\frac{C_{p,mix}}{k_{mix}} \delta \mu_{mix} \right)^2 + \left(\frac{\mu_{mix}}{k_{mix}} \delta C_{P,mix} \right)^2 + \left(-\frac{\mu_{mix} C_{p,mix}}{k_{mix}^2} \delta k_{mix} \right)^2 \right\}^{1/2} \quad \text{4A.19}$$

Here, the component uncertainties are taken from the stated model accuracies. For the viscosity, the average deviation is stated at 2 percent. The accuracy of the specific heats (taken from empirical data) was 0.5 percent, while that of the specific heat capacity was 4 percent.

Finally, the uncertainty in the freestream conditions were calculated. The uncertainties associated with the procedure described in Section 4A.1.2 are several, and most stem from the uncertainty in the incoming Mach number. A slightly different method was employed to calculate the uncertainty in the Mach number. Herein, the uncertainty range was found by varying the initial condition over the tabulated range, and the subsequent range of Mach numbers generated by running them through the same iterative algorithm. Here, the incoming Mach number and uncertainty therein are tabulated as functions of the velocity uncertainty and that of the stagnation temperature as expressed in Eqs. 4A.20 and 4A.21, respectively.

$$M_\infty = U_\infty / \left(\gamma R T_o - \frac{\gamma - 1}{2} U_\infty^2 \right)^{1/2} \quad \text{4A.20}$$

$$\delta M_\infty = \left\{ \left(\frac{\gamma R T_o}{\left(\gamma R T_o - \frac{\gamma - 1}{2} U_\infty^2 \right)^{3/2}} \delta U_\infty \right)^2 + \left(\frac{\gamma R U_\infty}{2 \left(\gamma R T_o - \frac{\gamma - 1}{2} U_\infty^2 \right)^{3/2}} \delta T_o \right)^2 \right\}^{1/2} \quad \text{4A.21}$$

The results for the Mach number uncertainty analysis are found in Figs 4A.7 and 4A.8 for the planar and hypermixing injectors, respectively. Once the uncertainty in the freestream and local Mach numbers have been found in the above fashion, the same methodology of substituting the range into the overall function was used for calculating the uncertainties in the freestream temperature and pressures. The results for these uncertainty calculations are found in Figs. 4A.9 through 4A.12.

4A.5 – PIV UNCERTAINTY

The general procedure for calculating the uncertainty in a PIV measurement has been outlined in Appendix 3C, and as such the details of what the various component uncertainties are, and from which they arise, are herein omitted. The various estimates for these uncertainties will be stated here as well as the total calculated uncertainty. It should be reiterated that this analysis is intended for the statistical quantities..

4A.5.1 – Convergence of Data

Plots of the convergence in the three mean velocity components and their fluctuations are shown in Figs 4A.13 and 4A.14. Here it is seen that the mean components reach a minimum converge to a residual value of 10-2, while the others attained were more converged. The RMS velocities attain a similar degree of convergence to that of the mean.

4A.5.2 – Peak-locking

PDFs for the three velocity components are shown in Figs 4A.15 through 4A.20. Here it can be seen that there is no evidence of the pixel-locking effects which were observed to in the side-view planar PIV of Chapter 3 (see Appendix 3C). Thus, a standard uncertainty of 0.1 px will be added to the combined uncertainty in the PIV measurement.

4A.5.3 – Particle-lag Effects

There are two potential issues to consider in regard to the particle lag effects. One new effect to consider in the present study is that there are two types of particles being utilized (solid and liquid), which could potentially have disparate response times. As shown in Appendix 2A, the response time of the liquid particles is about 2.1 μs, while that of the solid particles was shown to be around 2.6 μs [**116**]. Thus, the response times are quite similar, and the effects related to variable response need not be considered away from shockwaves (which the fields of view in the studies of Chapter 4 are).

The next consideration is the effect of the relevant time scales of the flow. As was described in Appendix 3C, a relevant time scale for used in studying the shear layers was suggested by Samimy and Lele [**127**] as $\tau_f = 10\delta_\omega/\Delta U$. Using this as the reference time scale, the particle Stokes numbers for the first field of are presented in Fig 4A.21 and 4A.22. The maximum Stokes number for the planar injector flowfield is seen to be 0.043 and 0.046 for the hypermixing injector flowfield, which correspond to maximum RMS slip velocities of 0.75 percent by the data of the same authors. Thus, at peak the contributed uncertainty is 0.18 px and is added to the cumulative uncertainty.

4A.5.4 – Convergence Errors

The same method of repeated subset analysis is utilized here as was used in Appendix 3C. These results show the uncertainty in the statistical quantities due to incomplete convergence of the data. The results for this convergence analysis for the planar injector are pictured in Fig 4A.23, while those for the hypermixing injector are shown in Fig 4A.24. It is seen here that the peak uncertainties are found in the stream-wise velocity component, reaching a maximum of roughly 3 px in the vicinity of the low correlation region. The transverse and span-wise velocity components peak at 1.25 px. In

general the uncertainties in the hypermixing injector flowfields were slightly lower than that of the planar injector, but the difference is minimal.

4A.5.5 – Processing Errors

Flow induced errors again arise from high shearing in the flow. To quantify this uncertainty, the non-dimensional vorticity for the plane were calculated and compared to the data of Fincham and Delerce [**128**]. The results for the two planar and hypermixing injectors are depicted in Figs 4A.25 and 4A.26, respectively. Here, much as was seen in the previous side-view PIV, the error is negligible in this flow.

As was described in Appendix 3C, one part of the processing procedure for stereoscopic PIV is to set an allowable range of reconstruction errors in the multi-pass post-processing. This threshold was set higher in the side-view PIV than was the case in the end-view stereoscopic PIV (2 pixels in this case in lieu of the 1 pixel set in the former case). While in general the error was below this threshold, in the interest of measuring the maximum, the threshold was used as the maximum.

4A.5.6 – Errors in temporal displacement

The uncertainties in the measured temporal displacement were identical to that stated in Appendix 3C. To recapitulate, there is a 1.86 ns jitter in the pulse timing and a 30 ns voltage-induced uncertainty. The only thing of difference to note in this case is that the voltage-induced uncertainty represents a much larger uncertainty in this case, since the temporal separation is less than half (400 ns) used in the previous side-view and end-view studies.

4A.5.7 – Total Velocity Uncertainty

Combining all of the above-mentioned uncertainties yields the total uncertainties depicted in Figs 4A.27 and 4A.28 for the planar injector and hypermixing injector flowfields,

respectively. It is seen here that there is a global background uncertainty of 8 percent within these wake regions. The uncertainty grows with distance into the wake, and is found to decrease with downstream distance. The maximum uncertainty here is found to be around 15 percent, which is consistent with the uncertainties found in the side-view PIV from Chapter 3.

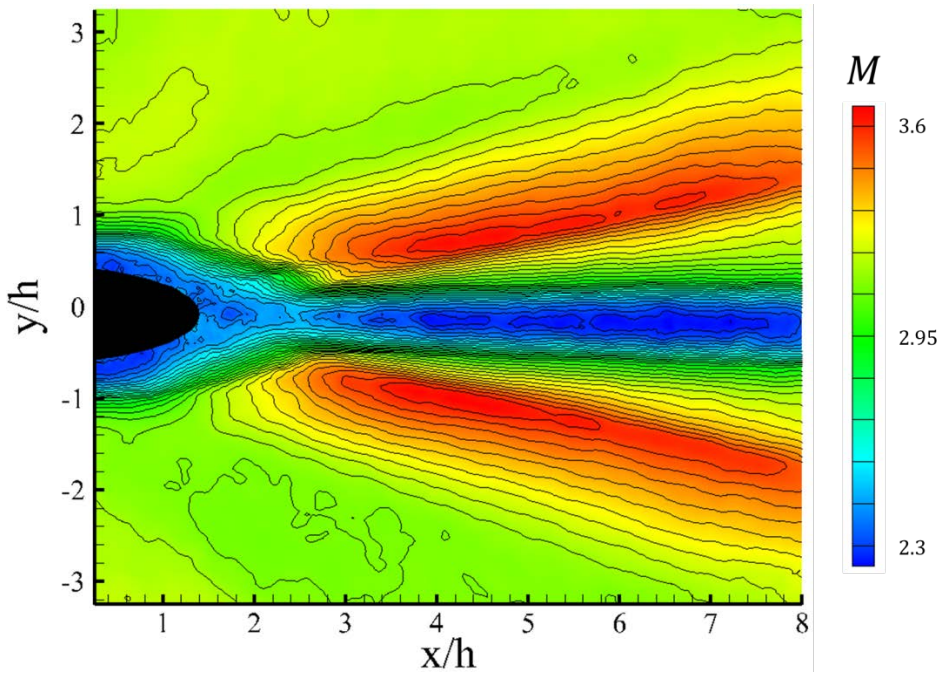

Figure 4A.1: Estimated centerline Mach number contours for near-field of planar injector flowfield

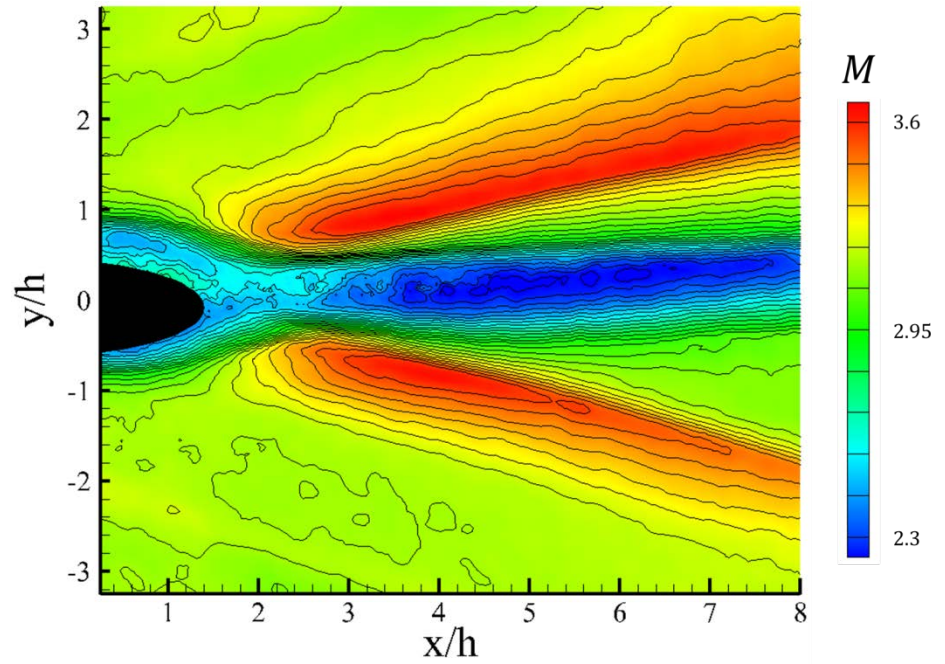

Figure 4A.2: Estimated centerline Mach number contours for near-field of hypermixing injector flowfield

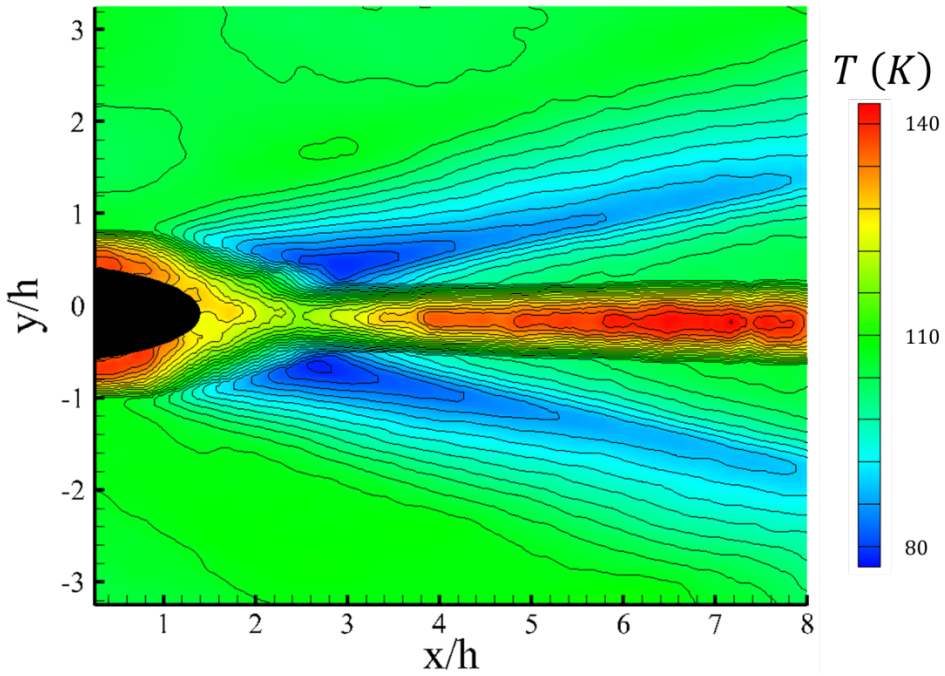

Figure 4A.3: Estimated centerline static temperature contours for near-field of planar injector flowfield

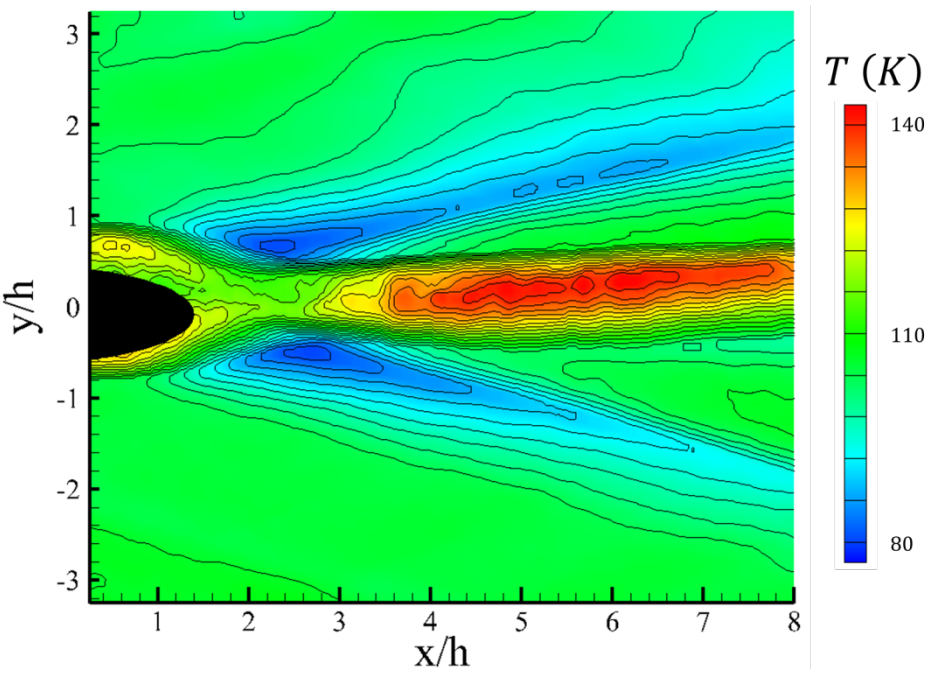

Figure 4A.4: Estimated centerline static temperature contours for near-field of hypermixing injector flowfield

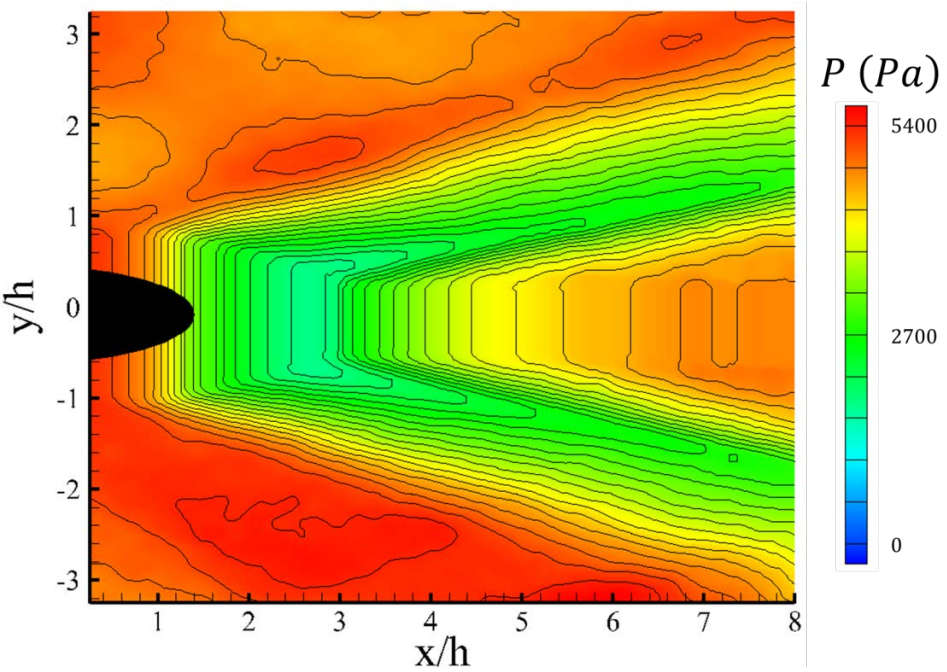

Figure 4A.5: Estimated centerline static pressure contours for near-field of planar injector flowfield

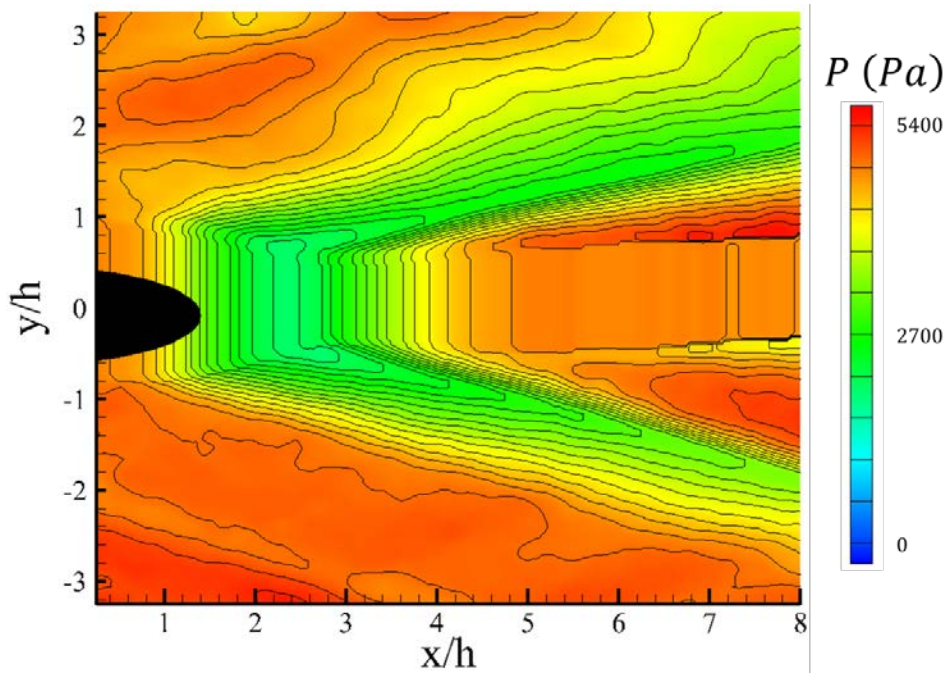

Figure 4A.6: Estimated centerline static pressure contours for near-field of hypermixing injector flowfield

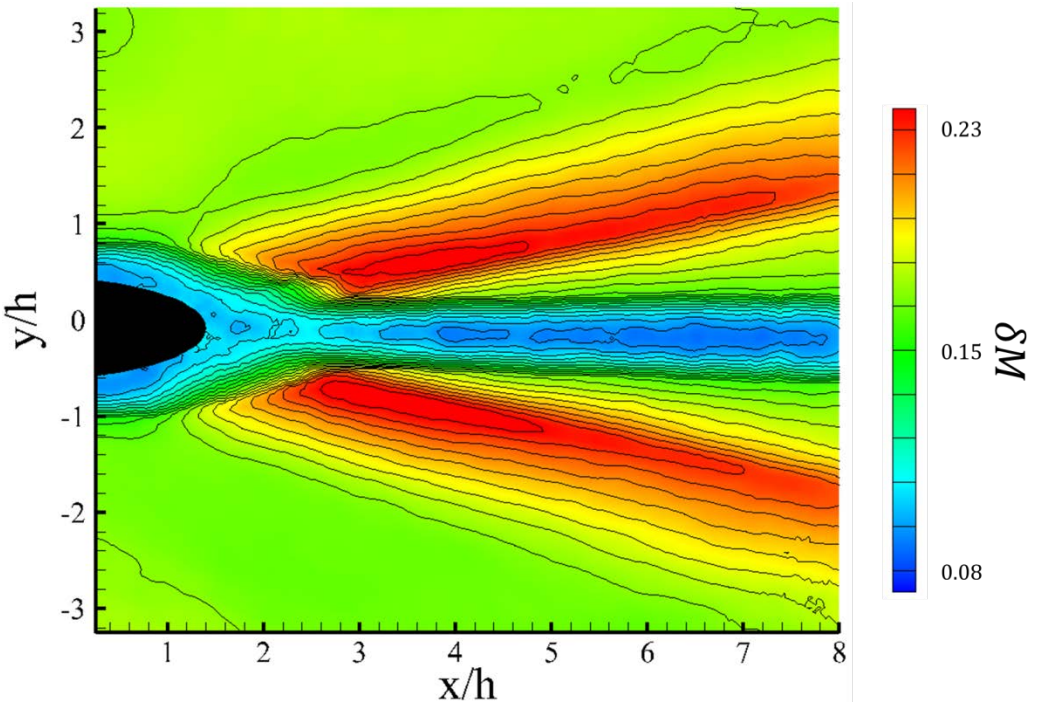

Figure 4A.7: Uncertainty in centerline Mach number for planar injector flowfield

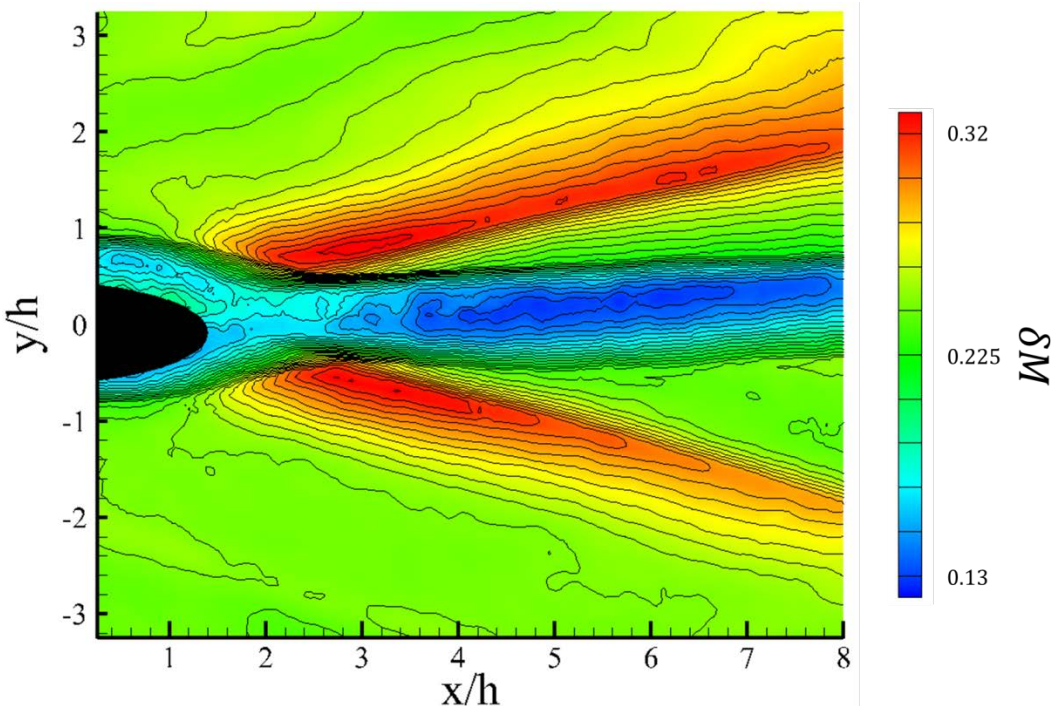

Figure 4A.8: Uncertainty in centerline Mach number for hypermixing injector flowfield

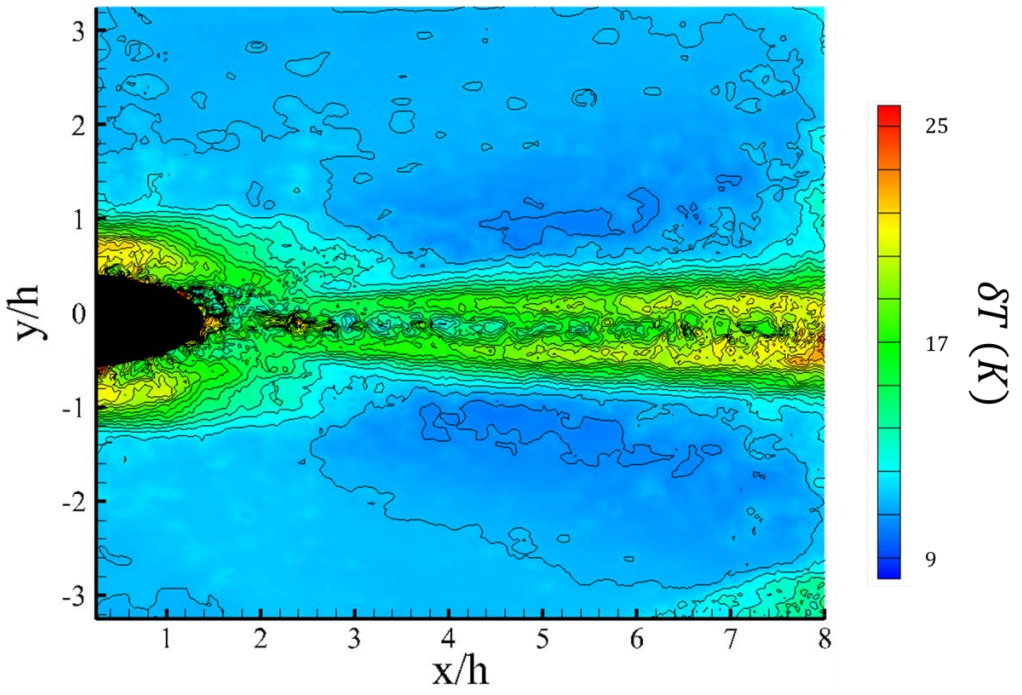

Figure 4A.9: Uncertainty in centerline static temperature for planar injector flowfield

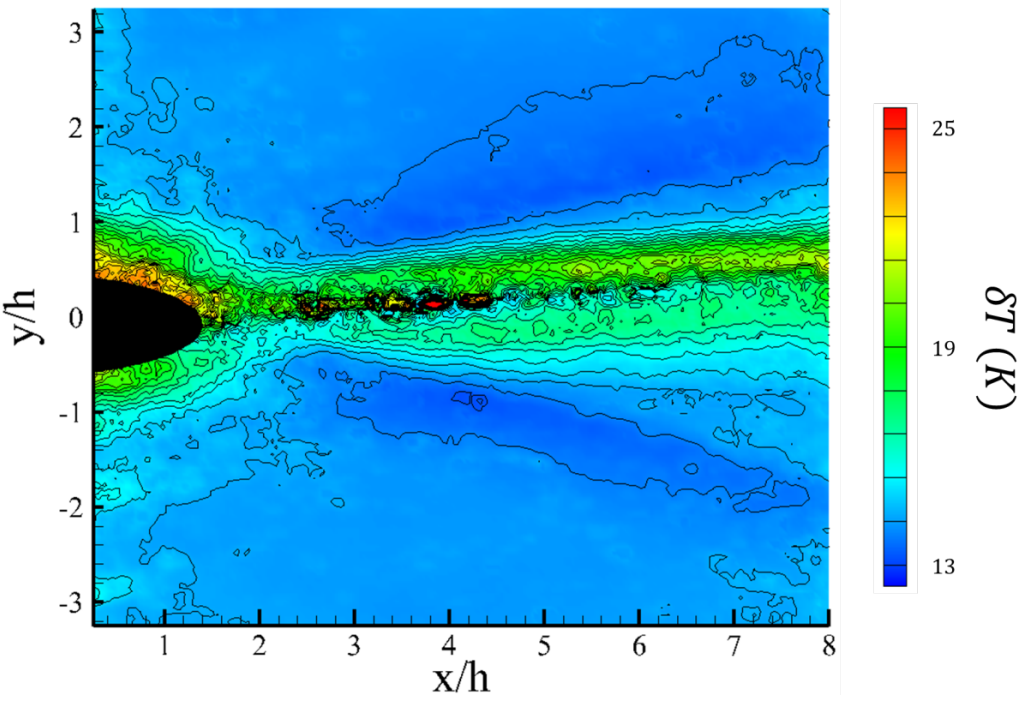

Figure 4A.10: Uncertainty in centerline static temperature for hypermixing injector flowfield

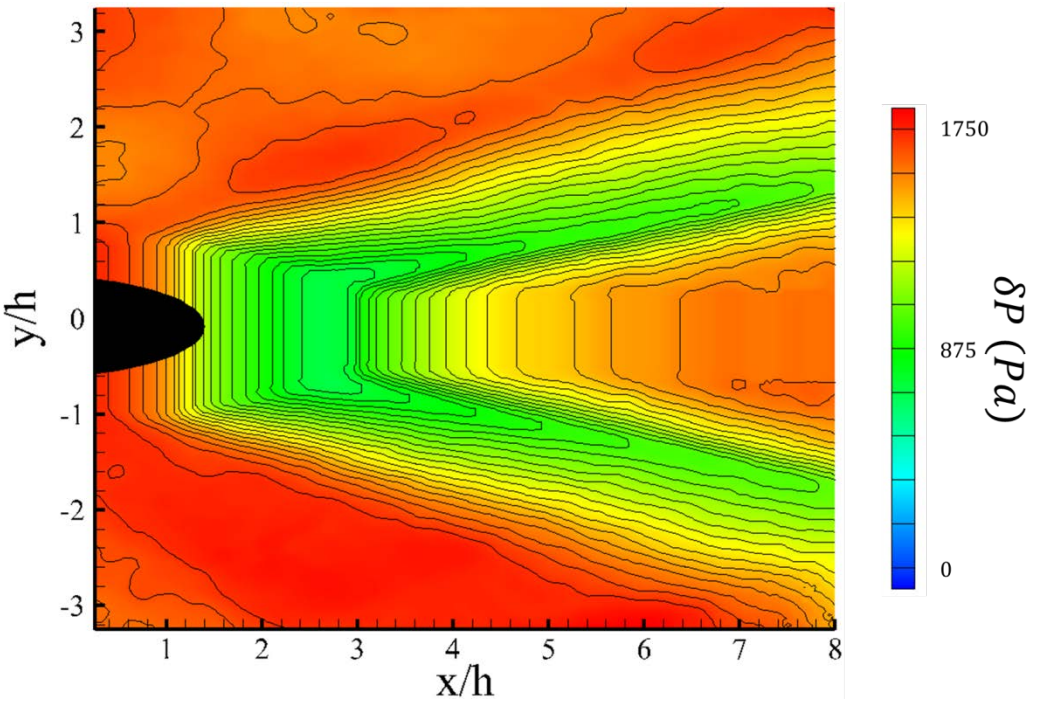

Figure 4A.11: Uncertainty in pressure for planar injector flowfield

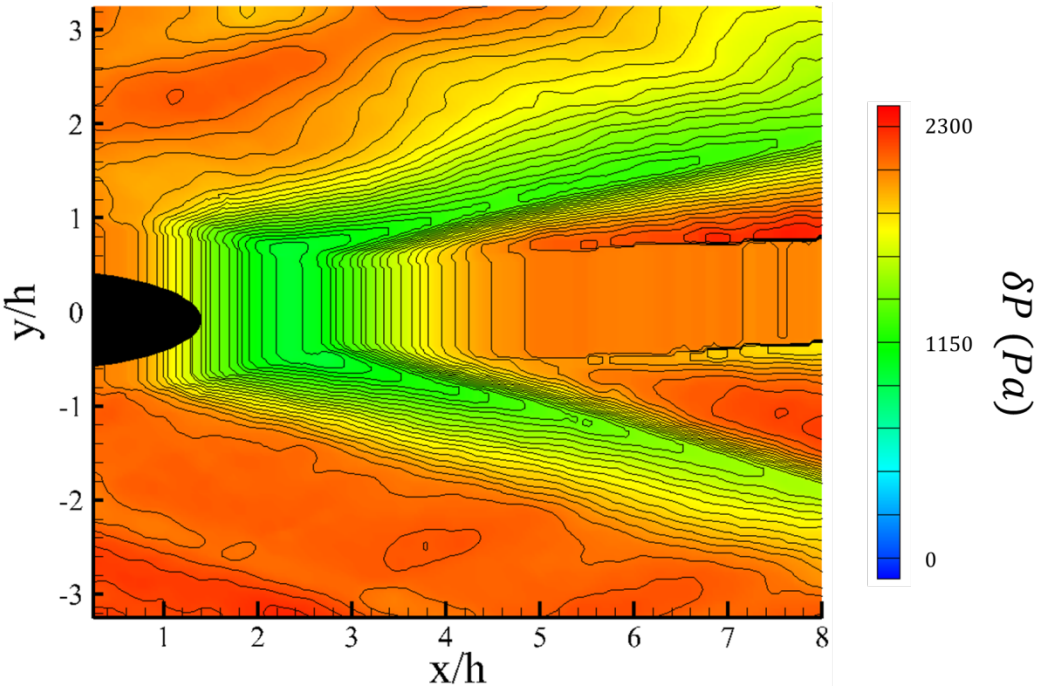

Figure 4A.12: Uncertainty in pressure for hypermixing njector flowfield

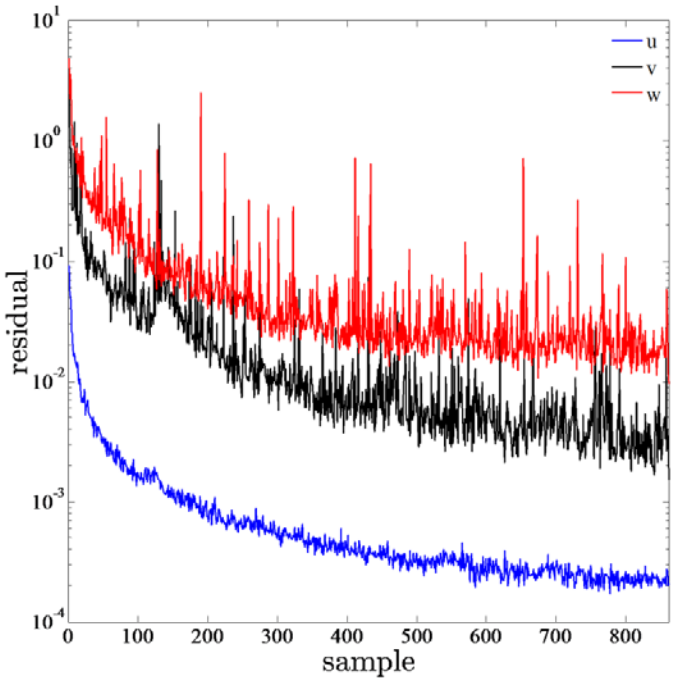

Figure 4A.13: Convergence of mean flow statistics for planar injector flowfield

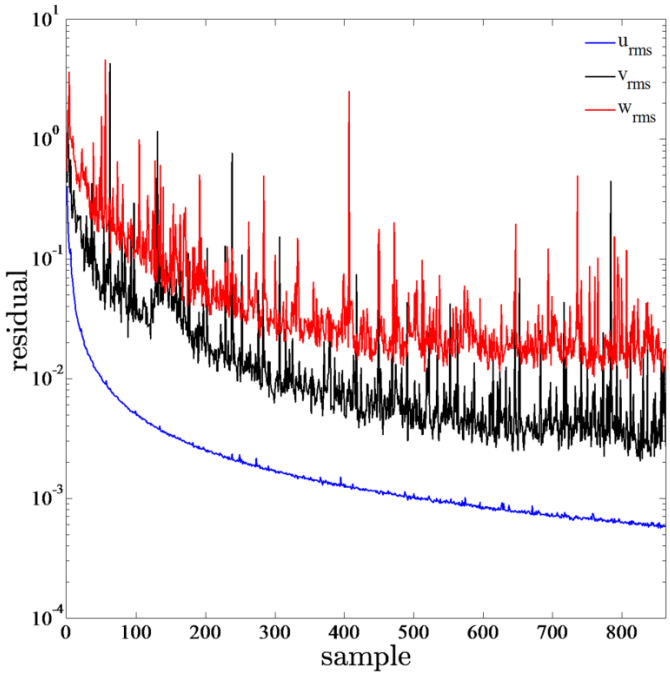

Figure 4A.14: Convergence of fluctuation flow statistics for planar injector flowfield

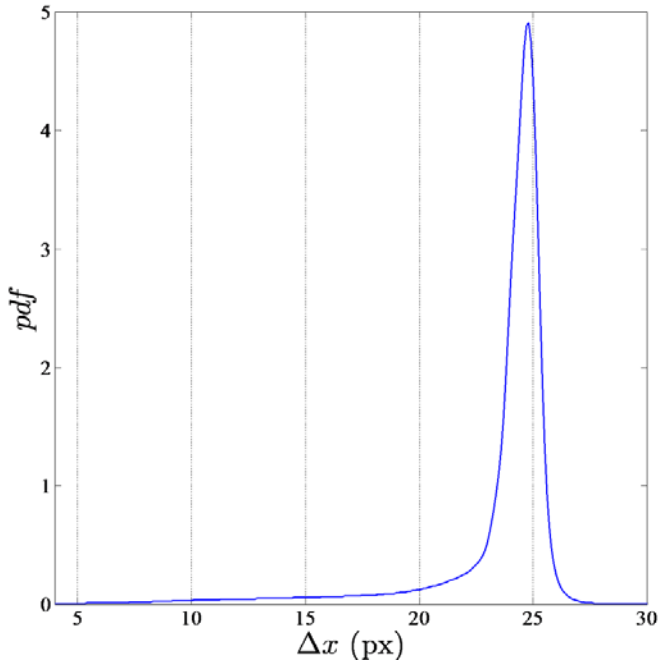

Figure 4A.15: PDF of stream-wise pixel displacements for planar injector flowfield, FOV 1S

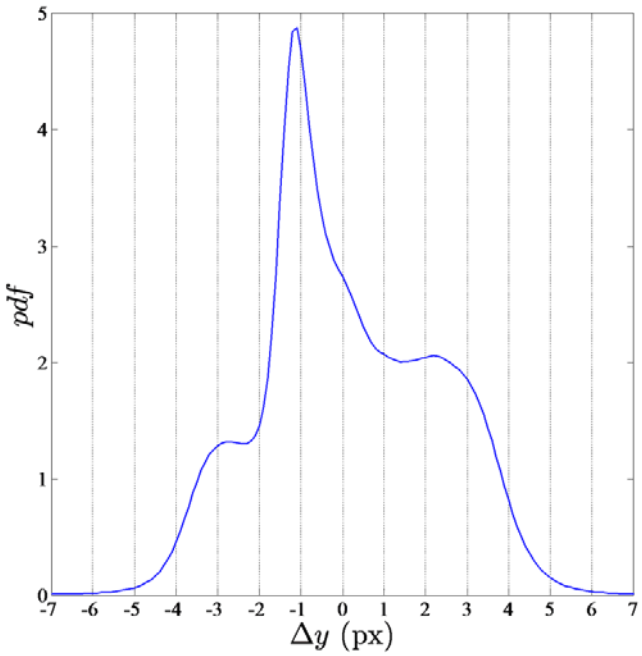

Figure 4A.16: PDF of transverse pixel displacements for planar injector flowfield, FOV 1S

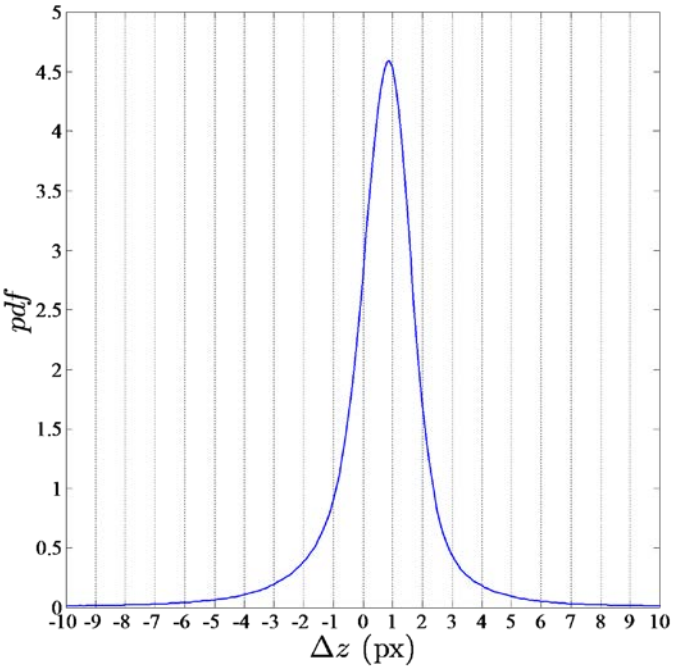

Figure 4A.17: PDF of span-wise pixel displacements for planar injector flowfield, FOV 1S

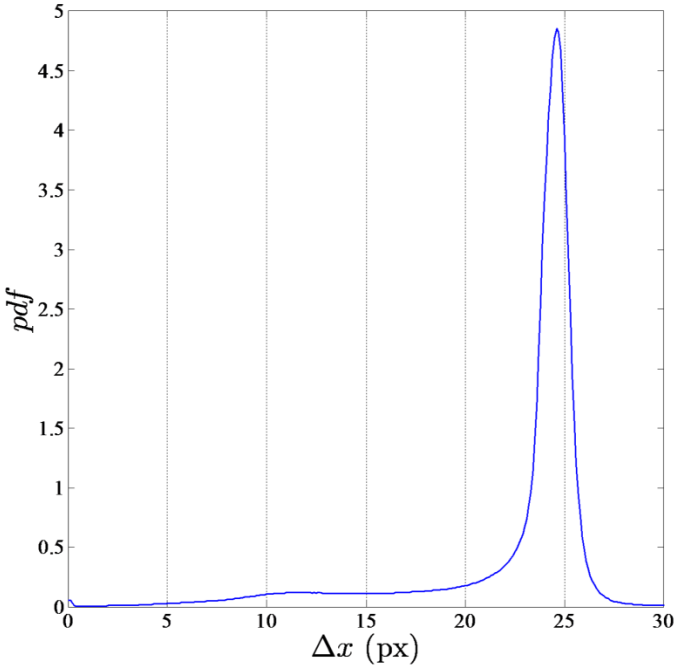

Figure 4A.18: PDF of stream-wise pixel displacements for hypermixing injector flowfield, FOV 1S

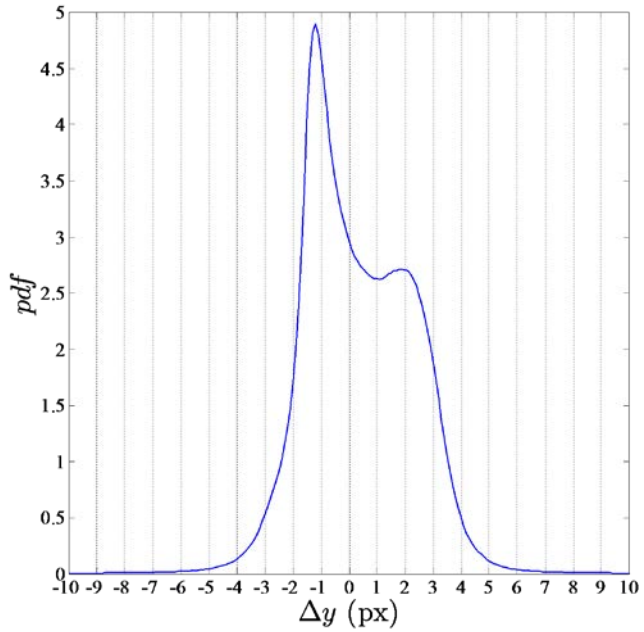

Figure 4A.19: PDF of transverse pixel displacements for hypermixing injector flowfield, FOV 1S

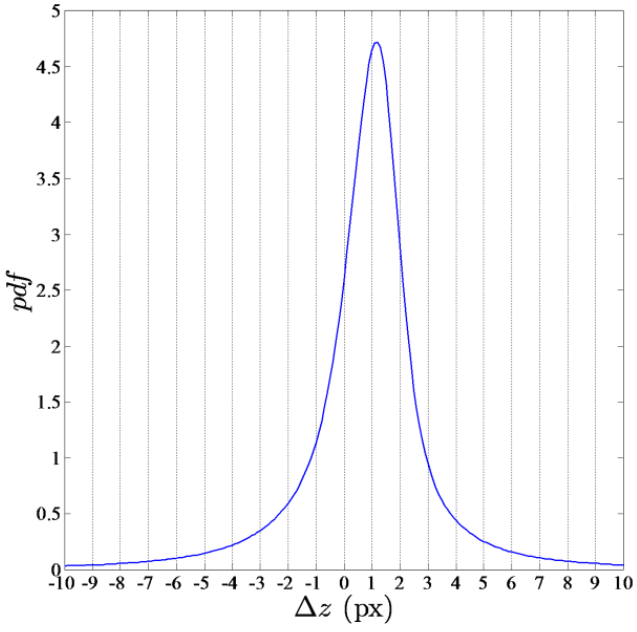

Figure 4A.20: PDF of span-wise pixel displacements for hypermixing injector flowfield, FOV 1S

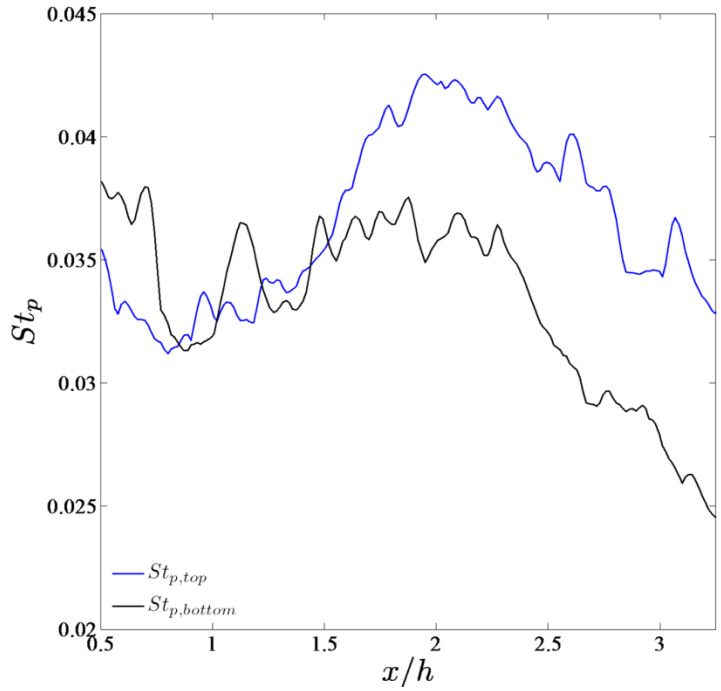

Figure 4A.21: Particle Stokes numbers for planar injector flowfield, FOV 1S

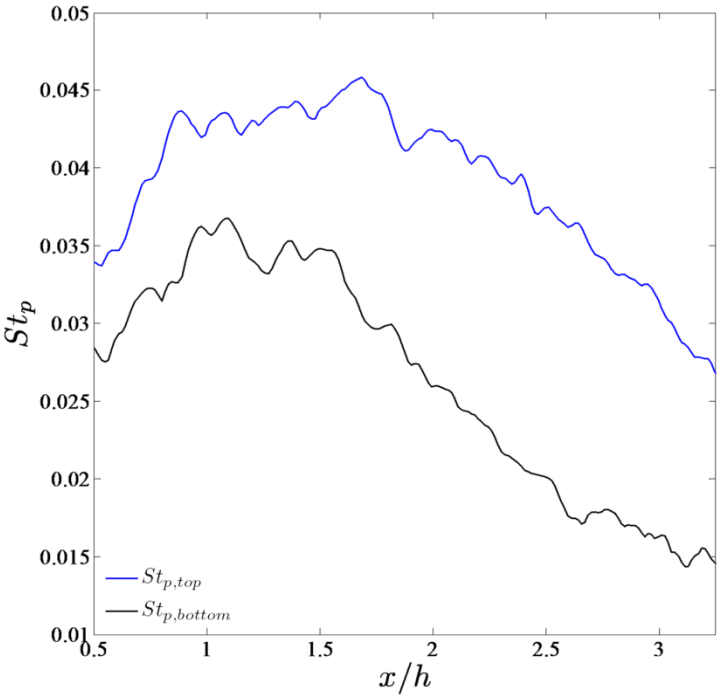

Figure 4A.22: Particle Stokes numbers for hypermixing injector flowfield, FOV 1S

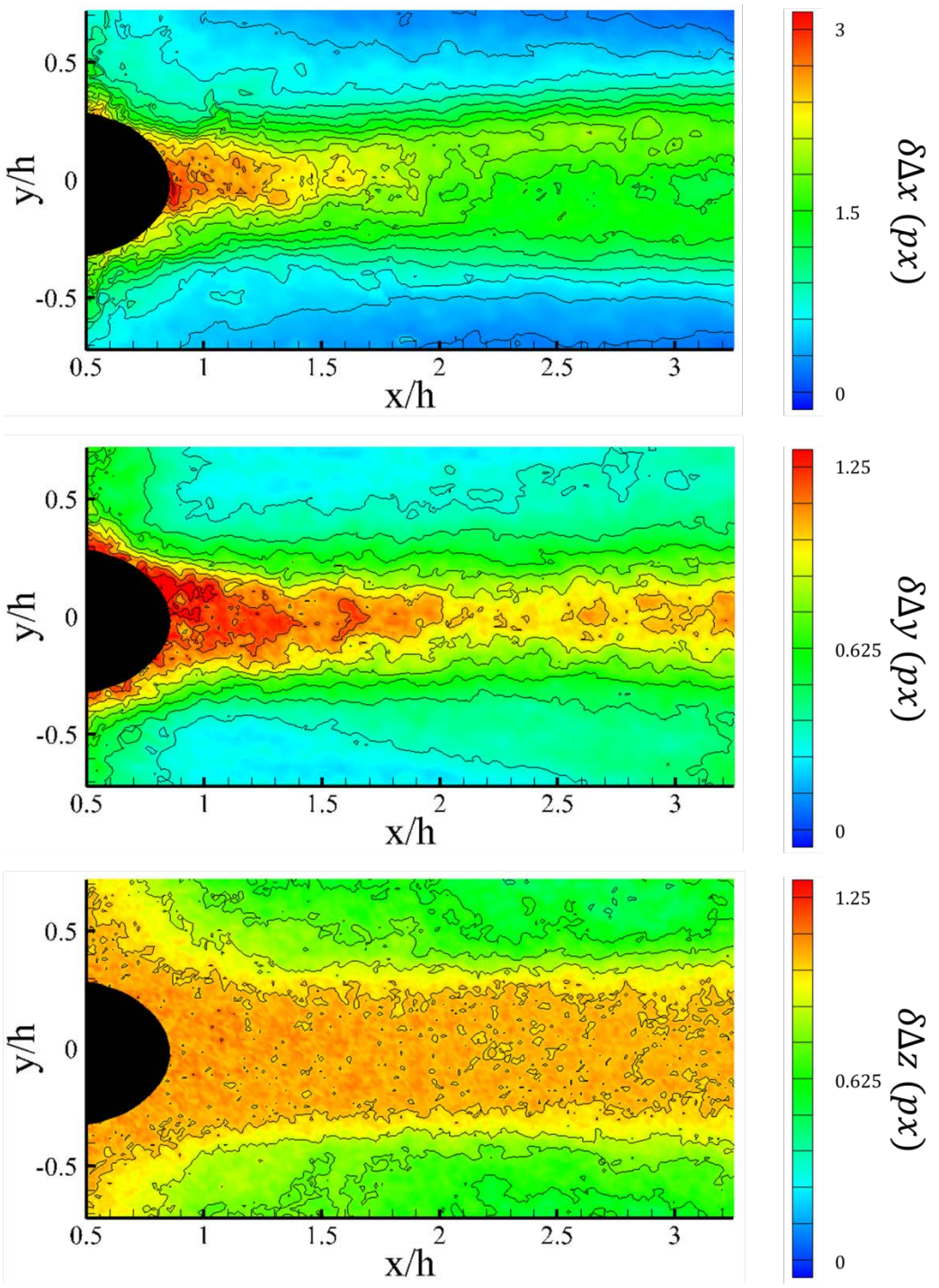

Figure 4A.23: Displacement uncertainties due to convergence errors for planar injector flowfield, FOV 1S. Top – stream-wise, middle – transverse, and bottom – span-wise.

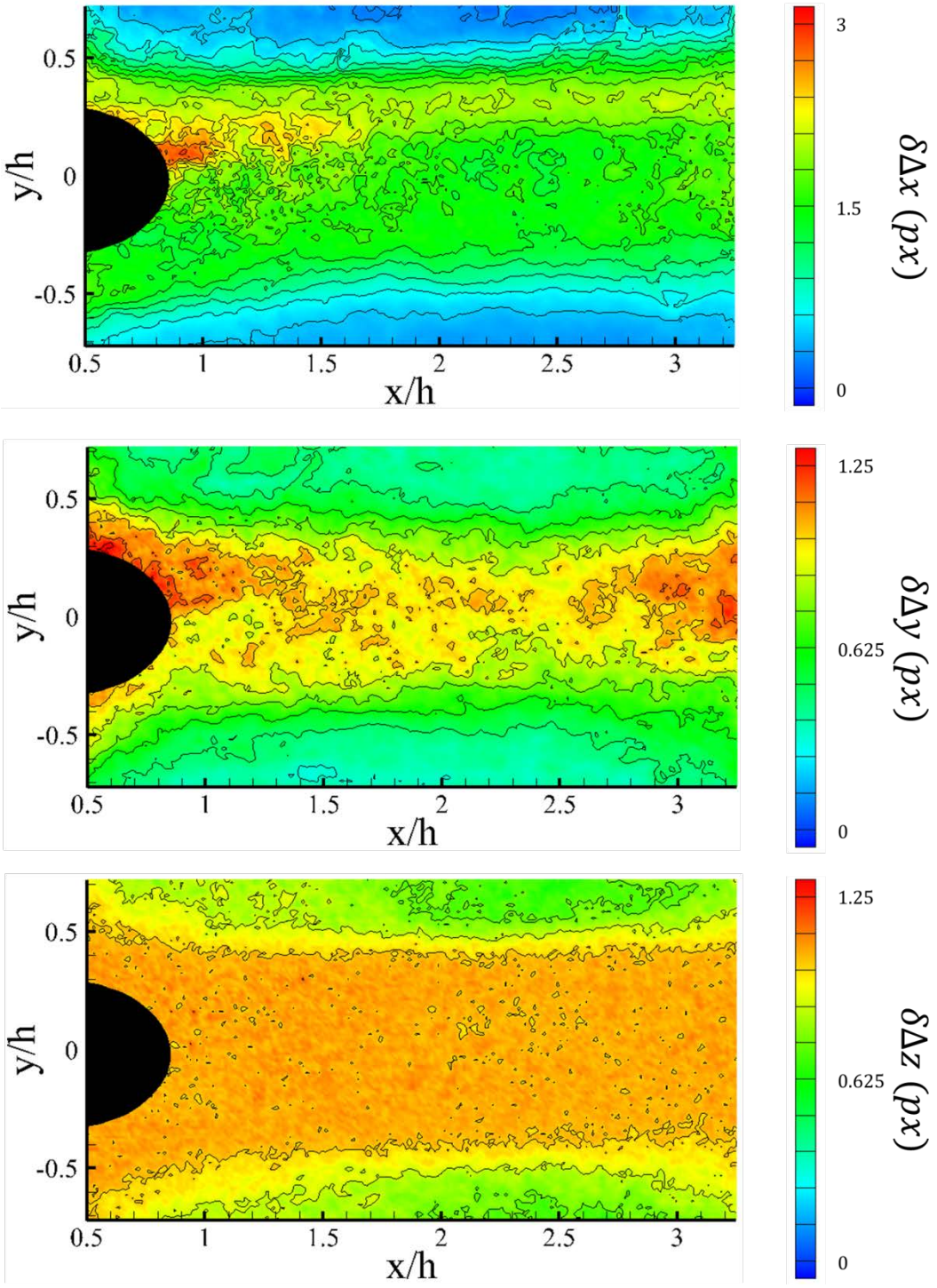

Figure 4A.24: Displacement uncertainties due to convergence errors for hypermixing injector flowfield, FOV 1S. Top – stream-wise, middle – transverse, and bottom – span-wise.

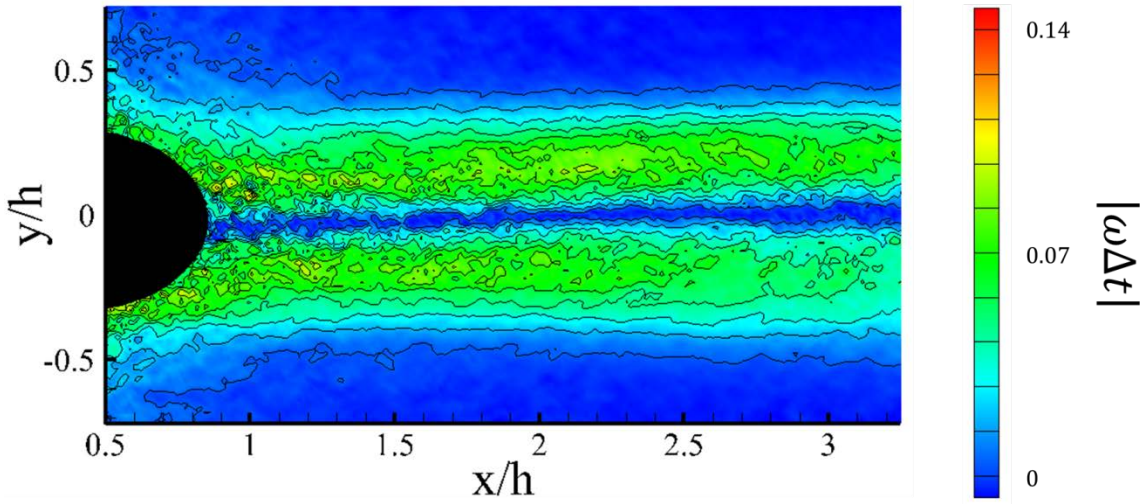

Figure 4A.25: Non-dimensional shear for planar injector flowfield, FOV 1S

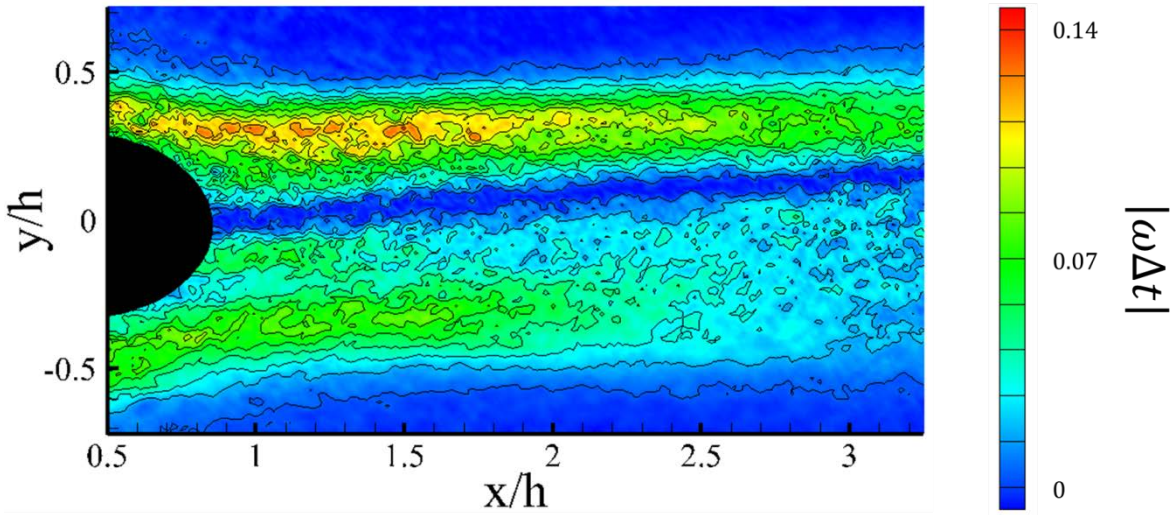

Figure 4A.26: Non-dimensional shear for hypermixing injector flowfield, FOV 1S

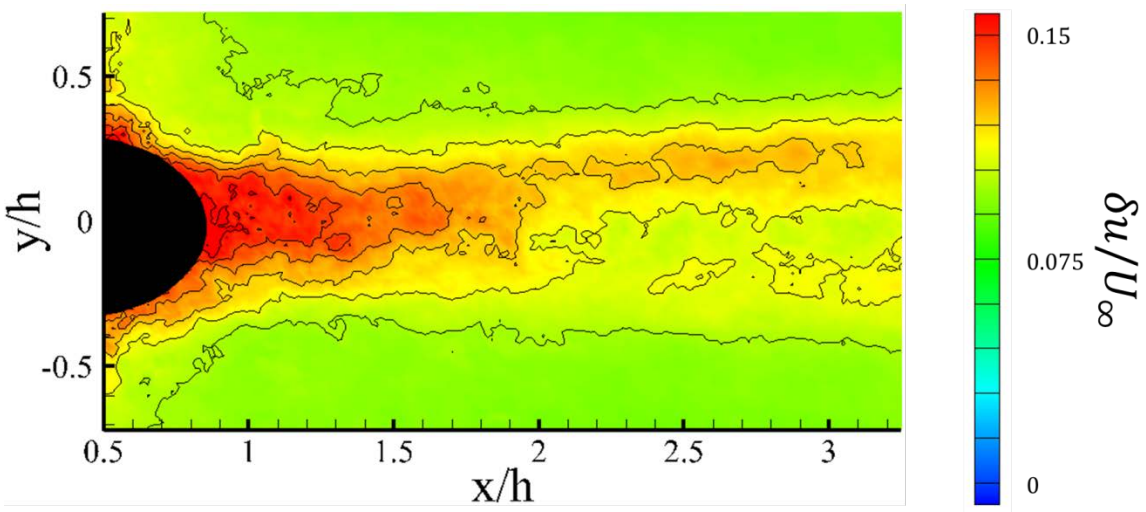

Figure 4A.27: Total velocity uncertainty for planar injector flowfield, FOV 1S

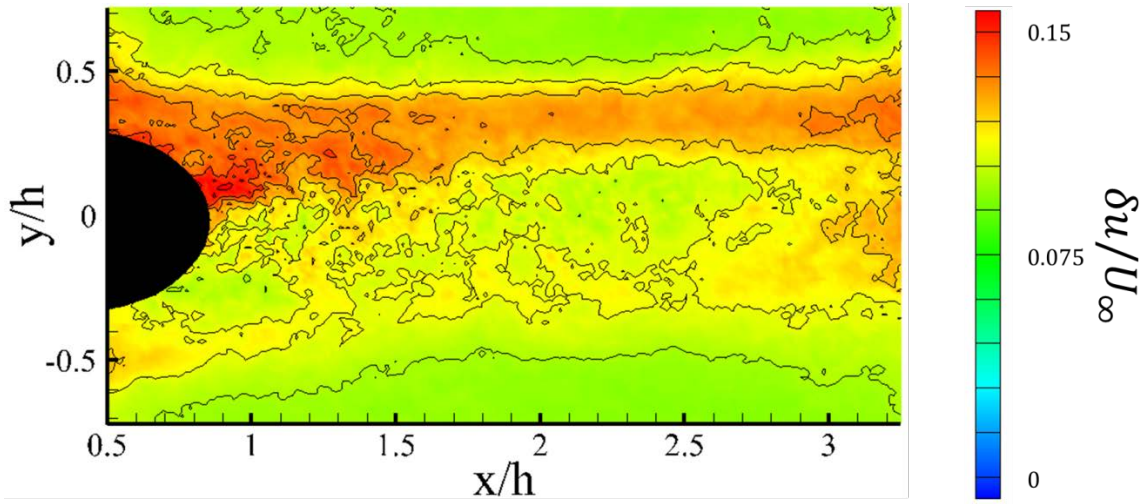

Figure 4A.28: Total velocity uncertainty for hypermixing injector flowfield, FOV 1S

References

1 Curran, E. T., "Scramjet engines: the first forty years," *Journal of Propulsion and Power*, Vol. 17, No. 6, 2001, pp. 1138-1148.

2 Anderson, J. D. *Modern Compressible Flow: With Historical Perspective,* 3rd ed.; McGraw-Hill, 2002.

3 Raffel, M., Willert, C. E., Werely, S. T., and Kompenhans, J. *Particle Image Velocimetry: A Practical Guide,* 2nd ed.; Springer, New York, NY, 2007.

4 Su, L. K. and Clemens, N. T., "The structure of fine-scale scalar mixing in gas-phase planar turbulent jets," *Journal of Fluid Mechanics*, Vol. 488, 2003, pp. 1-29.

5 Oberkampf, W. L. and Trucano, T. G., "Verification and validation in computational fluid dynamics," *Progress in Aerospace Sciences*, Vol. 38, 2002, pp. 209-272.

6 Bradshaw, P., "Compressible Turbulent Shear Layers," *Annual Review of Fluid Mechanics*, Vol. 9, 1977, pp. 33-54.

7 Birch, S. L. and Eggers, J. M., "A critical review of the experimental data for developed free turbulent shear layers," *NASA SP-321*, 1973, pp. 943-949.

8 Brown, G. L. and Roshko, A., "On density effects and large structures in turbulent mixing layers," *Journal of Fluid Mechanics*, Vol. 64, 1974, pp. 775-781.

9 Bogdanoff, D. W., "Compressibility effects in turbulent shear layers," *AIAA Journal*, Vol. 21, No. 6, 1983, pp. 926-927.

10 Papamoschou, D. and Roshko, A., "The compressible turbulent shear layer: an experimental study," *Journal of Fluid Mechanics*, Vol. 197, 1988, pp. 453-477.

11 Clemens, N. T. and Mungal, M. G., "A planar Mie scattering technique for visualizing supersonic mixing flows," *Experiments in Fluids*, Vol. 11, 1991, pp. 175-185.

12 Clemens, N. T. and Mungal, M. G., "Large-scale structure and entrainment in the supersonic mixing layer," *Journal of Fluid Mechanics*, Vol. 284, 1995, pp. 171-216.

13 Clemens, N. T. and Mungal, M. G., "Two- and Three-Dimensional Effects in the Supersonic Mixing Layer," *AIAA Journal*, Vol. 30, No. 4, 1992, pp. 973-981.

14 Clemens, N. T., Paul, P. H., Mungal, M. G., and Hanson, R. K. "Scalar Mixing in the Supersonic Shear Layer," *22nd AIAA Fluid Dynamics, Plasma Dynamics & Lasers Conference*, Honolulu, HI, 1991.

15 Barre, S., Quine, C., and Dussauge, J. P., "Compressibility effects on the structure of supersonic mixing layers: experimental results," *Journal of Fluid Mechanics*, Vol. 259, 1994, pp. 47-78.

16 Elliot, G. S. and Samimy, M., "Compressibility effects in free shear layers," *Physics of Fluids*, Vol. 2, 1990, pp. 1231-1240.

17 Elliot, G. S., Samimy, M., and Arnette, S. A., "The characteristics and evolution of large-scale structures in compressible mixing layers," *Physics of Fluids*, Vol. 7, 1995, pp. 864-876.

18 Sarkar, S., "The stabilizing effect of compressibility in turbulent shear flow," *Journal of Fluid Mechanics*, Vol. 282, 1995, pp. 163-185.

19 Zukoski, E. E. and Spaid, F. W., "Secondary Injection of Gases into a Supersonic Flow," *AIAA Journal*, Vol. 2, No. 10, 1964, pp. 1689-1696.

20 Hermanson, J. C. and Winter, M. "Imaging of a transverse, sonic jet in supersonic flow," *27th AIAA/SAE/ASME Joint Propulsion Conference*, Sacramento, CA, 1991.

21 Hermanson, J. C. and Winter, M., "Mie scattering imaging of a transverse, sonic jet in supersonic flow," *AIAA Journal*, Vol. 31, No. 1, 1993, pp. 129-132.

22 Cohen, L. S., Coulter, L. J., and Egan, W. J., "Penetration and Mixing of Multiple Gas Jets Subjected to a Cross Flow," *AIAA Journal*, Vol. 9, No. 4, 1971, pp. 718-724.

23 Schetz, J. A. and Billig, F. S., "Penetration of gaseous jets injected into a supersonic stream," *Journal of Spacecaft*, Vol. 3, No. 11, 1966, pp. 1658-1665.

24 Schetz, J. A., Hawkins, P. F., and Lehman, H., "Structure of highly underexpanded

transverse jets in a supersonic stream," *AIAA Journal*, Vol. 5, No. 5, 1967, pp. 882-884.

25 Rothstein, A. D. and Wantuck, P. J. "A study of the normal injection of hydrogen into a heated supersonic flow using planar laser-induced fluorescence," *28th AIAA/SAE/ASME/ASEE Joint Propulsion Conference and Exhibit*, Nashville, TN, 1992.

26 Gruber, M. R., Nejad, A. S., Chen, T. H., and Dutton, J. C., "Mixing and penetration studies of sonic jets in a Mach 2 freestream," *Journal of Propulsion and Power*, Vol. 11, No. 2, 1995, pp. 315-323.

27 Auvity, B., Etz, M. R., and Smits, A. J., "Effects of transverse helium injection on hypersonic boundary layers," *Physics of Fluids*, Vol. 13, 2001, pp. 3025-3032.

28 Ben-Yakar, A., Mungal, M. G., and Hanson, R. K., "Time evolution of mixing characteristics of hydrogen and ethylene transverse jets in supersonic crossflows," *Physics of Fluids*, Vol. 18, No. 2, 2006.

29 Schetz, J. A. and Gilreath, H. E., "Tangential Slot Injection in Supersonic Flow," *AIAA Journal*, Vol. 5, No. 12, 1967, pp. 2149-2154.

30 Burrows, M. C. and Kurkov, A. P., "An Analytical and Experimental Study of Supersonic Combustion of Hydrogen in Vitiated Air Stream," *AIAA Journal*, Vol. 11, No. 9, 1973, pp. 1217-1218.

31 Hyde, C. R., Smith, B. R., Schetz, J. A., and Walker, D. A., "Turbulence measurements for heated gas slot injection in supersonic flow," *AIAA Journal*, Vol. 28, No. 9, 1990, pp. 1605-1614.

32 Lewis, D. P. and Schetz, J. A., "Tangential injection from overlaid slots into a supersonic stream," *Journal of Propulsion and Power*, Vol. 13, No. 1, 1997, pp. 59-63.

33 Bogdanoff, D. W., "Advanced Injection and Mixing Techniques for Scramjet Combustors," *Journal of Propulsion and Power*, Vol. 10, No. 2, 1994, pp. 183-190.

34 Gruenig, C., Avrashkov, V., and Mayinger, F., "Fuel Injection into a Supersonic Airflow by Means of Pylons," *Journal of Propulsion and Power*, Vol. 16, No. 1, 2000, pp. 29-34.

35 Hsu, K. Y., Carter, C. D., Gruber, M. R., and Tam, C. J. "Mixing Study of Strut Injectors in Supersonic Flows," *45th AIAA/ASME/SAE/ASEE Joint Propulsion Conference & Exhibit*, Denver, CO, 2009, AIAA-2009-5226.

36 Rock, C., Schetz, J. A., and Ungewitter, R. "Experimental and Numerical Studies of a Strut Injector for Round Scramjet Combustors," *16th AIAA/DLR/DGLR International Space Planes and Hypersonic Systems and Technologies Conference*, Bremen, Germany, 2009, AIAA-2009-7313.

37 Tomioka, S., Murakami, A., Kudo, K., and Mitani, T., "Combustions tests of a staged supersonic combustor with a strut," *Journal of Propulsion and Power*, Vol. 17, No. 2, 2001, pp. 293-300.

38 Masuya, G., Komuro, T., Murakami, A., Shinozaki, N., Nakamura, A., Murayama, M., and Ohwaki, K., "Ignition and combustion performance of scramjet combustors with fuel injection struts," *Journal of Propulsion and Power*, Vol. 11, No. 2, 1995, pp. 301-307.

39 Gruber, M. R., Nejad, A. S., Chen, T. H., and Dutton, J. C., "Transverse injection from circular and elliptic nozzles into a supersonic crossflow," *Journal of Propulsion and Power*, Vol. 16, No. 3, 2000, pp. 449-457.

40 Barber, M. J., Schetz, J. A., and Roe, L. A., "Normal, sonic helium injection through a wedge-shaped orifice into supersonic flow," *Journal of Propulsion and Power*, Vol. 13, No. 2, 1997, p. 257.

41 Tomioka, S., Jacobsen, L. S., and Schetz, J. A., "Sonic injection from diamond-shaped orifices into a supersonic crossflow," *Journal of Propulsion and Power*, Vol. 19, No. 1, 2003, pp. 104-114.

42 Bowersox, R. D. W., Fan, H., and Lee, D., "Sonic injection into a mach 5.0

freestream through diamond orificies," *Journal of Propulsion and Power*, Vol. 20, No. 2, 2004, pp. 280-287.

43 Tomioka, S., Kohchi, T., Masumoto, R., Izumikawa, M., and Matsuo, A., "Supersonic combustion with supersonic injection through diamond-shaped orifices," *Journal of Propulsion and Power*, Vol. 27, No. 6, 2011, pp. 1196-1203.

44 Hirano, K., Matsuo, A., Kouchi, T., Izumikawa, M., and Tomioka, S. "New injector geometry for penetration enhancement of perpendicular jet into supersonic flow," *43rd AIAA/ASME/SAE/ASEE Joint Propulsion Conference and Exhibit*, Cincinatti, OH, 2007.

45 Kouchi, T., Hirano, K., Matsuo, A., Kobayashi, K., Tomioka, S., and Izumikawa, M. "Combustion performance of supersonic combustor with stinger-shaped fuel injector," *44th AIAA/ASME/SAE/ASEE Joint Propulsion Conference and Exhibit*, Hartford, CT, 2008.

46 Hollo, S. D., McDaniel, J. C., and Hartfield, R. J., "Quantitative investigation of compressible mixing: staged transverse injection into a Mach 2 flow," *AIAA Journal*, Vol. 32, No. 3, 1994, pp. 528-534.

47 Lee, S. H., "Characteristics of dual transverse injection in scramjet combustor, part 1: mixing," *Journal of Propulsion and Power*, Vol. 22, No. 5, 2006, p. 1012.

48 Lee, S. H., "Characteristics of dual transverse injection in scramjet combustor, part 2: combustion," *Journal of Propulsion and Power*, Vol. 22, No. 5, 2006, pp. 1020-1026.

49 Schetz, J. A., Cox-Stouffer, S., and Fuller, R. "Integrated CFD and experimental studies of complex injectors in supersonic flows," *20th AIAA Advanced Measurement and Ground Testing Technologies Conference*, Albuquerque, NM, 1998.

50 Fuller, R. P., Wu, P. K., Nejad, A. S., and Schetz, J. A., "Comparison of physical and aerodynamic ramps as fuel injectors in supersonic flow," *Journal of Propulsion and*

Power, Vol. 14, No. 2, 1998, pp. 135-145.

51 Cox-Stouffer, S. K. and Gruber, M. R. "Effects of spanwise injector spacing on mixing characteristics of aerodynamic ramp injector," *34th AIAA/ASME/SAE/ASEE Joint Propulsion Conference and Exhibit*, Cleveland, OH, 1998.

52 Cox-Stouffer, S. K. and Gruber, M. R. "Effects of injector yaw on mixing characteristics of aerodynamic ramp injectors," *37th AIAA Aerospace Sciences Meeting and Exhibit*, Reno, NV, 1999.

53 Cox-Stouffer, S. K. and Gruber, M. R. "Further investigation of the effects of "aerodynamic ramp" design upon mixing characteristcs," *35th AIAA/ASME/SAE/ASEE Joint Propulsion Conference and Exhibit*, Los Angeles, CA, 1999.

54 Jacobsen, L. S., Gallimore, S. D., Schetz, J. A., O'Brien, W. F., and Goss, L. P., "Improved aerodynamic-ramp injector in supersonic flow," *Journal of Propulsion and Power*, Vol. 19, No. 4, 2003, pp. 663-673.

55 Maddalena, L., Campioli, T. L., and Schetz, J. A. "Experimental and computational investigation of an aeroramp injector in a mach four cross flow," *13th AIAA/CIRA International Space Planes and Hypersonics Systems and Technologies*, Capua, Italy, 2005.

56 Maddalena, L., Campioli, T. L., and Schetz, J. A., "Experimental and computational investigation of light-gas injectors in Mach 4.0 crossflow," *Journal of Propulsion and Power*, Vol. 22, No. 5, 2006, pp. 1027-1038.

57 Jacobs, J. W., "Shock-induced mixing of a light-gas cylinder," *Journal of Fluid Mechanics*, Vol. 234, 1992, pp. 629-649.

58 Houwing, F., Bishop, A., Gaston, M., Fox, J., Danehy, P., and Mudford, N. "Simulated fuel-jet/shock-wave interaction," *23rd International Symposium on Shock Waves*, Fort Worth, TX, 2001.

59 Lee, S. H., Jeung, I. S., and Yoon, Y., "Computational investigation of shock-

enhanced mixing and combustion," *AIAA Journal*, Vol. 35, No. 12, 1997, pp. 1813-1820.

60 Lee, S. H., Jeung, I. S., and Yoon, I. S., "Computational investigation of shock-enhanced mixing: application to circular cross-section combustor," *AIAA Journal*, Vol. 36, No. 11, 1998, pp. 2055-2062.

61 Northam, G. B., Greenberg, I., Byington, C. S., and Capriotti, D. P., "Evaluation of parallel injector configurations for Mach 2 combustion," *Journal of Propulsion and Power*, Vol. 8, No. 2, 1992, pp. 491-499.

62 Hardfield, R. J., Hollo, S. D., and McDaniel, J. C., "Experimental investigation of a supersonic swept ramp injector using laser-induced iodine fluorescence," *Journal of Propulsion and Power*, Vol. 10, No. 1, 1994, pp. 129-135.

63 Donohue, J. M., McDaniel, J. C., and Haj-Hariri, H., "Experimental and Numerical Study of Swept Ramp Injection into a Supersonic Flowfield," *AIAA Journal*, Vol. 32, No. 9, 1994, pp. 1860-1867.

64 Riggins, D. W., McClinton, C. R., Rogers, R. C., and Bittner, R. D., "Investigation of Scramjet Injection Strategies for High Mach Number Flows," *Journal of Propulsion and Power*, Vol. 11, No. 3, 1995, pp. 409-418.

65 Hoenig, R., Theisen, D., Fink, R., Lachner, R., Kappler, G., Rist, D., and Andressen, P. "Experimental Investigation of a scramjet model combustor with injection through a swept ramp using laser-induced fluorescence with tunable eximer lasers," *26th Symposium on Combustion*, Naples, Italy, 1996.

66 Fox, J. S., Gaston, M. J., Houwing, A. F. P., Danehy, P. M., Mudford, N. R., and Gai, S. L. "Instantaneous Mole-Fraction PLIF Imaging of Mixing Layers Behind Hypermixing Injectors," *37th AIAA Aerospace Sciences Meeting & Exhibit*, Reno, NV, 1999.

67 Fox, J. S., Houwing, A. F. P., Danehy, P. M., Gaston, M. J., Mudford, N. R., and Gai, S. L., "Mole-Fraction-Sensitive Imaging of Hypermixing Shear Layers,"

Journal of Propulsion and Power, Vol. 17, No. 2, 2001, pp. 284-292.

68 Gaston, M. J., Houwing, F., Mudford, N. R., Danehy, P. M., and Fox, J. S., "Fluorescence imaging of mixing flowfields and comparisons with computational fluid dynamic simulations," *Shock Waves*, Vol. 12, No. 2, 2002, pp. 99-110.

69 Gaston, M. J., Mudford, N. R., and Houwing, F. "A Comparison of Two Hypermixing Fuel Injectors in a Supersonic Combustor," *36th AIAA Aerospace Sciences Meeting & Exhibit*, Reno, NV, 1998, AIAA-98-0964.

70 Doster, J. C., King, P. I., Gruber, M. R., and Maple, R. C. "Pylon Fuel Injector Design for a Scramjet Combustor," *43rd AIAA/ASME/SAE/ASEE Joint Propulsion Conference & Exhibit*, Cincinnati, OH, 2007, AIAA 2007-5404.

71 Doster, J. C., King, P. I., Gruber, M. R., Carter, C. D., Ryan, M. D., and Hsu, K. Y. "Experimental Investigation of Air and Methane Injection from In-stream Fueling Pylons," *44th AIAA Joint Propulsion Conference & Exhibit*, Hartford, CT, 2008, AIAA 2008-4501.

72 Doster, J. C., King, P. I., Gruber, M. R., Carter, C. D., Ryan, M. D., and Hsu, K. Y., "In-stream hypermixer fueling pylons in supersonic flow," *Journal of Propulsion and Power*, Vol. 25, No. 4, 2009, pp. 885-901.

73 Sunami, T., Wendt, M. N., and Nishioka, M. "Supersonic Mixing and Control Using Streamwise Vortices," *34th AIAA/ASME/SAE/ASEE Joint Propulsion Conference and Exhibit*, Cleveland, OH, 1998.

74 Sunami, T., Murakami, A., Kudo, K., Kodera, M., and Nishioka, M. "Mixing and conbustion control strategies for efficient scramjet operation in wide range of flight Mach numbers," *11th AIAA/AAAF International Conference Space Planes and Hypersonic Systems and Technologies*, Orleans, Frannce, 2002, AIAA 2002-5116.

75 Sunami, T. and Scheel, F. "Analysis of mixing enhancement using streamwise vortices in a supersonic combustor by application of laser diagnostics," *11th AIAA/AAAF International Conference Space Planes and Hypersonic Systems and*

Technologies, Orleans, France, 2002.

76 Sunami, T., Magre, P., Bresson, A., Grisch, F., Orain, M., and Kodera, M. "Experimental Study of Strut Injectors in a Supersonic Combustor Using OH-PLIF," *13th AIAA/CIRA International Space Planes and Hypersonics Systems and Technologies Conference*, Capua, Italy, 2005, AIAA-2005-3304.

77 Desikan, S. L. N. and Kurian, J. "Mixing Studies in Supersonic Flow Employing Strut Based Hypermixers," *41st AIAA/ASME/SAE/ASEE Joint Propulsion Conference & Exhibit*, Tucson, AZ, 2005, AIAA 2005-3643.

78 Vergine, F. and Maddalena, L. "Evolution of Large-Scale Structures Generated by a Strut Injector in a Mach 2.5 Flow," *50th AIAA Aerospace Sciences Meeting Including the New Horizons Forum and Aerospace Exposition*, Nashville, TN, 2012, AIAA 2012-0332.

79 Vergine, F., Cristani, M., and Maddalena, L. "Investigation of the Merging Process and Dynamics of Streamwise Vortices Generated by a Flow-Mixing Device in a Mach 2.5 Flow," *51st AIAA Aerospace Sciences Meeting Including the New Horizons Forum and Aerospace Exposition*, Grapevine, TX, 2013, AIAA 2013-0699.

80 Vergine, F., Maddalena, L., Miller, V., and Gamba, M. "Supersonic Combustion and Flame-Holding Characteristics of Pylon Injected Hydrogen in a Mach 2.4 High Enthalpy Flow," *50th AIAA Aerospace Sciences Meeting Including the New Horizons Forum and Aerospace Exposition*, Nashville, TN, 2012, AIAA 2012-0333.

81 Miller, J. C., "Two-photon resonant multiphoton ionization and stimulated emission in krypton and xenon," *Physical Review A*, Vol. 40, No. 12, 1989, pp. 6969-6976.

82 Whitehead, C. A., Poumasr, H., Bruce, M. R., Cai, H., Kohel, J., Layne, W. B., and Keto, J. W., "Deactivation of two-photon excited Xe (5p5 6p, 6p', 7p) and Kr(4p5 5p) in xenon and krypton," *Journal of Chemical Physics*, Vol. 102, No. 5, 1995, pp. 1965-1980.

83 Hsu, A. G., Narayanaswamy, V., Clemens, N. T., and Frank, J. H., "Mixture fraction

imaging in turbulent non-premixed flames with two-photon LIF of krypton," *Proceedings of the Combustion Institute*, Vol. 33, 2011, pp. 759-766.

84 Eichhorn, C., Loehle, S., Knapp, A., and Auweter-Kurtz, M. "On Calibration of Laser-Induced Fluorescence Measurements in Plasma Flows Using Rare Gases," *14th International Symposium on Applications of Laser Techniques to Fluid Mechanics*, Lisbon, Portugal, 2008.

85 Eichhorn, C., Fritzsche, S., Loehle, S., Knapp, A., and Auweter-Kurtz, M., "Time-resolved fluorescence spectroscopy of two-photon laser-excited 8p, 9p, 5f, and 6f levels in neutral xenon," *Physical Review E*, Vol. 80, 2009, pp. 026401-0261-6.

86 Loehle, S. and Auweter-Kurtz, M., "Laser-Induced Fluorescence Measurements of Atomic Oxygen Using Two Calibration Methods," *Journal of Thermophysics and Heat Transfer*, Vol. 21, No. 3, 2007, pp. 623-629.

87 Bamford, D. J., Jusinki, L. E., and Bischel, W. K., "Absolute two-photon absorption and three-photon ionization cross-sections for atomic oxygen," *Physical Review A*, Vol. 34, No. 1, 1986, pp. 185-198.

88 Glauber, R. J., "Coherent and Incoherent States of the Radiation Field," *Physical Review*, Vol. 131, No. 6, 1963, pp. 2766-2788.

89 McKenzie, R. L. and Gross, K. P., "Two-photon excitation of nitric oxide fluorescence as a temperature indicator in unsteady gasdynamic processes," *Applied Optics*, Vol. 20, No. 12, 1981, pp. 2153-2166.

90 Narayanaswamy, V., Burns, R., and Clemens, N. T., "Kr-PLIF for scalar imaging in supersonic flows," *Optics Letters*, Vol. 36, No. 21, 2011, pp. 4185-4187.

91 Siegman, A. E. *Lasers*, University Science Books, Sausalito, CA, 1986.

92 Halfmann, T., Rickes, T., Vitanov, N. V., and Bergmann, K., "Lineshapes in coherent two-photon excitation," *Optics Communication*, Vol. 220, 2003, pp. 353-359.

93 Vaughan, J. M., "Self-Broadening and the Resonance Oscillator Strengths in

Krypton," *Physical Review*, Vol. 166, No. 1, 1968, pp. 13-17.

94 Vaughan, J. M. and Smith, G., "Interpretation of Foreign-Gas Broadening and Shift in Krypton," *Physical Review*, Vol. 166, No. 1, 1968, pp. 17-21.

95 Ferrell, W. R., Payne, M. G., and Garrett, W. R., "Resonance broadening and shifting of spectral lines in xenon and krypton," *Physical Review A*, Vol. 36, No. 1, 1987, pp. 81-89.

96 Niemi, K., Schulz-von der Gathen, V., and Doebele, H. F., "Absolute calibration of atomic density measurements by laser-induced fluorescence spectroscopy with two-photon excitation," *Journal of Physics D: Applied Physics*, Vol. 34, 2001, pp. 2330-2335.

97 Niemi, K., Schulz-von der Gathen, V., and Doebele, H. F., "Absolute atomic oxygen density measurements by two-photon absorption laser-induced fluorescence spectroscopy in an RF-excited atmospheric pressure plasma jet," *Plasma Sources Science and Technology*, Vol. 14, 2005, pp. 375-386.

98 Narayanaswamy, V. *Investigation of a pulsed-plasma jet for separation shock / boundary layer interaction control*, The University of Texas at Austin, Austin, TX, 2010.

99 Burns, R. A. and Clemens, N. T. "Scalar and Velocity Measurements in a Mach 3 Hypermixing Flowfield," *50th AIAA Aerospace Sciences Meeting including the New Horizons Forum and Aerospace Exposition*, Nashville, Tennessee, 2012, AIAA 2012-0438.

100 Burns, R. A. and Clemens, N. T. "Planar Imaging Investigation of Supersonic Hypermixing Configurations," *51st AIAA Aerospace Sciences Meeting including the New Horizons Forum and Aerospace Exposition*, Grapevine, TX, 2013, AIAA 2013-1123.

101 Kondo, A., Hayase, H., Sakaue, S., and Arai, T. "Effect of Expansion Ramp Angle on Supersonic Mixing and Streamwise Vorticies," *16th AIAA/DLR/DGLR*

International Space Planes and Hypersonics Systems and Technologies Conference, Bremen, Germany, 2009, AIAA-2009-7314.

102 Arai, T., Sakaue, S., Hayase, H., Hiejima, T., Sunami, T., and Nishioka, M. "Streamwise Vortices Introduced by 'Hyper-Mixer' on Supersonic Mixing," *17th AIAA International Space Planes and Hypersonic Systems and Technologies Conference*, San Francisco, CA, 2011, 2342.

103 Scarano, F. and van Oudheusden, B. W., "Planar velocity measurements of a two-dimensional compressible wake," *Experiments in Fluids*, Vol. 34, No. 3, 2003, pp. 430-441.

104 Smith, K. M. and Dutton, J. C., "Investigation of Large-Scale Structures in Supersonic Planar Base Flows," *AIAA Journal*, Vol. 34, No. 6, 1996, pp. 1146-1152.

105 Donohue, J. M. and McDaniel, J. C., "Complete Three-Dimensional Multiparameter Mapping of a Supersonic Ramp Fuel Injector Flowfield," *AIAA Journal*, Vol. 34, No. 3, 1996, pp. 455-462.

106 Burns, R. A., Koo, H., Clemens, N. T., and Raman, V. "Experimental and Computational Studies of Mixing in Supersonic Flow," *41st AIAA Fluid Dynamics Conference*, Honolulu, HI, 2011, AIAA 2011-3936.

107 Chen, J. H., Cantwell, B. J., and Mansour, N. M., "The effect of Mach number on the stability of a plane supesonic wake," *Physics of Fluids A*, Vol. 2, No. 6, 1990, pp. 984-1004.

108 Jiang, M., Machiraju, R., and Thompson, D. "A Novel Approach to Vortex Core Region Detection," *Joint EUROGRAPHICS - IEEE TCVG Symposium on Visualization*, Barcelona, Spain, 2002.

109 Bonnet, J. P., Jayaraman, V., and Alziary de Roquefort, T., "Structure of a high-Reynolds-number turbulent wake in supersonic flow," *Journal of Fluid Mechanics*, Vol. 143, 1984, pp. 277-304.

110 Demetriades, A., "Turbulence Measurements in a Supersonic Two-Dimensional

Wake," *Physics of Fluids*, Vol. 13, No. 7, 1970, pp. 1672-1678.

111 Genin, F. and Menon, S., "Simulation of Turbulent Mixing Behind a Strut Injector in Supersonic Flow," *AIAA Journal*, Vol. 48, No. 3, 2010, pp. 526-539.

112 McCormick, D. C. and Bennet, J. C., "Vortical and Turbulent Structure of a Lobed Mixer Free Shear Layer," *AIAA Journal*, Vol. 32, No. 9, 1994, pp. 1852-1859.

113 Hu, H., Saga, T., Kobayashi, T., and Taniguchi, N., "Research on the vortical and turbulent structures in the lobed jet flow using laser induced fluorescence and particle image velocimetry techniques," *Measurement Science and Technology*, Vol. 11, 2000, pp. 697-711.

114 White, F. M. *Viscous Fluid Flow*, McGraw Hill, New York, NY, USA, 2006.

115 Bird, R. B., Stewart, W. E., and Lightfoot, E. N. *Transport Phenomena*, John Wiley & Sons, New York, NY, 1960.

116 Hou, Y. X. *Particle Image Velocimetry Study of Shock-Induced Turbulent Boundary Layer Separation*, Department of Aerospace Engineering and Engineering Mechanics, The University of Texas at Austin, Austin, TX, 2003.

117 Berezin, M. Y. and Achilefu, S., "Fluorescence Lifetime Measurements and Biological Imaging," *Chemical Reviews*, Vol. 110, No. 5, 2010, pp. 2641-2684.

118 Oulianov, D. A., Tomov, I. V., Dvornikov, A. S., and Rentzepis, P. M., "Observations on the measurement of two-photon absorption cross-section," *Optics Communications*, Vol. 191, 2001, pp. 235-243.

119 Crowe, C. T., Troutt, T. R., and Chung, J. N., "Numerical models for two-phase turbulent flows," *Annual Review of Fluid Mechanics*, Vol. 28, 1996, pp. 11-43.

120 Humble, R. A., Scarano, F., and van Oudheusden, B. W., "Particle image velocimetry measurements of a shock wave / turbulent boundary layer interaction," *Experiments in Fluids*, Vol. 43, 2007, pp. 173-183.

121 Ragni, D., Schrijer, F., van Oudheusden, B. W., and Scarano, F., "Particle tracer response across shocks measured by PIV," *Experiments in Fluids*, Vol. 50, 2011, pp.

53-64.

122 Schrijer, F., Scarano, F., and van Oudheusden, B. W., "Application of PIV in a Mach 7 double-ramp flow," *Experiments in Fluids*, Vol. 41, 2006, pp. 353-363.

123 Urban, W. D. and Mungal, M. G., "Planar Velocity Measurements in Compressible Mixing Layers," *Journal of Fluid Mechanics*, Vol. 431, 2001, pp. 189-222.

124 LaVision, "Davis," 2007.

125 Melling, A., "Seeding gas flows for laser anemometry," *AGARD Advanced Instrumentation for Aero Engine Components* , 1986, pp. 14-31.

126 Schaaf, S. A., Chambre, P. L., and Emmons, H. W. Fundamentals of gas dynamics. In *High speed aerodynamics and jet propulsion, vol. 3;*, 1958; Vol. 3, pp 689-693.

127 Samimy, M. and Lele, S. K., "Motion of particles with inertia in a compressible free shear layer," *Physics of Fluids*, Vol. 3, 1991, pp. 1915-1923.

128 Fincham, A. and Delerce, G., "Advanced optimization of correlation imaging velocimetry," *Experiments in Fluids*, Vol. 29, No. 1 Supplement, 2000, pp. S13-S22.

129 Thurber, M. C. and Hanson, R. K., "Simultaneous imaging of temperature and mole fraction using acetone planar laser-induced fluorescence," *Experiments in Fluids*, Vol. 30, 2001, pp. 93-101.

130 Vander Wal, R. L., Zhou, Z., and Choi, M. Y., "Laser-induced incandescence calibration via gravimetric sampling," *Combustion and Flame*, Vol. 105, No. 4, 1996, pp. 462-470.

131 van Cruyningen, L., Lozano, A., and Hanson, R. K., "Quantitative imaging of concentration by planar laser-induced fluorescence," *Experiments in Fluids*, Vol. 10, 1990, pp. 41-49.

132 Buch, K. A. and Dahm, W. J. A., "Experimental study of the fine scale structure of conserved scalar mixing in turbulent shear flows," *Journal of Fluid Mechanics*, Vol. 317, 1996, pp. 21-71.